REACTOR PHYSICS: METHODS AND APPLICATIONS

EDITED BY: Tengfei Zhang, Ding She, Shripad T. Revankar, Jun Wang and Qian Zhang

PUBLISHED IN: Frontiers in Energy Research

frontiers Research Topics

ISSN 1664-8714
ISBN 978-2-88976-457-0
DOI 10.3389/978-2-88976-457-0

About Frontiers

Frontiers is more than just an open-access publisher of scholarly articles: it is a pioneering approach to the world of academia, radically improving the way scholarly research is managed. The grand vision of Frontiers is a world where all people have an equal opportunity to seek, share and generate knowledge. Frontiers provides immediate and permanent online open access to all its publications, but this alone is not enough to realize our grand goals.

Frontiers Journal Series

The Frontiers Journal Series is a multi-tier and interdisciplinary set of open-access, online journals, promising a paradigm shift from the current review, selection and dissemination processes in academic publishing. All Frontiers journals are driven by researchers for researchers; therefore, they constitute a service to the scholarly community. At the same time, the Frontiers Journal Series operates on a revolutionary invention, the tiered publishing system, initially addressing specific communities of scholars, and gradually climbing up to broader public understanding, thus serving the interests of the lay society, too.

Dedication to Quality

Each Frontiers article is a landmark of the highest quality, thanks to genuinely collaborative interactions between authors and review editors, who include some of the world's best academicians. Research must be certified by peers before entering a stream of knowledge that may eventually reach the public - and shape society; therefore, Frontiers only applies the most rigorous and unbiased reviews.
Frontiers revolutionizes research publishing by freely delivering the most outstanding research, evaluated with no bias from both the academic and social point of view. By applying the most advanced information technologies, Frontiers is catapulting scholarly publishing into a new generation.

What are Frontiers Research Topics?

Frontiers Research Topics are very popular trademarks of the Frontiers Journals Series: they are collections of at least ten articles, all centered on a particular subject. With their unique mix of varied contributions from Original Research to Review Articles, Frontiers Research Topics unify the most influential researchers, the latest key findings and historical advances in a hot research area! Find out more on how to host your own Frontiers Research Topic or contribute to one as an author by contacting the Frontiers Editorial Office: frontiersin.org/about/contact

REACTOR PHYSICS: METHODS AND APPLICATIONS

Topic Editors:
Tengfei Zhang, Shanghai Jiao Tong University, China
Ding She, Tsinghua University, China
Shripad T. Revankar, Purdue University, United States
Jun Wang, University of Wisconsin-Madison, United States
Qian Zhang, Harbin Engineering University, China

Citation: Zhang, T., She, D., Revankar, S. T., Wang, J., Zhang, Q., eds. (2022). Reactor Physics: Methods and Applications. Lausanne: Frontiers Media SA. doi: 10.3389/978-2-88976-457-0

Table of Contents

frontiers | Frontiers in Energy Research

EDITORIAL
published: 06 June 2022
doi: 10.3389/fenrg.2022.928836

Editorial: Reactor Physics: Methods and Applications

Tengfei Zhang[1]*, *Ding She*[2], *Qian Zhang*[3], *Jun Wang*[4] and *Shripad T. Revankar*[5]

[1]School of Mechanical Engineering, Shanghai Jiao Tong University, Shanghai, China, [2]Institute of Nuclear and New Energy Technology, Tsinghua University, Beijing, China, [3]School of Physics, Zhejiang University, Hangzhou, China, [4]College of Engineering, University of Wisconsin-Madison, Madison, WI, United States, [5]School of Nuclear Engineering, Purdue University, West Lafayette, IN, United States

Keywords: nuclear reactor, reactor physics analysis, neutron transport and diffusion, nuclear reactor design, sensitivity and uncertainty analysis

Editorial on the Research Topic

Reactor Physics: Methods and Applications

The goal of reactor physics is to investigate the interactions of neutrons and matter in nuclear reactors using both analytical and numerical models. Nuclear physics modeling can be used to obtain critical neutronic information about the reactor core, such as the multiplication factor and the neutron flux (fission power) distribution. This field has profited from the development of both deterministic and Monte Carlo approaches. The deterministic technique employs a multi-step process for solving a problem that involves selectively combining a variety of neutronic models based on reactor type and application objectives. The Monte Carlo method is a straightforward and accurate approach for simulating neutron motions within a nuclear reactor. To comprehend the neutronic properties of nuclear reactors, reactor physics approaches are required, as they act as the foundation for reactor design and analysis.

In recent decades, reactor physics methods have advanced at an unprecedented rate. These advancements have had a profound effect on the nuclear energy industry. This study area examines advanced mathematical and numerical modeling techniques used in the field of reactor physics in order to provide an update on current reactor physics methodologies. This Research Topic comprises 26 papers on a variety of research topics, including nuclear data processing and resonance calculation models, cross-section homogenization techniques, steady-state and transient neutron transport methods, Monte Carlo approaches and applications, nuclear reactor design and analysis, and methods for sensitivity and uncertainty analysis. We classify and describe the substance of the featured papers in "*Reactor Physics: Methods and Applications*" in the sections that follow.

"*Reactor Physics: Methods and Applications*" contains three papers on nuclear data processing and model-based resonance computation. Choi et al. developed the pointwise energy slowing-down technique (PSM) to account for the nonuniformity of the fuel pellet's material composition and temperature profile. This method eliminates the need for a pre-generated table and instead directly calculates the collision probability in all subdivided regions of the fuel pellet when solving the slowing-down equation. Extensive comparative analysis was conducted using models that simulated a variety of conceivable operating situations for a light water reactor (LWR) design. PSM predicts the eigenvalue with errors of over 2000 pcm for the pin-cell problem with steep temperature profiles and material compositions, whereas PSM-CPM predicts the eigenvalue accurately with errors of less than 100 pcm. Zu et al. investigated the effect of traditional approaches on thermal neutron scattering data using zirconium hydride as

OPEN ACCESS

Edited by:
Muhammad Zubair, University of Sharjah, United Arab Emirates

Reviewed by:
Donny Hartanto, Oak Ridge National Laboratory (DOE), United States

Correspondence:
Tengfei Zhang
zhangtengfei@sjtu.edu.cn

Specialty section:
This article was submitted to Nuclear Energy, a section of the journal Frontiers in Energy Research

Received: *26 April 2022*
Accepted: *17 May 2022*
Published: *06 June 2022*

Citation:
Zhang T, She D, Zhang Q, Wang J and Revankar ST (2022) Editorial: Reactor Physics: Methods and Applications. Front. Energy Res. 10:928836. doi: 10.3389/fenrg.2022.928836

an example. The numerical results indicate that the incident energy grid has a significant effect on the eigenvalue, and that considering both coherent and incoherent elastic scattering simultaneously has a tens-of-pcm effect on the eigenvalue.

Advanced homogenization approaches are required for reliable prediction of nuclear reactor neutronic characteristics. To account for the environment effect in whore-core pin-by-pin computations, Zhang et al. conducted a systematic analysis of the relative errors of pin-cell homogenized group constants and determined the significance of adjusting pin-cell discontinuity factors (PDF) of the thermal group. The relationship between the thermal group PDF and the core parameters is functionalized and analyzed using the least-square method. Lei et al. investigated the connection between the reactivity calculation deviation and the optical length in order to determine the influence of double heterogeneity on homogenizing neutron cross sections for dispersed particle type fuels. They hypothesized and examined the two-step ring reactivity-equivalent physical transformation (TRRPT). It was demonstrated that the TRRPT method is more accurate in calculating reactivity and has a broader transformation range than the standard improved reactivity-equivalent physical transformation (IRPT).

The steady-state and time-dependent particle transport equations have formed the bedrock of the computational reactor physics area. Among them, the combined fission matrix theory has been praised for its high efficiency, fidelity, and resolution in solving the neutron transport equation in thermal nuclear reactors. He et al.investigated the viability of the combined fission matrix theory in fast reactors, concluding that approximations to the fission matrix elements will result in considerable errors in fast reactors. The combined fission matrix theory's application to fast reactors requires additional changes and refinement. Zhao et al.developed the SHARK nuclear reactor neutronics code. The code comprises a treatment of construct solid geometry (CSG), a method for subgroup resonance, and a two-dimensional/1-dimensional method of characteristics (MOC). The C5G7, BEAVRS, and VERA benchmarks are discussed numerically. Kang et al.presented a multilevel predictor-corrector quasi-static technique (AML-PCQM) for pin-resolved neutron kinetics problems in transient instances. The approach is established by integrating neutron transport, multi-group coarse mesh finite difference (CMFD), one-group coarse mesh finite difference (CMFD), and the point-kinetics equation. Additionally, one work on neutron transport acceleration has been approved for this Research Topic. Xu et al. applied the sign preservation rule from the field of numerical heat transfer to the CMFD framework in order to address the stability difficulties in CMFD. The updated method, dubbed rCMFD, outperformed previous CMFD methods in terms of efficiency.

As is widely known, Monte Carlo (MC) methods are used to solve the particle transport equation due to their precision and capacity to handle complex geometries. Ma et al. compared the single-node performance of history-based and event-based multigroup MC algorithms on CPUs and GPUs. This research may shed light on the proper selection of techniques for parallelizing MC codes on various architectures. Li et al. used the MC approach to model and analyze the initial criticality of HTR-PM. This work is noteworthy for its use of the discrete element method (DEM) code LAMMPS to explicitly describe randomly packed TRi-structural ISOtropic (TRISO) particles.

Computational reactor physics advances have significantly increased the breadth of nuclear reactor design and analysis. Zhao et al. used the RMC Monte Carlo code to perform pre-conceptual design of spectral-shift control rods in a small lead-based reactor. They observed improvements in the burnup depth and fuel usage rate. Wang et al. designed the scheme and analyzed the data for a major physical experiment involving a hexagonal casing type fuel reactor. The performance of fully ceramic microencapsulated fuel in a supercritical CO_2 (S-CO_2) cooled reactor was investigated by Lu et al. To maximize neutron moderation in the high-performance S-CO_2 reactor assembly, the arrangement of moderator rods and fuel enrichment partition is investigated. Xu et al. investigated the properties of burnable poisons and neutronics in a long-life PWR plate fuel assembly. It was demonstrated that enriched 157Gd, enriched 167Er, B4C, 231Pa, PACS-J, PACS-Er, and PACS-Pa can be chosen and mixed as burnable poisons for plate-fuel assemblies without incurring large reactivity penalties. She et al. used the in-house deterministic code PANGU to simulate the HTR-10 reactor. In all steady-state power periods, numerical comparisons to measured data revealed good agreement. The difference in k_{eff} was within 500 pcm, and the difference in coolant outlet temperature was less than 5°C. Additionally, it was discovered that graphite impurity has minor impacts at the conclusion of the operating history, resulting in an discrepancy of up to 1,500 pcm.

The cost of the accompanying experiments for validating the computer models is a barrier to the deployment of reactor design improvements. To address this Research Topic, a criterion is required for determining whether a particular experiment, whether past or future, is relevant to the application of interest. Ma et al. introduced a generalized perturbation theory (GPT) based on an implicit sensitivity calculation method for evaluating the sensitivity and uncertainty associated with reactor physics modeling. Seo et al. stressed the concept of experimental relevance in their study, which extends the fundamental similarity score to account for the influence of previous experiments and associated experimental uncertainties. The suggested metric, dubbed ACCURE, is validated through a series of criticality experiments in order to determine the relevance of a group of tests to a certain application. Using a tritium breeding blanket, Qu et al. investigated the density perturbation calculation approach. Li et al. suggested a lightweight verification approach for nuclear reactor codes based on the metamorphic connection. The advantage of this method is that it determines the accuracy of the code by examining if the program meets the metamorphic relation, rather than manually solving or benchmarking the code. By combining observational data and a reduced model, the generalized empirical interpolation method (GEIM) is frequently employed to estimate the physical field. Gong et al. applied a smooth restriction on the GEIM to address the observation noise problem. The model constraints the

H1 semi-norm of the reconstructed field of the reduced model and proves to be efficient.

AUTHOR CONTRIBUTIONS

All authors listed have made a substantial, direct, and intellectual contribution to the work and approved it for publication.

Conflict of Interest: The authors declare that the research was conducted in the absence of any commercial or financial relationships that could be construed as a potential conflict of interest.

frontiers in Energy Research

ORIGINAL RESEARCH
published: 14 June 2021
doi: 10.3389/fenrg.2021.704116

Simulation of the HTR-10 Operation History With the PANGU Code

Ding She, Fubing Chen, Bing Xia and Lei Shi*

Institute of Nuclear and New Energy Technology, Tsinghua University, Beijing, China

The 10 MW High Temperature Gas-cooled Reactor-Test Module (HTR-10) is the first High Temperature Gas-cooled Reactor (HTGR) in China, which was operated from January 2003 to May 2007. The HTR-10 operation history provides very important data for the validation of HTGR codes. In this paper, the HTR-10 operation history is simulated with the PANGU code, which has been recently developed for HTGR reactor physics analysis and design. Models and parameters are constructed based on the measured data of the actual conditions. The simulation results agree well with the measurements in all steady-state power periods. The discrepancy of keff is generally below 0.5%, and the discrepancy of coolant outlet temperature is generally below 5°C. It is also figured out that the burnup of graphite impurities has considerable influence on the keff at the end of the operation history, which can cause over 1.5% discrepancy when neglecting the burnup of graphite impurities. By this work, the PANGU code's applicability in actual HTGR fuel cycle simulations is demonstrated.

Keywords: PANGU, HTR-10, operation history, simulation, validation

OPEN ACCESS

Edited by:
Mingjun Wang,
Xi'an Jiaotong University, China

Reviewed by:
Chen Hao,
Harbin Engineering University, China
Jinfeng Li,
Imperial College London, United Kingdom
Dunfu Shi,
Institute of Applied Physics and Computational Mathematics (IAPCM), China

****Correspondence:***
Bing Xia
xiabing@tsinghua.edu.cn

Specialty section:
This article was submitted to Nuclear Energy, a section of the journal Frontiers in Energy Research

Received: *01 May 2021*
Accepted: *31 May 2021*
Published: *14 June 2021*

Citation:
She D, Chen F, Xia B and Shi L (2021) Simulation of the HTR-10 Operation History With the PANGU Code. Front. Energy Res. 9:704116. doi: 10.3389/fenrg.2021.704116

INTRODUCTION

The 10 MW High Temperature Gas-cooled Reactor-Test Module (HTR-10) Wu et al. (2002), designed, constructed, and operated by Institute of Nuclear and New Energy Technology (INET), Tsinghua University, and is the first High Temperature Gas-cooled Reactor (HTGR) in China. HTR-10 achieved the full power operation in January 2003, and then it was intermittently operated up to May 2007 with various power levels. During this period, kinds of tests were carried out on this reactor. Through the operation and test results of the HTR-10, its inherent safety features were fully demonstrated.

The HTR-10 operation history provides very valuable data to validate the codes employed in the HTGR analysis and design. Some of these data have been explored as benchmark test cases Methnani and Tyobeka (2013) to validate the system analysis codes such as TINTE Gerwin et al. (1989), but the validation work on reactor physics codes have not been well reported.

The PANGU code She et al. (2018b) has been recently developed at INET for pebble-bed HTGR neutronics analyses and fuel cycle simulations. Compared with the legacy codes such as VSOP Rütten et al. (2005), PANGU implements a lot of new methodologies, models, and capabilities (She et al., 2017; She et al., 2018a; Wang et al., 2019). In the work, preliminary validation of the PANGU code was done by code-to-code comparisons. This paper presents a further validation of the PANGU code utilizing the HTR-10 operation history. It is a comprehensive examination on the PANGU code's applicability in actual HTGR fuel cycle simulations.

Due to the complexity of the HTR-10 operation history, big efforts have been made to prepare the models and parameters for the simulation work. First, fine time steps are employed in the step-by-step fuel cycle simulation, and the input parameters are processed from the measured data in all

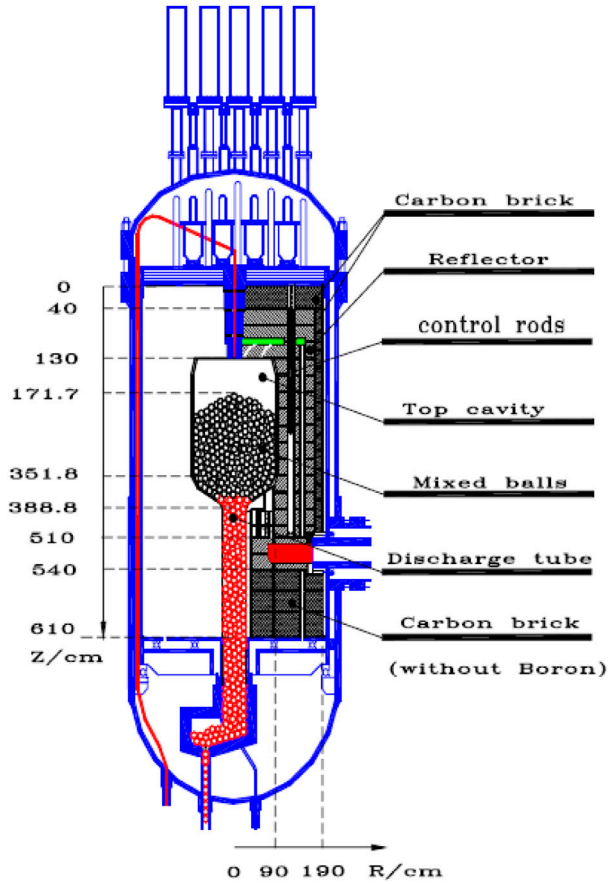

FIGURE 1 | The scheme of the HTR-10.

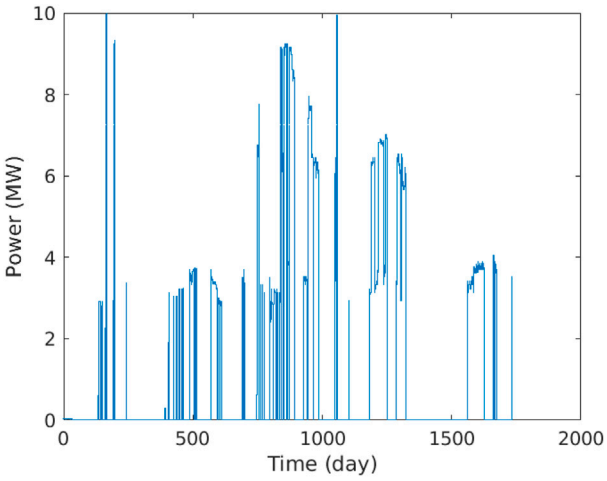

FIGURE 2 | HTR-10 detailed power history.

TABLE 1 | Summary of HTR-10 power history (Chen et al., 2014).

Year	Power operation time (days)	Integrated power (Mwd)
2003	106	258.9
2004	168	708.5
2005	149	821.4
2006	97	532
2007	49	182.6
Total	569	2503.4

detailed power periods. Second, the pebble flow and shuffling model is constructed based on the actual pebble loading and discharging records. Third, the burnup of graphite impurity is considered to overcome the keff discrepancy at the end of operation history. As such, satisfactory simulation results are finally obtained with the PANGU code.

The remainder of this paper is organized as follows. *The HTR-10 operation history* gives a description of the HTR-10 operation history. *Parameters and models used in the simulation* introduces the key input parameters and calculation models used in the PANGU code simulation. The simulation results are shown and analyzed in *Results and analysis*. Concluding remarks are provided in *Conclusion*.

THE HTR-10 OPERATION HISTORY

Figure 1 give the scheme of the HTR-10 reactor. The HTR-10 first criticality was attained on December 2000. At this initial core (IC) state, the core bottom conical region and the fuel discharging tube was filled with graphite pebbles, while the cylindrical part of the core was filled with 16,890 fuel and graphite mixing pebbles with the ratio of 57:43. Following the IC state, mixing pebbles were gradually added into the core, while the reactor was not operated until August 2002. From August 2002 to the end of the year, HTR-10 was intermittently operated below a power level of 3 MW. In January 2003, HTR-10 reached the designed full power level of 10 MW and a coolant outlet temperature of 700°C.

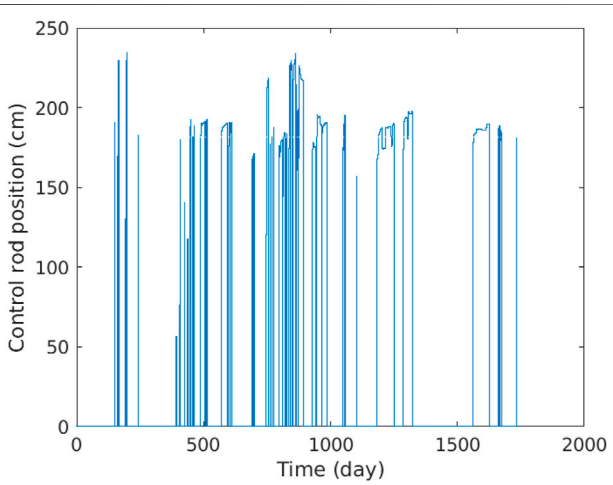

FIGURE 3 | Control rod position (averaged) during the operation history.

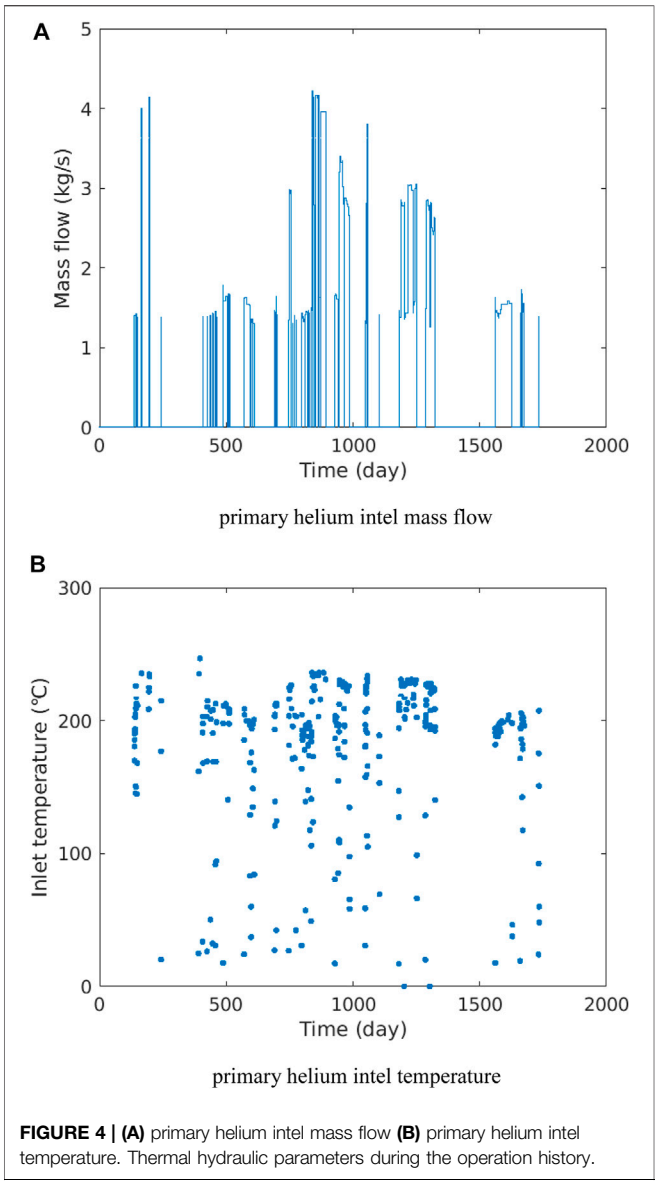

FIGURE 4 | (A) primary helium intel mass flow **(B)** primary helium intel temperature. Thermal hydraulic parameters during the operation history.

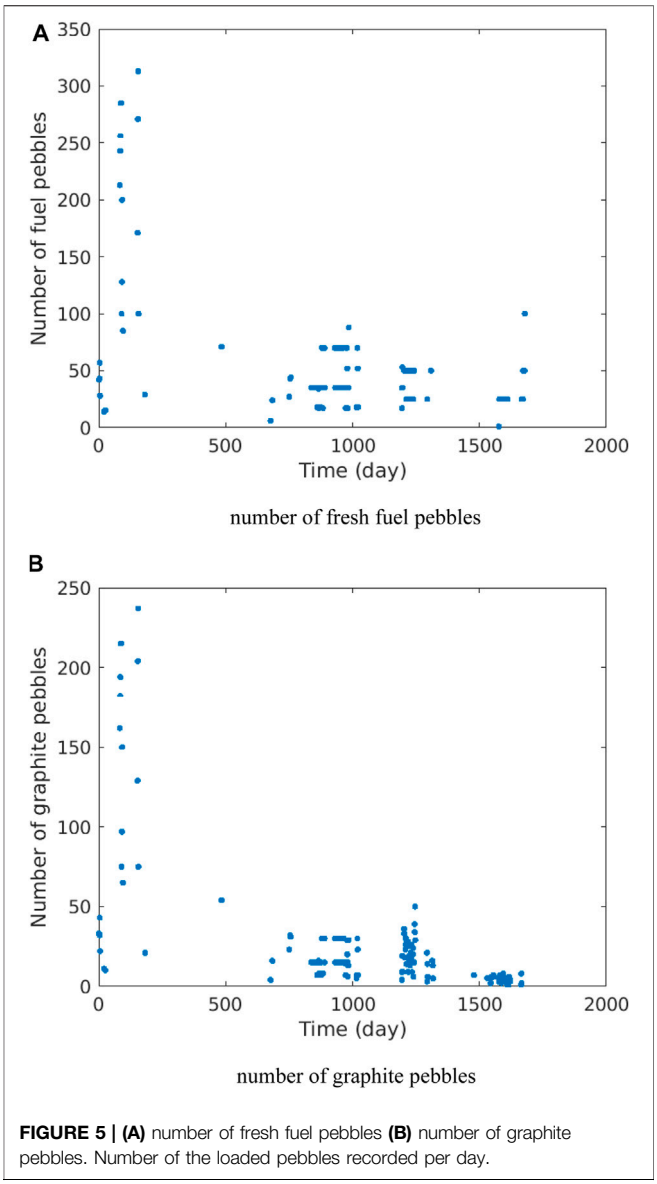

FIGURE 5 | (A) number of fresh fuel pebbles **(B)** number of graphite pebbles. Number of the loaded pebbles recorded per day.

At this full power initial core (FPIC) state, there were 23,900 mixing pebbles in the pebble bed core. By December 2004, the number of mixing pebbles increased up to about 27,000, which is defined as the full core (FC) state.

Following the FC state, the pebbles in the core started recycling. The graphite pebbles were at first discharged from the fuel discharging tube and the core bottom, which were partially replaced with fresh fuel pebbles and then reloaded into the core. Thus, the ratio of the fuel pebbles in the core was increased gradually. With the progress of pebble recycling, the mixing pebbles also began to be discharged. The first discharged fuel pebble was recorded in April 2005.

TABLE 2 | Input-parameter table used in PANGU simulation (example data).

Step	Time (day)	Time periods (day)	Power (MW)	System pressure (MPa)	Inlet mass flow (kg/s)	Inlet temperature (°C)	Control rod position (cm)
1	—	—	—	—	—	—	—
2	—	—	—	—	—	—	—
...	—	—	—	—	—	—	—
1,020	—	—	—	—	—	—	—

Pebble flow and shuffling model.

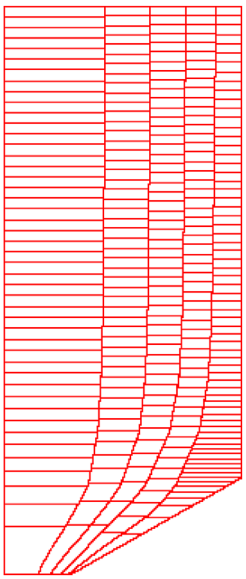

FIGURE 6 | Pebble-flow model used in PANGU simulation.

The HTR-10 operation history simulated in this work is ranging from August 2002 to May 2007, lasting for about 1,700 days. The corresponding power history is shown in **Figure 2** and summarized in **Table 1**. It can be seen that HTR-10 experienced frequent and relatively long-period shutdown, while the power operation only took around 30% of the whole operation days. Besides, the power was frequently varied during the power operation periods.

During the HTR-10 operation history, some important data were measured in details. As for the fuel cycle simulation, the following three categories of measured data need be utilized. The first-category data is the measured control rod position in each power period, as shown in **Figure 3**. The *y*-axis value corresponds to the distance between the bottom of the control rod and the bottom of the pebble bed core. The second-category data is the measured thermal hydraulic parameters of the primary helium, mainly including the inlet temperature and the mass flow that are depicted in **Figure 4**. The third-category data is the number of loaded and discharged pebbles recorded per day. For example, the numbers of loaded fresh fuel pebbles and graphite pebbles are shown in **Figure 5**.

PARAMETERS AND MODELS USED IN THE SIMULATION

Time Steps and Input Parameters

The HTR-10 power history includes a total of 1,020 time periods. A lot of the power periods are quite short, reflecting the transient state of reactor starting up, shutting down, or changing power. Since the PANGU code is mainly used for the steady-state analysis, this work is focused on the simulation results of the steady-state power periods. Nevertheless, in order to conform to the realistic burnup and decay history, all of the detailed 1,020 power periods are explicitly treated by step-by-step fuel cycle simulations with PANGU, without any combination of the short power periods.

Noting that the original thermal-hydraulic data were measured in longer time periods compared with the power data, the thermal-hydraulic input parameters of the fine time steps are calculated by linear interpolation. Because PANGU employs a 2D R-Z model for whole core criticality calculations, it uses an averaged control rod position in each power period, which is calculated from the measured data. Finally, a complete input-parameter table is built for the subsequent simulations, the example data of which is shown in **Table 2**.

One main challenge in simulating the pebble-bed HTGR operation is related to the treatment of on-line refueling. In

TABLE 3 | Mixing ratio of loaded pebbles in the shuffle steps.

Shuffling step	Fresh fuel pebble	Depleted fuel pebble	Graphite pebble
1	0.57	0.00	0.43
2	0.57	0.00	0.43
3	0.67	0.00	0.33
4	0.70	0.00	0.30
5	0.70	0.00	0.30
6	0.70	0.00	0.30
7	0.70	0.00	0.30
8	0.70	0.00	0.30
9	0.70	0.00	0.30
10	0.70	0.00	0.30
11	0.71	0.02	0.27
12	0.63	0.07	0.30
13	0.48	0.22	0.30
14	0.50	0.24	0.26
15	0.50	0.29	0.21
16	0.50	0.29	0.21
17	0.27	0.41	0.33
18	0.27	0.41	0.33
19	0.49	0.42	0.09
20	0.35	0.59	0.07
21	0.34	0.62	0.05

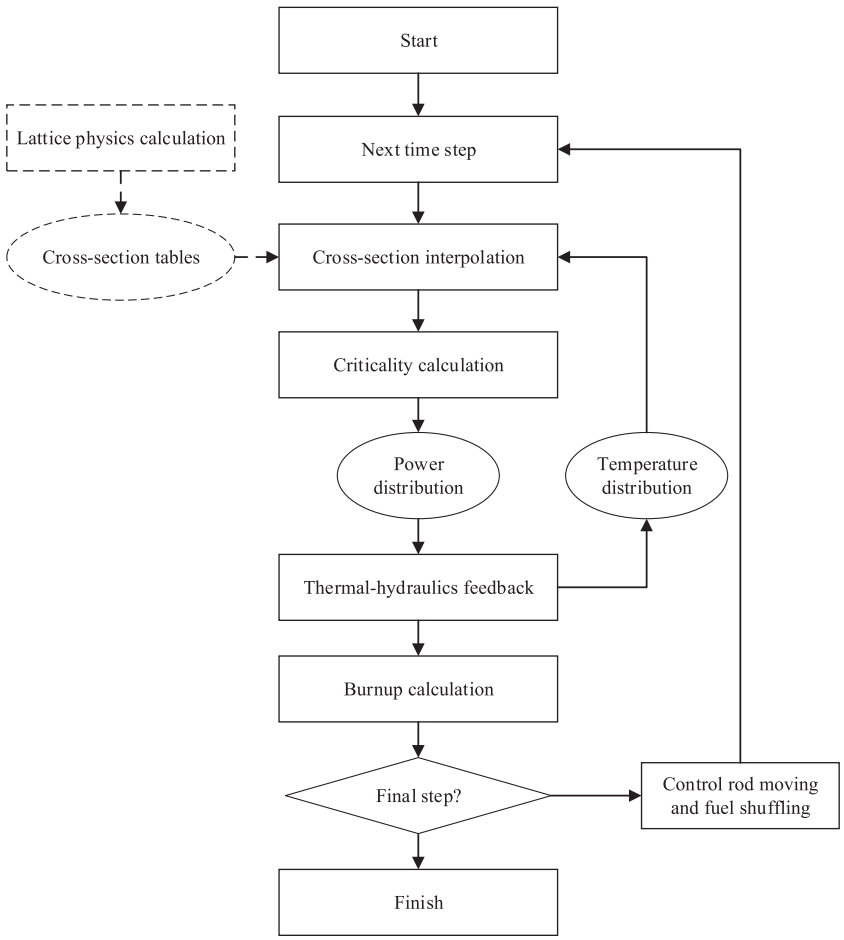

FIGURE 7 | Calculation flow of the PANGU code simulation.

the first stages of the HTR-10 operation history, i.e. from the initial core to the full core state, mixing pebbles were loaded and the core height increased along with the reactor operation. In the second stages, the pebbles were recycled through the core and the graphite pebbles were gradually replaced with the fuel pebbles. The two stages are referred as loading stage and recycling stage, respectively.

The pebble flow model in PANGU is improved from the model used in the VSOP code (Hao and Li., 2014). The pebble-bed zone is radially divided into several flow channels, whose boundaries can be either straight or curved surfaces depending on the flow pattern. Each channel is equally divided into several layers. As such, the core is divided into a number of regions with equal volume. Besides, the pebbles in a region can further include different batches, so that each batch has the same composition. Compared with the VSOP code, PANGU provides a more flexible way of describing arbitrary mixing ratio of batches during the fuel shuffling process.

As shown in **Figure 6**, the following pebble flow model is employed in PANGU to simulate the HTR-10 fuel loading and recycling procedures. The pebble-bed zone is radially divided into five curved flow channels. Each channel is divided into different number of equal-volume regions, in order to illustrate the flow speed distributions among the channels. Considering there are 27,000 pebbles in the full core state, the core is divided into 270 regions, and each region occupies a volume of 100 pebbles.

Then, a number of shuffling steps are defined in the PANGU fuel cycle simulation. In the beginning of the loading stage, the regions in certain top layers are set as vacuum according to the actual core height of the first time step. With the increase of the loading height, the vacuum regions are filled with mixing pebbles level by level. During the recycling stage, the pebbles flow down along the channel, so that the pebbles of the bottom layer are discharged and the top layer is filled with new loaded pebbles. In each shuffling step, there are 500 mixing pebbles loaded into the core. The mixing ratio of these pebbles are evaluated from the pebble loading data in the operation history, by simply counting the ratio of the loaded fresh fuel, depleted fuel and graphite pebbles in every 500 pebbles. **Table 3** gives the mixing ratio of loaded pebbles in each shuffling step.

Besides, based on the recorded number of discharged pebbles and their mixing ratios, the flow speed of each channel can be roughly estimated. For instance, the flow speed of the central channel is estimated according to the time that the first fuel pebble was

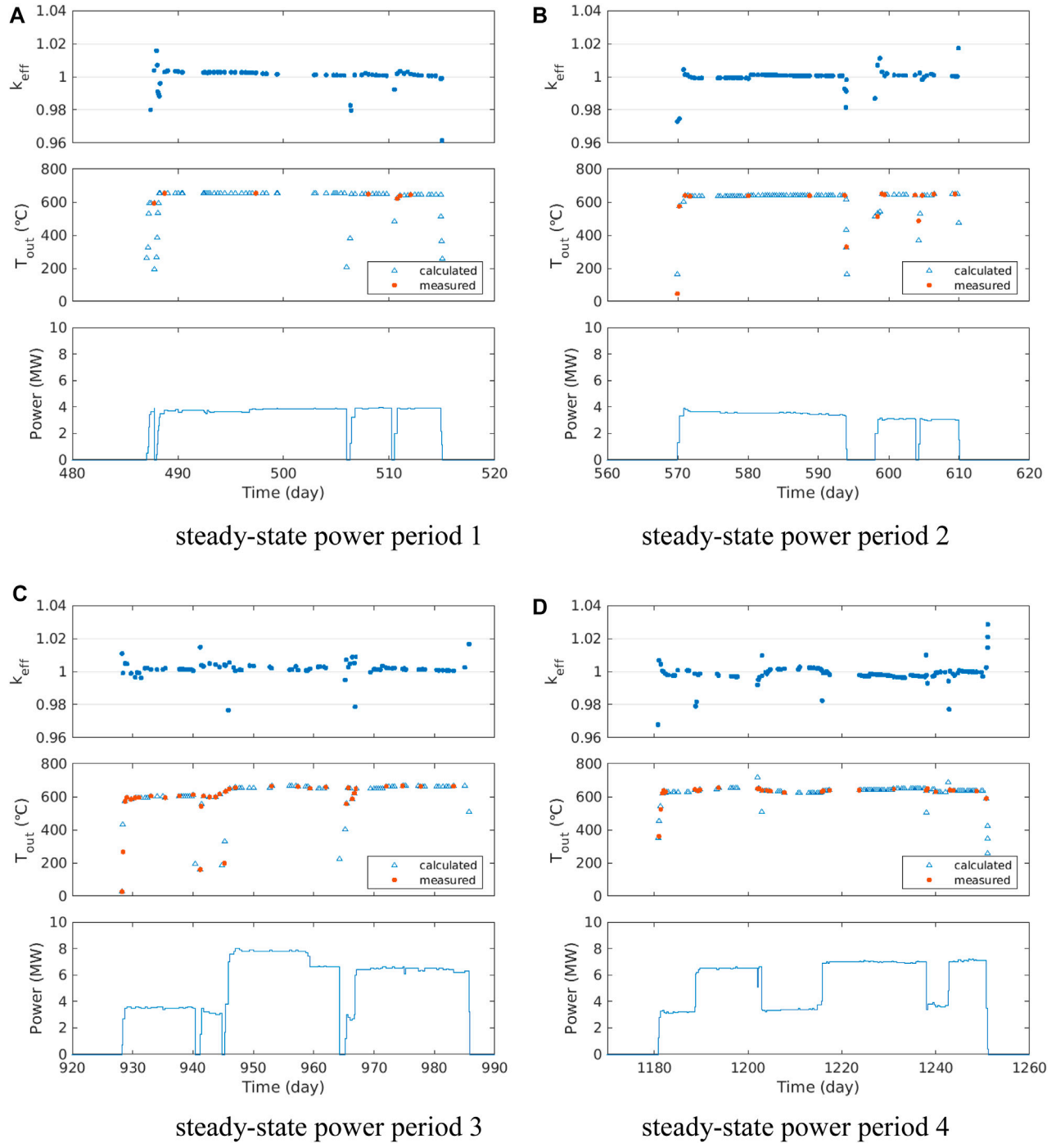

FIGURE 8 | (A) steady-state power period 1 **(B)** steady-state power period 2 **(C)** steady-state power period 3 **(D)** steady-state power period 4 **(E)** steady-state power period 5 **(F)** steady-state power period 6 **(G)** steady-state power period 7. Simulation results of the HTR-10 operation history.

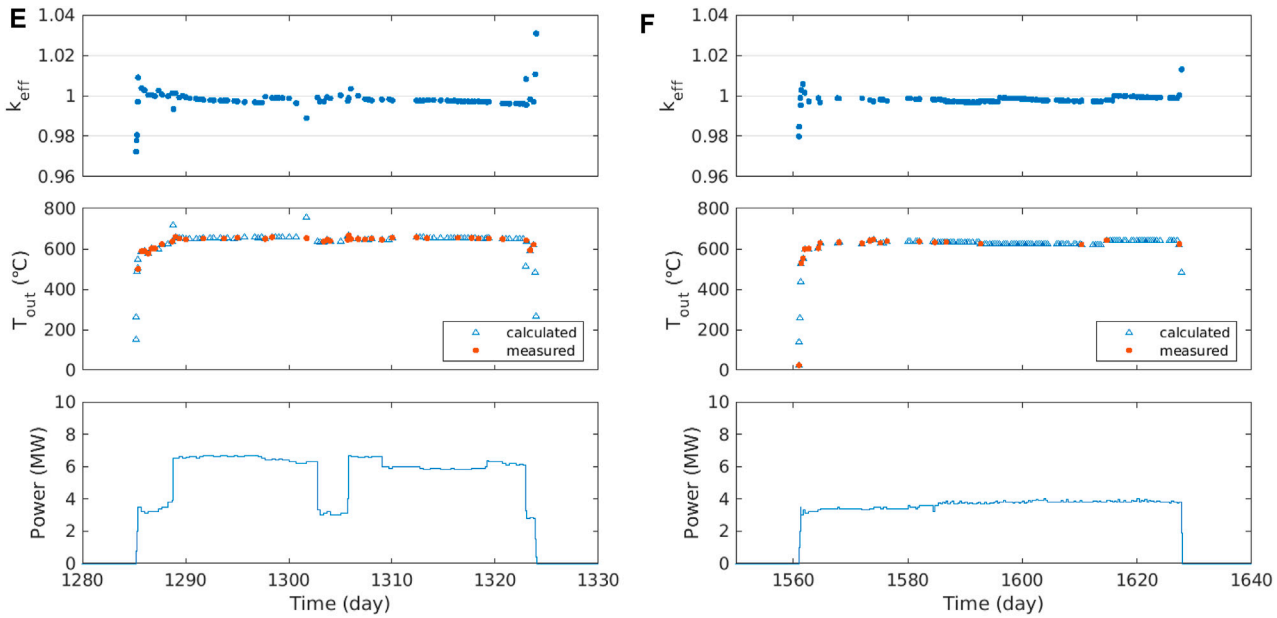

steady-state power period 5

steady-state power period 6

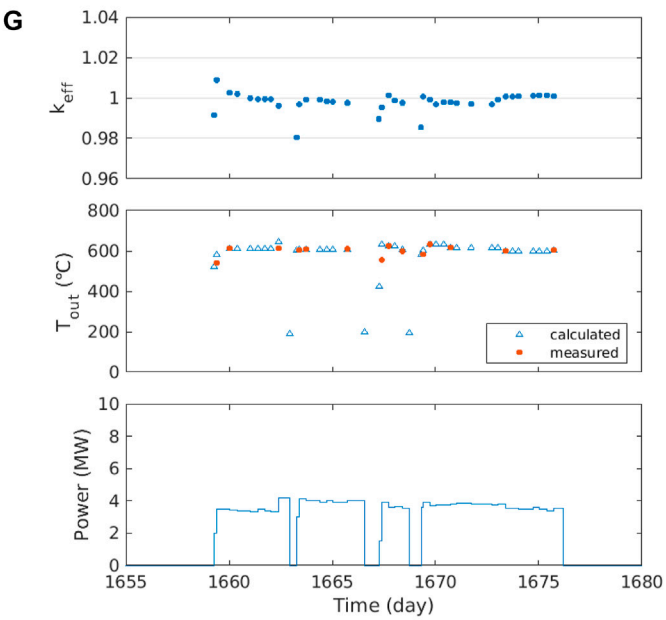

steady-state power period 7

FIGURE 8 | (Continued)

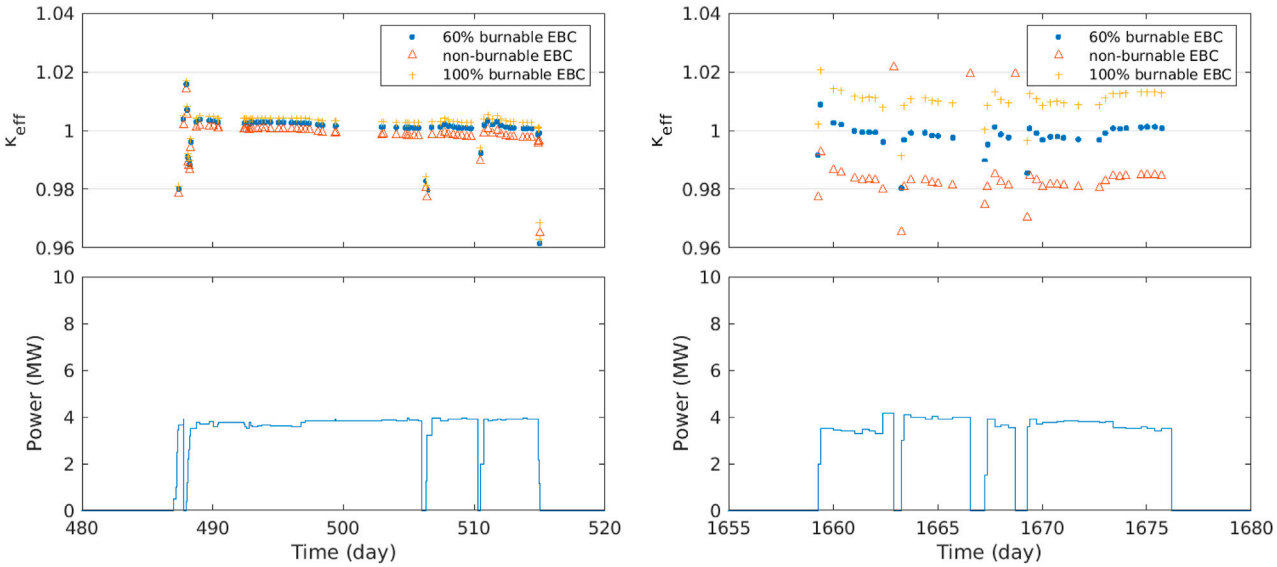

FIGURE 9 | Influence of the EBC burnup

discharged. In this work, the number of regions in the five channels are 46, 50, 51, 55, and 68 respectively.

Burnup of Graphite Impurity

In the HTGR graphite, there are dozens of impurity isotopes, such as boron, chlorine, barium, iron, cadmium, and so on, which has considerable influence on keff. In the practical design of HTGR, the graphite impurities are described by the equivalent boron content (EBC) ASTM (2013) which preserves the neutron absorption of the original impurity isotopes. However, it is a problem on how to treat the EBC in burnup calculations.

In our previous study Li et al. (2018), the burnup characteristics of the graphite impurities in HTR-PM Zhang et al. (2006) was investigated to found that about 60% of the impurity isotopes are burnable. In order to simulate the burnup behavior of the graphite impurities, PANGU adopts a simple burnup model to update the time-dependent density of B-10 in EBC:

$$n_t = n_0 b e^{-\sigma_a \phi t} + n_0 (1 - b) \quad (1)$$

where n_0 is the initial B-10 density, b is the user-input burnable ratio, σ_a is the one-group absorption cross section of B-10, and ϕ is the total neutron flux. In principle, the burnable ratio depends on the fraction of the graphite impurity isotopes. But unfortunately such data of HTR-10 graphite is not provided in the design report. Therefore, the burnable ratio of HTR-PM graphite impurity, i.e. 60%, is used in this simulation.

Calculation Flow

PANGU adopts a two-step calculation scheme. Burnup and temperature dependent cross-section tables are pre-generated with the lattice code XPZ She et al. (2016) and the multi-group data library processed from the ENDF/B VIII.0. These cross-section tables are then used in the fuel cycle simulations with the PANGU code.

The whole fuel cycle simulation contains 1,020 time steps. In each time step, there are iterations between the criticality calculation and the steady-state thermal hydraulics feedback, to obtain the converged keff and temperatures. After that, burnup or decay calculation is performed for the current-step time period. When required, the control rod position and the fuel shuffling is treated at the end of the step. The overall calculation flow is shown in **Figure 7**.

RESULTS AND ANALYSIS

Figure 8 gives the calculated results of keff and the coolant outlet temperatures during all of the steady-state power periods. In general, the simulation results agree well with the measured data. The difference between the calculated keff and the experimental critical value (keff = 1.0) are generally within 0.5%. The differences between the calculated and measured coolant outlet temperatures are generally below 5°C. The errors in the head and the tail of each power period are relatively larger, because these transient states are beyond the scope of steady-state simulation in this work.

In order to analyze the influence caused by the burnup of the EBC, comparison simulations are done by changing the burnable ratio to 0 and 100%, respectively. In case of the non-burnable EBC, the graphite impurities (represented by EBC) are not burned during the power operation, which is expected to cause reactivity penalty in the fuel cycle calculation. In contrary, the 100% burnable EBC calculation condition is expected to result in extra reactivity. In **Figure 9**, it is seen that the calculated keff at the end of operation history is depressed by about 1.5–2% with the non-burnable EBC assumption, while it is overestimated by about 1–1.5% with the 100% burnable EBC assumption. Thus it is

figured that the burnable ratio of EBC has significant influence on the HTGR fuel cycle calculation.

The large uncertainties caused by the nuclear data in HTGR simulations have been reported in some previous work (Bostelmann et al., 2020; Zhang et al., 2020). In our simulation of the HTR-10 operation history, it is found that the keff obtained by ENDF/B VII.0 is about 0.7% higher than that by ENDF/B VIII.0. As one limitation of this work, the difference caused by the nuclear data is not analyzed up to now.

CONCLUSION

The HTR-10 operation history has been simulated with the PANGU code, using delicate models and parameters converted from the measured data. The simulation results are satisfactory, and the PANGU code's applicability is validated. Future work could be done to investigate the sensitivities and uncertainties caused by the nuclear data and some other input parameters in the simulation. Also, it would be of interest to propose and publish a practical burnup benchmark based on the HTR-10 operation data.

DATA AVAILABILITY STATEMENT

The raw data supporting the conclusion of this article will be made available by the authors, without undue reservation.

AUTHOR CONTRIBUTIONS

DS: code development, numerical simulation, and manuscript writing. FC: operation data analysis. BX: operation data preparation, and simulation result evaluation. LS: guidance and consultancy.

FUNDING

This work is supported by the National S&T Major Project (Grant No. ZX06901/ZX06902) of China, and CNNC Youth Research project.

REFERENCES

ASTM (2013). *Standard Practice for Determining Equivalent Boron Contents of Nuclear Materials*, -09, C1233.

Bostelmann, F., Ilas, G., and Wieselquist, W. A. (2020). *Key Nuclear Data Impacting Reactivity in Advanced Reactors (No. ORNL/TM-2020/1557)*. Oak Ridge, TN (United States): Oak Ridge National Lab.(ORNL). doi:10.2172/1649145

Chen, F., Dong, Y., Zheng, Y., Shi, L., Zhang, Z., and Li, F. (2014). July. Progress of the HTR-10 Measured Data Utilization, 2014 22nd International Conference on Nuclear Engineering. American Society of Mechanical Engineers Digital Collection. doi:10.1115/icone22-30088

Gerwin, H., Scherer, W., and Teuchert, E. (1989). The TINTE Modular Code System for Computational Simulation of Transient Processes in the Primary Circuit of a Pebble-Bed High-Temperature Gas-Cooled Reactor. *Nucl. Sci. Eng.* 103 (3), 302–312. doi:10.13182/nse89-a23682

Hao, C., and Li, F. (2014). Investigation on the Pebble Bed Flow Model in VSOP. *Nucl. Eng. Des.* 271, 352–355.

Li, J., She, D., and Shi, L. (2018). Burnup Characteristics Analyses of Graphite Impurities in HTGR Fuel Element. *Ann. Nucl. Energ.* 118, 165–169. doi:10.1016/j.anucene.2018.04.018

Methnani, M., and Tyobeka, B. (2013). *Evaluation of High Temperature Gas Cooled Reactor Performance: Benchmark Analysis Related to the PBMR-400, PBMM, GT-MHR, HTR-10 and the ASTRA Critical Facility*. IAEA-TECDOC-1694.

Rütten, H. J., Haas, K. A., Brockmann, H., and Scherer, W. (2005). *VSOP (99/05) Computer Code System*. doi:10.4324/9780203987117

She, D., Guo, J., Liu, Z., and Shi, L. (2018b). PANGU Code for Pebble-Bed HTGR Reactor Physics and Fuel Cycle Simulations. *Ann. Nucl. Energ.* 126, 48–58.

She, D., Liu, Z., Guo, J., and Shi, L. (2018a). Leakage Correction in Group-Constant Generation for Pebble-Bed HTGRs. *Prog. Nucl. Energ.* 105, 76–82. doi:10.1016/j.pnucene.2017.12.015

She, D., Liu, Z., and Shi, L. (2017). An Equivalent Homogenization Method for Treating the Stochastic Media. *Nucl. Sci. Eng.* 185 (2), 351–360. doi:10.1080/00295639.2016.1272363

She, D., Liu, Z., and Shi, L. (2016). XPZ: Development of a Lattice Code for HTR. *Ann. Nucl. Energ.* 97, 183–189. doi:10.1016/j.anucene.2016.07.017

Wang, Q., She, D., Xia, B., and Shi, L. (2019). Evaluation of Pebble-Bed Homogenized Cross Sections in HTGR Fuel Cycle Simulations. *Prog. Nucl. Energ.* 117, 103041. doi:10.1016/j.pnucene.2019.103041

Wu, Z., Lin, D., and Zhong, D. (2002). The Design Features of the HTR-10. *Nucl. Eng. Des.* 218 (1), 25–32. doi:10.1016/s0029-5493(02)00182-6

Zhang, L., She, D., and Shi, L. (2020). Influence of Graphitization Degree of Nuclear Graphite on HTGR Reactor Physics Calculation. *Ann. Nucl. Energ.* 143, 107458. doi:10.1016/j.anucene.2020.107458

Zhang, Z., Wu, Z., Sun, Y., and Li, F. (2006). Design Aspects of the Chinese Modular High-Temperature Gas-Cooled Reactor HTR-PM. *Nucl. Eng. Des.* 236 (5), 485–490. doi:10.1016/j.nucengdes.2005.11.024

Conflict of Interest: The authors declare that the research was conducted in the absence of any commercial or financial relationships that could be construed as a potential conflict of interest.

frontiers in Energy Research

ORIGINAL RESEARCH
published: 23 July 2021
doi: 10.3389/fenrg.2021.705823

Evaluation of Single-Node Performance of Parallel Algorithms for Multigroup Monte Carlo Particle Transport Methods

Donghui Ma[1], *Bo Yang*[1], *Qingyang Zhang*[1], *Jie Liu*[1,2] *and Tiejun Li*[1]*

[1]Science and Technology on Parallel and Distributed Processing Laboratory, National University of Defense Technology, Changsha, China, [2]Laboratory of Software Engineering for Complex Systems, National University of Defense Technology, Changsha, China

Monte Carlo (MC) methods have been widely used to solve the particle transport equation due to their high accuracy and capability of processing complex geometries. History-based and event-based algorithms that are applicable to different architectures are two methods for parallelizing the MC code. There is a large work on evaluating and optimizing parallel algorithms with continuous-energy schemes. In this work, we evaluate the single-node performance of history-based and event-based algorithms for multigroup MC methods on both CPUs and GPUs with Quicksilver, a multigroup MC transport code that has already implemented the history-based algorithms. We first implement and optimize the event-based algorithm based on Quicksilver and then perform the evaluation work extensively on the Coral2 benchmark. Numerical results indicate that contrary to continuous-energy schemes, the history-based approach with multigroup schemes outperforms the event-based algorithm on both architectures in all cases. We summarize that the performance loss of the event-based algorithm is mainly due to: 1) extra operations to reorganize particles, 2) batched atomic operations, and 3) poor particle data locality. Despite the poor performance, the event-based algorithm achieves higher memory bandwidth utilization. We further discuss the impact of memory access patterns and calculation of cross sections (xs) on the performance of the GPU. Built on the analytics, and shed light on the algorithm choice and optimizations for paralleling the MC transport code on different architectures.

Keywords: parallel computing, performance evaluation, history-based, event-based, particle transport

OPEN ACCESS

Edited by:
Qian Zhang,
Harbin Engineering University, China

Reviewed by:
Rongliang Chen,
Shenzhen Institutes of Advanced Technology (CAS), China
Xiaowen Xu,
Institute of Applied Physics and Computational Mathematics (IAPCM), China
Kenli Li,
Hunan University, China
Qingming He,
Xi'an Jiaotong University, China

***Correspondence:**
Tiejun Li
tjli@nudt.edu.cn

Specialty section:
This article was submitted to Nuclear Energy, a section of the journal Frontiers in Energy Research

Received: *06 May 2021*
Accepted: *25 June 2021*
Published: *23 July 2021*

Citation:
Ma D, Yang B, Zhang Q, Liu J and Li T (2021) Evaluation of Single-Node Performance of Parallel Algorithms for Multigroup Monte Carlo Particle Transport Methods. Front. Energy Res. 9:705823. doi: 10.3389/fenrg.2021.705823

1 INTRODUCTION

Particle transport problems such as shielding radiations and power reactor calculations require solving the Boltzman equation, which describes how particles transport through and interact with materials. Deterministic methods solve such problems by numerical calculations to obtain the required physical quantities. Different from deterministic methods, Monte Carlo (MC) methods (Metropolis and Ulam, 1949) construct a stochastic model through statistical sampling and particle weighting and are capable of handling complex geometry and physics models. The expected value of a physical quantity is then estimated by the weighted average of behaviors of numerous independent particles. Random numbers following the specific probability distributions are used to model various

events (collision, fission, capture, etc.), thus causing statistical uncertainty. Increasing the number of particle histories is usually used to reduce uncertainty, but meanwhile, it comes at a significant computational cost. To reduce the runtime, MC transport codes such as Shift (Pandya et al., 2016), OpenMC (Romano and Forget, 2013), and MCNP (Forster and Godfrey, 1985) are usually targeted at large-scale parallelization on high-performance supercomputers with tens of thousands of computing nodes.

There are two parallel algorithms for MC methods, history-based and event-based algorithms. History-based algorithms loop over a large number of independent particles, each of which is simulated from the birth to the death by a fixed thread. Because each particle has an independent trajectory and a different history length, history-based algorithms are appropriate for multiple-instruction multiple-data (MIMD) architectures. The MC transport loop over particles is not suitable for vectorization because different instructions are required at different times. To exploit the vectorization capabilities of computing architectures, the event-based MC method was proposed in the 1980s (Brown and Martin, 1984). This approach processes a batch of particles based on the next event that particles will undergo. Particles that have the same next event will be processed together.

Traditionally, MC codes are parallelized on CPU-based machines. To achieve higher floating-point operations per second (FLOPS), supercomputers tend to rely on vectorized, single-instruction multiple-data (SIMD) or single-instruction multiple-threads (SIMT) architectures such as graphical processing unit (GPU) and Intel Xeon Phi processors (MIC). A large amount of research uses vectorized architectures to obtain better performance. Li et al. (2017) proposed a multi-stream approach based on GPU for matrix factorization to accelerate stochastic gradient descent and achieved 5–10× speedup. Yan et al. (2020) presented an optimized implementation for single-precision Winograd convolution on GPUs. Its implementation achieved up to 2.13× speedup on Volta V100 and up to 2.65× speedup on Turing RTX2070. Existing research shows that computation-intensive programs can obtain a significant performance improvement.

A number of MC codes on vectorized architectures (Du et al., 2013; Liu et al., 2014; Bergmann and Vujić, 2015) have been developed. Most recent studies of GPU-based MC methods (Choi et al., 2019; Hamilton and Evans, 2019) have focused on event-based algorithms. The WARP code (Bergmann and Vujić, 2015) adapted event-based algorithms to the new GPU hardware and realized a generalized GPU-based implementation for continuous-energy MC transport. Substantial gains in performance are achieved by using event-based algorithms in the Shift code (Hamilton and Evans, 2019), a continuous-energy MC neutron transport solver. All of the GPU-based studies above are based on continuous energy, on which the event-based approach outperforms the history-based method by a large margin.

We consider the single-node performance of the history-based and event-based algorithms for multigroup MC methods. Compared with continuous-energy MC methods, the multigroup scheme has a simpler logic. The energy ranges in the multigroup energy spectrum are usually subdivided into a few hundred groups and averaged in different ways over the continuous-energy schemes, thus avoiding the need to carry out a lookup over very large cross section tables, which constitute a significant fraction of runtime. Therefore, multigroup MC methods have extremely different memory access patterns and conditional branches. To further optimize the performance of the multi-group MC programs, it is necessary to evaluate the performance of history-based and event-based algorithms on modern architectures. Hamilton et al. (2018) provided a comparison of history-based and event-based algorithms for multigroup MC methods on GPUs. However, it lacks a comparative analysis of the multigroup and continuous energy schemes, as well as a comparative analysis of performance on the CPU and GPU.

This article is aimed at providing a detailed analysis of the single-node performance difference between different parallel algorithms with different cross section schemes on both CPUs and GPUs. The studies were performed using Quicksilver (Richards et al., 2017), a proxy application for the MC transport code Mercury (LLNL, 2017). It implements the history-based algorithm on both CPUs and GPUs through a thin-threads approach (Bleile et al., 2019).

The main contributions of this work are that:

- We implement the event-based algorithm for multigroup MC methods in the Quicksilver code on both CPUs and GPUs. The implementation details, including modification of data structures, loop organization, and optimization on the GPU, are provided.
- We explore the performance difference of the history-based and event-based algorithms for multigroup MC methods on both CPUs and GPUs. The results show that the event-based algorithm for multigroup MC methods is over 1.5× slower than the history-based algorithm on both architectures, but achieves a higher memory bandwidth.
- We analyze the performance-affecting factors, including memory access patterns and xs schemes. Built on the analytics, we provide suggestions for optimizations and algorithm choices for the MC transport code on different architectures.

2 BACKGROUND

2.1 Monte Carlo particle Transport

MC methods are very different from deterministic transport methods. MC methods solve the transport equation by simulating individual particles and recording some aspects (tallies) of their average behavior. The average behavior of particles in the physical systems is then inferred (using the central limit theorem) from the average behavior of the simulated particles. Deterministic methods typically give fairly complete information throughout the phase space of the problem, while MC methods supply information only about specific tallies requested by the user.

MC methods transport particles between events (for example, collisions) that are separated in space and time. The individual probabilistic events that comprise a process are simulated sequentially. The probability distributions governing these events are statistically sampled to describe the total phenomenon. Probability distributions are randomly sampled using transport data to determine the outcome at each step of its life.

2.2 History-Based Algorithm

As the particle histories are independent, it is natural to achieve parallelism over individual particles. This means each thread or process will process a single particle for its whole life cycle until it is absorbed, escapes from the system, or reaches the end of a time step. Algorithm 1 is the basic history-based algorithm with a loop over simulated particles. The loop body sequentially processes particle histories that would alternate between moving particle to collision site and processing particle collision. Moving particle to collision site involves calculating several distances, including sampling distance to next collision and other geometric operations. Processing particle collision encompasses the most sophisticated control flow, which involves sampling the nuclide to interact with the reaction type.

Algorithm 1 History-based algorithm

```
get vector of source particles
for each particle do
    repeat
        Move particle to collision site
        Process particle collisions
    until terminated
end for
```

In the GPU implementation, the loop is replaced by a CUDA kernel launch where the total number of CUDA threads is equal to the number of particles. The number of particles is much larger than the number of threads the device can physically execute simultaneously to hide the latency of accessing global memory. Owing to the limited GPU resources, particles are usually simulated in batches. In Algorithm 1, each particle has a different history length and therefore will collide at different times, which represents a thread divergence of MC methods at the highest level.

2.3 Quicksilver

This work was performed in the Quicksilver code (Bleile et al., 2019; Richards et al., 2017), a proxy application of the full production code Mercury developed and maintained by Lawrence Livermore National Laboratory (LLNL). Quicksilver is designed to represent the key features of Mercury and offers an approximation of the critical physical routines that form the essential part of the full production code. It only implements some of the most common physical interactions but keeps enough to represent crucial computational patterns. Mercury supports meshes with multiple types and solid geometry, while Quicksilver is limited to only a 3D polyhedral mesh. Additionally, Mercury uses both continuous and multigroup cross sections, while Quicksilver only supports the multigroup nuclear data.

Quicksilver offers only two types of predefined tallies: balance tallies and a cell-based scalar flux tally. Balance tallies record the total number of times specific events occur (such as collisions, facet crossings). Scalar flux tally scores the flux of particles through each mesh cell. In addition, Quicksilver implements history-based algorithms on both CPUs and GPUs. Thread safety is handled by using atomic operations. In this article, we implement the event-based approach.

TABLE 1 | Summary of notations.

Symbol	Meaning
N	The number of particles in a cycle
B	The number of particles in a batch
E	Event type
Vp	Initial particle vector
V_b	Particle bank
Q_{xs}	Queue that handles xs calculations
Q_{ad}	Queue that handles particle advancing
Q_{cl}	Queue that handles collisions
Q_{cf}	Queue that handles facet crossings

3 EVENT-BASED ALGORITHM

In this section, we implement the basic event-based algorithm on both CPUs and GPUs and present some optimizations on GPUs. Instead of being simulated by a fixed task from the creation to completion, event-based transport processes particles with the same next event (e.g., calculate total macro cross section) together. It offers an opportunity to exploit vectorization capabilities. As discussed in Ozog et al. (2015), employing an event-based algorithm to the MC transport code is not trivial because nearly all the data structures and loop organization require to be modified.

The notations used in this work are listed in **Table 1**.

3.1 Basic Event-Based Algorithm

Suppose there are N particles to be simulated in a cycle. N particles form the *initial particle vector*. Because storing the attributes of N particles simultaneously is not feasible on a GPU, the number of particles in a given batch is often limited to at most B particles. We refer to a vector of particles to be processed in a batch as a *particle bank*. We denote the initial particle vector and particle bank by V_p and V_b, respectively. Before the particles undergo the next event together, they should be banked. As described in Romano and Siegel (2017), there are two main variations on how to bank particles that have the same event type. In the first method, the particles within a particle bank execute the same event at any given time. But some may be masked because they either have different undergoing events or have already been terminated, which might cause the occurrence of idle threads. The other approach is the queue-driven approach, in which several event queues are maintained and particle indices

in the particle bank are pushed into or popped off the queues according to the next event type. This article is based on the queue-driven method and will extend the algorithm to improve the performance of GPUs.

3.1.1 Event-CPU Algorithm

Algorithm 2 is the basic event-based algorithm on CPUs. The algorithm begins by getting a batch of particles from the initial particle vector (line 2). The next step is an initialization (line 4) of event queues that correspond to four event types: computing cross sections, advancing, collision, and crossing facet. Four event queues are abbreviated as Q_{xs}, Q_{ad}, Q_{cl}, and Q_{cf}, respectively. Computing cross sections is to access cross section data corresponding to the particle's current energy group and calculate total macro cross sections at the current cell. Advancing is to move a particle to the next location, which involves computing three distances, including the distance to cencus, the distance to facet, and the distance to reaction. Collision means sampling reaction type (scatter, fission, or absorption) and processing sampled reaction. The crossing facet aims to determine whether the particle crosses to the neighbor cell located on the current rank or the neighbor cell located on the other rank.

Algorithm 2 Basic event-based algorithm

```
1:  while any particles in V_p are alive do
2:      get a batch of particles and stored in V_b
3:      H ← {Q_xs, Q_ad, Q_cl, Q_cf}
4:      initialize event queues
5:      while any particles in V_b are alive do
6:          max_size ← max_{q∈H}(size(q))
7:          if max_size == size(Q_xs) then
8:              calculate cross sections
9:          else if max_size == size(Q_ad) then
10:             move particle to next location
11:         else if max_size == size(Q_cf) then
12:             process particle collisions
13:         else
14:             process particle facet crossing
15:         end if
16:     end while
17: end while
```

Before generating trajectories, all particles must first calculate the cross sections, which is the first event of the particle. Therefore, the initialization of event queues is to put all particles in the bank into Q_{xs}. It should be noted that each event queue is an array storing the particle indices into the particle bank. Storing only particle indices avoids a large amount of memory transfer, which frequently occurs when performing pushes and/or pops on the event queues.Following the initialization is a while loop (lines 5–16), the body of which is to process the particles in the longest queue until all the particles in V_b are simulated. When dealing with collisions, the secondary particles produced by fission are added to the fission bank by performing an atomic add on the length of the fission bank. At the end of each event processing, active particles require to be redistributed to event queues. Each thread performs an atomic operation to put the particle index into the corresponding queue. In particular, after computing cross sections each particle will move to the next location, that is, all the particles in Q_{xs} will be put into Q_{ad}. Therefore, there is no need to perform atomic operations because each particle's position in Q_{ad} can be directly obtained by adding its position in Q_{xs} to the length of Q_{ad}.

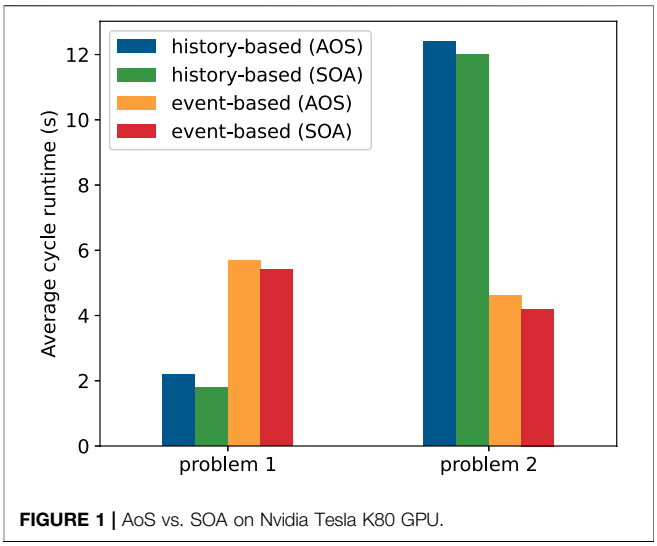

FIGURE 1 | AoS vs. SOA on Nvidia Tesla K80 GPU.

3.1.2 Event-GPU Algorithm

The basic event-based algorithm on GPUs is still as shown in Algorithm 2, but all the events are processed through GPU kernels. Compared with the large kernel in the history-based algorithm, a smaller event kernel means that most branching logic is handled outside the kernel, resulting in less thread divergence within kernels and therefore an improved utilization of vectorization. In addition, smaller kernels are capable of providing the reduced computational complexity and therefore each thread occupies fewer GPU resources (registers, etc.). Because of a fixed amount of resources available, more threads can be executed simultaneously to achieve a higher occupancy, which is an important consideration for improving GPU performance. The performance of multigroup MC methods on GPUs is affected by many factors, one of which is thread divergence. Reducing thread divergence results in an improved arithmetic performance, but may also bring some changes in other aspects, such as memory access patterns, which may cause more serious performance losses.

3.1.2.1 Tallies

An essential concern is the update of tallies. Quicksilver only provides two kinds of tallies, one of which is the scalar flux tally. One way to update the scalar flux tally is to allocate a copy for each particle in V_b. Each particle updates its copy and finally, a

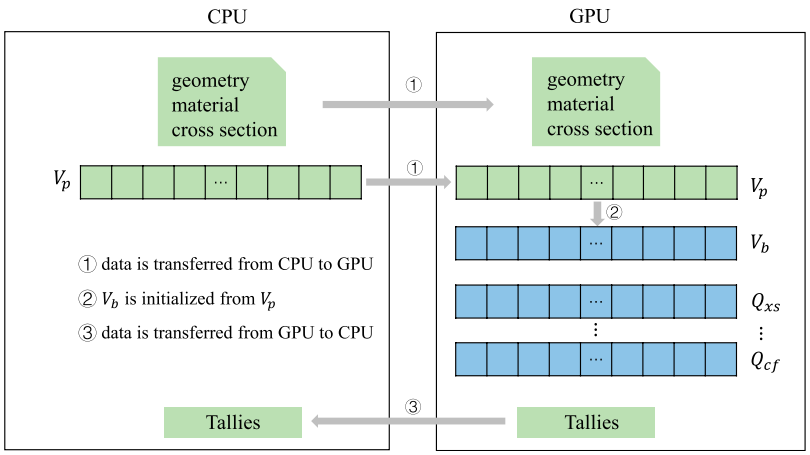

FIGURE 2 | Memory management of main data structures in the event-GPU algorithm.

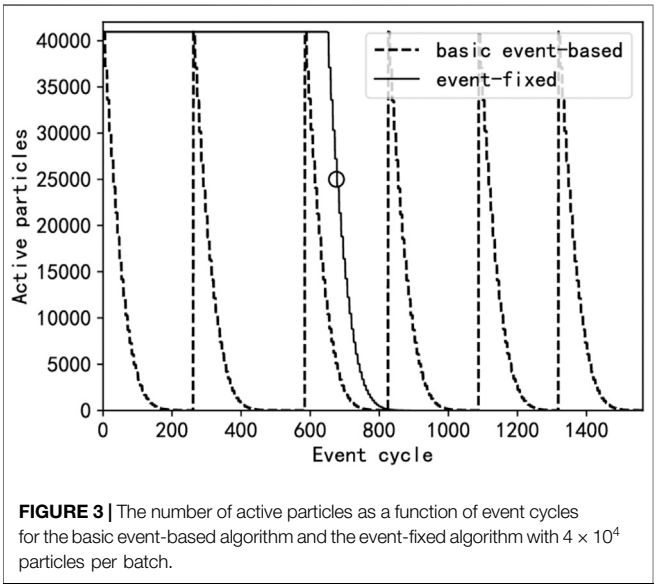

FIGURE 3 | The number of active particles as a function of event cycles for the basic event-based algorithm and the event-fixed algorithm with 4×10^4 particles per batch.

reduction operation is performed on all copies. However, this method requires a large amount of memory since numerous particles will be simulated. A batch method is employed in this article. Fixed-length (much less than B) scalar flux copies are maintained in GPU. Each particle updates the corresponding copy indexed by the remainder of its index divided by the length of the copies.

3.1.2.2 Data Structure

The particle's basic information, including position, energy, direction, velocity, etc., is represented by a data structure. One approach for storing the initial particle vector and particle bank is to allocate an array of these structures, which is known as AOS. The second method is to store each data component of these structures in distinct arrays, which is usually called SOA. On CPUs, AOS is often used to improve cache efficiency due to its better locality. The SOA pattern is usually recommended to be used for GPU so that coalesced memory accesses can be efficiently utilized. We explored the performance difference between AOS and SOA on the GPU. The results in **Figure 1** demonstrate that, on the GPU, the SOA pattern performs better on both problem 1 and problem 2 (see **Section 4.1** for the introduction of these two problems), but only brings very little performance gains. In the following experiments, we use AOS for CPU implementations and SOA for GPU.

3.1.2.3 Memory Management

Figure 2 shows the memory management of the event-GPU algorithm. Since all operations of event queues, including event kernels and initialization, can be handled on the GPU, the memory of event queues only needs to be allocated on the GPU, avoiding data movement between host and device. Data on geometry, materials, and multigroup cross sections are all transferred from the CPU to the GPU during the initialization of Quicksilver and will not be modified in the subsequent execution. The initial particle vector V_p is allocated memory on both the CPU and the GPU. At the beginning of each cycle, particles generated on the CPU are transferred from the CPU to the GPU and simulated on the device until all particles die. Similar to event queues, we only allocate memory for particle bank V_b on the GPU and V_b are initialized by a GPU kernel at the beginning of each batch. Tallies are accumulated on the GPU and transferred from the GPU to the CPU at the end of the simulation.

3.1.2.4 Event Kernel Switch

The kernel that handles events in the longest queue (this means that GPU can concurrently simulate a maximum number of particles) is launched each time. To know which queue is the longest, we allocate memory for an array of length four using *cudaMallocManaged* and maintain it to represent current lengths of event queues. Then the maximum length can be determined on the host. Kernels are switched over and over until all the particles in that batch are simulated.

3.2 Optimization on GPUs

In the basic event-GPU algorithm, particles will be terminated when it is absorbed, escapes from the system (or subdomain), or reaches the end of a time step, leading to a gradual decrease in the number of active particles in V_b. In case the number of particles within a batch drops to a threshold that cannot efficiently occupy GPUs, the overall performance of the GPU will be reduced significantly. The dotted line in **Figure 3** is the change in the number of active particles within a cycle in the basic event-GPU algorithm. It can be seen that the performance degradation caused by the decrease in GPU occupancy will occur multiple times within a cycle because a cycle contains multiple batches. To maximize GPU occupancy, we first implement the "Source Event" method proposed in Hamilton et al. (2018) and then propose the hybrid method.

3.2.1 Occupancy Enhancement

Hamilton et al. (2018) proposed to replace terminated particles with new particles to maximize GPU occupancy, which keeps the number of active particles in a cycle for a significant fraction of cycle runtime. To achieve this, instead of killing terminated particles directly, we replace terminated particles in V_b with new particles from V_p and also put their indices into Q_{xs}. We refer to this method as event-fixed. The solid line in **Figure 3** shows the change in the number of particles within a cycle in the event-fixed method. In this way, the performance degradation only occurs at the end of the cycle.

It should be noted that the meaning of "batch" is no longer the same as the original meaning. The difference is that "batch" in the event-fixed method is based on the number of terminated particles, not source particles. Specifically, a global counter is maintained and incremented atomically when particles are terminated. Once the counter rises above B, it is considered that a batch of particles has been processed.

At the conclusion of event processing atomic operations are utilized to redistribute active particles. However, the atomic operation would have a great impact on the overall performance because the GPU will typically execute many more threads simultaneously and the redistribution operation will occur frequently. We consider another method based on prefix sum to collect the indices of active particles, thus avoiding atomic operations on queues.

For event queue Q_E with a given event type E, indices of particles whose next event type is E are collected through the method shown in Algorithm 3. There are two auxiliary arrays in Algorithm 3, V_{map} and V_{offset}. At the end of the previous event kernel, each particle will get a 1 in V_{map} at its index location if its next event is E; otherwise, it will get a 0 (line 1). V_{offset} is the exclusive prefix sum of V_{map} (line 2) and is also the offset of the particle's position in Q_E relative to the current length of Q_E. After generating V_{map} and V_{offset}, a CUDA kernel is executed to update Q_E (lines 4–8).

TABLE 2 | Problem definition in the Cora 2 benchmark. Two problems have different numbers of isotopes and reactions.

Problem	Isotope	Reaction	Energy group
Problem 1	20	9	230
Problem 2	10	3	230

Algorithm 3 Particle redistribution based on prefix sum

1: generate V_{map} for event E
2: compute V_{offset} by performing exlusive scan on V_{map}
3: $l \leftarrow$ size(Q_E)
4: **for** $i \leftarrow 0, 1, \ldots, B-1$ **do in parallel**
5: **if** $V_{map}[i] == 1$ **then**
6: $Q_E[l + V_{offset}[i]] \leftarrow i$
7: **end if**
8: **end for**
9: $l \leftarrow l + (V_{offset}[B-1] + V_{map}[B-1])$
10: set_size(Q_E, l)

3.2.2 Hybrid Method

When the number of active particles falls below a threshold. For example, from the circle in **Figure 3**, the cost of multiple event kernel startups will exceed the benefits brought by the event-based algorithm itself. The main reason is that the event kernel cannot be executed efficiently for a small number of particles in flight. From the threshold, we switch to the history-based algorithm to track the residue particles. We refer to this method as an event-hybrid approach. Before switching to the history-based algorithm each particle may be going to undergo a different next event, which means that all event queues are not empty. Performing the following three steps, all particles will be merged into Q_{xs}.

- Execute advancing kernel. After this step, surviving particles in Q_{ad} are moved to the next location and then will collide or cross the nearest facet. As a result, at the end of the kernel, all survive particles in Q_{ad} will be put into Q_{cl} or Q_{cf}. Now Q_{ad} is empty.
- Execute collision kernel. After colliding with sampled nuclides, survive particles will enter Q_{xs} to recompute cross sections. Now both Q_{ad} and Q_{cl} are empty.
- Execute crossing kernel. Particles in Q_{cf} may be terminated (escape from the system or subdomains on local rank), or enter other subdomains on the local rank. Consequently, all survive particles in Q_{cf} will be put into Q_{xs}. Now all the other three event queues except Q_{xs} are empty.

Finally, we perform a history-based algorithm on all particles in Q_{xs}.

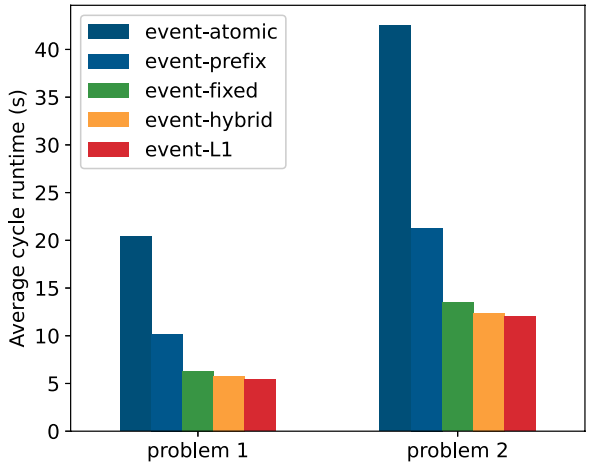

FIGURE 4 | Average cycle runtime of different event-GPU algorithms on problem 1 and problem 2.

4 PERFORMANCE EVALUATION

In this section, we present a single-node performance comparison of the history-based and event-based algorithms of Quicksilver on both CPUs and GPUs. In addition, some experiments were conducted to further explain the reasons for the performance evaluation results.

4.1 Experiment Setup

For performance evaluations, we perform some experiments on the Tianjin HPC1 system, each node of which contains two fourteen-core Intel Xeon E5-2690 v4 CPUs operating at 2.6 GHz along with four NVIDIA Tesla K80 GPUs. L1 cache is one of the factors that can affect performance on GPUs. On the Kepler architecture, all memory transactions only use an L2 cache, but the L1 cache is disabled by default and must be enabled using the compiler flag "-Xptxas -dlcm –ca." In the following experiments on GPUs, L1 cache is enabled. To simplify the execution within a rank, we use one rank for a GPU and 4 ranks per node as a result of running on 4 Tesla K80 GPUs.

We utilize a single problem, Godiva in water (Cullen et al., 2003), as the basis of our study. This problem was generated to be used as a Cora 2 benchmark in Quicksilver due to its balanced reactions and balanced nature to match a classic MC test problem. The benchmark is defined by multiple parts, including cross sections, materials, and geometries. The cross sections define the detailed information to describe reactions that will occur when colliding with different isotopes. Materials mainly define physical information, such as the number of isotopes and the number of reactions considered in the corresponding material. Geometries contain the size of the mesh and the size of subdomains related to domain decomposition.

This benchmark defines a Cartesian mesh with $10 \times 10 \times 10$ elements per rank. There are two specific problems in the Cora 2 benchmark. **Table 2** shows the specific definitions. There are 20 isotopes and nine reactions in problem 1, while in problem 2 there are only 10 isotopes and three reactions. The biggest difference between these two problems is that cross sections in problem 1 are tailored to give a broader energy spectrum for the particles and a different reaction mix compared to problem 1. Both of these two problems use 230 energy groups.

4.2 Event-GPU Algorithm Comparison

We describe the implementation details of the basic event-based algorithm on GPUs in **Section 3.1.2** and implement three optimized methods (event-fixed, event-hybrid, and event-prefix) for enhancing the GPU performance. We now perform a comparison of these algorithms. Besides, we also investigate the performance gains by enabling L1 cache (event-based, L1). **Figure 4** shows the average cycle runtime for different GPU algorithms on both problem 1 and problem 2, respectively. Results are obtained using 100 cycles and 4×10^6 neutrons per cycle. Each algorithm in **Figure 4** is modified based on the previous one. As expected, both the algorithmic developments and the availability of the L1 cache bring performance improvements.

The results indicate that there is a big gap between the performance of the atomic-based and prefix-sum-based methods. The prefix sum method outperforms the atomic method by a factor of approximately two on the problems considered. This proves that there is a significant benefit to replacing atomic operations with the prefix sum method when redistributing survive particles. The event-fixed approach achieves an obvious performance increase. This is because GPU efficiency is reduced multiple times within a cycle due to the decrease in the number of particles in each batch, which keeps the GPU not fully occupied for a large fraction of the calculation. Replacing terminated particles with new source particles allows the GPU to maintain a high occupancy rate until the end of each cycle. Compared with the event-fixed approach, the event-hybrid algorithm brings little performance gains, which is not surprising. The tracking using the hybrid algorithm at the end of each cycle only accounts for very few calculations; therefore, the performance gains by using event-hybrid are very limited.

It is worth noting that the L1 cache only brings a slight advantage due to the event-based algorithm's inability to efficiently exploit the L1 cache. There are several reasons. One reason is that the light kernel offers little opportunity for event-based methods to reuse data. Particle data are only used during the execution of short-lived event kernels, the data required by the previous kernel are often different from the next event kernel, leading to frequent invalidation of the cache of earlier loaded data. Another reason is that the particle redistribution results in less spatial locality. In event-based methods, although the first access to a particle data will cause the particle to be cached in the L1 cache, very few components of a particle data would be accessed later in the same event kernel. Therefore, the event-GPU algorithms obtain a small performance increase by enabling the L1 cache due to its insensitivity to the L1 cache.

4.3 History vs. Event Performance

This article now explores the single-node performance of the history-based and event-based algorithms on both CPUs and

TABLE 3 | Tracking rate ($10^4 n/s$) and achieved memory bandwidth (*GB/s*) of history-based and event-based algorithms on CPUs and GPUs for problem1 and problem 2.

Algorithm	Problem 1		Problem 2	
	Tracking rate	Memory bandwidth	Tracking rate	Memory bandwidth
History-CPU	87.9	9	38.5	7
Event-CPU	48.4	15	21.9	14
History-GPU	224.8	95	95.2	93
Event-GPU	72.9	140	27.3	135

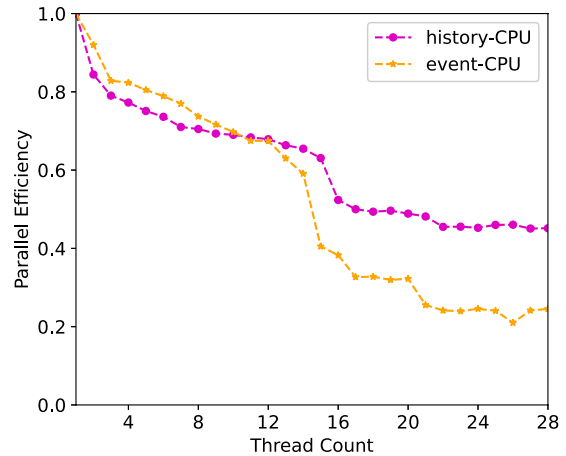

FIGURE 5 | Thread parallel efficiency of problem 1 on the two-sockets of Intel Xeon E5-2690 v4 14 core CPU. Only one process is used.

GPUs. All experiments on GPUs are based on event-hybrid algorithm and L1 cache is enabled.

4.3.1 Particle-Tracking Rate

Table 3 provides the particle-tracking rate for the history-based and event-based algorithms on both CPUs and GPUs. It can be seen from **Table 3** that, on the CPU, the history-based algorithm is over 1.5x faster than the event-based algorithm in all cases. The serious performance degradation of event-CPU relative to history-CPU is mainly caused by the following reasons:

1) Extra operations: Event-CPU requires extra operations to organize the particles periodically to ready them for the different event-processing routines. These additional operations introduce extra overhead compared to the history-based algorithm on the CPU.
2) Atomic operations: The atomic operations in history-CPU are randomly distributed along the history of each particle, whereas the atomic operations in event-CPU are batched into a single-event loop. Therefore, more threads are waiting for atomic operations in the event-CPU.
3) Particle data locality: There are more opportunities for history-CPU to reuse data. In history-CPU, particle data can be cached in registers; thus consecutive particle data access can be hit directly in registers. However, in event-CPU, data required by the current event loop are often part of the complete particle data and are often different from the previous loop. Very few components of particle data would be accessed later in the current event loop.

TABLE 4 | Percentage (%) of time spent on subroutines of event-based algorithm on CPU and GPU for problem 1 and problem 2.

Subroutine	Event-CPU		Event-GPU	
	Problem 1	Problem 2	Problem 1	Problem 2
xs calculation	6.7	4.1	7.8	5.6
Advancing	63.4	44.6	64.7	45.2
Collision	17.3	44.0	15.4	42.1
Crossing facet	12.6	7.3	12.1	7.1

It should be noted that the event-GPU algorithm did not achieve the speedup as expected and only provides 19–23 equivalent CPU cores that are 3x slower than history-GPU. Different from previous studies on the continuous-energy MC code (Bergmann and Vujić, 2015; Choi et al., 2019; Hamilton and Evans, 2019) where the lookup of energy grids occupies a very large portion of the calculation. **Table 3** shows the remarkably superior performance of the history-based method relative to the event-based approach on the GPU. The main advantage of event-GPU is that the top level branches of history-GPU are removed, which decreases thread divergence on the GPU. Nevertheless, event-GPU has many disadvantages that would significantly affect the performance of the event-GPU algorithm for the multigroup transport code. Apart from the drawbacks related to extra operations, atomic operations, and particle data locality, memory access pattern is another factor. We will design several experiments in **Section 4.4** to analyze the factor in detail.

4.3.2 Memory Bandwidth Utilization

MC transport is a random memory access problem, and the memory bandwidth of each algorithm requires to be measured. We measured the memory bandwidth using the perf and nvprof tools. On the Intel Xeon E5-2690 v4 CPU, the available memory bandwidth is measured by the STREAM benchmark. **Table 3** shows the achievable memory bandwidth of the history-based and event-based algorithms on the CPU and GPU. On problem 1, the history-based algorithm achieves approximately 9 GB/s or roughly 9% of available memory bandwidth on the CPU, while the event-based algorithm achieves roughly 15%. The result on the GPU is similar to that on the CPU. The history-based algorithm achieves 95 GB/s memory bandwidth, whereas the

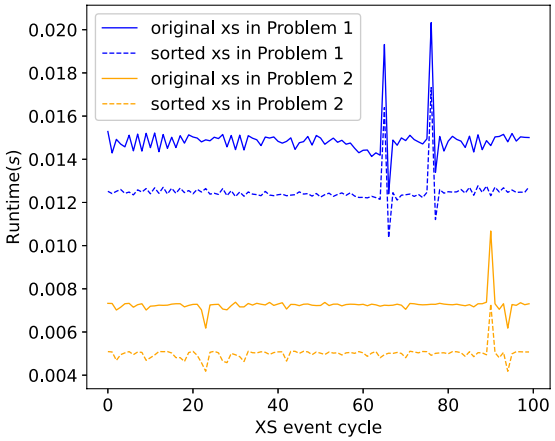

FIGURE 6 | Runtime of original and sorted xs kernel on Problem 1 and Problem 2. The *x*-axis represents the number of xs events in the execution of event-GPU.

event-based algorithm achieves 140 GB/s or roughly 40% of the available memory bandwidth. The results on both architectures demonstrate that despite the poor performance, the event-based algorithm can achieve higher memory bandwidth.

It should be noted that the memory bandwidth cannot be saturated by the MC code due to its random memory access patterns, especially for the history-based algorithm. In most cases, only one item in the cache line can be used, because of which the performance of MC methods is bounded by memory access latency. The ability of GPU to support more concurrent memory requests and to hide memory access latency makes the performance on the GPU better (**Table 3** shows two algorithms are faster on the GPU).

4.3.3 Thread Scaling

Figure 5 shows the parallel efficiency as the thread count (one process) is increased on the CPU. We can see that both the history-based and event-based algorithms achieve over 60% parallel efficiency when using less than 14 threads (within one socket), while the parallel efficiency drops rapidly when the second socket is used. This is because nonunified memory access occurs when the second socket is consumed. Compared to the event-based algorithm, the parallel efficiency of the history-based algorithm drops and becomes slower since more threads are waiting for the atomic operations in the event-based algorithm, as demonstrated in **Section 4.3.1**. We further use two processes with 14 threads per rank and find that the parallel efficiency of the two algorithms increases to more than 50% when scaling to 28 threads. This shows that the MC particle transport code is sensitive to memory access latency and using MPI across sockets reduces the impact of nonunified memory access.

4.3.4 Runtime of Subroutines

Table 4 provides a comparison of time spent on different event subroutines on both CPUs and GPUs. The experiments were carried out using one rank. The process of generating source particles is excluded during the measurement. As observed, xs calculation only occupies less than 8%. This is because in the multigroup MC simulation, macroscopic cross section corresponding to a specific energy group is computed only once and subsequent calls to the function of xs calculation directly return the cached value. The results indicate that calculating cross sections in the multigroup scheme is not as time-consuming as in the continuous-energy scheme. The time spent on xs calculation for problem 2 constitutes a larger fraction than problem 1 on both two architectures due to more isotopes and reactions in problem 2.

4.4 Discussion of Performance on GPUs

The intra-node results provided in **Section 4.3.1** indicate that for the multigroup particle transport code, history-GPU outperforms event-GPU by factors of three to four across a range of the problems considered, whereas previous studies on continuous-energy schemes demonstrate that event-GPU is faster than history-GPU. The reasons for this performance difference mainly contain two factors: memory access pattern and calculation of cross sections. In this section we will design several experiments to answer the following two questions:

1) How does the memory access pattern affect the performance of the history-based and event-based algorithms for multigroup MC transport methods on the GPU?
2) Why is the event-based algorithm for continuous-energy MC transport methods faster than the history-based algorithm on the GPU?

4.4.1 Question 1

On the GPU, a good coalesced access can be achieved when the neighboring threads access neighboring locations in memory. Memory coalescing offers an opportunity to combine multiple memory accesses into a single transaction, greatly improving efficiency.

4.4.1.1 Theoretical Analysis

In the history-based algorithm, contiguously stored particles are assigned to neighboring threads, leading to a good coalesced access. In the event-based algorithm, however, disjoint memory accesses are encountered because of the reallocation of particles to different threads at the conclusion of each event cycle. This prevents the event-based algorithm from utilizing memory coalescing. Therefore, the cost caused by poor memory access patterns may outweigh the benefit of reducing thread divergence.

TABLE 5 | Runtime (*s*) of continuous-energy cross section lookups on CPU and GPU in XSBench.

Algorithm	History-CPU	Event-GPU
Nuclide grid	38.2	1.6
Unionized grid	7.7	0.6
Hash-based	9.4	0.8

TABLE 6 | Percentage (%) of time spent on different subroutines in the Pincell case, which is simulated using event-based implementation in OpenMC with the continuous-energy scheme.

Subroutine	Event-CPU
xs calculation	64.4
Advancing	17.2
Collision	9.9
Crossing surface	8.5

TABLE 7 | Tracking rate (10^4 *n/s*) for problem 1 and problem 2 in the continuous-energy Quicksilver code.

Algorithm	Problem 1	Problem 2
History-CPU	21.0	6.4
History-GPU	40.6	17.2
Event-GPU	61.0	21.1

4.4.1.2 Experimental Analysis

To demonstrate the impact of disjoint memory accesses, we modify the memory access patterns of event-GPU. We sort the particle bank before executing each event kernel so that contiguously stored particles are assigned to neighboring threads. Then we compare the runtime of the original and sorted event kernel. **Figure 6** shows the runtime of the original and sorted xs kernel. The sorted xs kernel achieves lower runtime on both two problems every time the cross sections are calculated, indicating that there is a significant performance loss for the original xs kernel. However, the performance of sorted xs kernel cannot be achieved as sorting the particle bank is very expensive.

4.4.2 Question 2

Numerous studies on continuous-energy MC methods achieve the opposite results to the conclusion of this article that is based on multigroup schemes. The major difference between the continuous-energy and multigroup schemes is the former needs time-consuming energy lookups. Several algorithms for accelerating energy lookups have been proposed, such as the unionized grid method (Leppänen, 2009) and hash-based approach (Brown, 2014; Walsh et al., 2015), which can provide speedups of up to 20x over conventional schemes.

4.4.2.1 Theoretical Analysis

In the history-based algorithm, it would take much more time to calculate cross sections in the continuous-energy scheme than that in the multigroup scheme. Fortunately, there are some existing optimization techniques on the GPU to accelerate the continuous-energy xs event kernel in the event-based algorithm, such as sort event queue by material or energy, and kernel splitting, etc. For the continuous-energy scheme, the speedup of accelerating xs event kernel would exceed the cost caused by poor memory access patterns. Therefore, the event-GPU is faster than history-GPU with the continuous-energy scheme.

4.4.2.2 Experimental Analysis

We will design experiments with XSBench (Tramm et al., 2014), a mini app representing continuous-energy cross section kernel, to investigate the impact of calculations of cross sections. XSBench has already implemented both conventional and optimized energy lookup algorithms. To show the difference in the time of xs calculation between continuous-energy and multigroup MC, we also performed an experiment with OpenMC.

Experiment with XSBench and OpenMC. To verify the theoretical analysis, we first test XSBench on the GPU to show the significant speedup of the continuous-energy xs kernel. **Table 5** shows the runtime of three algorithms implemented in XSBench on the CPU and GPU. The history-based and event-based methods are used on the CPU and GPU respectively. The results are obtained on the same CPU and GPU shown in **Section 4.1**. On the CPU, the number of particles is set to 5×10^5 and the number of lookups to perform per particle is set to 34. On the GPU, the number of lookups is set to 1.7×10^7. It can be seen from **Table 5** that the use of event-based method on the GPU for all these three algorithms achieves more than 10× speedup relative to the history-based method on the CPU.

OpenMC has implemented the event-based algorithm with the continuous-energy scheme. We simulated Pincell case (Horelik et al., 2013) using OpenMC to show the percentage of time spent on different subroutines when using continuous-energy cross sections. **Table 6** shows the results. Compared with the results in **Table 4**, it can be seen that the time percentage needed to compute xs in the continuous-energy scheme is much larger than that in the multigroup scheme.

Experiment with XSBench and Quicksilver. We modify Quicksilver by adding accesses to continuous-energy cross sections for each particle. The modified code is aimed at approximating the program features of the continuous-energy MC code by bridging the major gap between the multigroup scheme and the continuous-energy scheme. For history-CPU and history-GPU, it is only necessary to add relative implementation in XSBench at the location where the distance to the next collision is computed. For event-GPU, an event kernel that performs calculations of continuous-energy cross sections is called.

Table 7 shows the tracking rate of modified algorithms for problem 1 and problem 2. Event-GPU outperforms other algorithms by factors of approximately 1.2–1.5 after adding accesses to continuous-energy cross sections. The superior performance of event-GPU relative to history-based algorithms is dominantly due to two factors. On the one hand, calculating continuous-energy cross sections on the GPU using the event-based method is capable of obtaining a significant speedup as shown in **Table 5**. The speedup of computing continuous-energy cross sections exceeds the cost of disjoint access to particle data. On the other hand, the calculation of continuous-energy cross sections is much more time-consuming than the multigroup scheme, causing more serious thread divergence in history-GPU. This means that continuous-energy event-GPU would reduce much more thread divergence than multigroup, that is to say, the corresponding benefit would be larger.

4.5 Evaluation Summary

We have characterized history-based and event-based algorithms for multigroup MC transport code. Built on the analytics, we make the following summaries.

4.5.1 Algorithm Choice on the CPU and GPU

For multigroup MC transport methods, the event-based algorithm suffers from performance loss caused by extra operations to organize particles, batched atomic operations, and poor particle data locality. Besides, memory access pattern is another factor that weakens the performance of event-GPU. The history-based algorithm outperforms the event-based algorithm on both two architectures in all cases. Thus the history-based algorithm is recommended on both the CPU and GPU for multigroup MC transport methods.

For continuous-energy MC methods, the event-based algorithm is faster on the GPU due to the overwhelming speedup of the cross section kernel. We recommend using the history-based algorithm on the CPU and the event-based algorithm on the GPU.

4.5.2 Optimizations for Multigroup Scheme on the GPU

The history-based algorithm suffers from serious thread divergence on the GPU. One reason is that each particle has a different history length. To reduce branches, we can limit each particle to a prescribed number of collisions. In addition, the proposed optimizations, including event-fixed and event-hybrid, can also be applied to event-based implementation with continuous-energy schemes.

4.5.3 Suitable Architecture for MC Methods

Despite the fact that the event-based algorithm can achieve higher memory bandwidth utilization on both the CPU and GPU, the memory bandwidth cannot be saturated since the majority of the memory access patterns are random. We have characterized the MC transport code as memory latency bound. GPU can hide the latency to access memory by executing many more threads than the device can physically execute simultaneously, which helps GPU provides higher performance. In terms of memory access, a suitable architecture for executing the MC transport code should be a many-core architecture that can support a large number of simultaneous memory requests and hide memory access latency. The more the number of cores, the better the performance. Considering the issue of power consumption, each core requires to be specially designed in accordance with the characteristics of the MC particle transport code. To obtain a hundredfold speedup on a single node, an MC-specified architecture should be designed.

5 CONCLUSION

This article evaluates the performance of the history-based and event-based algorithms for the multigroup MC particle transport on CPUs and GPUs using Quicksilver, a multigroup MC code with only the history-based implementation. In this article, we first implement and optimize the event-based algorithm. The queue-based method is used to implement the event-based algorithm. To improve the performance on the GPU, terminated particles are replaced with new particles so that the number of active particles will remain fixed for most of the time. A hybrid history and event-based method is also implemented. The results show that both two methods benefit the basic event-based algorithm.

Then we used the Coral2 benchmark to evaluate the intra-node performance and other factors of history-based and event-based algorithms. The event-based algorithm suffers from performance loss due to extra operations to reallocate particles, batched atomic operations, and poor particle data locality. We further focus on the performance affecting factors on the GPU and the performance difference between the multigroup and continuous-energy MC code. Different from the results on continuous-energy MC codes, the history-based algorithm on the GPU with the multigroup scheme outperforms the event-based algorithm by a factor of around three. This is because the disjointed memory accesses are encountered in the event-based algorithm, which prevents the kernel from utilizing memory coalescing. The cost of poor memory access patterns outweighs the benefit of reducing thread divergence. For continuous-energy MC code, the speedup of accelerating xs event kernel would exceed the cost by poor memory access patterns, thus the event-based algorithm for the continuous-energy MC code obtains a superior performance.

The evaluation results build on our analytics. For multigroup MC codes, despite the poor performance, the event-based algorithm can achieve higher memory bandwidth utilization on both CPU and GPU. Compared with the CPU, the GPU is more suitable for executing the MC transport code due to its capability of supporting a large number of simultaneous memory requests and hiding memory access latency. In future research, we plan to optimize the MC transport code on modern architectures and develop MC-specified architecture.

DATA AVAILABILITY STATEMENT

Publicly available datasets were analyzed in this study. This data can be found here: https://github.com/LLNL/Quicksilver/tree/master/Examples/CORAL2_Benchmark.

AUTHOR CONTRIBUTIONS

DM designed the research. TL and JL guided the research. DM drafted the manuscript. BY helped perform experiments and organize the manuscript. QZ helped revise the paper. DM revised and finalized the paper.

FUNDING

This research work was supported in part by the National Key Research and Development Program of China (2017YFB0202104 and 2018YFB0204301).

REFERENCES

Bergmann, R. M., and Vujić, J. L. (2015). Algorithmic Choices in WARP - A Framework for Continuous Energy Monte Carlo Neutron Transport in General 3D Geometries on GPUs. *Ann. Nucl. Energ.* 77, 176–193. doi:10.1016/j.anucene.2014.10.039

Bleile, R., Brantley, P., Richards, D., Dawson, S., McKinley, M. S., and O'Brien, M. (2019). "Thin-threads: An Approach for History-Based Monte Carlo on Gpus," in 2019 International Conference on High Performance Computing & Simulation (HPCS), Dublin, Ireland (Tentative), June 15–19, 2019 (IEEE), 273–280. doi:10.1109/HPCS48598.2019.9188080

Brown, F. B., and Martin, W. R. (1984). Monte Carlo methods for radiation transport analysis on vector computers. *Progress in Nuclear Energy* 14 (3). (Elsevier), 269–299. doi:10.1016/0149-1970(84)90024-6

Brown, F. B. (2014). New Hash-Based Energy Lookup Algorithm for Monte Carlo Codes. Technical Report. Los Alamos, NM (United States). Los Alamos National Lab.(LANL).

Choi, N., Kim, K. M., and Joo, H. G. (2019). "Initial Development of Pragma–A Gpu-Based Continuous Energy Monte Carlo Code for Practical Applications," in Transactions of the Korean Nuclear Society Autumn Meeting, Goyang, Korea, October 24–25, 2019 (Goyang, Korea), 24–25.

Cullen, D. E., Clouse, C. J., Procassini, R., and Little, R. C. (2003). Static and Dynamic Criticality: Are They Different?. Technical Report.

Du, X., Liu, T., Ji, W., Xu, X. G., and Brown, F. B. (2013). "Evaluation of Vectorized Monte Carlo Algorithms on Gpus for a Neutron Eigenvalue Problem," in Proceedings of International Conference on Mathematics and Computational Methods Applied to Nuclear Science & Engineering, Sun Valley, Idaho, May 5–9, 2014 (Sun Valley, Idaho, USA), 2513–2522.

Forster, R., and Godfrey, T. (1985). Mcnp-a General Monte Carlo Code for Neutron and Photon Transport 77, 33–55. doi:10.1007/BFb0049033

Hamilton, S. P., and Evans, T. M. (2019). Continuous-energy Monte Carlo Neutron Transport on Gpus in the Shift Code. *Ann. Nucl. Energ.* 128, 236–247. doi:10.1016/j.anucene.2019.01.012

Hamilton, S. P., Slattery, S. R., and Evans, T. M. (2018). Multigroup Monte Carlo on Gpus: Comparison of History-And Event-Based Algorithms. *Ann. Nucl. Energ.* 113, 506–518. doi:10.1016/j.anucene.2017.11.032

Horelik, N., Herman, B., Forget, B., and Smith, K. (2013). "Benchmark for Evaluation and Validation of Reactor Simulations (Beavrs), V1. 0.1," in Proceedings of International Conference on Mathematics and Computational Methods Applied to Nuclear Science and Engineering, Sun Valley, Idaho, May 5–9, 2014. 5–9

Leppänen, J. (2009). Two Practical Methods for Unionized Energy Grid Construction in Continuous-Energy Monte Carlo Neutron Transport Calculation. *Ann. Nucl. Energ.* 36, 878–885. doi:10.1016/j.anucene.2009.03.019

Li, H., Li, K., An, J., and Li, K. (2017). Msgd: A Novel Matrix Factorization Approach for Large-Scale Collaborative Filtering Recommender Systems on Gpus. *IEEE Trans. Parallel Distributed Syst.* 29, 1530–1544. doi:10.1109/TPDS.2017.2718515

Liu, T., Du, X., Wei, J., Xu, X. G., and Brown, F. B. (2014). "A Comparative Study of History-Based versus Vectorized Monte Carlo Methods in the Gpu/cuda Environment for a Simple Neutron Eigenvalue Problem," in SNA + MC 2013 - Joint International Conference on Supercomputing in Nuclear Applications + Monte Carlo, Paris, October 27–31, 2013. doi:10.1051/snamc/201404206

[Dataset] LLNL (2017). Mercury. Available at: https://wci.llnl.gov/simulation/computer-codes/mercury (Accessed February 18, 2020).

Metropolis, N., and Ulam, S. (1949). The Monte Carlo Method. *J. Am. Stat. Assoc.* 44, 335–341. doi:10.1080/01621459.1949.10483310

Ozog, D., Malony, A. D., and Siegel, A. R. (2015). "A Performance Analysis of Simd Algorithms for Monte Carlo Simulations of Nuclear Reactor Cores," in 2015 IEEE International Parallel and Distributed Processing Symposium, Hyderabad, India, May 25–29, 2015 (IEEE), 733–742. doi:10.1109/IPDPS.2015.105

Pandya, T. M., Johnson, S. R., Evans, T. M., Davidson, G. G., Hamilton, S. P., and Godfrey, A. T. (2016). Implementation, Capabilities, and Benchmarking of Shift, a Massively Parallel Monte Carlo Radiation Transport Code. *J. Comput. Phys.* 308, 239–272. doi:10.1016/j.jcp.2015.12.037

Richards, D. F., Bleile, R. C., Brantley, P. S., Dawson, S. A., McKinley, M. S., and O'Brien, M. J. (2017). "Quicksilver: a Proxy App for the Monte Carlo Transport Code Mercury," in 2017 IEEE International Conference on Cluster Computing (CLUSTER), Hawaii, United States, September 5–8, 2017 (IEEE), 866–873. doi:10.1109/CLUSTER.2017.121

Romano, P. K., and Forget, B. (2013). The Openmc Monte Carlo Particle Transport Code. *Ann. Nucl. Energ.* 51, 274–281. doi:10.1016/j.anucene.2012.06.040

Romano, P. K., and Siegel, A. R. (2017). Limits on the Efficiency of Event-Based Algorithms for Monte Carlo Neutron Transport. *Nucl. Eng. Techn.* 49, 1165–1171. doi:10.1016/j.net.2017.06.006

Tramm, J. R., Siegel, A. R., Islam, T., and Schulz, M. (2014). Xsbench-the Development and Verification of a Performance Abstraction for Monte Carlo Reactor Analysis. PHYSOR 2014 - The Role of Reactor Physics Toward a Sustainable Future, The Westin Miyako, Kyoto, Japan, September 28, 2014.

Walsh, J. A., Romano, P. K., Forget, B., and Smith, K. S. (2015). Optimizations of the Energy Grid Search Algorithm in Continuous-Energy Monte Carlo Particle Transport Codes. *Comput. Phys. Commun.* 196, 134–142. doi:10.1016/j.cpc.2015.05.025

Yan, D., Wang, W., and Chu, X. (2020). "Optimizing Batched Winograd Convolution on Gpus," in Proceedings of the 25th ACM SIGPLAN Symposium on Principles and Practice of Parallel Programming, San Diego, California, February 22–26, 2020, 32–44. doi:10.1145/3332466.3374520

Conflict of Interest: The authors declare that the research was conducted in the absence of any commercial or financial relationships that could be construed as a potential conflict of interest.

frontiers in Energy Research

ORIGINAL RESEARCH
published: 30 July 2021
doi: 10.3389/fenrg.2021.702952

Feasibility Study for the Fast Periodic Pulsed Reactor with UO_2 Fuel

Liang Zhang[1†], *Xinbiao Jiang*[1*†], *Xinyi Zhang*[1,2†], *Tengyue Ma*[1,2], *Sen Chen*[1], *Lipeng Wang*[1], *Da Li*[1] *and Lixin Chen*[1]

[1]State Key Laboratory of Intense Pulsed Radiation Simulation and Effect (Northwest Institute of Nuclear Technology), Xi'an, China, [2]Xi'an High Technology Institute, Xi'an, China

In order to study the feasibility of the fast periodic pulsed reactor with UO_2 as fuel (abbreviated as FPPRU), the core models with different load schemes are designed. Neutronic characteristics of two typical design schemes are compared, and the better design scheme is determined. The critical search method is established for analyzing the reactor dynamics. Furthermore, the theoretical estimation formulas are derived to study the factors affecting the reactor dynamics clearly and intuitively. The reactor dynamics of the fast periodic pulsed reactor with UO_2 and PuO_2 as fuel are compared. The thermal hydraulic characteristic of FPPRU is studied with the sub-channel model. The results show that the design scheme of the FPPRU meets the demand of neutronics and thermal hydraulics safety. Meanwhile, the pulse parameter quality of the FPPRU with UO_2 as fuel is not as good as that of IBR-2 with PuO_2 as fuel.

Keywords: pulse parameters, periodic, pulsed reactor, UO_2, feasibility

OPEN ACCESS

Edited by:
Qian Zhang,
Harbin Engineering University, China

Reviewed by:
Peiwei Sun,
Xi'an Jiaotong University, China
Quan Gan,
Hefei Institutes of Physical Science (CAS), China
Jinsen Xie,
University of South China, China

****Correspondence:***
Xinbiao Jiang
zhangliang9@nint.ac.cn

†These authors have contributed equally to this work and share first authorship

Specialty section:
This article was submitted to Nuclear Energy, a section of the journal Frontiers in Energy Research

Received: *30 April 2021*
Accepted: *25 June 2021*
Published: *30 July 2021*

Citation:
Zhang L, Jiang X, Zhang X, Ma T, Chen S, Wang L, Li D and Chen L (2021) Feasibility Study for the Fast Periodic Pulsed Reactor with UO_2 Fuel. Front. Energy Res. 9:702952. doi: 10.3389/fenrg.2021.702952

INTRODUCTION

The fast periodic pulsed reactor uses rotating reflectors to introduce periodic reactivity, making the core generate power pulses at a certain frequency. The fast periodic pulsed reactor IBR-2 had been built in 1984 in the Joint Institute for Nuclear Research of Russia and had retired in 2006. And then the modernized reactor IBR-2M was designed and built and was put into use in 2011 (Dragunov et al., 2012). After successful operation for as long as 37 years, the fast periodic pulsed reactor IBR-2/IBR-2M has been proven to be safe. IBR-2/IBR-2M could provide pulsed neutron flux with narrow half-width and high intensity. Lots of research has been carried out in a wide range of scientific fields, including condensed physics, biology, chemistry, material, geophysics, new superconductivity, and heavy metal nuclear database (Marina, 2011; Ata-Allah et al., 2016; Avdeev et al., 2019; Badawy et al., 2020; Golovin et al., 2020; Turchenko et al., 2020).

So far, lots of studies are performed on many aspects of IBR-2/IBR-2M, such as operation lifetime, neutron flux, reactor dynamics, and reactor safety. For example, in order to increase the operation lifetime of IBR-2M, in 2020, Ananiev studied the way to optimize the reactor fuel run by reshuffling fuel assemblies, giving more uniform fuel burn up and increasing the core lifetime by almost 1/4 (Ananiev et al., 2020). For improving the neutron flux, in 2018, Ananiev considered the neutronic aspect of the IBR-2 reactor optimization and studied the way to increase the thermal neutron flux theoretically (Ananiev et al., 2019). In 2013, Kulikov studied the way to optimize the cold-neutron yield and found the best material for use in IBR-2M cold moderators (Kulikov and Shabalin, 2013). The reactor dynamics plays a very important role in the operation and safety of this kind of reactor. In 2017, Pepelyshev analyzed the transient processes caused by intentional periodic oscillations of the reactivity and investigated the fast feedback parameters of IBR-2M (Pepelyshev et al., 2017). In 2015, Pepelyshev simulated the transitional processes at a wide range of reactivity change and power

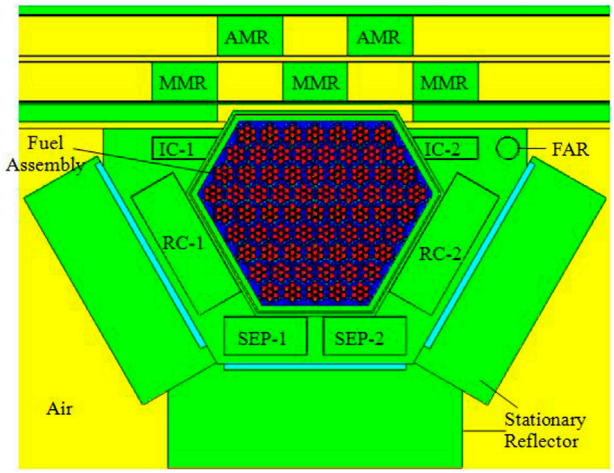

FIGURE 1 | IBR-2M core.

change, and the result is in good accordance with the detected one (Pepelyshev et al., 2015). In 2010, Chan and Pepelyshev studied the IBR-2 dynamics with power shedding (Chan and Pepelyshev, 2010). In 2008, Chan and Pepelyshev studied the power feedback dynamics taking account of slow components (Chan and Pepelyshev, 2008). In 2006, Pepelyshev analyzed the power pulse shape measured over the entire dynamic range of neutron flux variation and found out how to obtain best approximation to the experimental data (Pepelyshev and Popov, 2006a). And Pepelyshev successfully used the dynamical method to determine the reactivity effects of two types of moving reflectors in the pulsed regime of IBR-2 reactor operating at power (Pepelyshev and Popov, 2006b). For the modernization from IBR-2 to IBR-2M, Dragunov

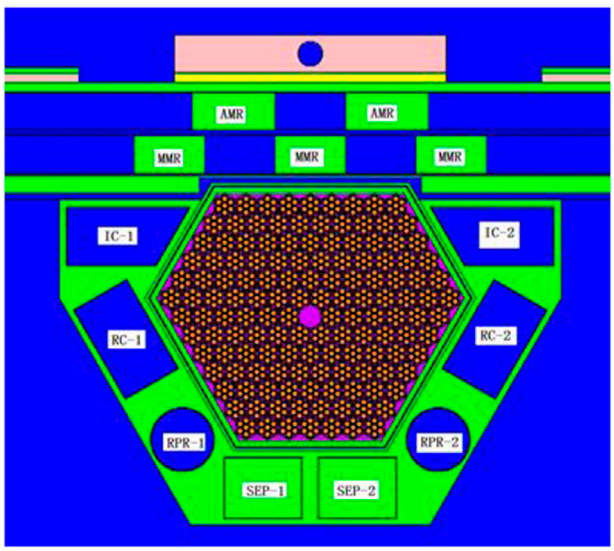

FIGURE 2 | Design scheme of FPPRU1.

introduced the project modernizing the reactor and the technical characteristics before and after modernization (Dragunov et al., 2012). For the safety of IBR-2, in 2010, Pepelyshev discussed the safety and reliability of the reactor and showed how a series of safety problems related to IBR-2 reactor physics are resolved (Pepelyshev et al., 2010).

Till now, almost all the research studies aimed at the IBR-2 type reactor with PuO_2 as fuel. As UO_2 fuel is very widely used in nuclear reactors, the use of UO_2 may promote the development of the fast periodic pulsed reactor. The study on the feasibility of such reactor using UO_2 fuel is very meaningful. The fast periodic pulsed reactor with UO_2 fuel (abbreviated as FPPRU) is designed in this article. And the feasibility is studied from the view of neutronics, dynamics, thermal hydraulics, and so on.

METHODS AND RESULTS

Conceptual Design of the FPPRU

Brief Description of IBR-2M

As the conceptual design of the fast periodic pulsed reactor with UO_2 as fuel is on the basis of IBR-2M, the structure of IBR-2M is briefly introduced here. As shown in **Figure 1**, the IBR-2M core is of an irregular hexagonal shape consisting of 69 PuO_2 fuel assemblies and is cooled by liquid sodium. Outside the core, there are two kinds of reflectors. One is the stationary reflector and the other is the moving reflector, which consists of one main moving reflector (MMR in **Figure 1**) and one auxiliary moving reflector (AMR in **Figure 1**). Seven control rods are used to regulate the reactivity, including two regulating rods (IC-1 and IC-2 in **Figure 1**), two compensating rods (RC-1 and RC-2 in **Figure 1**), two safety rods (SEP-1 and SEP-2 in **Figure 1**), and one fine adjusting rod (FAR in **Figure 1**). The material of all the reflectors and control rods is stainless steel. MMR and AMR are located on one side, opposite the core. The unique feature of the reactor is that it controls the periodic change of reactivity through the movable reflectors MMR and AMR outside the reactor and generates continuous pulses at a certain frequency. The rotating speeds of MMR and AMR are 600r/min and 300r/min, respectively, and the rotating directions are opposite. At a period of 200 ms, the two reflectors pass simultaneously opposite the core. At the very moment, the combination of the two reflectors could cover the neutron flight direction toward the core's periphery, and the core changes from deep subcritical state to transient supercritical state, generating continuous power pulses at a frequency of 5 Hz. The average thermal power and peak pulse power are 2 and 1500 MW, respectively.

Design Schemes of the FPPRU

In this article, different conceptual design schemes for the fast periodic pulsed reactor with UO_2 as fuel (FPPRU) are made. And two schemes are analyzed in detail. One is named as FPPRU1, whose reflectors and control rods are made of stainless steel, the same as IBR-2M. The other is named as FPPRU2, whose reflectors use beryllium, which could effectively reduce the number of UO_2 fuel assemblies. The material of FPPRU2

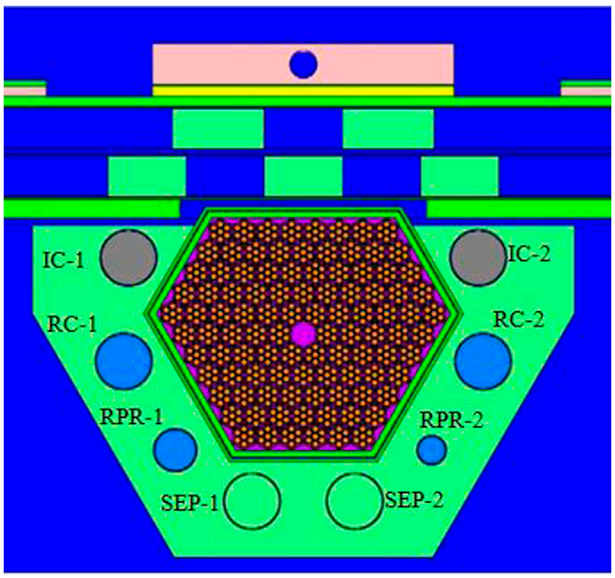

FIGURE 3 | Design scheme of FPPRU2.

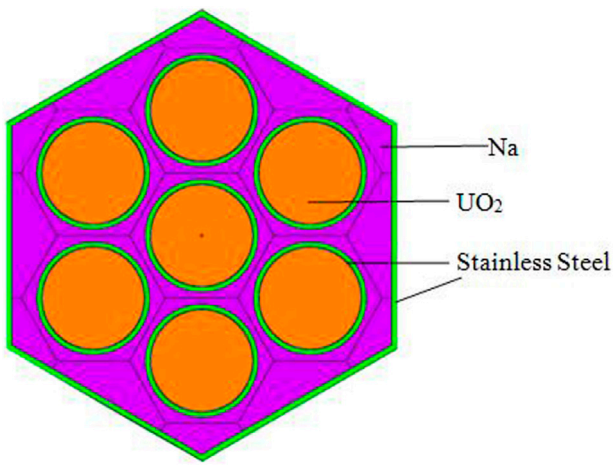

FIGURE 4 | Structure of the fuel assembly of FPPRU1 and FPPRU2.

control rods is B_4C. FPPRU1 and FPPRU2 are shown in **Figures 2**, **3**, respectively. In **Figure 2** and **Figure 3**, from the left to the right is the direction of the X-axis, and from the bottom to the top is the direction of the Y-axis. The coordinate of the center of the core on the X-axis is 0. The structure of the fuel assembly of FPPRU1 and FPPRU2 is the same, as shown in **Figure 4**. It could be seen that, compared to IBR-2M, more UO_2 fuel assemblies are needed to reach criticality for FPPRU. The main reason is that the critical mass of U-235 reactor is greater than that of Pu-239 reactor.

FPPRU1 consists of 139 hexagonal assemblies, including 138 UO_2 fuel assemblies and one neutron source assembly located in the center of the core, as shown in **Figure 2**. The reflector of FPPRU1 contains the stationary reflector and the moving reflector. Inside the stationary reflector there are eight control rods for regulating the reactivity, including two regulating rods (IC-1 and IC-2 in **Figure 2**), two cubic compensating rods (RC-1 and RC-2 in **Figure 2**), two cylindrical compensating rods (RPR-1 and RPR-2 in **Figure 2**), and two safety rods (SEP-1 and SEP-2 in **Figure 2**). The moving reflector consists of one main moving reflector MMR and one auxiliary moving reflector AMR, which are both arranged opposite one side of the core, as shown in **Figure 2**. The material of both reflectors and control rods is stainless steel. The periodic reactivity is accomplished by the combination of the moving reflector MMR and auxiliary moving reflector AMR (MMR and AMR in **Figure 2**). The rotation speeds of MMR and AMR are 600 r/min and 300 r/min, respectively. For each period (T = 200 ms), when AMR and MMR arrive at the position in **Figure 2**, the two reflectors completely block the leakage path of neutrons outward, and the reactivity reaches the maximum. After AMR and MMR move away from the position in **Figure 2**, the reactivity gradually decreases and finally stabilizes to the minimum ρ_b, forming the change of reactivity and power shown in **Figure 5**.

As shown in **Figure 5**, under the stable operation of the fast periodic pulsed reactor, the reactivity $\rho(t)$ and power $P(t)$ vary periodically at a certain frequency. T is the period, and each period could be divided into two phases: pulse phase and background phase. For the first period from time 0~T, OAB (from time 0~t_b) stands for the pulse phase and BC (from time t_b~T) stands for the background phase. t_h is the half-width of the pulse. ρ_{max} is the maximum reactivity, and ρ_b is the background reactivity. P_{max} is the maximum power, and P_b is the background power. There is little change in the reactivity within BC, and ρ_b could be approximated as a constant. In one period, the integral of power from 0~T and from t_b ~T are the total energy E_t and the background energy E_b, respectively. The integral of power from 0 ~ t_b is the pulse energy E_p, and $E_p = E_t - E_b$.

FPPRU2 consists of 101 hexagonal assemblies, including 100 UO_2 fuel assemblies and one neutron source assembly located in the center of the core. All the assemblies are arranged in a double-layer stainless steel barrel. The reflector of FPPRU contains the stationary reflector and the moving reflector. Inside the stationary reflector, there are eight control rods for regulating the reactivity, including two regulating rods (IC-1 and IC-2 in **Figure 3**), four compensating rods (RC-1, RC-2, RPR-1, and RPR-2 in **Figure 3**), and two safety rods (SEP-1 and SEP-2 in **Figure 3**). The moving reflector consists of one main moving reflector MMR and one auxiliary moving reflector AMR (MMR and AMR in **Figure 3**), which are both arranged opposite to one side of the core, as shown in **Figure 3**. FPPRU2 produces power pulses in the same way with FPPRU1. Different from FPPRU1, the materials of the reflectors and control rods of FPPRU2 are beryllium and B_4C, respectively.

As shown in **Figure 4**, each fuel assembly consists of seven fuel elements and 0.5 mm thick outer stainless steel cladding. The outer radius of the fuel assembly is 3.464 cm. The distance between adjacent fuel elements in the assembly is 1.11 cm. Each fuel element is made up of UO_2, He gas gap, and

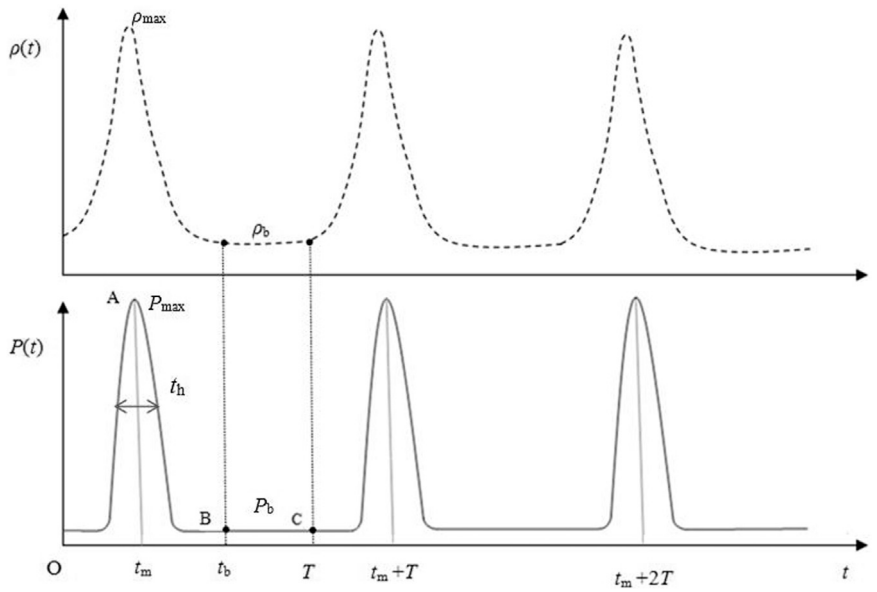

FIGURE 5 | Power and reactivity change of the fast periodic pulsed reactor.

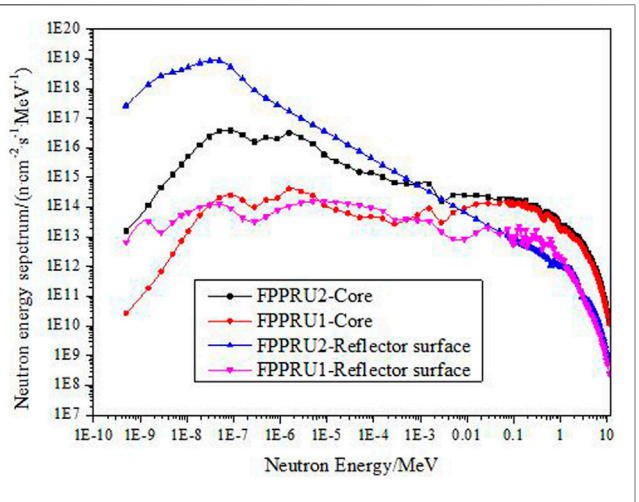

FIGURE 6 | Maximum effective multiplication factor k_{eff} vs. the enrichment of U-235.

stainless steel cladding from inside to outside, and the outer radius are 0.45, 0.46, and 0.50 cm, respectively. The length of the UO_2 active zone of the fuel element is 50 cm. Up and down the active zone are both the axial reflectors with 10 cm length. The materials of the axial reflectors of FPPRU1 and FPPRU2 are stainless steel and beryllium, respectively.

Calculation of Neutronic Parameters and Determination of Core Design Schemes

The neutronic parameters of FPPRU1 and FPPRU2, including the criticality, dynamic parameters, neutron energy spectrum, and power distribution, are calculated in the paper using the MCNP code. And based on the neutronic characteristics, the core design scheme is determined.

Criticality

In the design of the FPPRU, considering the burn up during the reactor lifetime, the uncertainty of U-235 enrichment, and the impurity of the reactor reflector, the reserved reactivity ρ_r should not be less than about 45 mk (1mk = 0.001), ensuring the long-term operation for the reactor. **Figure 6** shows the relationship between the maximum effective multiplication factor k_{eff} vs. the enrichment of U-235 for several core design schemes.

As shown in **Figure 6**, for FPPRU1, when U-235 enrichment is 75%, the reserved reactivity ρ_r ($\rho_r = (k_{eff}-1)/k_{eff}$) is 47.69 mk. For FPPRU2, when U-235 enrichment is 77%, the reserved reactivity ρ_r is 44.87 mk. These two core loading schemes basically meet the requirement of reserved reactivity and can reach a shutdown margin over −25 mk (−28.63 mk and −27.05 mk for FPPRU1 and FPPRU2, respectively).

The maximum effective multiplication factor k_{eff} of IBR-69UO_2 is also given in **Figure 6**. IBR-69UO_2 is the reactor that only replaces the PuO_2 fuel of the IBR-2M reactor with the UO_2 fuel. The k_{eff} of IBR-69UO_2 clearly shows that more fuel assemblies must be used to reach criticality if UO_2 is used as fuel.

Dynamic Parameters

The effective delayed neutron fraction β_{eff} and neutron generation time Λ play very important roles in reactor dynamics. For the fast periodic pulsed reactor, these two dynamic parameters have great influence on the dynamics under periodic pulse operation. β_{eff} and Λ are calculated for several reactors with different reflector materials using the MCNP code, as shown in **Table 1**.

TABLE 1 | Calculating results of the effective delayed neutron fraction β_{eff} and neutron generation time Λ.

Reactor	Fuel	Fuel assembly number	Reflector material	Λ/ns	$\beta_{eff}/10^{-5}$
IBR-2M	95% PuO_2	69	Stainless steel	65 Pepelyshev and Popov (2006a)	216 Pepelyshev and Popov (2006a)
			Beryllium	327	203
FPPRU1	75% UO_2	138	Stainless steel	114.9	728
FPPRU2	77% UO_2	100	Beryllium	1,477	736

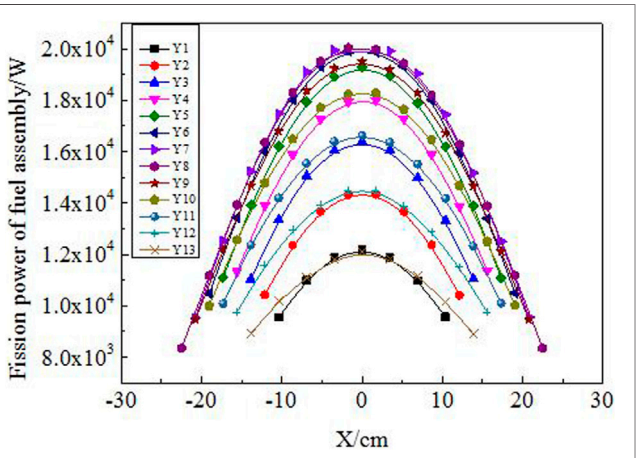

FIGURE 7 | Neutron energy spectrum.

The IBR-2M reactor uses PuO_2 as fuel, and the reflector is made of stainless steel. The neutron generation time is 65 ns, and the half-width of the pulse is 245 μs (Pepelyshev and Popov, 2006a). In general, the smaller the neutron generation time, the narrower the half-width of the pulse. Since the design is intended to achieve a narrower half-width, it is hoped that the neutron generation time could be as small as possible. As could be seen from **Table 1**, if the material of the IBR-2M reflector is replaced with beryllium, the neutron generation time Λ will increase significantly to 327 ns. Compared with stainless steel, beryllium is a much better material for slowing down neutrons. More fast neutrons will be moderated to thermal neutrons in the reflector and would be reflected back to the core, which will both make the neutrons disappear much slower and increase the neutron generation time Λ significantly. For the same reason, the FPPRU2 reactor using beryllium as the reflector material requires fewer fuel assemblies to reach criticality than FPPRU1 using stainless steel as the reflector material. The neutron generation time Λ of FPPRU2 is as high as 1,477 ns, much higher than 114.9 ns of FPPRU2. Therefore, from the view of the half-width of the pulse, FPPRU1 with a stainless steel reflector would be better. It can also be seen from **Table 1** that the effective delayed neutron fraction β_{eff} of FPPRU1 and FPPRU2 with UO_2 as fuel are similar, and are both much higher than that of IBR-2M with PuO_2 as fuel. It is mainly due to that more delayed neutrons are released in the fission of U-235. In addition, the difference between energy spectrums of IBR-2 and FPPRU also has some influence.

Neutron Energy Spectrum

Figure 7 shows the neutron energy spectrum in the core and on the stationary reflector surface of FPPRU1 and FPPRU2 at average power 2 MW. **Table 2** shows the neutron flux density and the average neutron energy in the core and on the stationary reflector surface. The neutrons are divided into four groups by energy, that is, the thermal group (0–0.414 eV), the epithermal group (0.414 eV–10 keV), the fast group one (0.01–0.1 MeV), and the fast group two (0.1–10 MeV). The mean neutron energy in the cores of FPPRU1 and FPPRU2 are 0.9243 and 0.9186 MeV, respectively. The average neutron energy on the stationary reflector surface of FPPRU1 and FPPRU2 are 0.5505 and 0.3596 MeV, respectively. The neutron energy spectrum on the surface of FPPRU2 reflector is softer than that on the surface of FPPRU1. It means that FPPRU2 is inferior to obtain a faster neutron beam. The main reason is that much more neutrons are moderated by beryllium in FPPRU2. As faster neutron beam is expected to be achieved in the design, from the view of the neutron energy spectrum, the FPPRU1 core scheme is preferred in this article. In addition, the fast neutron flux density (>0.01 MeV) in the core and on the stationary reflector surface of FPPRU1 are 8.88×10^{13} n/(cm^2·s) and 8.10×10^{12} n/(cm^2·s), respectively.

Power Distribution

The fission power distribution of FPPRU1 and FPPRU2 fuel assemblies at average power 2 MW is shown in **Figures 8**, **9**, respectively. From the bottom to the top of FPPRU1 core (**Figure 2**), Y1,Y2, . . ., Y13 in **Figure 8** stand for the first layer, second layer, . . . thirteenth layer fuel assemblies, respectively. And from the bottom to the top of FPPRU2 core (**Figure 3**), Y1,Y2, . . ., Y11 in **Figure 9** stand for the first layer, second layer, . . . eleventh layer fuel assemblies, respectively. X in **Figures 8**, **9** represents the coordinate of each fuel assembly in the direction of the X axis, and the coordinate of the center of the core on the X axis is 0.

From **Figures 8**, **9** it could be seen that the closer the fuel assembly to the center of FPPRU1 core, the greater the fission power basically. However, for FPPRU2, the fission power of Y1 layer fuel assemblies is the largest. As the safety rods of FRRPU2 (SEP-1 and SEP-2 in **Figure 3**) are at the top in the calculation, downside the Y1 layer fuel assemblies are all beryllium reflector. Beryllium moderates neutrons and reflects neutrons back to the core. The thermal neutrons are much more in the Y1 layer fuel assemblies, and thus, the fission power is higher than that of other layer fuel assemblies. It could also be seen from **Figure 9** that the fission power of FPPRU2

TABLE 2 | Neutron flux density and average neutron energy for FPPRU1 and FPPRU2.

Reactor	Counting range	Neutron flux density/(n·cm^{-2}·s^{-1})				Average energy/MeV
		0–0.414 eV	0.414 eV–10 keV	0.01–0.1 MeV	0.1–10 MeV	
FPPRU1	Core	5.7608×10^{7}	6.6636×10^{11}	1.1875×10^{13}	7.6966×10^{13}	0.9243
	Stationary reflector surface	6.4718×10^{7}	1.5492×10^{11}	1.2734×10^{12}	6.8292×10^{12}	0.5505
FPPRU2	Core	9.1157×10^{9}	3.5443×10^{12}	1.7740×10^{13}	9.8845×10^{13}	0.9186
	Stationary reflector surface	1.0545×10^{12}	4.0293×10^{12}	1.5076×10^{12}	3.3023×10^{12}	0.3596

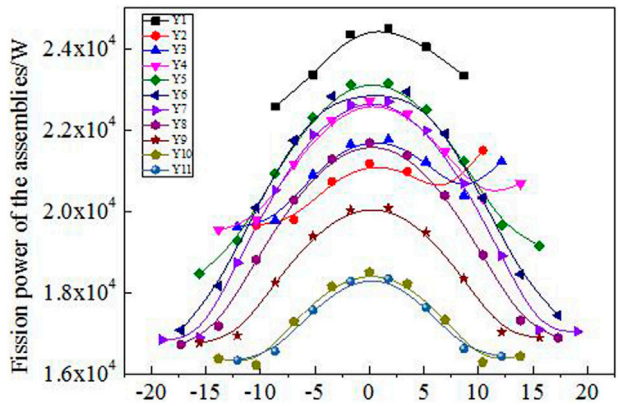

FIGURE 8 | Fission power distribution of FPPRU1.

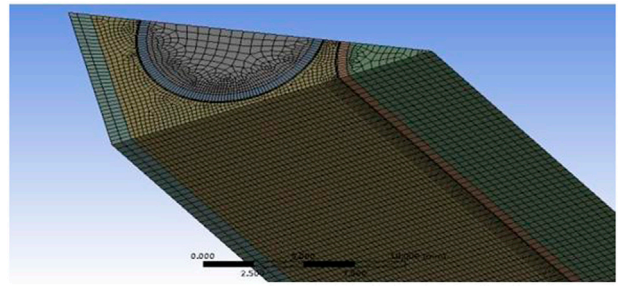

FIGURE 9 | Fission power distribution of FPPRU2.

Y1,Y2,Y3, and Y4 layers is not symmetric. The reason is that the size of the two compensating rods RPR-1 and RPR-2 in **Figure 3** is not the same in the design.

The fission energy deposition and gamma energy deposition in the core components, including the auxiliary moving reflector, the control rod, and the fuel assembly, are shown in **Table 3**. According to **Table 3**, at average power 2 MW, the maximum energy deposition in the fuel assembly of FPPRU1 and FPPRU2 is 19.65 and 22.86 kW, respectively. The nonuniformity coefficient of FPPRU1 radial power is 1.383, which is larger than 1.225 of FPPRU2. The reason is that FPPRU2 reflector (beryllium) could moderate neutrons much better and the power of the outer fuel assemblies is relatively higher.

The energy deposition in the stationary beryllium reflector of FPPRU2 is 12 kW, which is 3.72 times as much as that in the stationary stainless steel reflector of FPPRU1. The material of FPPRU1 and FPPRU2 control rods is stainless steel and B_4C, respectively. Among the eight control rods of FPPRU2, the compensating rod (RC-1 or RC-2 in **Figure 3**) has the largest energy deposition 2.48 kW. For FPPRU1, the compensating rod (RC-1 or RC-2 in **Figure 2**) also has the largest energy deposition, and the value is 0.71 kW. Therefore, under the condition of natural air cooling, the thermal safety of the stationary reflector of FPPRU1 is better.

Determination of Core Design Schemes

Compared with the FPPRU1 design scheme, the advantages of FPPRU2 design scheme are that less fuel assemblies are needed to reach criticality, and the nonuniformity coefficient of the radial power is smaller. However, the disadvantages of FPPRU2 are more obvious. The neutron generation time of FPPRU2 is too long to achieve ideal neutron pulse with narrow half-width. The neutron energy spectrum of FPPRU2 is softer, not beneficial for producing more fast neutrons. The energy deposition in the stationary reflector is much more, not conductive to heat dissipation. As the purpose of the design is to achieve narrower half-width pulse and harder neutron energy

TABLE 3 | Energy deposition of core components for FPPRU1 and FPPRU2.

Core components	FPPRU1		FPPRU2	
	Fission energy deposition/W	Gamma energy deposition/W	Fission energy deposition/W	Gamma energy deposition/W
Stationary reflector	7.1943×10^{2}	2.5041×10^{3}	8.0620×10^{3}	3.9391×10^{3}
Main moving reflector (MMR)	1.7433×10^{2}	1.4613×10^{3}	1.3332×10^{3}	5.0261×10^{2}
Auxiliary moving reflector (AMR)	1.2036×10^{2}	1.3960×10^{3}	8.9480×10^{2}	4.2971×10^{2}
Control rods (RC-1 or RC-2)	9.5287×10^{1}	6.1124×10^{2}	2.2962×10^{3}	1.8339×10^{2}
Fuel assembly (maximum)	1.8756×10^{4}	9.0146×10^{2}	2.2761×10^{4}	1.0494×10^{3}
Fuel assembly (minimum)	7.8222×10^{3}	3.2879×10^{2}	1.5172×10^{4}	5.9180×10^{2}

spectrum, the design scheme of FPPRU1 is selected. The cost is that more fuel assemblies are needed to reach criticality and the nonuniformity coefficient of the radial power is relatively high.

Reactor Dynamics

Reactor dynamics plays a very important role for the fast periodic pulsed reactor. So far, lots of research have been performed on the dynamics for the IBR-2 type reactor (Pepelyshev and Popov, 2006a; Pepelyshev and Popov, 2006b; Chan and Pepelyshev, 2008; Chan and Pepelyshev, 2010; Pepelyshev et al., 2015; Pepelyshev et al., 2017; Brezhnev et al., 2017). In this article, the critical search method for studying reactor dynamics is established based on the basic characteristics of the fast periodic pulsed reactor. Furthermore, the theoretical estimation formula which could show the difference between FPPRU1 dynamics and IBR-2 dynamics clearly and intuitively is also derived. And the pulse parameters of FPPRU1 and IBR-2 are compared using the critical search method and the theoretical estimation formula.

Critical Search Method

The critical search method is based on the point kinetic model:

$$\frac{\mathrm{d}P(t)}{\mathrm{d}t} = \frac{\rho(t) - \beta_{\mathrm{eff}}}{\Lambda} P(t) + \sum_{i=1}^{6} \lambda_i C_i(t), \tag{1}$$

$$\frac{\mathrm{d}C_i(t)}{\mathrm{d}t} = \frac{\beta_{\mathrm{eff}} \cdot \alpha_i}{\Lambda} P(t) - \lambda_i C_i(t). \tag{2}$$

In **Eqs. 1**, **2**, $\alpha_i = \beta_{\mathrm{eff},i}/\beta_{\mathrm{eff}}$. $\rho(t)$ and $P(t)$ are the reactivity and power in **Figure 5**, respectively. β_{eff} and $\beta_{\mathrm{eff},i}$ are the total and the i^{th}-group effective delayed neutron fraction, respectively. Λ is the neutron generation time and $C_i(t)$ is the density of the i^{th}-group delayed neutron precursor concentration.

From **Eqs. 1**, **2**, $P(t)$ would be obtained if $\rho(t)$ is known. By changing the position of MMR and AMR gradually, the relative change of reactivity $\rho(t)$ could be obtained by calculation or by experiment. Thus, the shape of reactivity $\rho(t)$is known. The shape function is defined as $f(t)$, and then the relationship between $\rho(t)$ and $f(t)$ is as follows:

$$\rho(t) = f(t) + D. \tag{3}$$

In **Eq. 3**, D is a constant. It is known that when the fast periodic pulsed reactor is under the stable operation, the peak power of every period is approximately equal, as shown in **Figure 5**. By gradually changing the value of D and solving **Eqs. 1**, **2** until every peak power is found to approach the same, D could be determined. In the calculation, if the peak power of the 200th period $P_{\max}$ (200) and the peak power of the 500th period $P_{\max}$ (500) could meet the condition $|(P_{\max}(200) - P_{\max}(500))/P_{\max}(500)| < 0.1\%$, then the D value is what we search for.

The dynamic characteristic of the fast periodic pulsed reactor is very special. It is that only one fixed D value exists if the basic parameters of the reactor, including $f(t)$, β_{eff}, Λ, are determined. And with D being one fixed value, the ratio of peak power to average power $P_{\max}/P_{\mathrm{t}}$ and the ratio of background energy to total energy $E_{\mathrm{b}}/E_{\mathrm{t}}$ are also unchangeable. Meanwhile, the absolute power $P_{\max}$ and the absolute energy E_{b} could be adjusted by rising or dropping the control rods in the stationary reflector.

Theoretical Estimation Formula

Pulse parameters under stable operation, including relative power $P_{\max}/P_{\mathrm{t}}$ and relative energy $E_{\mathrm{b}}/E_{\mathrm{t}}$, are critically important in measuring the dynamic performance of the fast periodic pulsed reactor. In order to study $P_{\max}/P_{\mathrm{t}}$ and $E_{\mathrm{b}}/E_{\mathrm{t}}$ in detail and to show the difference between IBR-2 and FPPRU1 dynamics intuitively, the theoretical estimation formulas are derived in the article.

From **Eq. 2**, the following could be obtained:

$$\int_0^T \sum_{i=1}^{6} \frac{\mathrm{d}C_i(t)}{\mathrm{d}t}\mathrm{d}t = \int_0^T \sum_{i=1}^{6} \alpha_i \frac{\beta_{\mathrm{eff}}}{\Lambda} P(t)\mathrm{d}t - \int_0^T \sum_{i=1}^{6} \lambda_i C_i(t)\mathrm{d}t. \tag{4}$$

When the reactor is under stable periodic pulse operation, the production and the decay of delayed neutron precursors reach a balance; as a result, $C_i(0) \approx C_i(T)$ and $\int_0^T \sum_{i=1}^{6} \frac{\mathrm{d}C_i(t)}{\mathrm{d}t}\mathrm{d}t \approx 0$. As the peroid T is about several milliseconds, the variation of the delayed neutron precursors concentration in one period is very small, and $\sum_{i=1}^{6} \lambda_i C_i(t) \approx S$ (S is a constant) is reasonable. Then the following could be obtained:

$$E_{\mathrm{t}} = \frac{\Lambda T}{\beta_{\mathrm{eff}}} S. \tag{5}$$

As shown in **Figure 5**, from time t_{b}, the core reactivity stabilizes at ρ_{b} and the following is obtained:

$$\frac{\mathrm{d}P(t)}{\mathrm{d}t} = \frac{\rho_{\mathrm{b}} - \beta_{\mathrm{eff}}}{\Lambda} P(t) + \sum_{i=1}^{6} \lambda_i C_i. \tag{6}$$

Integrating **Eq. 6** on both side from t_{b} to T, the following is obtained:

$$\int_{t_{\mathrm{b}}}^{T} \frac{\mathrm{d}P(t)}{\mathrm{d}t}\mathrm{d}t = \int_{t_{\mathrm{b}}}^{T} \frac{\rho_{\mathrm{b}} - \beta_{\mathrm{eff}}}{\Lambda} P(t)\mathrm{d}t + \int_{t_{\mathrm{b}}}^{T} \sum_{i=1}^{6} \lambda_i C_i \mathrm{d}t. \tag{7}$$

From time t_{b}, the power decreases at the decay rate of the delayed neutron precursors, as shown in **Figure 5**. As the change of power within time $t_{\mathrm{b}} \sim T$ is very little, the left-hand term of **Eq. 7** is approximately 0. Then it could be achieved as follows:

$$E_{\mathrm{b}} = \frac{S\Lambda}{\beta_{\mathrm{eff}} - \rho_{\mathrm{b}}} (T - t_{\mathrm{b}}). \tag{8}$$

From **Eqs. 5**, **7**, $E_{\mathrm{b}}/E_{\mathrm{t}}$ takes the form as follows:

$$\frac{E_{\mathrm{b}}}{E_{\mathrm{t}}} = \frac{\beta_{\mathrm{eff}}}{\beta_{\mathrm{eff}} - \rho_{\mathrm{b}}} \frac{T - t_{\mathrm{b}}}{T}. \tag{9}$$

Assuming the integral pulse energy Ep is proportional to the product of peak power $P_{\max}$ and half-width t_{h}, then the following can be obtained:

$$E_{\mathrm{P}} = kP_{\max}t_{\mathrm{h}}. \tag{10}$$

k in **Eq. 10** is the proportional coefficient. For IBR-2 with PuO_2 as fuel, according to the experimental data, $k \approx 1$. For FPPRU1,

TABLE 4 | Comparison of FPPRU1 pulse parameters with IBR-2 pulse parameters.

Parameters	IBR-2			FPPRU1	
	Critical search method	Theoretical estimation formula	Experimental data	Critical search method	Theoretical estimation formula
E_b/E_t	6.61%	6.50%	~7% Bondarchenko et al. (2001)	27.74%	28.05%
P_{max}/P_t	687.73	763.30	~750 Dragunov et al. (2012)	185.46	183.25
t_h/μs	236.50	—	245 Pepelyshev and Popov (2006a)	790.95	—
$\rho_{max}/10^{-5}$	301.97	—	304.5–306 Pepelyshev and Popov (2006a)	523.5	—

according to the numerical results of the critical search method, $k \approx 1.5$. Using **Eqs. 9**, **10**, the following could be obtained:

$$\frac{P_{max}}{P_t} = \frac{E_p / (kt_h)}{E_t / T} = \frac{T}{kt_h}\left(1 - \frac{\beta_{eff}}{\beta_{eff} - \rho_b}\frac{T - t_b}{T}\right). \quad (11)$$

Eqs. 9, **11** are the theoretical estimation formula describing E_b/E_t and P_{max}/P_t respectively. As can be seen intuitively from **Eqs. 9**, **11**, P_{max}/P_t increases with the rise of $|\rho_b|$ and T, and with the drop of β_{eff} and t_h. E_b/E_t decreases with the rise of $|\rho_b|$ and the drop of β_{eff}. Thus, the theoretical estimation formula provides a simple way to analyze the factors affecting the pulse parameters clearly and intuitively, and establish a theoretical basis for improving the quality of the pulse parameters.

Comparison of Pulse Parameters of IBR-2 and FPPRU1

The qualities of pulse parameters of the fast periodic pulsed reactors with different fissile materials as fuel are quite different. In this article, the pulse parameters of IBR-2 with PuO_2 as fuel are compared with those of FPPRU1 with UO_2 as fuel. The results are shown in **Table 4**.

As shown in **Table 4**, both the critical search method and the theoretical estimation formula are used to calculate the pulse parameters. For IBR-2, the results obtained with the critical search method are in good agreement with the experimental data on the whole. E_b/E_t calculated with the two methods is in good accordance, proving both the two methods are feasible. It should be noted that P_{max}/P_t obtained with the theoretical estimation formula is on the assumption that k is known in the calculation ($k = 1$ for IBR-2 and $k = 1.5$ for FPPRU1).

It could be known from **Table 4** that, the relative peak power P_{max}/P_t of FPPRU1 is much lower and the relative background energy E_b/E_t is much higher. Thus, the quality of pulse parameters of FPPRU1 is worse than that of IBR-2. From **Eq. 9**, it is known that if β_{eff} is larger, then E_b/E_t is larger and P_{max}/P_t is smaller, which means the quality of pulse parameters is worse. The number of the delayed neutron produced by U-235 and Pu-239 per fission are 0.0068 and 0.00215 (Huang, 2007), respectively. And β_{eff} of FPPRU1 and IBR-2 are 0.00728 and 0.00216, respectively. Thus, the pulse parameters of FPPRU1 are of relative poor quality compared to that of IBR-2.

From **Eqs. 9**, **11**, we know that some measures could be taken to increase the quality of pulse parameters of FPPRU1. For example, the period T could be increased by reducing the rotating speed of moving reflectors. And the half-width t_h could be decreased by optimizing the reactor design. However, the measures may conflict with each other. For instance, reducing the rotation speed of the moving reflectors would also increase the half-width t_h at the same time.

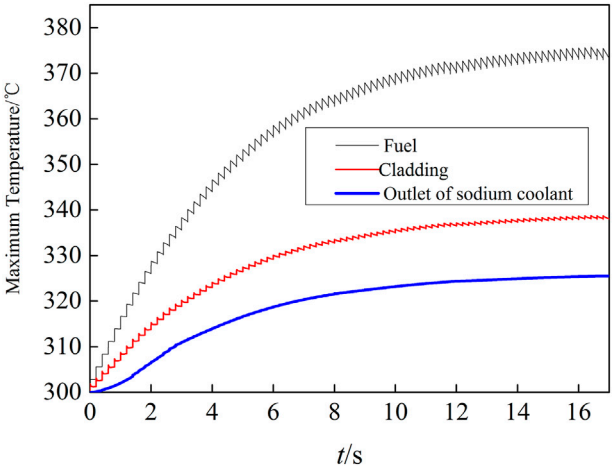

FIGURE 10 | The sub-channel model of the fuel assembly.

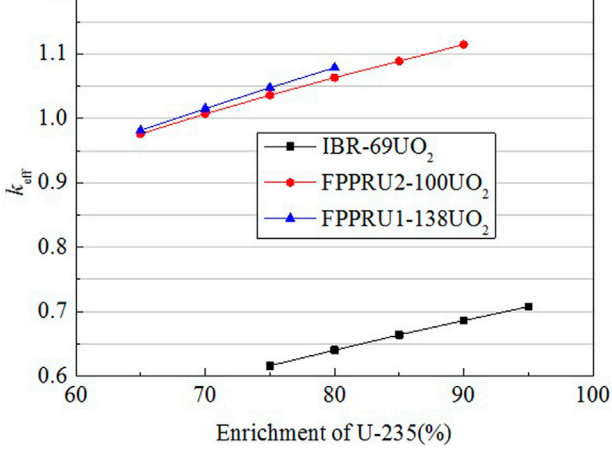

FIGURE 11 | Changes of the maximum temperature.

Thermal Hydraulics Calculation

When FPPRU1 is under stable periodic operation at the average power 2MW, the peak power is about 370.92 MW. For the fuel assembly with the maximum power, the energy deposition in one pulse is about 4 kJ. The pulse frequency is 5 Hz and the half-width is 523.5 μs. The sub-channel model of the fuel assembly with the maximum power for analyzing the thermal hydraulic characteristics is established with FLUENT, as shown in **Figure 10**.

The model in **Figure 10** is 1/12 of the whole fuel assembly shown in **Figure 4**. In the calculation, it is assumed that the inlet temperature of the sodium coolant is 300 ˚C and the flow rate of sodium coolant in one fuel assembly is 800 L/h. The changes of the maximum temperature of the fuel and the cladding and the maximum outlet temperature of sodium coolant are shown in **Figure 11**.

As seen from **Figure 11**, the temperature of the fuel and the coolant rise gradually and reach the balance after operating for about 17 s. The pulses only cause small jagged fluctuations to the temperature. The maximum fuel temperature and the coolant outlet temperature are 375 and 325 ˚C respectively, which means that the thermal safety under stable periodic operation could be guaranteed.

DISCUSSION

The sodium cooling fast periodic pulsed reactor with UO_2 as fuel (FPPRU) is designed, and the feasibility is studied in this article. Two typical core load schemes (FPPRU1 and FPPRU2) with stainless steel or beryllium as the reflector are compared. It is found that FPPRU1 with the stainless steel as the reflector has better performance such as narrower half-width of the pulse, harder neutron energy spectrum on the reflector surface, and less energy deposition in the stationary reflector. On the other hand, the downside of FPPRU1 is that more fuel assemblies have to be loaded to reach criticality. In order to study the reactor dynamics, the critical search method is established. Furthermore, the theoretical estimation formula which could clearly show the difference between the pulse parameters of FPPRU1 and IBR-2 is derived. The two methods are verified by the IBR-2 experimental data and are applied to the calculation of FPPRU1. The results show that the quality of the pulse parameters of FPPRU1 is not as good as that of IBR-2. In order to study the thermal safety under stable periodic operation, the sub-channel model of the FPPRU1 fuel assembly is built, and it is found that the maximum fuel temperature is not very high and thus is acceptable. On the whole, the sodium cooling fast periodic pulsed reactor with UO_2 as fuel is feasible in neutronics and thermal hydraulics, but the quality of the pulse parameters needs to be improved further.

DATA AVAILABILITY STATEMENT

The original contributions presented in the study are included in the article/Supplementary Material; further inquiries can be directed to the corresponding author.

AUTHOR CONTRIBUTIONS

All authors listed have made a substantial, direct, and intellectual contribution to the work and approved it for publication.

REFERENCES

Ananiev, V. D., Lukasevich, I. B., Popov, V. E., and Romanova, N. V. (2020). IBR-2 Run Optimization Suggestions. *At. Energ.* 127 (3), 131–133. doi:10.1007/s10512-020-00598-3

Ananiev, V. D., Pepelyshev, Y. N., and Rogov, A. D. (2019). Optimization Study of the IBR-2 Reactor. *Phys. Atom. Nuclei* 82 (8), 1162–1174. doi:10.1134/S1063778819080039

Ata-Allah, S. S., Balagurov, A. M., Hashhash, A., Bobrikov, I. A., and Hamdy, S. (2016). Refinement of Atomic and Magnetic Structures Using Neutron Diffraction for Synthesized Bulk and Nano-Nickel Zinc Gallate Ferrite. *Physica B: Condensed Matter* 481 (481), 118–123. doi:10.1016/j.physb.2015.10.030

Avdeev, M. V., Rulev, A. A., Ushakova, E. E., Kosiachkin, Y. N., Petrenko, V. I., Gapon, I. V., et al. (2019). On Nanoscale Structure of Planar Electrochemical Interfaces Metal/liquid Lithium Ion Electrolyte by Neutron Reflectometry. *Appl. Surf. Sci.* 486, 287–291. doi:10.1016/j.physb.2015.10.03010.1016/j.apsusc.2019.04.241

Badawy, W. M., Duliu, O. G., Frontasyeva, M. V., El-Samman, H., and Mamikhin, S. V. (2020). Dataset of Elemental Compositions and Pollution Indices of Soil and Sediments: Nile River and delta -Egypt. *Data in Brief* 28 (105009), 105009–105010. doi:10.1016/j.dib.2019.105009

Bondarchenko, E. A., Pepyolyshev, Y. N., and Popov, A. K. (2001). Influence of Automatic Regulator Parameters on Power Transition Processes of the IBR-2 Reactor. *Ann. Nucl. Energ.* 28, 63–78. doi:10.1016/j.anucene.2006.04.002

Brezhnev, A. I., Gulevich, A. V., Kukharchuk, O. F., and Fokina, O. G. (2017). Assessment of the Critical Condition for the Operation of an IBR Reactor with a Subcritical Unit in an Equilibrium Mode. *Nucl. Energ. Tech.* 3 (2), 127–132. doi:10.1016/j.nucet.2017.05.007

Chan, L. Y., and Pepelyshev, Y. N. (2010). IBR-2 Dynamics with Power Shedding. *At. Energ.* 109 (2), 75–80. doi:10.1007/s10512-010-9326-8

Chan, L. Y., and Pepelyshev, Y. N. (2008). Model of IBR-2 Power Feedback Dynamics Taking Account of Slow Components. *At Energy* 104 (4), 262–267. doi:10.1007/s10512-008-9026-9

Dragunov, Y. G., Tretiyakov, I. T., Lopatkin, A. V., Romanova, N. V., Lukasevich, I. B., Ananyev, V. D., et al. (2012). Modernization of the IBR-2 Pulsed Research Reactor. *At Energy* 113 (1), 29–38. doi:10.1007/s10512-012-9591-9

Golovin, I. S., Mohamed, A. K., Bobrikov, I. A., and Balagurov, A. M. (2020). Time-Temperature-Transformation from Metastable to Equilibrium Structure in Fe-Ga. *Mater. Lett.* 263 (127257), 127257–127264. doi:10.1016/j.matlet.2019.127257

Huang, Z. Q. (2007). *Basis of Nuclear Reactor Dynamics*. Beijing, China: Peking University Press.

Kulikov, S. A., and Shabalin, E. P. (2013). Optimization of IBR-2M Moderator Parameters. *At Energy* 115 (1), 48–52. doi:10.1007/s10512-013-9747-2

Marina, F. (2011). Neutron Activation Analysis in the Life Sciences. *Phys. Particles Nuclei* 42 (2), 332–378. doi:10.1134/S1063779611020043

Pepelyshev, Y. N., and Popov, A. K. (2006). Influence of the Nearest Environment of the Core on the Power Pulse Dynamics in the IBR-2 Reactor. *Ann. Nucl. Energ.* 33, 813–819. doi:10.1016/j.anucene.2006.04.002

Pepelyshev, Y. N., and Popov, A. K. (2006). Investigation of Dynamical Reactivity Effects of IBR-2 Moving Reflectors. *At Energy* 101 (2), 549–554. doi:10.1007/s10512-006-0129-x

Pepelyshev, Y. N., Popov, A. K., and Sumkhuu, D. (2017). IBR-2M Reactor Power Feedback Parameters Evaluation Using Square Reactivity Oscillations. *At Energy* 122 (5), 75–80. doi:10.1007/s10512-017-0238-8

Pepelyshev, Y. N., Popov, A. K., and Sumkhuu, D. (2015). Model of the IBR-2M Pulsed Reactor Dynamics for Investigating Transition Processes in a Wide

Range of Power Variation. *Ann. Nucl. Energ.* (85), 488–493. doi:10.1016/j.anucene.2015.06.002

Pepelyshev, Y. N., Vinogradov, A. V., and Rogov, A. D. (2010). "On Some Issues of Safety of Research Pulsed Reactor IBR-2," in International Conference on Current Problems in Nuclear Physics and Atomic Energy, Kiev (Ukraine), June 7–12.

Turchenko, V., Kostishyn, V. G., Trukhanov, S., Damay, F., Porcher, F., Balasoiu, M., et al. (2020). Crystal and Magnetic Structures, Magnetic and Ferroelectric Properties of Strontium Ferrite Partially Substituted with in Ions. *J. Alloys Compounds* 821 (153412), 153412–153417. doi:10.1016/j.jallcom.2019.153412

Conflict of Interest: The authors declare that the research was conducted in the absence of any commercial or financial relationships that could be construed as a potential conflict of interest.

Publisher's Note: All claims expressed in this article are solely those of the authors and do not necessarily represent those of their affiliated organizations, or those of the publisher, the editors and the reviewers. Any product that may be evaluated in this article, or claim that may be made by its manufacturer, is not guaranteed or endorsed by the publisher.

frontiers in Energy Research

ORIGINAL RESEARCH
published: 11 August 2021
doi: 10.3389/fenrg.2021.704307

The Ring RPT Method for DH Systems Containing Dispersed Particle-Type of Fuel and Burnable Poisons

Lei Lou, Xingjie Peng, Xiaoming Chai, Dong Yao, Mancang Li, Lianjie Wang and Liang Chen*

Science and Technology on Reactor System Design Technology Laboratory, Nuclear Power Institute of China, Chengdu, China

Because dispersed particle-type fuel and burnable poisons both have double heterogeneity (DH), using the traditional volumetric homogenization method (VHM) to treat DH systems will bring about large reactivity calculation deviation. The improved reactivity-equivalent physical transformation (IRPT) method can be applied to DH systems which have both dispersed particle-type fuel and burnable poisons because of the features of simplicity and high calculation accuracy. In this article, the calculations show that the IRPT method becomes invalid for some DH systems when the volume fraction of dispersed particle-type burnable poisons is relatively high or the absorb cross section of burnable poison particles is relatively large. Then the two-step ring reactivity-equivalent physical transformation (TRRPT) method is proposed to be applied to the DH systems with both dispersed particle-type fuel and burnable poisons. Results of reactivity at zero burnup and depletion calculations for different types of dispersed particle-type fuel and burnable poisons and the comparison with Monte Carlo results of grain models prove the validity of the TRRPT method, and it has been proven that the TRRPT method has higher accuracy in reactivity calculation and a wider scope of transformation than the IRPT method.

Keywords: particle-type fuel, particle-type burnable poisons, double-heterogeneous systems, volumetric homogenization method, IRPT method, ring RPT method

OPEN ACCESS

Edited by:
Tengfei Zhang,
Shanghai Jiao Tong University, China

Reviewed by:
Jian Li,
Tsinghua University, China
Song Li,
Harbin Engineering University, China

****Correspondence:***
Xiaoming Chai
chaixm@163.com

Specialty section:
This article was submitted to Nuclear Energy, a section of the journal Frontiers in Energy Research

Received: *02 May 2021*
Accepted: *30 June 2021*
Published: *11 August 2021*

Citation:
Lou L, Peng X, Chai X, Yao D, Li M, Wang L and Chen L (2021) The Ring RPT Method for DH Systems Containing Dispersed Particle-Type of Fuel and Burnable Poisons. Front. Energy Res. 9:704307. doi: 10.3389/fenrg.2021.704307

1 INTRODUCTION

Dispersed particle-type fuels (IAEA-TECDOC-1797, 2014) and burnable poisons (van Dam, 2000) have attracted much attention due to their unique physical properties. Dispersed particle-type fuel can contain fission products under high temperature and deep burnup conditions and has accident-resistant characteristics. Dispersed particle-type burnable poisons can increase the surface compatibility of particles and the matrix by adding a coating layer, and at the same time, it can control the burnup rate through its own space self-shielding effect and improve the flexibility of using burnable poisons in reactivity control. Dispersed particle-type fuel and burnable poisons have double heterogeneity (DH), that is, on the basis of the heterogeneity of the fuel pin, cladding, and moderator, the heterogeneity of the dispersed particles in the fuel pin and the matrix is added. The DH cannot be described in the current traditional neutronics calculation program, and the direct use of the volume homogenization method will bring about a larger reactivity calculation deviation.

A large number of studies have been conducted on the DH of dispersed materials at home and abroad. At present, there are two major types of methods for DH. The first is the Monte Carlo method, which can be used to directly simulate the dispersed particles using the Monte Carlo program, but the calculation will take a long time and require lots of memory. The second category is the deterministic method, which involves adding a certain algorithm to the present deterministic

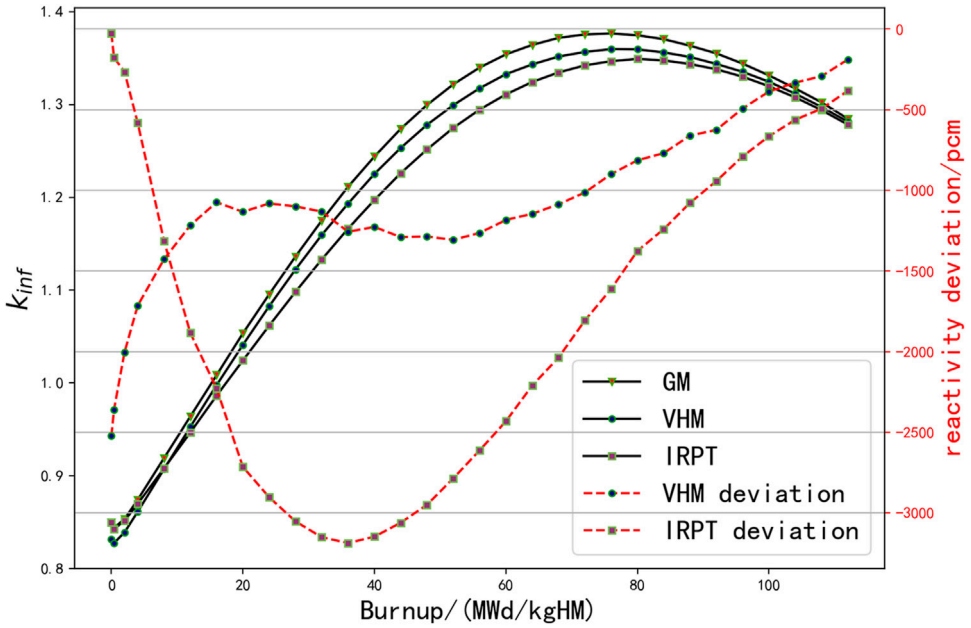

FIGURE 1 | Reactivity curve of FCM fuel with dispersed particle-type B_4C.

program to realize the treatment of DH. There are also many deterministic treatment methods for DH (Zhang et al., 2017a). One is the equivalent homogenization method of Shmakov (Shmakov et al., 2000) and She Ding (Ding et al., 2017), which can handle the DH effects of the cross section of the nonresonant energy group, and the resonance energy groups need to be dealt with separately using other methods such as the Dancoff factor correction or the Monte Carlo method. Sanchez's DH treatment method based on the method of characteristic (MOC) and the collision probability method (CPM) (Sanchez and Masiello, 2002; Zhang et al., 2017b) can also be applied to DH. The equivalent homogenization method and Sanchez's method both require more formula derivation and a lot of modifications to existing programs. Another method is the reactivity-equivalent physical transformation (RPT) method proposed by Yonghee Kim (Kim et al., 2006) in South Korea, which converts the DH system into a single-heterogeneous (SH) system by performing a reactive equivalent transformation of the system based on the reactivity of the Monte Carlo particle model at the time of zero burnup. Then the traditional neutronics program is used to calculate. The method is simple to operate, but the calculation accuracy is acceptable.

In 2018, Jian Li (Li et al., 2018) from Tsinghua University proposed an improved reactivity-equivalent physical transformation (IRPT) method, which is an improved RPT method for fully ceramic microencapsulated (FCM) fuel dispersed both particle-type fuel and burnable poisons. When processed using the IRPT method, the FCM fuel region is divided into three ring zones which will be homogenized separately. Numerical results of FCM fuel show that the IRPT method can be used to treat these cases containing both dispersed particle-type fuel and burnable poisons.

In 2020, we conducted in-depth research based on the RPT method and proposed a ring RPT (RRPT) method, which can be used to process the single particle-type DH system of dispersed particle-type fuel or burnable poisons (Lou et al., 2020a; Lou et al., 2020b). The reactivity calculation accuracy is higher than that of the traditional RPT method. In order to be able to deal with the two types of particle DH systems containing both dispersed particle-type fuel and burnable poisons, this article will conduct a more in-depth study.

In this article, it is found that for the cases with dispersed particle-type burnable poisons, when its macro cross section is relatively large or its volumetric fraction is relatively high or its particle size is relatively large or its burnup is relatively deep, the IRPT method will also have large deviations. **Figure 1** shows the reactivity curve of FCM fuel with dispersed particle-type B_4C. In this case, the diameter of the B_4C particle is 100 μm, and its volumetric fraction is 5%.

For the issue above, in this article, the RRPT method for systems with dispersed particles is proposed. With the RRPT method, all the dispersed particles are compressed to be a ring column for a cylindrical cell or a ring shell for a spherical cell, and the double-heterogeneous system is also transformed into an SH system as the traditional RPT method does. When the DH system contains both particle dispersed fuel and burnable poisons, the RRPT method can be used twice to transform the fuel particles and burnable poison particles into corresponding rings which are an SH system and can be modeled using the traditional neutronic program. The calculation results and comparison with Monte Carlo results show that the RRPT method can deal with systems containing both fuel particles and burnable poison particles and has higher calculation accuracy in reactivity calculation and a wider scope of application than the original IRPT method.

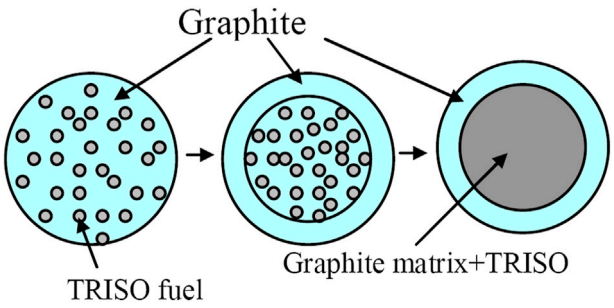

FIGURE 2 | Schematic diagram of the traditional RPT method.

2 METHODOLOGY

2.1 RPT and IRPT Methods

In the traditional RPT method, the DH problem with dispersed particles will be transformed into an SH system which can be modeled using a traditional program. The transformation process contains two steps: first, gather all the particles into a smaller circular area with a higher packing fraction than before in the center region, and second, the new smaller circular area is treated using the VHM (see **Figure 2** (Kim et al., 2006)) The RPT radius which is the radius of the smaller circular area is determined by keeping the k_{inf} of the system equivalent to the reference value which is usually calculated using the Monte Carlo or high-fidelity deterministic programs.

For the DH system with both dispersed particle-type fuel and burnable poison, the schematic diagram of the IRPT method is shown in **Figure 3** (Li et al., 2018). First, we assume that the DH system does not contain burnable poison particles, only fuel particles, and then the RPT radius can be obtained using the traditional RPT method. Then burnable poison is reverted to the fuel region within the RPT radius, and the traditional RPT method is used twice to get a smaller RPT radius. After being processed twice using the traditional RPT method, the FCM fuel region is divided into three circular areas. The outer region contains only matrix material, the middle zone contains the matrix and particle-type fuel, and the inner zone contains the matrix, particle-type fuel, and particle-type burnable poisons. The dispersed particles in the inner zone and the middle zone are homogenized separately.

2.2 RRPT and TRRPT Methods

The RRPT method can also transform the DH problem into an SH one which can be modeled using the traditional neutronic program. The whole process of the RRPT method contains only one step, which is shown in **Figure 4**. First, all dispersed particle material is compressed into a ring area in the matrix material, and the center of the ring is consistent with the fuel cell. There is a corresponding relationship between the inner and outer radii of the ring when keeping the entire dispersed particle material constant during the transformation. The radius of the ring is determined by keeping the k_{inf} of the system equivalent to the

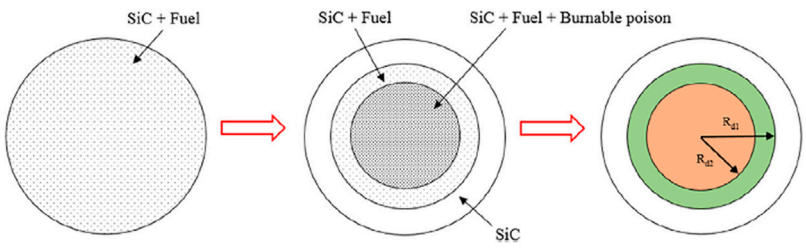

FIGURE 3 | Schematic diagram of the IRPT method.

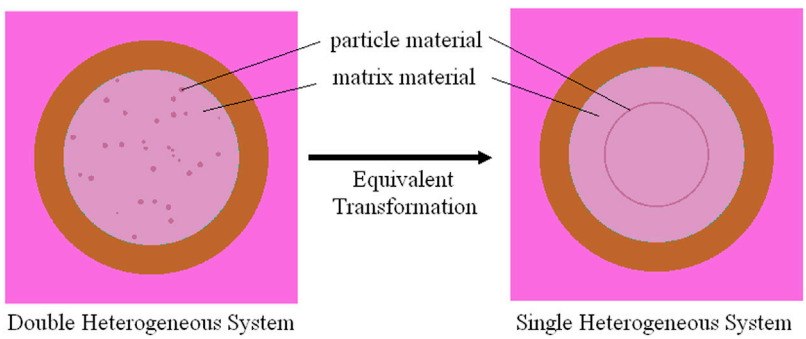

FIGURE 4 | Schematic diagram of the RRPT method.

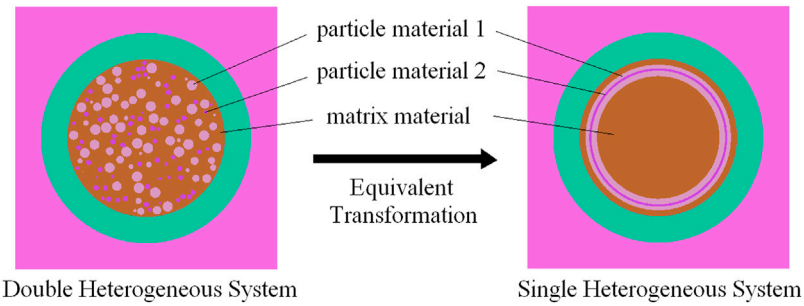

FIGURE 5 | Schematic diagram of the TRRPT method.

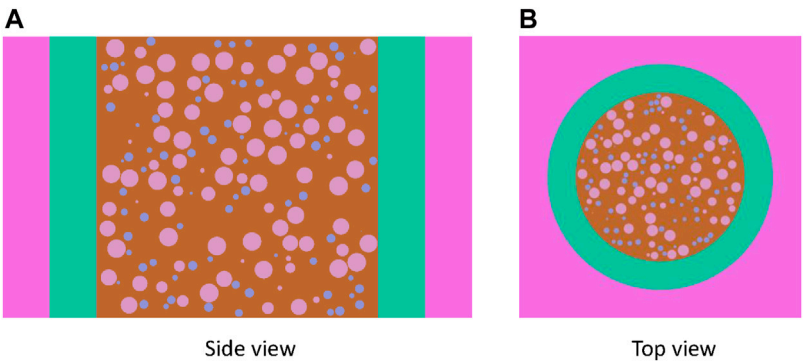

FIGURE 6 | DH system containing two types of dispersed particles. **(A)** Side view. **(B)** Top view.

reference results of the Monte Carlo or high-fidelity deterministic program.

When the DH systems contain two types of dispersed particles, such as fuel particles and burnable poison particles, the RRPT method can also be used with the IRPT idea. First, we assume that the DH system does not contain burnable poison particles, only fuel particles, and then the radius of the fuel ring can be determined using the RRPT method. Then burnable poison is reverted to the fuel region, and a new radius of the burnable poison ring can be determined using the RRPT method. After being processed twice using the RRPT method, the FCM fuel region is divided into three circular areas, namely, the matrix zone, the fuel zone, and the burnable poison zone. The matrix zone contains only matrix material, the fuel zone contains only fuel material, and the burnable poison zone contains only burnable poison, which is shown in **Figure 5**.

In the TRRPT and IRPT methods, the first step of treatment needs to remove the dispersed burnable poison particles in the system, and the second step of treatment needs to add the dispersed burnable poison particles to the fuel region in the system. The reason for removing and regaining burnable poison particles is that the traditional RPT method and the RRPT method are both applied to single-type particles. When the DH system contains both particle-dispersed fuel and burnable poison, the two types of particles need to be treated separately. The new methods of treating with the traditional RPT and RRPT methods twice are the IRPT and TRRPT methods.

Generally, the content of burnable poison particles is much less than that of fuel particles, and so the area of the burnable poison ring is much smaller than that of the fuel ring. In all the

TABLE 1 | Parameters of the calculation model.

Physical parameter	Value
Fuel cell	
Radius of the fuel region, cm	0.3
Thickness of the gas gap, cm	0.0008
Thickness of the zirconium cladding, cm	0.1
Density of the zirconium cladding, g/cm^3	6.5
Density of the zirconium matrix, g/cm^3	6.5
Density of the moderator, g/cm^3	1.0
Fuel particle	
Radius of the UO_2 kernel, μm	200
Enrichment of the UO_2 kernel, %	20
Volume fraction of the UO_2 kernel, %	20
Density of UO_2, g/cm^3	10.41
Burnable poison particle	
Radius of the burnable poison kernel, μm	100
Volume fraction of the burnable poison kernel, %	5/1
Density of the Ag kernel, g/cm^3	10.5
Density of the B_4C kernel, g/cm^3	1.9
Density of the Dy_2O_3 kernel, g/cm^3	7.8
Density of the Er_2O_3 kernel, g/cm^3	8.6
Density of the Eu_2O_3 kernel, g/cm^3	7.42
Density of the Hf kernel, g/cm^3	13.0
Density of the In kernel, g/cm^3	7.31

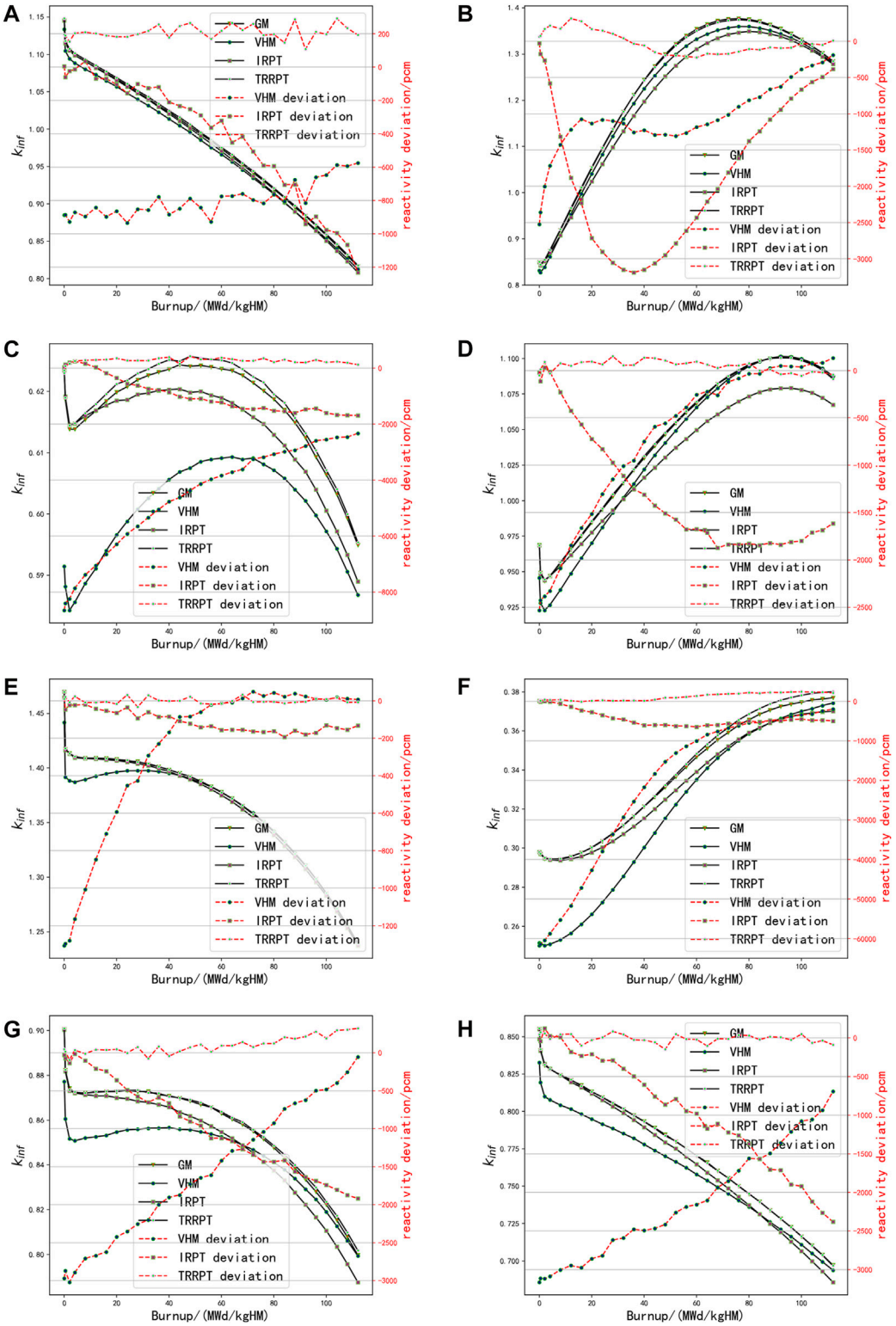

FIGURE 7 | Reactivity and calculation deviation of different methods. **(A)** Ag-V5%. **(B)** B4C-V5%. **(C)** Dy2O3-V5%. **(D)** Er2O3-V5%. **(E)** Er2O3-V1%. **(F)** Eu2O3-V5%. **(G)** Hf-V5%. **(H)** In-V5%.

examples verified in this study, the burnable poison ring is contained inside the fuel ring, as shown in **Figure 5**.

3 NUMERICAL RESULTS

In this article, the Monte Carlo program RMC (Wang et al., 2013), which was developed by Tsinghua University, is used to describe the random distribution of dispersed particles in the matrix and to provide a benchmark solution. When fuel particles with a radius of 200 μm and a volume fraction of 20% and burnable poison particles with a radius of 100 μm and a volume fraction of 5% are dispersed randomly in the zirconium matrix, the schematic diagram of distribution is shown in **Figure 6**. The parameters of the calculation model are shown in **Table 1**. In the two-type dispersed particle system, the dispersed particles are burnable poison and UO_2. The parameters of the calculation model are shown in **Table 1**.

The models with dispersed particle-type fuel and burnable poisons are, respectively, calculated using the grain model (GM), the VHM, the IRPT method, and the TRRPT method, and the results of reactivity and calculation deviation are shown in **Figure 7**.

In **Figure 7**, the GM is the results of the grain model of the DH systems and is the benchmark. In the calculation, the burnable poison particles are divided into 10 burnup zones for accurate results.

When the volume fraction of burnable poison is relatively low, such as Er_2O_3 with a volume fraction of 1% as shown in (e) of **Figure 7**, the IRPT and TRRPT methods can both treat such problems with low reactivity deviation. But when the volume fraction becomes large, such as 5%, the reactivity calculating deviation of the IRPT method becomes large, the deviation will gradually increase with the depletion, and the maximum deviation will exceed 500 pcm.

When the TRRPT method is used, not only can the cases the IRPT method is suitable for get perfect results but also the reactivity calculation deviation of the cases with a relatively large volume fraction and burnable poison with a large absorb cross section such as B_4C stays within 500 pcm during the depletion. The TRRPT method which transforms the dispersed particle-type burnable poisons into a ring can better simulate the space self-shielding effect of the particles in the DH systems than the IRPT method.

4 CONCLUSION

In this study, the IRPT method, improved from the traditional RPT method, is introduced to deal with the DH system with dispersed particle-type fuel and burnable poisons; results compared with Monte Carlo show that the reactivity calculation deviation of the IRPT method will be relatively large for the DH systems with burnable poison particles which have a relatively large volume fraction or a large absorption cross section. Then the RRPT method can be used twice to treat the DH system with two types of dispersed particles. The TRRPT method is proposed, which can not only treat the cases the IRPT method is suitable for but also the cases that the IRPT method cannot treat; the maximum reactivity calculation deviation stays within 500 pcm during the depletion. The calculation results and comparison with Monte Carlo show that the TRRPT method has higher accuracy in reactivity calculation and a wider scope of transformation than the IRPT method.

DATA AVAILABILITY STATEMENT

The raw data supporting the conclusion of this article will be made available by the authors, without undue reservation.

AUTHOR CONTRIBUTIONS

LL: conceptualization, methodology, and software. XP: conceptualization. XC: conceptualization. DY: conceptualization. ML: visualization and investigation. LW: funding acquisition and supervision. LC: funding acquisition and supervision.

FUNDING

This work is supported by the National Natural Science Foundation of China (Approved no.: 1170051016).

REFERENCES

Ding, S., Liu, Z., and Shi, L. (2017). An Equivalent Homogenization Method for Treating the Stochastic Media, *Nucl. Sci. Eng.*, volume 185, 351–360.

IAEA-TECDOC-1797 (2014). "Accident Tolerant Fuel Concepts for Light Water Reactor." in Proceedings of a Technical Meeting held at Oak Ridge National Labratories, United States of America, 13-16.

Kim, Y., Kim, K-S., and Noh, J. M. (2006). *Preservation of Fuel Characteristics in the RPT Method*, Transactions of the Korean Nuclear Society Spring Meeting, Chuncheon, Korea.

Li, J., She, D., and Shi, L. (2018). An Improved Reactivity-Equivalent Physical Transformation for Treating FCM Fuel with Burnable Poisons. *Ann. Nucl. Energ.* 121, 577–581. doi:10.1016/j.anucene.2018.08.024

Lou, L., Chai, X., Yao, D., Peng, X., Chen, L., Li, M., et al. (2020). Research of Ring RPT Method on Spherical and Cylindrical Double-Heterogeneous Systems. *Ann. Nucl. Energ.* 147, 107741. doi:10.1016/j.anucene.2020.107741

Lou, L., Yao, D., Chai, X., Peng, X., Li, M., Li, W., et al. (2020). A Novel Reactivity-Equivalent Physical Transformation Method for Homogenization of Double-Heterogeneous Systems. *Ann. Nucl. Energ.* 142, 107396. doi:10.1016/j.anucene.2020.107396

Sanchez, R., and Masiello, E. (2002). *Treatment of the Double Heterogeneity with the Method of Characteristics*. Seoul, Korea: PHYSOR. (. (7-10 October, 2002).

Shmakov, V. M., Lyutov, V. D., and Dean, V. F. (2000). Effective Cross Sections for Calculations of Criticality of Dispersed Media, *Proc Advances in Reactor Physics, and Mathematics and Computation into the Next Millennium* (PHYSOR 2000, Pittsburgh, Pennsylvania).

van Dam, H. (2000). Long-term Control of Excess Reactivity by Burnable Particles. *Ann. Nucl. Energ.* 27, 733–743. doi:10.1016/s0306-4549(00)82014-9

Wang, K., Li, Z. G., and She, D. (2013). *RMC-A Monte Carlo Code for Reactor Physics analysisJoint International Conference on Supercomputing in Nuclear Applications and Monte Carlo*. Paris: France.

Zhang, T., Lewis, E. E., Smith, M. A., Yang, W. S., and Wu, H. (2017). A Variational Nodal Approach to 2D/1D Pin Resolved Neutron Transport for Pressurized Water Reactors. *Nucl. Sci. Eng.* 186 (2), 120–133. doi:10.1080/00295639.2016.1273023

Zhang, T., Wang, Y., Lewis, E. E., Smith, M. A., Yang, W. S., and Wu, H. (2017). A Three-Dimensional Variational Nodal Method for Pin-Resolved Neutron Transport Analysis of Pressurized Water Reactors. *Nucl. Sci. Eng.* 188 (2), 160–174. doi:10.1080/00295639.2017.1350002

Conflict of Interest: All authors were employed by company Nuclear Power Institute of China.

Publisher's Note: All claims expressed in this article are solely those of the authors and do not necessarily represent those of their affiliated organizations, or those of the publisher, the editors and the reviewers. Any product that may be evaluated in this article, or claim that may be made by its manufacturer, is not guaranteed or endorsed by the publisher.

frontiers in Energy Research

ORIGINAL RESEARCH
published: 17 August 2021
doi: 10.3389/fenrg.2021.747148

The Advanced Multilevel Predictor-Corrector Quasi-Static Method for Pin-Resolved Neutron Kinetics Simulation

Le Kang[1], *Chen Hao*[1]*, *Qiang Zhao*[1] *and Yunlin Xu*[2]

[1]Fundamental Science on Nuclear Safety and Simulation Technology Laboratory, Harbin Engineering University, Harbin, China, [2]School of Nuclear Engineering, Purdue University, West Lafayette, IN, United States

The Advanced Multilevel Predictor-Corrector Quasi-static Method (AML-PCQM) is proposed in this work. The four computational levels, including transport, Multi-Group (MG) Coarse Mesh Finite Difference (CMFD), One-Group (1G) CMFD, and Exact Point-Kinetics Equation (EPKE), are coupled with a new dynamic iteration strategy. In each coupling algorithm, the original Transient Fixed Source Problem (TFSP) is solved in the predictor process using coarse time step, and then the flux distribution is factorized to the functions of amplitude and shape in the next corrector process. Finally, multiple fine time steps are used to adjust the predicted solution. Two heterogeneous single assembly problems with the prompt control rod withdrawal event are used to verify the AML-PCQM scheme's accuracy and efficiency. The numerical results obtained by different cases are compared and analyzed. The final results indicate that the AML-PCQM performs the remarkable advantages of efficiency and accuracy with the reference cases.

Keywords: transient, predictor-corrector quasi-static method, multilevel, TFSP, AML-PCQM

OPEN ACCESS

Edited by:
Ding She,
Tsinghua University, China

Reviewed by:
Jiong Guo,
Tsinghua University, China
Xiafeng Zhou,
Huazhong University of Science and Technology, China
Qicang Shen,
University of Michigan, United States

***Correspondence:**
Chen Hao
haochen.heu@163.com

Specialty section:
This article was submitted to Nuclear Energy, a section of the journal Frontiers in Energy Research

Received: *25 July 2021*
Accepted: *03 August 2021*
Published: *17 August 2021*

Citation:
Kang L, Hao C, Zhao Q and Xu Y (2021) The Advanced Multilevel Predictor-Corrector Quasi-Static Method for Pin-Resolved Neutron Kinetics Simulation. Front. Energy Res. 9:747148. doi: 10.3389/fenrg.2021.747148

INTRODUCTION

Since the high-performance computing clusters have significant advances recently, the state-of-the-art computer simulation for nuclear reactors is three-dimensional (3D) whole-core time-dependent modeling with high-fidelity pin-resolved features. The nuclear industry relied on the simulation technique to understand many complicated processes and possibly decrease safety conservatism for design accidents, thus increasing nuclear power's overall costs (Shen et al., 2019). Meanwhile, a significant challenge of the dramatically computational cost has happened to the direct simulation utilizing conventional 3D neutron transport techniques, the 3D complete nuclear reactor core. The real total number of numerical unknowns for a typical reactor core is much too large, approaching 10^{15} for steady-state simulation but significantly more for time-dependent simulation (Collins et al., 2016). As a replacement for the direct 3D reactor simulation, a viable solution uses the two-dimensional (2D)/one-dimensional (1D) method. The 2D/1D approach, which is commonly used in high-fidelity codes to solve the forward transport equation, employs two-dimensional heterogeneous transport computations in the radial direction and a lower-order transport calculation in the 1D axial direction, such as the CRX code (Cho et al., 2002), DeCART (Joo et al., 2004), nTRACER (Jung et al., 2013), MPACT (Collins et al., 2016; Kochunas et al., 2017; Shen et al., 2019), NECP-X (Liu et al., 2018), Tiger-3D (Wu, 2014), PANX (Zhang, et al., 2017a; Zhang, et al., 2017b) and PROTEUS-MOC (Zhang et al., 2019). The 2D/1D scheme has been successful in actual reactor applications in those

high-fidelity codes, where the Method of Characteristics (MOC) was most often used for solving the 2D radial problem, and for the 1D axial computation, a variety of techniques are employed.

When utilizing huge time steps to reduce the number of transport options, it is challenging to maintain accuracy (Zhu et al., 2016), considering the time-dependent transient analysis's high computational intensiveness. Among the most frequently utilized and preferred techniques to efficiently solve the time-dependent Boltzmann equation is the quasi-static method (Henry, 1958; Henry and Curlee, 1958), which was then modified as the Improved Quasi-Static (IQS) method (Ott and Meneley, 1969). The basic idea of the quasi-static method is to assume that the neutron flux can be factorized into the amplitude and shape function because the flux amplitude varies considerably faster than the flux shape. Thus, the shape function in the IQS technique may be solved using a modified time-dependent Boltzmann equation with a specified amplitude function. And for the amplitude function, the Exact Point-Kinetics Equations (EPKEs) are usually used, which are obtained by combining the time-dependent Boltzmann equation and the known shape function. The shape and amplitude functions would then be solved using a shape constraint function until the iteration converged (Zhu et al., 2016).

A fine-mesh/coarse-mesh based IQS method was provided to extend the nodal/EPKE based IQS method by introducing a coarse-mesh-wise amplitude function to replace the whole-core amplitude function, which was named Multigrid Amplitude Function (MAF) and was later implemented in a transport-based transient solver (Ban et al., 2012; Shaner et al., 2013; Tsujita et al., 2013; Tsujita et al., 2020). In addition, a factorization technique known as the Predictor-Corrector Quasi-static Method (PCQM) has lately gained popularity in addition to the IQS/MAF method (Kao and Henry, 1989). Rather than solving the shape and amplitude functions iteratively, the PCQM directly calculates the neutron flux in the predictor step and corrects the flux using the amplitude function evaluated in the corrector step, resulting in improved accuracy and computational efficiency the traditional IQS method (Caron et al., 2015). To overcome the unacceptable computing burden of the Multi-Group (MG) Coarse Mesh Finite Difference (CMFD) calculation with the fine time steps in PCQM, the MPACT team at the University of Michigan proposed a new multilevel transient solver named the Transient MultiLevel (TML) method, where the first level couples the transient solver and the MG CMFD solver, and the second level involves the coupling between the MG CMFD solver and the EPKE solver to capture the flux variation in the fine time range (Zhu et al., 2016).

Even so, the computational burden of the MG CMFD is still large and achieves almost 70% of the transient transport burden even with the TML method in the MPACT code (Zhu, 2016). To decrease the cost of the MG CMFD, a two-level generalized equivalence theory-based CMFD (gCMFD) acceleration system was developed, in which an analogous One-Group (1G) CMFD is created to efficiently accelerate the MG CMFD solutions and the 3D whole-core transport computation (Hao et al., 2018; Kang et al., 2020). Then, Shen et al. from the University of Michigan implemented the 1G CMFD method in the MPACT code as a new scheme of TML named TML-4. The TML-4 scheme reduced the total run time of the original TML scheme by at least 16%, even 47% for certain large-scale, full-core problems (Shen et al., 2021). However, the TML-4 remains the original TML's time step structure, in which the transport level still has a significant computational expense.

The Advanced Multilevel Predictor-Corrector Quasi-static Method (AML-PCQM) scheme is proposed in this work to achieve further efficiency performance with the same accuracy.

The AML-PCQM scheme involves the coupling among four TFSP solvers, including the transient transport solver, the MG CMFD solver, the 1G CMFD solver, and the EPKE solver. For the time step structure, the AML-PCQM scheme makes 1G CMFD level replace the MG CMFD level totally at the second finest time step and expands the time steps of both transport and MG CMFD levels. With the new time step structure, the computational burdens of transport and MG CMFD can be effectively reduced, while the 1G CMFD can help maintain the overall accuracy. The TML and AML-PCQM schemes are implemented in the high-fidelity neutron transport code HNET to verify the functional performance. The HNET code is developed in C language with Message Passing Interface (MPI) parallel strategy, whose transient solver is based on a 2D/1D transport solver accelerated by the two-level time-dependent gCMFD (generalized equivalence theory-based coarse mesh finite difference) technique (Kang et al., 2020). Comparison and analysis of TML and AML-PCQM are provided using two heterogeneous single assembly problems with control rod withdrawal events.

The paper is structured as follows. *Transient Methodology* provides a comprehensive description of the transient solver at all four levels, i.e., the transport, the MG CMFD, the 1G CMFD, and EPKE transient formulations. The implementation of the AML-PCQM for all levels in HNET is described in *Iteration Strategy of the AML-PCQM Scheme*. *Numerical Results* demonstrates the comparison and the evaluation of the numerical results for the heterogeneous single assembly problems with control rod withdrawal events. Finally, *Conclusion* covers current performance and problems and a work plan for the future.

TRANSIENT METHODOLOGY

This section shows the specifics of the equations for the four levels of the transient solution. The 3D transient transport equations are presented first, followed by the 3D MG CMFD transient equations, the 3D 1G CMFD transient equations, and the EPKEs.

3D Transport Transient Fixed Source Equation

The 3D transient transport solution begins with the 3D time-dependent multi-group neutron transport equation with

isotropic scattering approximation in the Cartesian coordinate system, as shown below.

$$\frac{1}{\nu_g\left(\vec{r}\right)}\frac{\partial\varphi_g\left(\vec{r},\vec{\Omega},t\right)}{\partial t}=R_g\left(\vec{r},\vec{\Omega},t\right), \tag{1A}$$

$$\begin{aligned}R_g\left(\vec{r},\vec{\Omega},t\right)=&-\Omega\cdot\nabla\varphi_g\left(\vec{r},\vec{\Omega},t\right)\\&-\Sigma_{t,g}\left(\vec{r},t\right)\varphi_g\left(\vec{r},\vec{\Omega},t\right)+S_{s,g}\left(\vec{r},\vec{\Omega},t\right)\\&+\frac{1}{4\pi}S_F\left(\vec{r},t\right)\left[\chi_{p,g}+\sum_k\beta_k\left(\chi_{d,k,g}-\chi_{p,g}\right)\right]\\&+\frac{1}{4\pi}\sum_k\chi_{d,k,g}\left[\lambda_kC_k\left(\vec{r},t\right)-\beta_kS_F\left(\vec{r},t\right)\right].\end{aligned} \tag{1B}$$

As well as the delayed neutron precursors are determined as follows,

$$\frac{\partial C_k\left(\vec{r},t\right)}{\partial t}=\beta_kS_F\left(\vec{r},t\right)-\lambda_kC_k\left(\vec{r},t\right),\qquad k=1,2,\ldots, \tag{2}$$

where φ is the angular flux and C_k is the delayed neutron precursor density for the delayed group k. S_F is the total fission neutron source, and its value is modified by the calculated eigenvalue in the steady-state calculation, and $S_{s,g}$ is the scatter neutron source for the angle $\vec{\Omega}$ and the group g. χ_p and χ_d are the prompt and delayed neutron spectrums, respectively. β_k is the delayed neutron fraction and λ_k is decay constant of the k group delayed neutron precursor.

The time-dependent angular flow may be represented using the exponential transformation as,

$$\varphi_g\left(\vec{r},\vec{\Omega},t\right)=\tilde{\varphi}_g\left(\vec{r},\vec{\Omega},t\right)e^{\alpha_g^n\left(\vec{r},\vec{\Omega}\right)\left(t-t_{n-1}\right)},\ t\in[t_{n-1},t_n], \tag{3A}$$

where the α^n can be obtained by the power p of time $t_{n\text{-}1}$ and $t_{n\text{-}2}$ as,

$$\alpha_g^n\left(\vec{r},\vec{\Omega}\right)=\frac{1}{\Delta t_{n-1}}\ln\frac{p^{n-1}}{p^{n-2}}. \tag{3B}$$

Then the left term of **Eq. 1A** can be transformed into the following form,

$$\begin{aligned}&\frac{1}{\nu_g(\vec{r})}\frac{\partial\varphi_g(\vec{r},\vec{\Omega},t)}{\partial t}=\frac{1}{\nu_g(\vec{r})}\left(e^{\alpha_g^n(t-t_{n-1})}\frac{\partial\tilde{\varphi}_g(\vec{r},\vec{\Omega},t)}{\partial t}\right.\\&\left.+\alpha_g^ne^{\alpha_g^n(t-t_{n-1})}\tilde{\varphi}_g(\vec{r},\vec{\Omega},t)\right)\\&=R_g(\vec{r},\vec{\Omega},t)\end{aligned} \tag{3C}$$

Then,

$$\begin{aligned}\frac{1}{\nu_g\left(\vec{r}\right)}\frac{\partial\tilde{\varphi}_g\left(\vec{r},\vec{\Omega},t\right)}{\partial t}=e^{-\alpha_g^n\left(t-t_{n-1}\right)}&\left(R_g\left(\vec{r},\vec{\Omega},t\right)\right.\\&\left.-\frac{\alpha_g^n}{\nu_g}\varphi_g\left(\vec{r},\vec{\Omega},t\right)\right).\end{aligned} \tag{3D}$$

For a given Δt_n at time step n, **Eq. 3D** may be further discretized for time using the first order Backward Euler technique (implicit method), as shown below,

$$\begin{aligned}&\Omega\cdot\nabla\varphi_g^n\left(\vec{r},\vec{\Omega}\right)+\left[\Sigma_{t,g}^n\left(\vec{r}\right)+\frac{\alpha^n}{\nu_g\left(\vec{r}\right)}\right]\varphi_g^n\left(\vec{r},\vec{\Omega}\right)\\&=-\frac{\varphi_g^n\left(\vec{r},\vec{\Omega}\right)}{\Delta t_n\nu_g\left(\vec{r}\right)}+\frac{\varphi_g^{n-1}\left(\vec{r},\vec{\Omega}\right)}{E_g^n\left(\vec{r},\vec{\Omega}\right)\Delta t_n\nu_g\left(\vec{r}\right)}+S_{s,g}^n\left(\vec{r},\vec{\Omega}\right)\\&+\frac{1}{4\pi}\left\{S_F^n\left(\vec{r}\right)\left[\chi_{p,g}+\sum_k\beta_k\left(\chi_{d,k,g}-\chi_{p,g}\right)\right]\right.\\&\left.+\sum_k\chi_{d,k,g}\left[\lambda_kC_k^n\left(\vec{r}\right)-\beta_kS_F^n\left(\vec{r}\right)\right]\right\},\end{aligned} \tag{4A}$$

where

$$E_g^n\left(\vec{r},\vec{\Omega}\right)=e^{-\alpha_g^n\left(t_n-t_{n-1}\right)}, \tag{4b}$$

Regarding the precursor equation,

$$\begin{aligned}\frac{d}{dt}\left(C_k\left(\vec{r},t\right)e^{\lambda_kt}\right)&=e^{\lambda_kt}\frac{dC_k\left(\vec{r},t\right)}{dt}+e^{\lambda_kt}\lambda_kC_k\left(\vec{r},t\right)\\&=\beta_kS_F\left(\vec{r},t\right)e^{\lambda_kt}.\end{aligned} \tag{5}$$

Assuming that the fission source is linear over a time step,

$$G\left(\vec{r},t\right)=S_F\left(\vec{r},t\right)e^{-\alpha\left(t-t_{n-1}\right)}=G^n\left(\vec{r}\right)w+G^{n-1}\left(\vec{r}\right)(1-w), \tag{6A}$$

$$w=\frac{t-t_{n-1}}{\Delta t_n}. \tag{6B}$$

Then, integrating precursor equations over a time step ($t_{n\text{-}1}$, t_n),

$$\begin{aligned}C_k^n\left(\vec{r}\right)=e^{-\tilde{\lambda}_k^n}C_k^{n-1}\left(\vec{r}\right)+e^{\alpha^n\Delta t_n}\beta_k\Delta t_n&\left\{G^n\left(\vec{r}\right)\kappa_1\left(\tilde{\lambda}_k^n\right)\right.\\&\left.+G^{n-1}\left(\vec{r}\right)\left[\kappa_0\left(\tilde{\lambda}_k^n\right)-\kappa_1\left(\tilde{\lambda}_k^n\right)\right]\right\}\end{aligned} \tag{7A}$$

where

$$\tilde{\lambda}_k^n=(\lambda_k+\alpha^n)\Delta t_n \tag{7B}$$

$$\hat{\lambda}_k^n=\lambda_n\Delta t_n \tag{7C}$$

$$G^n\left(\vec{r}\right)=S_F^n\left(\vec{r}\right)e^{-\alpha^n\Delta t_n} \tag{7D}$$

$$\kappa_0(x)=(1-e^{-x})/x \tag{7E}$$

$$\kappa_1(x)=(1-\kappa_0(x))/x \tag{7F}$$

If the precursor equations are plugged into the Boltzmann transient equation with a first-order approximation of the fission source in one step, the transient fixed source equation is obtained,

$$\Omega \cdot \nabla \varphi_g^n\left(\vec{r},\vec{\Omega}\right) + \left(\Sigma_{t,g}^n\left(\vec{r}\right) + \frac{\alpha^n}{\nu_g\left(\vec{r}\right)}\right)\varphi_g^n\left(\vec{r},\vec{\Omega}\right) = S_{s,g}^n\left(\vec{r},\vec{\Omega}\right) + \frac{\widetilde{\chi}_g\left(\vec{r}\right)}{4\pi} S_F^n\left(\vec{r}\right) + \frac{1}{4\pi}\sum\nolimits_k \chi_{d,k,g}\lambda_k \widehat{C}_k^{n-1}\left(\vec{r}\right) - \frac{\varphi_g^n\left(\vec{r},\vec{\Omega}\right)}{\Delta t_n \nu_g\left(\vec{r}\right)} + \frac{\varphi_g^{n-1}\left(\vec{r},\vec{\Omega}\right)}{E_g^n\left(\vec{r},\vec{\Omega}\right)\Delta t_n \nu_g\left(\vec{r}\right)} \tag{8A}$$

where

$$\widetilde{\chi}_g^n\left(\vec{r}\right) = \chi_{p,g} + \sum\nolimits_k \chi_{d,k,g}\lambda_k\beta_k\Delta t_n\kappa_1\left[\widetilde{\lambda}_k^n\left(\vec{r}\right)\right] - \chi_{p,g}\beta_k, \tag{8B}$$

$$\widehat{C}_k^{n-1}\left(\vec{r}\right) = e^{-\widetilde{\lambda}_k^n} C_k^{n-1}\left(\vec{r}\right) + e^{\alpha^n\Delta t_n}\beta_k\Delta t_n S_F^{n-1}\left(\vec{r}\right)\left[\kappa_0\left(\widetilde{\lambda}_k^n\right) - \kappa_1\left(\widetilde{\lambda}_k^n\right)\right]. \tag{8C}$$

In this case, an isotropic approximation of the time-dependent angular flux in the source terms is used for different time steps, which has been shown to be acceptable by some state-of-the-art time-dependent transport solvers (Zhu et al., 2016), and then part of the source terms can be simplified further as,

$$\frac{\varphi_g^{n-1}(\vec{r},\vec{\Omega})}{E_g^n(\vec{r},\vec{\Omega})\Delta t_n\nu_g(\vec{r})} - \frac{\varphi_g^n(\vec{r},\vec{\Omega})}{\Delta t_n\nu_g(\vec{r})} \approx \frac{1}{4\pi}\left(\frac{\phi_g^{n-1}(\vec{r})}{E_g^n(\vec{r})\Delta t_n\nu_g(\vec{r})} - \frac{\phi_g^n(\vec{r})}{\Delta t_n\nu_g(\vec{r})}\right), \tag{9A}$$

where

$$E_g^n\left(\vec{r}\right) = e^{-\alpha^n\Delta t_n}. \tag{9B}$$

Substituting **Eq. 9A** into **Eq. 8A**,the functional transient fixed source equation is therefore as follows,

$$\Omega \cdot \nabla \varphi_g^n(\vec{r},\vec{\Omega}) + \widetilde{\Sigma}_{t,g}^n(\vec{r})\varphi_g^n(\vec{r},\vec{\Omega}) = \frac{1}{4\pi}\left[S_{s,g}^n(\vec{r}) + \widetilde{\chi}_g(\vec{r})S_F^n(\vec{r}) + S_{tr,g}^n(\vec{r})\right], \tag{10A}$$

$$\widetilde{\Sigma}_{t,g}^n(\vec{r}) = \Sigma_{t,g}^n(\vec{r}) + \frac{\alpha^n}{\nu_g(\vec{r})}, \tag{10B}$$

$$S_{tr,g}^n(\vec{r}) = S_{dc,g}^{n-1}(\vec{r}) + S_{dt,g}^{n-1}(\vec{r}) - \frac{\phi_g^n(\vec{r})}{\Delta t_n\nu_g(\vec{r})}, \tag{10C}$$

$$S_{dc,g}^{n-1}(\vec{r}) = \sum\nolimits_k \chi_{d,k,g}\lambda_k \widehat{C}_k^{n-1}(\vec{r}), \tag{10D}$$

$$S_{dt,g}^{n-1}(\vec{r}) = \frac{\phi_g^{n-1}(\vec{r})}{E_g^n(\vec{r})\Delta t_n\nu_g(\vec{r})}. \tag{10E}$$

Eq. 10 may therefore be solved using any conventional steady-state neutron transport solver. A 2D/1D methodology is utilized in this study, in which the 2D radial MOC (method of characteristics) and 1D axial NEM (nodal expansion method) are linked with transverse leakage terms. These techniques' concepts are described in the referenced article (Kang et al., 2020).

3D MG CMFD Transient Equation

The time-dependent diffusion equation with precursor equations for the CMFD formulation is provided in **Eq. 11**.

$$\frac{1}{\nu_g\left(\vec{r}\right)}\frac{\partial\phi_g\left(\vec{r},t\right)}{\partial t} = \nabla\cdot D_g\left(\vec{r},t\right)\nabla\phi_g\left(\vec{r},t\right) - \Sigma_{t,g}\left(\vec{r},t\right)\phi_g\left(\vec{r},t\right) + S_{s,g}\left(\vec{r},t\right) + \frac{1}{4\pi}S_F\left(\vec{r},t\right)\left[\chi_{p,g} + \sum\nolimits_k\beta_k\left(\chi_{d,k,g} - \chi_{p,g}\right)\right] + \frac{1}{4\pi}\sum\nolimits_k\chi_{d,k,g}\left[\lambda_k C_k\left(\vec{r},t\right) - \beta_k S_F\left(\vec{r},t\right)\right] \tag{11A}$$

$$\frac{\partial C_k\left(\vec{r},t\right)}{\partial t} = \beta_k S_F\left(\vec{r},t\right) - \lambda_k C_k\left(\vec{r},t\right), \qquad k = 1,2,\cdots, \tag{11B}$$

With similar approximations in the transient transport equations, the CMFD TFSP equation can be derived by incorporating the transport TFSP equation (**Eq. 10**) over 4π in the coarse mesh as follows,

$$\sum_{q\in neighbor} J_{g,c,q}^{n,l}A_{c,q} + V_c\left[\left(\overline{\Sigma}_{t,g,c}^n + \frac{1}{\Delta t_n\nu_{g,c}}\right)\overline{\phi}_{g,c}^{n,l} - \sum_{g'}\overline{\Sigma}_{g'\to g,c}^n\overline{\phi}_{g',c}^{n,l}\right] = V_c\left(\frac{\overline{\chi}_g^n}{k_{eff}^{ss}}\sum_{g'}\nu\overline{\Sigma}_{f,g',c}^n\overline{\phi}_{g',c}^{n,l-1} + \overline{S}_{dc,g,c}^{n-1} + \overline{S}_{dt,g,c}^{n-1}\right) \tag{12}$$

where, c is the index of the center node and the neighbor node corresponds to the index q. n is the index of time step and the l indicates the iteration number. The $\overline{S}_{dc}^{n-1}$ and $\overline{S}_{dt}^{n-1}$ are delay neutron sources from the last time step and will be constant in a certain time step. The $\nu\overline{\Sigma}_f^n$, $\overline{\Sigma}_{g,g'}^n$ and $\overline{\chi}^n$are the average fission, scattering cross-sections, and fission spectrum with standard definitions in nuclear reactor physics, while the $\overline{\Sigma}_t^n$ represents the average value in a node of the altered total cross-section. The k_{eff}^{ss} is the eigenvalue of the steady-state transport calculation.

According to the CMFD methodology, the interface current from node c to node q in **Eq. 11** can be quantified as follows,

$$J_{g,c,q}A_{c,q} = \widetilde{D}_{g,c,q}\overline{\phi}_{g,c} - \widetilde{D}_{g,q,c}\overline{\phi}_{g,q} \tag{13}$$

where the "D-tilde" terms on the interface from node c to node q and the one from node q to node c are defined respectively as,

$$\widetilde{D}_{g,c,q} = A_{c,q}\frac{2f_{g,c,q}^{dis}}{\frac{f_{g,c,q}^{dis}h_{c,q}}{f_{g,c,q}^{dif}D_{g,c}} + \frac{f_{g,q,c}^{dis}h_{q,c}}{f_{g,q,c}^{dif}D_{g,q}}} \tag{14A}$$

$$\widetilde{D}_{g,q,c} = A_{c,q}\frac{2f^{dis}_{g,q,c}}{\frac{f^{dis}_{g,c,q}h_{c,q}}{f^{dif}_{g,c,q}D_{g,c}} + \frac{f^{dis}_{g,q,c}h_{q,c}}{f^{dif}_{g,q,c}D_{g,q}}}. \tag{14B}$$

An albedo boundary condition is utilized for the boundary node treatment, and the "D-tilde" is provided as,

$$\widetilde{D}^{boundary}_{g,c,q} = \frac{2f^{dis}_{g,c,q}}{\frac{f^{dis}_{g,c,q}h_{c,q}}{f^{dif}_{g,c,q}D_{g,c}} + \frac{2}{\alpha}}, \tag{14C}$$

where $h_{c,q}$ is the thickness of node c in the direction from node c to node q. The D_g is the standard diffusion coefficient. The albedo α has different values for each different boundary condition, e.g., 0.5 for the vacuum boundary condition and 0 for the reflective boundary condition. Additionally, $f^{dis}_{c,q}$and$f^{dif}_{q,c}$ are referred to the Nodal Discontinuity Factor (NDF) and Modified Diffusion coefficient Factor (MDF), respectively, quantified using the surface current, surface flux, and average flux information obtained from the radial MOC and axial NEM calculations. The variables' specifics may be found in the referenced article (Xu et al., 2012; Hao et al., 2018).

Because the "D-tilde" is used to compel the interface to be the same as produced by higher-order techniques in the 2D/1D solution, the CMFD's node average fluxes and interface currents will be equal with the transport solutions after global convergence is reached. Therefore, an analogous 3D MG CMFD TFSP linear system is built using the new definition of "D-tilde" and homogenized XSs given by the radial planer MOC and the axial two-node NEM in the transport TFSP solutions, as follows,

$$\begin{aligned}
&V_c\left[-\sum_{g'}\overline{\Sigma}^{n}_{g'\to g,c}\overline{\phi}^{n,l}_{g',c} + \left(\overline{\Sigma}^{n}_{t,g,c} + \frac{1}{\Delta t_n \nu_{g,c}}\right)\overline{\phi}^{n,l}_{g,c}\right] \\
&+\begin{pmatrix}\widetilde{D}^{n}_{g,c,W} + \widetilde{D}^{n}_{g,c,N} + \widetilde{D}^{n}_{g,c,E} \\ +\widetilde{D}^{n}_{g,c,S} + \widetilde{D}^{n}_{g,c,T} + \widetilde{D}^{n}_{g,c,B}\end{pmatrix}\overline{\phi}^{n,l}_{g,c} \\
&-\begin{pmatrix}\widetilde{D}^{n}_{g,W,c}\overline{\phi}^{n,l}_{g,W} + \widetilde{D}^{n}_{g,N,c}\overline{\phi}^{n,l}_{g,N} + \widetilde{D}^{n}_{g,E,c}\overline{\phi}^{n,l}_{g,E} \\ +\widetilde{D}^{n}_{g,S,c}\overline{\phi}^{n,l}_{g,S} + \widetilde{D}^{n}_{g,T,c}\overline{\phi}^{n,l}_{g,T} + \widetilde{D}^{n}_{g,B,c}\overline{\phi}^{n,l}_{g,B}\end{pmatrix} \\
&= V_c\left(\frac{\overline{\chi}^{n}_{g}}{k^{ss}_{eff}}\sum_{g'}\nu\overline{\Sigma}^{n}_{f,g',c}\overline{\phi}^{n,l-1}_{g',c} + \overline{S}^{n-1}_{dc,g,c} + \overline{S}^{n-1}_{dt,g,c}\right)
\end{aligned} \tag{15}$$

where W, E, S, N, T and B represent the node's west, east, north, south, top, and bottom surfaces. In this situation, the fixed source solver in this work may solve the conventional steady-state fixed source transport equation with an extra transient source component for each time step. The CMFD TFSP iteration must continue to use the eigenvalue from the steady-state computation with no updates.

3D 1G CMFD Transient Equation

Because the original multi-group CMFD has a high condition number, and the condition number becomes much larger if the Wielandt shift is applied to speed the inverse power iteration, the one-level MG CMFD linear system may converge considerably more slowly (Hao et al., 2018). However, since the 1G CMFD linear system is considerably less expensive to solve, it is advantageous to use the fission source from the 1G CMFD and to update the MG nodal scalar flux to decrease the computing load of the MG CMFD calculation (Kang et al., 2020).

The cross-sections, flux, and current information from the MG CMFD TFSP linear system create the 1G CMFD TFSP linear system. Except for the unique handling of "D-tilde," all other terms in the 1G CMFD TFSP are derived by compressing the corresponding terms in the MG CMFD TFSP over all energy groups. After calculating the coefficients of the 1G CMFD TFSP, the 1G nodal scalar flux is computed by solving

$$\begin{aligned}
&\begin{pmatrix}\widetilde{D}^{n}_{c,W} + \widetilde{D}^{n}_{c,N} + \widetilde{D}^{n}_{c,E} \\ +\widetilde{D}^{n}_{c,S} + \widetilde{D}^{n}_{c,T} + \widetilde{D}^{n}_{c,B}\end{pmatrix}\overline{\phi}^{n,l}_{c} - \begin{pmatrix}\widetilde{D}^{n}_{W,c}\overline{\phi}^{n,l}_{W} + \widetilde{D}^{n}_{N,c}\overline{\phi}^{n,l}_{N} + \widetilde{D}^{n}_{E,c}\overline{\phi}^{n,l}_{E} \\ +\widetilde{D}^{n}_{S,c}\overline{\phi}^{n,l}_{S} + \widetilde{D}^{n}_{T,c}\overline{\phi}^{n,l}_{T} + \widetilde{D}^{n}_{B,c}\overline{\phi}^{n,l}_{B}\end{pmatrix}, \\
&+ V_c\left(\overline{\Sigma}^{n}_{a,c} + \frac{\alpha^n}{\nu_c} + \frac{1}{\Delta t_n \nu_c}\right)\overline{\phi}^{n,l}_{c} = V_c\left(\frac{1}{k^{ss}_{eff}}\nu\overline{\Sigma}^{n}_{f}\overline{\phi}^{n,l-1}_{c} + \overline{S}^{n-1}_{dc,c} + \overline{S}^{n-1}_{dt,c}\right)
\end{aligned} \tag{16A}$$

where

$$\overline{\phi}^{n}_{c} = \sum_{g}\overline{\phi}^{n}_{g,c}, \tag{16B}$$

$$J^{n}_{c,s} = \sum_{g}J^{n}_{g,c,s}, \tag{16C}$$

$$\overline{\Sigma}_{x} = \frac{1}{\overline{\phi}^{n}}\sum_{g}\overline{\Sigma}_{x,g}\overline{\phi}^{n}_{g}, \tag{16D}$$

$$D = \frac{1}{\overline{\phi}^{n}}\sum_{g}D\overline{\phi}^{n}_{g}, \tag{16E}$$

$$\overline{S}^{n-1}_{c} = \sum_{g}\overline{S}^{n-1}_{g,c}. \tag{16F}$$

The discontinuity factor and diffusion coefficient correction factor in 1G CMFD TFSP are calculated using the interface current from MG CMFD, which varies from the MG CMFD TFSP. Once the MG current at an interface is known, the 1G discontinuity factor and diffusion coefficient correction factor may be calculated, as described in the referenced article (Hao et al., 2018). The 1G CMFD TFSP linear system may therefore be built from the MG CMFD TFSP.

In addition, to solve the MG and 1G CMFD TFSP linear systems, a novel, efficient parallel RSILU preconditioned GMRES (Xu et al., 2019) solver has been developed. RSILU preconditioned GMRES may achieve excellent parallelization efficiency without multi-color ordering and has substantial benefits in reducing iterations and computational cost in parallel computing to find answers to the CMFD fixed source issue.

Exact Point Kinetics Equation

The EPKE can be obtained by integrating the 3D time-dependent diffusion equation with the adjoint MG CMFD fluxes as the weighting function, which is written as

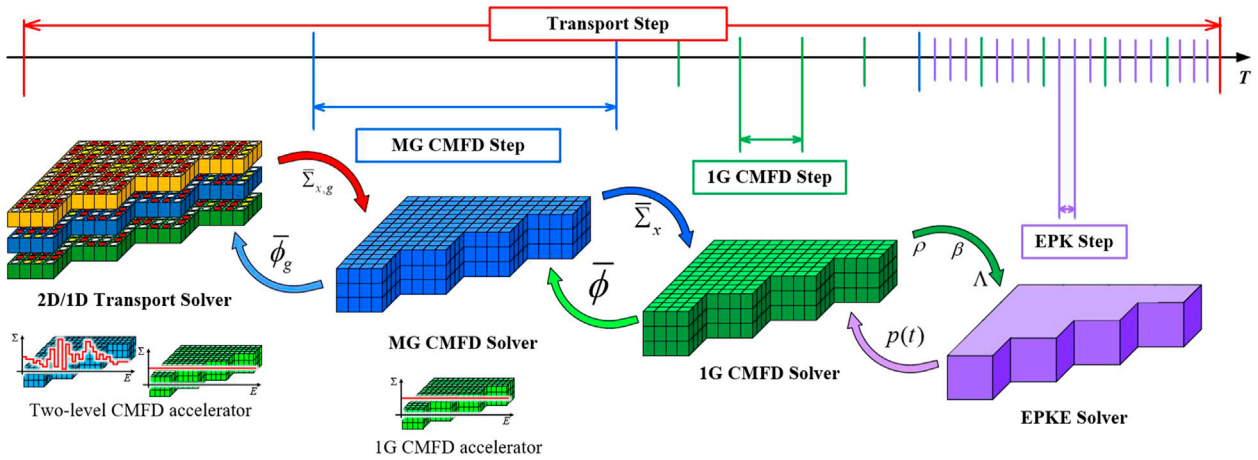

FIGURE 1 | Time step illustration of the AML-PCQM scheme in HNET.

$$\frac{dp(t)}{dt} = \frac{\rho(t) - \beta^{eff}(t)}{\Lambda(t)} p(t) + \frac{1}{\Lambda(0)} \sum_k \tilde{\lambda}_k(t) \zeta_k(t), \tag{17A}$$

and

$$\frac{d\zeta_k(t)}{dt} = \frac{\Lambda(0)}{\Lambda(t)} \beta^{eff}(t) p(t) - \tilde{\lambda}_k(t) \zeta_k(t), \quad k = 1, 2, \ldots, \tag{17B}$$

where p is the core amplitude function, and ζ_k is the adjoint flux weighted precursor concentration for the delayed group k. The reactivity, delayed neutron fractions, neutron generation time, and delayed neutron constants all have the regular definition as follows,

$$\rho(t) = \frac{1}{F(t)} < \phi^* \left(\vec{r}, E \right) (F - M) \phi \left(\vec{r}, E, t \right) >, \tag{18A}$$

$$\beta_k^{eff}(t) = \frac{1}{F(t)} < \phi^* \left(\vec{r}, E \right) \chi_{d,k} \left(\vec{r}, E \right) \beta_k \left(\vec{r} \right) S_F \left(\vec{r}, t \right) >, \tag{18B}$$

$$\Lambda(t) = \frac{1}{F(t)} < \phi^* \left(\vec{r}, E \right) \frac{1}{v_g} \phi \left(\vec{r}, E, t \right) >, \tag{18C}$$

$$\tilde{\lambda}_k(t) = \frac{< \phi^* \left(\vec{r}, E \right) \lambda_k \left(\vec{r} \right) \chi_{d,k} \left(\vec{r}, E \right) C_k \left(\vec{r}, E \right) >}{< \phi^* \left(\vec{r}, E \right) \chi_{d,k} \left(\vec{r}, E \right) C_k \left(\vec{r}, E \right) >}, \tag{18D}$$

where the cumulative spectrum of all fission neutrons is obtained by steady-state transport as following

$$\begin{aligned} &\chi_{cum}(E) \iint \nu\Sigma_f \left(\vec{r}, E' \right) \psi \left(\vec{r}, \vec{\Omega'}, E' \right) d\vec{\Omega'} dE' \\ &= \chi_p(E) \iint \left[1 - \beta \left(\vec{r}, E' \right) \right] \nu\Sigma_f \left(\vec{r}, E' \right) \psi \left(\vec{r}, \vec{\Omega'}, E' \right) d\vec{\Omega'} dE', \\ &+ \sum_k \chi_{d,k}(E) \iint \beta_k \left(\vec{r}, E' \right) \nu\Sigma_f \left(\vec{r}, E', t \right) \psi \left(\vec{r}, \vec{\Omega'}, E' \right) d\vec{\Omega'} dE' \end{aligned} \tag{18E}$$

the factor $F(t)$ is defined as

$$F(t) = < \phi^* \left(\vec{r}, E \right) \chi_{cum}(E) S_F \left(\vec{r}, t \right) >, \tag{18F}$$

and the total effective delayed neutron fraction is the summation of all delayed neutron groups as follows,

$$\beta^{eff}(t) = \sum_k \beta_k^{eff}(t). \tag{18G}$$

Then, **Eq. 17** is solved using precisely the exact discretization for the transient transport equation in *3D Transport Transient Fixed Source Equation*.

ITERATION STRATEGY OF THE AML-PCQM SCHEME

The AML-PCQM is based on the standard PCQM, while the essential idea is inspired by the TML method in MPACT. The time step setting for all levels is illustrated in **Figure 1**. Through this transient solver, the combination of three-level spatial grids and two-level energy grids can maintain a consistent accuracy and minimize the overall computational burden for the transient simulation.

In the AML-PCQM scheme, there are four solutions with three coupling levels, in which a new iteration strategy is applied to capture the neutron fluxes varies on each specific level. The overall flowchart is given in **Figure 2**; the four perpendicular blocks present the iterations strategy of the ATML algorithm. Each vertical block presents one level of the ATML solution. The most left vertical blocks represent the transient transport iteration scheme, in which the predictor angular flux shape on the sub-pin level is assumed to be accurate. Then, as shown in the second left vertical blocks, the scalar flux on the pin mesh is obtained by solving MG CMFD steps and correcting the transport solution's pin-wise amplitude function.

In the same way, the energy shape function by MG CMFD on the pin mesh is presumed accurate, and the 1G scalar flux corrects the whole-energy-space amplitude from 1G CMFD steps. Finally, the core-wise shape function is predicted by 1G CMFD, and the core-wise amplitude is corrected by the finest EPKE steps in the most right vertical blocks. The details of the coupling scheme are introduced as follows.

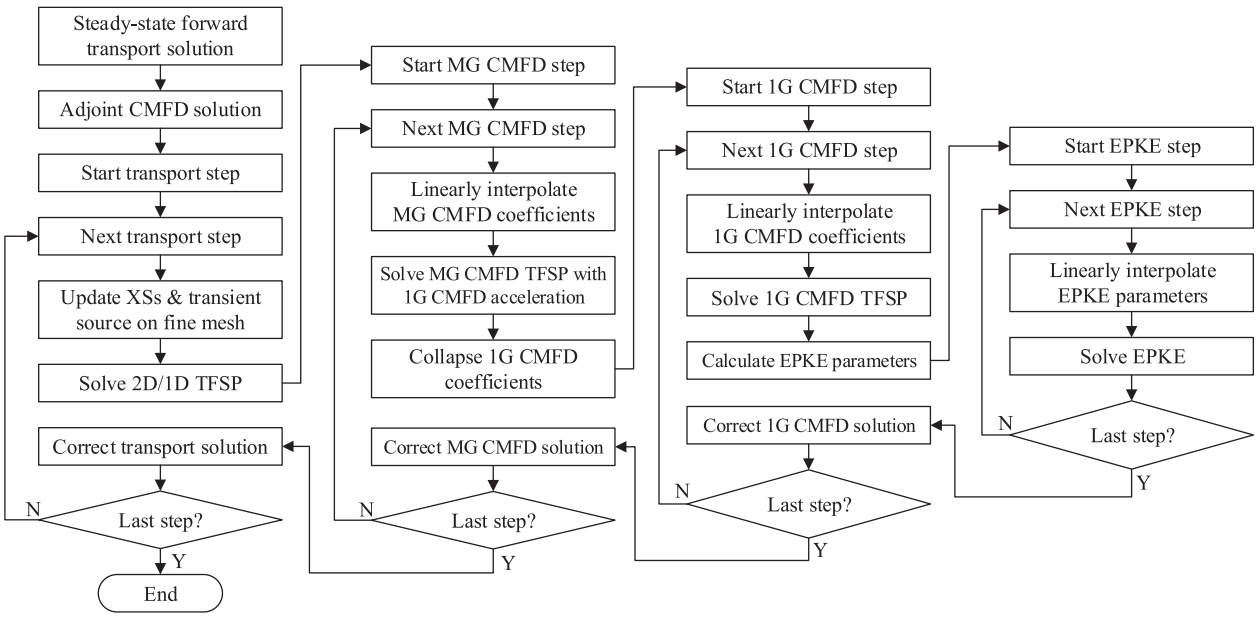

FIGURE 2 | Flowchart of the ATML iteration scheme in HNET.

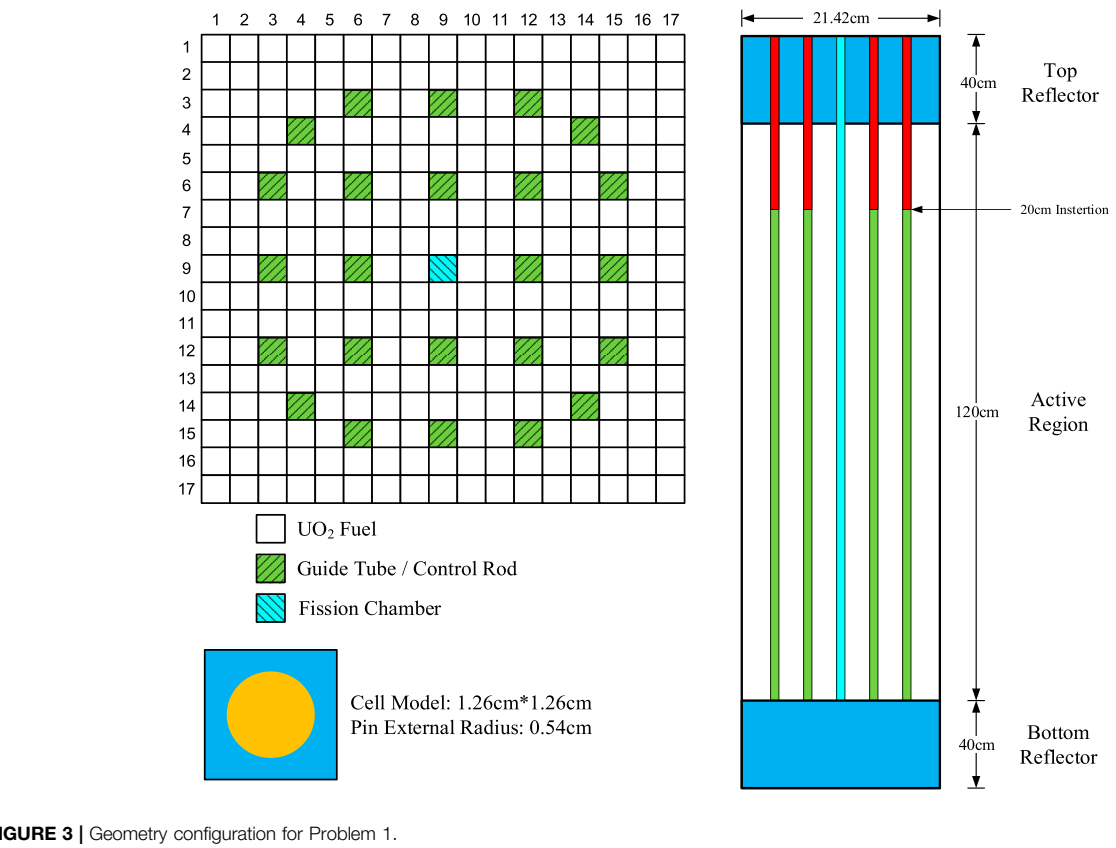

FIGURE 3 | Geometry configuration for Problem 1.

TABLE 1 | PCQM options for the cases in Problem 1.

Case ID	Transport time step (ms)	1G accelerator[a]	N_{MG}	N_{1G}	N_{PK}
1.1	0.2	No	—	—	—
1.2	0.2	Yes	—	—	—
1.3	5	Yes	—	—	25
1.4	5	No	5	—	5
1.5	5	Yes	5	—	5
1.6	5	Yes	2	2	6
1.7	5	Yes	3	3	3

[a]*1G Accelerator: 1G CMFD acceleration for iterations of MG CMFD solution.*

The first coupling level is between the transport TFSP solution and the MG CMFD TFSP solution. According to the PCQM theory, the angular flux can be factored into an amplitude and shape function in a coarse mesh *i*.

$$\varphi_g\left(\vec{r},\vec{\Omega},t\right)=P_i(t)\psi_g\left(\vec{r},\vec{\Omega},t\right),r\in i, \tag{19}$$

where P is the amplitude function, which is flat in the coarse mesh, and ψ represents the angular flux shape function on the fine meshes.

Since the amplitude and shape function definition, an artificial constraint for the shape function is necessary. Here the integral of the spatial shape function in the single coarse mesh is required to be unity as,

$$\frac{1}{V_i}\int_{\vec{r}\in i}\int_{\vec{\Omega}}\psi_g\left(\vec{r},\vec{\Omega},t\right)d\vec{\Omega}d\vec{r}=1. \tag{20}$$

After integrating the **Eq. 19** over angle and space in the \coarse mesh and using the **Eq. 20** as the constraint, the spatial amplitude function in the coarse mesh happens to be identical to the corresponding CMFD scalar flux. Thus, the angular flux can be corrected with the MG CMFD TFSP solution as in **Eq. 21**.

$$\varphi_g^{Corrected}\left(\vec{r},\vec{\Omega},t\right)=\varphi_g^{Predictor}\left(\vec{r},\vec{\Omega},t\right)\frac{\overline{\phi}_{i,g}^{Corrector}(t)}{\overline{\phi}_{i,g}^{Predictor}(t)},r\in i. \tag{21}$$

In **Eq. 21**, the term $\varphi_g^{Predictor}(\vec{r},\vec{\Omega},t)$ is the predictor angular flux by the transport TFSP solution on the transport step Δt_n, the term $\overline{\phi}_{i,g}^{Predictor}(\vec{r},t)$ is the predictor coarse-mesh scalar flux homogenized from the transport TFSP solution, and the term $\overline{\phi}_{i,g}^{Corrector}(\vec{r},t)$ is the corrector coarse-mesh scalar flux by the MG CMFD TFSP solution. The MG CMFD level is solved using the finer time step $\Delta t_n'$ with the linearly interpolated multi-group coefficients during Δt_n.

The second coupling level is for the MG CMFD and 1G CMFD. The multi-group coarse-mesh scalar flux is factored into an amplitude and shape function in a certain energy interval, but for the 1G CMFD the certain energy interval means the whole energy space. Then the factoring equation becomes as follows,

$$\overline{\phi}_{i,g}(t)=P_i'(t)\psi_{i,g}'(t), \tag{22}$$

where ψ' represents the coarse-mesh flux shape in the energy space.

The normalization condition is

$$\int_E \psi_{i,g}'(t)dE=1. \tag{23}$$

Then the energy amplitude function can be found identical to the corresponding 1G CMFD scalar flux. Similar to **Eq. 21**, the multi-group scalar flux can be corrected with the 1G CMFD TFSP solution as in **Eq. 24**. The 1G CMFD level is solved using the finer time step $\Delta t_n''$ with the linearly interpolated one-group coefficients during $\Delta t_n'$.

$$\overline{\phi}_{i,g}^{Corrected}(t)=\overline{\phi}_{i,g}^{Predictor}(t)\frac{\overline{\phi}_i^{Corrector}(t)}{\overline{\phi}_i^{Predictor}(t)} \tag{24}$$

The last level is the coupling of the 1G CMFD and EPKEs, and the factorization is still necessary, as shown in **Eq. 25**.

$$\overline{\phi}_i(t)=p(t)\psi_i''(t), \tag{25}$$

where $\overline{\phi}$, p and ψ'' represent the 1G CMFD scalar flux, the core-wise amplitude, and the spatially dependent shape function, respectively.

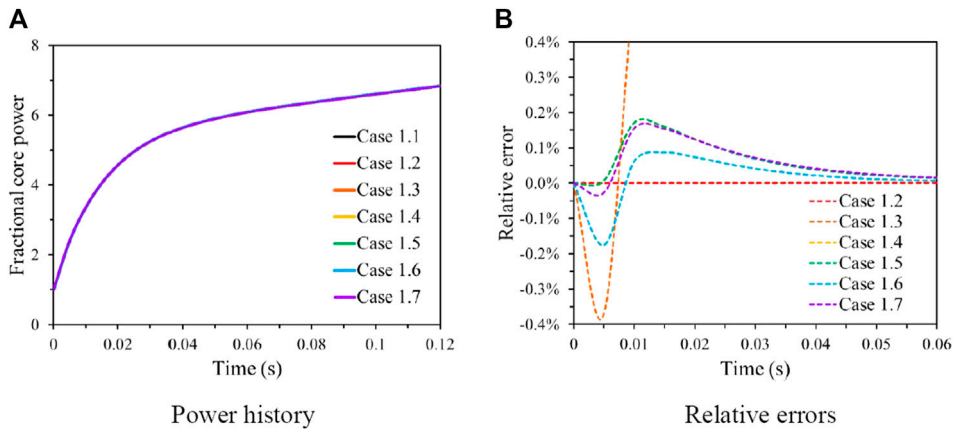

FIGURE 4 | Fractional core power results for heterogeneous UO_2 assembly problem. **(A)** Power history **(B)** Relative errors.

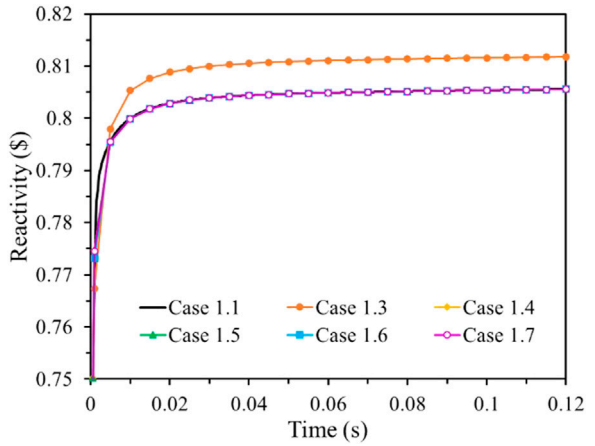

FIGURE 5 | Reactivity history for heterogeneous UO_2 assembly problem.

The constraint here is obtained using the multi-group coarse-mesh scalar flux since the EPKE is integrated from the MG CMFD, as shown in **Eq. 26**.

$$C = <\phi^*_{i,g}(0)\frac{1}{\nu_g}\psi_{i,g}(0)> = <\phi^*_{i,g}(0)\frac{1}{\nu_g}\psi_{i,g}(t)>, \quad (26)$$

where $<\quad>$ is the integration operator overall spatial regions and energy groups and C is a constant as in standard PCQM.

As a result, the 1G CMFD scalar flux can be corrected by **Eq. 27**. And the coefficients in the EPKE are linearly interpolated during the step $\Delta t''_n$.

$$\overline{\phi}_i^{Corrected}(t) = \frac{\overline{\phi}_i^{Predictor}(t)\, p^{Corrector} C}{<\phi^*_{i,g}(0)\frac{1}{\nu_g}\overline{\phi}^{Predictor}_{i,g}(t)>} \quad (27)$$

NUMERICAL RESULTS

Numerical results are presented in this section. Two heterogeneous single assembly problems are used to verify the performance of the AML-PCQM: 1) a UO_2 assembly problem based on C5G7-TD to check the ability of 1G CMFD acceleration for iterations and overall scheme, 2) a 51-group single assembly problem to analyze the performance of AML-PCQM for the control rod withdrawal event. The HNET code simulates all cases with the 2.30 GHz Intel Xeon E5-2699 v3 CPU. The 2D/1D hybrid scheme is performed for transient transport in which the radial 2D calculation uses the planer MOC solver, and the axial 1D equation is solved with the NEM.

Problem 1: A UO_2 Assembly Problem Based on C5G7-TD

Problem 1 is based on a UO_2 assembly from the C5G7-TD benchmark's TD4 exercise (Hou et al., 2017). The macro cross-sections are shown in a 7-group structure, whereas the kinetics parameters are presented in an 8-delayed group neutron representation. A ray spacing of 0.05 cm with 48 azimuthal angles and a Tabuchi-Yamamoto polar quadrature (Yamamoto et al., 2007) using 3 polar angles per half-space are utilized for the planer MOC ray-tracing module. All active pin cells are divided into 32 flat source regions consisting of 3 fuel rings and 1 moderator rings with 8 azimuthal divisions, and the reflector cells use the 6 × 6 type grid. For the 3D configuration, the 2D geometry mesh is extruded with eight 10-cm-thick layers, eight 5-cm-thick layers, and two 20-cm-thick axial layers for both the top and bottom reflector regions. The vacuum boundary condition is applied to the core's axial boundaries, while the radial boundaries are all reflective. The configuration is provided in **Figure 3**.

Six cases of Problem 1 are simulated for the preliminary verification of the AML-PCQM scheme. The transient event in Problem 1 is a prompt withdrawal of 24 control rods at the beginning of the 0.12 s transient. The assembly is partly rodded for the initial condition, where the control rods stay at 20 cm of insertion. Cases 1.1 and 1.2 are with the pure transient transport scheme with the time step of 0.2 ms. All other cases are with a 5 ms time step for the transient transport level. The case 1.3 is provided as the original PCQM case with transport and EPK method. Cases 1.4 and 1.5 use the TML method with a recommended ratio for each PCQM level in MPACT (Zhu et al., 2016). Cases 1.6 and 1.7 present the AML-PCQM scheme with four levels of different time steps, where the 5 ms transport time step and the 0.2 ms EPKE time step are identical to

TABLE 2 | Results of accuracy and efficiency for the cases in Problem 1.

Case ID	RMSE	Solvers' run time (s)				Iterations			
		Total	MOC	MG[a]	1G[b]	EPK	MOC	MG[a]	1G[b]
1.1	–	535.339	443.088	92.251	–	–	1,293	66,586	–
1.2	0.0071%	464.442	440.256	7.511	16.675	–	1,293	5,425	55,516
1.3	19.2815%	111.898	99.789	3.175	8.934	0.795	279	1976	26,309
1.4	0.2638%	218.284	86.521	131.772	–	0.715	275	90,726	–
1.5	0.2616%	77.145	61.181	3.656	12.317	0.718	198	2,811	41,746
1.6	0.1630%	81.462	61.439	3.196	16.827	0.730	199	2,242	53,539
1.7	0.2579%	83.746	61.500	3.491	18.755	0.868	199	2,412	58,745

[a]*MG: MG CMFD.*
[b]*1G: 1G CMFD.*

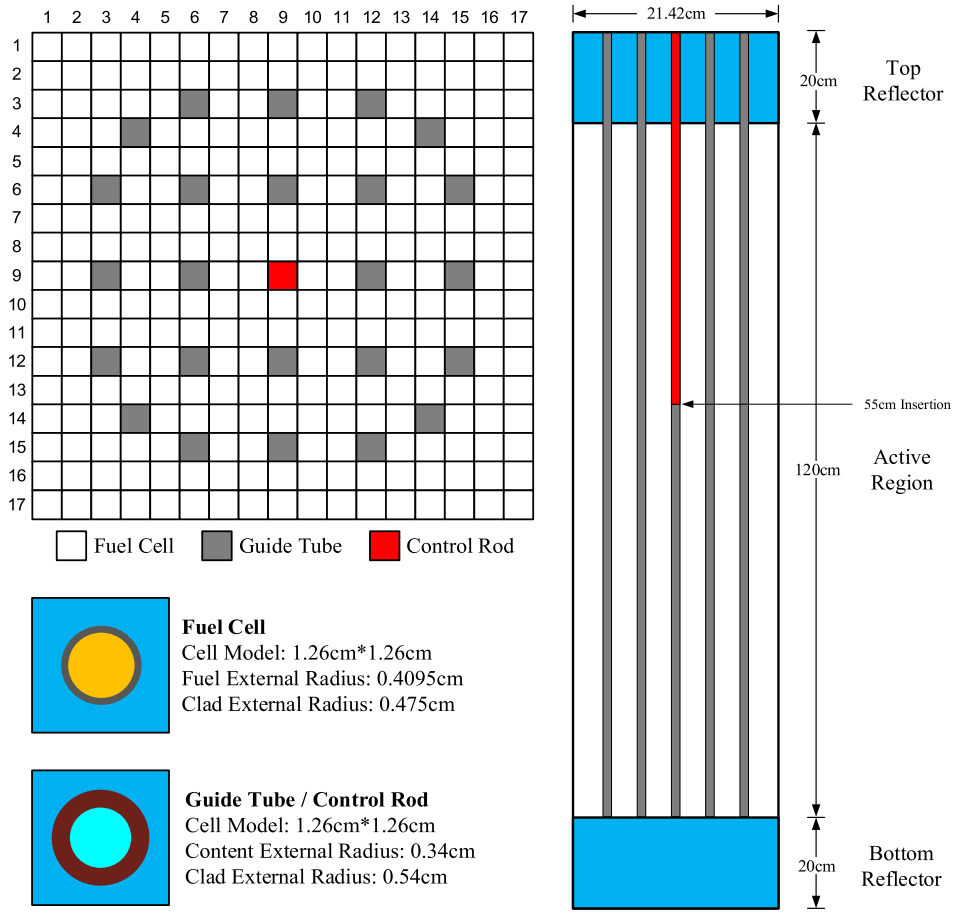

FIGURE 6 | Geometry configuration for Problem 2.

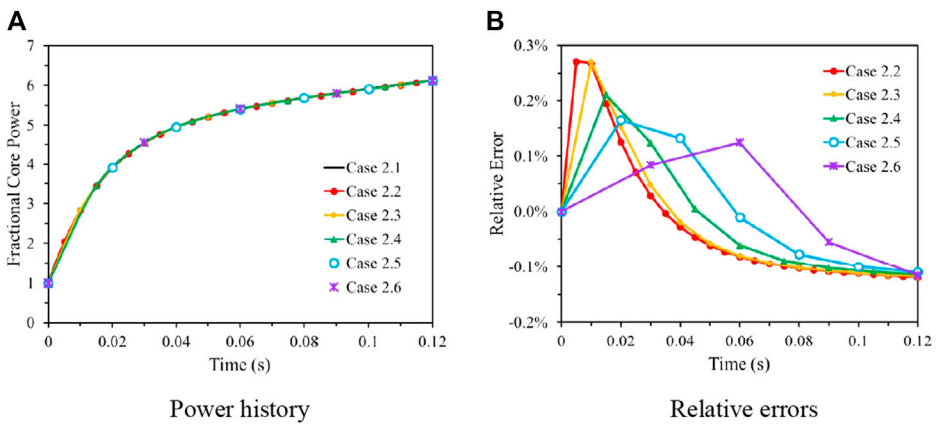

FIGURE 7 | The TML cases's results in Problem 2. **(A)** Power history **(B)** Relative errors.

other mentioned cases, but the time step for MG CMFD and 1G CMFD are different.

Cases 1.1 and 1.4 aim to reference the pure transient transport and the TML scheme from MPACT. Then, the case 1.2 and 1.5 are intended to present the 1G CMFD acceleration for the MG CMFD iterations in case 1.1 and 1.4. Further, the case 1.6 and 1.7 are run to show the preliminary performance of the AML-PCQM scheme. **Table 1** provides the details of these cases, where the

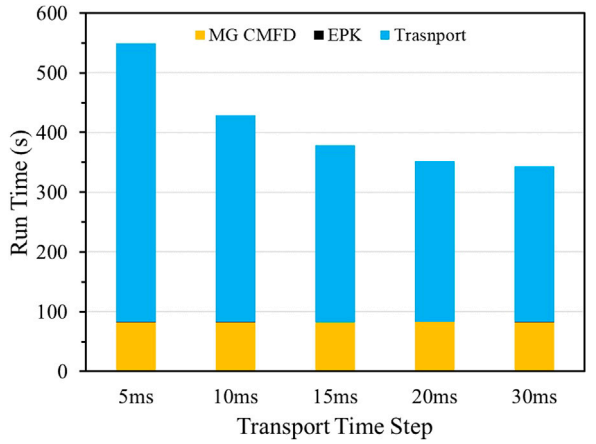

FIGURE 8 | Comparison of total solver run time for different TML cases.

"N_{MG}", "N_{1G}", and "N_{PK}" represent the number of MG CMFD steps per transport step, the number of 1G CMFD steps per MG CMFD step, and the number of EPKE steps per MG or 1G CMFD step, respectively.

The fractional core power history is shown in **Figure 4** in terms of accuracy. The relative errors of the fractional core power in cases 1.2 to 1.7 are also provided in **Figure 4**, where case 1.1 results are performed as the reference. Also, the reactivity history is presented in **Figure 5**. Finally, the Root Mean Squared Error (RMSE) of the fractional core power history, the solver run time, and the iteration numbers for each case are summarized in **Table 2**, where the index "MG" and "1G" represent MG CMFD and 1G CMFD respectively.

For the accuracy of the fractional core power, the relative errors are all less than 0.2%, except the standard PCQM case 1.3. The reason is that the reactivity insertion caused by the prompt rod withdrawal does not change as a ramping line during the first several steps, which makes the linear interpolation of the EPK parameters lead to higher relative errors. However, the multilevel quasi-static cases present better reactivity results because the middle-level CMFD solvers capture the flux change in the pin meshes during the middle time steps.

As indicated, reference case 1.1 requires a considerable computational time of 535 s for all solvers, which is about 6 times larger than other PCQM cases because of the large number of time steps for pure transport. On the other hand, in case 1.2, the MG CMFD solver's iterations and run time effectively decrease due to the 1G CMFD acceleration for the MG CMFD solution, which has been discussed in the referenced paper (Kang et al., 2020). First, the standard PCQM results are presented as case 1.3 for the comparison to the multilevel quasi-static cases. Then, cases 1.4 and 1.5 are compared to check the

TABLE 3 | Results of accuracy and efficiency for the TML cases in Problem 2.

Case ID	Time step			RMSE	PCQM solver run time (s)			
	Transport	MG[a]	EPK		Total	Transport	MG[a]	EPK
2.1	0.2 ms	—	—	—	4487.887	4487.887	—	—
2.2	5 ms	1 ms	0.2 ms	0.5331%	549.704	466.896	81.926	0.882
2.3	10 ms	1 ms	0.2 ms	0.5506%	428.602	345.682	82.137	0.783
2.4	15 ms	1 ms	0.2 ms	0.5550%	378.676	296.555	81.578	0.543
2.5	20 ms	1 ms	0.2 ms	0.5526%	351.563	268.162	82.957	0.444
2.6	30 ms	1 ms	0.2 ms	0.5478%	343.264	260.615	82.313	0.336

[a]*MG: MG CMFD.*

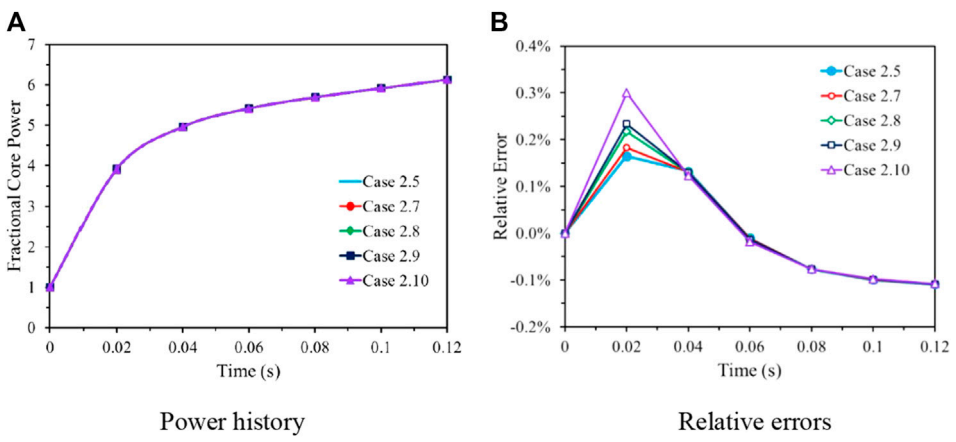

FIGURE 9 | The AML-PCQM cases' results in Problem 2. **(A)** Power history **(B)** Relative errors.

TABLE 4 | Results of accuracy and efficiency for the AML-PCQM cases in Problem 2

Case ID	Time step				RMSE (%)	PCQM solver run time (s)				
	Transport	MG[a]	1G[b]	EPK		Total	Transport	MG[a]	1G[b]	EPK
2.5	20 ms	1 ms	—	0.2 ms	0.5526	351.563	268.162	82.957	—	0.444
2.7	20 ms	2 ms	1 ms	0.2 ms	0.5661	310.251	265.881	43.937	5.593	0.433
2.8	20 ms	4 ms	1 ms	0.2 ms	0.5935	290.232	264.267	25.571	5.764	0.394
2.9	20 ms	5 ms	1 ms	0.2 ms	0.6079	294.298	269.628	24.286	5.669	0.384
2.10	20 ms	10 ms	1 ms	0.2 ms	0.6728	293.710	272.810	20.534	5.523	0.366

[a]*MG: MG CMFD.*
[b]*1G: 1G CMFD.*

ability of the 1G CMFD iteration accelerator for the TML scheme, where the CMFD solvers' rum time and the total solvers' time are reduced by about 87.9 and 64.7%, respectively. Finally, in the case 1.6 and 1.7, several 1G CMFD steps replace specific MG CMFD steps, which both achieve a partial reduction of the MG CMFD's expense.

The multilevel quasi-static cases show the reasonably good performance of the reference case, which indicates that the TML and AML-PCQM applied in HNET perform superiorly in capturing the amplitude and shape functions' evolution. Although the AML-PCQM has shown its advantage in decreasing the MG CMFD run time, it is notable that the total solver run time seems to be affected reversely between the TML cases and AML-PCQM cases. The main reason is that the energy group number of C5G7 cross-sections is not many enough for the 1G CMFD level to access an obvious advantage on efficiency. For the same reason, the MG CMFD solver's run time becomes less than expected, making the comparison inconspicuous. Therefore, a 51-group single assembly control rod withdrawal problem is presented and discussed in the next sub-section.

Problem 2: A Single Assembly Problem With 51-Group Cross-Sections

Problem 2 is present here to further analyze the accuracy and efficiency performance of the AML-PCQM. Problem 2 is a typical 17 × 17 type fuel assembly problem. The C5G7-TD benchmark is used to design the pin cell architecture (Boyarinov et al., 2016). The macro cross-sections are given in a 51-group structure, and the kinetics parameters are also provided in an 8 delayed group neutron representation (Kim, 2016). The MOC ray spacing is fixed to 0.05 cm, and 64 azimuthal angles and a Tabuchi-Yamamoto polar quadrature (Yamamoto et al., 2007) with 2 polar angles per half-space are used. The active pin cells are divided into 40 flat source regions consisting of 3 fuel rings, 1 clad ring, and 1 moderator ring with 8 azimuthal divisions, and the axial reflector cells also use the 6 × 6 type grid. The axial configuration includes 24 fuel layers of 5 cm thickness and 2 axial reflector layers of 10 cm thickness both at the top and bottom of the reflector areas, as shown in **Figure 6**. The boundary condition of Problem 2 is the same as Problem 1. The transient event in Problem 2 is a prompt withdrawal of the central control rod at the beginning of the 0.12 s transient. The assembly is partly rodded for the initial condition, where the central control rod stays at 55 cm of insertion.

Before further verification for the AML-PCQM, one must explain how the multilevel PCQM scheme works. In the standard PCQM, the flux distribution is separated into an amplitude and shape function, solved by transient transport and EPK, respectively. Then, the EPK replaces the transport and captures the amplitude varies on the fine time step, while the transient transport is moved to a coarse time step for the slower changes of the shape function. Therefore, the overall transient simulation has a much lower computational expense with reasonable accuracy. The first coarse time step in the TML technique becomes the medium time step, on which the transient transport is replaced again by MG CMFD. As a result, the transport time step grows coarser. As a result, the overall computational burden decreases again.

Although the MPACT team has implemented the 1G CMFD into the TML system referred to as TML-4 (Shen et al., 2021), the 1G CMFD was only used to remit the computing expense the MG CMFD level. As a result, the transient transport time step in TML-4 was unchanged, which means the largest computational burden is still not

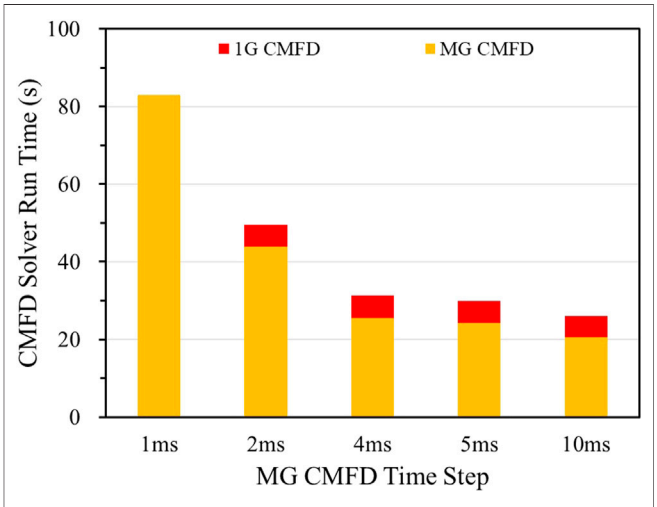

FIGURE 10 | Acceleration performance of AML-PCQM cases on CMFD run time.

TABLE 5 | Overall acceleration performance for the AML-PCQM scheme in Problem 2

case ID	Time step				RMSE	Total solver time (s)	Speedup
	Transport	MG[a]	1G[b]	EPK			
2.1	0.2 ms	—	—	—	—	4487.887	—
2.2	5 ms	1 ms	—	0.2 ms	0.5331%	549.704	8.16
2.8	20 ms	4 ms	1 ms	0.2 ms	0.5935%	290.232	15.46

[a]*MG: MG CMFD level.*
[b]*1G: 1G CMFD level.*

improved. However, it is completely reasonable and possible to extend the transport time step once again through 1G CMFD level between MG CMFD and EPK, which is exactly the primitive purpose of the AML-PCQM.

Cases 2.1 to 2.6 are presented to observe the influence of the transport step in TML cases. The fractional core power history and relative errors are shown in **Figure 7**. In **Table 3**, the transport time step grows coarser through cases 2.2–2.6, where the MG CMFD step and the EPK step stay unaltered to capture the flux varies. Case 2.1 with a transport step of 0.2 ms is used as the reference case for accuracy. The RMSE of the fractional core power history indicates that the TML scheme in the HNET code does maintain an excellent agreement of about 0.55% to the reference case. The transient transport also requests less execution time when the time step was growing coarser, and the over computational burden is reduced, as it represents in **Figure 8**. Unfortunately, though, the MG CMFD solution demands a larger ratio of the transport run time, even nearly 35%, although the MG CMFD level maintains the original expense on solutions.

In this circumstance, the 1G CMFD level can be applied to reduce the MG CMFD run time like the cases 1.5 and 1.6 in Problem 1. **Figure 9** provides the fractional core power history and the relative errors for the AML-PCQM case 2.7 to 2.10. **Table 4** and **Figure 10** show that the 1G CMFD substitutes the original 1 ms time step for the MG CMFD. As a result, the RMSE of the fractional core power history slightly increases to about 0.6%, but it is still an excellent agreement to the reference case. This is because the total burden of CMFD solvers keeps decreasing when the MG CMFD time is step getting large, and the tendency to be limited appears after the MG CMFD time step is larger than 5 ms. Even so, approximately 70% of the CMFD solver's run time can be depressed again because of the AML-PCQM scheme.

The results here indicate that the 1G CMFD level makes an essential contribution to the intermediate time step in capturing variations in the whole-energy-space amplitude magnitude in front of EPKE. Also, the 1G CMFD level is more computationally efficient in predicting changes in the pin-wise amplitude function on the whole energy space. Therefore, it can be practical to minimize the MG CMFD solver's computational expense, as shown in **Table 5**, and presents a considerable potential to handle the circumstances with the larger geometry modeling.

CONCLUSION

A new multilevel predictor-corrector quasi-static method for pin-resolved neutron kinetics simulation named AML-PCQM is proposed to implement a scheme in the HNET code.

The transient formulation for the multi-group neutron transport equation is given first, followed by two gCMFD TFSP solutions and a summary of the EPKE scheme. Following that, the AML-PCQM algorithm is presented, in which the PCQM iteration technique is used to couple the transport/MG CMFD level, the MG CMFD/1G CMFD level, and the 1G CMFD/EPKE level. In each level, the initial TFSP is solved using a coarse time step in the predictor process, and the flux distribution is factorized to the amplitude and shape functions in the subsequent corrector process, where the predicted solution is rectified using numerous fine time steps. For example, in the transport/MG CMFD level coupling, the spatial shape functions of the angular sub-pin flux are assumed to change slowly over time, and the MG CMFD pin-wise amplitude function is calculated using a multi-step MG CMFD transient equation. The MG CMFD scalar flux calculated in its time step is then corrected by the 1G CMFD scalar flux in the second level. For the last level, the predictor 1G CMFD scalar flux is then corrected by a core-wise amplitude magnitude generated by the EPKE. Finally, two prompt rod withdrawal problems are chosen for the primary verification of the accuracy and efficiency performance of the AML-PCQM solution and to compare different quasi-static modes. The numerical results indicate that the speedup results of AML-PCQM cases reach over 15, and the errors remain less than 0.6% with the reference case of a pure transient transport solution. Further, the AML-PCQM scheme performs remarkable overall efficiency advantages compared to the TML method and shows a considerable potential to handle the larger geometry modeling circumstances.

In general, the preliminary numerical results for the prompt rod withdrawal problems show that the AML-PCQM scheme in HNET has successfully utilized several TFSP solvers in a multilevel quasi-static calculation framework, the good agreement of the fractional core power and reactivity to the reference cases has been achieved, and the balance between the accuracy and efficiency can be adjusted through different quasi-static mode or time step set. More verifications are required in the future, particularly for simulations with non-smooth reactivity insertion or explicitly modeled rod movement. Another ongoing research emphasis is the development of the thermal-hydraulic feedback module.

DATA AVAILABILITY STATEMENT

The original contributions presented in the study are included in the article/Supplementary Material, further inquiries can be directed to the corresponding author.

AUTHOR CONTRIBUTIONS

LK: Develop the transient transport code and the AML-PCQM algorithm; Transient analysis of the benchmark problems. Writing. CH: Propose ideas to AML-PCQM scheme; Develop the AML-PCQM algorithm and verification. Writing - Review and Editing, Supervision. QZ: Verification of the AML-PCQM implementation. YX: Ideas to conduct the AML-PCQM scheme and transient transport. Provide details of the theory and advices to solve problems in the process of the research. Supervision.

FUNDING

This study is supported by the Chinese National Natural Science Foundation Project 12075067 and the National Key R and D Program of China (2018YFE0180900).

REFERENCES

Ban, Y., Endo, T., and Yamamoto, A. (2012). A Unified Approach for Numerical Calculation of Space-dependent Kinetic Equation. *J. Nucl. Sci. Tech.* 49 (5), 496–515. doi:10.1080/00223131.2012.677126

Boyarinov, F., Fomichenko, P., Hou, J., Kostadin, N., Jason, J., Ivanov, V., et al. (2016). *Deterministic Time-dependent Neutron Transport Benchmark without Spatial Homogenization (C5G7-TD)*. Paris, France: Nuclear Energy Agency Organisation for Economic Co-operation and Development (NEA-OECD).

Caron, D., Dulla, S., and Ravetto, P. (2016). New Aspects in the Implementation of the Quasi-Static Method for the Solution of Neutron Diffusion Problems in the Framework of a Nodal Method. *Ann. Nucl. Energy* 87, 34–48.

Cho, N. Z., Lee, G. S., and Park, C. J. (2002). Fusion of Method of Characteristics and Nodal Method for 3-d Whole-Core Transport Calculation. *Trans. Am. Nucl. Soc.* 87, 322–324.

Collins, B., Stimpson, S., Kelley, B. W., Young, M. T. H., Kochunas, B., Graham, A., et al. (2016). Stability and Accuracy of 3D Neutron Transport Simulations Using the 2D/1D Method in MPACT. *J. Comput. Phys.* 326, 612–628. doi:10.1016/j.jcp.2016.08.022

Hao, C., Kang, L., Xu, Y., Song, P., Zhao, Q., and Zhang, Z. (2018). 3D Whole-Core Neutron Transport Simulation Using 2D/1D Method via Multi-Level Generalized Equivalence Theory Based CMFD Acceleration. *Ann. Nucl. Energ.* 122, 79–90. doi:10.1016/j.anucene.2018.08.014

Henry, A. F., and Curlee, N. J. (1958). Verification of a Method for Treating Neutron Space-Time Problems. *Nucl. Sci. Eng.* 4, 727–744. doi:10.13182/NSE4-727

Henry, A. F. (1958). The Application of Reactor Kinetics to the Analysis of Experiments. *Nucl. Sci. Eng.* 3, 52–70. doi:10.13182/NSE58-1

Hou, J. J., Ivanov, K. N., Boyarinov, V. F., and Fomichenko, P. A. (2017). OECD/NEA Benchmark for Time-Dependent Neutron Transport Calculations Without Spatial Homogenization. *Nucl. Eng. Des.* 317, 117–189.

Joo, H. G., Cho, J. Y., Kim, K. S., Lee, C. C., Zee, S. Q., et al. (2004). *Methods and Performance of a Three Dimensional Whole-Core Transport Code DeCART*. Chicago, Illinois, US: PHYSOR 2004–The Physics of Fuel Cycles and Advanced Nuclear Systems.

Jung, Y. S., Shim, C. B., Lim, C. H., and Joo, H. G. (2013). Practical Numerical Reactor Employing Direct Whole Core Neutron Transport and Subchannel thermal/hydraulic Solvers. *Ann. Nucl. Energ.* 62, 357–374. doi:10.1016/j.anucene.2013.06.031

Kang, L., Hao, C., Zhao, Q., and Xu, Y. (2020). Two-level Time-dependent GET Based CMFD Acceleration for 3D Whole Core Transient Transport Simulation Using 2D/1D Method. *Ann. Nucl. Energ.* 142 (2020), 107405. doi:10.1016/j.anucene.2020.107405

Kao, P., and Henry, A. (1989). "Supernodal Analysis of PWR Transients," in Proc. Topl. Mtg. Advances in Nuclear Engineering Computation and Radiation Shielding, Santa Fe, New Mexico, April 9–13, 1989 (American Nuclear Society).

Kim, K. (2016). *Generation of the V4.2m5 AMPX and MPACT 51 and 252-Group Libraries with ENDF/B-VII.0 and VII.1*. Oak Ridge, TN: Oak Ridge National Laboratory. Report No. CASL-U-2016-1177-000 Rev. 0. https://info.ornl.gov/sites/publications/files/Pub70361.pdf. doi:10.2172/1337852

Kochunas, B., Collins, B., Stimpson, S., Salko, R., Jabaay, D., Graham, A., et al. (2017). VERA Core Simulator Methodology for Pressurized Water Reactor Cycle Depletion. *Nucl. Sci. Eng.* 185 (1), 217–231. doi:10.13182/NSE16-39

Liu, Z., Liang, L., Chen, J., Zhao, C., and Wu, H. (2018). Accuracy and Analysis of the Iteratively Coupling 2D/3D Method for the Three-Dimensional Transport Calculations. *Ann. Nucl. Energ.* 113, 130–138. doi:10.1016/j.anucene.2017.10.020

Ott, K. O., and Meneley, D. A. (1969). Accuracy of the Quasistatic Treatment of Spatial Reactor Kinetics. *Nucl. Sci. Eng.* 36, 402–411. doi:10.13182/NSE36-402

Shaner, K., Forget, B., and Smith, K. (2013). "Sensitivity Analysis and Performance of the Adiabatic, Theta, and Multigrid Amplitude Function Kinetics Methods in 2D MOC Neutron Transport," in Proc. Int. Conf. Mathematics and Computational Methods Applied to Nuclear Science and Engineering (M&C 2013), Sun Valley, Idaho, May 5–9, 2013 (American Nuclear Society).

Shen, Q., Kochunas, B., Xu, Y., Choi, S., and Downar, T. (2021). Transient Multilevel Scheme with One-Group CMFD Acceleration. *Nucl. Sci. Eng.* 195, 741–765. doi:10.1080/00295639.2020.1866388

Shen, Q., Wang, Y., Jabaay, D., Kochunas, B., and Downar, T. (2019). Transient Analysis of C5G7-TD Benchmark with MPACT. *Ann. Nucl. Energ.* 125, 107–120. doi:10.1016/j.anucene.2018.10.049

Tsujita, K., Endo, T., and Yamamoto, A. (2020). Application of the Multigrid Amplitude Function Method for Time-dependent MOC Based on the Linear Source Approximation. *J. Nucl. Sci. Tech.* 57 (6), 646–662. doi:10.1080/00223131.2019.1709993

Tsujita, K., Endo, T., and Yamamoto, A. (2013). "Application of the Multigrid Amplitude Function Method for Time-dependent Transport Equation Using MOC," in Proc. Int. Conf. Mathematics and Computational Methods Applied to Nuclear Science and Engineering (M&C 2013), Sun Valley, Idaho, May 5–9, 2013 (American Nuclear Society).

Wu, W. (2014). *Research on 2D/1D Coupled 3D Whole-Core Transport Calculations Based on Parallel Computation*. Beijing: Tsinghua University. Ph.D. thesis.

Xu, Y., and Downar, T. (2012). Convergence analysis of a CMFD method based on generalized equivalence theory. Knoxville, TN: PHYSOR 2012–Advances in Reactor Physics-Linking Research, Industry, and Education.

Xu, Y., and Hao, C. (2019). A Novel and Efficient Hybrid RSILU Preconditioner for the Parallel GMRES Solution of the Coarse Mesh Finite Difference Equations for Practical Reactor Simulations. *Nucl. Sci. Eng.* 194 (2), 104–119.

Yamamoto, A., Tabuchi, M., Sugimura, N., Ushio, T., and Mori, M. (2007). Derivation of Optimum Polar Angle Quadrature Set for the Method of Characteristics Based on Approximation Error for the Bickley Function. *J. Nucl. Sci. Tech.* 44 (2), 129–136. doi:10.1080/18811248.2007.9711266

Zhang, G., Hsieh, A., Yang, W. S., and Jung, Y. S. (2019). Consistent pCMFD Acceleration Schemes of the Three-Dimensional Transport Code

PROTEUS-MOC. *Nucl. Sci. Eng.* 193 (8), 828–853. doi:10.1080/00295639.2018.1560854

Zhang, T., Lewis, E. E., Smith, M. A., Yang, W. S., and Wu, H. (2017a). A Variational Nodal Approach to 2D/1D Pin Resolved Neutron Transport for Pressurized Water Reactors. *Nucl. Sci. Eng.* 186, 120–133. doi:10.1080/00295639.2016.1273023

Zhang, T., Wang, Y., Lewis, E. E., Smith, M. A., Yang, W. S., and Wu, H. (2017b). A Three-Dimensional Variational Nodal Method for Pin-Resolved Neutron Transport Analysis of Pressurized Water Reactors. *Nucl. Sci. Eng.* 188 (2), 160–174. doi:10.1080/00295639.2017.1350002

Zhu, A. (2016). *Transient Methods for Pin-Resolved Whole Core Transport*. Ann Arbor: University of Michigan. Ph.D. thesis.

Zhu, A., Xu, Y., and Downar, T. (2016). A Multilevel Quasi-Static Kinetics Method for Pin-Resolved Transport Transient Reactor Analysis. *Nucl. Sci. Eng.* 182 (4), 435–451. doi:10.13182/NSE15-39

Conflict of Interest: The authors declare that the research was conducted in the absence of any commercial or financial relationships that could be construed as a potential conflict of interest.

Publisher's Note: All claims expressed in this article are solely those of the authors and do not necessarily represent those of their affiliated organizations, or those of the publisher, the editors and the reviewers. Any product that may be evaluated in this article, or claim that may be made by its manufacturer, is not guaranteed or endorsed by the publisher.

frontiers in Energy Research

ORIGINAL RESEARCH
published: 26 August 2021
doi: 10.3389/fenrg.2021.701437

Large-Scale Heterogeneous Computing for 3D Deterministic Particle Transport on Tianhe-2A Supercomputer

Biao Li[1,2], *Jie Liu*[1,2]*, *Xiaoxiong Zhu*[1,2] *and Shengjie Ding*[1,2]

[1]Science and Technology on Parallel and Distributed Processing Laboratory, National University of Defense Technology, Changsha, China, [2]Laboratory of Software Engineering for Complex System, National University of Defense Technology, Changsha, China

Scalable parallel algorithm for particle transport is one of the main application fields in high-performance computing. Discrete ordinate method (S_n) is one of the most popular deterministic numerical methods for solving particle transport equations. In this paper, we introduce a new method of large-scale heterogeneous computing of one energy group time-independent deterministic discrete ordinates neutron transport in 3D Cartesian geometry (Sweep3D) on Tianhe-2A supercomputer. In heterogeneous programming, we use customized Basic Communication Library (BCL) and Accelerated Computing Library (ACL) to control and communicate between CPU and the Matrix2000 accelerator. We use OpenMP instructions to exploit the parallelism of threads based on Matrix 2000. The test results show that the optimization of applying OpenMP on particle transport algorithm modified by our method can get 11.3 times acceleration at most. On Tianhe-2A supercomputer, the parallel efficiency of 1.01 million cores compared with 170 thousand cores is 52%.

Keywords: heterogeneous parallel algorithm, HPC, openmp, particle transport, SN method

OPEN ACCESS

Edited by:
Qian Zhang,
Harbin Engineering University, China

Reviewed by:
Liang Liang,
Harbin Engineering University, China
Tengfei Zhang,
Shanghai Jiao Tong University, China
Peitao Song,
China Institute for Radiation Protection, China

***Correspondence:**
Jie Liu
liujie@nudt.edu.cn

Specialty section:
This article was submitted to Nuclear Energy, a section of the journal Frontiers in Energy Research

Received: *28 April 2021*
Accepted: *09 August 2021*
Published: *26 August 2021*

Citation:
Li B, Liu J, Zhu X and Ding S (2021) Large-Scale Heterogeneous Computing for 3D Deterministic Particle Transport on Tianhe-2A Supercomputer. Front. Energy Res. 9:701437. doi: 10.3389/fenrg.2021.701437

1 INTRODUCTION

Particle transport plays an important role in modeling many physical phenomena and engineering problems. Particle transport theory has been applied in (Atanassov et al., 2017) astrophysics (Chandrasekhar, 2013), nuclear physics (Marchuk and Lebedev, 1986), medical radiotherapy (Bentel, 2009), and many other fields. The particle transport equation (Boltzmann equation) is a mathematical physics equation describing the particle transport process, and its solution algorithm has always been the key to research in this field. The existing commonly used solutions are divided into two categories, one is the deterministic methods for solving algebraic equations through discrete space, including spherical harmonic method (Marshak, 1947), discrete ordinates method (Carlson, 1955), etc. The other is the stochastic methods, for instance, the Monte Carlo method (Eckhardt, 1987), which simulates particle space using probability theory (Atanassov et al., 2017). With the development of science and technology, simulations of particle transport is more and more demanding of precision and realtimeness. Therefore, facing the rapidly expanding scale of computation and the need for higher performance, it is necessary for researchers to study scalable parallel algorithms for large-scale particle transport.

Currently, the performance of multi-core processors is limited by frequency, power consumption, heat dissipation, etc. And the process of adding cores in a single CPU has encountered bottlenecks. In order to further improve computing performance under existing conditions, the many-integrated-core processors have begun to be used to build high-performance computing systems, including NVIDIA's GPU (Wittenbrink et al., 2011) and Intel's MIC (Duran and Klemm, 2012). The latest Top500 list released in November 2020 (TOP500.ORG, 2020), most of the top ten are multi-core heterogeneous systems, including Summit, Sierra, Piz Daint, ABCI, which are based on NVIDIA-GPU and Trinity which uses Intel Xeon Phi processors. The Tianhe-2A supercomputer replaces the Intel Xeon Phi 31S1P accelerators with the independently developed Matrix2000 multi-core accelerators. The whole system has a total of 17,792 heterogeneous nodes, which reaches a peak performance of 100.68 PFlops, and the measured performance reaches at 61.40 PFlops. Heterogeneous parallel computing based on coprocessor has become a trend in the field of high-performance computing, and some achievements have been made in the fields of particle transport (Panourgias et al., 2015), fluid mechanics (Cao et al., 2013) and molecular dynamics (Pennycook et al., 2013).

Scalable parallel algorithm for particle transport is one of the main application fields in high-performance computing. Since the solution of the particle transport equation is related to spatial coordinates, motion direction, energy, and time, its high-precision solution is very time-consuming (Marchuk and Lebedev, 1986). Over the years, the simulation overhead of particle transport problems has dominated the total cost of multiphysics simulations (Downar et al., 2009). Using the current discrete simulation algorithm, a transport solver that completely discretizes all coordinates will require 10^{17}–10^{21} degrees of freedom (Baker et al., 2012) for each step, even beyond the reach of the Exascale Computing.

Sweep3D (LANL, 2014) is a program for solving single-group steady-state neutron equations and also the benchmark for large-scale neutron transport calculations in the Accelerated Strategic Computing Initiative (ASCI) program established by the U.S. Department of Energy. Many researchers have ported and optimized Sweep3D to heterogeneous systems. Petrini et al. (2007) and Lubeck et al. (2009) migrated Sweep3D to the Cell stream processor in single MPI process mode and multiple MPI process mode, respectively. Gong et al. (2011) and Gong et al. (2012) designed a large-scale heterogeneous parallel algorithm based on GPU by mining fine-grained thread-level parallelism of particle transport problems, which breaked the limitations of the particle simulation and took full advantage of GPU architecture. Wang et al. (2015) designed Sweep3D with thread-level parallelism and vectorization acceleration, and ported Sweep3D to the MIC many-core coprocessors, then applied the Roofline model to access the absolute performance of the optimizations. Liu et al. (2016) presented a parallel spatial-domain-decomposition algorithm to divide the tasks among the available processors and a new algorithm for scheduling tasks within each processor, then combined these two algorithms to solve two-dimensional particle transport equations on unstructured grids.

Based on Sweep3D, we design and develop the method of large-scale heterogeneous computing for 3D deterministic particle transport on Tianhe-2A supercomputer. Compared with original Sweep3D program, this method develops OpenMP thread-level parallelism and implements heterogeneous computing functions based on the Basic Communication Library (BCL) and the Accelerated Computing Library (ACL), which are highly customized for Tianhe-2A.

2 BACKGROUND

2.1 Sweep3D

The particle transport equation mainly describes the process of collision with the nucleus when the particle moves in the medium, and with its solution we can obtain the distribution of the particle with respect to space and time. According to the particle conservation relationship, the unsteady integral-differential particle transport equation can be obtained. **Eq. 1** gives the particle angular flux density expression of the transport equation. $\psi(\vec{r},\vec{\Omega},E,t)$ represents the particle angular flux density, which is a function of the moving direction $\vec{\Omega}$, time t, the energy E and the spatial point $\vec{r}$, and $v(E)$ represents the velocity of the kinetic energy E particle, $\sigma_t(\vec{r},E)$ indicating the sum of the cross sections of the particle's collision with the nucleus at the position $\vec{r}$ and energy E. $\sigma_s(\vec{r},\vec{\Omega}'\rightarrow\vec{\Omega},E'\rightarrow E)$ indicates that the moving particles at position $\vec{r}$ are scattered from energy E and direction $\vec{\Omega}'$ to energy E and direction $\vec{\Omega}$. $Q_t(\vec{r},\vec{\Omega},E,t)$ represents source items, including fission sources and exogenous sources.

$$\frac{1}{v(E)}\frac{\partial}{\partial t}\psi(\vec{r},\vec{\Omega},E,t)+\vec{\Omega}\cdot\nabla\psi(\vec{r},\vec{\Omega},E,t)+\sigma_t(\vec{r},E)\psi(\vec{r},\vec{\Omega},E,t)$$
$$=Q_t(\vec{r},\vec{\Omega},E,t)+\int_{4\pi}\sigma_s(\vec{r},\vec{\Omega}'\rightarrow\vec{\Omega},E'\rightarrow E)\psi(\vec{r},\vec{\Omega}',E',t)d\vec{\Omega}'\,dE'. \quad (1)$$

By discretizing the variables t and E in **Eq. 1**, we can obtain the time-independent single-group particle transport equation, as shown in **Eq. 2**.

$$\vec{\Omega}\cdot\nabla\psi(\vec{r},\vec{\Omega})+\sigma_t(\vec{r})\psi(\vec{r},\vec{\Omega})=Q_{ext}(\vec{r},\vec{\Omega})+\int_{4\pi}\sigma_s(\vec{r},\vec{\Omega}'\rightarrow\vec{\Omega})\psi(\vec{r},\vec{\Omega}')d\vec{\Omega}'. \quad (2)$$

The right-hand side of the equation is the source item, including the scattering source and external source. $Q_{ext}(\vec{r},\vec{\Omega})$ expresses the external source.

In Sweep3D, the discrete ordinate method S_n is used to discretize the angular-direction Ω into a set of quadrature points and discretize the space into a finite mesh of cells. In the angular direction, we choose several specific discrete angular directions Ω_m (m = 1, 2, …, N), so that the integral concerning the direction of Ω is approximated by numerical summation instead, as shown in **Eq. 3**, where w_m is the weight of integration in the discrete direction Ω_m.

$$\psi(\vec{r}) = \int_{4\pi} \psi(\vec{r}, \vec{\Omega}) d\vec{\Omega} = \sum_{m=1}^{M} w_m \psi(\vec{r}, \vec{\Omega}_m). \tag{3}$$

Integrating both sides of **Eq. 2** over the neighboring angular-directions region, $\Delta\Omega_m$, of a given discrete angle Ω_m (μ_m, η_m, ξ_m) where μ_m, η_m, ξ_m represent the components of the unit vector of the particle in the direction Ω_m on the X, Y, Z coordinates with respect to $\mu_m^2 + \eta_m^2 + \xi_m^2 = 1$, we get the balanced equation as follows:

$$\mu_m \frac{\partial \psi_m}{\delta x} + \eta_m \frac{\partial \psi_m}{\delta y} + \xi_m \frac{\partial \psi_m}{\delta z} + \sigma_t(\vec{r}) \psi_m = Q_m(\vec{r}). \tag{4}$$

The three-dimensional discrete solution of the space is solved by the finite difference method, and the XYZ geometry is represented by an IJK logically rectangular grid of cells, shown in **Figure 3**. The finite difference method discretizes the geometric space $(x_i, y_j, z_k) = (i\Delta x, j\Delta y, k\Delta z)$, $i = 0, 1, \ldots, I$; $j = 0, 1, \ldots, J$; $k = 0, 1, \ldots, K$, where $\Delta x = \frac{x_{max}}{I}$, $\Delta y = \frac{y_{max}}{J}$, $\Delta z = \frac{z_{max}}{K}$. Then we can get the difference equation as follows:

$$\mu_m \frac{\psi_{i+\frac{1}{2},j,k,m} - \psi_{i-\frac{1}{2},j,k,m}}{\Delta x} + \eta_m \frac{\psi_{i,j+\frac{1}{2},k,m} - \psi_{i,j-\frac{1}{2},k,m}}{\Delta y} + \xi_m \frac{\psi_{i,j,k+\frac{1}{2},m} - \psi_{i,j,k-\frac{1}{2},m}}{\Delta z} + \sigma_{t,i,j,k} \psi_{i,j,k,m} = Q_{i,j,k,m}. \tag{5}$$

To solve the difference **Eq. 5**, additional auxiliary relations, such as the rhombic difference relation, need to be added:

$$\begin{aligned} \psi_{i,j,k,m} &= \frac{\psi_{i+\frac{1}{2},j,k,m} + \psi_{i-\frac{1}{2},j,k,m}}{2}; \\ \psi_{i,j,k,m} &= \frac{\psi_{i,j+\frac{1}{2},k,m} + \psi_{i,j-\frac{1}{2},k,m}}{2}; \\ \psi_{i,j,k,m} &= \frac{\psi_{i,j,k+\frac{1}{2},m} + \psi_{i,j,k-\frac{1}{2},m}}{2}. \end{aligned} \tag{6}$$

Sweep3D uses the Source Iteration (SI) method to solve the discrete **Eq. 5**. Each iteration includes computing the iterative source, wavefront sweeping, computing flux error, and judging whether the convergence condition is met or not. Wavefront sweeping is the most time-consuming part. In the Cartesian geometries (XYZ coordinates and IJK directions), each octant of angle sweeps has a different sweep direction through the mesh grid, and all angles in a given octant sweep the same way. In SI method, $Q_{i,j,k,m}$ is known. The sweep of S_n method generically is named wavefront (Lewis and Miller, 1984). A wavefront sweep for a given angle proceeds as follows. Every cell (mesh grid) has 4 equations (**Eq. 5** plus **Eq. 6**) with seven unknowns (6 faces plus one central). Boundary conditions initialize the sweep and allow the system of equations to be completed. For any given cell, three known inflows allow the cell center and three outflows to be solved, and then the three outflows provide inflows to three adjoining cells in particle traveling directions. Therefore, there is recursive dependence in all three grid directions. The recursive dependence causes the sweep to be performed in a diagonal wave across the physical space, and **Figure 1A** gives a sweep of the wavefront from state (a) to state (d).

Therefore, the parallelism is limited by the length of the JK-diagonal line in **Figure 2**. To alleviate this problem, MMI angles for each octant are pipelined on JK-diagonal lines to increase the number of parallel I-lines. MMI is the number of angles for blocking and can be chosen as desired, but it must be a integral factor of the number of angles in each octant. Moreover, Sweep3D utilizes Diffusion Synthetic Acceleration (DSA) (Adams and Larsen, 2002) to improve its convergence of source iteration scheme. So wavefront sweeping subroutine mainly involves computing sources from spherical harmonic (P_n) moments, solving S_n equation recursively with or without flux fixup, updating flux from Pn moments, and updating DSA face currents, as shown in **Algorithm 1**.

Algorithm 1 Wavefront sweeping subroutine in Sweep3D

```
for iq = 1 to 8 do//octants
  for mo = 1 to mmo do//angle pipelining loop.
    for kk = 1 to kb do//k-plane pipelining loop
      RECV EAST/WEST//recv block I-inflows
      RECV SOUTH/NORTH//recv block J-inflows
      for idiag = 1 to jt + nk − 1 + mmi − 1 do.
        for jkm = 1 to ndiag do//I-lines grid columns
          for i = 1 to it do
            Calculate discrete source term in Pn moments
          if not do fixup then
            for i = 1 to it do
              Solve Sn equation
          else
            for i = 1 to it do
              Solve Sn equation with fixup
          for i = 1 to it do
            Update flux from Pn moments
          for i = 1 to it do
        Update DSA face currents
        SEND East/West//send block I-inflows. SEND North/
South//send block J-inflows
```

2.2 Matrix2000 Accelerator

In the Tianhe-2A supercomputer, each node consists of two Intel Xeon microprocessors and two Matrix2000 accelerators, as shown in **Figure 3**.

Each of these Intel Xeon microprocessors is a 12-core processor operating at 2.2 GHz, based on the Intel Ivy Bridge microarchitecture (Ivy Bridge-EX core), with a 22 nm process and a peak performance of 0.2112TFLOPS. The Matrix2000 consists 128 cores, eight DDR4 memory channels, and x16 PCIe lanes. The chip consists of four supernodes (SN) consisting of 32 cores each operating at 1.2 GHz with a peak power dissipation of 240 Watts. Operating at 1.2 GHz, each core has a peak performance of 19.2 GFLOPs (1.2 GHz * 16 FLOP/cycle). With 32 such cores in each SuperNode, the peak

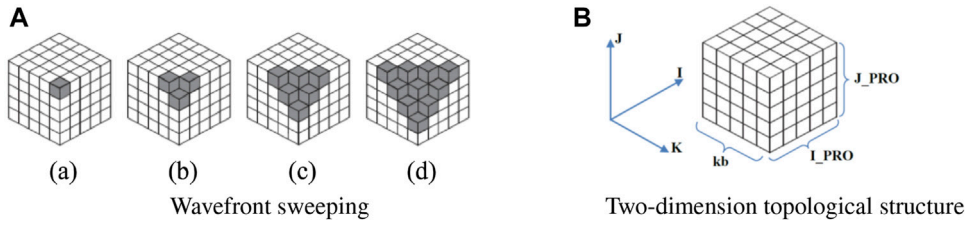

FIGURE 1 | Wavefront sweeping and two-dimension topological structure.

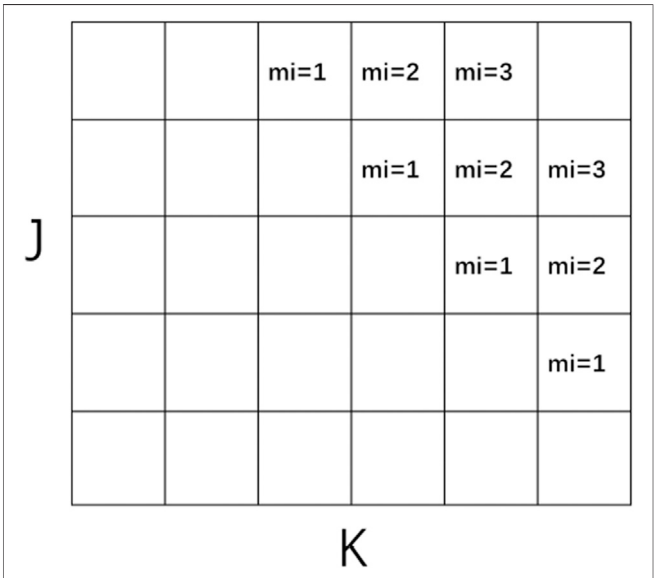

FIGURE 2 | This MMI-pipelined JK-diagonal wavefront is depicted below at the fourth stage of a 3-deep wavefront that started in the upper right corner.

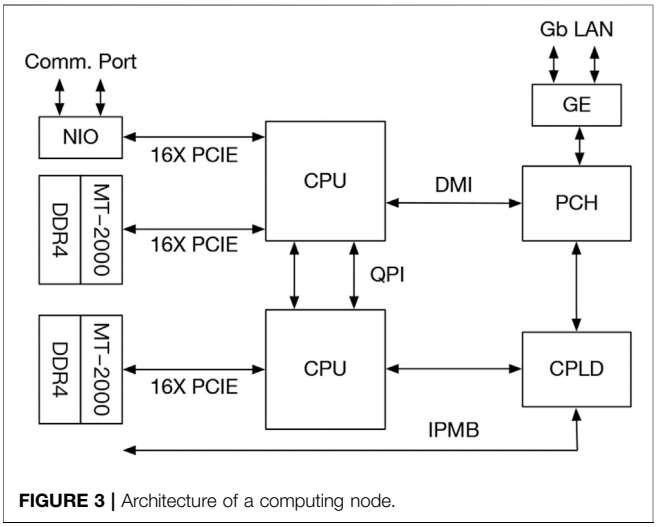

FIGURE 3 | Architecture of a computing node.

performance of each SN is 614.4 GFLOPS. Likewise, with four SN per chip, the peak chip performance is 2.458 TFLOPS double precision or 4.916 TFLOPS single-precision.

3 SCALABLE PARALLEL ALGORITHM FOR PARTICLE TRANSPORT

3.1 Heterogeneous Parallel Algorithms

The process-level parallel algorithm with our method, as shown in **Figure 1B**, divides the overall mesh space from three directions: I, J, and K. We use a two-dimensional process topology division along the I, J direction for the spatial mesh, so that each K-column mesh along the K direction is stored in a process. Due to the strong data dependency of the sweeping algorithm, in order to improve the parallelism, we need to subdivide the K direction so that each process can quickly complete the data computation of the small mesh and then pass the results to the adjacent meshes in the three directions. The I and J directions are controlled by the process numbers I_PRO and J_PRO, and K direction is controlled by parameter kb. Then we get a mesh space divided into I_PRO*J_PRO*kb mesh of cells.

The sweep calculation is the core of the whole algorithm. Sweeping is running in the diagonal direction of IJK, as shown in **Figure 1A**. Firstly, in subfigure (a), only the process where the data of the small gray mesh is located performs the calculation, and then passes the results to the three adjacent gray grids along the IJK direction, as shown in subfigure (b), where the two small meshes in the IJ direction are in other processes and the small mesh in the K direction is still in the current process. There is no data dependency between these three small meshes, which can be executed in parallel. Then, the results are transmitted to three adjacent directions, and this operation is repeated to obtain the wavefront sweeping in the order from (a) to (d). Since adjacent mesh involve data dependence, adjacent mesh need to communicate during wavefront sweeping, and lines 4-5 and 20-21 in **Algorithm 1** describe this communication process. The idea of our heterogeneous algorithm design is to put all the computations on the Matrix 2000, while the processes on the CPU are only responsible for the MPI communication during the wavefront sweeping.

The heterogeneous communication interfaces supported by the Tianhe-2A supercomputer include OpenMP 4.5, BCL and ACL. Among them, BCL is a simple and efficient symmetric transmission interface, which enables data to be transmitted on the coprocessor and CPU through the PCI-E bus. Although the program migration is more complicated, the transmission rate is faster and the transplant flexibility of the program is better. The heterogeneous program based on the BCL interface

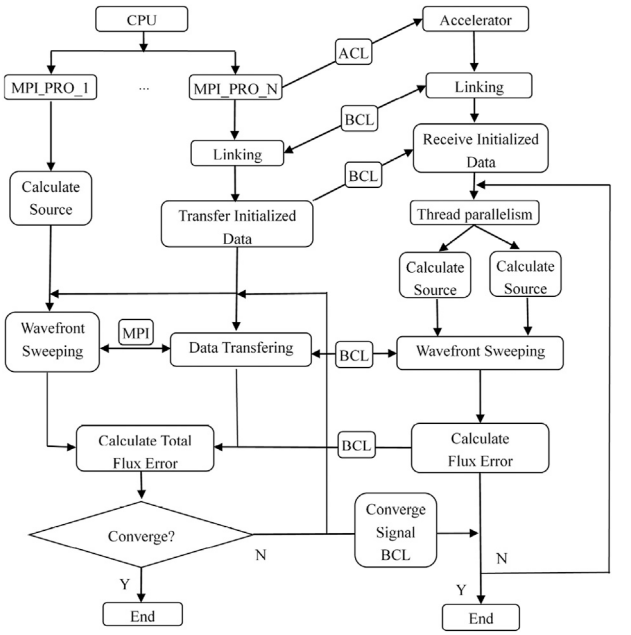

FIGURE 4 | Heterogeneous logic flowchart.

needs to compile two sets of programs, which will be running simultaneously on the CPU and the accelerator. First, one of the program is initialized on the CPU, and then the ACL interface is activated to load the other program running on accelerator of the Matrix 2000. The heterogeneous mode flow of our method is given, as shown in **Figure 4** and **Algorithm 2**.

First, the CPU starts the MPI to initialize the process, the master process reads the file data, divides the task according to the computing capability, and then transfers the task size to the slave process. Each slave process controls a Matrix2000 supernode and uses the ACL interface to load the programs that need to run on the accelerator of the Matrix 2000, and then establishes a connection between the CPU and the Matrix2000 supernode via the BCL interface. Once the connection is established, the slave processes on the CPU side can communicate with the Matrix2000 *via* the BCL interface. Then, a small number of parameters are transferred from the slave process to Matrix 2000. The program on the Matrix2000 side receives the parameters and initializes the data directly on the accelerator and proceeds to calculate the iterative source, wavefront sweeping, and compute flux error. Since there is no communication interface between Matrix2000 supernodes, resulting in Matrix2000 supernodes cannot communicate directly and need to go through CPU transition to achieve communication between supernodes. The main function of Matrix2000 supernodes is responsible for intensive data computation. In the wavefront sweeping **algorithm 1**, the incoming flux and outgoing flux in lines four to five and lines 20-21, respectively, need to involve communication between Matrix2000 supernodes, so the communication between them needs CPU processes to assist.

Algorithm 2 Heterogeneous logic algorithm

if *rank_id* = 0 **then**//master process
  Read file and Initialize
  MPI_Send task to slave processes
else
  slave process MPI_Recv the task assigned by the master process//slave process
if *rank_id* ≠ 0 **then**//slave process
  Invoke ACL to start the accelerator Matrix2000
  Establish the connection between CPU and Matrix2000
  Invoke BCL to transport initialized data to Matrix2000
  /* the Source Iteration (SI) running on Matrix 2000 */
  #pragma omp parallel for
  {
  Calculate source//Matrix2000
  }
  /* Wavefront sweeping in **algorithm 1** */
  for *iq* = 1 *to* 8 **do**
    for *mo* = 1 *to mmo* **do**
      for *kk* = 1 *to kb* **do**
        MPI recv east/west block I-inflows//CPU *rank_id*
        MPI recv south/north block J-inflows//CPU *rank_id*
        Invoke BCL to recv the block I-inflows from slave process//Matrix2000
        Invoke BCL to recv the block J-inflows from slave process//Matrix2000
        #pragma omp parallel for
        {
        Calculate discrete source in P_n moments//Matrix2000
        Solve S_n equation//Matrix2000
        Update flux//Matrix2000
        }
        Invoke BCL to send block I-inflows to slave process//Matrix2000
        Invoke BCL to send block J-inflows to slave process//Matrix2000
        MPI send east/west block I-outflows//CPU *rank_id*
        MPI send south/north block J-outflows//CPU *rank_id*
  /* Calculate flux error */
  Calculate flux error and invoke BCL to sen//Matrix2000

  Calculate total flux error//CPU
  if *Converge* **then**
    Invoke BCL to send converge signal to Matrix2000
    Break
  else
    Continuing the calculation in lines 10-30

3.2 OpenMP Thread Level Parallelism

A supernode in Matrix2000 contains 32 cores. In order to fully utilize the performance of Matrix 2000, we use OpenMP instructions to implement thread-level parallelism. **Figure 5** shows the optimization process based on OpenMP thread-level

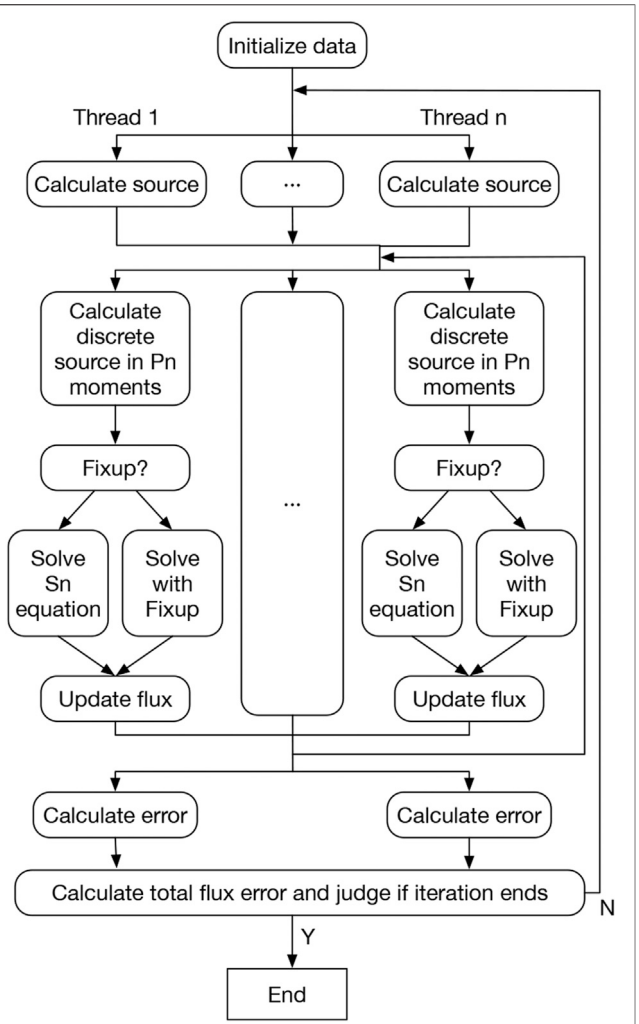

FIGURE 5 | OpenMP thread parallelism flowchart.

parallelism. Among them, the calculation of iterative source, wavefront scanning, and flux error calculation can be performed in thread-level parallel optimization.

The iterative source is equal to the sum of the external and scattering iterative sources. As shown in **Eq. 7**, the scattering iterative source is equal to the product of the flux moment and the discrete cross section, where i represents the ith iteration, and when $i = 1$, the scattering source can be initialized by any non-negative value.

$$Q(\vec{r}_i) = \sigma_s(\vec{r})\psi(\vec{r})_{i-1} + Q_{ext}(\vec{r}) \tag{7}$$

When calculating, the grids are independent of each other and have no data dependency. If the single grid is used as the parallel granularity, the overhead of OpenMP scheduling will be too large. Therefore, the IJ plane is used as the parallel granularity, and only the OpenMP thread-level parallelism is performed in the K direction. As shown in **Algorithm 3**, it is divided into two cases where the discrete order of P_n is 0 and 1.

Algorithm 3 OpenMP thread-level parallelism in source iteration

```
if isct. Eq. (0) then
  #pragma omp parallel for
  for k = 0; k < kt; k + + do
    for j = 0; j < jt; j + + do.
      for i = 0; i < it; i + + do
        Src(1,k,j,i) = Srcx (k,j) + Sigs (1,k,j,i)*Flux (1,k,j,i)
Pflux (k,j,i) = Flux (1,k,j,i) Flux (1,k,j,i) = 0.0
else
  #pragma omp parallel for
  for k = 0; k < kt; k + + do
    for j = 0; j < jt; j + + do
      for i = 0; i < it; i + + do
        Src(1,k,j,i) = Srcx (k,j,i) + Sigs (1,k,j,i)*Flux (1,k,j,i)
        Src(2,k,j,i) = Sigs (2,k,j,i)*Flux (2,k,j,i)
        Src(3,k,j,i) = Sigs (3,k,j,i)*Flux (3,k,j,i)
        Src(4,k,j,i) = Sigs (4,k,j,i)*Flux (4,k,j,i)
        Pflux (k,j,i) = Flux (1,k,j,i)
        Flux (1,k,j,i) = 0.0
        Flux (2,k,j,i) = 0.0
        Flux (3,k,j,i) = 0.0
        Flux (4,k,j,i) = 0.0
```

Algorithm 4 Iterative OpenMP optimization algorithm in wavefront scanning

```
#pragma omp parallel for
for jkm = 1 to ndiag do.
  for i = 1 to it do
    Compute source from P_n moments
  if not do fixup then
    for i = 1 to it do
      Solve S_n equation
  else
    for i = 1 to it do
      Solve S_n equation with fixups
  for i = 1 to it do
    Update flux from P_n moments
  for i = 1 to it do
    Update DSA face currents
```

During the wavefront scanning process, there is a strong data dependency between the wavefronts, and it is not possible to perform calculations in multiple directions at the same time. However, the calculation of all I-line grids in the wavefront of a single direction is independent of each other. OpenMP thread-level parallelism is performed on the I-line grid column, as shown in **Algorithm 4**. The parallel granularity of threads is limited by the number of I-line grid columns on the JK diagonal. The number of I-line grid columns changes with particles' movements. The minimum is one and the maximum is the larger of J and K. flushleft.

We determine the flux error by calculating the flux for twice in succession, as shown in **Eq. 8**, setting the maximum relative error as the overall error value. The calculation of each grid is

independent of each other in the process. The JK plane is used as the parallel granularity, and the OpenMP thread-level parallelism is performed from the I direction. The *max* value in all threads is calculated by the OpenMP reduction statement.

$$Error_{max} = max\left|\frac{\psi(\vec{r}_i) - \psi(\vec{r}_{i-1})}{\psi(\vec{r}_i)}\right| \tag{8}$$

3.3 Flux Fixup

Sweep3D solves a single-group, time-independent set of S_n equations on each grid cell. The set of equations consists of the discretized balanced **Eq. 9** with three rhombic difference auxiliary **Eq. 10**, where **Eq. 9** is transformed from **Eq. 5** combined with the rhombic difference auxiliary equations.

$$\psi_{i,j,k,m} = \frac{1}{D}\left[Q_{i,j,k,m} + A \cdot \psi_{i-\frac{1}{2},j,k,m} + B \cdot \psi_{i,j-\frac{1}{2},k,m} + C \cdot \psi_{i,j,k-\frac{1}{2},m}\right]. \tag{9}$$

$$\begin{aligned}
\psi_{i+}\frac{1}{2}, j, k, m &= 2 \cdot \psi_{i,j,k,m} - \psi_{i-}\frac{1}{2}, j, k, m \\
\psi_{i,j+}\frac{1}{2}, k, m &= 2 \cdot \psi_{i,j,k,m} - \psi_{i,j-}\frac{1}{2}, k, m \\
\psi_{i,j,k+}\frac{1}{2}, m &= 2 \cdot \psi_{i,j,k,m} - \psi_{i,j,k-}\frac{1}{2}, m.
\end{aligned} \tag{10}$$

where $\psi_{i-\frac{1}{2},j,k,m}$, $\psi_{i,j-\frac{1}{2},k,m}$, $\psi_{i,j,k-\frac{1}{2},m}$ are the input fluxes of the grid cell (i, j, k) in the I, J and K directions, respectively, $\psi_{i,j,k,m}$ is the central flux of the cell (i, j, k) for the current dispersion angle, and D, A, B and C represent the relative difference parameters. P_n(spherical harmonic) moments have been used to obtain the source term $Q_{i,j,k,m}$. Thus, for a single grid cell in the I-line grid column, the input flux is known, and the central flux of the cell grid can be found, and then the output fluxes $\psi_{i+\frac{1}{2},j,k,m}$, $\psi_{i,j+\frac{1}{2},k,m}$, and $\psi_{i,j,k+\frac{1}{2},m}$ are immediately obtained from the rhombic difference auxiliary **Eq. 10**. Moreover, in **Eq. 9**, the central flux $\psi_{i,j,k,m}$ cannot be negative as long as the input fluxes $\psi_{i-\frac{1}{2},j,k,m}$, $\psi_{i,j-\frac{1}{2},k,m}$, and $\psi_{i,j,k-\frac{1}{2},m}$ are not negative, but the output flux obtained by equation **Eq. 10** can be negative.

When the negative flux is transmitted along the iterative solution direction, more negative fluxes may be generated, thus triggering fluctuations in the simulation results, and in this case, a negative flux correction is required. In Sweep3D, a zero-setting method is used to correct the negative flux. The iterative solution of the S_n equation with flux correction is similar to that without flux correction, except that the process of negative flux correction is added. The process of flux correction is full of judgments and branches, so it is difficult to exploit the data-level parallelism. Therefore, the iterative solution of the S_n equation with flux correction is still implemented in a serial manner. Lines 5-10 in **Algorithm 4** give two different cases of solving the S_n equation with and without flux correction, respectively. For the test cases with different grid sizes and number of threads, the experimental results in **Section 4** will give the difference between flux correction or not.

4 EXPERIMENT AND RESULTS

The benchmark code Sweep3D represents the heart of a real ASCI(Accelerated Strategic Computing Initiative) application established by the U.S. Department of Energy. It solves a 1-group time-independent discrete ordinates (S_n) 3D Cartesian (XYZ) geometry neutron transport problem. Sweep3d is not a program that solves realistic applications, but a realistic S_n code would solve a multi-group problem, which in simple terms is nothing more than a group-ordered iterative solution on top of what Sweep3D does. To keep the problem setup simple, the cross section, external source and geometric array are set to constants in the Sweep3D code. The case of our calculation also follow exactly this simple problem setup.

TABLE 1 | Specification of the experiment platform.

Processor	Intel Xeon E5-2692v2 12C 2.2 GHz
Accelerator	Matrix2000
Interconnect	TH Express-2
Operating System	Kylin Linux
Host-side Compiler	ICC, MPICH3.2
Acce-side Compiler	Customized Cross-compiler

The test platform is the Tianhe-2A supercomputer. Since ACL and BCL instructions only provide C/C++ interfaces, the implementation of our method is a hybrid encoding of FORTRAN and C. The CPU-side program is compiled with Intel compiler and high-speed network-based MPICH3.2. The accelerator side uses a customized cross-compiler, which supports OpenMP instructions. The compilation option takes "−O3". The specifications of test environment and parameters configured for Sweep3D are as shown in **Table 1**.

4.1 OpenMP Performance Optimization Test

In order to effectively evaluate the performance of the OpenMP thread parallel optimization, we run a test with the single-process mode on a CPU core and a Matrix2000 super-accelerated node (32 cores). There are two primary ways to scale Sweep3D on Matrix 2000, including strong scaling and week scaling. Strong scaling means that more cores are applied to the same problem size to get results faster. Weak scaling refers to the concept of increasing the problem size as Sweep3D runs on more cores. This subsection focuses on strong scaling tests, weak scaling tests will be discussed in the next subsection. **Table 2** gives the configuration of some parameters of the program during the openMP test.

Figure 6 shows the results of four sets of strong scalability tests, where the size of the (I, J, K)-grid is increased from $32 \times 32 \times 256$ to $256 \times 256 \times 256$. To test the performance of the OpenMP algorithm, the four sets of results in **Figure 6** give the comparison results for two scenarios with and without flux correction at different (I, J, K)-grid sizes, and each subplot gives the comparison results of time and speedup ratio separately, where the bars indicate the time and the dashes indicate the speedup ratio curves. It can be seen that the computation time of the case without flux correction is less than that of the case with flux correction for all four different problem sizes because performing flux correction increases the number of conditional statements and computation steps in the program code, which leads to an increase in time. From the viewpoint of the speedup ratio, the difference between the speedup ratio curves

TABLE 2 | Parameters configured for sweep3D.

32–256	# Grid points in I-direction
32–256	# Grid points in J-direction
256	# Grid points in K-direction
0.1	# delta-x for I-direction
0.1	# delta-y for J-direction
0.1	# delta-z for K-direction
3	# angles for blocking
6	# angles per octant
Reflective	# BC flag for I/J/K-direction
1	# Pn scattering order
off/on	# flux fixup flag

with and without flux correction is not significant when the grid size is 32 × 32 × 256, especially when the number of threads is 32, the speedup ratio of both cases is approximately equal to 4.7. However, the **Figures 6B–D** show that as the grid size increases, the difference between the speedup ratio curves of the two cases is small for the number of threads below 8, but the difference becomes larger for 16 and 32 threads. For example, in **Figures 6B–D**, the network sizes are 64 × 64 × 256, 128 × 128 × 256 and 256 × 256 × 256, respectively, corresponding to a speedup ratio difference of 0.3, 1.2, and 0.9 for 16 threads, and 0.5, 1.6, and 1.8 for 32 threads, respectively.

To more intuitively distinguish the difference between with flux fixup and without flux fixup as the grid size increases, **Figure 7** exhibits the speedup of Sweep3D running on all 32 cores of Matrix2000 supernode in comparison with that on only one core under different problem sizes. Both with and without flux fixup, the speedup rises gradually with problem size at the beginning, and the speedup between the two flux fixup is still very close at the grid sizes of 32 × 32 × 256, but the difference is gradually increasing as the scale increases, reaching a maximum at 256 × 256 × 256. As the problem size is equal to 256 × 256 × 256, the maximum speedup reach 11.18 and 13.02 for with flux fixup and without flux fixup, respectively. This is because performing flux fixup increases the number of conditional statements and computational

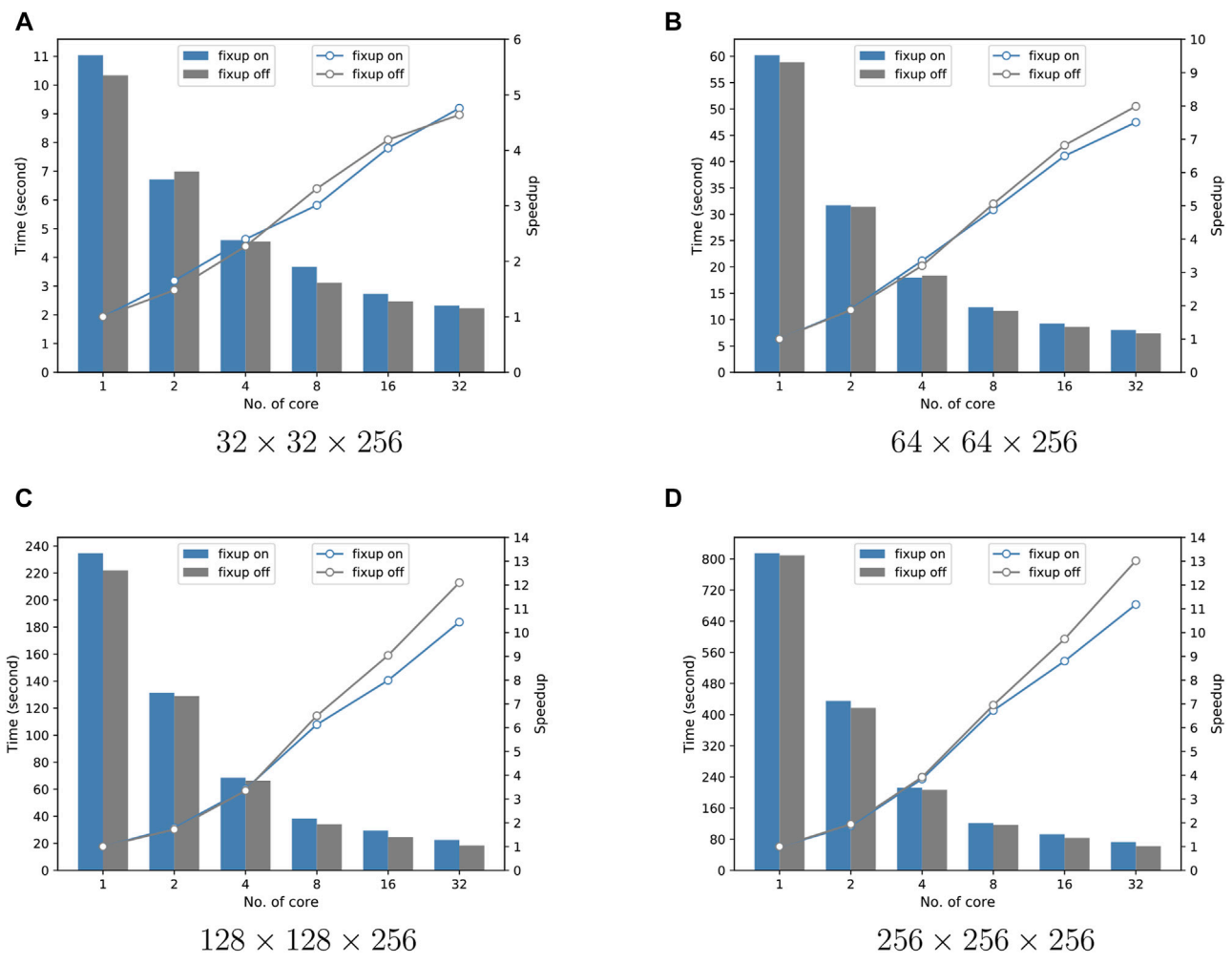

FIGURE 6 | Execution time of Sweep3D running on different number of cores in Matrix2000 supernode and speedup in comparison with the simulation on only one core of Matrix 2000. The comparison results for two scenarios with and without flux correction at different (I, J, K)-grid size.

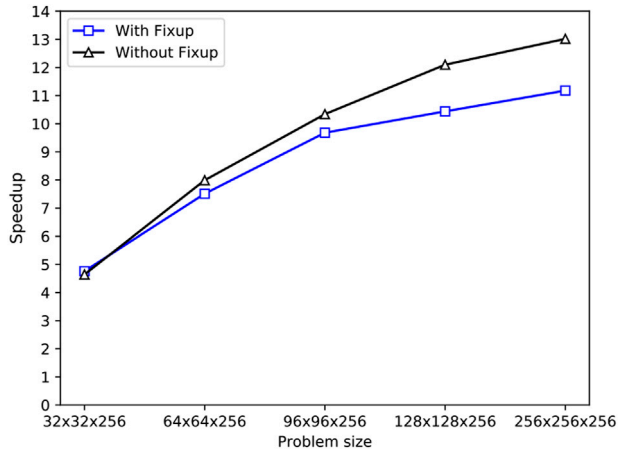

FIGURE 7 | Speedup of Sweep3D running on all 32 cores of Matrix 2000 supernode in comparison with that on only one core under different problem sizes.

threads reaches 32. There are two main reasons: First, although thread-level parallelism does not involve MPI communication, the computational process in the mesh of a single process is exactly similar to the full-space computational process, which also requires the computational wavefront sweeping process, i.e., the adjacent regions in the mesh also have data dependencies and are also limited by the length of the JK diagonal in the mesh as in **Figure 2**; Second, the communication between the CPU and Matrix2000 also takes time, which cannot be eliminated by increasing the number of threads.

4.2 Large-Scale Extension Test on Tianhe-2A Supercomputer

We performed a weak scalability test for our method. During the test, we run 8 processes on each node, using 8 CPU cores and 8 Matrix2000 supernodes, and each Matrix2000 supernode starts 32 threads. For the problem sizes, the grid size on a single process remains 32 × 32 × 256, and the size of the K dimension is fixed to

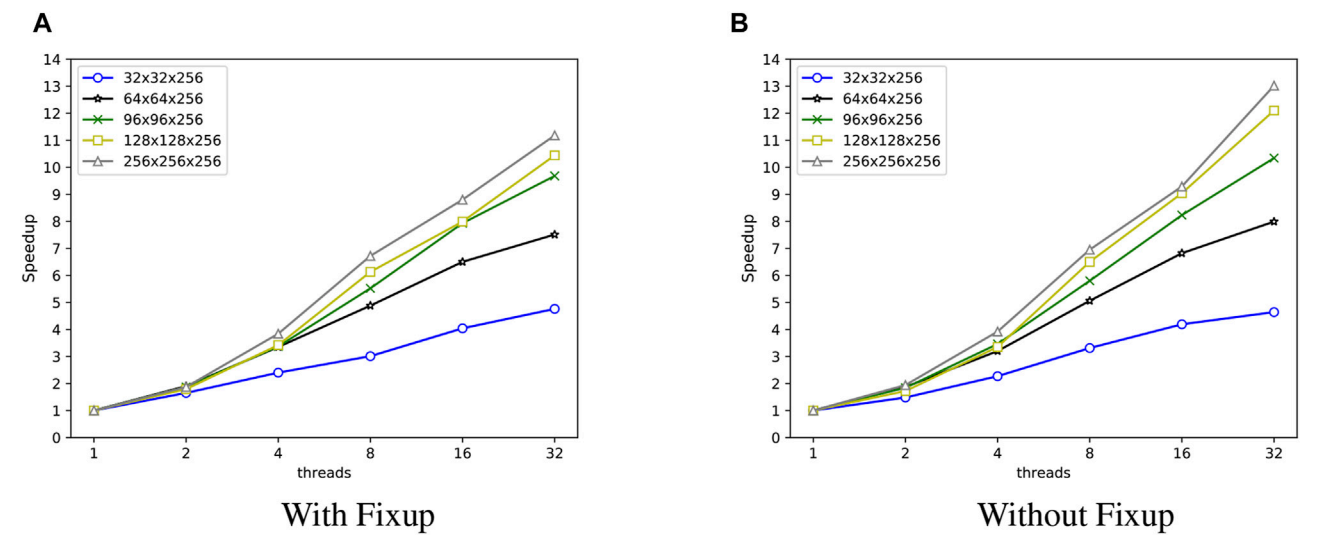

FIGURE 8 | Speedup of Sweep3D running on the different problem sizes after by OpenMP optimizing in the two cases of with and without flux fixup.

steps in the program code, which leads to an increase in time. The time gap between flux fixup and no-fixup becomes smaller as the number of threads increases, but because the single-core time for flux fixup is larger than the no-fixup time, resulting in a smaller speedup ratio, which affects parallel efficiency.

To better illustrate the results of the strong scaling test for thread-level parallelism, we combine the above data to obtain the results in **Figure 8**. **Figure 8** gives the strong scaling results for a variety of different scales in both with flux fixup and without flux fixup cases. Both subplots show that the performance of the strong scaling test gets better as the size increases, but the efficiency does not reach the desired value as the number of 256 while the sizes of the I and J dimensions keep a linear relationship with the number of processes. The test results are given in **Table 3**.

The correlation between core size and efficiency and time is shown in **Figure 9**, where the computation time increases slowly and linearly with the number of cores, and the efficiency decreases slowly and linearly with the number of cores. The decisive effect on the parallel efficiency is mainly the strong data dependency between two adjacent wavefronts in the wavefront sweeping algorithm, which requires data communication. As the size increases, that is, the I and J increases, leading to an increase in the number of wavefronts required to complete a global spatial grid sweep, which leads to an increase in communication and causes a decrease in parallel efficiency. Another

TABLE 3 | Weak scaling evaluation.

Node	Core	Problem sizes	time(s) without flux fixup	Efficiency
640	168,960	(64 × 32) × (80 × 32) × 256	61.07	100.00
1,024	270,336	(64 × 32) × (128 × 32) × 256	70.93	86.08
2048	540,672	(128 × 32) × (128 × 32) × 256	84.63	72.15
2,560	675,840	(128 × 32) × (160 × 32) × 256	97.69	62.50
2,816	743,424	(128 × 32) × (176 × 32) × 256	103.92	58.76
3,072	811,008	(128 × 32) × (192 × 32) × 256	110.68	55.17
3,840	1013760	(128 × 32) × (240 × 32) × 256	117.35	52.03

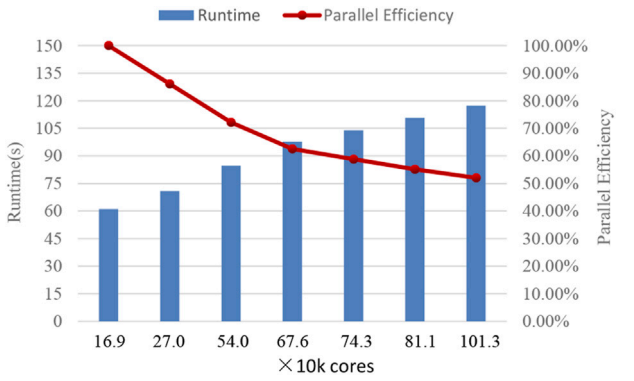

FIGURE 9 | Runtime and parallel efficiency on Tianhe-2A.

factor is that the communication between Matrix2000 needs to be relayed through CPUs, which leads to a three-step communication process, adding two CPUs to the Matrix2000 supernode communication process compared to the simple inter-process communication. Although the efficiency decreases as the size increases, our algorithm can still maintain the efficiency of the 540,000 cores versus 170,000 cores is 72%, and the efficiency of the 1.01 million cores versus 170,000 cores is 52% which means much better scalability.

5 CONCLUSION AND FUTURE WORK

We introduce a new method of large-scale heterogeneous computing for 3D deterministic particle transport, which is designed for Tianhe-2A supercomputer. The CPU and Matrix2000 data transmission is completed through the BCL and ACL interfaces. We construct a heterogeneous parallel algorithm to optimize OpenMP on the thread-level parallelism on the Matrix2000 side to improve performance. Our optimization on thread-level parallelism includes iteration source calculation, I-line grid column calculation, and flux error calculation. In the single node test, this method achieves a maximum of 11.3 speedups on the Matrix2000 super-acceleration node. The extension test of the million-core scale was completed on the Tianhe-2A supercomputer, the test efficiency was high, and the program has good scalability. As a part of the future work, we will study on the performance and scalability issues of particle transport algorithms on next-generation China CPU/Accelerator heterogeneous clusters.

DATA AVAILABILITY STATEMENT

The original contributions presented in the study are included in the article/**supplementary material**, further inquiries can be directed to the corresponding author.

AUTHOR CONTRIBUTIONS

BL and JL designed heterogeneous parallel algorithm; BL and XZ carried out experiments; BL and SD analyzed experimental results. BL, XZ, and SD wrote the manuscript.

FUNDING

This work was supported by the National Key Research and Development Program of China (2017YFB0202104, 2018YFB0204301).

SUPPLEMENTARY MATERIAL

The Supplementary Material for this article can be found online at: https://www.frontiersin.org/articles/10.3389/fenrg.2021.701437/full#supplementary-material

REFERENCES

Adams, M. L., and Larsen, E. W. (2002). Fast Iterative Methods for Discrete-Ordinates Particle Transport Calculations. *Prog. Nucl. Energ.* 40, 3–159. doi:10.1016/s0149-1970(01)00023-3

Atanassov, E., Gurov, T., Ivanovska, S., and Karaivanova, A. (2017). Parallel Monte Carlo on Intel Mic Architecture. *Proced. Comp. Sci.* 108, 1803–1810. doi:10.1016/j.procs.2017.05.149

Baker, C., Davidson, G., Evans, T. M., Hamilton, S., Jarrell, J., and Joubert, W. (2012). "High Performance Radiation Transport Simulations: Preparing for Titan," in SC'12: Proceedings of the International Conference on High

Performance Computing, Networking, Storage and Analysis (IEEE), Salt Lake, November 10–16, 2012, 1–10. doi:10.1109/sc.2012.64

Bentel, G. C. (2009). *Radiation Therapy Planning*. New York, NY: McGraw Hill Professional.

Cao, W., Xu, C. F., and Wang, Z. H. (2013). Heterogeneous Computing for a CFD Solver on GPU/CPU Computer. *Adv. Mater. Res.* 791, 1252–1255. doi:10.4028/www.scientific.net/amr.791-793.1252

Carlson, B. G. (1955). "Solution of the Transport Equation by Sn Approximations,". Technical Report (N. Mex: Los Alamos Scientific Lab). doi:10.2172/4376236

Chandrasekhar, S. (2013). *Radiative Transfer*. New York, NY: Courier Corporation.

Downar, T., Siegel, A., and Unal, C. (2009). *Science Based Nuclear Energy Systems Enabled by Advanced Modeling and Simulation at the Extreme Scale*. Citeseer.

Duran, A., and Klemm, M. (2012). "The Intel® many Integrated Core Architecture," in 2012 International Conference on High Performance Computing & Simulation (HPCS) (IEEE), Madrid, Spain, July 2–6, 2012, 365–366. doi:10.1109/HPCSim.2012.6266938

Eckhardt, R. (1987). Stan ulam, john von neumann, and the monte carlo method. *Los Alamos Sci.* 15, 131–136.

Gong, C., Liu, J., Chi, L., Huang, H., Fang, J., and Gong, Z. (2011). Gpu Accelerated Simulations of 3d Deterministic Particle Transport Using Discrete Ordinates Method. *J. Comput. Phys.* 230, 6010–6022. doi:10.1016/j.jcp.2011.04.010

Gong, C., Liu, J., Huang, H., and Gong, Z. (2012). Particle Transport with Unstructured Grid on Gpu. *Comp. Phys. Commun.* 183, 588–593. doi:10.1016/j.cpc.2011.12.002

LANL (2014). [Dataset]. The Asci Sweep3d Benchmark. Available at: http://wwwc3.lanl.gov/pal/software/sweep3d/.

Lewis, E., and Miller, W. (1984). *Computational Methods of Neutron Transport*. New York, NY: John Wiley and Sons, Inc.

Liu, J., Lihua, C., Qing Lin, W., Chunye, G., Jie, J., Xinbiao, G., et al. (2016). Parallel Sn Sweep Scheduling Algorithm on Unstructured Grids for Multigroup Time-dependent Particle Transport Equations. *Nucl. Sci. Eng.* 184, 527–536. doi:10.13182/NSE15-53

Lubeck, O., Lang, M., Srinivasan, R., and Johnson, G. (2009). Implementation and Performance Modeling of Deterministic Particle Transport (Sweep3d) on the Ibm Cell/be. *Sci. Program.* 17, 199–208. doi:10.1155/2009/784153

Marchuk, G., and Lebedev, V. (1986). *Numerical Methods in the Theory of Neutron Transport*. New York, NY: Harwood Academic Pub.

Marshak, R. (1947). Note on the Spherical Harmonic Method as Applied to the Milne Problem for a Sphere. *Phys. Rev.* 71, 443. doi:10.1103/PhysRev.71.443

Panourgias, I., Weiland, M., Parsons, M., Turland, D., Barrett, D., and Gaudin, W. (2015). "Feasibility Study of Porting a Particle Transport Code to Fpga," in International Conference on High Performance Computing, Frankfurt, Germany, July 12–16 (Springer), 139–154. doi:10.1007/978-3-319-20119-1_11

Pennycook, S. J., Hughes, C. J., Smelyanskiy, M., and Jarvis, S. A. (2013). "Exploring Simd for Molecular Dynamics, Using Intel® Xeon® Processors and Intel® Xeon Phi Coprocessors," in 2013 IEEE 27th International Symposium on Parallel and Distributed Processing (IEEE), Cambridge, MA, May 20–24, 2013, 1085–1097. doi:10.1109/IPDPS.2013.44

Petrini, F., Fossum, G., Fernández, J., Varbanescu, A. L., Kistler, M., and Perrone, M. (2007). "Multicore Surprises: Lessons Learned from Optimizing Sweep3d on the Cell Broadband Engine," in 2007 IEEE International Parallel and Distributed Processing Symposium (IEEE), Rome, March 26–30, 2007, 1–10. doi:10.1109/IPDPS.2007.370252

TOP500.ORG (2020). [Dataset]. Top500 List. Available at: https://www.top500.org/lists/top500/.

Wang, Q., Liu, J., Xing, Z., and Gong, C. (2015). Scalability of 3d Deterministic Particle Transport on the Intel Mic Architecture. *Nucl. Sci. Tech.* 26. doi:10.13538/j.1001-8042/nst.26.050502

Wittenbrink, C. M., Kilgariff, E., and Prabhu, A. (2011). Fermi Gf100 Gpu Architecture. *IEEE Micro* 31, 50–59. doi:10.1109/mm.2011.24

Conflict of Interest: The authors declare that the research was conducted in the absence of any commercial or financial relationships that could be construed as a potential conflict of interest.

Publisher's Note: All claims expressed in this article are solely those of the authors and do not necessarily represent those of their affiliated organizations, or those of the publisher, the editors and the reviewers. Any product that may be evaluated in this article, or claim that may be made by its manufacturer, is not guaranteed or endorsed by the publisher.

frontiers in Energy Research

ORIGINAL RESEARCH
published: 27 August 2021
doi: 10.3389/fenrg.2021.729552

Burnable Poison Selection and Neutronics Analysis of Plate Fuel Assemblies

Shikun Xu[1,2], *Tao Yu*[1,2]*, *Jinsen Xie*[1,2]*, *Lei Yao*[1,2] and *Zhulun Li*[1,2]

[1]School of Nuclear Science and Technology, University of South China, Hengyang, China, [2]Hunan Engineering and Technology Research Center for Virtual Nuclear Reactor, University of South China, Hengyang, China

Burnable poisons play a critical role in long-life pressurized water reactors. Plate fuel elements have good application prospects in long-life pressurized water reactors. In long-life pressurized water reactors with large initial residual reactivity in the core, a reasonable selection of burnable poisons can suppress the large residual reactivity at beginning of lifetime and can achieve a long burnup depth at end of lifetime. Therefore, the selection of burnable poisons is a crucial factor to be considered in the design of long-life pressurized water reactors. In this study, the selection of burnable poisons and neutronics characteristics of long-life PWR plate fuel assembly were studied. The transport-burnup calculations of different burnable poison fuel assemblies were carried out. Some candidate BPs are selected to realize the effective control of reactivity. The results show that when the enriched isotopes ^{157}Gd, ^{167}Er and B_4C are used as burnable poisons, there is almost no reactivity penalty; when PACS-J and ^{231}Pa are used as burnable poisons, due to their own characteristics, not only does not cause reactivity penalty at end of lifetime, but also the fuel assembly life is extended, the fuel utilization rate is improved. The combination of PACS-J and the slow-burnup burnable poisons can obtain a better reactivity curve. The results of this article show that the plate fuel assemblies can be selected with enriched isotope ^{157}Gd, enriched isotope ^{167}Er, B_4C, ^{231}Pa and PACS-J as burnable poisons, and the combinations of burnable poisons can be selected with two combination schemes, PACS-Er and PACS-Pa.

Keywords: long-life PWR, assembly life, combination schemes, neutronics characteristic, burnable poison

OPEN ACCESS

Edited by:
Qian Zhang,
Harbin Engineering University, China

Reviewed by:
Xubo Ma,
North China Electric Power University, China
Tiejun Zu,
Xi'an Jiaotong University, China

***Correspondence:**
Jinsen Xie
jinsen_xie@usc.edu.cn
Tao Yu
yutao29@sina.com

Specialty section:
This article was submitted to Nuclear Energy, a section of the journal Frontiers in Energy Research

Received: *23 June 2021*
Accepted: *09 August 2021*
Published: *27 August 2021*

Citation:
Xu S, Yu T, Xie J, Yao L and Li Z (2021) Burnable Poison Selection and Neutronics Analysis of Plate Fuel Assemblies. Front. Energy Res. 9:729552. doi: 10.3389/fenrg.2021.729552

INTRODUCTION

Long-life reactor designs are currently available in the United States, Russia and other countries, such as the MIT-designed submarine reactor (Ippolito, 1990) and the Russian KLT-40 series of reactors (Gontov et al., 2019). Nuclear propulsion power reactors are an important area of pressurized water reactors (PWRs) development. Small nuclear reactor is the ideal main power units for large marine vessels due to its high power density and small size. The refueling of reactor core in marine reactors is time-consuming, expensive, and has extreme requirements for nuclear waste management and radiation protection, which can directly affect the utilization rate of nuclear marine reactors. Reducing the number of reactor core refueling during the service of such reactors can substantially improve their economic viability and reduce the amount of nuclear waste. By increasing the core fuel enrichment, the initial residual reactivity of the core is improved and the core can be operated for a longer period of time with a single fuel load. The long-life reactor

design can reduce or eliminate the frequency of reactor refueling, allowing large marine vessels to operate for 10–20 years or more with a single fuel load.

The power level and reactor core lifetime are the crucial performance indexes of nuclear reactors. An ideal nuclear power reactor must have both long core lifetime and high power. Plate fuel has a large heat transfer area, short distance between fuel center and coolant channel, and high heat transfer efficiency (Cheng and Xiong, 2020). Lower fuel pellet and surface temperatures can be obtained at the same power level and coolant flow rate, or when the fuel pellet and surface temperature does not exceed the limit, nuclear reactors are allowed to operate at higher power. Further, plate fuel has a compact structure, which is conducive to the miniaturization of reactor core (ZCongpeiDshouhui, 1987; Song, 2013). Plate fuel is a commonly used fuel geometry for high flux research reactors and compact nuclear power reactors with high power density (Ye, 1997; Afshin et al., 2007; Gong et al., 2015; Mohamed and Mohamed, 2019). Long-life reactors based on plate fuel exhibit immense potential in applications that require both power and lifetime.

The reactor core lifetime can be enhanced by increasing the loading or conversion ratio of fissile nuclides. In pressurized water reactors (PWRs), it is difficult to achieve ultra-long reactor core lifetime by simply increasing the conversion ratio because the conversion ratio is much less than 1. Meanwhile, another challenge is that the leakage probability of the primary circuit pressure boundary increases the power distribution of reactor core and the positive temperature coefficient of moderator. Burnable poisons (BPs) has a strong capacity to absorb neutron, and the product formed after neutron absorption can either be a "transparent" nuclide or a nuclide that can continue to absorb neutron, so it has flexible residual reactivity control ability (Li et al., 2019). Therefore, BP design is a significant method to control the core residual reactivity of long-life PWR. The existing studies on the selection of burnable poisons for pressurized water reactors had been studied (Anwar and Cao, 2010; Li et al., 2019; Xu et al., 2021), but most of the current studies are based on conventional rod-shaped with low-enrichment fuel assemblies, and there are fewer studies on the selection of burnable poisons for high-enrichment plate fuel assemblies with better burnable poison neutronics characteristics. Long-life PWRs have high enrichment fuel, so long-life PWRs have large initial residual reactivity. If reactivity control is performed using traditional BPs, it may be difficult to achieve a smooth release and control of reactivity over the lifetime of a long-life PWRs.

In this study, long-life PWR plate fuel assemblies are studied. Calculations are carried out using different BPs schemes for plate fuel assemblies, and the performance of different BPs is analyzed by the variation in the k_{inf} of assembly containing different BPs as a function of burnup to obtain the better BPs. This study can provide a reference for the selection and design of BPs for long-life PWRs.

CALCULATION PROCEDURE AND MODEL

Calculation Procedure

The DRAGON program is used for the transport-burnup calculation. DRAGON (Marleau et al., 2016) is a deterministic reactor lattice calculation program developed by Montreal University of Technology, Canada. Many numerical method modules can be used to solve 1D/2D/3D neutron transport problems, such as interface flow method, collision probability method, discrete ordinate method, characteristic method, and spherical harmonic function method. The DRAGON can handle fuel assemblies with different geometric structures (e.g., tube bundles, plates, hexagons) and different reactor types (e.g., light water reactor, heavy water reactor), so it has a strong geometric applicability and flexibility (Guangwen and Shengyi, 2010). The feasibility of DRAGON for plate assembly calculation has been verified (Haitao et al., 2005; Ma et al., 2015; Zhao, 2017; Yu et al., 2020). DRAGON can also perform accurate calculations for nuclides with complex burnup chains (Canbakan and Hébert, 2015; Xia et al., 2021).

There are many modules available inside the DRAGON, so in this article, the subgroup method module is chosen for resonance self-shielding calculations, the Sanchez module is chosen to handle the double non-uniformity problem, and the MOC module is chosen to handle the transport calculations. The cross section library is selected from the 172-groups WIMSD.

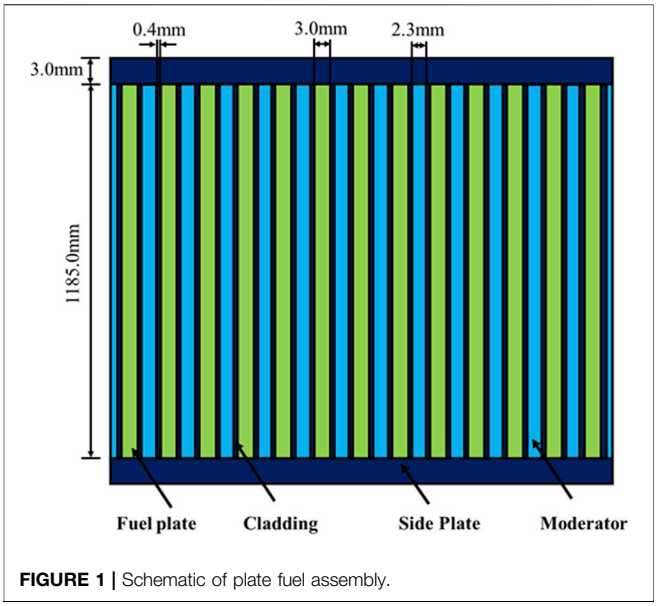

FIGURE 1 | Schematic of plate fuel assembly.

Calculation Model

The Schematic of plate fuel assembly is shown in **Figure 1**. The assembly consists of 13 fuel plates, two support plates, and water gaps (H_2O), where UO_2 particles, which is dispersed in the ^{4}Zr matrix, is selected as the fuel, and ^{4}Zr alloy is used as the material for the cladding, support plates, and matrix. The thicknesses of fuel core, fuel cladding, water gap between two fuel plates, the support plate, and fuel plate height are 3.0, 0.4, 2.3, 3.0, and 1,185.0 mm, respectively. Dispersion fuel has the advantages of reasonable irradiation stability, excellent thermal conductivity, good corrosion resistance, long service life, and high burnup, thus it is widely used in long-life PWR. The enrichment of UO_2 in this study is 60%. The loading arrangement of BPs is as follows: the

TABLE 1 | Calibration results.

Program	DRAGON	Openmc	Error (pcm)
k_{inf}	1.688579	1.688435	14.4

BPs are uniformly mixed with the fuel to facilitate dispersion loading, and a symmetrical arrangement of fuel plates containing BPs is considered. To ensure the accuracy of the design, the calibration results are shown in **Table 1**.

CANDIDATE BPs

Unlike conventional low-enrichment rod fuel assemblies, assemblies within long-life core have higher initial reactivity. From a neutronics perspective, the selection of either natural nuclides or enriched isotopes as BPs should follow three principles: (1) BPs should suppress a large initial reactivity at beginning of lifetime; (2) BPs need to ensure a gentle release of reactivity during the lifetime; (3) Small or no reactivity penalties at end of lifetime for assemblies containing BPs allow reactors to achieve longer days of full power operation (Xie et al., 2017). In this study, the relevant physical properties of candidate BPs are evaluated in terms of suppression of initial reactivity at beginning of lifetime, reactivity released during life and reactivity penalty at end of lifetime, and BPs suitable for high enrichment long-life PWR are selected. By reducing the loading in the fuel plate, different BPs are added to make the initial value of infinite medium multiplication coefficient (k_{inf}) as 1.20 in the assembly. Further, by changing the content of BPs in the single board and the number of BP boards in the assembly, the reactivity control requirements are satisfied and a smaller reactivity penalty is achieved finally.

Here, BP materials including non-proliferative BPs, actinide BPs, and advanced polymeric BPs are selected as the research object for the analysis.

Non-proliferative BPs

The components of non-proliferative BP materials are naturally abundant, and the main materials are B_4C, Dy_2O_3, Er_2O_3, Eu_2O_3, Gd_2O_3, and Sm_2O_3.

Actinide BPs

Some actinide nuclides can be converted into fissile nuclides after absorbing neutron. When these nuclides are used as BPs, they can inhibit excessive reactivity by absorbing neutron at the beginning of lifetime, and they can also use the converted fissile nuclides to prolong the life of the assembly and enhance the reactivity. Finally, it leads to a gentle variation in the residual reactivity. The actinide nuclides selected in this study are ^{231}Pa, ^{241}Am, ^{237}NP, ^{238}Pu, and ^{240}Pu.

PACS: Advanced Polymeric BP

Polycarboborane-siloxane-ethynyl (PACS) has good corrosion resistance and stability, thus it is an effective BP [21]. **Figure 2** shows the chemical structure of PACS. In this study, two advanced polymeric BPs: PACS-J and PACS-L (Allen et al., 2003), are selected, and their compositions are shown in **Table 2**.

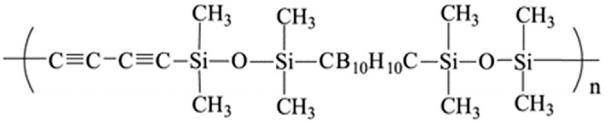

FIGURE 2 | Chemical structure of PACS.

TABLE 2 | Composition of PACS [22].

BP	Density (g/cm^3)	Number of atoms per molecule				
		C	H	B	O	Si
PACS-J	1.0	14	34	10	2	4
PACS-L	0.9	44	84	10	5	12

RESULTS AND ANALYSIS

Calculation Results

The candidate BPs burnup curves are shown in **Figure 3**. As seen in **Figure 3A**, only ^{231}Pa of the actinide BPs extends the life of the assembly at k_{inf} = 1.0 in the case of high fuel enrichment, and all other actinide BPs showed reactive penalties of different magnitudes.

Figure 3B shows that at k_{inf} = 1.0, the two advanced polymer BPs extend the life of the assembly at end of lifetime due to their own properties. At an initial k_{inf} = 1.20, assemblies containing both advanced polymer BPs showed a large reactive release in the middle and late life cycle and difficulties in reactivity control. The rate of reactive release of BPs was reduced by increasing the BPs content in a single plate (increasing the BPs self-shielding effect) to slow down the rate of BPs consumption. The fuel burnup curve of PACS-L does not meet the requirements for safe reactor operation because the reactivity fluctuates widely throughout the assembly lifetime and the reactivity is more difficult to control. The reactivity fluctuation of the burnup curve of the assembly containing PACS-J did not exceed 0.2 throughout the lifetime at the initial k_{inf} = 1.04, but the reactivity showed a large release in the middle and late stages of the lifetime, which prolonged the assembly lifetime but made the reactivity control difficult.

As seen in **Figure 3C**, the assembly containing the B_4C had no reactivity penalty at end of lifetime, but the assemblies containing the other BPs all caused a reactivity penalty. The nuclides have a small absorption cross section in BPs with different natural ratios, and the nuclides produced by offspring have different absorption cross sections and half-lives. This can lead to reactivity penalty if k_{inf} = 1.0. For highly enrichment assemblies, the use of natural ratios of non-proliferative BPs is not optimal.

Therefore, in this study, the natural proportion of non-proliferative BPs (Er_2O_3, Eu_2O_3, Gd_2O_3, and Sm_2O_3) corresponding to enriched isotope oxides ($^{167}Er_2O_3$, $^{151}Eu_2O_3$,

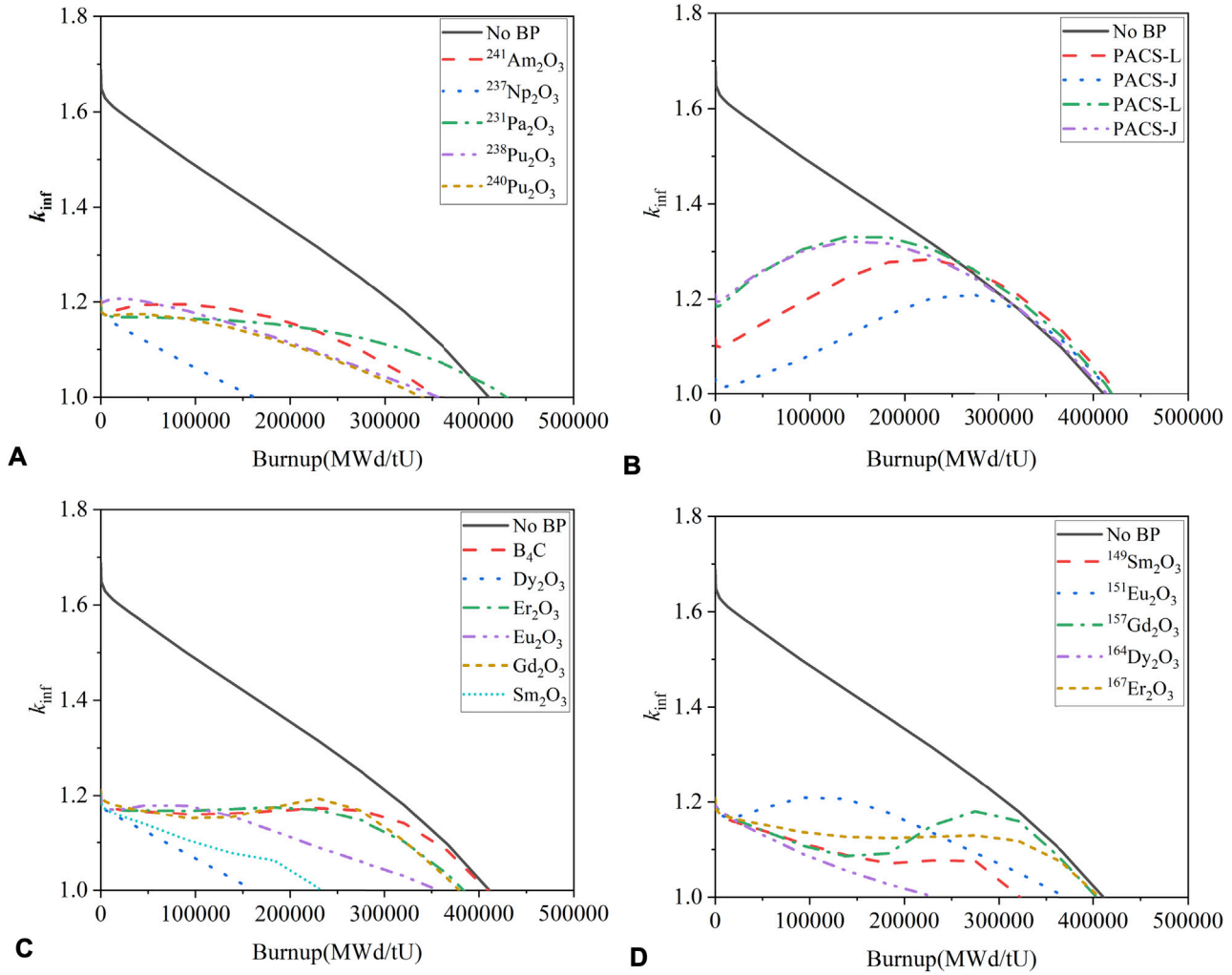

FIGURE 3 | Variation in the k_{inf} of assembly with different BPs schemes.

$^{157}Gd_2O_3$, and $^{149}Sm_2O_3$) are selected, and all the separated isotopes are enriched at 100%.As seen in **Figure 3D**, at high fuel enrichment, the enriched isotope is consumed more quickly as BPs, causing less reactivity penalty at end of lifetime and greater burnup of the assembly than what can be achieved with naturally proportioned BPs. The use of enriched isotopes as BPs reduces the production of daughter nuclides in the burnup chain, resulting in a reduction of some daughter nuclides with absorption cross sections, reducing the reactivity penalty at end of lifetime and improving fuel utilization.

Through the above calculations, this article conducted a selection study on different types of BPs. The results show that ^{231}Pa, B, ^{157}Gd, ^{167}Er, and PACS-J is more suitable than other BPs for long-life reactors. The reactive release of B_4C and ^{167}Er as BPs was smooth throughout the burnup cycle, with no significant fluctuations throughout the life cycle and little to no reactive penalty at end of lifetime. ^{157}Gd, when used as BPs, causes only a small reactivity penalty, but the reactivity is released more rapidly over the life span. When ^{231}Pa and PACS-J are used as BPs, the lifetime of the assembly is extended beyond that of non-BPs fuel assemblies due to ^{231}Pa own burnup chain and PACS-J own characteristics, resulting in improved fuel utilization. However, when PACS-J is used as a single BPs, there are difficulties in lifetime reactivity control.

Neutronics Characteristics Analysis of BPs

From ***Calculation Rresults***, it can be seen that ^{231}Pa, B, ^{157}Gd, ^{167}Er and PACS-J showed better results than other BPs. Therefore, this article performs neutronics characteristics analysis for ^{231}Pa, B, ^{157}Gd, ^{167}Er and PACS-J.

The analysis parameters of ^{231}Pa, B, ^{157}Gd, ^{167}Er and PACS-J are shown in **Table 3**. The neutron absorption cross sections for the different BPs are given in **Table 3**. **Table 3** also contains the BPs content in a single plate, the number of plates in the assembly containing different BPs and the reactivity penalty at end of lifetime, which are the input parameters and results of the selection calculations performed in ***Calculation Rresults***. In order to visualize the arrangement of fuel plates containing BPs in the assembly, **Figure 4** shows the arrangement of fuel plates containing different BPs in the assembly.

TABLE 3 | Analysis parameters for different BPs.

Analysis parameters	Parameter values for different BPs				
	$^{157}Gd_2O_3$	B_4C	$^{167}Er_2O_3$	$^{231}Pa_2O_3$	PACS-J
Neutron absorption cross section/$10^{-24}cm^2$ Renier. (2003)	253,254	3,838(^{10}B)	644	202	3,838(^{10}B)
Mass fraction (% of BP in single board)	5.20	13.00	4.50	2.27	70.00
Change in the cycle length of assembly with BPs as compared to without BPs (MWd/tU)	2,291.680	458.336	916.672	−4,583.360	−3,666.688
Number of fuel plates with BP	3	2	6	13	4

The neutron absorption cross section of ^{157}Gd is the largest among the selected BPs. When ^{157}Gd is used as BPs, the initial residual reactivity can be suppressed by adding only 5.20% of $^{157}Gd_2O_3$ at beginning of lifetime, but the large absorption cross section makes the BPs consume faster, and a large reactivity release occurs in the middle and late stages of the lifetime, producing reactivity fluctuations. There is a certain neutron absorption cross section for the daughter nuclides produced by the absorption of neutrons by ^{157}Gd, which causes a small reactivity penalty at end of lifetime.

The neutron absorption cross section of ^{10}B is the largest of the two isotopes, and the burnup chain of B is very simple, absorbing neutrons and converting them directly to helium and lithium, which are essentially "transparent" to neutrons, with essentially no reactivity penalty at end of lifetime, but as a diffuse BPs the swelling of fuel elements due to helium release needs to be considered.

^{167}Er has a smaller neutron absorption cross section compared to ^{157}Gd, but has a certain neutron absorption cross section that burnup slower compared to ^{157}Gd, reducing the BPs content in a single plate and making $^{167}Er_2O_3$ as completely consumed as possible at end of lifetime. The daughter nuclides produced by the absorption of neutrons by ^{167}Er have a certain neutron absorption

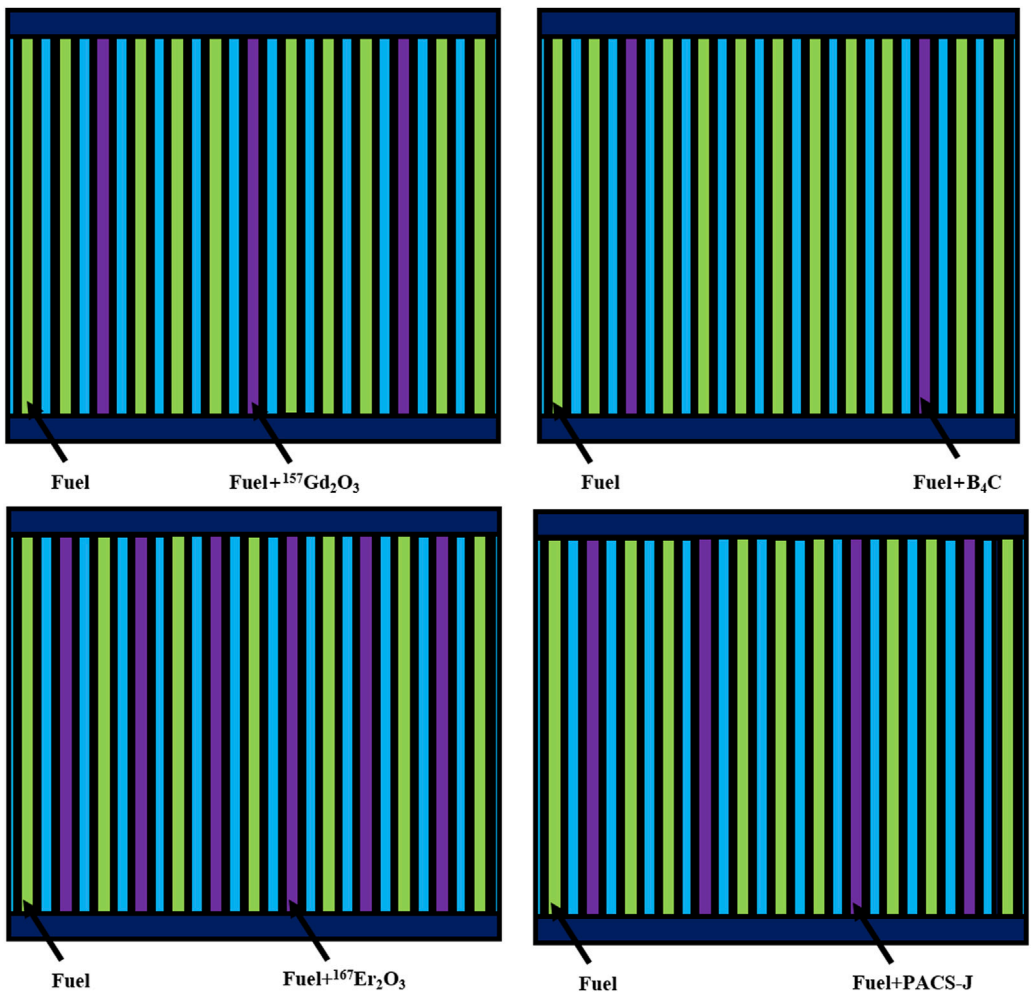

FIGURE 4 | Layout scheme of different burnable poison assemblies.

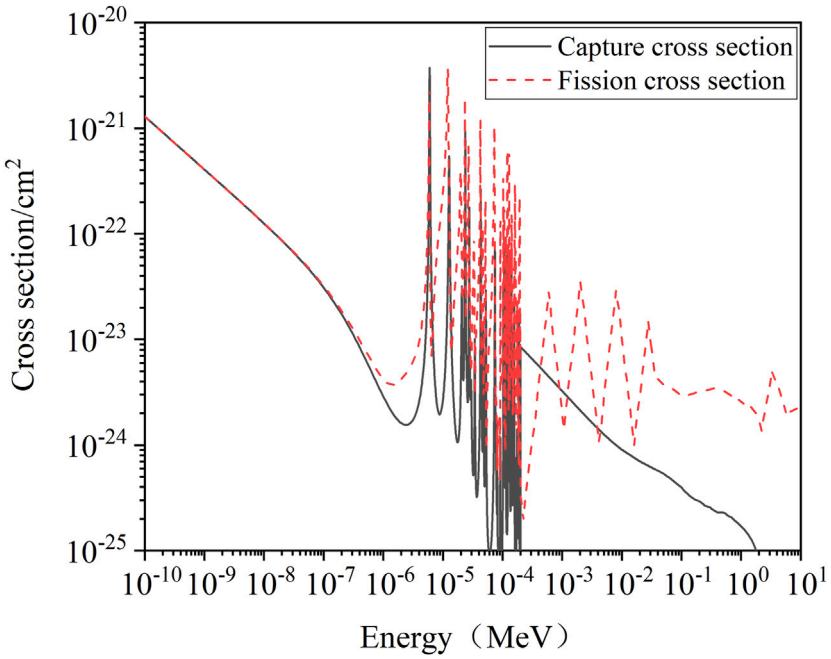

FIGURE 5 | Capture and fission cross sections of ^{232}U.

cross section, which causes a small reactivity penalty at end of lifetime.

The neutron absorption cross section of ^{231}Pa is relatively small compared to ^{157}Gd and ^{167}Er, so the burnup rate is significantly slower and better control of reactivity can be achieved. The burnup chain of ^{231}Pa is different from the other nuclides (Kulikov et al., 2017). ^{231}Pa acts as the parent nucleus of this burnup chain, and fissionable ^{232}U and ^{233}U exist directly in the burnup chain. ^{232}Pa is generated after the capture of neutrons by ^{231}Pa, and ^{232}Pa has a half-life of only 1.3 days and decays to form ^{232}U. The fission and capture cross sections of ^{232}U are very similar, which allows ^{232}U to both capture neutrons to produce the fissile nuclide ^{233}U and to fission directly to supplement reactivity. The capture and fission cross section of ^{232}U is shown in **Figure 5**. The special burnup chain of ^{231}Pa offers the possibility to achieve high burnup with ^{231}Pa assemblies.

PACS-J has a high hydrogen content and high boron content, and its high hydrogen content makes PACS-J have its own slowing effect as BPs, which can better slow down neutrons at end of lifetime, improve thermal neutron utilization, and promote the consumption of fission nuclide Pu. Therefore, PACS-J can extend the burnup and improve fuel utilization at end of lifetime when used as BPs.

From the above neutronics characteristics analysis, it is known that the main neutron absorber in PACS-J is ^{10}B, and the absorption cross section of ^{10}B is 3,838barn.Because the higher fuel enrichment makes the life time initial reactivity larger, when PACS-J is used as a single BP for reaction control, although increasing the content (70%) of BP in a single plate to increase the self-shielding effect, the assembly reactivity fluctuation is still the largest among the selected BPs. Therefore, in the case of high fuel enrichment, PACS-J can be considered in combination with BPs with small neutron absorption cross section (slow-burnup).

COMBINATION OF BPs

In this article, a preliminary study of BPs combinations was conducted without changing the BPs content in a single plate and only adjusting the number of BPs plates containing PACS-J, $^{167}Er_2O_3$ and $^{231}Pa_2O_3$ in the assemblies.

For the combination of PACS-J and $^{167}Er_2O_3$, the number of BPs plates containing PACS-J and $^{167}Er_2O_3$ is 1 and 4, respectively, and the others are pure fuel plate elements. For the combination of PACS-J and $^{231}Pa_2O_3$, the number of BPs plates containing PACS-J and $^{231}Pa_2O_3$ is 1 and 10, respectively, and the others are pure fuel plate elements. The schematic diagram of the assemblies arrangement is shown in **Figure 6**.

Figure 7 shows the burnup curves of PACS-J combined with $^{167}Er_2O_3$ and $^{231}Pa_2O_3$. It can be seen that the initial k_{inf} of the assembly is about 1.10 after the combination of PACS-J with BPs of small neutron absorption cross section, and there is no large fluctuation in the reactivity of assemblies throughout the lifetime, and the reactivity is released smoothly during the lifetime. There was no reactivity penalty at the end of life and the lifetime was extended by 2,750.016 MWd/tU at end of lifetime for the PACS-Er combination and 9,625.056 MWd/tU for the PACS-Pa combination. The reactivity fluctuations for both BPs combination scenarios were about 0.1 over the entire lifetime.

PACS-J has a large neutron absorption cross section as BPs, and because the assemblies has a large initial reactivity, if single

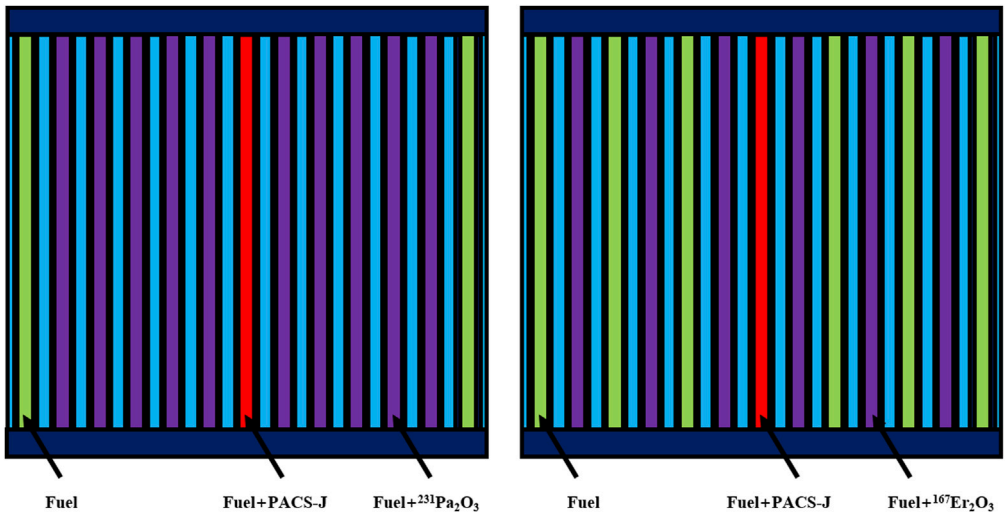

FIGURE 6 | Layout scheme of assembly with different numbers of burnable poisons.

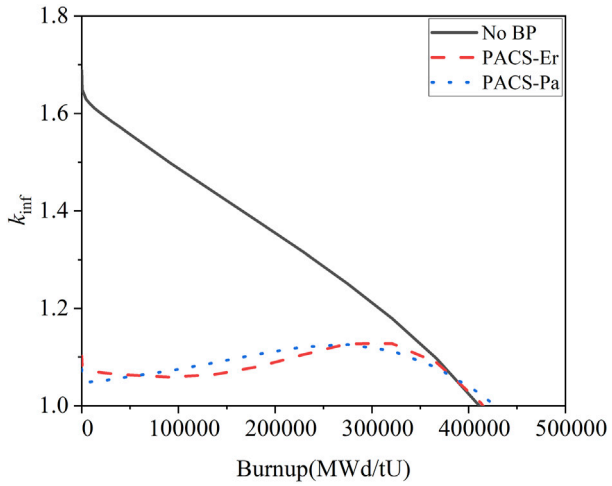

FIGURE 7 | Variation in the k_{inf} of assembly with different BP combination schemes.

BPs with a large neutron absorption cross section is used for reactivity control, the initial residual reactivity can be suppressed at beginning of lifetime. However, as the burnup deepens, the reactivity is released more quickly and the assemblies show large reactivity fluctuations. The combination of "fast-burnup" BPs with "slow-burnup" BPs can compensate the disadvantage of difficult assembly reactivity control at high enrichment, thus obtaining better reactive burnup curve.

CONCLUSION

In this study, based on high enrichment plate fuel assemblies, BPs selection and neutronics characterization studies are carried out, transport-burnup calculations are performed for different BPs, and BPs with better neutronics performance are selected. The specific conclusions are as follows:

1) For plate fuel assemblies, oxides of ^{157}Gd and ^{167}Er in enriched isotopes can be used as BPs to reduce the reactivity penalty at end of lifetime; there is almost no reactivity penalty at end of lifetime when B_4C is used as BPs. Also ^{231}Pa and PACS-J, when used as BPs, both extend the assemblies burnup at end of lifetime and improve fuel utilization. The ^{157}Gd, ^{167}Er, ^{231}Pa and PACS-J can be used as candidates for long-life PWRs when they are obtained economically.
2) At high fuel enrichment, some of the "fast-burnup" BPs are not suitable for reactive control as a single BPs in the assembly, but a better reactive burnup curve can be obtained by a reasonable combination with "slow-burnup" BPs. For example, PACS can be combined with "slow-burnup" BPs Er and Pa to increase the control of reactivity.

DATA AVAILABILITY STATEMENT

The raw data supporting the conclusions of this article will be made available by the authors, without undue reservation.

AUTHOR CONTRIBUTIONS

SX designed the Scheme and performed simulations, analyzed data, and drafted or provided the revision of the article. TY, JX, LY participated in the work and co-wrote the article. ZL supervised the research and resolved appropriately, provided the revision of the article, and approved of the final version to be published. All authors contributed to the article and approved the submitted version.

FUNDING

This study is supported by the science and technology innovation Program of Hunnan Province (Nos.2020RC4053) and National Natural Science Foundation of China (No. 11875162).

ACKNOWLEDGMENTS

The authors would like to show their great appreciations to NEAL (Nuclear Engineering and Application Laboratory) Team for its contribution to this research.

REFERENCES

Afshin, H., Hadi, D., and Jalil, J. (2007). Loss of Coolant Accident Analyses on Tehran Research Reactor by RELAP5/MOD3.2 Code[J]. *Prog. Nucl. Energ.* 49 (7), 511–528.

Allen, K., Baney, R., and Butt, D. (2003). An Advanced Burnable Poison for Pressurized Water Reactors[C]. *Proc. Conf. Adv. Nucl. Fuel Manag.*, 5–8.

Anwar, H., and Cao, X. (2010). Small PWR Core Design with Coated Particle Based Fuel with a Novel Composition[J]. *Prog. Nucl. Energ.* 52 (6), 531–535.

Canbakan, A., and Hébert, A. (2015). Accuracy of a 2-level Scheme Based on a Subgroup Method for Pressurized Water Reactor Fuel Assembly Models. *Ann. Nucl. Energ.* 81, 164–173. doi:10.1016/j.anucene.2015.03.034

Cheng, R., and Xiong, J. (2020). Numerical Analysis of Flow Blockage Accidents in Inlet of Plate-type Fuel Assembly[J]. *Nucl. Power Eng.* 41 (S2), 92–97.

Congpei, Z., and Shouhui, D. (1987). UO2 Ceramic Plate Fuel Assembly[J]. *Nucl. Power Eng.* 8 (1), 74–78, 88.

Gong, D., Huang, S., Wang, G., and Wang, K. (2015). Heat Transfer Calculation on Plate-type Fuel Assembly of High Flux Research Reactor. *Sci. Tech. Nucl. Installations* 2015, 1–13. doi:10.1155/2015/198654

Gontov, V. S., Anikin, N. A., and Chernov, L. V. The Study of the Probability of Increasing the Operating Time of the Nuclear Reactor KLT-40 S through the Use of Perspective Nuclear Fuel Cycles[C]//Физикоќтечнические Проблемы В Наукењ Промышленности И Медицине ЋФТШНШМќЫЩЪыЦЬ Сборник Научныч трудов Международной НаучноќПрактической конференции Студентовњ асПирантов И Молодыч ученычњ Гћ Томскњ ЬЩ СентябряќЩЭ октября ЫЩЪы ГћТомскњ ЫЩЪыћ ЫЩЪыь ЬЬЬЭћ

Guangwen, B., and Shengyi, S. (2010). "Validation and Analysis of the DRAGON Program for Pressurized Water Reactor Fuel Assembly Calculations [C]," in The 13th Reactor Numerical Calculation and Particle Transport Conference and 2010 Reactor Physics Conference. Chinese Nuclear Society.

Haitao, J., Hongchun, W., and Dong, Y.. Computer Simulation of Variform Fuel Assemblies Using Dragon Code[C]. In 13th International Conference on Nuclear Engineering. 2005.

Ippolito, T. D. (1990). Effects of Variation of Uranium Enrichment on Nuclear Submarine Reactor Design[D]. *Mass. Inst. Tech.*

Kulikov, G. G., Kulikov, E. G., Shmelev, A. N., and Apse, V. A. (2017). Protactinium-231 - New Burnable Neutron Absorber. *Nucl. Energ. Tech.* 3 (4), 255–259. doi:10.1016/j.nucet.2017.10.002

Li, M., Yu, Y., and Xiao, P. (2019). Nuetronic Analysis on Separated Isotope Burnable Poisons for Long-Life Reactor Core[J]. *Sci. Tech. Nucl. Installations* 40 (S2), 74–77. doi:10.1155/2015/198654

Ma, J., Wang, G., and Yuan, S. (2015). An Improved Assembly Homogenization Approach for Plate-type Research Reactor[J]. *Ann. Nucl. Energ.* 85, 1003–1013. doi:10.1016/j.anucene.2015.07.018

Marleau, G., Hebert, A., and Roy, R. (2016). *A User Guide for DRAGON Version4, Report IGE-294[R]*. Canada: Ecole Polytechnique de Montreal.

Mohamed, A. G., and Mohamed, A. (2019). Analysis of Natural Circulation loop in MTRs Using CONVEC Code[J]. *Prog. Nucl. Energ.* 117, 110–114.

Renier, J. A. (2003). *Development of Improved Burnable Poisons for Commercial Nuclear Power Reactors*. Final Report on NERI project Number 99-0074[J]. US: Department of Energy.

Song, L. (2013). Numerical Analysis of Flow Blockage Accident of Plate Fuel Assembly[D]. *Harbin Eng. Univ.*

Xia, Y., Xie, J., and Xu, S. (2021). Neutronic Design and Analysis of Dispersed Particle Burnable Poison for Long Cycle PWR[J/OL]. *At. Energ. Sci. Tech.* 1-8 , 2021 available at: http://kns.cnki.net/kcms/detail/11.2044.TL.20210317.1611.012.html.

Xie, M., Chen, Y., and Lei, Y. (2017). Analysis for Burnup Characteristics of Advanced Polymeric Burnable Poison[J]. *Nucl. Sci. Eng.* 37 (2), 320–326.

Xu, S., Yu, T., and Xie, J. (2021). Burnable Poison to Improve Life of UO2 Fuel Small PWR Core[J]. *At. Energ. Sci. Tech.* 55 (2), 265–271.

Ye, C. (1997). China Advanced Research Reactor (CARR): A New Reactor to Be Built in China for Neutron Scattering Studies. *Physica B: Condensed Matter* 241-243, 48–49. doi:10.1016/s0921-4526(97)00509-7

Yu, T., Liu, J., and Xie, J. (2020). Study on Burnup Characteristics of Actinide Burnable Poisons in Plate-type Fuel Assembly[J]. *Nucl. Power Eng.* 41 (03), 1–7.

Zhao, W. (2017). *Study of TRU Transmutation and Th-U Proliferation Characteristics in Molten Salt Stacks [D]*. Hengyang: University of South China.

Conflict of Interest: The authors declare that the research was conducted in the absence of any commercial or financial relationships that could be construed as a potential conflict of interest.

Publisher's Note: All claims expressed in this article are solely those of the authors and do not necessarily represent those of their affiliated organizations, or those of the publisher, the editors and the reviewers. Any product that may be evaluated in this article, or claim that may be made by its manufacturer, is not guaranteed or endorsed by the publisher.

frontiers in Energy Research

ORIGINAL RESEARCH
published: 21 September 2021
doi: 10.3389/fenrg.2021.756106

Application of the Spectral-Shift Effect in the Small Lead-Based Reactor SLBR-50

Chen Zhao, Lei Lou, Xingjie Peng, Bin Zhang and Lianjie Wang*

Science and Technology on Reactor System Design Technology Laboratory, Nuclear Power Institute of China, Chengdu, China

In the design of a nuclear reactor, improving fuel utilization and extending burnup are two of the most important goals. A concept design of spectral-shift control rods is presented to extend cycle length and fuel utilization. First, a small lead-based reactor, SLBR-50, is preliminarily designed, and the design rationality is proved. Next, the concept design of spectral-shift control rods is presented and analyzed. Finally, numerical results of the small reactor design show that the burnup depth is extended by 73.3% and the fuel utilization rate for ^{235}U and ^{238}U is improved by 66.6 and 68.4%. All results are calculated using a Monte-Carlo code RMC. These results show advantages of the concept design for the spectral-shift control rod.

Keywords: spectral-shift effect, SLBR-50, RMC, fuel utilization, extending burnup

OPEN ACCESS

Edited by:
Tengfei Zhang,
Shanghai Jiao Tong University, China

Reviewed by:
Shen Qu,
Southwestern Institute of Physics, China
Zhitao Xu,
North China University of Water Resources and Electric Power, China

****Correspondence:***
Xingjie Peng
pengxingjiets@126.com

Specialty section:
This article was submitted to Nuclear Energy, a section of the journal Frontiers in Energy Research

Received: *10 August 2021*
Accepted: *02 September 2021*
Published: *21 September 2021*

Citation:
Zhao C, Lou L, Peng X, Zhang B and Wang L (2021) Application of the Spectral-Shift Effect in the Small Lead-Based Reactor SLBR-50. Front. Energy Res. 9:756106. doi: 10.3389/fenrg.2021.756106

INTRODUCTION

Improving fuel utilization, extending burnup depth, and improving the nuclear plant economy are several important reactor design targets (Zhang et al., 2020a; Zhang et al., 2020b). It is still an open question when it comes to extending burnup depth with certain fuel weights. The spectral-shift effect is one of the solutions for the problem.

The spectral-shift effect was studied and the spectral-shift control concept was first proposed in 1961 in the Babcock and Wilcox company report (Mars and Gans, 1961). After that, the spectral-shift effect was studied in the pressurized water reactor design (Ronen and Galperin, 1980; Ronen and Fahima, 1984; Martin, 1988) and extended to the boiling water reactor design (Yokomizo et al., 1993). In the 21st century, the spectral-shift effect research was applied in the new-type advanced reactor. In the ABWR-II core design, spectral-shift rods were adopted and analyzed (Anegawa et al., 2001; Moriwaki et al., 2004). Results show that the average discharge burnup was improved by 5% and uranium weight was saved by 6~7%. Recently, the spectral-shift control design was applied in other advanced reactors, such as SmAHTR (Greene, 2010; Ilas et al., 2014; Kotlyar et al., 2017; Mehta and Kotlyar, 2019), small modular reactors (Lindley and Parks, 2016), and molten salt reactors (Betzler et al., 2018). SmAHTR is a small advanced high-temperature graphite-moderator reactor designed by Oak-Ridge. The cycle length can be extended by up to 20% or coated particle (TRISO) fuel can be reduced by 15% while maintaining the cycle length with the spectral-shift effect (Kotlyar et al., 2017; Mehta and Kotlyar, 2019). In these new-type advanced reactor analyses, a reactor design with spectral-shift effect shows good improvements of the fuel utilization rate and cycle length extension. However, few research studies have been carried out on spectral-shift lead-based reactors (LBRs) or the spectral-shift for extending cycle length and the fuel utilization rate.

In this study, a 50-MWt small lead-based fast reactor, SLBR-50, is conceptually designed at the Nuclear Power Institute of China (NPIC) for research. Besides, detailed parameters of the SLBR-50 are introduced. Based on the SLBR-50, the concept design of control rods with the spectral-shift

TABLE 1 | Basic parameters of the SLBR-50.

Items	Parameter	Items	Parameter
Reactor power	50 MWt	Fuel diameter	8.0 mm
Hot-condition average temperature	700 K	Air gap thickness	0.1 mm
^{235}U enrichment	19.95%	Clad thickness	0.6 mm
U total weight	3,835.3 kg	Clad outer diameter	9.4 mm
CR absorber material	B_4C	Fuel rod distance	10.9 mm
Reflector material	BeO	Assembly box thickness	2 mm
Clad material	Stainless steel	Assembly center distance	93.5 mm
Coolant material	Lead	Assembly inner distance	88.0 mm
Barrel material	Stainless steel	Assembly outer distance	92.0 mm
Fuel assembly amount	144	Active core height	95 cm
Control rod assembly amount	18	Outer reflector diameter	82 cm
Reflector assembly amount	48	—	—

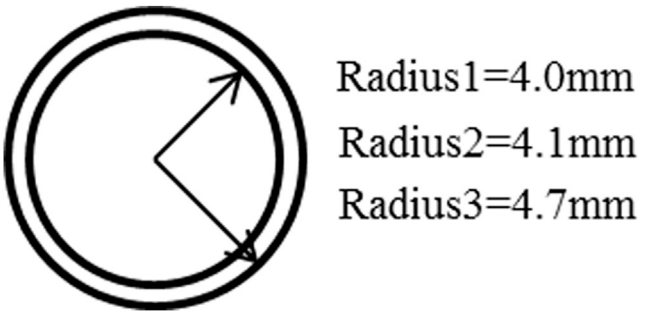

FIGURE 1 | Pin cell geometry of the SLBR-50; **(A)** fuel assembly, **(B)** reflector assembly, and **(C)** control rod assembly.

effect are proposed and analyzed, including the spectral-shift effect analyses and reactor performance improvement.

A continuous-energy Monte-Carlo reactor physics code, RMC (She et al., 2013; Wang et al., 2015; Liu et al., 2017), is adopted for the small reactor design. RMC has been developed by the Department of Engineering Physics, Tsinghua University, from 2010 as a tool for a reactor core analysis platform. It has several functions, such as complicated geometry modeling, criticality calculation, burnup calculation, and critical position searching calculation. Until now, RMC has already been used for reactor design and validation. In this study, all geometry modeling and calculation results are provided using RMC.

DESIGN OF SLBR-50

Design of SLBR-50

The SLBR-50 is conceptually designed for research. Several basic parameters of the reactor are shown in **Table 1**. Thermal power of the SLBR-50 is 50 MW. The hot-condition average temperature is 700 K. As for materials, 19.95% enrichment UO_2 is applied as the fuel. The uranium total weight is 3835.3 kg in the SLBR-50. B_4C is chosen as the control rod absorber material. In each pin cell, stainless steel is conducted as the clad material. Outside of the active core, BeO is applied as the reflector and stainless steel is conducted as the barrel. Heavy metal lead is adopted as the coolant in the lead-based reactor SLBR-50. Other parameters will be introduced in geometry modeling.

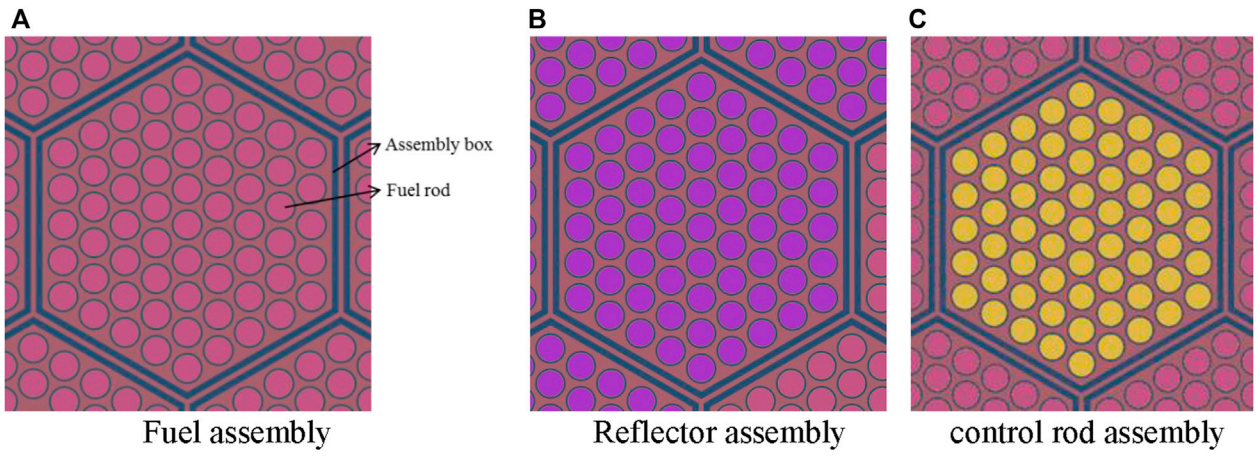

FIGURE 2 | Hexagonal assembly geometry of the SLBR-50.

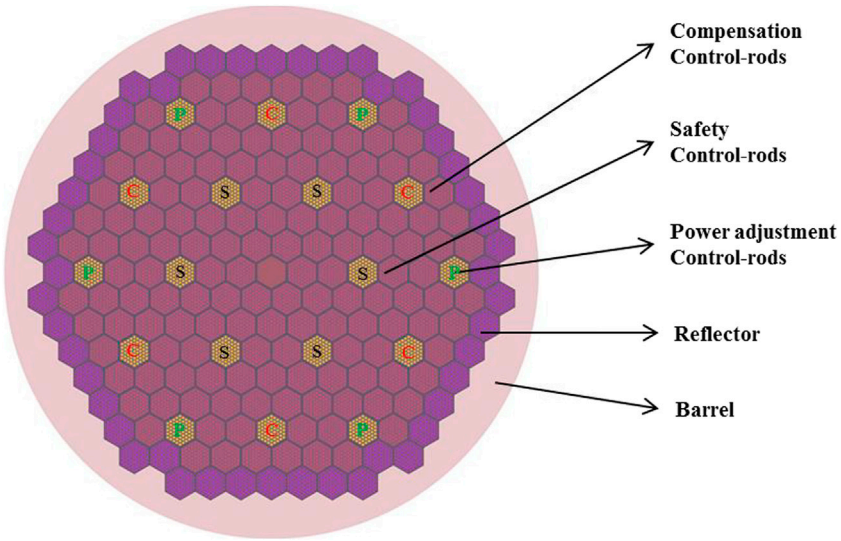

FIGURE 3 | Radial cut of the SLBR-50.

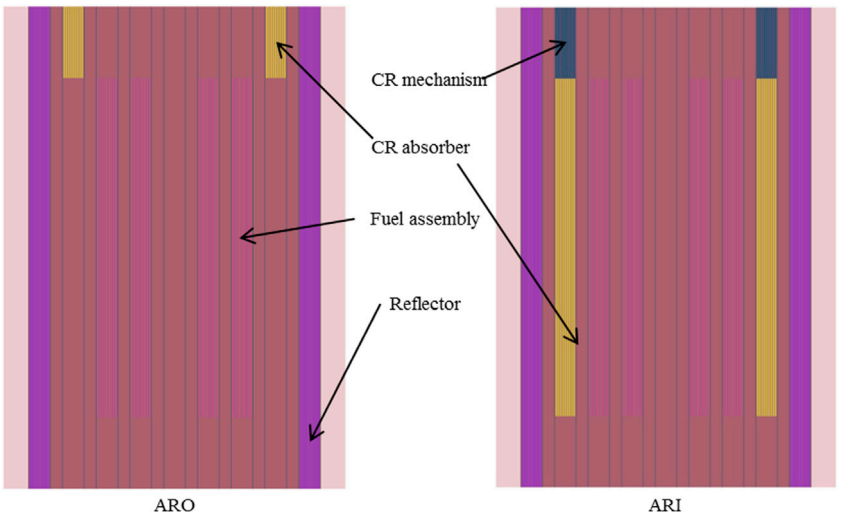

FIGURE 4 | Axial cut of the SLBR-50.

The geometry modeling of the SLBR-50 is divided into the pin cell, the lattice, and the whole core. The basic pin cell geometry is shown in **Figure 1**. The radius of the fuel region is 4.0 mm. The thickness of the air gap between the fuel and the clad is 0.1 mm, which is hard to show in the figure. The 0.6-mm-thick clad lies outside of the pin cell.

The hexagonal assembly geometry of the fuel, reflector, and control rod lattice are shown in **Figure 2**. The basic geometry is totally the same for these assemblies. 61 rods are arranged in regular matrix form. The thickness of the stainless steel assembly box is 2 mm. The assembly inner and outer distances are 88.0 and 92.0 mm separately. The assembly center distance is 93.5 mm.

The radial cut of SLBR-50 whole-core modeling is shown in **Figure 3**, and axial cuts of all rods out (ARO) and all rods in (ARI) cases are shown in **Figure 4**. The whole core consists of 144 fuel assemblies, 48 reflector assemblies, 18 control rod assemblies, and center guide tube assembly. Control rod assemblies are divided into three groups, including compensation, safety, and power adjustment. Besides, reflector assemblies are located outside of the active core. The barrel is explicitly modeled and the diameter of the barrel is 82 cm. In the axial cut, the height of the active core is 95 cm. On the top and the bottom of the active core, a 20-cm-high coolant reflector is arranged.

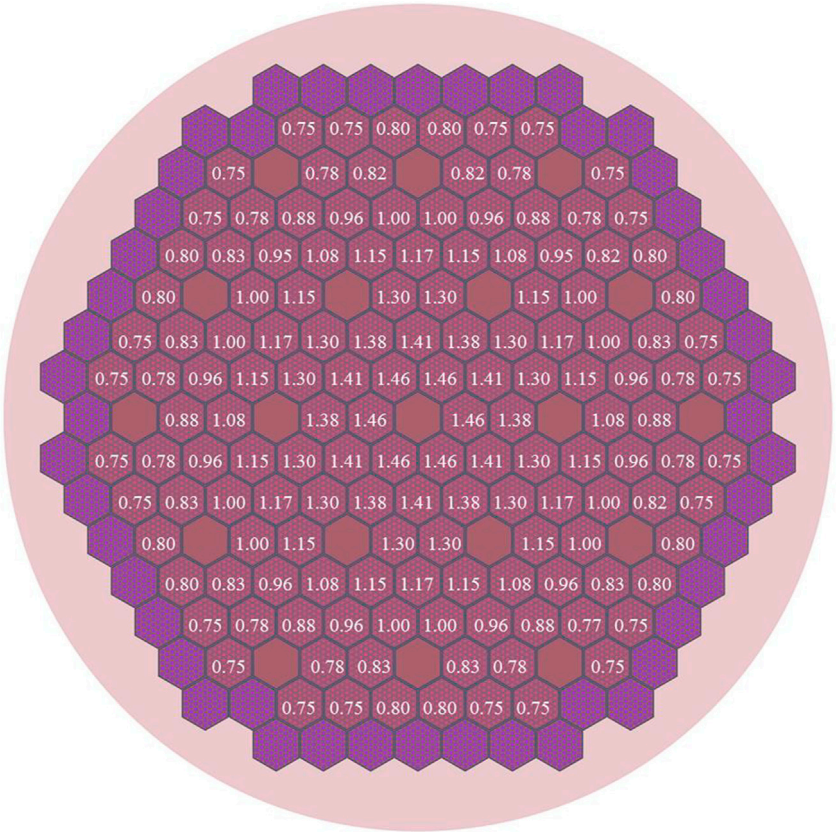

FIGURE 5 | Radial assembly power result of the SLBR-50.

Nuclear Design Results of SLBR-50

Nuclear design calculations for the power distribution and control rod worth were conducted using the Monte-Carlo code RMC. In the calculation, the ENDF-VII.0 library was adopted. 10 layers were divided in the axial direction of the active core. To obtain the detailed power distribution results, a relatively refined calculation condition was applied in the calculation. 8 billion active particles were used (800 generations consisting of 10 million neutrons per generation, of which 300 generations were skipped). Normalized radial assembly power and axial power distribution results of the ARO case are shown in **Figures 5**, **6**. In the radial assembly power result, the maximum assembly power is 1.46, which lies in the center of the reactor. In the axial power distribution, the maximum power is 1.268.

In the control rod worth calculation, 60 million active particles are used (600 generations consisting of 100 thousand neutrons per generation, of which 200 generations are skipped). The control rod worth results are shown in **Table 2**. Three sets of control rods are calculated. Integral rod worth (IRW) results are 6,915, 4,114, and 16,022 pcm for compensation, power adjustment, and safety control rod sets separately. Both differential rod worth (DRW) and integral rod worth (IRW) results show the shutdown depth is adequate for reactor control.

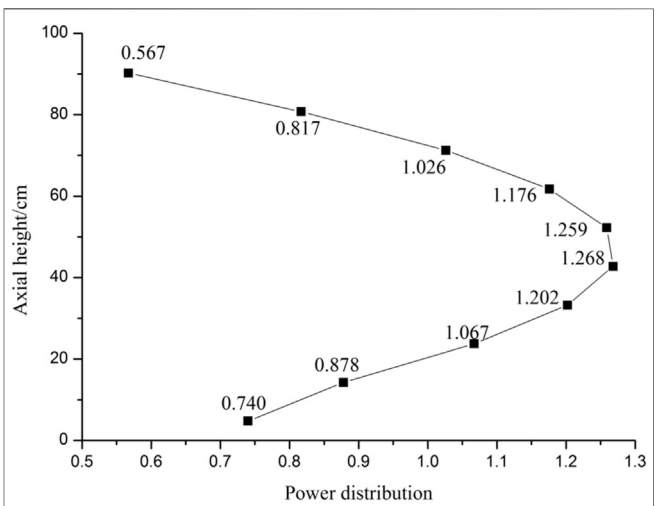

FIGURE 6 | Axial power distribution result of the SLBR-50.

Rationality of the primary design for the SLBR-50 is confirmed by these nuclear design results. Apparently, parameters in the reactor design need to be researched to improve the reactor characteristic. In this study, the spectral-shift effect is researched and analyzed based on the SLBR-50.

TABLE 2 | Control rod worth of the SLBR-50.

CR insert depth/cm	Compensation CR			Power adjustment CR			Safety CR		
	Eigenvalue	DRW/pcm	IRW/pcm	Eigenvalue	DRW/pcm	IRW/pcm	Eigenvalue	DRW/pcm	IRW/pcm
0	1.02244 ± 9pcm	/	/	1.02244 ± 9pcm	/	/	1.02244 ± 9pcm	/	/
9.5	1.01985 ± 9pcm	259	259	1.02101 ± 9pcm	143	143	1.01667 ± 9pcm	577	577
19	1.01505 ± 9pcm	480	739	1.01770 ± 9pcm	331	474	1.00639 ± 9pcm	1,028	1,605
28.5	1.00769 ± 9pcm	736	1,475	1.01332 ± 9pcm	438	912	0.99156 ± 9pcm	1,483	3,088
38	0.99858 ± 9pcm	911	2,386	1.00766 ± 9pcm	566	1,478	0.97255 ± 9pcm	1901	4,989
47.5	0.98803 ± 9pcm	1,055	3,441	1.00132 ± 9pcm	634	2,112	0.94940 ± 9pcm	2,315	7,304
57	0.97704 ± 9pcm	1,099	4,540	0.99477 ± 9pcm	655	2,767	0.92328 ± 9pcm	2,612	9,916
66.5	0.96689 ± 9pcm	1,015	5,555	0.98900 ± 9pcm	577	3,344	0.89761 ± 9pcm	2,567	12,483
76	0.95947 ± 9pcm	742	6,297	0.98472 ± 9pcm	428	3,772	0.87743 ± 9pcm	2018	14,501
85.5	0.95480 ± 9pcm	467	6,764	0.98201 ± 9pcm	271	4,043	0.86563 ± 9pcm	1,180	15,681
95	0.95329 ± 9pcm	151	6,915	0.98130 ± 9pcm	71	4,114	0.86222 ± 9pcm	341	16,022

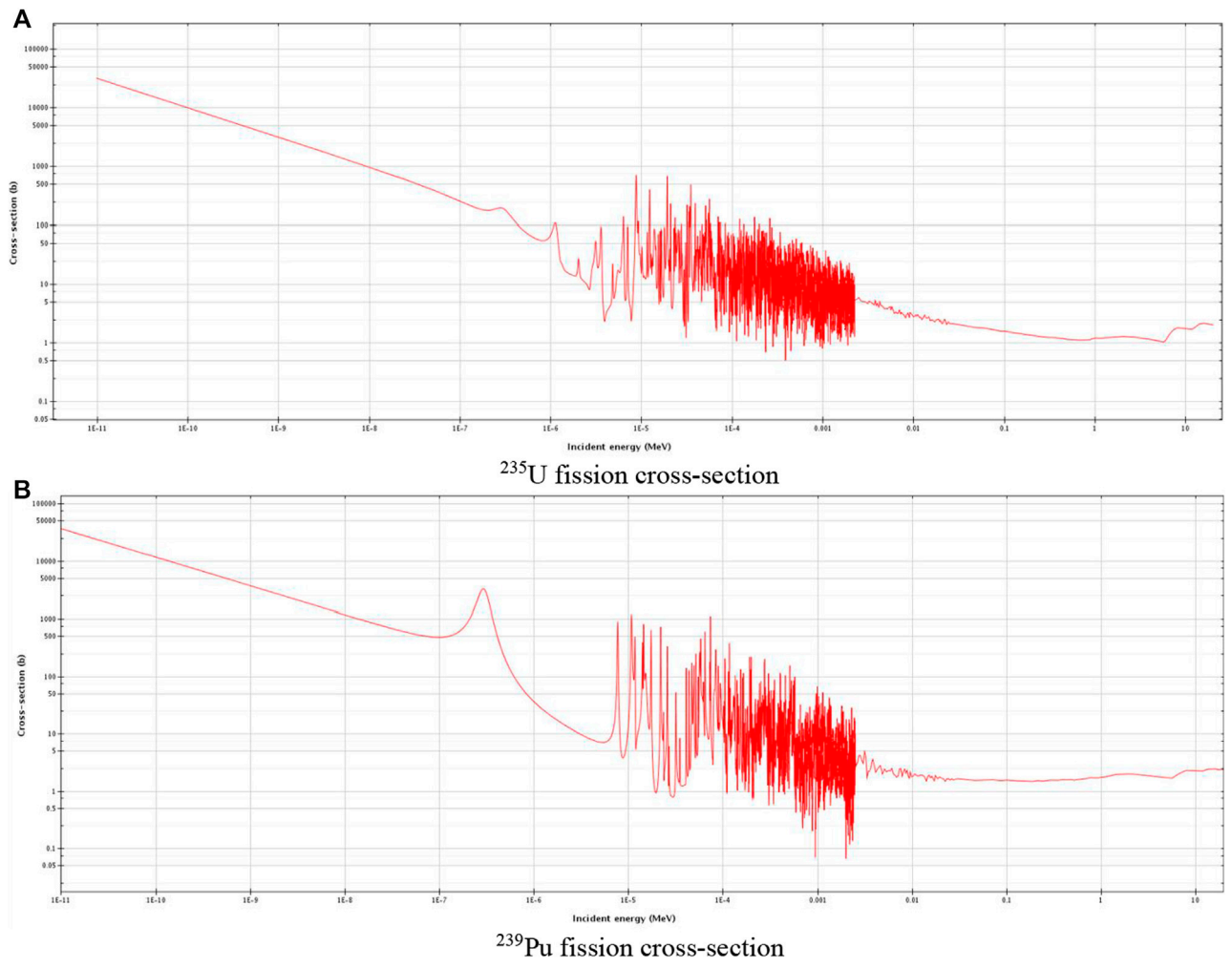

FIGURE 7 | Diagram of the fission cross-sections for typical fuel nuclides. **(A)** ^{235}U fission cross-section. **(B)** ^{239}Pu fission cross-section.

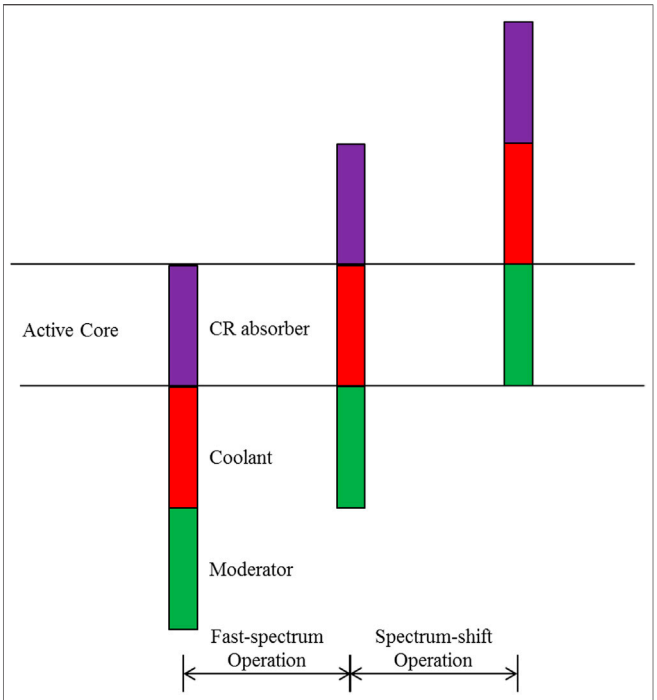

FIGURE 8 | Concept design of the control rod for the spectral-shift scheme.

THE CONCEPT DESIGN OF SPECTRAL-SHIFT CONTROL RODS

The basis of the spectral-shift effect is the difference of the fission absorption capacity in different energy ranges. ^{235}U and ^{239}Pu are dominant fission nuclides. As is shown in **Figure 7**, fission cross-sections of ^{235}U and ^{239}Pu show a similar pattern; the cross-section in the thermal energy region is larger than that in the fast energy region. Besides, ^{238}U can absorb fast neutrons and convert to ^{239}Pu. In this way, fuel breeding happens in the fast-spectrum reactor. Based on the fuel nuclides analysis of the different energy ranges, it can be concluded that the spectral-shift effect can balance the fuel breeding in the fast energy range and fission absorption in the thermal energy range. As a result, the fuel utilization rate will increase by the spectral-shift effect.

In this study, a concept design of a control rod with the spectral-shift effect is analyzed to realize the spectral-shift effect in the small lead-based reactor SLBR-50. The concept design of spectral-shift control rods is shown in **Figure 8**. Three sections are divided axially, including the control rod absorber, coolant, and moderator from the top to the bottom. Compared to the traditional control rod, the spectral-shift rod adds coolant and moderator sections. In the beginning of the spectral-shift scheme, the absorber section is inserted into the core active region. Spectral-shift control rods are withdrawn in the burnup procedure. With all absorbers withdrawn outside of the active core and the coolant section raised into the core, the fast-spectral operation procedure is finished. In the fast-spectrum operation, the reactor is operated in the fast spectrum to realize fuel proliferation. After that, spectral-shift rods continue withdrawing and moderators are moving to the core. In the spectrum-shift operation, neutrons will be moderated and the energy spectrum is softened. In this way, fuel utilization can be improved with the spectral-shift effect. The control rod moving procedure is shown in **Figure 9**. In the SLBR-50, YH_2 is applied as the moderator material.

THE SPECTRAL-SHIFT EFFECT ANALYSES AND NUMERICAL RESULTS

Cycle Length Results

The burnup depth and critical rod position results for the small reactor design are shown in **Table 3**. Three sets of control rods are withdrawn in the order of safety rods, power adjustment rods, and compensation rods. The initial rod position is −95 cm, where the control rod absorbers are totally inserted. The fast-spectrum operation is from the beginning of life to 1500 EFPD. In

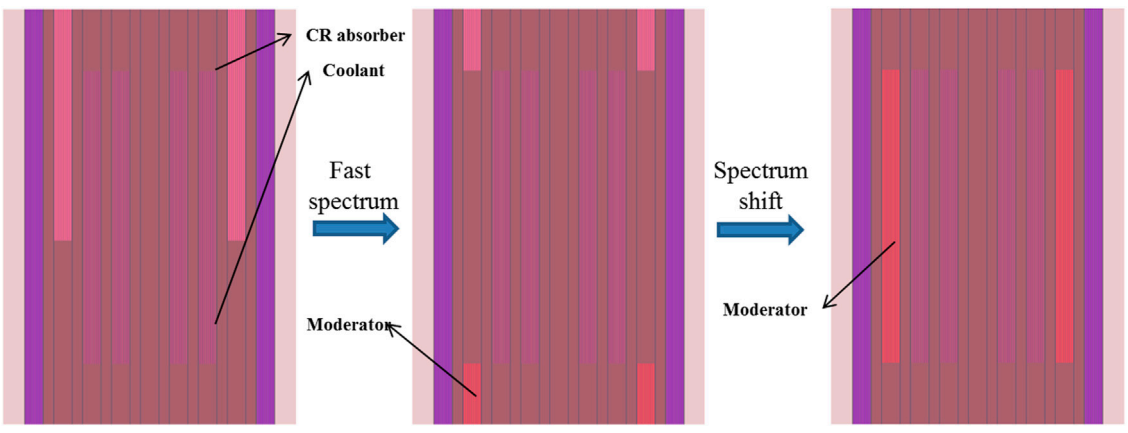

FIGURE 9 | Detailed axial cut in the spectral-shift rod withdrawing procedure.

TABLE 3 | Results of the critical rod position for the SLBR-50 spectral-shift control rod design.

Operation	Burnup/EFPD	Rod position/cm		
		Compensation CR	Power adjustment CR	Safety CR
Fast-spectrum operation	0	−44.79	0	0
	5	−43.81	0	0
	30	−43.4	0	0
	100	−45.07	0	0
	200	−41.87	0	0
	300	−39.58	0	0
	400	−37.28	0	0
	500	−34.72	0	0
	600	−32.3	0	0
	700	−29.82	0	0
	800	−27.35	0	0
	900	−24.82	0	0
	1,000	−20.75	0	0
	1,100	−19.06	0	0
	1,200	−14.89	0	0
	1,300	−9.51	0	0
	1,400	0	0	0
	1,500	0	0	0
Spectral-shift operation	1,600	0	0	7.38
	1700	0	0	24.31
	1800	0	0	23.86
	1900	0	0	23.27
	2000	0	0	64.75
	2,100	0	0	67.97
	2,200	0	0	95
	2,300	0	0	95
	2,400	30.66	95	95
	2,500	60.42	95	95
	2,600	95	95	95
—	2,700		Subcritical	

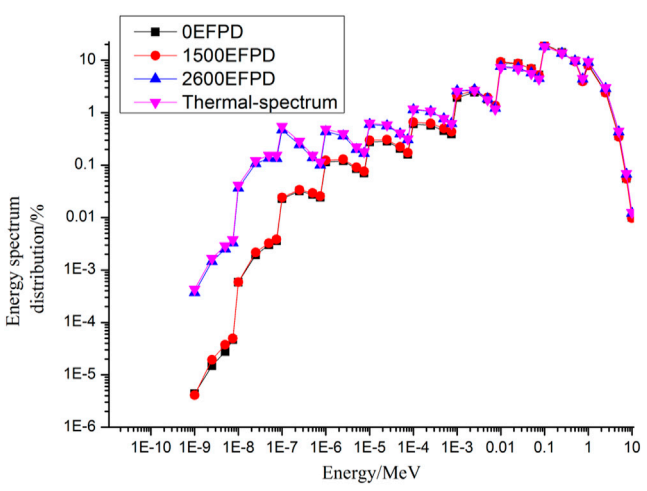

FIGURE 10 | Energy spectrum results of the spectral-shift scheme in the SLBR-50.

1500 EFPD, all control rod absorbers are withdrawn and the spectrum-shift operation begins. The spectral-shift effect can extend the cycle length from 1500 EFPD to 2600 EFPD, which has a 73.3% improvement for the cycle length with the same fuel weight. Besides, the spectral-shift design has the same shutdown margin as the fast-spectrum design.

Energy Spectrum Results

The kernel of the spectral-shift effect is the energy spectrum shift. Therefore, the energy spectrums are analyzed in typical burnup steps, shown in **Figure 10**. Energy sections are divided by an order of magnitude, from 1.0e-9 to 10 MeV. Each line shows the energy spectrum along all energy sections for the certain burnup. The energy spectrum analyses need to match with the spectral-shift rod withdrawal procedure. Besides, the thermal-spectrum result is provided in the beginning of life with all moderator rods inserted. The thermal-spectrum result can be shown as a reference in the spectrum-shift analysis. In the fast-spectrum operation from 0 EFPD to 1500 EFPD, energy spectrums are similar. Control absorber insertion has little influence on the energy spectrum. In the spectral-shift operation from 1500 EFPD to 2600 EFPD, moderators are inserted, and the spectrum-shift phenomenon can be observed in the energy spectrum analyses. The energy spectrum distribution of 2600 EFPD is similar to the thermal spectrum. It can be concluded that the spectrum-shift control rod design takes advantage of the spectrum-shift effect sufficiently in the SLBR-50.

TABLE 4 | Density of typical nuclides in the spectral-shift scheme.

Operation	Burnup/EFPD	Nuclide density/b−1cm−1			Utilization rate[a]/%	
		^{235}U	^{238}U	^{239}Pu	^{235}U	^{238}U
Fast-spectrum operation	0	1.960E+03	7.767E+03	0.000E+00	/	/
	5	1.960E+03	7.766E+03	2.130E-01	0.00	0.00
	30	1.956E+03	7.764E+03	2.418E+00	0.20	0.13
	100	1.945E+03	7.756E+03	8.756E+00	0.77	0.13
	200	1.929E+03	7.746E+03	1.774E+01	1.58	0.26
	300	1.913E+03	7.736E+03	2.653E+01	2.40	0.39
	400	1.898E+03	7.725E+03	3.518E+01	3.16	0.51
	500	1.882E+03	7.715E+03	4.370E+01	3.98	0.77
	600	1.867E+03	7.705E+03	5.209E+01	4.74	0.90
	700	1.852E+03	7.694E+03	6.033E+01	5.51	1.03
	800	1.837E+03	7.684E+03	6.845E+01	6.28	1.16
	900	1.822E+03	7.674E+03	7.647E+01	7.04	1.29
	1,000	1.807E+03	7.663E+03	8.437E+01	7.81	1.42
	1,100	1.793E+03	7.653E+03	9.214E+01	8.52	1.54
	1,200	1.778E+03	7.643E+03	9.976E+01	9.29	1.67
	1,300	1.764E+03	7.633E+03	1.073E+02	10.00	1.80
	1,400	1.750E+03	7.622E+03	1.147E+02	10.71	1.93
	1,500	1.735E+03	7.612E+03	1.220E+02	11.48	2.06
Spectral-shift operation	1,600	1.721E+03	7.602E+03	1.292E+02	12.19	2.19
	1700	1.707E+03	7.591E+03	1.363E+02	12.91	2.32
	1800	1.693E+03	7.581E+03	1.432E+02	13.62	2.45
	1900	1.680E+03	7.571E+03	1.499E+02	14.29	2.57
	2000	1.666E+03	7.561E+03	1.565E+02	15.00	2.70
	2,100	1.652E+03	7.551E+03	1.628E+02	15.71	2.83
	2,200	1.639E+03	7.541E+03	1.688E+02	16.38	2.96
	2,300	1.625E+03	7.531E+03	1.748E+02	17.09	3.09
	2,400	1.612E+03	7.522E+03	1.804E+02	17.76	3.22
	2,500	1.599E+03	7.513E+03	1.857E+02	18.42	3.35
	2,600	1.585E+03	7.503E+03	1.909E+02	19.13	3.47

[a]*Utilization rate = Consumed nuclides/Total nuclides*100%*

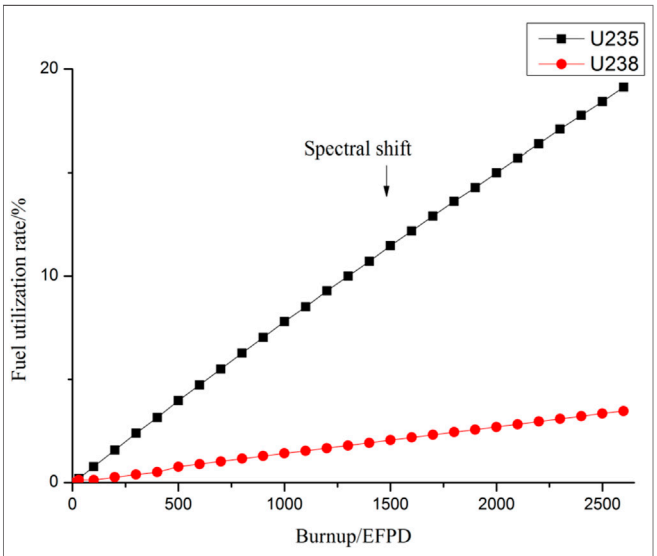

FIGURE 11 | Nuclide density variation in 200 EFPD for several typical fuel nuclides in the burnup.

Fuel Utilization Rate Results

Nuclide density variation is an important result for the spectral-shift effect. In the nuclide density analysis, only the spectral-shift scheme is conducted because that is the only scheme influenced by the spectral-shift effect. Considering the breeding of ^{238}U to ^{239}Pu, the fission reaction of ^{235}U, ^{238}U, and ^{239}Pu is the dominant nuclear reaction in the burnup. ^{235}U, ^{238}U, and ^{239}Pu are analyzed as the typical nuclides. The nuclide densities for these three nuclides are listed in **Table 4**, and the utilization rate variations in the burnup are shown in **Figure 11**.

As is shown in the table, the nuclide density of ^{235}U and ^{238}U is decreasing both in the fast-spectrum operation and the spectrum-shift operation, and the nuclide density of ^{239}Pu is increasing. The phenomenon is caused by the relatively hard energy spectrum. In the burnup procedure, even though the spectrum-shift effect makes the energy spectrum softer than the original fast spectrum, the spectrum-shift effect is unable to change the harder energy spectrum in the SLBR-50. Therefore, the breeding of ^{239}Pu is stronger than the fission absorption in the burnup procedure. All in all, the spectral-shift improves the fuel utilization of ^{235}U and ^{238}U from 11.5 to 19.1% and from 2.06 to 3.47%.

CONCLUSION

A 50-MWt small lead-based reactor, SLBR-50, is conceptually designed at the NPIC for research. The detailed design parameters are provided, as well as power distribution and control rod worth calculation results. These results verify the rationality of the preliminary design for the SLBR-50.

Based on the SLBR-50, the concept design of the spectral-shift control rod is analyzed for extending the burnup depth and improving fuel utilization. The basic configuration of the spectral-shift control rod is introduced in detail. Three sections are divided axially, including the control rod absorber section, the coolant section, and the moderator section. In the burnup procedure, the first section is the fast-spectrum operation. Control rod absorbers are withdrawn in this section and it is totally the same as the traditional control rod design. The second section is the spectral-shift operation with moderators inserted into the active core. The spectral-shift effect is realized in this section, and the burnup depth can be extended.

DATA AVAILABILITY STATEMENT

The original contributions presented in the study are included in the article/Supplementary Material; further inquiries can be directed to the corresponding author.

AUTHOR CONTRIBUTIONS

CZ: main researcher in the group and writer of the manuscript. LL: main researcher in the group. XP: leader in the group. BZ: researcher in the group. LW: main adviser and director.

FUNDING

This work is supported by the National Natural Science Foundation of China (grant nos. 12005214 and 11905214) and the China Association for Science and Technology (Young Elite Scientists Sponsorship Program 2019QNRC001).

REFERENCES

Anegawa, T., Aoyama, M., Fennern, L. E., and Koh, F. (2001). "The Status of Development Activities of ABWR-II," in Proc. 9th Int. Conf. Nuclear Engineering, Nice, France. ICONE-9, 8–12. April.

Betzler, B. R., Robertson, S., Powers, E. E. J. J., Worrall, A., Dewan, L., and Massie, M. (2018). Fuel Cycle and Neutronic Performance of a Spectral Shift Molten Salt Reactor Design. *Ann. Nucl. Energ.* 119, 396–410. doi:10.1016/j.anucene.2018.04.043

Greene, S. R. (2010). *Pre-Conceptual Design of a Fluoride-Salt-Cooled Small Modular Advanced High-Temperature Reactor (SmAHTR)*. Tennessee: ORNL/TM-201/199.

Ilas, D., Holcomb, D. E., and Gehin, J. C. (2014). *SmAHTR-CTC Neutronic Design*. Kyoto, Japan: Proc Physor.

Kotlyar, D., Lindley, B. A., and Mohamed, H. (2017). Improving Fuel Utilization in SmAHTR with Spectral Shift Control Design: Proof of Concept. *Ann. Nucl. Energ.* 104, 53–63. doi:10.1016/j.anucene.2016.12.037

Lindley, B. A., and Parks, G. T. (2016). The Spectral Shift Control Reactor as an Option for Much Improved Uranium Utilisation in Single-Batch SMRs. *Nucl. Eng. Des.* 309, 75–83. doi:10.1016/j.nucengdes.2016.08.041

Liu, S., Liang, J., Wu, Q., Guo, J., Huang, S., Tang, X., et al. (2017). BEAVRS Full Core Burnup Calculation in Hot Full Power Condition by RMC Code. *Ann. Nucl. Energ.* 101, 434–446. doi:10.1016/j.anucene.2016.11.033

Mars, D., and Gans, D. (1961). *Spectral Shift Control Reactor Design and Economic study[R]. BAW-1241*. United States: Babcock and Wilcox Company.

Martin, W. (1988). *The Slightly-Enriched Spectral Shift Control Reactor [R]*. DOE/ER/12809-4.

Mehta, V., and Kotlyar, D. (2019). Core Analysis of Spectral Shift Operated SmAHTR. *Ann. Nucl. Energ.* 123, 46–58. doi:10.1016/j.anucene.2018.09.013

Moriwaki, M., Aoyama, M., Anegawa, T., Okada, H., Sakurada, K., and Tanabe, A. (2004). ABWR-II Core Design with Spectral Shift Rods for Operation with All Control Rods Withdrawn. *Nucl. Tech.* 145, 247–256. doi:10.13182/nt04-a3474

Ronen, Y., and Fahima, Y. (1984). Combination of Two Spectral Shift Control Methods for Pressurized Water Reactors with Improved Power Utilization. *Nucl. Tech.* 67 (1), 46–55. doi:10.13182/nt84-a33528

Ronen, Y., and Galperin, A. (1980). A Comparison between Spectral Shift Control Methods for Light Water Reactors [J]. *Ann. Nucl. Energ.* 7, 55–64. doi:10.1016/0306-4549(80)90007-9

She, D., Liu, Y., Wang, K., Yu, G., Forget, B., Romano, P. K., et al. (2013). Development of Burnup Methods and Capabilities in Monte Carlo Code RMC. *Ann. Nucl. Energ.* 51, 289–294. doi:10.1016/j.anucene.2012.07.033

Wang, K., Li, Z., She, D., Liang, J. g., Xu, Q., Qiu, Y., et al. (2015). RMC - A Monte Carlo Code for Reactor Core Analysis. *Ann. Nucl. Energ.* 82, 121–129. doi:10.1016/j.anucene.2014.08.048

Yokomizo, O., Kashiwai, S., Nishida, K., Orii, A., Yamashita, J., and Mochida, T. (1993). Spectral Shift Rod for the Boiling Water Reactor. *Nucl. Eng. Des.* 144, 223–236. doi:10.1016/0029-5493(93)90139-z

Zhang, T., Liu, X., Xiong, J., and Cheng, X. (2020). Comparisons of Reduced Moderation Small Modular Reactors with Heavy Water Coolant[J]. *Front. Energ. Res.* 8, 15. doi:10.3389/fenrg.2020.00027

Zhang, T., Xiong, J., Liu, X., Chai, X., Li, W., and Cheng, X. (2020). Conceptual Design of an Innovative Reduced Moderation Thorium-Fueled Small Modular Reactor with Heavy-Water Coolant[J]. *Int. J. Energ. Res.* 43, 82868298. doi:10.1002/er.4827

Conflict of Interest: The authors declare that the research was conducted in the absence of any commercial or financial relationships that could be construed as a potential conflict of interest.

Publisher's Note: All claims expressed in this article are solely those of the authors and do not necessarily represent those of their affiliated organizations, or those of the publisher, the editors, and the reviewers. Any product that may be evaluated in this article, or claim that may be made by its manufacturer, is not guaranteed or endorsed by the publisher.

frontiers in Energy Research

METHODS
published: 01 October 2021
doi: 10.3389/fenrg.2021.760339

Environment Effect Treatments in PWR Whole-Core Pin-by-Pin Calculation

Bin Zhang[1]*, *Yunzhao Li*[2] *and Hongchun Wu*[2]

[1]Science and Technology on Reactor System Design Technology Laboratory, Nuclear Power Institute of China, Chengdu, Sichuan, [2]School of Nuclear Science and Technology, Xi'an Jiaotong University, Xi'an, China

The environment effect arises when pin-cell homogenized parameters are generated with reflective boundary conditions. To treat it in whore-core pin-by-pin calculation, two works are summarized in this article. Firstly, by analyzing the relative errors of pin-cell homogenized group constants and the relative importance of pin-cell discontinuity factors (PDF) in each group, the importance of correcting the PDF of the thermal group is recognized. Secondly, the least-squares method for a multivariate polynomial is utilized to functionalize the relation of the thermal group PDF and the core parameters, including diffusion coefficient, removal cross-section, neutron source, and normalized surface flux. The C5G7 and KAIST benchmarks are employed to evaluate the performance of the PDF predication. Numerical results indicate its effectiveness in reducing the errors of eigenvalue and pin power, especially for the cases with the fuel pins located near the interface between different assemblies.

Keywords: PWR, pin-by-pin, environment effect, least-squares method, functionalization

OPEN ACCESS

Edited by:
Tengfei Zhang,
Shanghai Jiao Tong University, China

Reviewed by:
Kun Zhuang,
Nanjing University of Aeronautics and Astronautics, China
Xubo Ma,
North China Electric Power University, China
Zhuo Li,
Sun Yat-sen University, China

***Correspondence:**
Bin Zhang
jsszwtzb@163.com

Specialty section:
This article was submitted to Nuclear Energy, a section of the journal Frontiers in Energy Research

Received: *18 August 2021*
Accepted: *07 September 2021*
Published: *01 October 2021*

Citation:
Zhang B, Li Y and Wu H (2021) Environment Effect Treatments in PWR Whole-Core Pin-by-Pin Calculation. Front. Energy Res. 9:760339. doi: 10.3389/fenrg.2021.760339

INTRODUCTION

For Pressurized Water Reactor (PWR) simulation, the computational cost of one-step calculation with fully detailed description is still too expensive for routine calculation using either stochastic or deterministic methods, even with the currently most advanced computing powers. Therefore, approximations in spatial, energy, and angular spaces have been developed to provide efficient solutions with acceptable accuracy. With the advantages of small storage and high computing speed, the two-step calculation schemes have successfully been applied to PWR analysis for decades.

In the last few decades, the nodal diffusion calculation accompanied by assembly homogenization has been widely employed (Smith, 1986). It contains 2D lattice neutron-transport calculation and 3D whole-core neutron diffusion calculation. The 2D lattice neutron-transport calculations are carried out for each type of assemblies with reflective boundary conditions to provide assembly-homogenized parameters (including cross-sections, diffusion coefficients, and discontinuity factors) and pin-power form functions. The whole-core diffusion solver determines the nodal power shape and then reconstructs the 3D pin-power distribution (Smith, 1980). One of the most important error sources in the scheme is applying the reflective boundary condition in the lattice calculation. For most large-scale PWRs, the neutron leakage model applied in the assembly homogenization can lead to an accurate result without any other corrections for the reflective boundary condition. There are several reasons. First, the environmental effect is not so strong for large-scale commercial PWRs. Second, fuel assemblies are optically thick which contain more than five neutron-free paths.

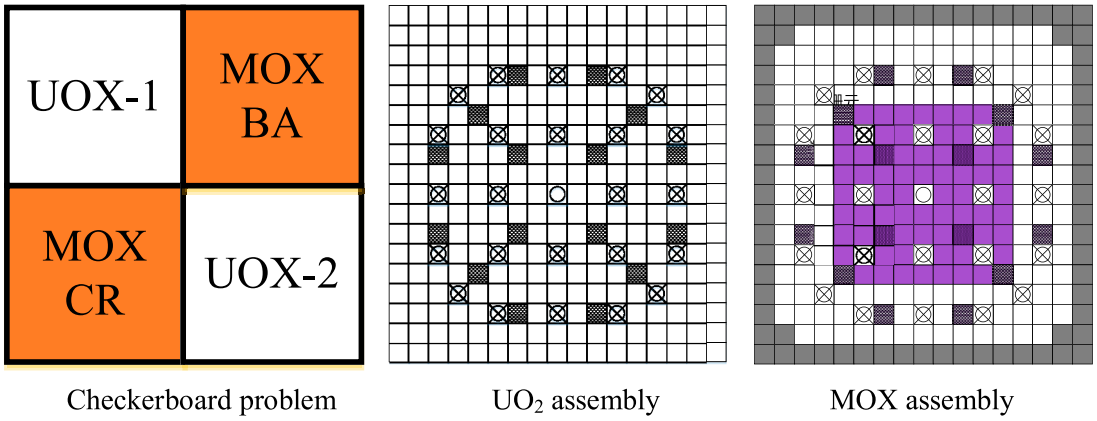

FIGURE 1 | Configuration of the checkerboard problem.

With the development of computing technology, an improved scheme named pin-by-pin calculation has become popular in recent years (Park and Park, 2001; Sugimura and Ushio, 2006). Different from the traditional two-step calculation, only the heterogeneous structure within each pin is homogenized, leaving the assembly heterogeneous during the three-dimensional whole-core calculation. It eliminates the assembly homogenization and the pin-power reconstruction. Alone with the development of the pin-cell homogenization technology (Kozlowski et al., 2011; Zhang et al., 2017), the reflective boundary condition used in the process of the pin-cell homogenized parameters becomes the main error source. In principle, the homogenized cross-sections, diffusion coefficients, and the pin-cell discontinuity factors can preserve the neutron leakage and reaction rates only for the boundary conditions at which they were created, i.e., for the reflective boundary condition. However, the exact boundary condition of an assembly in the active core cannot be known a priori for the two-step scheme. What is more, the size of the homogenization region in the pin-by-pin calculation is almost equal to the averaged neutron-free path, making the pin-cell homogenized parameters more dependent on the assembly environment compared with the assembly-homogenized parameters.

In order to achieve further accuracy of the pin-by-pin calculation, several embedding homogenization methods have been estimated (Yamaji et al., 2006; Zhang et al., 2008). These methods usually utilize the embedded heterogeneous assembly calculations to update the group constants on-line. The artificial neural network (ANN) method has also been developed to fit the group constants (Kozlowski et al., 2004; Yu et al., 2017). However, the methods are unstable because of the unpredictable ANN training and uncertainty in the quality of the fitted function. Focused on the environment effect, first in *Analysis of Pin-Cell Homogenized Parameters*, this article analyzed the errors of the pin-cell homogenized parameters and the relative importance of pin-cell discontinuity factors in each group (Kozlowski, 2005). Secondly, the least-squares method (LSM) utilized for the functionalization of PDF (Kozlowski, 2004) is introduced in the *Method for the PDF Predication* section. In order to numerically analyze the performance of the method, C5G7 (Smith et al., 2003) and KAIST (Cho, 2000) benchmarks are evaluated in this summary.

ANALYSIS OF PIN-CELL HOMOGENIZED PARAMETERS

A typical checkerboard assembly problem based on the KAIST benchmark (Cho, 2000), as shown in **Figure 1**, is utilized to analyze the pin-cell homogenized data. In the pin-cell homogenization, the flux-volume-weight method is used to generate the homogenized cross-sections:

$$\overline{\Sigma}_g = \frac{\sum\limits_{h\in g}\int_V \Sigma_h(\mathbf{r})\phi_h(\mathbf{r})d\mathbf{r}}{\int_V \phi_g(\mathbf{r})d\mathbf{r}}, \tag{1}$$

where h, g stands for the energy group and $\overline{\Sigma}$ stands for the homogenized cross-section.

Because of the reflective boundary condition performed in the assembly calculations, neither the axial nor radial leakage rate is considered within the heterogeneous assembly calculation. The heterogeneous leakage model (Li et al., 2017) is applied in this work; the heterogeneous leakage equations are shown as follows:

$$\begin{aligned}
&\Omega\cdot\nabla\varphi(\mathbf{r},E,\Omega)+\Sigma(\mathbf{r},E)\varphi(\mathbf{r},E,\Omega)=\frac{1}{4\pi}\left[Q(\mathbf{r},E)-iB\varphi_1(\mathbf{r},E)\right]\\
&\mathbf{\Omega}\cdot\nabla\varphi_1(\mathbf{r},E,\mathbf{\Omega})+\Sigma(\mathbf{r},E)\varphi_1(\mathbf{r},E,\mathbf{\Omega})=\\
&\frac{1}{4\pi\gamma\left[B,\overline{\Sigma}(E)\right]}\left[\frac{1}{3}\varphi_0(\mathbf{r},E)B^2+\int_0^\infty \mathrm{d}E'\Sigma_{s1}(\mathbf{r},E\leftarrow E')\varphi_1(\mathbf{r},E')\right].
\end{aligned} \tag{2}$$

The pin-cell diffusion coefficient for core pin-by-pin calculation would be determined by the space-dependent leakage coefficient from the heterogeneous leakage model.

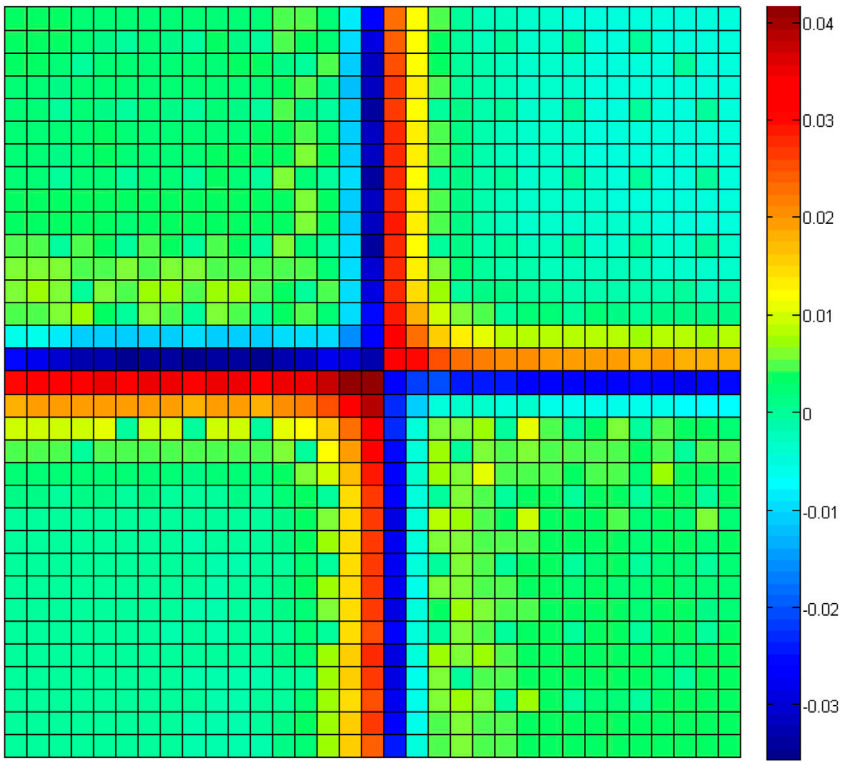

FIGURE 2 | Distribution of the pin-power relative error.

$$D_g = \frac{1}{B}\frac{i\int_V \varphi_{1,g}(\mathbf{r})d\mathbf{r}}{\int_V \varphi_g(\mathbf{r})d\mathbf{r}}. \quad (3)$$

The GET method was applied in this work. For single-assembly calculation with a specific boundary condition (zero current), the heterogeneous information can be provided by lattice code, while the homogeneous information is supposed to be obtained from the homogeneous neutron diffusion calculation. To get rid of the nonlinear relationship between the homogeneous surface flux and the PDF, a procedure is used to estimate the homogeneous surface flux accurately for the SP3 method using the heterogeneous information (Zhang et al., 2017). The discontinuity factor is defined as the ratio of the heterogeneous over the homogeneous surface fluxes:

$$f_g^s = \frac{\phi_g^{s,het}}{\phi_g^{s,hom}}, \quad (4)$$

where $\phi_g^{s,het}$ and $\phi_g^{s,hom}$ stand for the pin-cell heterogeneous surface flux and the homogeneous one.

Two sets of 7-group pin-cell homogenized parameters are generated for the colorset problem:

- The first set is obtained from the whole-core checkerboard calculation in order to eliminate the single-assembly zero net current boundary conditions assumption and incorporate the correct interface spectrum effect between UO_2 and MOX assemblies into the homogenized parameters.

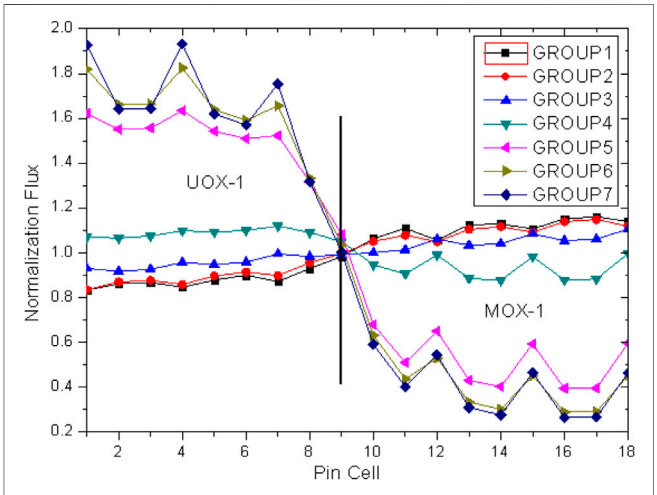

FIGURE 3 | The normalization neutron flux distribution.

- The pin-cell homogenized parameters in the second case are determined by single-assembly calculations with reflective boundary conditions.

Pin-Power Distribution

Figure 2 shows the pin-power relative error distribution of the pin-by-pin SP_3 calculation utilized in the second library set. The

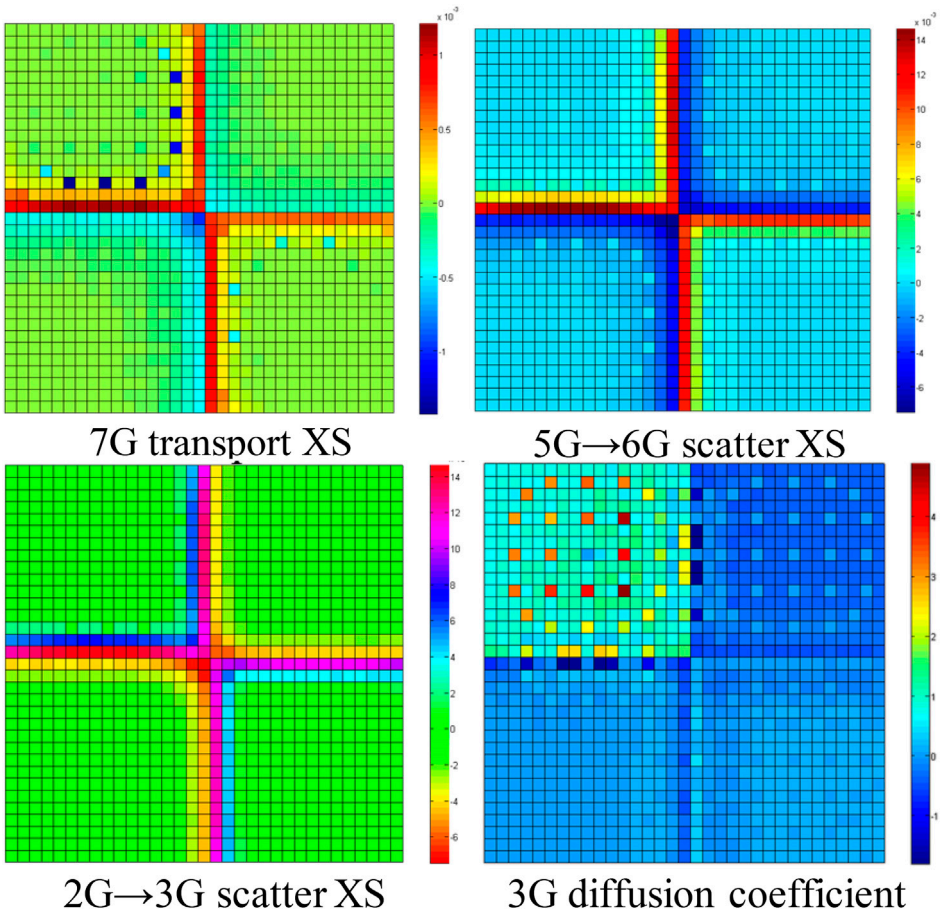

FIGURE 4 | Relative error distributions of the cross-sections.

reference solution is provided by the 2D whole-core one-step transport calculation. It can be found that large pin-power errors always occur in the pins close to the interface between two assemblies due to the large spectral mismatch between the single-assembly and full-core conditions in those locations. The maximum of the relative errors is more than 4% at the interface, while that of other locations would be about 1%.

Pin-Cell Homogenized Parameters

Figure 3 shows the neutron flux profile between the UO_2 and MOX assemblies. Dramatic changes can be found close to the interface of the thermal energy group. The spectrum interference effect between UO_2 and MOX is very strong for the fast groups (5–7 groups) while being weak for the thermal group (1–4 groups).

Part of the relative error distributions of the cross-sections is shown in **Figure 4**. It can be found that the errors of the pin-cell homogenized cross-sections are small, and the spectrum interference effect of the thermal group is so strong. The maximum error is less than 1.5%.

The relative error distributions of the PDF ratio of the first and seventh energy groups are shown in **Figure 5**. It can be found that the errors of the PDF ratios of fast groups are negligible. It is because that the spectrum interference effect of the fast groups is very weak. In contrast, the errors of the PDF ratios of the thermal groups are very large because of the strong spectrum interference effect between different assemblies. The maximum PDF error of the thermal groups would be more than 10%.

Relative Importance of PDF in Each Group

Single-assembly calculations of four different assemblies mentioned in the checkerboard problem were carried out to determine the relative importance of PDF in each group and analyze the interaction effect of the PDF between different energy groups.

Several calculations are carried out as follows:

- The reference solutions are obtained from the transport calculation by the house-developed Bamboo lattice code, which uses the MOC method as the transport solver (Chen et al., 2008; He et al., 2014; Li et al., 2015; Huang et al., 2016).
- The second one is the pin-by-pin SP_3 calculation without PDF (Yang et al., 2013; Li et al., 2013; Li et al., 2014; Yang et al., 2016).

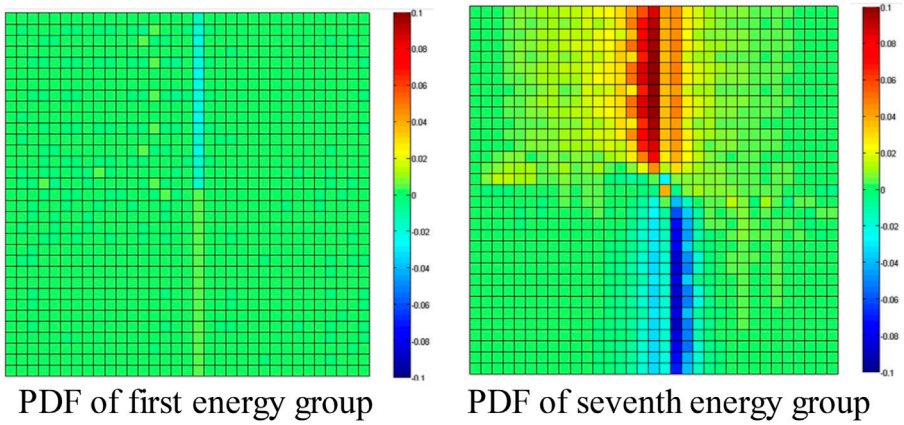

FIGURE 5 | Error distributions of the PDF ratio.

TABLE 1 | Single-assembly calculation results.

Case	k_{inf}	Eigenvalue difference (pcm) pin-power % RMS error		
		Without PDF	PDF effect	
			Fast group = 1.0 Thermal group = exact	Fast group = exact Thermal group = 1.0
UOX-1	1.49161	141 0.57	28 0.09	113 0.59
UOX-2	1.44302	453 1.09	−9 0.19	461 1.04
MOX-1	1.40060	847 1.86	−31 0.56	881 1.47
MOX-1 CR	1.35576	1,429 1.63	18 0.34	1,410 1.45

- The third results come from the calculation with exact PDF in fast groups or thermal groups and then turned off (set to 1.0) in all other groups.

From the results presented in **Table 1**, several important conclusions can be made. First, the results with the correct PDF of the thermal group are more accurate than the calculation with the correct PDF of the fast group. It is indicated that the PDF of the thermal group are more important and contribute more to the error than the fast group ones. Secondly, the sum of the eigenvalue differences of each exact PDF equals the calculation results without PDF. It is indicated that the PDF satisfy the neutron balance equation in a group-by-group way. Thirdly, correct PDF in one group with those of other groups set as 1.0 might not improve the solution accuracy; however, they do not make the results worse.

METHOD FOR THE PDF PREDICATION

The thermal group PDF have the largest relative errors and the thermal group is more important. Thus, attention should be paid to the correction of the thermal group PDF. In this work, the least-squares method (LSM) for multivariate polynomial is utilized to functionalize the relation of the thermal group PDF and the core parameters. The PDF predication function would be created with heterogeneous solutions obtained from several single-assembly calculations and several spectral geometry calculations. It is expected to predicate PDF with a whole-core homogeneous solution.

The least-squares method (LSM) for multivariate polynomial is written in the way by assuming that $\boldsymbol{x}$ is a vector variable with two or more components:

$$y = f(x) = a_0 + \sum_{i=1}^{N} a_i x_i + \sum_{i=1}^{N} \sum_{j=1}^{i} a_{ij} x_i x_j + \sum_{i=1}^{N} \sum_{j=1}^{i} \sum_{k=1}^{j} a_{ijk} x_i x_j x_k + \cdots, \tag{5}$$

where y stands for the function variable, which is the pin-cell homogenized parameters in our study, such as the cross-section and the pin-cell discontinuity factors; x_i stands for the core-parameter vector $\boldsymbol{x}$, a_i is the undetermined coefficient, which can be determined using the discrete state points $(\boldsymbol{x}_n, y_n)$.

TABLE 2 | Relative fitting errors of the different energy-group PDF by different predication function.

Polynomial order	Number of coefficients	RMS error/%						
		1	2	3	4	5	6	7
0	1	2.09	1.21	1.82	5.69	5.77	8.33	8.17
1	8	1.42	0.29	0.41	1.25	2.14	3.11	3.27
2	36	0.50	0.15	0.22	0.69	0.95	1.66	0.95
3	120	0.30	0.09	0.05	0.10	0.30	0.26	0.23

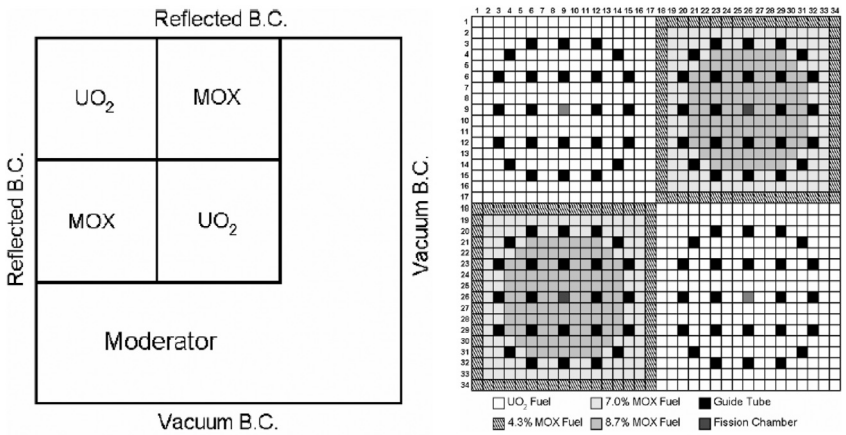

FIGURE 6 | 2D C5G7 benchmark.

The selection of the core parameters for the function of PDF predication plays an important role in the accuracy of the solutions. In this article, several elements are taken into consideration to pick up the core parameters. First, neutron behaviors are different in different energy groups. Therefore, the core parameters should be selected in a group-by-group manner. Second, the parameters should be associated with the method used in the core nodal solver. Different core methods would lead to different PDF. Third, the parameters should be suitable for any case that appeared in the problem.

In this article, the choice of core parameters is based on the physics underlying core neutronics behavior: neutron leakage, removal, and generation. Thus, there are seven core parameters as follows:

$$x_1 = D_{inode,g}\ x_2 = \Sigma_{r,inode,g}\ x_3 = \frac{S_{inode,g}}{\overline{\phi}_{inode,g}}\ x_i = \frac{\phi^s_{inode,g}}{\overline{\phi}_{inode,g}},\ (s = E,W,S,N), \tag{6}$$

where subscripts i and g stand for the node and the energy group; D represents the diffusion coefficient (cm); Σ_r represents the removal cross-section (cm^{-1}); S is the sum of the fission source and the scatter source (cm^{-3}); $\overline{\phi}$ is the average neutron flux (s^{-1} cm^{-2}); ϕ^s is the nodal surface flux (s^{-1} cm^{-2}); superscript s represents pin-cell surface in the different directions, $s = E,W,S,N$.

Based on the selected seven inputs, the coefficient a_i of the PDF predication function can be determined using the discrete state points ($\boldsymbol{x}_n$, y_n) via the least-squares method. For the whole-core pin-by-pin calculation, the state points ($\boldsymbol{x}_n$, y_n) would be provided by the single-assembly transport calculations and colorset problem calculation.

In order to determine the order of the PDF predication function, several calculations of different orders are carried out. The relative fitting errors of the PDF predication function are presented in **Table 2**. It can be found that when the polynomial order of the function is three, the maximum root-mean-square (RMS) error is less than 1%.

In this work, the function of PDF predication is selected as **follows**:

$$PDF = f(x) = a_0 + \sum_{i=1}^{N} a_i x_i + \sum_{i=1}^{N}\sum_{j=1}^{i} a_{ij} x_i x_j + \sum_{i=1}^{N}\sum_{j=1}^{i}\sum_{k=1}^{j} a_{ijk} x_i x_j x_k. \tag{7}$$

Taking into consideration the different neutron behaviors between the internal and peripheral locations of the core, two different functions of PDF predication were established for the internal fuel pins and the peripheral fuel, respectively. The PDF predication of reflector pins is considered separately.

NUMERICAL RESULTS

The 2D C5G7 benchmark (Smith et al., 2003) shown in **Figure 6** is carried out and the results are summarized in **Table 3**. The pin-power error distributions are shown in **Figure 7**. The "MC" in

TABLE 3 | Summary of the results.

Solutions	k_{eff}	Eigenvalue difference/pcm	Pin-power Max/RMS error (%)
MC	1.18655	—	—
SA	1.18493	−162	9.62/2.18
LSM	1.18772	117	3.09/0.57

TABLE 4 | Summary of the results.

Solutions	k_{eff}	Eigenvalue difference/pcm	Pin-power max/RMS error (%)
MOC	0.97948	—	—
SA	0.97914	−34	3.29/0.70
LSM	0.97896	−52	−2.13/0.70

Table 3 represents the reference solutions of Monte Carlo calculation obtained from the benchmark. The "SA" represents that the whole-core SP_3 calculation is carried out with the cross-sections and the PDF generated by the single-assembly calculation. The "LSM" represents the PDF of thermal groups obtained by the predication function and the other parameters are just the same as the "SA." The reference k_{eff} is 1.18655 ± 0.00006 within the confidence interval of 98%.

Takingg into consideration the different neutron behaviors between the internal and peripheral locations of the core, two functions of PDF predication were established for the internal fuel pins and the peripheral fuel or reflector pins, respectively. Numerical results indicate that the application of LSM can accurately predicate the PDF of the thermal group and reduce the error of eigenvalue and pin power effectively. Compared with the "SA" calculation, which causes about −162 pcm error in k_{eff}

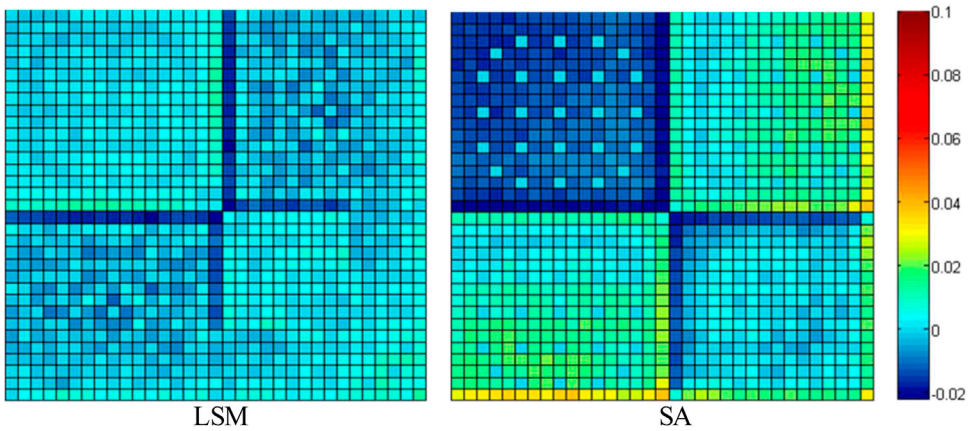

FIGURE 7 | Pin-power relative error distributions.

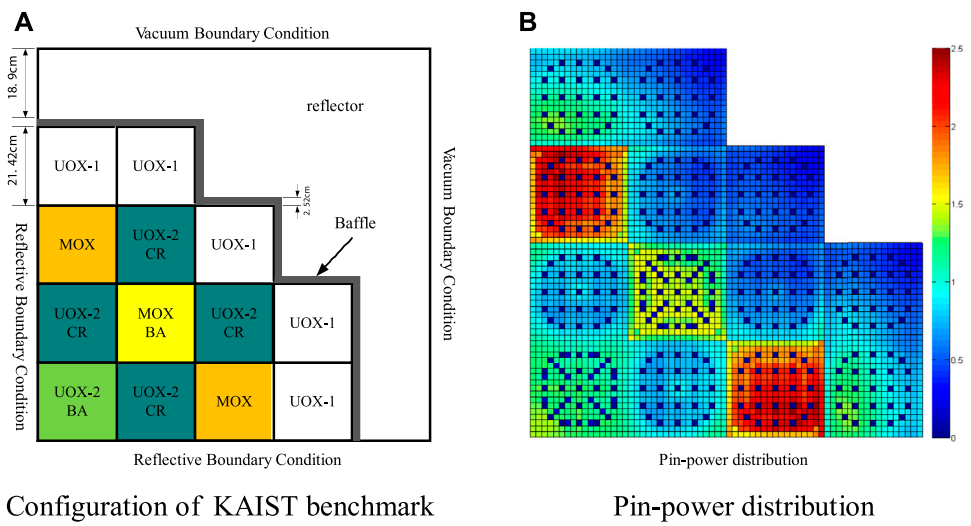

FIGURE 8 | 2D whole-core problem of KAIST benchmark. **(A)** Configuration of KAIST benchmark. **(B)** Pin-power distribution.

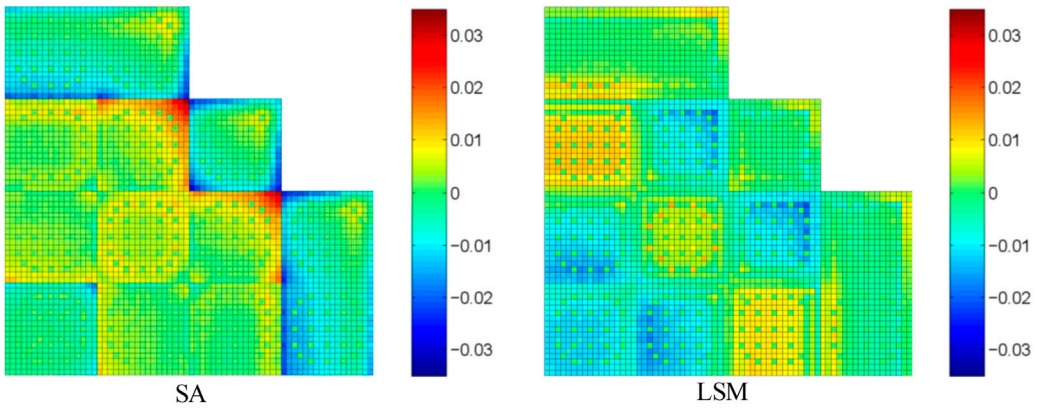

FIGURE 9 | Pin-power relative error distributions.

and 9.62% maximum pin-power error, the "LSM" calculation reduces these errors, respectively, to 117 pcm and 3.09%. The root-mean-square (RMS) pin-power error is also reduced from 2.18 to 0.57%.

The 2D whole-core problem of the KAIST benchmark (Cho, 2000) shown in **Figure 8A** is also carried out to analyze the performance of the method. **Figure 8B** is the pin-power distribution of the reference solution, which comes from the one-step transport calculation. The "SA" and "LSM" have the same meaning as those in the C5G7 benchmark problem. Results are summarized in **Table 4**. The pin-power error distributions are shown in **Figure 9**. It leads to the same conclusion. The function of thermal PDF predication works effectively. It can reduce the error and improve the accuracy of the pin-power distribution, especially for the interface locations between different assemblies.

CONCLUSION

All the pin-cell homogenized parameters are analyzed based on a checkerboard problem. It can be found that the errors of the PDF ratios of the thermal groups are very large, while others are negligible. What is more, the relative importance of the PDF of thermal groups is larger than that of other parameters. Attention would be paid to the correction of the thermal group PDF.

The PDF of the thermal group is functionalized using the least-squares method. The PDF predication function is created with given solutions. It has been proved that the predicated PDF of thermal groups can lead to a more accurate core solution.

Results of the C5G7 and KAIST benchmarks indicate that the PDF predication of the thermal group works effectively in reducing the error of eigenvalue and pin power, especially for the pins located near the interface between different assemblies.

DATA AVAILABILITY STATEMENT

The original contributions presented in the study are included in the article/Supplementary Material; further inquiries can be directed to the corresponding author.

AUTHOR CONTRIBUTIONS

YL contributed significantly to analysis and manuscript preparation; HW helped perform the analysis with constructive discussions.

FUNDING

This research was carried out under financial support by the National Natural Science Foundation of China (No.11775171).

REFERENCES

Smith, M. A., Lewis, L. L., and Na, B-C. (2004). Benchmark on Deterministic 2-D MOX Fuel Assembly Transport Calculations Without Spatial Homogenization. *Progress Nuclear Energy* 45, 107–118. doi:10.1016/j.pnueene.2004.09.003

Chen, Q., Wu, H., and Cao, L. (2008). Auto MOC-A 2D Neutron Transport Code for Arbitrary Geometry Based on the Method of Characteristics and Customization of AutoCAD. *Nucl. Eng. Des.* 238, 2828–2833. doi:10.1016/j.nucengdes.2008.04.014

Cho, N. Z. (2000). *Benchmark Problem in Reactor and Particle Transport Physics*. Daejeon, Korea. Korea Advanced Institute of Science and Technology.

He, L., Wu, H., and Cao, L. (2014). Improvements of the Subgroup Resonance Calculation Code SUGAR. *Ann. Nucl. Energ.* 66, 5–12. doi:10.1016/j.anucene.2013.11.029

Huang, Kai., Wu, H. C., and Cao, L. Z. (2016). Improvements to the Transmutation Trajectory Analysis of Depletion Evaluation. *Ann. Nucl. Energ.* 87, 637–647. doi:10.1016/j.anucene.2015.10.013

Kozlowski, T., Lee, D. J., and Downer, T. (2004). *The Use of an Artificial Neural Network for On-Line Predication of Pin-Cell Discontinuity Factors in PARCS*. Chicago, Illinois, USA: PHYSOR2004.

Kozlowski, T. (2005). *Spatial Homogenization Methods for Pin-By-Pin Neutron Transport Calculations*, PhD Thesis. Westville, USA: Purdue University.

Kozlowski, T. (2004). *The Use of an Artificial Neural Network for On-Line Prediction of Pin-Cell Discontinuity Factors in PARCS*. Chicago, Illinois, USA: PHYSOR2004.

Kozlowski, T., Xu, Y., Downar, T. J., and Lee, D. (2011). Cell Homogenization Method for Pin-By-Pin Neutron Transport Calculations. *Nucl. Sci. Eng.* 169, 1–18. doi:10.13182/nse08-85

Li, Y. Z., Cao, L. Z., and Yuan, X. B. (2014). *High Order Source Approximation for the EFEN Method*. Japan: PHYSOR.

Li, Y., Zhang, B., Wu, H., and Shen, W. (2017). Heterogeneous Neutron-Leakage Model for PWR Pin-By-Pin Calculation. *Ann. Nucl. Energ.* 110, 443–452. doi:10.1016/j.anucene.2017.07.002

Li, Y. Z., Wu, H. C., and Cao, L. Z. (2013). Unstructured Triangular Nodal-SP_3 Method Based on an Exponential Function Expansion. *Nucl. Sci. Eng.* 174 (2), 163–171. doi:10.13182/nse11-111

Li, Y. Z., Zhang, B., and Tian, C. (2015). NECP-CACTI: Pressurized Water Reactor Lattice Code Development. *Tran. Nucl. Soc.* 112, 814–816.

Park, K., and Park, C. (2001). Pin-cell Homogenization via Generalized Equivalence Theory and Embedding Assembly Calculation. *Trans. Am. Nucl. Soc.* 85, 334.

Smith, K. S. (1986). Assembly Homogenization Techniques for Light Water Reactor Analysis. *Prog. Nucl. Energ.* 17, 303–335. doi:10.1016/0149-1970(86)90035-1

Smith, K. (1980). *Spatial Homogenization Methods for Light Water Reactors*, PhD Thesis. MIT.

Sugimura, N., and Ushio, T. (2006). *Calculation Models of AEGIS/SCOPE2, A Core Calculation System of Next Generation*. Vancouver, BC, Canada: PHYSOR2006.

Yamaji, K., Matsumoto, H., and Nakano, M. (2006). *Development of the New Pin-By-Pin Core Calculation Method with Embedded Heterogeneous Assembly Calculation*. Vancouver, BC, Canada: PHYSOR2006.

Yang, W., Zheng, Y. Q., Wu, H. C., Cao, L. Z., and Li, Y. Z. (2014). High-Performance Whole Core Pin-by-Pin Calculation Based on EFEN-SP3 Method. *Nucl. Power Eng.* 35, 164–167. doi:10.13832/j.jnpe.2014.05.0164

Yang, W., Li, Y. Z., and Wu, H. C. (2016). *Multi-group GMRES Algorithm for the Exponential Function Expansion Nodal SP_3 Method*. Idaho, USA: PHYSOR 2016, Sun Valley.

Yu, H., Rehman, H., and Kim, Y. H. (2017). *Artificial Neural Network Modeling for 2-group Pin-wise Group Constants*. San Francisco, CA, USA: ANS Annual Meeting.

Zhang, B., Wu, H., Li, Y., Cao, L., and Shen, W. (2017). Evaluation of Pin-Cell Homogenization Techniques for PWR Pin-By-Pin Calculation. *Nucl. Sci. Eng.* 186 (2), 134–146. doi:10.1080/00295639.2016.1273018

Zhang, S. H., Tang, C. T., and Huang, H. (2008). *Feasibility of Embedding Nodal Homogenization in Next Generation Methods for 3D Pin-By-Pin Core Simulation*. Interlaken, Switzerland: PHYSOR2008.

Conflict of Interest: The authors declare that the research was conducted in the absence of any commercial or financial relationships that could be construed as a potential conflict of interest.

Publisher's Note: All claims expressed in this article are solely those of the authors and do not necessarily represent those of their affiliated organizations, or those of the publisher, the editors and the reviewers. Any product that may be evaluated in this article, or claim that may be made by its manufacturer, is not guaranteed or endorsed by the publisher.

frontiers in Energy Research

ORIGINAL RESEARCH
published: 20 October 2021
doi: 10.3389/fenrg.2021.743642

Generalized Perturbation Theory Based Total Sensitivity and Uncertainty Analysis for High-Fidelity Neutronics Calculation

*Ji Ma, Chen Hao *, Guanghao Liu, Le Kang, Peijun Li and Florencia de los Angeles Renteria del Toro*

Fundamental Science on Nuclear Safety and Simulation Technology Laboratory, Harbin Engineering University, Harbin, China

Neutronics calculation for nuclear reactor with high-fidelity technology can significantly reduce the uncertainties propagated from numerical approximation error and model error. However, the uncertainty of input parameters inevitably exists, especially for nuclear data. On the other hand, resonance self-shielding calculation is essential for multi-group assumption based high-fidelity neutronics calculation, which introduce the implicit effect for calculation responses. In order to fully consider the implicit effects in the process of uncertainty quantification, a generalized perturbation theory (GPT) based implicit sensitivity calculation method is proposed in this paper. Combining the explicit sensitivity coefficient, which can be quantified using classic perturbation theory, the total sensitivity coefficient of calculation responses is obtained. Then the total sensitivity and uncertainty module is established in self-developed neutron transport code with high-fidelity technology-HNET. To verify the accuracy of the sensitivity calculation methods proposed in this paper, a two-dimensional fuel pin problem is chosen to verify the sensitivity results, and the numerical results show good agreement with results calculated by a direct perturbation method. Finally, uncertainty analysis for two-dimensional fuel pin problem is performed and some general conclusions are obtained from the numerical results.

Keywords: generalized perturbation theory, implicit/explicit effect, SU analysis, high-fidelity calculation, sensitivity verification

OPEN ACCESS

Edited by:
Ding She,
Tsinghua University, China

Reviewed by:
Qicang Shen,
University of Michigan, United States
Wenbin Wu,
Nuclear Power Institute of China (NPIC), China
Jiong Guo,
Tsinghua University, China

****Correspondence:***
Chen Hao
haochen.heu@163.com

Specialty section:
This article was submitted to Nuclear Energy, a section of the journal Frontiers in Energy Research

Received: *19 July 2021*
Accepted: *08 September 2021*
Published: *20 October 2021*

Citation:
Ma J, Hao C, Liu G, Kang L, Li P and Renteria del Toro FdlA (2021) Generalized Perturbation Theory Based Total Sensitivity and Uncertainty Analysis for High-Fidelity Neutronics Calculation. Front. Energy Res. 9:743642. doi: 10.3389/fenrg.2021.743642

INTRODUCTION

With the rapid development of high-performance computing power, high-fidelity calculation method has gradually become an essential method to depict neutron physical phenomena, and the calculation results affects the design, construction, and even the economic and safety aspects of the nuclear reactor. Nevertheless, uncertainties inevitably exist in the process of high-fidelity neutron physics calculations. In general, there are three basic uncertainty sources, including modeling error, numerical solution error and input parameter uncertainties (R.N. Bratton, et al., 2014). The first two uncertainty sources can be effectively decreased by using well-established high-fidelity numerical method for neutronics calculation, but the uncertainty of the multi-group cross sections is still significant (M. Pusa, 2012; C. Wan et al., 2017), especially for advanced reactor, e.g., High Temperature Gas-cooled Reactor (D. She et al., 2021). Meanwhile, the traditional conservative assumptions and large safety margins do not meet research requirements and Best-Estimation Plus Uncertainty (BEPU), which is proposed by IAEA, has now become the mainstream scheme for safety

analysis for nuclear power plant (IAEA, 2008). Therefore, the method used to propagate and quantify uncertainty needs to be taken into full consideration when BEPU is regarded as the evaluation criteria.

The basic uncertainty quantification method includes statistical sampling method and deterministic method. The deterministic method, also known as perturbation theory-based method, requires the sensitivity vectors of calculation responses with respect to nuclear cross sections, and finally the uncertainty can be quantified by using "Sandwich Formula", which is more suitable for high-fidelity neutron physics calculation due to its high efficiency in analyzing neutron reaction cross sections for all nuclides of the system. Forward and adjoint calculation for neutron transport equation based on the multi-group approximation for nuclear cross section library need to be solved firstly in order to obtain the sensitivity coefficient vectors. However, the neutron reaction cross section has significant resonance self-shielding phenomenon in the intermediate energy segment for some nuclides, and this phenomenon has a non-negligible impact on the numerical solutions in light water reactor (LWR). Therefore, the resonance self-shielding calculation needs to be firstly performed to obtain the effective resonance cross-section. Based on the idea of uncertainty propagation method, the uncertainty of the multi-group cross sections will be firstly propagated to the effective resonance cross section through the resonance self-shielding calculation. In order to ensure the reasonable propagation of the uncertainty, the uncertainty of effective resonance cross section needs to be quantified reasonably. At the same time, for the purpose of accurately describing the influence of the multi-group microscopic nuclear cross sections on system responses, sensitivity analysis of effective resonance cross-section with respect to the multi-group cross section must be quantified, in other words, the implicit sensitivity must be taken into consideration.

The uncertainty analysis based on the sensitivity coefficient vectors were firstly applied to the fast reactor analysis, in which the implicit impact has negligible influence on the uncertainty results, and the explicit sensitivity analysis scheme is proposed and established in this research (C.R. Weisbin, et al., 1976). Based on this scheme, explicit sensitivity analysis for LWR with high-fidelity deterministic transport simulation can be performed (Q. Wu, et al., 2018; J. Ma, et al., 2020). However, many sensitivity and uncertainty research neglect the influence of performing implicit sensitivity, from the research of (E. Greenspan, et al., 1978) and (M. L. Williams, et al., 2001), it is concluded that the implicit part had a similar influence compared with the explicit part to the total sensitivity results and in some problems, the implicit part had a magnitude that was more that 40% of the explicit part. In this case, the research of total sensitivity and uncertainty analysis has been performed by Y. Liu, et al. (2015), B. Foad, and Takeda (2015), M. Dion and Marleau (2013) and C. M. Perfetti and Rearden (2013). The results also indicated that for LWR problems, the implicit part cause significant effect, and the total sensitivity and analysis scheme should be established for LWR to provide convincing sensitivity and uncertainty analysis results for the calculated responses with respect to the multi-group microscopic cross sections. However, the analysis scheme is still not adequate enough because the above research introduced some assumptions. In this paper, total sensitivity including implicit and explicit sensitivity is studied based on the generalized perturbation theory, in which subgroup calculation method is applied when performing resonance calculation. Using the verified sensitivity analysis results, the total uncertainty analysis scheme is finally established for LWR problem.

In the following sections, the theory background of total sensitivity coefficient calculation method, classical perturbation theory based explicit sensitivity analysis, generalized perturbation theory based implicit sensitivity analysis, uncertainty analysis with Sandwich Rule is firstly present. Then the implementation of total sensitivity and uncertainty analysis scheme used in this research is descripted in detail. For the purpose of verifying the accuracy of sensitivity results, the direct perturbation (DP) sensitivity analysis is performed for VERA two-dimensional fuel pin problem. Finally, the total SU analysis of the VERA single cell problem is performed and total SU results are obtained.

THEORIES

Method of Quantifying the Total Sensitivity Coefficient

The sensitivity coefficient for k_{eff} with respect to multi-group microscopic cross section $\sigma^i_{x,g}$ can be expressed as:

$$S_{k_{eff},\sigma^i_{x,g}} = \frac{\sigma^i_{x,g}}{k_{eff}} \frac{dk_{eff}}{d\sigma^i_{x,g}} \tag{1}$$

x is reaction type identifier, i is nuclide identifier and g is energy group identifier. Considering that the effective resonance cross section of reaction y nuclide j in group h can be perturbated by$\sigma^i_{x,g}$, using the chain rule and **Eq. 1** can be then written as (B.T. Rearten and Jessee, 2016):

$$\begin{aligned} S^{tot}_{k_{eff},\sigma^i_{x,g}} &= \frac{\sigma^i_{x,g}}{k_{eff}} \frac{dk_{eff}}{d\sigma^i_{x,g}} = \frac{\sigma^i_{x,g}}{k_{eff}} \frac{\partial k_{eff}}{\partial \sigma^i_{x,g}} + \sum_j \frac{\sigma^j_{y,h}}{k_{eff}} \frac{\partial k_{eff}}{\partial \sigma^j_{y,h}} \times \frac{\sigma^i_{x,g}}{\sigma^j_{y,h}} \frac{\partial \sigma^j_{y,h}}{\partial \sigma^i_{x,g}} \\ &= S^{\exp}_{k_{eff},\sigma^i_{x,g}} + \sum_j S^{\exp}_{k_{eff},\sigma^j_{y,h}} S^{imp}_{\sigma^j_{y,h},\sigma^i_{x,g}} \end{aligned} \tag{2}$$

It can be found that the total sensitivity coefficient for k_{eff} with respect to multi-group cross section$\sigma^i_{x,g}$ consists of two parts: $S^{imp}_{\sigma^j_{y,h},\sigma^i_{x,g}}$ is the implicit sensitivity coefficient for effective resonance cross section $\sigma^j_{y,h}$with respect to multi-group cross section $\sigma^i_{x,g}$; $S^{\exp}_{k_{eff},\sigma^i_{x,g}}$ and $S^{\exp}_{k_{eff},\sigma^j_{y,h}}$ are both explicit sensitivity coefficients which represents the impact of cross sections on the responses directly through neutron transport equation. The methods for quantifying the implicit and explicit sensitivity are given below.

It needs to be emphasized that according to the division pattern for resonance nuclides and resonance energy group, total sensitivity analysis can be divided into three conditions:

1) For multi-group cross sections of non-resonance nuclides in resonance energy group, both implicit and explicit effect need to be taken into consideration;
2) For multi-group cross sections of resonance nuclides in resonance energy group, only the implicit effect needs to be considered;
3) For multi-group cross sections of both resonance and non-resonance nuclides in non-resonance energy group, only the explicit effect needs to be taken into consideration.

Method of Quantifying the Explicit Sensitivity

The classical perturbation theory can be used to quantify the sensitivity coefficients of k_{eff} to the effective resonance cross sections of different reaction type of different nuclides. In nuclear reactor physics system, the forward and adjoint neutron transport equations can be written as the operator forms,

$$(A-\lambda B)\Psi = 0 \tag{3a}$$

$$\left(A^{*}-\lambda^{*}B^{*}\right)\Psi^{*} = 0 \tag{3b}$$

A represents neutron leakage, absorption and scattering term, Brepresents the fission source term, $\Psi$is the forward neutron angular flux. $A^{*}$and$B^{*}$are the adjoint form of operators A and$B$. Ψ^{*}represents the adjoint neutron angular flux. λ and $\lambda^{*}$are the eigenvalue of forward and adjoint neutron transport equations, respectively. According to the mathematical derivation, the explicit sensitivity coefficient of k_{eff} due to the perturbation of effective resonance cross sections σcan be eventually expressed as (J. Ma et al., 2020),

$$S_{k_{eff},\sigma} = -\sigma\left\langle \Psi^{*}\left(\frac{\partial A}{\sigma}-\frac{1}{k_{eff}}\frac{\partial B}{\sigma}\right)\Psi\right\rangle \Big/ \left\langle \Psi^{*}\frac{1}{k_{eff}}B\Psi\right\rangle \tag{4}$$

Based on **Eq. 4**, the sensitivity coefficient of k_{eff} with respect to the effective resonance cross sections can be quantified, and only once forward transport calculation and adjoint calculation is required. **Equation 4** indicates that the denominator is the function of forward flux, adjoint flux, eigenvalue and the fission source operator, whereas numerator would vary with targeted reaction type. The denominator and the derivation term in numerator could be obtained based on the discrete form of neutron transport equation according to our previous research (J. Ma et al., 2020), and the exact form of explicit sensitivity coefficients won't be given in this paper.

Method of Quantifying the Implicit Sensitivity

As introduced in *Method of Quantifying the Total Sensitivity Coefficient*, the key issue in the study of implicit sensitivity is to study the effect of multi-group microscopic cross section on the effective resonance cross section. Generally, the effective resonance cross section in group g can be written as:

$$\sigma_{x,g} = \int_{g}\sigma_{x}(E)\phi(E)dE \Big/ \int_{g}\phi(E)dE \tag{5}$$

$\phi(E)$ is the neutron flux in group g; $\sigma_{x}(E)$ is fine-group cross section in group g。 According to the definition of sensitivity coefficient, the relative sensitivity of $\sigma_{x,g}$ with respect to multi-group microscopic cross section $\alpha_{g}$is：

$$\begin{aligned} S_{\sigma_{x,g},\alpha_{g}} &= \frac{d\sigma_{x,g}/\sigma_{x,g}}{d\alpha_{g}/\alpha_{g}} \\ &= \alpha_{g}\left\{\frac{\int_{g}\phi(E)\frac{\partial\sigma_{x}(E)}{\partial\alpha_{g}}dE}{\int_{g}\phi(E)\sigma_{x}(E)dE}+\frac{\int_{g}\sigma_{x}(E)\frac{\partial\phi(E)}{\partial\alpha_{g}}dE}{\int_{g}\phi(E)\sigma_{x}(E)dE}-\frac{\int_{g}\frac{\partial\phi(E)}{\partial\alpha_{g}}dE}{\int_{g}\phi(E)dE}\right\} \\ &= \underbrace{\alpha_{g}\frac{\int_{g}\phi(E)\frac{\partial\sigma_{x}(E)}{\partial\alpha_{g}}dE}{\int_{g}\phi(E)\sigma_{x}(E)dE}}_{S^{dir}} + \underbrace{\alpha_{g}\int_{g}\left(\frac{\sigma_{x}(E)}{\int_{g}\phi(E)\sigma_{x}(E)dE}-\frac{1}{\int_{g}\phi(E)dE}\right)\frac{\partial\phi(E)}{\partial\alpha_{g}}dE}_{S^{indir}} \end{aligned} \tag{6}$$

It can be found that **Eq. 6** can be divided into two parts: the first part is the direct part, it represent the change of effective resonance cross section $\sigma_{x}(E)$ caused directly by the perturbation of multi group cross section α_{g}; the second part is the indirect part, it represent multi group cross section α_{g}firstly influence the neutron flux $\phi(E)$, and further influence the effective resonance cross section $\sigma_{x}(E)$.

The neutron flux $\phi(E)$ in **Eq. 5** is the solution of neutron slowing-down equation. The operator form of slowing-down equation can be expressed as：

$$B\phi(E) = Q(E) \tag{7}$$

$B$is the disappearing term, Q is the effective source term. Take the derivative on each term of **Eq. 7** with multi group cross section α:

$$B\frac{\partial\phi(\mathrm{E})}{\partial\alpha} = \frac{\partial Q(E)}{\partial\alpha}-\frac{\partial B}{\partial\alpha}\phi(E) \tag{8}$$

Equation 8 describes the basic relationship between the perturbation of microscopic cross-section α and the weighting function $\phi(E)$. Theoretically, if the variation of the operators Q and$B$are obtained, the derivative term $\partial\phi(E)/\partial\alpha$ can be solved directly based on **Eq. 8**, and the relative sensitivity coefficients of effective resonance cross section $\sigma_{x,g}$with respect to microscopic cross section α can be calculated using **Eq. 6**. In fact, the derivative terms $\partial B/\partial\alpha$ and $\partial Q/\partial\alpha$can be calculated directly utilizing the direct perturbation method. However, the perturbation calculations need to be achieved for different nuclides, energy groups, and reaction types, which will introduce an unacceptable calculated amount and computational complexity in the study of implicit sensitivity analysis.

Fortunately, the indirect part of **Eq. 6** can be determined for multiple perturbations by combining the generalized adjoint equation and the slowing equation instead of explicitly calculating the derivative term $\partial\phi(E)/\partial\alpha$. Based on the generalized perturbation theory, introducing a generalized adjoint function $\Gamma^{*}_{x,g}(E)$ for reaction type x and energy group g, which represents the value of weighted function $\phi(E)$ to the effective resonance section $\sigma_{x,g}$ rather than the neutron value.

Then the generalized adjoint form of the slowing down equation can be written as:

$$B^{*}\Gamma^{*}_{x,g}(E) = \frac{\sigma_x(E)}{\int_g \phi(E)\sigma_x(E)dE} - \frac{1}{\int_g \phi(E)dE} \tag{9}$$

B^{*} is the adjoint form of operator B.

Multiply both sides of **Eq. 8** by the generalized adjoint function $\Gamma^{*}_{x,g}(E)$, and integrating over group g:

$$\int_g \left(B\frac{\partial\phi(E)}{\partial\alpha}\right)\Gamma^{*}_{x,g}(E)dE = \int_g \left(\frac{\partial Q(E)}{\partial\alpha} - \frac{\partial B}{\partial\alpha}\phi(E)\right)\Gamma^{*}_{x,g}(E)dE \tag{10}$$

According to the characteristics of the adjoint operator, the left term of **Eq. 10** can be written as:

$$\int_g \left(B\frac{\partial\phi(E)}{\partial\alpha}\right)\Gamma^{*}_{x,g}(E)dE = \int_g \left(\frac{\partial\phi(E)}{\partial\alpha}\right)B^{*}\Gamma^{*}_{x,g}(E)dE \tag{11}$$

Substituting **Eqs. 9–11** into **Eq. 6**, the relative sensitivity coefficient of effective resonance cross section with respect to a certain type microscopic cross section can be calculated by:

$$S_{\sigma_{x,g},\alpha_g} = \underbrace{\alpha_g \frac{\int_g \frac{\partial\sigma_x(E)}{\partial\alpha_g}\phi(E)dE}{\int_g \sigma_x(E)\phi(E)dE}}_{S^{dir}} + \underbrace{\alpha_g \int_g \Gamma^{*}_{x,g}(E)\left(\frac{\partial Q(E)}{\partial\alpha_g} - \frac{\partial B}{\partial\alpha_g}\phi(E)\right)dE}_{S^{indir}} \tag{12}$$

Subgroup method is using to perform resonance self-shielding calculation in HNET. Before performing the implicit sensitivity analysis, it is necessary to briefly introduce the subgroup resonance calculation method. Differ from the traditional resonance calculation method, which subdivides the energy group depending on the value of neutron energy, subgroups are defining according to the cross section itself which drastic changes. S o a few subgroups can contain the resonance energy interval. The neutron flux varies weakly due to the smooth value of cross section in one subgroup, which leads to a high efficiency resonance computation compared with the traditional resonance self-shielding calculation method, and subgroup method currently became one of the most widely used resonance calculation method.

According to the subgroup method, the cross section in the resonance energy group is divided into several intervals within one cross section range, and each interval is a so-called subgroup. Each subgroup corresponds to several discrete energy segments, the energy segment set is expressed as:

$$\Delta E_{g,i} \in \left\{E | \sigma_{g,i} < \sigma \le \sigma_{g,i+1}\right\} \tag{13}$$

Subgroup cross section and subgroup probability, which are called subgroup parameters, are used to describes the properties of subgroup, and can be expressed as:

$$\sigma_{x,g,i} = \frac{\int_{\Delta E_{g,i}} \sigma_x(E)\phi(E)\mathrm{d}E}{\int_{\Delta E_{g,i}} \phi(E)\mathrm{d}E} \tag{13a}$$

$$p_{g,i} = \frac{\Delta E_{g,i}}{\Delta E_g} \tag{13b}$$

After obtaining the subgroup parameters, the subgroup flux density can be obtained by solving the subgroup transport equation, then the subgroup flux is used as weight function to obtain the effective resonance self-shielding cross section. For energy group g, the transport equation of subgroup i is:

$$\mathbf{\Omega}\cdot\nabla\phi_{g,i} + \Sigma_{t,g,i}\phi_{g,i} = Q_{g,i} \tag{13a}$$

$$Q_{g,i} = p_{g,i}\Sigma_p \tag{13b}$$

$Q_{g,i}$is source term in subgroup i, Σ_p is potential cross section, $\Sigma_{t,g,i}$ is the total cross section in subgroup i. The operator form of slowing-down equation in subgroup i can be expressed as :

$$B_{g,i}\phi_{g,i} = Q_{g.i} \tag{14}$$

The flux density of subgroup i can be obtained by solving **Eq. 14**, then the effective resonance self-shielding cross section can be calculated by:

$$\sigma_{x,g} = \sum_{i=1}^{I} \sigma_{x,g,i}\phi_{g,i} \Big/ \sum_{i=1}^{I} \phi_{g,i} \tag{15}$$

Based on the generalized perturbation theory, the generalized adjoint subgroup transport equation needs to be established firstly in order to obtain the relative sensitivity coefficient of the effective resonance self-shielding cross section with respect to the multi-group cross section, the subgroup generalized adjoint transport equation can be written as:

$$-\mathbf{\Omega}\nabla\Gamma^{*}_{g,i} + \Sigma_{t,g,i}\Gamma^{*}_{g,i} = Q^{*}_{g,i} \tag{16}$$

The Operator Form Is

$$B^{*}_{g,i}\Gamma^{*}_{g,i} = Q^{*}_{g.i} \tag{17}$$

B^{*}_{g} is subgroup adjoint transport term, Γ^{*}_{g} is the generalized subgroup adjoint neutron flux, $Q^{*}_{g}$is the generalized adjoint source, which is defined by :

$$Q^{*}_{g,i} = \frac{\sigma_{x,g,i}}{\sum_{i=1}^{N}\int_V\int_\Omega \phi_{g,i}\sigma_{x,g,i}dVd\Omega} - \frac{1}{\sum_{i=1}^{N}\int_V\int_\Omega \phi_{g,i}dVd\Omega} \tag{18}$$

Once obtaining the specific form of the generalized adjoint source term, it then can be used as the external source term of the generalized adjoint equation solver in HNET in order to obtain the generalized adjoint function $\Gamma^{*}_{x,g}$.

Finally, considering the exact form of $\sigma_x(E)$ and $\Gamma^{*}_{x,g}$ when subgroup method is used to apply the subgroup method and combining **Eq. 18**, the relative sensitivity coefficient of the effective resonance self-shielding cross section with respect to the multi-group microscopic cross section can be calculated by:

$$S_{\sigma^j_{x,g},\alpha^k_{y,g'}} = \alpha^k_{y,g'} \sum_{i=1}^{I} \left(\frac{\int_\Omega \frac{\partial \sigma^j_{x,g,i}}{\partial \alpha^k_{y,g'}} \phi_{g,i} d\Omega}{\int_\Omega \sigma^j_{x,g,i} \phi_{g,i} d\Omega} \right) + \alpha^k_{y,g'} \sum_{i=1}^{I} \sum_{Z} V_Z \int_\Omega \Gamma^*_{x,g,i} \left(\frac{\partial Q_{g,i}}{\partial \alpha^k_{y,g'}} - \frac{\partial L_{g,i}}{\partial \alpha^k_{y,g'}} \phi_{g,i} \right) d\Omega \tag{19}$$

Method of Quantifying the Uncertainty

After obtaining the sensitivity vectors, the relative uncertainty can be then calculated using "Sandwich Formula". In the following part, the derivation of Sandwich Formula will be introduced briefly.

The nuclear reactor physics system k_{eff} can be written as the function of a series of multi-group microscopic cross sections, which is shown in **Eq. 20**.

$$k_{eff} = R(\sigma_1, \sigma_2, \ldots\ldots \sigma_n) \tag{20}$$

σrepresents the multi-group microscopic cross section for a nuclide reaction type, and$\bar{k}$, $\bar{\sigma}$represent the expected value. Using the first order linearity approximation, the Taylor expansion form of **Eq. 20** can be rewritten as,

$$k_{eff} = \bar{k}_{eff} + \delta k_{eff} = R(\bar{\sigma}_1, \bar{\sigma}_2, \cdots \bar{\sigma}_n) + \sum_i^n \frac{\partial k_{eff}}{\partial \sigma_i} \delta \sigma_i \tag{21}$$

Presumptively, the input parameters in reactor system satisfy the$p(\sigma_1, \sigma_2, \cdots, \sigma_n)$, which is a joint probability density function, the variance of k_{eff} can be calculated using the following form,

$$var\left(k_{eff}\right) = \int \left(\sum_{i=1}^{n} \left(\frac{\partial k_{eff}}{\partial \sigma_i} \right) \delta \sigma_i \right)^2 p(\sigma_1, \sigma_2, \cdots, \sigma_n) d\sigma_1 d\sigma_2 \cdots d\sigma_n = \sum_{i=1}^{n} \left(\frac{\partial k_{eff}}{\partial \sigma_i} \right)^2 D_{\sigma_i} + 2 \sum_{i \neq j=1}^{n} \frac{\partial k_{eff}}{\partial \sigma_i} \frac{\partial k_{eff}}{\partial \sigma_j} \Sigma_{\sigma_i \sigma_j} \tag{22}$$

$k\Sigma$ is the covariance of two parameters, $D$is the variance of a specific parameter. Then the relative variance of k_{eff}, i.e. the square of the k_{eff} relative uncertainty, due to multi-group microscopic cross sections can be written as

$$\frac{var\left(k_{eff}\right)}{k^2_{eff}} = \sum_{i=1}^{n} \left(\frac{\sigma_i}{k_{eff}} \frac{\partial k_{eff}}{\partial \sigma_i} \right)^2 \frac{D_{\sigma_i}}{\sigma_i^2} + 2 \sum_{i \neq j=1}^{n} \left(\frac{\sigma_i}{k_{eff}} \frac{\partial k_{eff}}{\partial \sigma_i} \right) \left(\frac{\sigma_j}{k_{eff}} \frac{\partial k_{eff}}{\partial \sigma_j} \right) \frac{\Sigma_{\sigma_i \sigma_j}}{\sigma_i \sigma_j} = \sum_{i=1}^{n} \left(S_{k_{eff},\sigma_i} \right)^2 D^{relative}_{\sigma_i} + 2 \sum_{i \neq j=1}^{n} S_{k_{eff},\sigma_i} S_{k_{eff},\sigma_j} \Sigma^{relative}_{\sigma_i \sigma_j} \tag{23}$$

Considering the definition of sensitivity coefficient, the matrix form of relative uncertainty of k_{eff} can be rewritten as,

$$\frac{var\left(k_{eff}\right)}{k^2_{eff}} = S_{k_{eff},\sigma} \Sigma^{relative} \left(S_{k_{eff},\sigma} \right)^T \tag{24}$$

Equation 24 is the so-called "Sandwich Rule". Once obtaining the sensitivity vectors for k_{eff} with respect to multi-group microscopic cross sections and the relative covariance matrix, **Eq. 24** can be used to quantify the relative uncertainty of nuclear reactor physics system k_{eff}.

IMPLEMENTATION

Implementation Flow

In this section, the total sensitivity and uncertainty analysis scheme with the calculation flow is established, and the details will be discussed. **Figure 1** shows the implementation flow of the total sensitivity and uncertainty analysis. The fundamental evaluated nuclear data library is WIMS 69 g library, which is the basic input for the resonance and transport calculations. And the ZZ-SCALE6.0/COV-44G library, which contains the uncertainty and correlation information for multi-group cross sections, is the basic uncertainty source. High-fidelity Neutron Transport program (HNET), which is a self-developed deterministic 3D high-fidelity neutron transport code, is applied to solve the subgroup transport equations, forward neutron transport equations, adjoint neutron transport equations, and the generalized adjoint equation. The effective resonance multi-group cross sections are calculated by using subgroup resonance calculation method. Then a total sensitivity and uncertainty analysis module is developed for quantifying the sensitivity and uncertainty of k_{eff} propagated from the multi-group microscopic nuclear cross sections in HNET. The computational steps of generalized perturbation theory-based total sensitivity and uncertainty (SU) analysis can be summarized as follows:

1) The relative covariance matrix in 69 g energy group structure is generated from the well-developed 44 g energy group relative covariance library by using home-developed covariance matrix generation code T-COCOO.
2) The subgroup resonance calculation is performed to calculate the effective multi-group macro cross sections using 69 g nuclear data library, the subgroup parameters and subgroup neutron flux for establishing generalized adjoint equation can be generated at the same time.
3) Based on the subgroup parameters and subgroup neutron flux obtained in step 2, the generalized adjoint equation can be established, and it can be solved by directly using adjoint neutron transport solver after adding a generalized neutron source in the source term.
4) The k_{eff} implicit sensitivity coefficient can be calculated using the solution in step 3 for all resonance nuclides and resonance energy groups.
5) The forward flux, adjoint flux and the eigenvalue is obtained by solving the forward and adjoint equations, and the k_{eff} explicit sensitivity coefficients for all nuclide is calculated.
6) Total k_{eff} sensitivity coefficients are calculated using both implicit and explicit sensitivity coefficients obtained in step 4 and step 5.
7) Using the total sensitivity obtained in step6 and the relative covariance obtained in step 1, total k_{eff} uncertainty can be quantified using the Sandwich Rule.

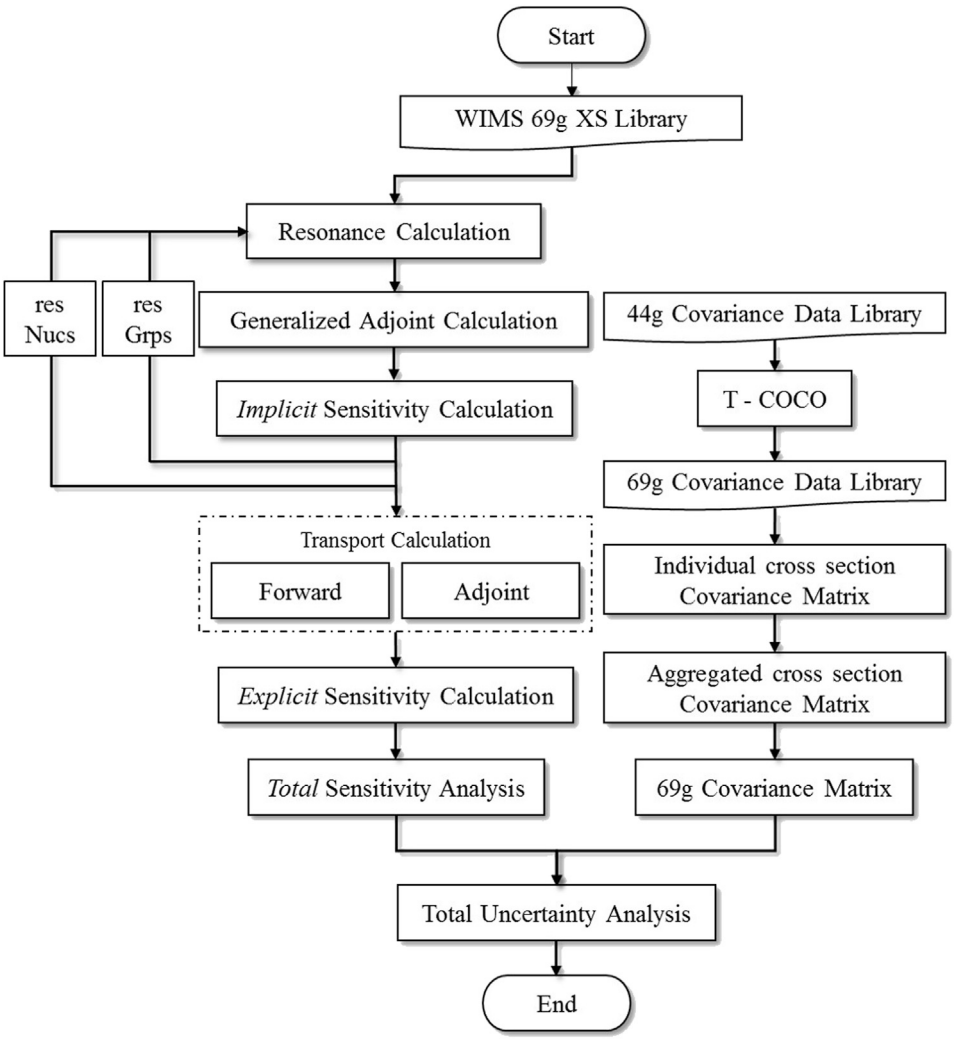

FIGURE 1 | Flowchart of the total sensitivity and uncertainty analysis.

TABLE 1 | Calculation parameters of this problem.

Parameters	Value
Ray spacing	0.01 cm
Polar angle	3
Azimuth angle	8
Flat source region	40

Direct Perturbation Scheme

Sensitivity coefficient calculated using central difference direct perturbation method is considered relatively precise if the linear relation is strong and the perturbation is feasible. In this way, this method is always used to verify the sensitivity coefficient calculated by other methods. For sensitivity coefficient of k_{eff} with respect to certain multi-group microscopic cross section using central difference direct perturbation method, the k_{eff} of the system is computed for three times: firstly, with the unperturbed cross sections$\alpha$and obtains unperturbed k_{eff} ; then with an adequate increased cross sectionα^+ and obtains $k_{eff}^{\alpha^+}$; with the same value decreased input cross section α^- and obtains $k_{eff}^{\alpha^-}$. Finally, DP method-based sensitivity coefficient of k_{eff} with respected to cross section α can be calculated by

$$S_{k_{eff},\alpha} = \frac{\left(k_{eff}^{\alpha^+} - k_{eff}^{\alpha^-}\right)/k_{eff}}{(\alpha^+ - \alpha^-)/\alpha} \tag{25}$$

In this paper, DP method is used to verify the sensitivity coefficient calculated using proposed generalized perturbation theory. Three types of sensitivity coefficient, including implicit, explicit and total sensitivity coefficient are verified, and the calculation methods can be summarized as follows:

1) Total sensitivity coefficients: Complete calculation including resonance self-shielding calculation and neutron transport calculation need to be performed for three times, with

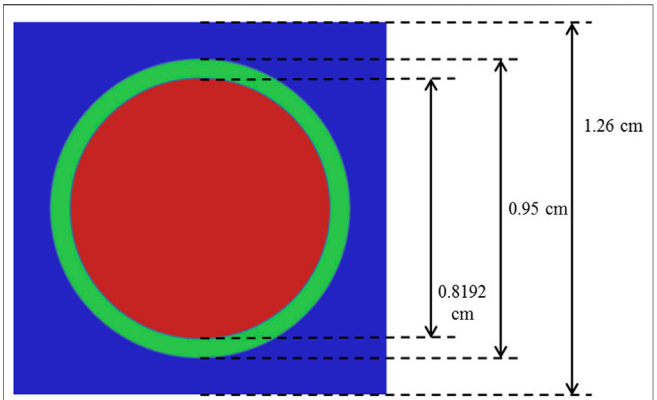

FIGURE 2 | Radial geometry for pin cell problem.

unperturbed, positive perturbed and negative perturbed multi-group cross sections respectively.

2) Explicit sensitivity coefficients: Only the neutron transport calculation needs to be performed for three times, with unperturbed, positive perturbed and negative perturbed effective resonance self-shielding cross sections respectively.
3) Implicit sensitivity coefficients: Firstly, resonance self-shielding calculation needs to be performed for three times, with unperturbed, positive perturbed and negative perturbed multi-group cross sections respectively. Secondly, the neutron transport calculation needs to be performed for three times, with unperturbed, positive perturbed and negative perturbed effective resonance self-shielding cross sections respectively.

Calculation Model and Uncertainty Sources

A two-dimensional fuel pin cell problem was chosen for the purpose of verifying the sensitivity coefficient calculated by using generalized perturbation theory proposed in this paper and perform total sensitivity and uncertainty analysis. More detail descriptions of this problem can be found in (A.T. Godfrey, 2013). The main calculation parameters of this problem is summarized in **Table 1**. The geometry information and computing mesh are illustrated in **Figure 2**. Meanwhile, the WIMS 69 energy group nuclear data library is used to perform subgroup resonance calculation, adjoint and transport calculations.

The sensitivity vectors are calculated using the WIMS 69-group structure nuclear data library, which is different from the 44 g group structure relative covariance library, so the problem-related 69 g relative covariance library needs to be firstly constructed from the well-evaluated 44 g group structure using a former proposed covariance matrix transforming method (D. Wang, et al., 2016). The comparison of relative covariance matrix of two typical nuclide neutron reaction cross section, including ^{235}U 5) and ^{238}U (n, γ) in 44 g group structure and 69 g group structure are shown in **Figures 3**, **4** respectively.

NUMERICAL RESULTS

Sensitivity Coefficient Verification

The 2D pin cell problem is firstly used to verify the implicit sensitivity coefficients calculated based on the proposed generalized perturbation theory method. According to the linear relationship test, 2% relative perturbation factor is in the region with strongest linear relationship, so a 2% relative perturbation of multigroup cross sections is used in the DP method for sensitivity verification. The comparisons of implicit sensitivity coefficients, which is divided into resonance nuclides and non-resonance nuclides, calculated by using the DP and GPT methods for some typical nuclides are illustrated in **Figures 5**, **6**, respectively.

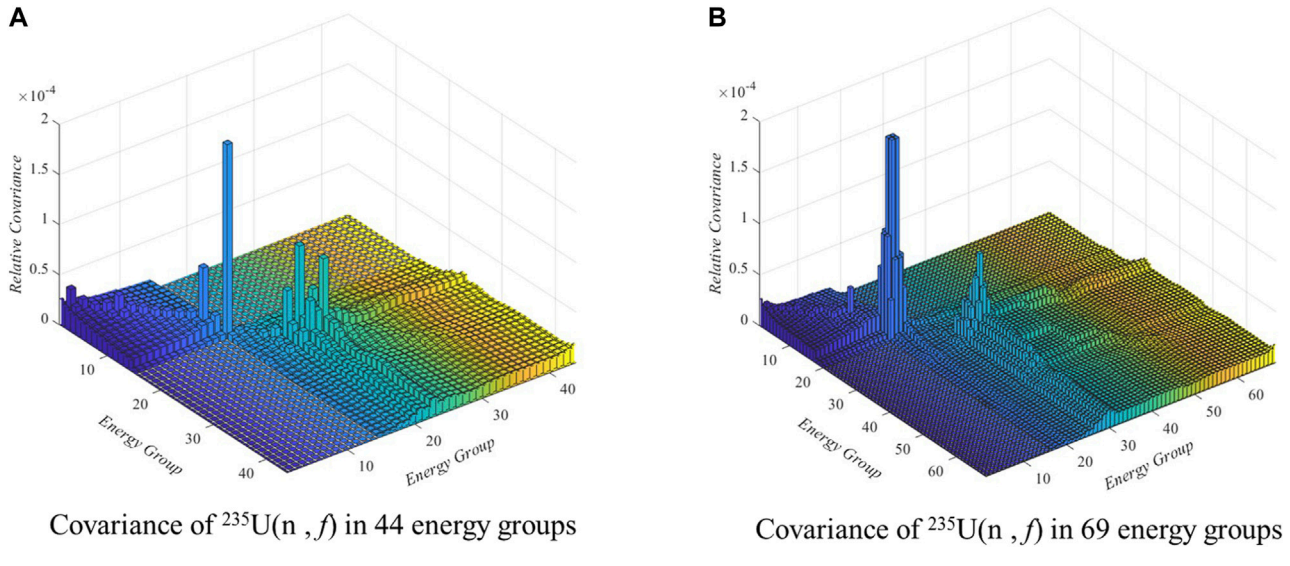

FIGURE 3 | Comparison of relative covariance matrix for ^{235}U (n, f).

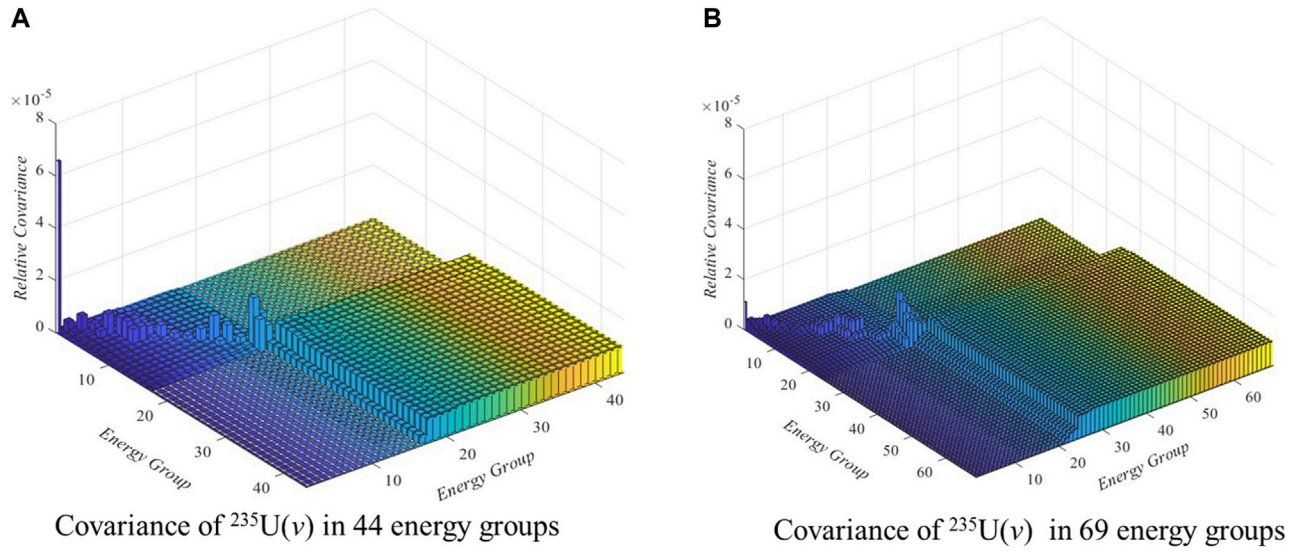

FIGURE 4 | Comparison of relative covariance matrix for ^{235}U (ν).

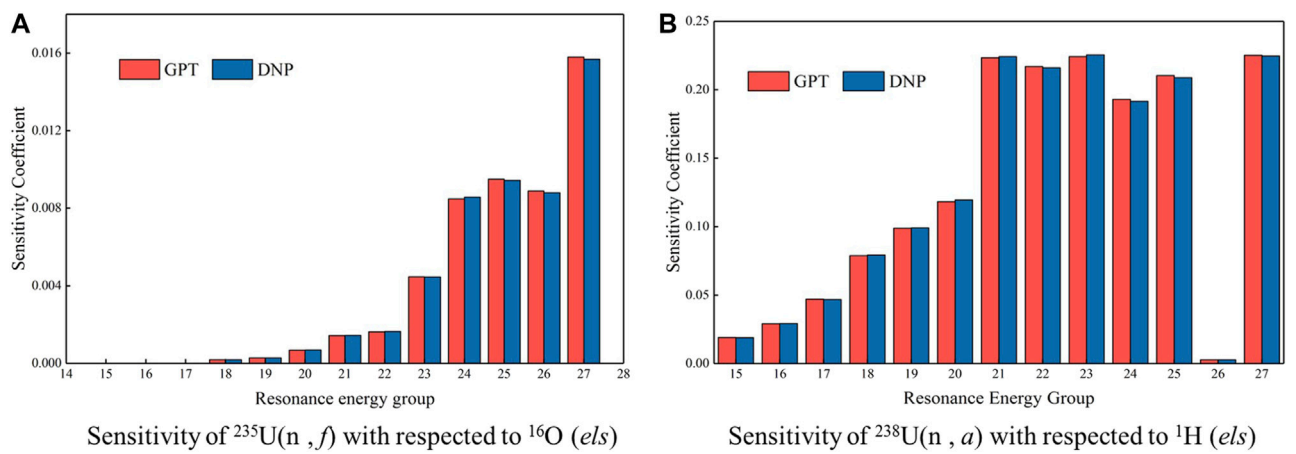

FIGURE 5 | Comparisons of implicit sensitivity coefficients for non-resonance nuclides.

Figures 5, **6** suggest that the implicit sensitivity coefficients for both resonance and non-resonance nuclides calculated by GPT and DP methods agree well for selected reaction types in all resonance energy groups. Most relative error in these energy groups is less than 1%, but in group 22, the relative error of implicit sensitivity coefficients of absorption cross section of ^{235}U with respect to radiative capture cross section of ^{235}U is 1.89%, which is a little large, but it is still acceptable. These comparisons indicate that acceptable accuracy of implicit sensitivity analysis is achievable by using generalized perturbation theory proposed in this paper.

It is worth noted that the ability of calculation for explicit sensitivity coefficient is verified in our precious work (J. Ma et al., 2020) and verification will not be performed in this paper. For the verification of total sensitivity, the integral sensitivity coefficients (integrating with volume and energy) of selected cross sections of representative isotopes and reaction types in resonance energy groups are summarized in **Table 2** for comparison. The comparison results also demonstrate that accurate total sensitivity coefficient can be obtained, and the total sensitivity and uncertainty can be then performed.

Total Sensitivity Analysis

Before performing the total sensitivity analysis, it is worth investigate that the relative importance of implicit sensitivity compared with the explicit part. **Figure 7** illustrates the implicit sensitivity, explicit sensitivity and total sensitivity of k_{eff} with respect to elastic scattering cross section of ^{1}H. According to **Figure 7**, in most energy group, the explicit sensitivity coefficients group are positive, while the implicit part are negative, thus the total sensitivity is less than explicit part in these energy groups. It suggests that if the

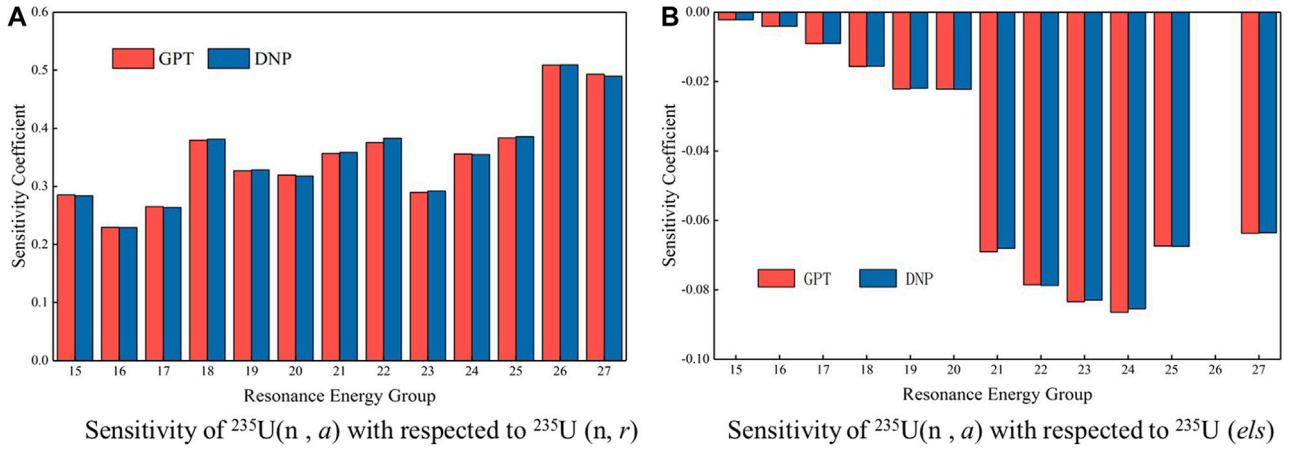

FIGURE 6 | Comparisons of implicit sensitivity coefficients for resonance nuclides.

TABLE 2 | Comparison of total sensitivity coefficients.

Reaction type	DP	PT	Relative error/%
U-238 σ_γ	−1.94818E-01	−1.96250E-01	0.735
U-235 σ_γ	−6.47168E-02	−6.44068E-02	0.479
U-235 σ_f	6.83782E-02	6.77714E-02	0.887
H-1 $_{els}$	1.70653E-01	1.71627E-01	0.571
O-16 $_{els}$	−9.38956E-03	−9.36846E-03	0.225
U-238 $_{els}$	4.08866E-03	4.12844E-03	0.973

implicit sensitivity is neglected, the sensitivity will be overestimated. It leads to a fact that the implicit sensitivity needs to be considered in detail when performing total SU analysis.

Three kinds of sensitivity coefficients, including total, explicit and implicit part of k_{eff} with respect to some representative reaction type cross section of both resonance and non-resonance nuclides are illustrated in **Table 3**. It also can be found in **Table.3** that the implicit effect has a nonnegligible impact for the sensitivity analysis for LWR, especially for the

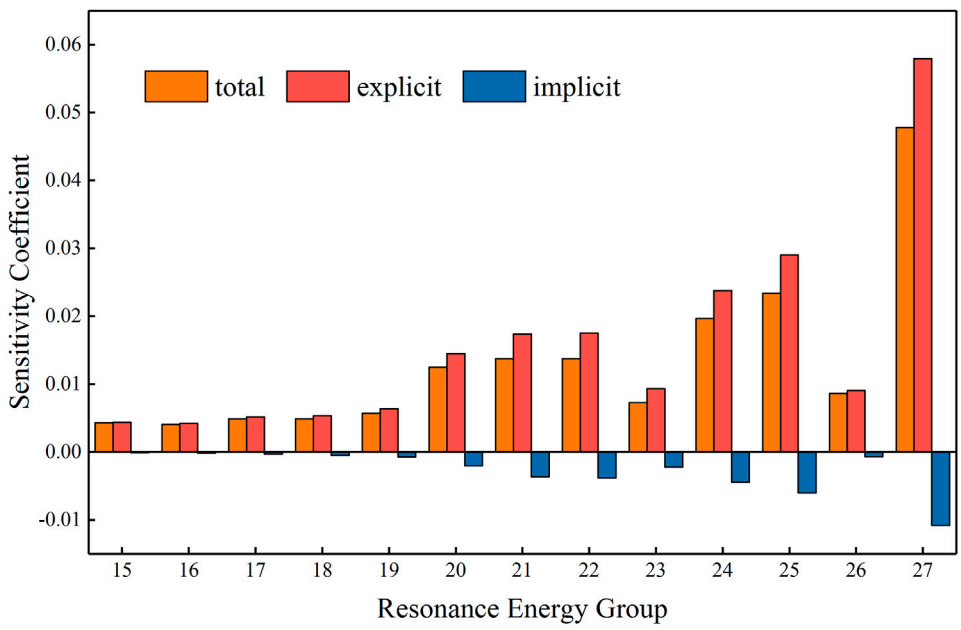

FIGURE 7 | Comparisons of implicit/explicit sensitivity coefficients.

TABLE 3 | Sensitivity coefficients of k_{eff} with respect to some. Representative reaction types of cross section.

Reaction type	Explicit	Implicit	Total
U-238 σ_γ	–3.0248E-01	1.8385E-02	–2.8410E-01
U-235 ν	9.5016E-01	0.0000E-01	9.5016E-01
U-235 σ_γ	–1.1262E-01	-8.9098E-05	–1.1271E-01
U-235 χ	–5.4498E-08	0.0000E-00	–5.4498E-08
U-235 σ_f	3.6389E-01	–1.9480E-04	3.6369E-01
U-238 σ_s	2.5765E-02	2.3585E-02	4.9350E-02
U-238 ν	4.9844E-02	0.0000E-00	4.9844E-02
H-1 σ_s	3.5150E-01	–3.3586E-02	3.1791E-01
U-238 χ	–1.0147E-10	0.0000E-00	–1.0147E-10
H-1 σ_γ	–1.0153E-01	–1.2715E-05	–1.0155E-01
U-238 σ_s	2.5765E-02	2.3585E-02	4.9350E-02
O-16 σ_s	–1.2233E-02	–1.0234E-03	–1.2467E-02

TABLE 4 | Implicit effect on uncertainty contributions.

Nuclide	Reaction pair	Uncertainty contribution to $\sigma k/k$ (%)	
		w	w/o
U-238	σ_γ-σ_γ	3.541E-01	3.578E-01
U-235	σ_γ-σ_γ	1.359E-01	1.414E-01
U-235	σ_f-σ_f	1.158E-01	1.212E-01
U-238	σs-σs	1.001E-01	1.005E-01
H-1	σ_s-σ_s	3.115E-02	3.124E-02
U-238	σ_f-σ_f	2.542E-02	2.697E-02
H-1	σ_γ-σ_γ	2.136E-02	2.087E-02
U-235	σ_s-σ_s	1.637E-03	1.454E-03

TABLE 5 | Total uncertainty contribution.

Nuclides	Reaction types	Total uncertainty contribution to $\sigma k/k$ (%)
U-238	σ_γ-σ_γ	3.541E-01
U-235	ν-ν	2.669E-01
U-235	σ_γ-σ_γ	1.359E-01
U-235	χ-χ	1.334E-01
U-235	σ_f-σ_f	1.158 E -01
U-238	σ_s-σ_s	1.001E-01
U-238	ν-ν	9.407E-02
H-1	σ_s-σ_s	3.115E-02
U-238	σ_f-σ_f	2.542E-02
H-1	σ_γ-σ_γ	2.136E-02
U-238	χ-χ	1.530E-02
O-16	σ_s-σ_s	4.772E-03
U-235	σ_s-σ_s	1.637E-03
Total	-	0.517

sensitivity coefficient for resonance nuclides in resonance energy groups.

Total Uncertainty Analysis

The uncertainty contribution of some important nuclide reaction cross section with and without considering the implicit part is presented in **Table 4**. It can be found in **Table 4** that although the implicit part is essential in sensitivity analysis, it has nonsignificant influences on uncertainty results. The first reason is that compared with the explicit part, the absolute value of implicit part is relatively small; the second reason is that uncertainty is quantified by using Sandwich Formula, the nuclide reaction cross section may have significant influence on eigenvalue, yet it has small uncertainty itself. Although the total uncertainty results barely effected by implicit sensitivity, considering the implicit influence ensure the reasonable propagation for uncertainty of input parameters, the implicit sensitivity needs to be fully investigated when performing total sensitivity and uncertainty analysis.

The total uncertainty contributions of some important reactions to k_{eff}, taken both implicit and explicit influence into consideration, are shown in **Table 5**. The most three significant contributors to the total uncertainty of k_{eff} are σ_γ of ^{238}U, ν of ^{235}U and σ_γ of ^{235}U respectively. This conclusion is similar to the uncertainty contribution results without considering the implicit effect. The total uncertainty contribution due to these representative nuclides reaction types to k_{eff} is 0.517%, compared with the results of 0.522% when implicit part is ignored, it also suggests that the implicit effect has little influence on the uncertainty quantification results.

CONCLUSION

In recent years, sensitivity and uncertainty quantification on nuclear reactor core physics key parameters, especially the simulation results calculated by high-fidelity simulation method, has raised more and more concerns. For LWR problems, total sensitivity analysis needs to be divided into explicit part, which can be calculated using classical perturbation theory, and implicit part, which is not studied widely. However, the implicit part needs to be investigated particularly for SU analysis on LWR problems.

In this paper, a generalized perturbation theory-based method is proposed to quantify the implicit sensitivity coefficient. Combining with the explicit sensitivity coefficient, total sensitivity of reactor core k_{eff} is quantified, and then total uncertainty contribution for typical nuclides and reaction types is calculated using "Sandwich Formula". For the purpose of verifying the accuracy of sensitivity coefficient quantified in this research, a two-dimensional fuel pin cell problem released in VERA core physics benchmark is firstly chosen to perform sensitivity quantification using both GPT method and DP method. The comparison results indicate that implicit sensitivity coefficient calculated in this paper by proposed GPT method has acceptable accuracy. Then the total sensitivity analysis is performed and the results suggest that implicit impact is nonnegligible when perform sensitivity analysis for LWR problems. Finally, total k_{eff} uncertainty of the two-dimensional fuel pin cell problem due to representative nuclides cross sections were quantified. According to the results, total uncertainty of k_{eff} propagated from multi-group cross sections is about 0.517%, and three most significant contributors are capture reaction of ^{238}U, average number of neutrons emitted per fission event of ^{235}U and capture reaction of ^{238}U. The numerical results also suggest

that the implicit part of sensitivity coefficient cannot be ignored, otherwise the reasonable uncertainty propagation cannot be ensured. While the implicit part has an unremarkable influence on the quantified total uncertainty of k_{eff} for the investigated problem.

DATA AVAILABILITY STATEMENT

The original contributions presented in the study are included in the article/Supplementary Material, further inquiries can be directed to the corresponding author.

AUTHOR CONTRIBUTIONS

CH is responsible for the research thought; JM is responsible for the formul derivation and code development; GL, LK, PL and FR help for the verification and a part of calculation.

FUNDING

This work was supported by the National Key R&D Program of China 2018YFE0180900 and the Chinese National Natural Science Foundation Project 12075067.

REFERENCES

Bratton, R. N., Avramova, M., and Ivanov, K. (2014). Oecd/nea Benchmark for Uncertainty Analysis in Modeling (Uam) for Lwrs - Summary and Discussion of Neutronics Cases (Phase I). *Nucl. Eng. Technology* 46 (3), 313–342. doi:10.5516/net.01.2014.710

Dion, M., and Marleau, G. (2013). *Resonance Self-Shielding Effects on Eigenvalue Sensitivity*. Idaho, USA: M&C 2013.

Foad, B., and Takeda, T. (2015). Sensitivity and Uncertainty Analysis for UO 2 and MOX Fueled PWR Cells. *Ann. Nucl. Energ.* 75 (JAN), 595–604. doi:10.1016/j.anucene.2014.08.068

Godfrey, A. T. (2013). *VERA Core Physics Benchmark Progression Problem Specifications, Revision 2. CASL-U-2012-0131-002*. Nashville, TN: Oak Ridge National Laboratory.

Greenspan, E., Karni, Y., and Gilai, D. (1978). *High Order Effects in Cross Section Sensitivity Analysis*. Beersheva (Israel): Negev Univ.

IAEA (2008). *Best Estimate Safety Analysis for Nuclear Power Plants: Uncertainty Evaluation*. in *Safety Reports Series 52*, 1–211.

Liu, Y., Cao, L., Wu, H., Zu, T., and Shen, W. (2015). Eigenvalue Implicit Sensitivity and Uncertainty Analysis with the Subgroup Resonance-Calculation Method. *Ann. Nucl. Energ.* 79, 18–26. doi:10.1016/j.anucene.2015.01.012

Ma, J., Hao, C., Liu, L., and Zhou, Y. (2020). Perturbation Theory-Based Whole-Core Eigenvalue Sensitivity and Uncertainty (SU) Analysis via a 2D/1D Transport Code. *Sci. Technology Nucl. Installations* 2020 (2), 1–13. doi:10.1155/2020/94285802020

Perfetti, C. M., and Rearden, B. T. (2013). "Continuous-energy Eigenvalue Sensitivity Coefficient Calculations in TSUNAMI-3D," in International Conference on Mathematics and Computational Methods Applied to Nuclear Science & Engineering (M&C 2013), Sun Valley, Idaho, USA, May 5-9, 2013 (LaGrange Park, Illinois: American Nuclear Society).

Pusa, M. (2012). Incorporating Sensitivity and Uncertainty Analysis to a Lattice Physics Code with Application to CASMO-4. *Ann. Nucl. Energ.* 40 (1), 153–162. doi:10.1016/j.anucene.2011.10.013

Rearden, B. T., and Jessee, M. A. (2016). *Oak Ridge National Laboratory, Oak Ridge, Tennessee. Available from Radiation Safety Information Computational Center as CCC-834. SCALE Code System, ORNL/TM-2005/39*. Version 6.2.1.

She, D., Xia, D., Guo, J., Wei, C-L., Zhang, J., Li, F., et al. (2021). Prediction calculations for the first criticality of the HTR-PM using the PANGU code. *Nucl. Sci. Tech.* 32, 90, 2021. doi:10.1007/s41365-021-00936-5

Wan, C., Cao, L., Wu, H., and Shen, W. (2017). Total Sensitivity and Uncertainty Analysis for LWR Pin-Cells with Improved UNICORN Code. *Ann. Nucl. Energ.* 99, 301–310. doi:10.1016/j.anucene.2016.09.014

Wang, D., Hao, C., Zhao, Q., and Wu, Z. (2016). Study of the Transform Method of Multi-Group Nuclear Cross Section Covariance Matrix. *Nucl. Power Eng.* 37 (No. 2). doi:10.13832/j.jnpe.2016.02.0001

Weisbin, C. R., Marable, J. H., Lucius, J. L., Peelle, R. W., Mynatt, F. R., Oblow, E. M., et al. (1976). Application of Forss Sensitivity and Uncertainty Methodology to Fast Reactor Benchmark Analysis. *Trans. Am. Nucl. Soc.* 24. doi:10.2172/7337288

Williams, M. L., Broadhead, B. L., and Parks, C. V. (2001). Eigenvalue Sensitivity Theory for Resonance-Shielded Cross Sections. *Nucl. Sci. Eng.* 138 (2), 177–191. doi:10.13182/nse00-56

Wu, Q., Yu, J., Shi, G., Tang, X., Yu, Y., Li, Q., et al. (2018). Eigenvalue Sensitivity and Uncertainty Analysis Based on a 2-D/1-D Whole-Core Transport Code KYADJ. *Ann. Nucl. Energ.* 122, 185–192. doi:10.1016/j.anucene.2018.08.044

Conflict of Interest: The authors declare that the research was conducted in the absence of any commercial or financial relationships that could be construed as a potential conflict of interest.

Publisher's Note: All claims expressed in this article are solely those of the authors and do not necessarily represent those of their affiliated organizations, or those of the publisher, the editors and the reviewers. Any product that may be evaluated in this article, or claim that may be made by its manufacturer, is not guaranteed or endorsed by the publisher.

frontiers in Energy Research

ORIGINAL RESEARCH
published: 19 November 2021
doi: 10.3389/fenrg.2021.764906

Study on Temperature Feedback Effect of Supercritical CO_2–Cooled Reactor

Lianjie Wang, Di Lu, Lei Yao, Hongzhi Xiang and Chen Zhao*

Science and Technology on Reactor System Design Technology Laboratory, Nuclear Power Institute of China, Chengdu, China

As a potential new-type reactor, the supercritical CO_2 (S-CO_2)–cooled reactor has several advantages, such as being a simple system, having high thermal efficiency, having a small size, and being lightweight. Due to the poor neutronics moderation performance, the S-CO_2–cooled reactor shows the disadvantage of a weak temperature feedback effect on reactivity. In this article, the neutronics performance of the reactor has been focused on, and the effects of temperature feedback on fuel, coolant, and moderator studied and the method to improve temperature feedback of the S-CO_2 reactor proposed.

Keywords: supercritical CO_2–cooled reactor, neutronics moderation performance, temperature feedback, solid moderator, potential new-type reactor

OPEN ACCESS

Edited by:
Tengfei Zhang,
Shanghai Jiao Tong University, China

Reviewed by:
Shichang Liu,
North China Electric Power University, China
Xiafeng Zhou,
Huazhong University of Science and Technology, China
Donghao He,
Shanghai Jiao Tong University, China
Zijing Liu,
University of South China, China

****Correspondence:***
Lianjie Wang
mcd2264@126.com

Specialty section:
This article was submitted to Nuclear Energy, a section of the journal Frontiers in Energy Research

Received: *26 August 2021*
Accepted: *25 October 2021*
Published: *19 November 2021*

Citation:
Wang L, Lu D, Yao L, Xiang H and Zhao C (2021) Study on Temperature Feedback Effect of Supercritical CO_2–Cooled Reactor. Front. Energy Res. 9:764906. doi: 10.3389/fenrg.2021.764906

INTRODUCTION

As a supercritical fluid, supercritical CO_2 (S-CO_2) presents a homogeneous fluid state. Moreover, it has special properties, i.e., low viscosity and high density, and is considered to be one of the most promising working mediums for energy transmission and energy conversion (Ahn et al., 2015). The S-CO_2–cooled reactor has the advantages of being a simple system, having high thermal efficiency, having a small size, and being lightweight and has become one of the most promising reactors. The United States (Michael, 2004; Carstens et al., 2006; Michael, 2006; Handwerk et al., 2007), the European Union (Petr and Kolovratnik, 1997), Japan (Kato et al., 2001; Kato et al., 2004; Tsuzuki et al., 2007), and South Korea (Eoh et al., 2008) have carried out research on the application of S-CO_2 to nuclear energy systems.

The reactivity temperature feedback effect is an important factor in maintaining the safety of the reactor (Xie, 1994), and it directly determines the inherent safety of the reactor. Unlike light water coolants or heavy water coolants (Zhang et al., 2019; Zhang et al., 2020), S-CO_2 has weak neutron-moderating performance. This "weak moderating" feature, on the one hand, leads to a weaker reactivity temperature effect of the coolant; when the temperature of the coolant rises, the effect of density variation on the moderating performance is limited, making the core coolant reactivity temperature effect weak and even positive; on the other hand, the harder energy spectrum of the neutrons reduces the fuel Doppler effect and makes the fuel temperature effect weak. When positive reactivity is imported into the reactor abnormally, relying on its own reactivity temperature effect, the core temperature must be increasing greatly to suppress reactivity elevating, which brings great challenge to the high temperature resistance of the fuel cladding and reactor structural materials and has an adverse effect on the safety of the reactor. This defect is more serious in the S-CO_2–cooled reactor.

Based on the "weak moderation" of S-CO_2, this article studies the influence mechanism of core reactivity temperature feedback effect from the aspects of fuel, moderator, and coolant, and then proposes a method to improve the reactivity temperature feedback effect of the S-CO_2–cooled reactor.

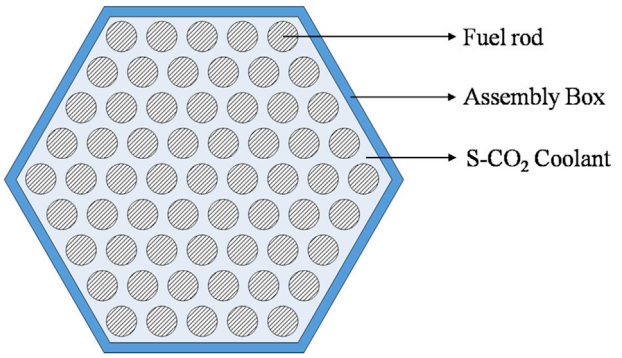

FIGURE 1 | The standard S-CO_2 fuel assembly.

TABLE 1 | Fuel assembly design parameters.

Paramenters	Value	Unit
Fuel rod diameter	8.00	mm
Fuel pitch	9.00	mm
Fuel number in assembly	61	—
^{235}U enrichment	20.00%	—
Center distance	92.00	mm

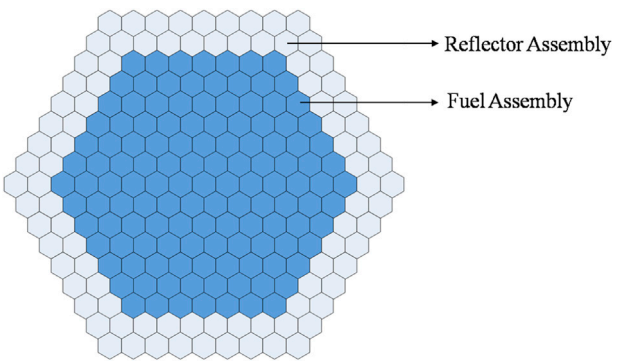

FIGURE 2 | The standard S-CO_2 assembly arrangement scheme.

THE STANDARD S-CO_2 REACTOR CORE DESCRIPTION

The Standard S-CO_2 Fuel Assembly

The standard fuel assembly of the S-CO_2–cooled reactor in this article is shown in **Figure 1**. A dense arrangement of fuels is adopted in assembly, and the fuels are placed in a regular triangular pattern. The assembly design parameters are given in **Table 1**.

The Standard S-CO_2 Assembly Arrangement Scheme

The standard S-CO_2 assembly arrangement scheme is shown in **Figure 2**. The standard S-CO_2–cooled reactor core consists of 127 assemblies, whose center distance is 92.00 mm, and the active core height is 1,000.00 mm. Two layers of stainless steel assemblies are arranged in the radial direction, and a 300.00-mm thick stainless steel layer is arranged in the axial direction.

TABLE 2 | Temperature feedback coefficient of standard design.

Calculation object	Feedback coefficient (pcm/K)
Fuel	−0.51
Coolant	−1.68
Moderator	—
Total	−2.19

Calculation Condition

This study uses the RMC (Reactor Monte Carlo code) for calculation and analysis. In order to calculate the reactivity feedback coefficient caused by the temperature change of each material, the calculated temperature is specified as follows:

Normal state: all the materials at 700 K.

Changed state: the temperature of each material was raised by 200 K. When performing coolant analysis, the coolant density also varies with temperature.

On the one hand, this calculation method can cover the temperature range of the reactor coolant; on the other hand, it can make reactivity change greatly and avoid the influence of program statistical deviation on the analysis result.

The calculation conditions of RMC are set as: 100,000 particles and 500 generations.

Calculation of Temperature Feedback Coefficient

The temperature feedback coefficient is shown in **Table 2**; the fuel temperature feedback coefficient is −0.51 pcm/K, coolant temperature feedback coefficient is −1.68 pcm/K, and total feedback coefficient is −2.19 pcm/K.

STUDY ON FUEL TEMPERATURE FEEDBACK EFFECT

The fuel temperature feedback effect is mainly affected by the Doppler broadening effect of the heavy nucleus. Among them, ^{238}U and ^{240}Pu contribute the most. As the fuel temperature increases, the effective resonance absorption cross section increases, and the reactivity decreases accordingly, so the fuel temperature coefficient is always negative. The main parameters that affect the Doppler broadening effect, including fuel type, fuel enrichment, and neutron energy spectrum, are studied in this article.

Fuel Type

Typical fuel materials are selected for research, including UN, UC, UO_2, and U-10Zr (U-Zr alloy, where the phase volume of Zr is 10%). The results are shown in **Table 3**. It shows that under typical enrichment, the use of UO_2 can obtain the strongest fuel temperature feedback effect, while U-10Zr the weakest one.

TABLE 3 | Fuel temperature feedback coefficient by fuel type.

Typical fuel materials	Feedback coefficient (pcm/K)
UN	−0.51
UC	−0.50
UO_2	−0.72
U-10Zr	−0.22

The feedback effect of different fuel materials is different when the ^{235}U enrichment remains the same. The reason for this phenomenon is that different fuel materials have different neutron energy spectrums due to their different densities and compositions, and then the different neutron energy spectrums and fuel densities lead to different fuel feedback effects. UO_2 has the softest neutron spectrum which gives it the strongest fuel temperature feedback effect.

Fuel Enrichment

Analyzing the influence of ^{235}U enrichment on the fuel temperature feedback effect.UO_2 is used for fuel material and the enrichment of ^{235}U varies within the range of 5–20%. The results are shown in **Figure 3**. With the increasing of ^{235}U enrichment, the fuel temperature feedback effect shows a downward trend.

When the enrichment increases, on the one hand, the content of ^{238}U decreases, and the Doppler broadening effect caused by ^{238}U is weakened, which leads to the weakening of the fuel temperature feedback effect; on the other hand, the content of ^{235}U increases, and the neutron energy spectrum then becomes harder, leading to the further weakening of the fuel temperature feedback effect.

The Neutron Energy Spectrum

Analyzing the influence of the neutron energy spectrum on the fuel temperature feedback effect. UO_2 is used for fuel material and the enrichment of ^{235}U is 15%. As shown in **Figure 4**, in order to achieve the neutron energy spectrum softening, the $ZrH_{1.6}$ rods, which have good moderating performance, replace parts of the fuel rods in the standard assembly. Densities of $ZrH_{1.6}$ are given different values, as shown in **Table 4**, to adjust the degree of neutron moderating, and then achieve different neutron energy spectrums. The calculation results are shown in **Figure 5**. The absolute value of the fuel temperature feedback coefficient presented earlier increases, and later decreases the trend.

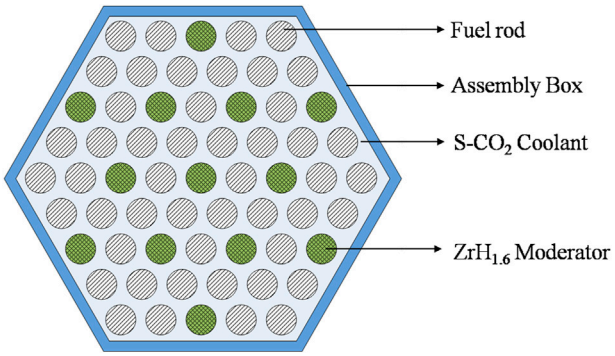

FIGURE 4 | S-CO_2 fuel assembly with $ZrH_{1.6}$ moderator.

The trend shown in **Figure 5** is related to the ^{238}U resonance absorption effect under different neutron energy spectrums. **Figure 6** shows the curve of the neutron flux changing with the $ZrH_{1.6}$ content in the ^{238}U resonance absorption region (**Figure 7**, 0.0l eV–10^4 eV), and it can be seen that the neutron flux in the resonance region shows a trend of first increasing and then decreasing, which is consistent with the trend of the fuel temperature feedback coefficient. The reasons for the above trend are as follows: in the low-density areas of $ZrH_{1.6}$, the neutrons cannot be sufficiently moderated. As the density of $ZrH_{1.6}$ increases, a large number of neutrons are moderated and fall into the resonance absorption region of ^{238}U, where the resonance effect is obvious, then this phenomenon makes the absolute value of the fuel temperature coefficient increase. In the high-density areas of $ZrH_{1.6}$, the neutron cannot be sufficiently moderated, as the density of $ZrH_{1.6}$ increases, lots of neutrons escape from the resonance region as they are further moderated, and then this phenomenon makes the absolute value of the fuel temperature coefficient decrease.

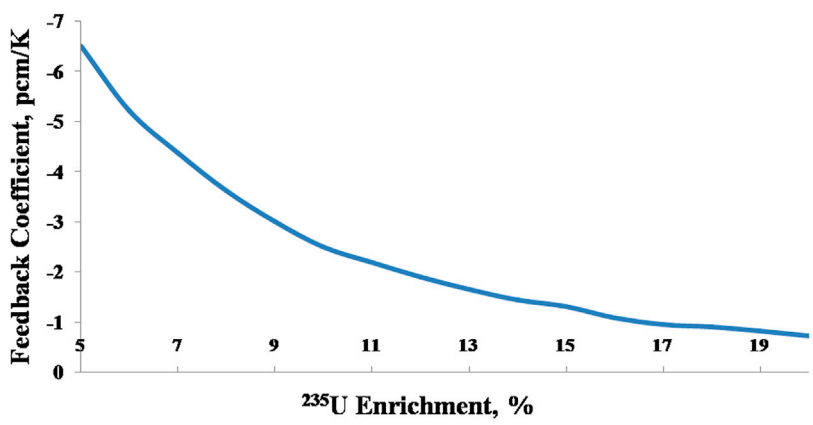

FIGURE 3 | Fuel temperature feedback coefficient variation with ^{235}U enrichment.

TABLE 4 | $ZrH_{1.6}$ density variation.

No	Relative density	Absolute density, g/cm^3
1	2.0	11.280
2	1.8	10.152
3	1.6	9.024
4	1.4	7.896
5	1.2	6.768
6	1.0	5.640
7	0.8	4.512
8	0.6	3.384
9	0.4	2.256
10	0.2	1.128
11	0.01	0.00564

STUDY ON COOLANT TEMPERATURE FEEDBACK EFFECT

When the temperature of the S-CO_2 coolant changes, the density of S-CO_2 changes. Due to the neutron moderation ability of the S-CO_2 being weak, the change in its density hardly affects its moderating performance. The change of S-CO_2 density mainly affects neutron leakage, which mainly affects the reactivity. The main parameters that affect the coolant temperature feedback effect, including coolant volume fraction and neutron energy spectrum, are studied in this article.

Coolant Volume Fraction

The coolant volume fraction in the core is mainly determined by the ratio of pitch to diameter (P/D), and there is a positive correlation between the coolant volume fraction and P/D. Under the premise of keeping the pitch constant, by setting different fuel rod diameters, the P/D is changed to obtain different coolant volume fractions (**Table 5**), and different fuel densities are set to keep the fuel weight the same in different rod diameters.

Figure 8 presents the coolant temperature feedback coefficient versus P/D. The absolute value of the coolant temperature feedback coefficient has an upward trend with the increase of P/D.

The trend shown in **Figure 8** is related to the influence of S-CO_2 density change on the leakage of neutrons. With the increase of coolant volume fraction, the influence of the neutron leakage on the temperature feedback effect is greater. Therefore, a higher P/D design is beneficial to improve the negative temperature feedback effect of the S-CO_2–cooled reactor.

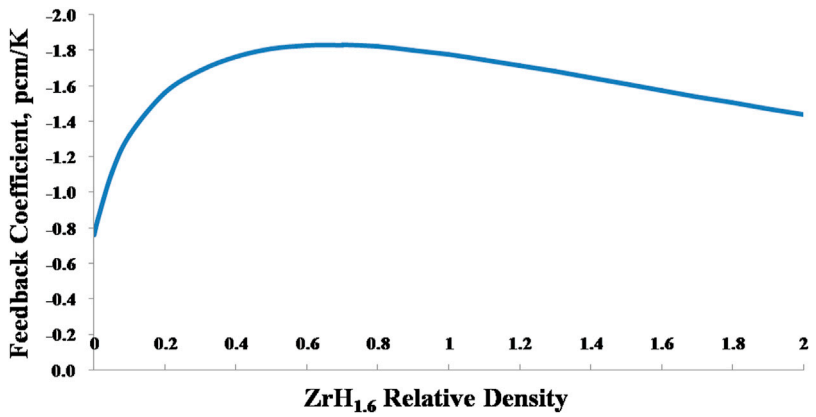

FIGURE 5 | Fuel temperature feedback coefficient versus $ZrH_{1.6}$ relative density.

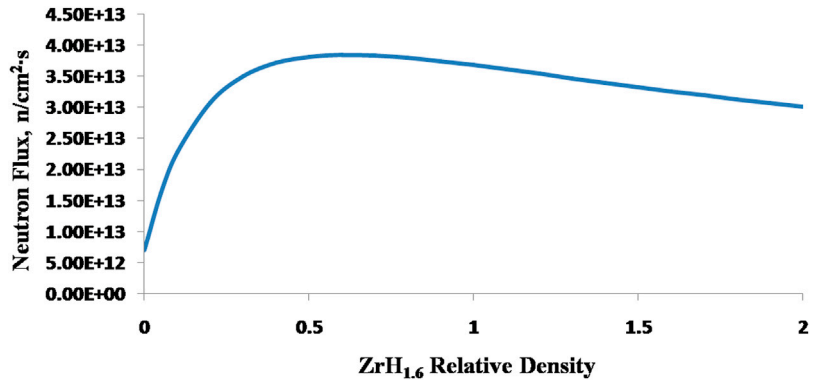

FIGURE 6 | Neutron flux versus $ZrH_{1.6}$ relative density (0.01 eV–10^4 eV).

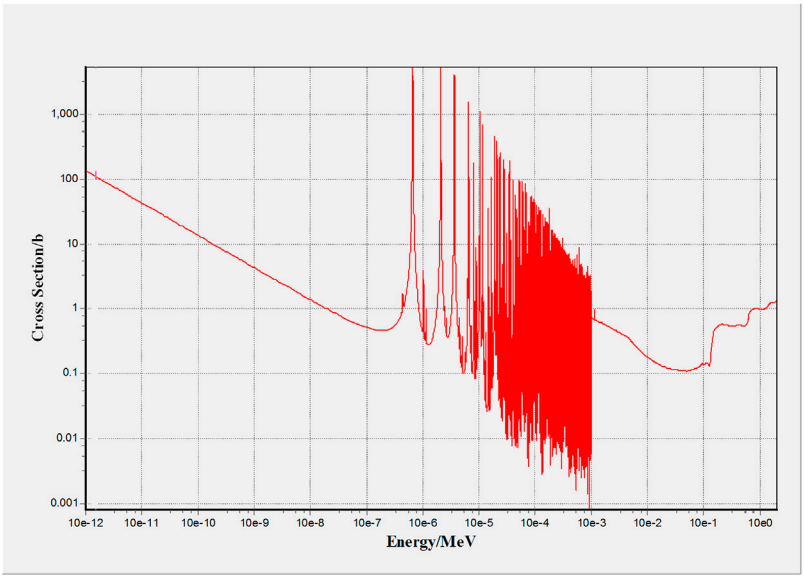

FIGURE 7 | ^{238}U resonance absorption cross section (600 K).

TABLE 5 | Fuel rod diameter variation.

No	Diameter, mm	P/D
1	8.0	1.13
2	7.5	1.20
3	7.0	1.29
4	6.5	1.38
5	6.0	1.50

The Neutron Energy Spectrum

Analyzing the influence of neutron energy spectrum on the fuel temperature feedback effect. The same moderating method as provided in The Neutron Energy Spectrum section under the Fuel Enrichment section is adopted: 13 $ZrH_{1.6}$ rods replace parts of the fuel rods, and different $ZrH_{1.6}$ densities are set to achieve different neutron energy spectrums.

Figure 9 presents the coolant temperature feedback coefficient versus $ZrH_{1.6}$ density. The absolute value of the coolant temperature feedback coefficient has a downward trend with the increase of $ZrH_{1.6}$ density.

The trend shown in **Figure 9** is related to the influence of the neutron energy spectrum on the neutron leakage. As the $ZrH_{1.6}$ density increases, the neutrons are moderated, resulting in a shorter neutron-free path, then the neutron leakage effect is reduced. Weakening the neutron leakage leads to a decrease of the feedback effect. Therefore, a harder neutron energy spectrum design is beneficial to improve the negative temperature feedback effect of the S-CO_2–cooled reactor.

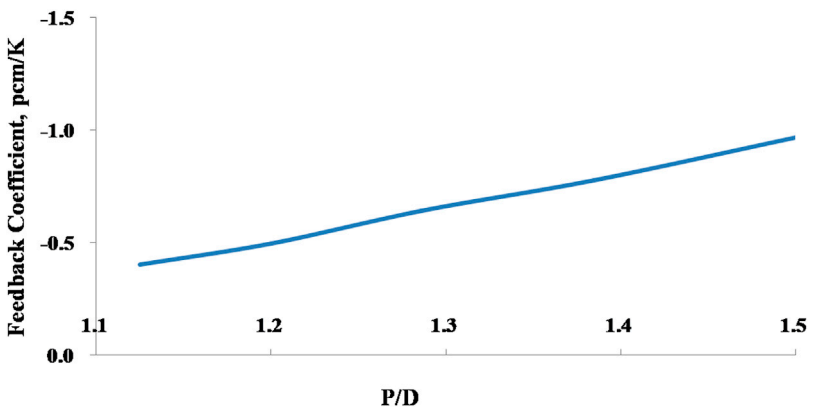

FIGURE 8 | Coolant temperature feedback coefficient versus P/D.

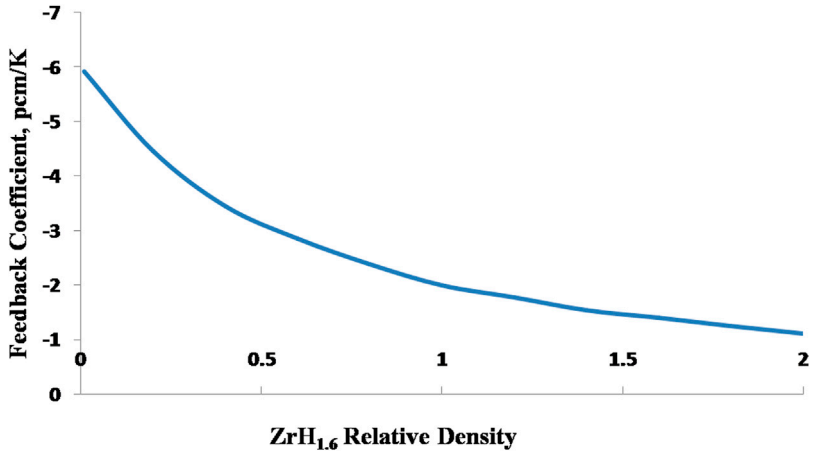

FIGURE 9 | Coolant temperature feedback coefficient versus $ZrH_{1.6}$ relative density.

STUDY ON MODERATOR TEMPERATURE FEEDBACK EFFECT

Due to the weak moderating performance of S-CO_2, the reactor usually uses the solid moderator in the assembly to achieve neutron moderating. Unlike water, the density of the solid moderator is negligible with temperature, and the temperature feedback effect of the moderator is mainly influenced by the cross section of the moderator. The main parameters that affect the temperature feedback effect of the moderator, including moderator material, and the moderator arrangement are studied in this article.

Moderator Type

Typical moderator materials are selected for research, including $ZrH_{1.6}$, BeO, and graphite. **Figure 4** presents the arrangement of moderators in assembly.

The calculation results are shown in **Table 4**. No matter what material is adopted, the feedback coefficient is close to zero.

The result shown in **Table 6** is caused by the negligible change in the moderation performance of solid moderators. Since the density changes very little with temperature, there is almost no change in the moderating performance, resulting in the temperature feedback effect of the solid moderator becoming negligible.

TABLE 6 | Moderator temperature feedback coefficient with different materials.

Moderator materials	Feedback coefficient (pcm/K)
$ZrH_{1.6}$	0.03
BeO	0.00
Graphite	0.00

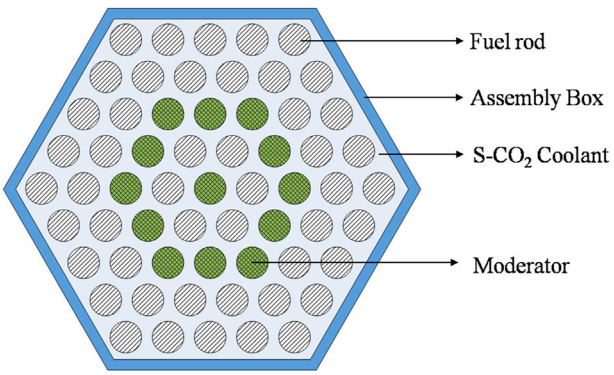

FIGURE 10 | S-CO_2 fuel assembly with moderator (circular arrangement).

Moderator Arrangement

Typical moderator arrangement forms are selected for research, including distributed arrangement (shown in **Figure 4**), circular arrangement (shown in **Figure 10**), and compact arrangement (shown in **Figure 11**).

The calculation results are shown in **Table 7**. For BeO and graphite, the temperature coefficient is close to zero regardless of the arrangement. For $ZrH_{1.6}$, the effect of the arrangement on the temperature feedback is very obvious. With compact arrangement, the temperature coefficient reaches +1.82 pcm/K, which cannot be ignored.

The above phenomenon is mainly caused by the "cell effect" of $ZrH_{1.6}$. In the $ZrH_{1.6}$ moderator, the hydrogen nuclei are trapped in the zirconium lattice. The fast neutrons collide with the hydrogen bound to the lattice and gain energy with an integer multiple of $h\nu$ = 0.137eV from the excited oscillators. As the temperature rises, the number of excited oscillators increases, thus increasing the probability of the neutrons gaining energy. The neutrons that gain energy escape from the moderator and enter the fuel region, and the probability of the neutrons being absorbed by the fuel increases, which increases the reactivity. This phenomenon is more obvious when the compact arrangement is adopted, thus introducing the positive temperature feedback effect. To further study the effect of the compact arrangement on the temperature feedback, we gradually increased the number of moderating rods in the study. The results are shown in **Table 8**, and these show that with the increase of the number of $ZrH_{1.6}$

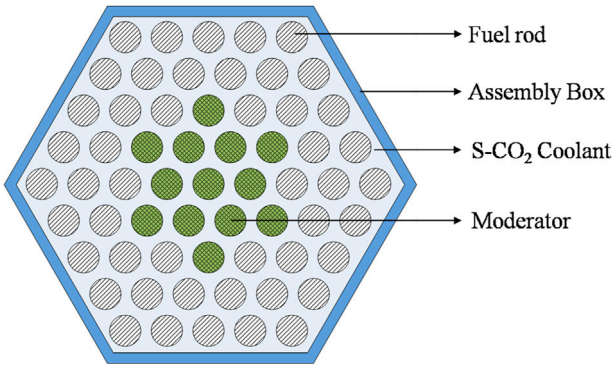

FIGURE 11 | S-CO_2 fuel assembly with moderator (compact arrangement).

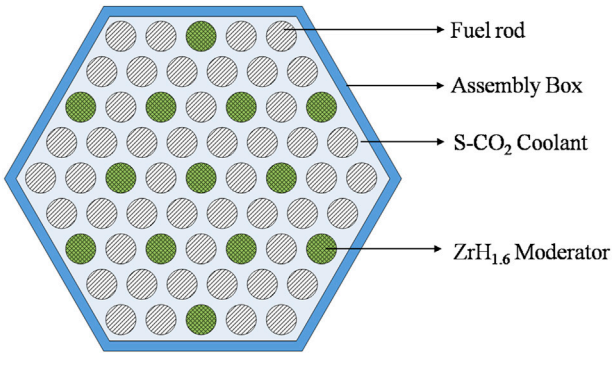

FIGURE 12 | Optimized design of S-CO_2 fuel assembly with moderator.

TABLE 7 | Moderator temperature feedback coefficient with different arrangement.

	Distributed	Circular	Compact
Moderator materials	**Feedback coefficient (pcm/K)**		
$ZrH_{1.6}$	0.03	0.05	0.20
BeO	0.00	0.00	0.00
Graphite	0.00	0.00	0.00

TABLE 8 | Moderator temperature feedback coefficient with different number of moderating rods.

Rods number	**13**	**25**	**37**
Typical moderator materials	**Feedback coefficient (pcm/K)**		
$ZrH_{1.6}$	0.20	1.01	1.82
BeO	0.00	0.00	0.00
Graphite	0.00	0.00	0.00

moderating rods, the positive temperature feedback effect brought by the compact arrangement is more and more obvious, and the temperature feedback effect constant zero when BeO or graphite is used as the moderator. Therefore, it is necessary to avoid the compact arrangement of $ZrH_{1.6}$ in the S-CO_2–cooled reactor design.

DESIGN ON S-CO_2–COOLED CORE FOR INCREASING TEMPERATURE FEEDBACK EFFECT

According to the study in the sections Study on Fuel Temperature Feedback Effect, Study on Coolant Temperature Feedback Effect, and Study on Moderator Temperature Feedback Effect, we obtain the method to enhance the temperature feedback effect. This method is applied to the S-CO_2–cooled core optimized design.

Optimized Design of Fuel Assembly

Based on the standard S-CO_2 fuel assembly, an optimized assembly design is adopted for increasing the temperature feedback effect. **Figure 12** presents the optimized design of the fuel assembly, and **Table 9** presents the comparison of the standard assembly and the optimized assembly. The optimization methods used for the optimized assembly are as follows:

1) Decreasing the fuel enrichment.

The effect of fuel enrichment on fuel temperature feedback is given in the Fuel Enrichment section. Using fuel with lower enrichment can effectively enhance the fuel temperature feedback effect, then the fuel enrichment decreases from 20 to 15% in the optimized assembly design.

2) Increasing the P/D.

The effect of the P/D on coolant temperature feedback is given in the Coolant Volume Fraction section. Using a larger P/D can effectively enhance the coolant temperature feedback effect, then the P/D increases from 1.125 to 1.200 in the optimized assembly design.

3) Adding moderating rods.

The effect of neutron energy spectrum on fuel temperature feedback is given in the The Neutron Energy Spectrum secton under the Fuel Enrichment section, and the effect of the moderator arrangement on moderator temperature feedback is

TABLE 9 | Comparison of the standard assembly an optimized assembly.

Design parameters	Standard assembly	Optimized assembly
Fuel material	UO_2	UO_2
Enrichment	20%	15%
P/D	1.125	1.200
Moderator material	—	$ZrH_{1.6}$
Number of moderating rods	—	13
Energy spectrum	fast	epithermal

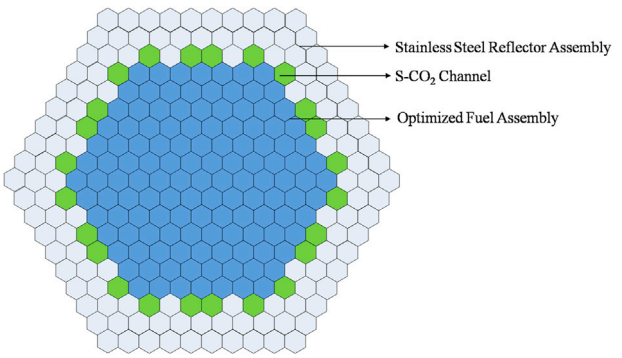

FIGURE 13 | The optimized S-CO_2–cooled core.

given in the Moderator Arrangement section. Using $ZrH_{1.6}$ moderator can effectively enhance the fuel temperature feedback effect, and a distributed arrangement is adopted to avoid the positive moderator temperature feedback. Therefore $ZrH_{1.6}$ moderator is adopted in the optimized design and the number of moderating rods is 13.

Optimized Design of S-CO_2–Cooled Core

Based on the standard S-CO_2 assembly arrangement scheme, the optimized core design is adopted for increasing temperature feedback effects. **Figure 13** presents the S-CO_2–cooled core, consisting of 127 optimized assemblies.

To further enhance the coolant temperature feedback effect, a larger coolant volume fraction is recommended in the Coolant Volume Fraction section. A circle of coolant channels is arranged around the fuel zone to increase the coolant volume fraction in the optimized core design.

Calculation of Temperature Feedback Coefficient

The temperature feedback coefficient is shown in **Table 10**; the fuel temperature feedback coefficient is −2.16 pcm/K, coolant temperature feedback coefficient is −2.07 pcm/K, moderator temperature feedback coefficient is 0.02 pcm/K, and the total feedback coefficient is −4.41 pcm/K.

In terms of fuel temperature feedback, $ZrH_{1.6}$ moderators are adopted in the optimized design. The energy spectrum is softened and the Doppler broadening effect increases. In addition, lower enrichment of fuel is selected in the optimized design. These designs can significantly enhance the fuel temperature feedback effect. The fuel temperature feedback coefficient changes from −0.51 pcm/K to −2.36 pcm/K.

TABLE 10 | Temperature feedback coefficient of optimized design.

Calculation object	Optimized design	Standard design
	Temperature feedback coefficient (pcm/K)	
Fuel	−2.36	−0.51
Coolant	−2.07	−1.68
Moderator	0.02	—
Total	−4.41	−2.19

In terms of coolant temperature feedback, although the softening of the energy spectrum will lead to the weakening of the feedback effect, the larger P/D design and coolant channel design can increase the coolant volume fraction, such that the feedback effect can be improved. The coolant temperature feedback coefficient changes from −1.68 pcm/K to −2.07 pcm/K.

In terms of moderator temperature feedback, the use of moderator imports moderator temperature feedback effect. The temperature coefficient of the moderator is only 0.02 pcm/K due to the distributed arrangement.

In conclusion, the total temperature feedback coefficient of the optimized design reaches −4.41 pcm/K, which is obviously stronger than the standard design.

CONCLUSIONS

Due to the poor neutronics moderation performance, the S-CO_2–cooled reactor shows the disadvantage of a weak temperature feedback effect on reactivity, which directly influences the inherent safety of the reactor.

In this article, the influence mechanism of core reactivity temperature feedback effect is studied, and the optimized design of an S-CO_2–cooled reactor which has a stronger temperature feedback effect on reactivity is proposed at last. The main conclusions of the study are as follows:

1) The main factors affecting S-CO_2–cooled reactor temperature feedback include fuel, coolant, and moderator.
2) In terms of fuel temperature feedback, using UO_2 fuel and low enrichment design can effectively improve temperature feedback effect. The neutron energy spectrum also has an important influence on the feedback effect, and increasing the neutron flux in the ^{238}U resonance region is conducive to enhancing the effect.
3) In terms of coolant temperature feedback, using larger coolant volume fraction and hard energy spectrum can improve temperature feedback effect.
4) In terms of moderator temperature feedback, the feedback effect of BeO and graphite moderators can be ignored no matter what arrangement is adopted. For $ZrH_{1.6}$, there is a strong positive temperature feedback effect when using the compact arrangement, which must be avoided in the design.

5) In terms of moderator temperature feedback, based on the study of fuel, coolant, and moderator temperature feedback effect mechanism, an optimized S-CO_2–cooled core is proposed, and a high-temperature feedback effect is obtained.

DATA AVAILABILITY STATEMENT

The original contributions presented in the study are included in the article/Supplementary Material, further inquiries can be directed to the corresponding author.

AUTHOR CONTRIBUTIONS

LW: conceptualization, methodology, and software; DL: visualization and investigation; LY: visualization and investigation; HX: funding acquisition and supervision; CZ: funding acquisition and supervision.

FUNDING

This work is supported by the National Natural Science Foundation of China (Approved no: 12075228).

REFERENCES

Ahn, Y., Bae, S. J., Kim, M., Cho, S. K., Baik, S., Lee, J. I., et al. (2015). Review of Supercritical CO_2 Power Cycle Technology and Current Status of Research and Development. *Nucl. Eng. Technol.* 47 (6), 647–661. doi:10.1016/j.net.2015.06.009

Carstens, N. A., Hejzlar, P., and Driscoll, M. J. (2006). "Control System Strategies and Dynamic Response for Supercritical CO_2 Power Conversion Cycle[R],". MIT-GFR-038, Topical Report of Center for Advanced Nuclear Energy Systems in MIT Nuclear Engineering Department.

Eoh, J.-H., Jeong, J.-Y., Han, J.-W., and Kim, S.-O. (2008). Numerical Simulation of a Potential CO_2 Ingress Accident in a SFR Employing an Advanced Energy Conversion System. *Ann. Nucl. Energ.* 35, 2172–2185. doi:10.1016/j.anucene.2008.09.012

Handwerk, C., Driscoll, M. J., and Hejzlar, P. (2007). "Core Design and Performance Assessment for a Supercritical-CO_2 Cooled Fast Reactor[R],". MIT-ANP-TR-113.

Kato, Y., Niktawaki, T., and Yoshizawa, Y. (2001). "A Carbon Dioxide Partial Condensation Direct Cycle for Advanced Gas Cooled Fast and Thermal Reactors[C]," in Proc. of Global 2001, Paris, France.

Kato, Y., Nitawaki, T., and Muto, Y. (2004). Medium Temperature Carbon Dioxide Gas Turbine Reactor. *Nucl. Eng. Des.* 230, 195–207. doi:10.1016/j.nucengdes.2003.12.002

Michael, A. P. (2004). "Reactor Physics Design of Supercritical CO_2-Cooled Fast Reactor [D]," (Cambridge, Massachusetts: Massachusetts Institute of Technology). Master Thesis.

Michael, A. P. (2006). "Thermal Hydraulics Design of a 2400MWth Direct Supercritical CO_2-Cooled Fast Reactor [D]," (Cambridge, Massachusetts: Massachusetts Institute of Technology). Ph.D Thesis.

Petr, V., and Kolovratnik, M. (1997). "A Study on Application of a Closed Cycle CO_2 Gas Turbine in Power Engineering [R],". Departmental report Z-523/97, Czech Technical niversity in Prague, Department of Fluid Dynamics and Power Engineering, Division of Power Engineering.

Tsuzuki, N., Kato, Y., and Ishiduka, T. (2007). High Performance Printed Circuit Heat Exchanger. *Appl. Therm. Eng.* 27, 1702–1707. doi:10.1016/j.applthermaleng.2006.07.007

Xie, Z. (1994). *Physical Analysis of Nuclear Reactor Property [M]*. Beijing: Atomic Energy Press, 68–71.

Zhang, T., Xiong, J., Liu, X., Chai, X., Li, W., and Cheng, X. (2019). Conceptual Design of an Innovative Reduced Moderation Thorium-fueled Small Modular Reactor with Heavy-Water Coolant. *International Journal of Energy Research* 43, 8286-8298.

Zhang, T., Liu, X., Xiong, J., and Cheng, X. (2020). Comparisons of Reduced Moderation Small Modular Reactors With Heavy Water Coolant. *Front. Energy Res.* 8, 7.

Conflict of Interest: The author declares that the research was conducted in the absence of any commercial or financial relationships that could be construed as a potential conflict of interest.

Publisher's Note: All claims expressed in this article are solely those of the authors and do not necessarily represent those of their affiliated organizations, or those of the publisher, the editors, and the reviewers. Any product that may be evaluated in this article, or claim that may be made by its manufacturer, is not guaranteed or endorsed by the publisher.

frontiers in Energy Research

ORIGINAL RESEARCH
published: 25 November 2021
doi: 10.3389/fenrg.2021.764905

Physical Design of High-Performance Fuel Assembly Based on Fully Ceramic Microencapsulated Fuel for Supercritical CO_2 Cooled Reactor

Di Lu, Lianjie Wang, Yun Cai, Dongyong Wang and Ce Zhang*

Nuclear Power Institute of China (NPIC), Chengdu, China

Fully ceramic microencapsulated fuel (FCM) is employed in the supercritical CO_2 (S-CO_2)-cooled reactor as accident tolerant fuel (ATF). Although the fuel and the assembly substrate contain SiC, the assembly cannot be sufficiently moderated due to the weak moderating performance of S-CO_2, which affects the neutronics economy seriously. In this study, a new fuel assembly based on FCM fuel is proposed for the S-CO_2 cooled reactor. Besides, the solid moderator rod is introduced into the design. Although the introduction of moderator rods can effectively improve the moderation performance of S-CO_2 reactor assembly, it will lead to the deterioration of uniform moderation. To further improve the uniform moderation, arrangement of moderator rods and fuel enrichment partition are studied. Finally, the results show clearly that a better balance between uniform moderation and sufficient moderation can be obtained in the high-performance S-CO_2 reactor assembly.

Keywords: supercritical CO_2 cooled reactor, fuel assembly (FA), FCM fuel, sufficient moderation, uniform moderation

OPEN ACCESS

Edited by:
Jun Wang,
University of Wisconsin-Madison, United States

Reviewed by:
Jie Cheng,
Harbin Engineering University, China
Guang Hu,
Xi'an Jiaotong University, China

****Correspondence:***
Lianjie Wang
mcd2264@126.com

Specialty section:
This article was submitted to Nuclear Energy, a section of the journal Frontiers in Energy Research

Received: *26 August 2021*
Accepted: *25 October 2021*
Published: *25 November 2021*

Citation:
Lu D, Wang L, Cai Y, Wang D and Zhang C (2021) Physical Design of High-Performance Fuel Assembly Based on Fully Ceramic Microencapsulated Fuel for Supercritical CO_2 Cooled Reactor. Front. Energy Res. 9:764905. doi: 10.3389/fenrg.2021.764905

INTRODUCTION

By taking advantage of the appropriate critical pressure, high density, stability, and sluggishness of CO_2 near its critical point, the use of supercritical CO_2(S-CO_2) as a coolant in the direct cycle reactor is evaluated (Ahn et al., 2015; Wu et al., 2020). The S-CO_2–cooled reactor, as a promising innovative reactor, has the advantages of simple system, high thermal efficiency, small volume, and light weight, and it represents an important development direction for nuclear energy innovation and development (Michael, 2004).

Safety and economics are the main objectives of the S-CO_2–cooled reactor. A new fuel concept is referred to as accident-tolerant fuels (ATFs) are capable of mitigating the potential consequences of beyond-design-basis accidents (Bragg-Sitton, 2014). The fully ceramic microencapsulated (FCM) fuel (Terrani et al., 2012) has become one among the ATF options which is based on tristructural isotropic (TRISO) (Bragg-Sitton and Carmack, 2015)–coated particles embedded in silicon carbide (SiC) matrix. FCM fuel borrows from the TRISO particle design from the high-temperature gas reactor (HTGR) technology but uses SiC as a matrix material rather than graphite in HTGR. Benefiting from the multiple barriers of TRISO and SiC matrix, FCM fuel has extremely high radioactivity retention capability compared to that of the conventional standard UO_2 fuel. By the advantages of safety, a new fuel assembly based on the FCM fuel is proposed for the S-CO_2–cooled reactor in this study.

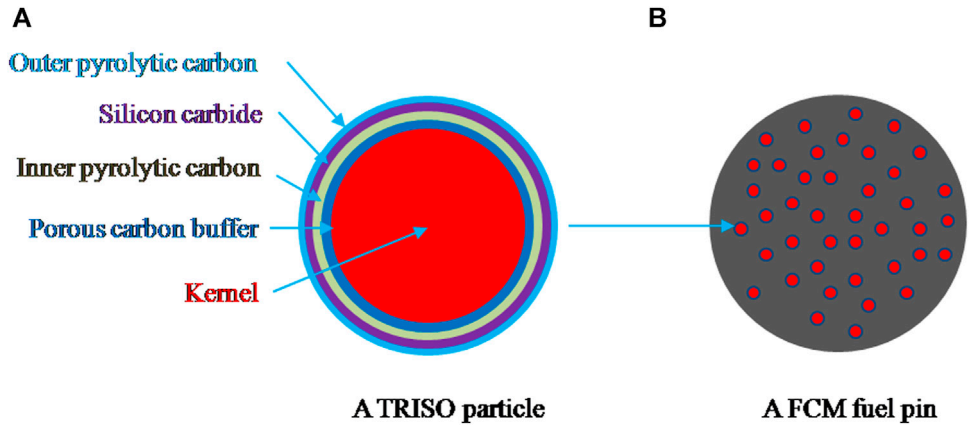

FIGURE 1 | Design of FCM fuel.

TABLE 1 | TRISO particle geometry and composition.

Layer	Radius (mm)	Density (g/cm^3)
Kernel	0.4000	10.41
Porous carbon buffer	0.4500	1.100
Inner pyrolytic carbon	0.4850	1.900
Silicon carbide	0.5200	3.180
Outer pyrolytic carbon	0.5400	1.900

TABLE 2 | FCM fuel design parameters.

Parameter	Value	Unit
Fuel compact outer radius	8.3500	mm
Gas gap outer radius	8.4000	mm
SiC Clad outer radius	8.9000	mm
^{235}U enrichment	19.75%	-
TRISO particle share	40%	-

In further research, although the FCM fuel contains moderation materials such as SiC, the assembly cannot be sufficiently moderated due to the weak moderating performance of S-CO_2, which affects the neutronics economy seriously. The study on improving the deficiency of weak moderating performance is described in this article.

Unlike the light water moderated or heavy water moderated (Zhang et al.,2019; Zhang et al.,2020) nuclear reactors, the S-CO_2 cooled reactor needs specific moderator rods to improve the slow-down of neutrons. The introduction of moderator rods can effectively improve the moderating performance of S-CO_2–cooled reactor, but it will lead to the deterioration of uniform moderation. To further improve the uniform moderation, moderator rod arrangement and fuel enrichment partition method are studied. Finally, this study shows clearly that a better balance between uniform moderation and sufficient moderation can be obtained in the high-performance S-CO_2–cooled reactor assembly.

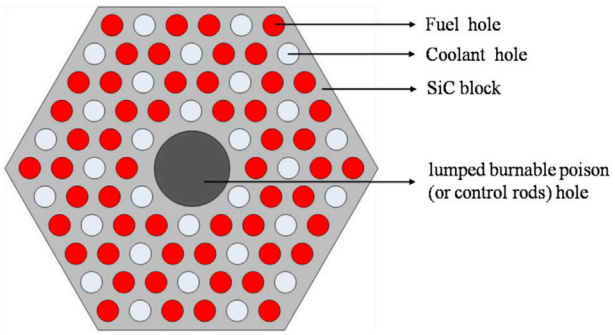

FIGURE 2 | S-CO_2–cooled reactor standard fuel assembly.

TABLE 3 | FCM fuel design parameters.

Parameter	Value	Unit
SiC block length	2,500.00	mm
SiC block width	240.00	mm
Fuel/Coolant hold diameter	18.00	mm
Minimum web thickness	6.00	mm
SiC Clad outer radius	8.90	mm
lumped burnable poison (or control rods) hole diameter	72.00	mm
Fuel hold number	54	-
Coolant hold number	30	-
U weight per assembly	44.48	kg

FULLY CERAMIC MICROENCAPSULATED FUEL ASSEMBLY OF S-CO_2–COOLED REACTOR DESIGN

Standard Fuel Assembly of S-CO_2–Cooled Reactor Design

An FCM fuel with a TRISO particle is shown in **Figure 1**. The TRISO particle geometry and composition are given in **Table 1** and the FCM fuel design parameters are given in **Table 2**. In this

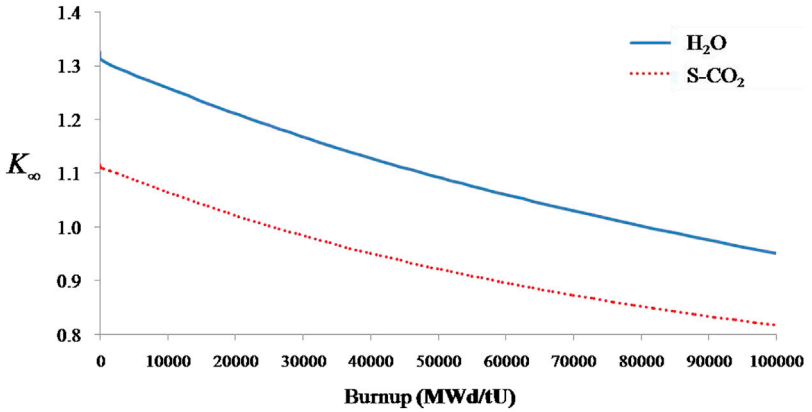

FIGURE 3 | K_∞ versus fuel burn up.

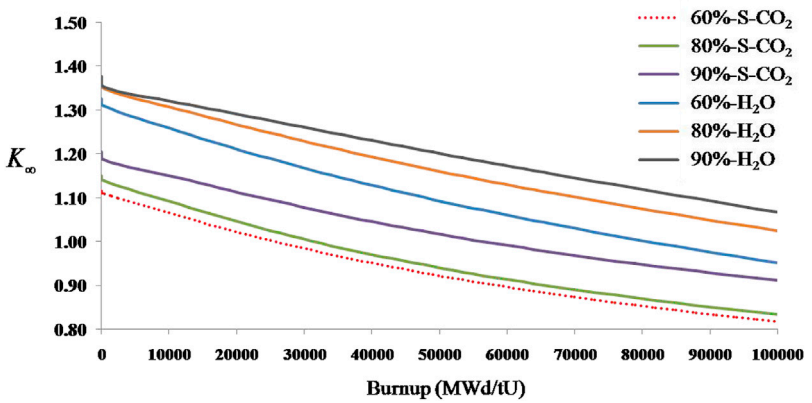

FIGURE 4 | K_∞ by different SiC matrix share versus burn up.

design, the TRISO particles account for 40% of the volume in FCM fuel and the enrichment of ^{235}U reaches 19.75%.

The standard fuel assembly of S-CO_2–cooled reactor in this study is shown in **Figure 2**; it contains SiC block, fuel holes, coolant holes, and lumped burnable poison (or control rods) hole. The assembly design parameters are given in **Table 3**. Each block is a right hexagonal prism with a dimension of 2,500 mm in length and 240 mm across the flats of the hexagonal cross section. Fuel and coolant holes run parallel through the length of the block in a regular triangular pattern of nominally two fuel holes per coolant hole. The pitch of the fuel and coolant hole array is 18 mm. The minimum web thickness between the fuel hold and coolant hole is 6 mm and this web provides an additional barrier to the release of metallic fission products. In order to get an effective control of reactivity, a lumped burnable poison (or control rods) hole (72 mm) is added to the center of standard fuel assembly.

TABLE 4 | $YH_{1.8}$ solid moderator pin geometry and composition.

Layer	Radius (mm)	Material
Kernel	8.4000	$YH_{1.8}$
Cladding	8.9000	stainless steel

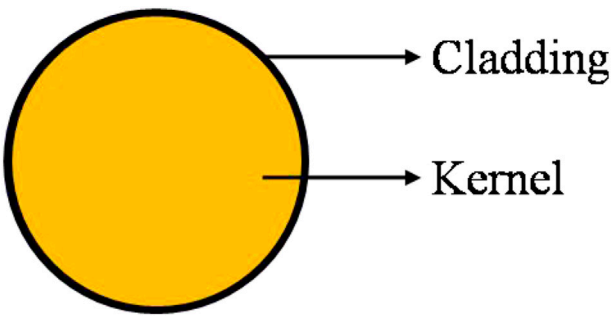

FIGURE 5 | $YH_{1.8}$ solid moderator pin.

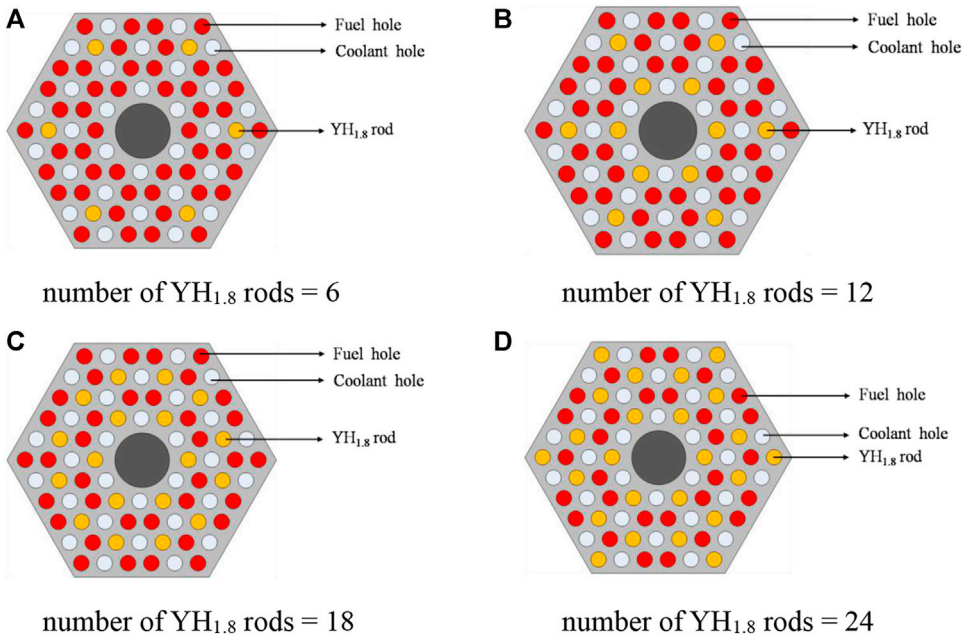

FIGURE 6 | Arrangements of $YH_{1.8}$ solid moderator rods in S-CO_2 assembly.

Neutron Moderating Performance Analysis for the Standard Assembly

To analyze neutron moderating performance for the standard assembly, the light water (H_2O) coolant fuel assembly is used for comparison in standard assembly cooling by S-CO_2. Other than replacing coolant with H_2O, the design parameters remain unchanged to compare S-CO_2 assembly and H_2O assembly in moderating analyses. The calculation in the study is done by using HANDF-E code package developed by the Nuclear Power Institute of China. This code has been used in the analysis of hexagonal assembly because of its high accuracy.

Infinite multiplication factor (K_∞) is the main parameter that characterizes fuel reactivity. In general, moderating performance largely determines the value of K_∞. $K_\infty$of each assembles as fuel burn up varies, as shown in **Figure 3**. $K_\infty$of S-CO_2 assembly is much less than that of H_2O under the same fuel burn up. The calculation results clearly show that S-CO_2 assembly has the defect of insufficient moderating performance.

Neutrons can be moderated in the SiC, and increasing the SiC matrix share of FCM fuel is the most direct way to improve the moderating performance. The SiC matrix share increases from 60 to 80%, or even 90%, and then K_∞ by different SiC matrix share as fuel burn up varies is shown in **Figure 4**. The calculation results clearly show that increasing SiC matrix share is beneficial to enhance moderating performance and improve fuel reactivity. **Figure 4** also presents K_∞ of H_2O assembly by different SiC matrix share as fuel burn up varies. Even if the matrix share changes, K_∞ of H_2O is still much greater than that of S-CO_2. These results show that the method of increasing the SiC matrix share has a limited effect on improving the moderating performance.

In fact, in terms of fuel burn up and core volume, increasing SiC matrix share is not a good idea; it means the TRISO particle share is reduced and fuel burn up will be grow greatly. To reduce fuel burn up, a larger number of assembles will be used in core, resulting in a larger core volume, and the large core volume makes the design of pressure vessels under high temperature and pressure a great challenge. Therefore, the method to improve the moderating performance should minimize the increase in core volume.

TABLE 5 | $YH_{1.8}$ solid moderator rods number setting.

	$YH_{1.8}$ rods number	Fuel rods number	Relative share of fuel
1	0	54	1.000
2	6	48	0.889
3	12	42	0.778
4	18	36	0.667
5	24	30	0.556

NEUTRONICS ANALYSIS FOR THE DESIGN OF $YH_{1.8}$ IN THE STANDARD ASSEMBLY

Because of stronger neutron moderating capacity, metal hydride has been used as a solid moderator in reactors. Yttrium hydride ($YH_{1.8}$) is more suitable to use in the S-CO_2 cooled reactor because it is more stable than zirconium hydride ($ZrH_{1.6}$) at high temperature.

The design of $YH_{1.8}$ solid moderator rod used in this study is shown in **Figure 5**. To reduce the release of hydrogen atoms,

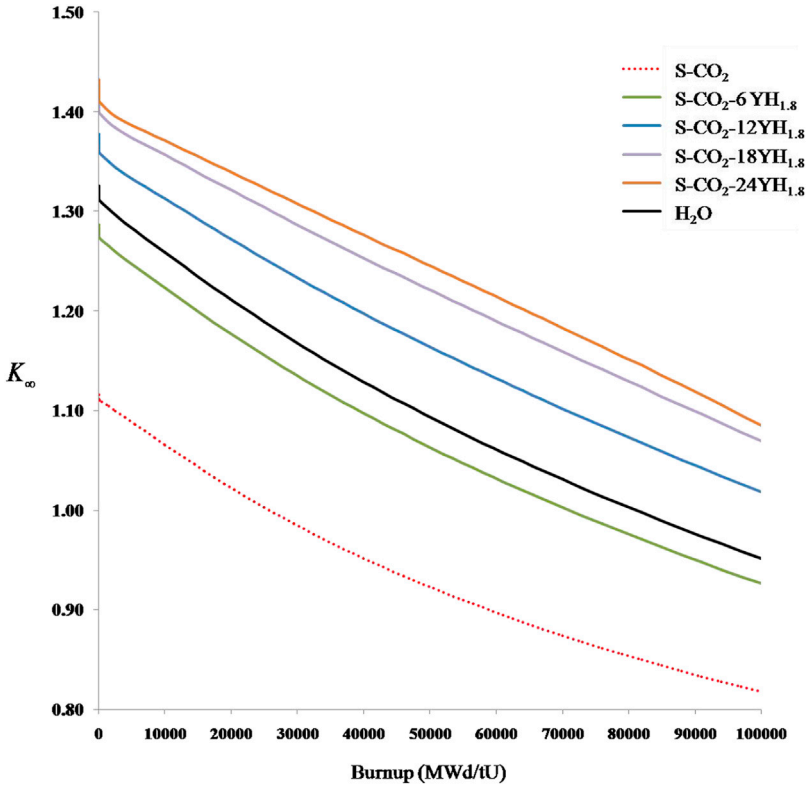

FIGURE 7 | K_∞ by different numbers of $YH_{1.8}$ rods versus burn up.

the solid moderator rod is coated with stainless steel. The $YH_{1.8}$ solid moderator rod geometry and composition are given in **Table 4**.

The moderating method is to insert the $YH_{1.8}$ solid moderator rod into part of fuel holds instead of the FCM fuel. The moderating performance of assembly can be changed by using different number of $YH_{1.8}$ solid moderator rods. The number of $YH_{1.8}$ solid moderator rod analyzed in this study is shown in **Table 5**, and the arrangements of the $YH_{1.8}$ solid moderator rods are shown in **Figure 6**.

K_∞ by different $YH_{1.8}$ solid moderator rod number as fuel burn up varies is shown in **Figure 7**. The calculation results clearly show that adding $YH_{1.8}$ solid moderator rod can significantly enhance moderating performance and then improve the fuel reactivity greatly. K_∞ of H_2O is also described in **Figure 6**. When the number of $YH_{1.8}$ solid moderator rods is greater than 12, the $K_\infty$of S-CO_2 assembly is significantly larger than that of H_2O assembly. These results show that moderating performance can be improved significantly by inserting the $YH_{1.8}$ solid moderator rod. When 12 $YH_{1.8}$ solid

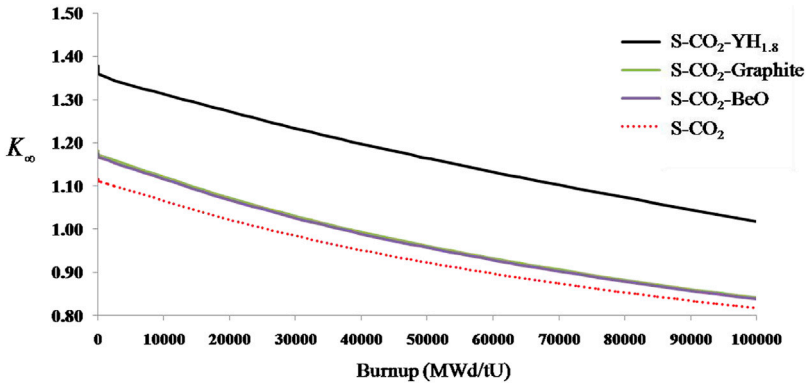

FIGURE 8 | K_∞ by different moderating materials versus burn up.

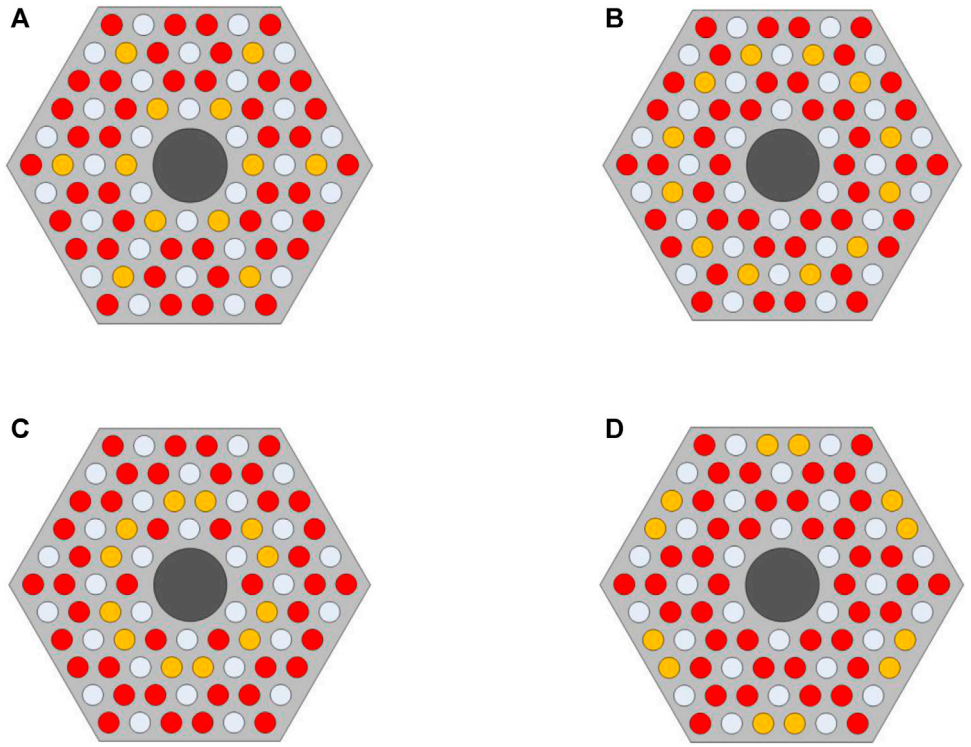

FIGURE 9 | Arrangements of 12 $YH_{1.8}$ solid moderator rods.

moderator rods were inserted, the S-CO_2 assembly was moderated sufficiently and the fuel share was reduced by only 22.2%.

The moderating effect of different materials was further studied. Commonly used moderating materials such as graphite and BeO are used for comparison with $YH_{1.8}$. K_∞ of different moderating materials as fuel burn up varies are shown in **Figure 8**. K_∞ of $YH_{1.8}$ is significantly larger than that of graphite and BeO. The results show that using $YH_{1.8}$ as a moderator is the best choice to improve the moderating performance of S-CO_2 assembly.

UNIFORM MODERATING DESIGN FOR THE S-CO_2 ASSEMBLY

Inserting the $YH_{1.8}$ solid moderator rods cause uneven moderating in the assembly. In order to get uniform moderating, the arrangement of the moderators must be studied.

The moderating effect and the change of fuel share were considered, and then the number of $YH_{1.8}$ solid moderator rods is selected as 12 in this section. The different arrangements of $YH_{1.8}$ solid moderator rods are shown in **Figure 9** and power uneven factor by different solid

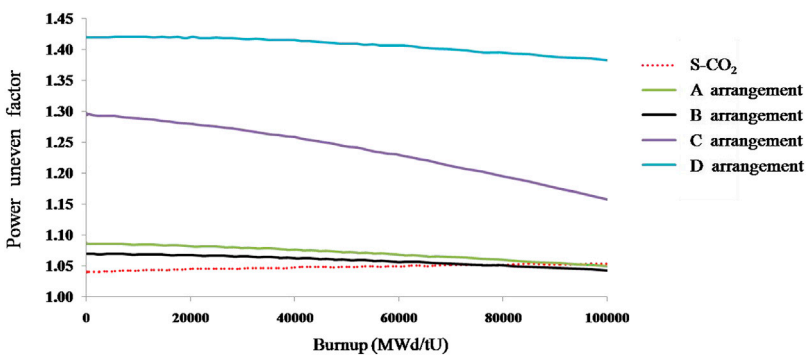

FIGURE 10 | Power uneven factor by different solid moderator arrangements.

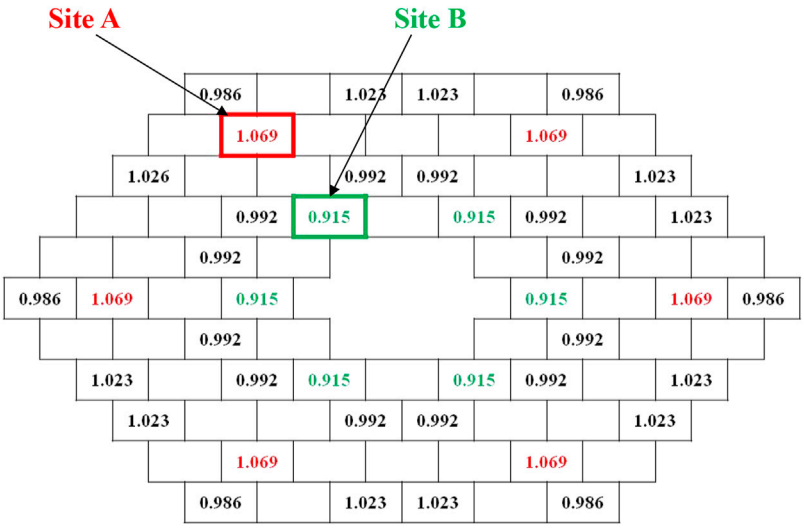

FIGURE 11 | Relative power distribution of S-CO_2 assembly using arrangement B (BOL).

moderator arrangements as fuel burn up varies are shown in **Figure 10**. The arrangement B of solid moderator obtains the lowest uneven factor and becomes the preferred arrangement in this study.

Figure 11 presents the BOL (**B**egin **O**f **L**ife) relative power distribution of S-CO_2 assembly using arrangement B. **Figure 11** clearly shows that the maximum power is at site A and the minimum power is at site B. In order to further realize the uniform moderating to reduce the power uneven factor, the fuel share of FCM partitioning method is applied in the S-CO_2 assembly design. The fuel share of FCM is reduced from 40 to 35% at site A which have maximum power and the fuel share of FCM is increased from 40 to 45% at site B which have minimum power. In addition, this partitioning method ensures that the fuel weight remains the same in the S-CO_2 assembly. The BOL relative power distribution of S-CO_2 assembly using the partitioning method is shown in **Figure 12**. The relative power at site A decreases from 1.069 to 0.964, the relative power at site B increases from 0.915 to 1.005, and then the uneven factor decreases from 1.069 to 1.028. **Figure 13** presents a power uneven factor by arrangement B with the partitioning method as fuel burn up varies; it shows that the fuel share of the FCM partitioning method can achieve more uniform moderating and power distribution.

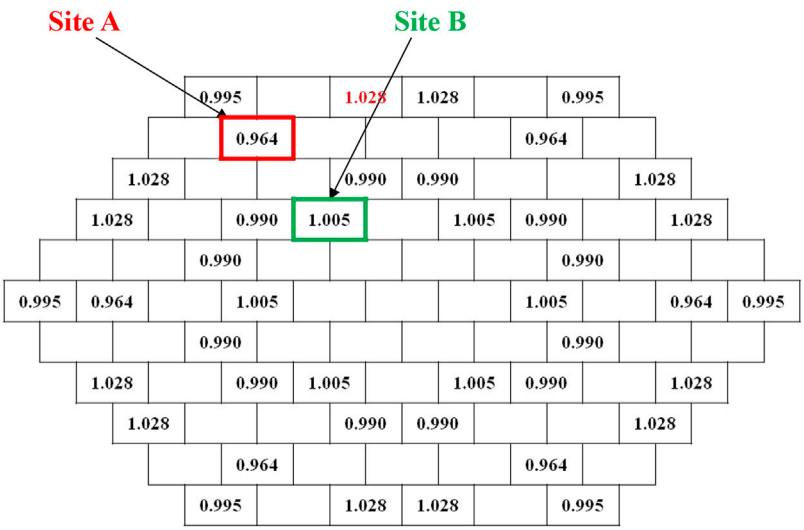

FIGURE 12 | Relative power distribution of S-CO_2 assembly using the partitioning method (BOL).

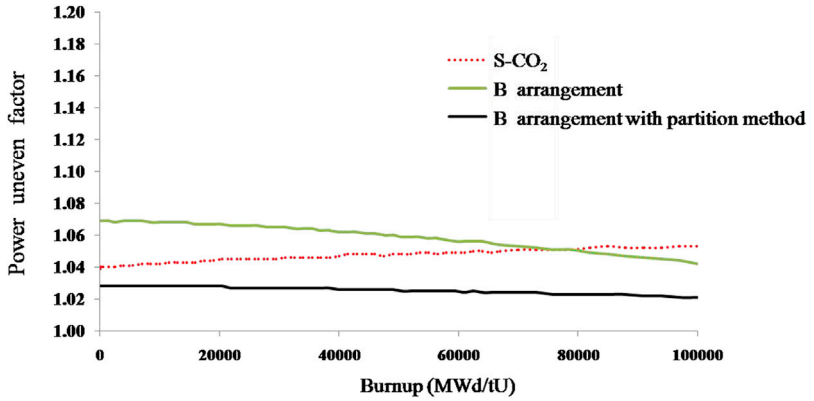

FIGURE 13 | Power uneven factor by arrangement B with the partitioning method.

CONCLUSION

As a new type reactor with development potential, the S-CO_2–cooled reactor has many advantages, such as simple system, high thermal efficiency, and small volume. FCM fuel which is a potential option of ATF is capable to mitigate the potential consequences of beyond-design-basis accidents and become the preferred type of fuel for the S-CO_2–cooled reactor.

In this article, a new fuel assembly design concept based on FCM fuel for S-CO_2–cooled reactor is proposed. Then, the design of $YH_{1.8}$ solid moderator rod was adopted to improve the moderating performance of the fuel assembly. In order to deal with the moderating non-uniformity caused by the moderator, the arrangement of moderators and the method of fuel share partitioning were well studied, and then the high-performance fuel assembly based on FCM fuel for S-CO_2–cooled reactor is proposed at last. The main conclusions of the study are as follows:

1) The fuel assembly based on the FCM fuel for the S-CO_2–cooled reactor was proposed because of the safety advantage. Due to the weak moderating performance of S-CO_2, the neutrons in this assembly cannot be sufficiently moderated and affects the neutronics economy seriously.
2) As it is superior to the method of adjusting the SiC matrix share, the design of $YH_{1.8}$ solid moderator rod is studied. With this design, the assembly can be sufficiently moderated.
3) The arrangement of $YH_{1.8}$ solid moderator rods is proposed, which can effectively improve the uniformity of moderating. The method of fuel share partitioning is studied at last and the fuel assembly is further uniformly moderated.
4) The high-performance fuel assembly based on the FCM fuel which has good safety and economics is suitable for S-CO_2–cooled reactor.

DATA AVAILABILITY STATEMENT

The raw data supporting the conclusions of this article will be made available by the authors, without undue reservation.

AUTHOR CONTRIBUTIONS

DL contributed to conceptualization, methodology, and design. LW contributed to conceptualization and methodology. YC performed the calcualtion and analysis. DW funding acquisition and supervision. CZ visualization and investigation.

FUNDING

This work is supported by the National Natural Science Foundation of China (Approved no.: 12,075,228).

REFERENCES

Ahn, Y., Bae, S. J., Kim, M., Cho, S. K., Baik, S., Lee, J. I., et al. (2015). Review of Supercritical CO2 Power Cycle Technology and Current Status of Research and Development. *Nucl. Eng. Technology.* 47 (6), 647–661. doi:10.1016/j.net.2015.06.009

Bragg-Sitton, S., and Carmack, W. J. (2015). Update on the DOE's ATF Development Program. *Nucl. News.* 58, 34–35.

Bragg-Sitton, S. (2014). Development of Advanced Accident Tolerant Fuels for Commercial LWRs. *Nucl. News.* 57, 83–91.

Michael, A. P. (2004). *Reactor Physics Design of Supercritical CO_2-Cooled Fast Reactor [D].* Cambridge, MA: Master Thesis of Massachusetts Institute of Technology.

Terrani, K. A., Kiggans, J. O., Katoh, Y., Shimoda, K., Montgomery, F. C., Armstrong, B. L., et al. (2012). Fabrication and Characterization of Fully Ceramic Microencapsulated Fuels. *J. Nucl. Mater.* 426, 268–276. doi:10.1016/j.jnucmat.2012.03.049

Wu, P., Ma, Y., Gao, C., Liu, W., Shan, J., Huang, Y., et al. (2020). A Review of Research and Development of Supercritical Carbon Dioxide Brayton Cycle Technology in Nuclear Engineering Applications. *Nucl. Eng. Des.* 368, 110767. doi:10.1016/j.nucengdes.2020.110767

Zhang, T., Xiong, J., Liu, X., Chai, X., Li, W., and Cheng, X. (2019). Conceptual Design of an Innovative Reduced Moderation Thorium-fueled Small Modular

Reactor with Heavy-water Coolant. *Int. J. Energy Res.* 43, 8286–8298. doi:10.1002/er.4827

Zhang, T., Liu, X., Xiong, J., and Cheng, X. (2020). Comparisons of Reduced Moderation Small Modular Reactors with Heavy water Coolant. *Front. Energy Res.* 8, 27.

Conflict of Interest: The authors declare that the research was conducted in the absence of any commercial or financial relationships that could be construed as a potential conflict of interest.

Publisher's Note: All claims expressed in this article are solely those of the authors and do not necessarily represent those of their affiliated organizations, or those of the publisher, the editors, and the reviewers. Any product that may be evaluated in this article, or claim that may be made by its manufacturer, is not guaranteed or endorsed by the publisher.

frontiers in Energy Research

ORIGINAL RESEARCH
published: 08 December 2021
doi: 10.3389/fenrg.2021.764897

Scheme Design and Data Analysis of Critical Physical Experiment for Hexagonal Casing Type Fuel Reactor

Wang Lianjie, Wei Yanqin, Lou Lei and Huang Shien*

Science and Technology on Reactor System Design Technology Laboratory, Nuclear Power Institute of China, Chengdu, China

Based on the requirement of Hexagonal Casing Type Fuel Reactor (HCTFR) nuclear design and the critical physical experiment design method introduced by a single factor, 11 core critical physical experiments are proposed to validate the calculation accuracy and reliability of the nuclear design code CPLEV2. The experiment loading scheme fully takes into account the various components and more than one irradiate hole in the HCTFR core, which is used as critical physical experiment schemes successfully. According to the critical physical experiment data, the reactivity calculation deviations of all critical physical experiments are within ±1.0%. The validation results show that the nuclear design code CPLEV2 has high calculation accuracy and reliability for the core of hexagonal casing type fuel, and it can be used for HCTFR nuclear design.

Keywords: hexagonal casing type fuel reactor (HCTFR), critical physical experiment, nuclear design code, experiment schemes, code validation

OPEN ACCESS

Edited by:
Tengfei Zhang,
Shanghai Jiao Tong University, China

Reviewed by:
Xiang Wang,
Harbin Engineering University, China
Wenbin Wu,
Sun Yat-sen University, China
Zeguang Li,
Tsinghua University, China

****Correspondence:***
Wang Lianjie
mcd2264@126.com

Specialty section:
This article was submitted to Nuclear Energy, a section of the journal Frontiers in Energy Research

Received: *26 August 2021*
Accepted: *05 November 2021*
Published: *08 December 2021*

Citation:
Lianjie W, Yanqin W, Lei L and Shien H (2021) Scheme Design and Data Analysis of Critical Physical Experiment for Hexagonal Casing Type Fuel Reactor. Front. Energy Res. 9:764897. doi: 10.3389/fenrg.2021.764897

1 INTRODUCTION

The nuclear design of Hexagonal Casing Type Fuel Reactor (HCTFR) adopted nuclear design program CPLEV2, which is a specific nuclear design code of the test reactor. As the hexagonal casing fuel core, irradiate hole scheme, fuel assembly, and control rod assembly of HCTFR are different from those of the existing reactor (Xu et al., 1990; Liu et al., 2000; Tang et al., 2011), it is necessary to carry out the critical physical experiment to test the calculation accuracy and reliability of nuclear design code CPLEV2 which has been applied to the design of HCTFR (Xie, 1994). The critical physical experiment of HCTFR included critical mass measurement, critical rod position measurement, shutdown depth measurement, and differential and integral value measurement of control rods.

According to the content of the critical physical experiment, in this paper 11 core critical physical experiment schemes and 2 supplemental schemes are proposed to validate the calculation accuracy and reliability of the nuclear design program CPLEV2. The validation results show that CPLEV2 has high calculation accuracy and reliability for the core of HCTFR, and it can be used for the nuclear design of HCTFR.

2 NUCLEAR DESIGN PROGRAM

The calculation of the core critical physical experiment used program CELL and CPLEV2, which constitute a two-step calculation framework.

CELL is a code for calculating the parameters of the few-group cross section of layered ring assembly. After calculating the effective absorption cross section of the resonance energy region and

TABLE 1 | Assembly type design in the experiment schemes.

Assembly type	Scheme number										
	1	2	3	4	5	6	7	8	9	10-1	10-2
Fuel assembly	√	√	√	√	√	√	√	√	√	√	√
Water reflector	√	√	√	√	√	√	√	√	√	√	√
Beryllium assembly (outside the active area)	×	√	×	√	×	√	√	√	√	√	√
Beryllium assembly (in active area)	×	×	√	√	×	×	√	√	√	√	√
Aluminum assembly	×	×	×	×	√	√	×	×	√	√	√
Ag–In–Cd control rod[a]	×	×	×	×	×	×	√	√	√	√	√
Target assembly	×	×	×	×	×	×	×	√	×	×	×
Loop (water)	×	×	×	×	×	×	×	×	×	√	×
Loop (air)	×	×	×	×	×	×	×	×	×	×	√

Note:
[a]*indicates whether the core contained Ag–In–Cd control rods in critical state.*

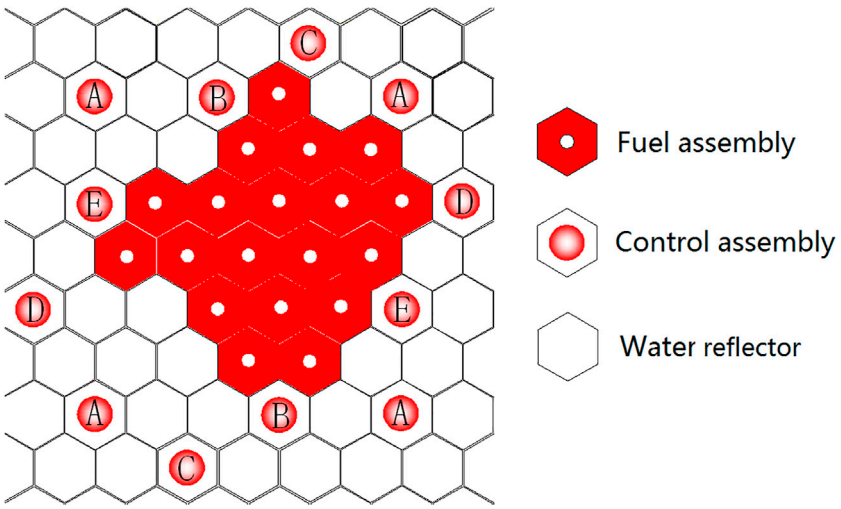

FIGURE 1 | Layout of core and control rods in Scheme 1 (layout and grouping of type 1 control rods).

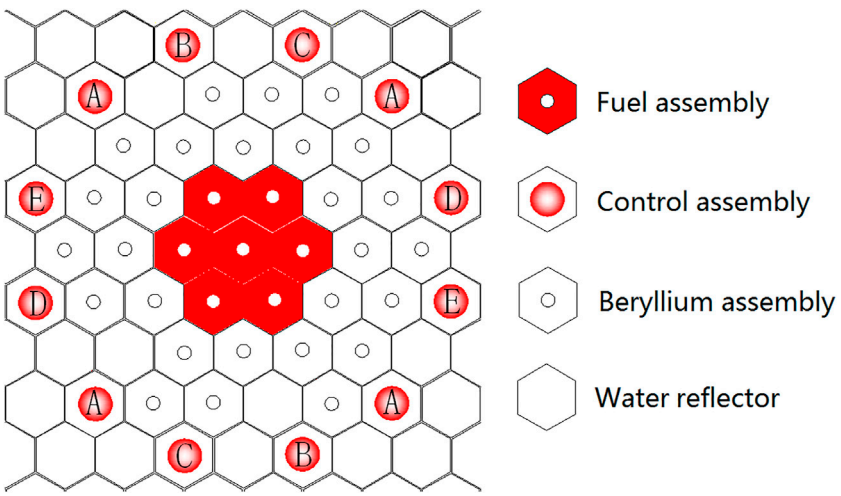

FIGURE 2 | Layout of core and control rods in Scheme 2 (layout and grouping of type 2 control rods).

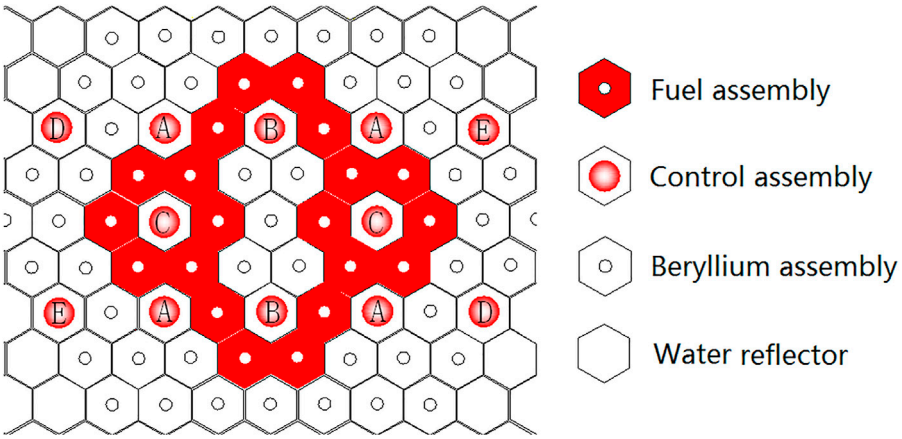

FIGURE 3 | Layout of core and control rods in Scheme 7 (layout and grouping of type 3 control rods).

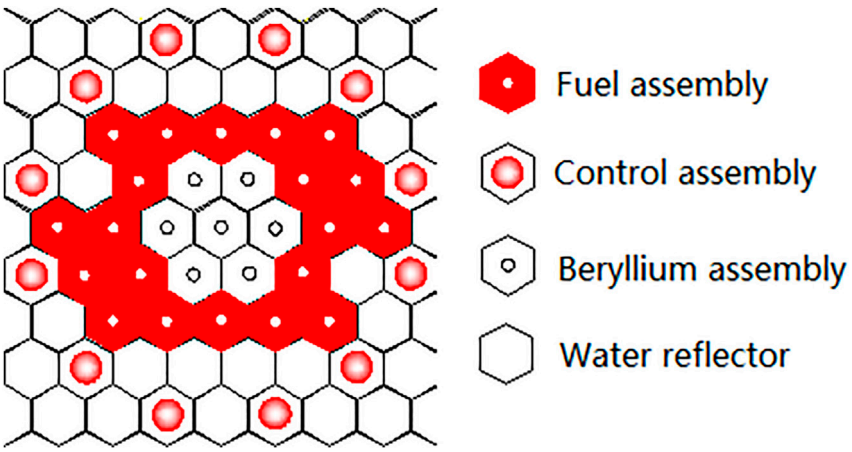

FIGURE 4 | Core arrangement of Scheme 3.

the thermal group cross section of temperature interpolation, the few-group micro or macro cross-section parameters of each nuclide are calculated, and the multigroup neutron integral transport equation is solved by the collision probability method. CELL can be used not only to calculate the few group cross-section parameters of fuel assembly and strong absorber assembly but also to calculate the few group constants of test loop or test fuel assembly.

CPLEV2 is a three-dimensional multigroup fuel management code based on the fine mesh finite difference method, which has both core fuel management calculation function and test loop calculation function. CPLEV2 can be used to calculate the core refueling and give the radial and axial power peak factors, core power density distribution, neutron flux distribution, the remaining amount of important nuclides at each burning time, the differential and integral values of control rods, and the effective delayed neutron yield. With multi-loop calculation function, CPLEV2 can give the power distribution and flux distribution in the test loop, as well as the fuel consumption of test fuel assembly at each fuel consumption moment.

3 SCHEME DESIGN OF CRITICAL PHYSICAL EXPERIMENT

The structure and materials of core components such as fuel assembly, beryllium assembly, aluminum assembly, control rod assembly (including absorber, follower and connecting section) and target assembly, and core water quality should be consistent with HCTFR.

Considering the experiment requirements and fuel manufacturing problems, it was determined that no more than 20 fuel assemblies should be used in the critical physical experiment of HCTFR. Considering the positional relationship between control rod assemblies, target assemblies, aluminum assemblies, beryllium assemblies, and fuel assemblies in the

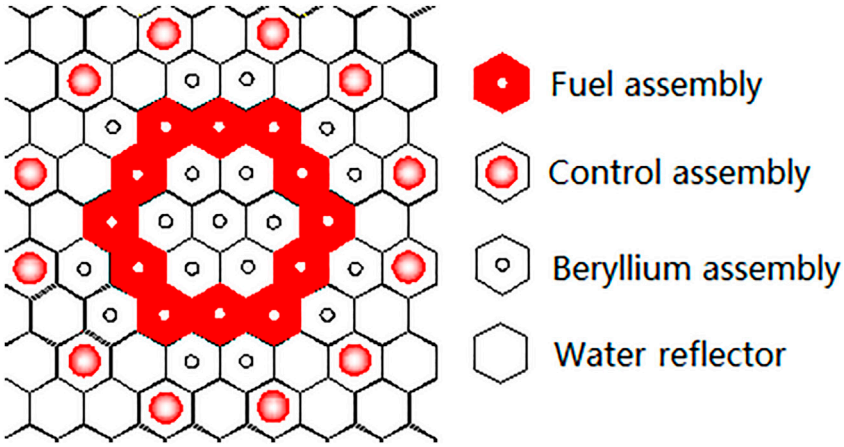

FIGURE 5 | Core arrangement of Scheme 4.

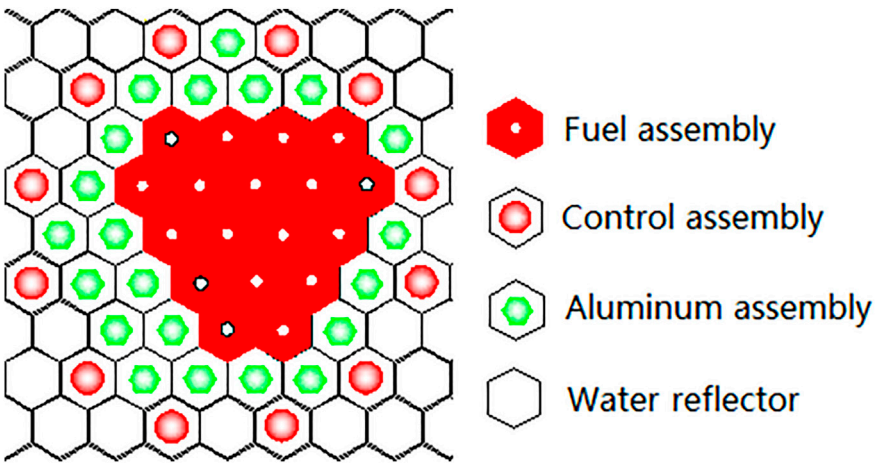

FIGURE 6 | Core arrangement of Scheme 5.

actual reactor core, 11 critical physical experiment schemes have been put forward, including 20 fuel assemblies, 72 aluminum assemblies, 47 beryllium assemblies, 4 target assemblies, and 12 control rod assemblies.

3.1 Assembly type design in the critical physical experiment

According to the principle of single-factor introduction, each assembly type was introduced one by one to form a series of critical physical experiment schemes, as shown in **Table 1**. All critical physical experiment schemes were generally divided into two categories. Scheme 1~Scheme 6 were critical mass measurement schemes; that is, the core reached critical under the state of all control rods outall control rods out. Scheme 7~Scheme 10-2 were critical rod position measurement schemes; that is, some control rods are not fully lifted out of the core when the core was critical.

3.2 Control rod layout and grouping design

Considering the critical experiment operation process, the control rod position in each experiment scheme should be kept as fixed as possible to simplify the experiment process. However, in the design it was found that the size of the active area in each experiment scheme was quite different, and the single control rod position and grouping design could not meet the reactivity control requirements.

According to the calculation and analysis, the control rod arrangement and grouping of all schemes were divided into three categories: the first type is shown in **Figure 1**, which was applicable to Scheme 1; the second type is shown in **Figure 2**, which was applicable to Schemes 2–6; and the third type is shown in **Figure 3**, which was applicable to Scheme 7~Scheme 10-2.

In Scheme 1, the core only contained fuel assemblies and the water reflector, and the active area of the core was smallest in size. If the second type control rod arrangement and grouping were arranged in Scheme 1, the value of rods would be too small to play

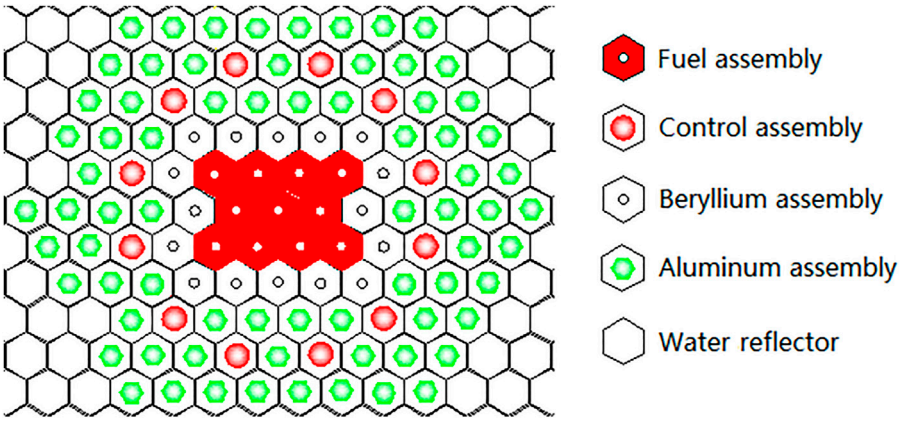

FIGURE 7 | Core arrangement of Scheme 6.

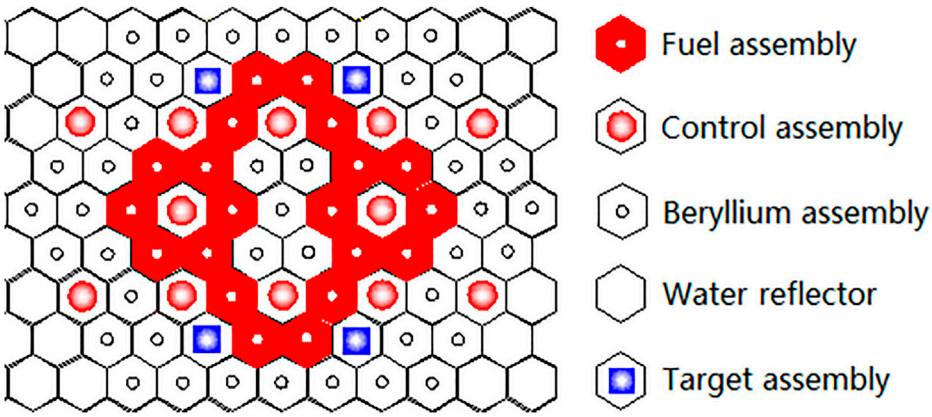

FIGURE 8 | Core arrangement of Scheme 8.

the role of critical safety supervision. Scheme 2~Scheme 6 adopted the second type control rod arrangement and grouping to meet the reactivity control requirements. The sizes of the core active area in Scheme 7~Scheme 10-2 were further increased, and the arrangement and grouping of control rods of the first and second types could no longer meet the reactivity control requirements. Therefore, all critical experiment schemes were divided into the above three categories, which not only simplified the arrangement and grouping of control rods but also met the reactivity control requirements of each experiment scheme.

3.3 Experiment schemes and fine-tuning strategy

3.3.1 Scheme 1

Figure 1 shows the core layout and control rod grouping in Scheme 1. The core contained fuel assemblies and water reflectors. There were 12 control rod assemblies in the core, which were divided into five groups, A~E. There were four safety rods in the A rod group and two rods in the B, C, D, and E rod groups.

In this test, 19 fuel assemblies were loaded, and the k_{eff} of all control rods out was 1.0016. The fuel assemblies could be adjusted when the calculation deviated from the actual situation. By adjusting the position of the fuel assemblies radially and increasing or decreasing fuel assemblies, the k_{eff} of the core could be increased or decreased, thus making the core critical.

3.3.2 Scheme 2

Figure 2 shows the core arrangement and control rod grouping in Scheme 2. The core contained fuel assemblies, beryllium assemblies (outside the active area) and water reflector. There were 12 control rod assemblies in the core, the positions of which were different from those in Scheme 1, but the grouping situation were the same.

In this test, 7 fuel assemblies and 27 beryllium assemblies were loaded, and the k_{eff} of all control rods out was 1.0002. When the calculation deviated from the actual situation, the beryllium assemblies could be adjusted. By adjusting the position of

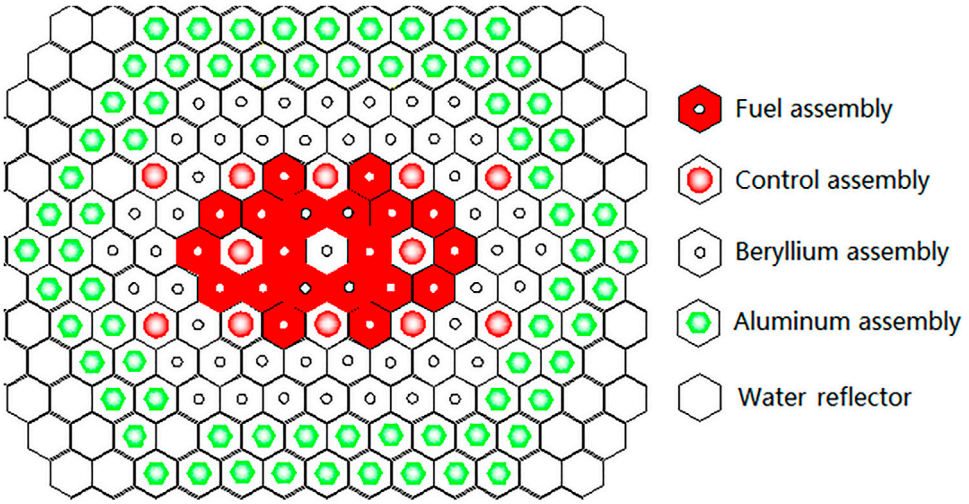

FIGURE 9 | Core arrangement of Scheme 9.

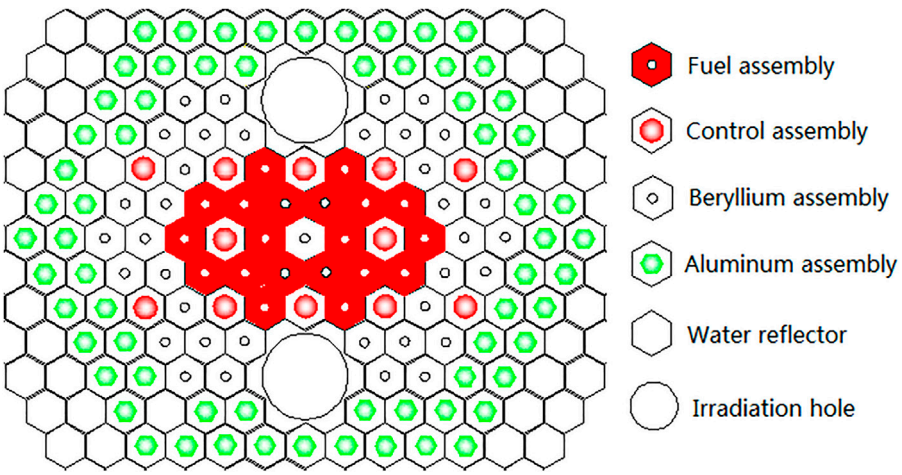

FIGURE 10 | Core arrangement of Scheme 10-1 and Scheme 10-2.

beryllium assemblies radially and increasing or decreasing beryllium assemblies, the k_{eff} of the core could be increased or decreased, thus making the core critical.

3.3.3 Scheme 3

Figure 4 shows the core arrangement of Scheme 3. The core contained fuel assemblies, beryllium assemblies (in the active area), and water reflector. The arrangement of control rod assemblies in the core was the same as Scheme 2.

In this test, 20 fuel assemblies and 7 beryllium assemblies were loaded, and the k_{eff} of the full lifting rod was 1.0003. When the calculation deviated from the actual value, the assemblies could be adjusted. By adjusting the position of the fuel assemblies radially, the k_{eff} of the core could be increased or decreased, thus making the core critical.

3.3.4 Scheme 4

Figure 5 shows the core arrangement of Scheme 4. The core contained fuel assemblies, beryllium assemblies (inside the active area), beryllium assemblies (outside the active area), and water reflector. The arrangement of control rod assemblies in the core was the same as that of Scheme 2.

In this test, 12 fuel assemblies and 18 beryllium assemblies (including 7 beryllium assemblies in the active area) were loaded, and the k_{eff} of all control rods out was 1.0031. When the calculation deviated from the actual situation, the beryllium assemblies could be adjusted. By adjusting the position of beryllium assemblies radially and increasing or decreasing beryllium assemblies, the k_{eff} of the core could be increased or decreased, thus making the core critical.

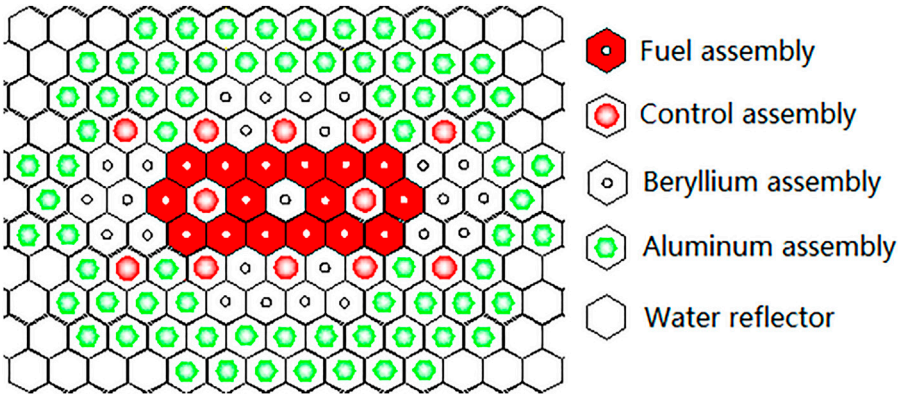

FIGURE 11 | Core arrangement of Scheme 9A.

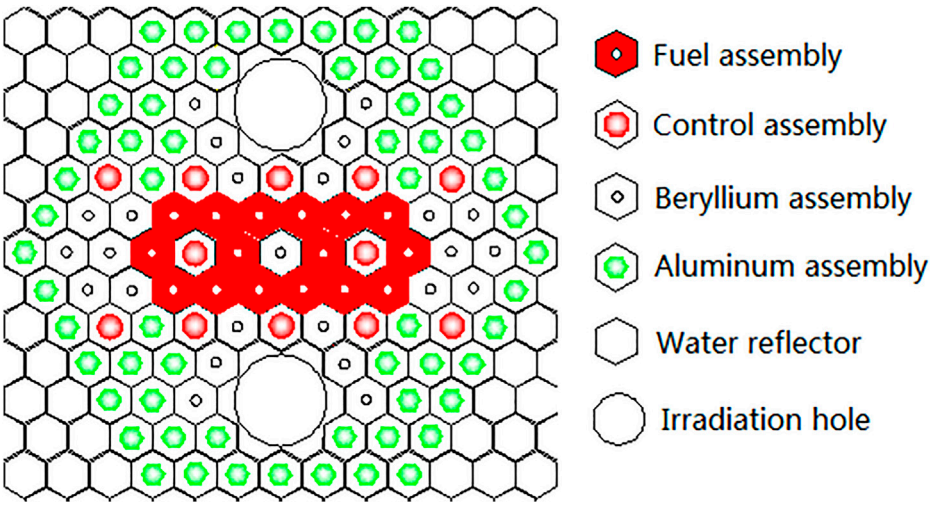

FIGURE 12 | Core arrangement of Scheme 10A.

3.3.5 Scheme 5

Figure 6 shows the core arrangement of Scheme 5. The core contained fuel assemblies, aluminum assemblies, and water reflector. The arrangement of control rod assemblies in the core was the same as that of Scheme 2.

In this test, 18 fuel assemblies and 21 aluminum assemblies were loaded, and the k_{eff} of all control rods out was 1.0000. When there was a deviation between calculation and practice, the core k_{eff} could be increased or decreased by adjusting the position of fuel assemblies and aluminum assemblies radially, increasing or decreasing aluminum assemblies and fuel assemblies, thus making the core critical.

3.3.6 Scheme 6

Figure 7 shows the core arrangement of Scheme 6. The core contained fuel assemblies, beryllium assemblies, aluminum assemblies, and water reflector. The arrangement of control rod assemblies in the core was the same as that of Scheme 2.

In this test, 11 fuel assemblies, 16 beryllium assemblies, and 72 aluminum assemblies were loaded, and the k_{eff} of all control rods out was 1.0015. When there was a deviation between calculation and practice, the k_{eff} of the core could be increased or decreased by adjusting the position of aluminum and beryllium assemblies radially, increasing or decreasing aluminum and beryllium assemblies, thus making the core critical.

3.3.7 Scheme 7

Figure 3 shows the core layout and control rod grouping in Scheme 7. The core contained fuel assemblies, beryllium assemblies (inside the active area), beryllium assemblies (outside the active area), water reflector, and Ag–In–Cd control rods. There were 12 control rod assemblies in the core, which were divided into five groups A~E. There were

TABLE 2 | k_{eff} verification calculation results of critical mass measurement test.

Scheme number	Experimental value	Calculation result	Relative deviation (%)
1	1.00000	1.00294	0.3
2	1.00173	0.99752	–0.4
3	1.00028	0.99262	–0.8
4	1.00039	0.99528	–0.5
5	1.00004	1.00071	0.1
6	1.00014	0.98967	–1.0

TABLE 3 | k_{eff} verification calculation results of core critical rod position.

Scheme number	Experimental value	Calculation result	Relative deviation (%)
7	1.00000	1.00207	0.2
8	1.00000	0.99674	–0.3
9	1.00000	1.00780	0.8
9A	1.00000	1.00357	0.4
10-1	1.00000	1.00414	0.4
10-2	1.00000	1.00278	0.3
10A	1.00000	0.99979	0.0

TABLE 4 | Calculation results of integral value of control rods.

Scheme number	Tested rod or rod group	Measurement interval (%)	Experimental value (pcm)	Calculation result (pcm)	Relative deviation (%)
7	B1	0~33.5	3,626	3,572	–1.5
	B2	0~33.6	3,626	3,580	–1.3
	B	0~20.35	3,736	3,896	4.3
	C1	0~35.8	3,650	3,565	–2.3
	C2	0~34.8	3,658	3,456	–5.5
	C	0~20.25	3,652	3,567	–2.3
8	B1	0~100	4,910	5,387	9.7
	B2	0~100	4,937	5,387	9.1
	B	0~100	10,688	11,753	10.0
	C1	0~100	6,646	6,990	5.2
	C2	0~100	6,571	6,985	6.3
	C	0~59.6	11,753	11,592	–1.4
9A	B1	0~100	4,260	4,634	8.8
	B2	0~100	4,157	4,631	11.4
	B	0~100	8,625	9,349	8.4
	C1	0~100	6,467	6,509	0.7
	C2	0~100	6,564	6,516	–0.7
	C	0~100	12,374	12,579	1.7
10A	B1	0~100	3,979	4,685	17.8
	B2	0~100	3,862	4,682	21.2
	B	0~100	7,792	9,390	20.5
	C1	0~100	7,471	6,587	–11.8
	C2	0~100	7,558	6,590	–12.8
	C	0~100	12,365	12,612	2.0

four safety rods in the A rod group and two rods in the B, C, D, and E rod groups.

In this test, 20 fuel assemblies and 47 beryllium assemblies were loaded, among which 5 beryllium assemblies were loaded in the active area. The k_{eff} of all control rods in was 0.8451, and that of all control rods out was 1.2226. Scheme 7 would measure the critical rod position, control rod value, and shutdown depth.

3.3.8 Scheme 8

Figure 8 shows the core arrangement of scheme 8. The core contained fuel assemblies, beryllium assemblies (inside the active area), beryllium assemblies (outside the active area), water reflector, Ag–In–Cd control rods, and target assemblies. The arrangement of control rod assemblies in the core was the same as that of Scheme 7.

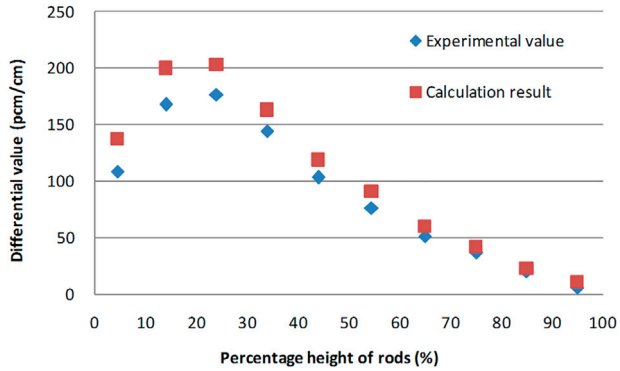

FIGURE 13 | Differential value curve of B rod group (Scheme 8).

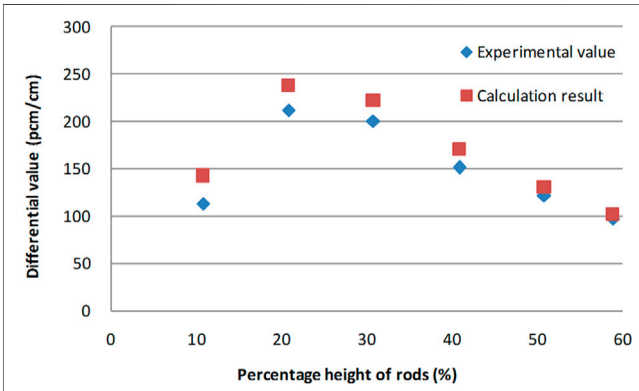

FIGURE 14 | Differential value curve of C rod group (Scheme 8).

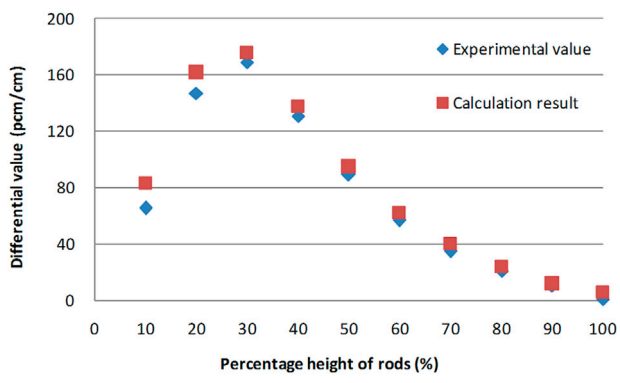

FIGURE 15 | Differential value curve of B rod group (Scheme 9A).

This test was loaded with 20 fuel assemblies, 43 beryllium assemblies (including 5 beryllium assemblies in the active area), and 4 target assemblies. The k_{eff} of all control rods in was 0.8026, and that of all control rods out was 1.1352. Scheme 8 would measure the critical rod position, control rod value, and shutdown depth.

3.3.9 Scheme 9

Figure 9 shows the core arrangement of scheme 9. The core contained fuel assemblies, beryllium assemblies, aluminum assemblies, water reflector, and Ag–In–Cd control rod assemblies. The arrangement of control rod assemblies in the core was the same as that of Scheme 7.

This test was loaded with 20 fuel assemblies, 47 beryllium assemblies (including 1 beryllium assembly in the active area), and 71 aluminum assemblies. The k_{eff} of all control rods in was 0.8836, and that of all control rods out was 1.2137. Scheme 9 would measure the critical rod position, control rod value, and shutdown depth.

3.3.10 Schemes 10-1 and 10-2

Figure 10 shows the core layout of Scheme 10-1. The core contained fuel assemblies, beryllium assemblies, aluminum assemblies, water reflector, Ag–In–Cd control rod assemblies, and irradiate holes, and the irradiate holes were filled with water. The arrangement of control rod assemblies in the core was the same as that of Scheme 7.

This test was loaded with 20 fuel assemblies, 37 beryllium assemblies (including 1 beryllium assembly in the active area) and 67 aluminum assemblies. The k_{eff} of all control rods in was 0.8684, and that of the full lifting rod was 1.1808. Scheme 10-1 would measure the critical rod position, control rod value, and shutdown depth.

Scheme 10-2 had the same core layout as Scheme 10-1, with the only difference being that the irradiate holes were filled with air.

The k_{eff} of all control rods in was 0.8721, and that of the full lifting rod was 1.1878. Scheme 10-2 would measure the critical rod position, control rod value, and shutdown depth.

3.3.11 Supplemental experiment schemes

During the critical physical experiment, it was found that full height differential and integral value measurement of some control rods could not be carried out because the loading schemes had large excess reactivity. According to the specific situation, two schemes of critical rod position measurement with less excess reactivity were supplemented by reducing the number of assemblies of Scheme 9 and Scheme 10-1, which were named as Scheme 9A and Scheme 10A.

Figure 11 shows the core arrangement of Scheme 9A. The core contained 16 fuel assemblies, 25 beryllium assemblies (including 1 beryllium assembly in the active area), and 71 aluminum assemblies. The k_{eff} of all control rods in was 0.8118, and that of all control rods out was 1.0955. Scheme 9A would measure the critical rod position, control rod value, and shutdown depth.

Figure 12 shows the core arrangement of Scheme 10A. The core contained 16 fuel assemblies, 25 beryllium assemblies (including 1 beryllium assembly in the active area), and 60 aluminum assemblies. The k_{eff} of all control rods in was 0.8055, and that of all control rods out was 1.0920. Scheme 10A would measure the critical rod position, control rod value, and shutdown depth.

TABLE 5 | Calculation results of shutdown depth.

Scheme number	Experimental value (pcm)	Calculation result (pcm)	Relative deviation (%)
7	−17,748	−18,953	6.8
8	−25,176	−24,952	−0.9
9	−16,070	−13,598	−15.4
9A	−27,694	−23,532	−15.0
10-1	−17,904	−16,004	−10.6
10-2	−17,797	−16,331	−8.2
10A	−26,193	−24,550	−6.3

4 VERIFICATION AND ANALYSIS OF CRITICAL MASS MEASUREMENT SCHEMES

Table 2 shows the verification calculation results of core k_{eff} for critical mass measurement schemes. It could be seen that the deviation of verification calculation in Scheme 1 is only 0.3%, which is in good agreement with the experimental result, which indicates that the nuclear design code has high accuracy in calculating the core of pure fuel assemblies. The calculation deviations of Schemes 2~4 are all within 0.8%, and they are all negative deviations, which indicates that the nuclear design code has higher accuracy in calculating the cores containing beryllium assemblies. Scheme 5 used fuel assemblies and aluminum assemblies, and the core k_{eff} calculation deviation is small and positive, which indicates that the aluminum assembly calculation model has high calculation accuracy. Scheme 6 used fuel assemblies, beryllium assemblies, and a large number of aluminum assemblies, and the core k_{eff} calculation deviation is negative and the absolute value is about 1.0%, which still can be accepted.

5 VERIFICATION AND ANALYSIS OF ZERO POWER PHYSICS TEST

5.1 Critical rod position k_{eff}

Table 3 shows k_{eff} verification calculation results of the core critical rod position. It could be seen that the calculation deviations of Scheme 7~Scheme 10 are within ±0.8%, which are in good agreement with the test results and indicate that the nuclear design code has high accuracy in calculating the critical rod positions of various core layout schemes.

5.2 Integral value of control rods

Table 4 shows the calculation results of the cold integral value of single control rod and rod groups with different schemes. It can be seen that the calibration deviation of the control rod integral value is within 20% except for B2 rod and B rod groups in Scheme 10A.

5.3 Differential value of control rods

Figures 13–15 and **Supplementary Figures S1–S3** show the cold differential value curves of different rod groups with different schemes. It can be seen that the calculated values of differential value curves of control rods in other cases are in good agreement with the experimental values except for the calculated values in Scheme 8.

5.4 Shutdown depth

Table 5 shows the calculation results of cold shutdown depth of each scheme. It can be seen that the calculated deviations of all schemes are within 20%, which is in good agreement with the experimental values.

6 CONCLUSION

Based on the requirement of the core critical physical experiment of HCTFR, 11 core critical physical experiment schemes and 2 supplemental schemes were proposed to validate the calculation accuracy and reliability of the nuclear design code CPLEV2. According to the critical physical experiment data, the reactivity calculation deviations of all critical rod position measurement schemes are within ±1.0%. The validation results show that the nuclear design code CPLEV2 has high calculation accuracy and reliability for the core of hexagonal casing type fuel and it can be used for HCTFR nuclear design.

DATA AVAILABILITY STATEMENT

The original contributions presented in the study are included in the article/**Supplementary Material**; further inquiries can be directed to the corresponding author.

AUTHOR CONTRIBUTIONS

WL: conceptualization, methodology, and software. WY: methodology, visualization, and investigation. LL: methodology, visualization, and investigation. HS: investigation, funding acquisition, and supervision.

SUPPLEMENTARY MATERIAL

The Supplementary Material for this article can be found online at: https://www.frontiersin.org/articles/10.3389/fenrg.2021.764897/full#supplementary-material

Supplementary Figure S1 | Differential value curve of C rod group (scheme 9A).

Supplementary Figure S2 | Differential value curve of B rod group (scheme 10A).

Supplementary Figure S3 | Differential value curve of C rod group (scheme 10A).

REFERENCES

Liu, J., Yao, D., Zeng, D., and Wang, Y. (2000). Low-enriched Core Nuclear Design of HFETR, Compilation of Literatures on the Twenty –Year Operation of HFETR (1980-2000). Shanghai: Nuclear Power Institute of China.

Tang, X., Wang, G., and Wu, Q. (2011). The Zero Power Physical Experiment of the HFETR LEU Core, Compilation of Literatures on the Thirty –Year Operation of HFETR (1980-2010). Shanghai: Nuclear Power Institute of China.

Xie, Z. (1994). Physical Analysis of Nuclear Reactor Property [M]. Beijing: Atomic Energy Press, 68–71.

Xu, J., Xu, H., Li, Z., Hu, Z., Zhao, J., Gu, Y., et al. (1990). The Physical Design and Calculation of HFETR, Compilation of Literatures on the First Ten –Year Operation of HFETR (1980-1990). Shanghai: Nuclear Power Institute of China.

Conflict of Interest: The authors declare that the research was conducted in the absence of any commercial or financial relationships that could be construed as a potential conflict of interest.

frontiers in Energy Research

ORIGINAL RESEARCH
published: 08 December 2021
doi: 10.3389/fenrg.2021.779261

Treatments of Thermal Neutron Scattering Data and Their Effect on Neutronics Calculations

*Tiejun Zu *, Yongqiang Tang, Zhanpeng Huang, Shuai Qin, Jie Li, Qingming He, Liangzhi Cao and Hongchun Wu*

School of Nuclear Science and Technology, Xi'an Jiaotong University, Xi'an, China

In the conventional method to generate thermal scattering cross section of moderator materials, only one of the coherent elastic scattering and incoherent elastic scattering is considered in neutronics calculations. For the inelastic scattering, fixed incident energy grid is used in the nuclear data processing codes. The multipoint linearization method is used to refine the incident energy grid for inelastic scattering. We select ZrH_x (zirconium hydride) as an example to analyze the effects of the above described treatments on the reactivity of several critical benchmarks. The numerical results show that the incident energy grid has an obvious effect on the effective multiplication factor (k_{eff}) of the analyzed reactors; simultaneously considering the coherent and incoherent elastic scattering also affects k_{eff} by tens of pcm.

Keywords: thermal scattering cross section, nuclear data processing, inelastic scattering, mixed elastic scattering, NECP-Atlas

OPEN ACCESS

Edited by:
Jun Wang,
University of Wisconsin-Madison, United States

Reviewed by:
Shichang Liu,
North China Electric Power University, China
Mohamad Hairie Rabir,
Malaysian Nuclear Agency, Malaysia
Ding She,
Tsinghua University, China
Prabhatasree Goel,
Bhabha Atomic Research Centre (BARC), India

****Correspondence:***
Tiejun Zu
tiejun@mail.xjtu.edu.cn

Specialty section:
This article was submitted to Nuclear Energy, a section of the journal Frontiers in Energy Research

Received: *18 September 2021*
Accepted: *15 October 2021*
Published: *08 December 2021*

Citation:
Zu T, Tang Y, Huang Z, Qin S, Li J, He Q, Cao L and Wu H (2021) Treatments of Thermal Neutron Scattering Data and Their Effect on Neutronics Calculations. Front. Energy Res. 9:779261. doi: 10.3389/fenrg.2021.779261

INTRODUCTION

In the neutronics analysis of nuclear reactors, accurate prediction of the thermal neutron distribution has an important effect on behaviors of the reactors. It is necessary to provide accurate thermal neutron scattering cross sections for neutronics codes to simulate the neutron thermalization. In the thermal energy region, the neutron scattering is sensitive to the atomic structure and motion in a moderator. In the Evaluated Nuclear Data Files (ENDF), the thermal scattering law (TSL) data are provided for some moderator materials to describe the thermal scattering of the bound atoms. Currently, individual TSL data files are contained in the major ENDFs, such as ENDF/B-VIII.0 (Brown et al., 2018), JEFF-3.3 (Plompen et al., 2020), and JENDL-4.0 (Shibata et al., 2011). The modern ENDFs adopt a common format, namely, ENDF-6 (Trkov et al., 2012), to store the evaluated nuclear data. In ENDF-6 format libraries, a specific file (MF) is used to store a certain data type, and among the files, File 7 (MF = 7) contains the TSL data for moderator materials.

Although several efforts have been made in Monte Carlo codes to directly use the TSL data (Čerba et al., 2013; Liu et al., 2016; Hart and Maldonado, 2017), for most cases, the TSL data should be first processed to calculate total scattering cross section and double-differential cross section and then converted to a specific format required by neutronics codes. For Monte Carlo codes, the obtained cross sections are converted to tabular data representing the energy and angle distributions of the secondary neutrons and stored in the ACE (A Compact ENDF) (Conlin and Romano, 2019) format library, whereas for deterministic-based codes adopting the multigroup approximation, the tabular data are further converted into multigroup cross sections and scattering matrices. The nuclear data processing codes, such as NJOY (Macfarlane et al., 2017) and NECP-Atlas (Zu et al., 2019), are designated for the above processing.

In the ENDF-6 format, the TSL data for elastic and inelastic scattering are provided in File 7 with different reaction number (MT), MT = 2 for elastic scattering and MT = 4 for inelastic scattering. According to the theory to generate the TSL data, there are two components in the elastic scattering, namely, coherent elastic scattering and incoherent elastic scattering (Squires, 2012). But, only one elastic scattering mode is given in the ENDF for a certain material, and the other one is ignored. In other words, the coherent and incoherent elastic scatterings are not simultaneously provided for a material. For example, the coherent elastic scattering is given for metal beryllium, and incoherent elastic scattering is given for the hydrogen bound in zirconium hydride (ZrH_x). The nuclear data processing codes just calculate corresponding elastic scattering cross section based on the data given in the ENDF. No works have been reported to show the effect of this treatment on neutronics calculations.

As for inelastic scattering, the ENDF provides the so-called $S(\alpha, \beta)$ data. The $S(\alpha, \beta)$ data are converted to a discrete tabular data for Monte Carlo calculations. The work by Conlin et al. (2012) showed that this representation can introduce noticeable deficiencies for differential calculations and recommended adopting a continuous $S(\alpha, \beta)$ table to represent the secondary energy and angle distributions. In the work by Hartling et al. (2018), it was found that in NJOY the inelastic scattering cross section is calculated on a fixed incident energy grid, and it has obvious effect on the Monte Carlo simulations. To solve this problem, an adaptive incident energy grid was implemented in the nuclear processing code NDEX (Wormald et al., 2020).

Recently, systematic researches have been done to calculate TSL data and thermal scattering cross sections in the nuclear data processing code NECP-Atlas. An advanced TSL data calculation module, called sab_calc (Tang et al., 2021), was developed. Using this module, accurate TSL data has been obtained for some materials, for example Be, ZrH_x (Zu et al., 2021). The TSL data can be directly used by the therm_calc module (Zu et al., 2019) to calculate total thermal scattering cross section and double-differential cross section. In the present work, we will investigate the effects of the aforementioned treatments for thermal neutron scattering data on the neutronics calculations. The analysis is carried out with the Monte Caro code NECP-MCX (He et al., 2021).

GENRATION OF THERMAL SCATTERING CROSS SECTION

Coherent Elastic Scattering Cross Section

According to the ENDF-6 format, the double-differential cross section of coherent elastic scattering is calculated as follows:

$$\sigma\left(E \to E', \mu_{\mathrm{LAB}}\right) = \frac{1}{E} S(E,T)\delta\left(\mu_{\mathrm{LAB}} - \mu_i\right)\delta\left(E - E'\right) \tag{1}$$

where E is incident neutron energy; E' is secondary neutron energy; T is temperature; μ_{LAB} is the scattering cosine in the laboratory reference system; $S(E,T)$ and μ_i are obtained as follows:

$$S(E,T) = \sum_{i=1}^{E_i < E} S_i(T) \tag{2}$$

$$\mu_i = 1 - \frac{2E_i}{E}. \tag{3}$$

In **Eqs 2**, **3**, E_i is the Bragg edges. The variable $S_i(T)$ is not given in ENDFs, but $S(E,T)$ is actually provided for each E_i. The total scattering cross section can be calculated as follows:

$$\sigma(E) = \frac{1}{E} S(E,T)/2\pi \tag{4}$$

In the ACE format library, the tabular data for coherent elastic scattering consists of the Bragg edges, and corresponding $S(E,T)$ are stored in the library.

Incoherent Elastic Scattering Cross Section

The double-differential cross section of coherent elastic scattering is calculated as follows:

$$\sigma\left(E \to E', \mu_{\mathrm{LAB}}\right) = \frac{\sigma_{\mathrm{b}}}{4\pi} e^{2EW(T)\left(1-\mu_{\mathrm{LAB}}\right)}\delta\left(E - E'\right) \tag{5}$$

where σ_{b} is the characteristic-bound cross section; $W(T)$ is the Debye–Waller coefficient for temperature T. These two variables are given in ENDF.

In the ACE format library, the tabular data for incoherent scattering contain the energy grid, total scattering cross section, and outgoing angular distribution. The total incoherent scattering cross section is obtained as follows:

$$\sigma(E) = \frac{\sigma_{\mathrm{b}}}{2}\left(\frac{1 - \mathrm{e}^{-4W(T)E}}{2W(T)E}\right) \tag{6}$$

For the angular distribution, the equally probable discrete cosine is stored in the library, which is calculated as follows:

$$\begin{aligned}\bar{\mu}_i(E \to E) = \frac{N}{2W(T)E}\Big[&\mathrm{e}^{-2W(T)E\left(1-\mu_i\right)}\left(2W(T)E\mu_i - 1\right)\\ &-\mathrm{e}^{-2W(T)E\left(1-\mu_{i-1}\right)}\left(2W(T)E\mu_{i-1} - 1\right)\Big]/\left(1 - \mathrm{e}^{-4W(T)E}\right)\end{aligned} \tag{7}$$

where N is the number of cosine bins; i is the index of cosine bins; μ_i is calculated as follows:

$$\mu_i = 1 + \frac{1}{2W(T)E}\ln\left[\frac{1 - \mathrm{e}^{-4W(T)E}}{N} + \mathrm{e}^{-4W(T)E\left(1-\mu_{i-1}\right)}\right] \tag{8}$$

with $\mu_0 = -1$.

Inelastic Scattering Cross Section

For inelastic scattering, the double-differential cross section can be calculated using the TSL data provided by ENDF as follows:

$$\sigma\left(E \to E', \mu_{\mathrm{LAB}}\right) = \frac{\sigma_{\mathrm{b}}}{4\pi k_{\mathrm{B}} T}\sqrt{\frac{E'}{E}}\mathrm{e}^{-\beta/2} S(\alpha, \beta, T) \tag{9}$$

where k_{B} is Boltzmann's constant; σ_{b} is the characteristic-bound cross section for the target nuclide; $S(\alpha, \beta, T)$ is given in ENDF for

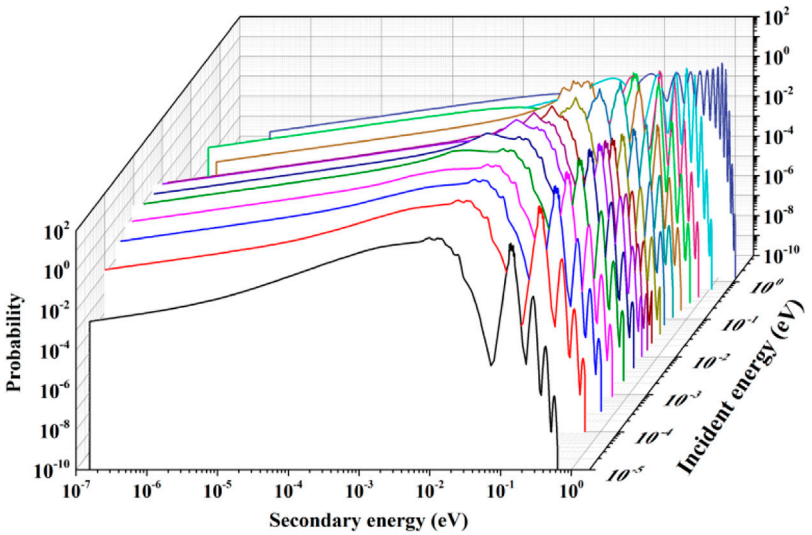

FIGURE 1 | Secondary energy distribution of the inelastic scattering from ZrH_x.

temperature T; α and β are momentum transfer and energy transfer, respectively, which are calculated as follows:

$$\alpha = \frac{E' + E - 2\mu_{\mathrm{LAB}}\sqrt{E'E}}{A_0 k_{\mathrm{B}} T} \tag{10}$$

$$\beta = \frac{E' - E}{k_{\mathrm{B}} T} \tag{11}$$

In the nuclear data processing code, the $S(\alpha, \beta, T)$ data are first used to calculate the double-differential cross sections at a certain incident energy grid according to **Eq. 9**, and then the double-differential cross sections are transferred to tabular data. The tabular data contain the scattering kernel $P(E \rightarrow E')$ representing the probability that the neutron with incident energy E exits with energy E' after scatter and the equally probable discrete cosines for each incident energy. $P(E \rightarrow E')$ is calculated as follows:

$$P\left(E \rightarrow E'\right) = \frac{\sigma\left(E \rightarrow E'\right)}{\sigma(E)} \tag{12}$$

where $\sigma(E \rightarrow E')$ is differential cross section obtained by integrating **Eq. 9** with respect to the outgoing cosine over $[-1, 1]$; $\sigma(E)$ is the total scattering cross section obtained by integrating **Eq. 9** with respect to the outgoing energy and cosine.

In NJOY, an incident energy grid with 118 points is fixed in the source code. As mentioned previously, some works have found that the fixed incident energy grid shows obvious effect on the Monte Carlo simulations. **Figure 1** shows the secondary distribution of the inelastic scattering from ZrH_x. At low incident energy region, the secondary distribution slowly varies with incident energy E, and it seems reasonable to use fixed incident energy grid. However, in the higher energy region, the shapes of the secondary energy distribution show obvious differences for different incident energies. Using the cross section calculated at fixed incident energy grid to interpolate cross sections at other energies will introduce a large error.

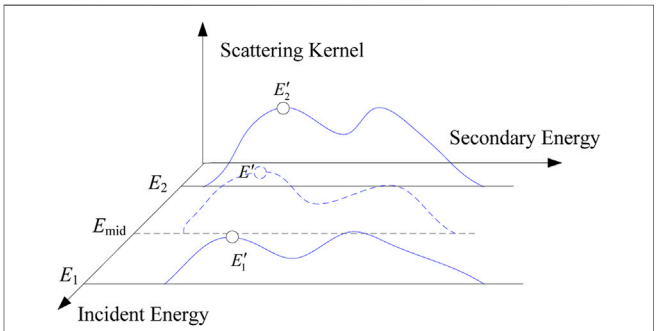

FIGURE 2 | Definition of the secondary energies for multipoint linearization.

In this work, we adopted the multipoint linearization method to refine the incident energy grid as follows. First, an initial incident energy grid is set, which can be selected from the fixed energies in NJOY. For each incident energy, the secondary energy of scattered neutrons is divided into two parts: the down-scattering part and up-scattering part, as shown in **Figure 2**. Several secondary energy points are respectively set in the down-scattering and up-scattering parts to check whether scattering probability can be linearly interpolated between two adjacent incident energies. In each secondary energy part, the set energy points divide the part into different intervals with identical logarithmic width. Therefore, for the down-scattering part, the energy points are determined as follows:

$$E'_{down,M} = \frac{E}{\exp\left(\frac{2\ln\left(E/E'_{\min}\right)}{(N+1)}\right) \cdot M}, \quad M = 1, 2, 3, \cdots, N-1 \tag{13}$$

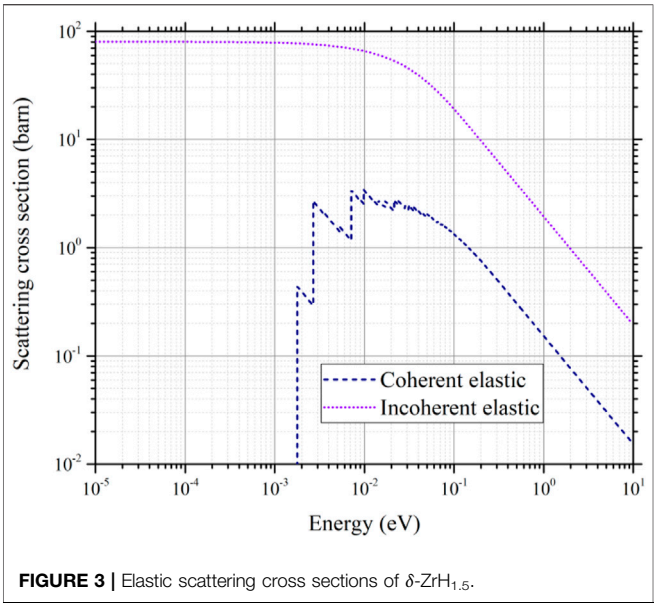

FIGURE 3 | Elastic scattering cross sections of δ-$ZrH_{1.5}$.

where E'_{min} is the minimum secondary energy; N is the total number of energy points added in the down-scattering part and is decided by the users; M is the index of the energy points. Similarly, in the up-scattering part, the energy points are determined as follows:

$$E'_{up,M} = \frac{E}{\exp\left(\frac{2\ln\left(E'_{max}/E\right)}{(N+1)}\right)\cdot M}, \quad M = 1, 2, 3, \cdots, N-1 \tag{14}$$

where E'_{max} is the maximum secondary energy. In addition to the energies determined as **Eqs 13**, **14**, the secondary energy that is equal to the incident energy is also used to check the convergence during the linearization procedure. The linearized procedure is described as follows.

For two adjacent incident energies and their midpoint, the scattering kernel, from incident energy E to each secondary energy E' defined as **Eqs 13**, **14**, is calculated according to **Eqs 13**, **14**. The scattering kernel for the midpoint is calculated again by linearly interpolating as follows:

$$P\left(E_{mid} \to E'\right) = P\left(E_1 \to E'_1\right) + P\left(E' - E'_1\right) \cdot \frac{P\left(E_2 \to E'_2\right) - P\left(E_1 \to E'_1\right)}{E'_2 - E'_1} \tag{15}$$

where E_1 and E_2 are adjacent incident energies; E_{mid} is the midpoint between E_1 and E_2; E'_1, E'_2, and E' are the secondary energy points in the panel for the incident energies E_1, E_2 and E_{mid}, respectively.

If the tolerance between the exact $P(E_{mid} \to E')$ calculated using **Eq. 12** and the one obtained by linear interpolation is less than a preset criterion, it is considered that the scattering kernel can be linearly interpolated. In this case, the E_1 and E_2 will be included in the final grid, and the midpoint will be removed. Otherwise, the midpoint is added to the final incident energy grid, and the interval-halving technique (Cacuci, 2010) is used to subdivide the interval between E_1 and E_2, until $P(E_{mid} \to E')$ can be linearly interpolated between two adjacent incident energies.

TABLE 1 | Bound scattering cross sections for several nuclides.

Nuclides	σ_{coh}	σ_{inc}
H-1	1.7583	80.27
H-2	5.592	2.05
Li-6	0.51	0.46
Li-7	0.619	0.78

RESULTS AND DISCUSSION

We select ZrH_x as an example material to analyze the treatments for thermal scattering data on neutronics calculations. Because the TSL data for coherent elastic scattering are not provided for ZrH_x in the ENDFs, in this work, we calculated these data for ZrH_x by the sab_calc module, which is developed based on the phonon expansion method (Squires, 2012; Wormald and Hawari, 2017). In the calculation of TSL data, the phonon density of states (PDOS) is the fundamental data. In this work, the PDOS of ZrH_x is obtained as described in our previous work (Zu et al., 2021). Besides, the incoherent scattering cross sections can be exactly calculated according to the method described previously, and it was also calculated using the same PDOS and will not be discussed in the following parts.

Coherent Elastic Scattering Cross Section

We calculated the coherent elastic scattering cross sections of hydrogen in ZrH_x at 300 K, based on the PDOS of δ-$ZrH_{1.5}$. The coherent elastics scattering cross sections are shown in **Figure 3**. It can be seen that the coherent scattering cross section is larger than 1 b above the second Bragg energy. Compared with the incoherent scattering cross section, the value is negligible, so the TSL data for coherent scattering are not provided in ENDFs. The reason for the little coherent elastic scattering cross section is explained as follows. According the theory to calculate TSL data, the coherent and incoherent elastic scattering cross sections can be calculated as follows (Tang et al., 2021):

$$\sigma_{el,coh}(E,\mu) = \frac{1}{2k_B T}\sqrt{\frac{E'}{E}}\sigma_{coh} S^0(\alpha,\beta) \tag{16}$$

$$\sigma_{el,inc}(E,\mu) = \frac{1}{2k_B T}\sqrt{\frac{E'}{E}}\sigma_{inc} S^0_s(\alpha,\beta) \tag{17}$$

where σ_{coh} and σ_{inc} are the characteristic-bound coherent cross section and incoherent cross section, which can be searched in the work by Sears (1992); $S^0(\alpha,\beta)$ and $S^0_s(\alpha,\beta)$ are the scattering law, which can be calculated by the LEAPR module in NJOY and sab_calc module in NECP-Atlas.

For hydrogen, the bound coherent cross section is much less than the bound incoherent cross section as listed in **Table 1**,

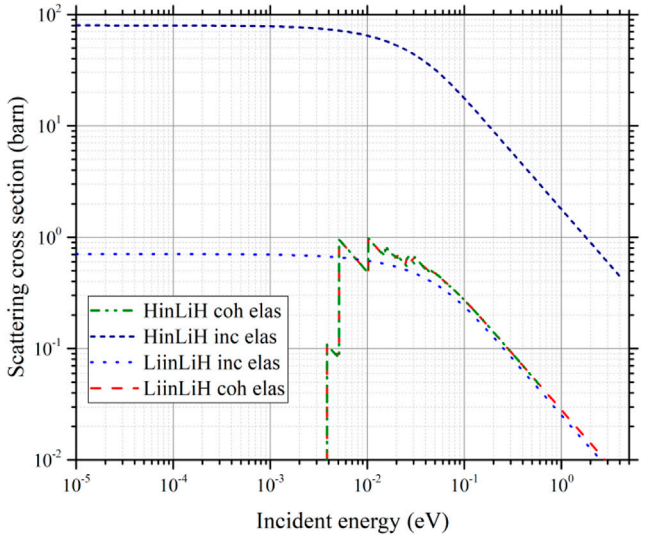

FIGURE 4 | Elastic scattering cross sections of LiH.

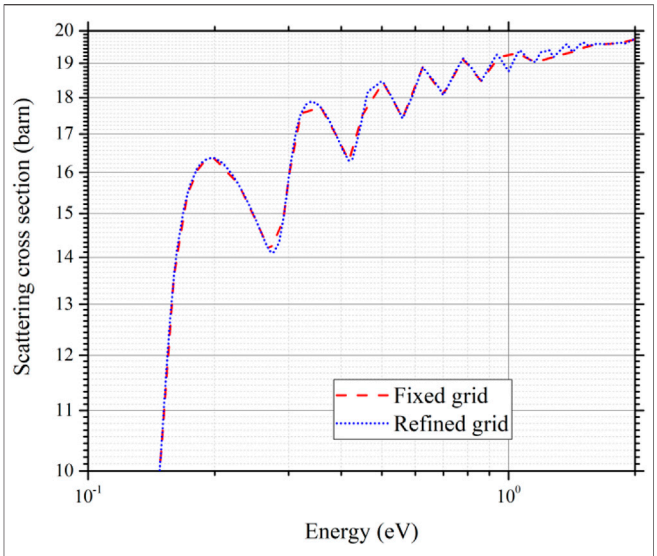

FIGURE 6 | Details of inelastic scattering cross section of δ-$ZrH_{1.5}$ above 0.1 eV.

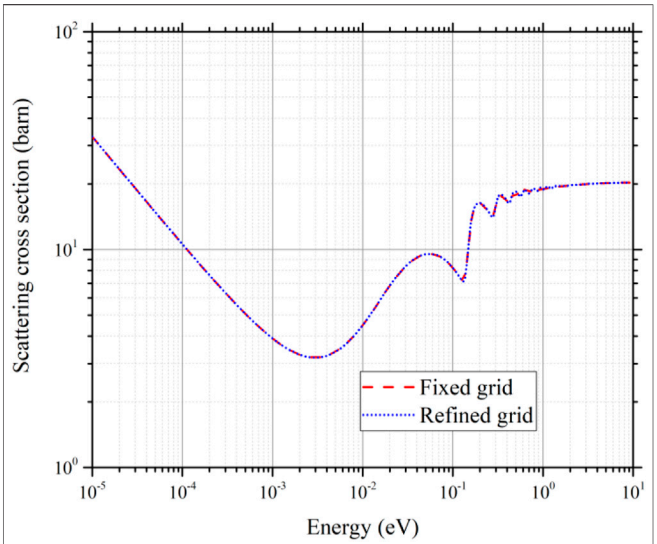

FIGURE 5 | Inelastic scattering cross section of δ-$ZrH_{1.5}$ as a function of energy.

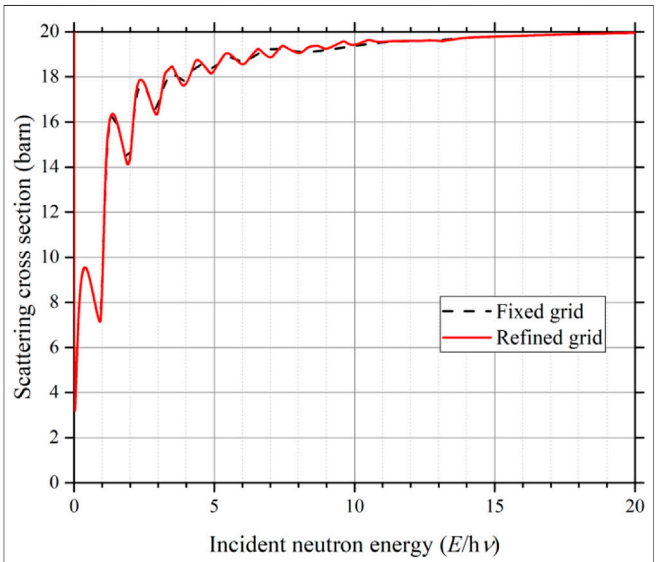

FIGURE 7 | Inelastic scattering cross section of δ-$ZrH_{1.5}$ as a function of numbers of $h\nu$.

which makes the final coherent scattering cross section much less than the incoherent scattering cross section. According to the work by Sears (1992), for most nuclides, the difference between the two bound scattering cross sections is very large. It seems reasonable to ignore the scattering mode with less bound cross sections. However, for some nuclides, the two bound cross sections are close, which will make the final coherent and incoherent scattering cross section comparable, for example, H-2, Li-6, and Li-7 listed in **Table 1**; **Figure 4** shows the coherent and incoherent cross section of LiH. It can be seen that the coherent and incoherent elastic scattering cross sections of Li in LiH are comparable.

Inelastic Scattering Cross Sections

The previously described multipoint linearization method was implemented in the therm_calc module in this work. The incident energy points for ZrH_x were generated with the multipoint linearization method, and the number of incident energy points between 1.0E-05 and 10 eV is 303. The inelastic scattering cross section of hydrogen in δ-$ZrH_{1.5}$ was calculated with the refined incident energy grid and compared with the results obtained using the fixed energy grid, as shown in **Figure 5**. The detailed cross section distribution for energies greater than 0.1 eV is given in **Figure 6**. The inelastic scattering cross section

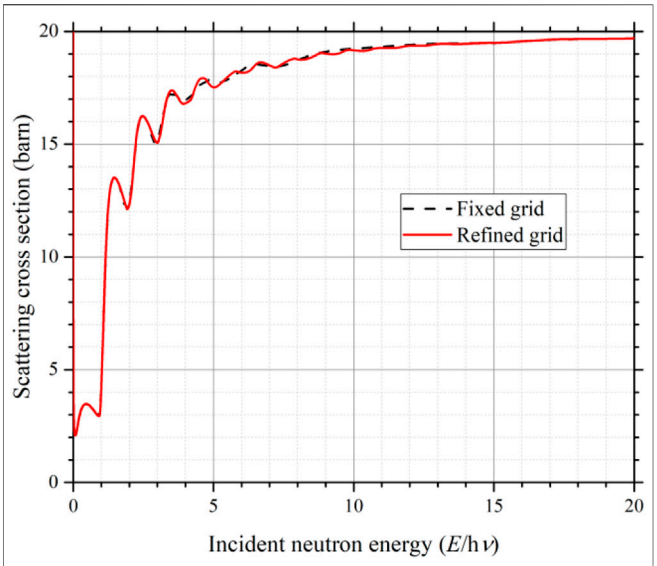

FIGURE 8 | Inelastic scattering cross section of YH2 as a function of numbers of *hv*.

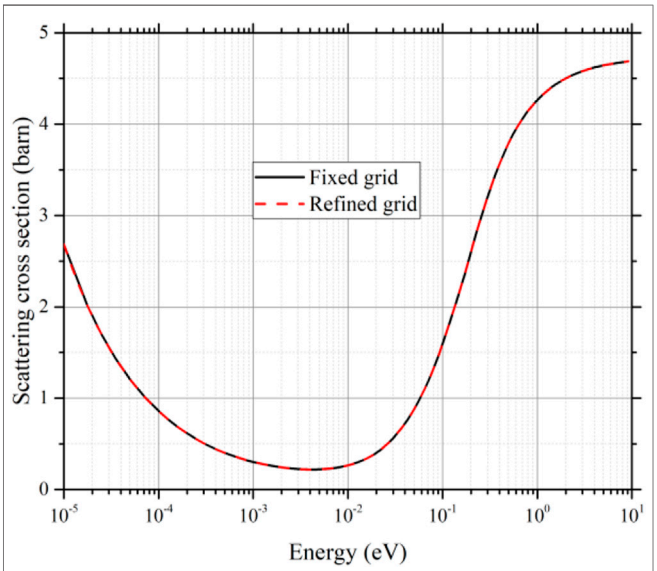

FIGURE 9 | Inelastic scattering cross sections of graphite.

shows oscillating along the energy. In the work by Whittemore (1964), the experimental and theoretical results revealed that the scattering cross section of hydrogen in ZrH_x is oscillating, and the valley of each oscillation occurs at integer values of harmonic frequency *hv*. The value of *hv* for δ-$ZrH_{1.5}$ is 0.143 eV. In **Figure 5**, the inelastic scattering cross section is represented as a function of energy, whereas in **Figure 6**, it is represented as a function of the numbers of *hv* **Figure 7** The refined grid obtained by multipoint linearization method captures more detailed variation of the cross section than the fixed grid. And the valley of the oscillation of the cross section appears at integers, which agrees with the experimental results by Whittemore (1964).

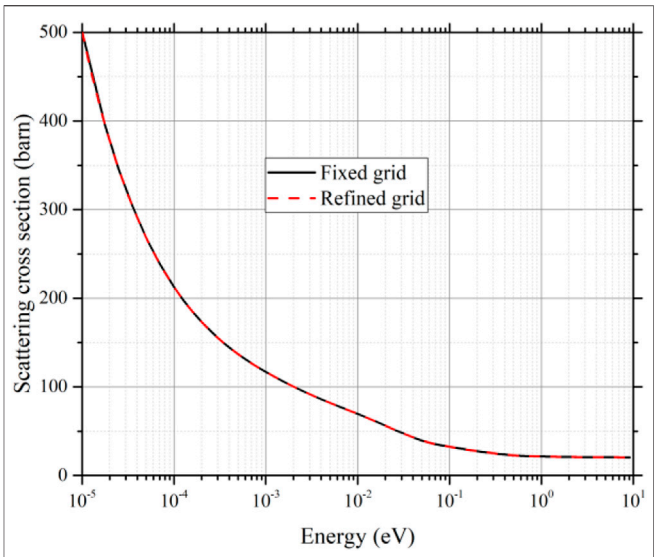

FIGURE 10 | Inelastic scattering cross sections of H_2O.

To show the effect of incident energy grid on the cross sections, we also analyzed the inelastic scattering cross sections of YH_2, graphite, and H_2O. **Figure 8** shows the inelastic scattering cross section of YH_2 represented as a function of the numbers of *hv*. In the calculations, the TSL data of YH_2 are obtained from ENDF/B-VIII.0. For YH_2, $h\nu$ = 0.119 eV. The inelastic scattering cross section distribution obtained using the refined incident energy grid captures more details of the oscillation. For graphite and H_2O, the inelastic scattering cross sections vary smoothly with energy as shown in **Figures 9**, **10**. The cross sections calculated based on fixed grid and refined grid are close to each other.

Results of Critical Benchmarks

To investigate the effects of the above treatments on the reactivity of reactors, a couple of critical benchmarks containing ZrH_x as moderator was calculated using the Monte Carlo code NECP-MCX, which is a new Monte Carlo code developed by the Nuclear Engineering Computational Physics (NECP) Laboratory of Xi'an Jiaotong University. NECP-MCX is developed based on a hybrid Monte Carlo deterministic method, where the deterministic method is utilized to generate consistent mesh-based weight-window and source-biasing parameters for the Monte Carlo method to reduce variance. The code has been verified against with various benchmarks (He et al., 2021; Li et al., 2021).

The critical benchmarks are selected from ICSBEP benchmark (OECD-NEA, 2016) and listed in **Table 2**, including ICT003 benchmarks and HCM003 benchmarks. The ICT003 benchmark experiments were performed in a TRIGA Mark II reactor, which is a light-water reactor with an annular graphite reflector. The fuel in the reactor is a homogeneous mixture of uranium and ZrH_x, with 12 wt% uranium of 20% enrichment. The temperature for all the materials in the benchmarks is 300 K. HCM003 benchmarks were performed on a reactor loaded with highly enriched uranium dioxide fuel (approximately 96% ^{235}U). The ZrH_x is

TABLE 2 | ICSBEP criticality benchmarks used in the comparison.

Short name of the benchmark	No. of cases	Title	H/Zr
ICT003	2	TRIGA MARK II reactor: u(20)—zirconium hydride fuel rods in water with graphite reflector	1.60
HCM003	6	Intermediate heterogeneous assembly with highly enriched uranium dioxide (96% ^{235}U) and zirconium hydride moderator	1.92

TABLE 3 | k_{eff} of the TRIGA benchmarks.

Benchmarks	Experimental results	Fixed grid and incoherent elastic scattering	Refined gird and incoherent elastic scattering	Refined gird and two elastic modes	Effect of incident grid (pcm)	Effect of elastic scattering (pcm)
HCM003_01	1.00000 ± 0	1.00203	1.00083	1.00045	−120	−38
HCM003_02	1.00000 ± 0	1.00279	1.00168	1.00109	−111	−59
HCM003_03	1.00000 ± 0	1.00242	1.00115	1.00049	−127	−66
HCM003_04	1.00000 ± 0	1.00265	1.00132	1.00091	−133	−41
HCM003_05	1.00000 ± 0	1.00263	1.00122	1.00067	−141	−55
HCM003_06	1.00000 ± 0	1.00229	1.00102	1.00036	−127	−66
ICT003_01	1.0006 ± 0.0056	0.99993	1.00204	1.00165	211	−39
ICT003_02	1.0046 ± 0.0056	1.00459	1.00682	1.00651	223	−31

used as moderator. In the benchmarks, the temperature for all the materials is 300 K. The models for ICT003 and HCM003 benchmarks used by NECP-MCX were established according to the typical MCNP input given in the handbook of ICSBEP, without any simplification.

In our previous work, it was shown that the TSL data given in ENDF/B-VIII.0 and JEFF-3.3 could introduce larger errors into the reactivity of the TRIGA reactors, because the TSL is not obtained from a realistic crystal structure of ZrH_x. Therefore, in this work, the TSL data calculated in the work by Zu et al. (2021) were adopted in the calculations: the thermal scattering cross sections obtained based on δ-$ZrH_{1.5}$ were adopted in ICT003 benchmarks; the thermal scattering cross sections obtained based on ε-ZrH_2 was adopted in HCM003 benchmarks. Except the TSL data, all the other nuclear data were extracted from the newly released CENDL-3.2. Ge et al. (2020) evaluated the nuclear data library.

In the thermal scattering library of ACE format, the flag IDPNC in the NXS array is used to indicate the elastic scattering mode for a material, IDPNC = 4 for coherent elastic scattering and IDPNC = 3 for incoherent elastic scattering. In order to use the two elastic scattering modes in the Monte Carol calculations, we extended the ACE library to include both the coherent and incoherent elastic scattering data (mixed elastic scattering) by setting IDPNC = 5. The indices for these data were added to the JXS array in the ACE library. Besides, in the conventional Monte Carlo codes, only one elastic scattering model is sampled in the simulations. In this work, NECP-MCX was modified to simultaneously sample the coherent and incoherent elastic scattering.

In the calculations of the above benchmarks using NECP-MCX, the statistical uncertainties of the effective multiplication factor k_{eff} were controlled within ±10 pcm. For ICT003, the calculations were run with 2,200 generations of 80,000 histories each, and the first 100 generations were excluded from statistics. For HCM003, 2,050 generations of 50,000 histories each were used, and the first 50 generations were excluded from statistics. Besides, in the calculations, only the scattering cross sections of ZrH_x are generated with techniques mentioned previously, and for other materials, the scattering cross sections are generated using the conventional methods.

The k_{eff} values calculated using different scattering cross sections are given in **Table 3**. The effect of the incident energy grid is given in the sixth column, which are values in the fourth column minus those in the third column. The effect of considering two elastic scattering modes is given in the last column, which is the value in the fifth column minus those in the fourth column. For HCM003 benchmarks, using the refined incident energy grid can reduce the k_{eff} by a range from 111 to 141 pcm, and when the coherent elastic scattering is considered in the calculations, the k_{eff} is further reduced by 38–66 pcm. Meanwhile, both the two factors make the k_{eff} closer to the experimental results, whereas for the two ICT003 benchmarks, the refined incident energy grid gives a larger k_{eff} of approximately 200 pcm than the fixed grid, and considering the coherent elastic scattering can predict a lesser k_{eff} of approximately 30 pcm. Although it seems that the refined incident energy grid makes the k_{eff} worse compared with the experimental, the uncertainties of experiment results of ICT003 are 560 pcm. The results of refined incident energy grid are still within the uncertainty range.

We also tested several assembly problems, including fuel pebble in HTR (She et al., 2021) and pressurized water reactor assembly benchmark VERA_2B (Godfrey, 2013). The results show that the incident energy grid has negligible effect on the k_{eff} of these assemblies, because the inelastic scattering cross sections of graphite and H_2O are smooth.

CONCLUSION

The treatments of thermal scattering cross sections are introduced in this article. The effects of ignoring one

elastic scattering mode in the evaluated nuclear data are analyzed using several critical benchmarks loaded with ZrH_x. It is found that considering the coherent and incoherent elastic scattering simultaneously in the neutronics calculations can affect the effective multiplication factor by tens of pcm. The multipoint linearization method is adopted to refine the incident energy grid for inelastic scattering. The numerical results show that the incident energy grid has obvious effect on the effective multiplication factor.

DATA AVAILABILITY STATEMENT

The raw data supporting the conclusions of this article will be made available by the authors, without undue reservation.

AUTHOR CONTRIBUTIONS

TZ: code development of NECP-Atlas, numerical calculation, results analysis, article writing. YT: code development of sab_calc module, numerical calculation. ZH: code development of NECP-MCX, modeling of TRIGA reactors. SQ: code development of NECP-MCX, modeling of TRIGA reactors. JL: code development of NECP-MCX for the treatment of mixed elastic scattering. QH: code development of NECP-MCX. LC: guidance and consultancy. HW: guidance and consultancy.

FUNDING

This research is supported by National Natural Science Foundation of China (No. 12075183, 12135019), and Key Laboratory of Nuclear Data (No. 6142A08190101B).

REFERENCES

Brown, D. A., Chadwick, M. B., Capote, R., Kahler, A. C., Trkov, A., Herman, M. W., et al. (2018). ENDF/B-VIII.0: The 8 Th Major Release of the Nuclear Reaction Data Library with CIELO-Project Cross Sections, New Standards and Thermal Scattering Data. *Nucl. Data Sheets* 148, 1–142. doi:10.1016/j.nds.2018.02.001

Cacuci, D. G. (2010). *Handbook of Nuclear Engineering*. Springer.

Čerba, Š., Damian, J. I. M., Lüley, J., Vrban, B., Farkas, G., Nečas, V., et al. (2013). Comparison of thermal Scattering Processing Options for S(α,β) Cards in MCNP. *Ann. Nucl. Energ.* 55, 18–22. doi:10.1016/j.anucene.2012.12.014

Conlin, J. L., Parsons, D. K., Brown, F. B., MacFarlane, R. E., Little, R. C., and White, M. C. (2012). Continuous-S (α, β) Capability in MCNP. *Transactions* 106, 501–504.

Conlin, J. L., and Romano, P. (2019). *A Compact ENDF (ACE) Format Specification (No. LA-UR-19-29016)*. Los Alamos, NM (United States): Los Alamos National Lab.

Ge, Z., Xu, R., Wu, H., Zhang, Y., Chen, G., Jin, Y., et al. (2020). CENDL-3.2: The New Version of Chinese General Purpose Evaluated Nuclear Data Library. *EPJ Web Conf.* 239, 09001. doi:10.1051/epjconf/202023909001

Godfrey, A. T. (2013). *VERA Core Physics Benchmarks Progression Problem Specifications (No. CASL-U-2012-0131-004)*. Oak Ridge, TN (United States): Oak Ridge National Lab.

Hart, S. W. D., and Maldonado, G. I. (2017). Implementation of the Direct S(α,β) Method in the KENO Monte Carlo Code. *Ann. Nucl. Energ.* 101, 270–277. doi:10.1016/j.anucene.2016.11.019

Hartling, K., Ciungu, B., Li, G., Bentoumi, G., and Sur, B. (2018). The Effects of Nuclear Data Library Processing on Geant4 and MCNP Simulations of the thermal Neutron Scattering Law. *Nucl. Instr. Methods Phys. Res. Section A: Acc. Spectrometers, Detectors Associated Equipment* 891, 25–31. doi:10.1016/j.nima.2018.02.053

He, Q., Zheng, Q., Li, J., Wu, H., Shen, W., Cao, L., et al. (2021). NECP-MCX: A Hybrid Monte-Carlo-Deterministic Particle-Transport Code for the Simulation of Deep-Penetration Problems. *Ann. Nucl. Energ.* 151, 107978. doi:10.1016/j.anucene.2020.107978

Li, J., Wu, H., He, Q., Shen, W., Zheng, Q., Cao, L., et al. (2021). The Neutron-Photon-Coupling Analysis of the Tritium-Breeding Blanket in CFETR by NECP-MCX. *Fusion Eng. Des.* 172, 108489. doi:10.1016/j.fusengdes.2021.112747

Liu, S., Yuan, Y., Yu, J., and Wang, K. (2016). Reaction Rate Tally and Depletion Calculation with On-The-Fly Temperature Treatment. *Ann. Nucl. Energ.* 92, 277–283. doi:10.1016/j.anucene.2016.02.006

Macfarlane, R., Muir, D. W., Boicourt, R. M., Kahler, I., Albert, C., and Conlin, J. L. (2017). *The NJOY Nuclear Data Processing System, Version 2016 (No. LA-UR-17-20093)*. Los Alamos, NM (United States): Los Alamos National Lab.

OECD-NEA (2016). *International Criticality Safety Benchmark Evaluation Project*. Paris, France: Nuclear Energy Agency, Organization for Ecomomic Cooperation and Development.

Plompen, A. J. M., Cabellos, O., De Saint Jean, C., Fleming, M., Algora, A., Angelone, M., et al. (2020). The Joint Evaluated Fission and Fusion Nuclear Data Library, JEFF-3.3. *Eur. Phys. J. A.* 56, 181. doi:10.1140/epja/s10050-020-00141-9

Sears, V. F. (1992). Neutron Scattering Lengths and Cross Sections. *Neutron News* 3, 26–37. doi:10.1080/10448639208218770

She, D., Chen, F., Xia, B., Shi, L., Zhang, J., Li, F., et al. (2021). Simulation of the HTR-10 Operation History with the PANGU Code. *Front. Energ. Res.* 9, 704116. doi:10.3389/fenrg.2021.704116

Shibata, K., Iwamoto, O., Nakagawa, T., Iwamoto, N., Ichihara, A., Kunieda, S., et al. (2011). JENDL-4.0: A New Library for Nuclear Science and Engineering. *J. Nucl. Sci. Tech.* 48, 1–30. doi:10.1080/18811248.2011.9711675

Squires, G. L. (2012). *Introduction to the Theory of Thermal Neutron Scattering*. Cambridge: Cambridge University Press.

Tang, Y., Zu, T., Yi, S., Cao, L., and Wu, H. (2021). Development and Verification of thermal Neutron Scattering Law Data Calculation Module in Nuclear Data Processing Code NECP-Atlas. *Ann. Nucl. Energ.* 153, 108044. doi:10.1016/j.anucene.2020.108044

Trkov, A., Herman, M., and Brown, D. A. (2012). *ENDF-6 Formats Manual Data Formats and Procedures for the Evaluated Nuclear Data Files ENDF/B-VI and ENDF/B-VII (No. BNL-90365-2009 Rev.2)*. Upton, NY (United States): Brookhaven National Lab.

Whittemore, W. L. (1964). *Neutron Interaction in Zirconium Hydride (No. GA-4490)*. Washington, DC, United States: General Atomic.

Wormald, J. L., and Hawari, A. I. (2017). Generation of Phonon Density of States and thermal Scattering Law Using Ab Initio Molecular Dynamics. *Prog. Nucl. Energ.* 101, 461–467. doi:10.1016/j.pnucene.2017.02.011

Wormald, J. L., Thompson, J. T., and Trumbull, T. H. (2020). Implementation of an Adaptive Energy Grid Routine in NDEX for the Processing of thermal Neutron Scattering Cross Sections. *Ann. Nucl. Energ.* 149, 107773. doi:10.1016/j.anucene.2020.107773

Zu, T., Tang, Y., Wang, L., Cao, L., and Wu, H. (2021). Thermal Scattering Law Data Generation for Hydrogen Bound in Zirconium Hydride Based on the Phonon Density of States from First-Principles Calculations. *Ann. Nucl. Energ.* 161, 108489. doi:10.1016/j.anucene.2021.108489

Zu, T., Xu, J., Tang, Y., Bi, H., Zhao, F., Cao, L., et al. (2019). NECP-atlas: A New Nuclear Data Processing Code. *Ann. Nucl. Energ.* 123, 153–161. doi:10.1016/j.anucene.2018.09.016

Conflict of Interest: The authors declare that the research was conducted in the absence of any commercial or financial relationships that could be construed as a potential conflict of interest.

Publisher's Note: All claims expressed in this article are solely those of the authors and do not necessarily represent those of their affiliated organizations, or those of the publisher, the editors, and the reviewers. Any product that may be evaluated in this article, or claim that may be made by its manufacturer, is not guaranteed or endorsed by the publisher.

frontiers in Energy Research

ORIGINAL RESEARCH
published: 08 December 2021
doi: 10.3389/fenrg.2021.784247

A New Numerical Nuclear Reactor Neutronics Code SHARK

Chen Zhao, Xingjie Peng, Hongbo Zhang, Wenbo Zhao, Zhang Chen, Junjie Rao, Kun Liu, Zhaohu Gong, Wei Zeng and Qing Li*

Science and Technology on Reactor System Design Technology Laboratory, Nuclear Power Institute of China, Chengdu, China

In order to establish the next-generation reactor physics calculation method based on the numerical nuclear reactor technology and realize high-fidelity modeling and calculation, a new numerical nuclear reactor neutronics code SHARK is developed. The code is based on the direct transport method with construct solid geometry (CSG) method, advanced subgroup resonance method, direct transport MOC method in rectangle and hexagonal geometry, large-scale parallel, and CMFD acceleration method. The C5G7, macro BEAVRS and VERA benchmarks are verified to show the accuracy of the code and method. Numerical results show good accuracy and calculation performance of SHARK, and the direct transport method can be adopted on numerical nuclear reactor calculation.

Keywords: numerical nuclear reactor, resonance method, direct transport method, shark, vera

OPEN ACCESS

Edited by:
Tengfei Zhang,
Shanghai Jiao Tong University, China

Reviewed by:
Donghao He,
Shanghai Jiao Tong University, China
Liang Liang,
Harbin Engineering University, China

****Correspondence:***
Xingjie Peng
pengxingjiets@126.com

Specialty section:
This article was submitted to Nuclear Energy, a section of the journal Frontiers in Energy Research

Received: *27 September 2021*
Accepted: *11 October 2021*
Published: *08 December 2021*

Citation:
Zhao C, Peng X, Zhang H, Zhao W, Chen Z, Rao J, Liu K, Gong Z, Zeng W and Li Q (2021) A New Numerical Nuclear Reactor Neutronics Code SHARK. Front. Energy Res. 9:784247. doi: 10.3389/fenrg.2021.784247

1 INTRODUCTION

Numerical nuclear reactor is based on the multi-physics coupling calculation with accurate theory and physical model from first principles. In this way, the approximation from experience and artificial adjustment is eliminated to the maximum extent. With the high-performance computing platform, high-fidelity and high-distinguishability numerical calculation for nuclear reactor is conducted to decrease the conservation of safety analysis (Casl, 2010; CASL Project Summary Slides, 2011). In numerical nuclear reactor physics calculation, the direct transport method avoids the spatial and energy group homogenization in the traditional two-step method. Besides, the resolution can be improved to the level of flat source region, and micro-phenomenon can be simulated.

The research of the direct transport method has become a hotspot in numerical nuclear reactor physics calculation. Several direct transport codes have been developed for numerical nuclear reactor physics calculation, including MPACT (Kelley and Larsen, 2013), nTRACER(Jung, 2013), DeCART(Hursin, 2010), STREAM (Choi et al., 2019), NECP-X (Chen et al., 2018), and PANX (Zhang et al., 2017a; Zhang et al., 2017b). PWR whole-core multi-physics coupling direct calculation has been conducted, and numerical results show good accuracy. However, most numerical nuclear reactor technologies are focused on the large-scale pressured water reactor. The direct transport method needs to be improved for further application on advanced nuclear reactors in the future.

In this paper, a new numerical nuclear reactor neutronics code SHARK (Zhao et al., 2021a; Zhao et al., 2021b) is developed, which is the initial abbreviation of the Simulation-based High-fidelity Advanced Reactor physics Kit. The traditional technical route is applied in the SHARK code, including geometry modeling, resonance method, and transport method. A significant objective of the code design lies in the calculation ability for advanced numerical nuclear reactor with complex geometry. Therefore, geometry adaptability is one of the most important characteristics for SHARK. The detailed description of framework and methods in each module will be introduced.

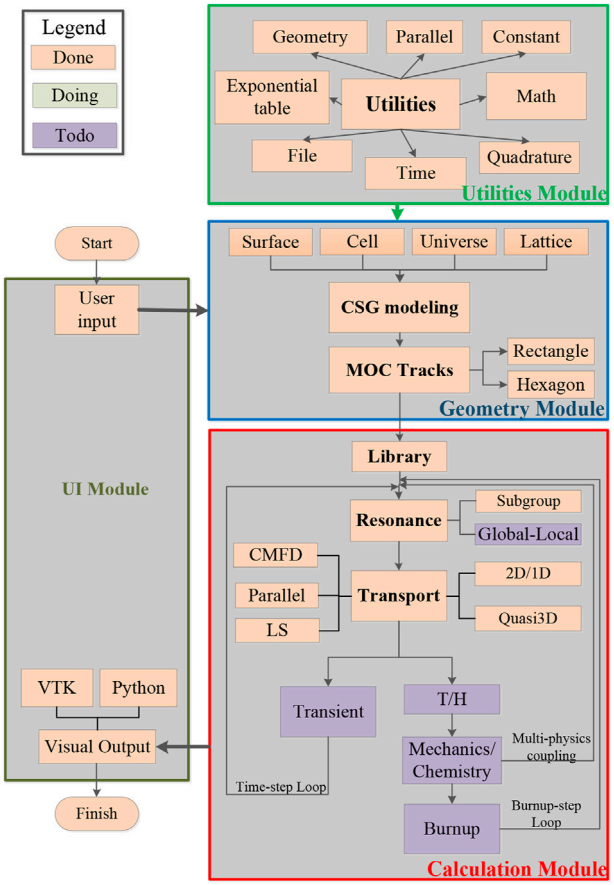

FIGURE 1 | The framework and modules of Simulation-based High-fidelity Advanced Reactor physics Kit (SHARK).

2 FRAMEWORK OF SIMULATION-BASED HIGH-FIDELITY ADVANCED REACTOR PHYSICS KIT

The numerical nuclear reactor neutronics code SHARK has four modules, including utilities, geometry, calculation, and UI. The overall framework and detailed modules of SHARK are shown in **Figure 1**.

In the utilities module, basic programming kits are provided, such as the math library, time function, and parallel parameters. In the geometry module, the reactor geometry model is built by surface, cell, universe, and lattice. Two-dimensional characteristic rays are generated in each layer. It supports rectangle and hexagonal ray tracing. The calculation module is the kernel of SHARK and includes several calculation sub-modules, including library, resonance, transport, transient, thermal-hydraulics, mechanics/chemistry multi-physics coupling, and burnup. Up to now, library, resonance, and transport have already been realized in SHARK. Other sub-modules will be developed in the future. In the UI module, user input and visual output are executed with Python programming language for expanding the visualization ability. As for programming, C++/Python hybrid programming is adopted to combine the data processing for Python and the numerical calculation for C++. Besides, object-oriented programming improves the readability, modularization, and reusability.

3 GEOMETRY MODELING

In the initial design of SHARK, two significant objectives are the accurate geometry modeling and calculation abilities for advanced numerical nuclear reactor with complex geometry. In SHARK, the constructive solid geometry (CSG) (Cao et al., 2019) method is adopted. The geometry model is built with objects by regular Boolean operation in the CSG method. In the geometry modeling procedure, several typical objects need to be predefined, including surface, cell, universe, and lattice. In this way, the geometry modeling ability can be extended to arbitrary geometry theoretically with complicated CSG objects. In the UI module, the geometry modeling can be visually displayed to verify the modeling correction. Complicated geometry modeling of hexagonal assembly and plate-type assembly has already been realized in SHARK. The geometry modeling of the plate-type assembly and the JRR-3 reactor (Iwasaki et al., 1985; Liu et al., 2015) are shown in the **Figure 2**.

4 RAY TRACING

SHARK is a MOC-based numerical nuclear reactor neutronics code, and ray tracing is an important section in the code design. Assembly module ray tracing method (Hong and Cho, 1998) is applied in ray tracing to save the memory cost. Up to now, rectangle and hexagon modular ray tracing has been developed in SHARK with the established method (Cho et al., 2008; Chen et al., 2018). In the future, the long characteristic method (Suslov, 2001) will be added for complicated geometry cases without regular assembly structure.

5 LIBRARY AND RESONANCE METHOD

5.1 Library

The multi-group cross-section library in SHARK is processed by NJOY (Muir et al., 2016) based on ENDF/B-VI.8. The 45-group energy group structure is applied in SHARK, which has been verified in the HELIOS method (HELIOS Methods, 2001). A new library based on the ENDF/B-VII.0 will be processed and researched in the future.

5.2 The subgroup resonance method

The subgroup method based on the equivalent cross-section interpolation table (Cullen, 1977; Wemple et al., 2008) is applied in resonance calculation. The diagram of the subgroup method is shown in **Figure 3**.

In the resonance region, according to the subgroup method, the cross section can be calculated in the form of the subgroup, shown as **Eq. 1**.

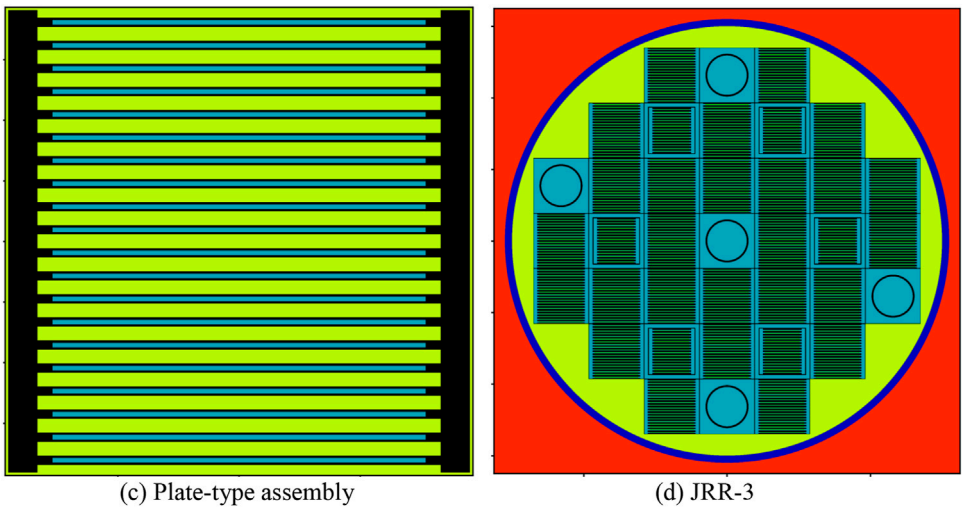

FIGURE 2 | Complicated geometry modeling of SHARK.

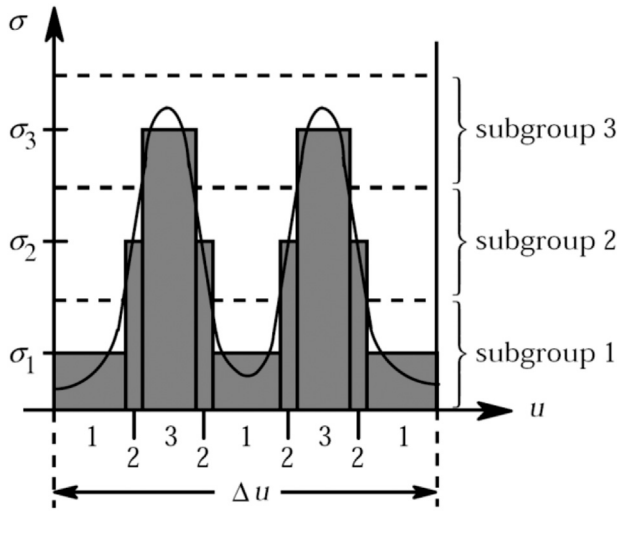

FIGURE 3 | The diagram of subgroup resonance method.

$$\sigma_{x,g} = \frac{\sum_{n_g=1}^{N_g} w_{x,n_g}\sigma_{x,n_g}\phi_{n_g}}{\sum_{n_g=1}^{N_g} w_{a,n_g}\phi_{n_g}} \tag{1}$$

where, n_g is the n subgroup in the resonance energy group g. N_g is the number of subgroups in energy group g. w_{x,n_g}, σ_{x,n_g}, ϕ_{n_g} are the weight, cross-section, and flux of the subgroup n_g.

In the equation, w_{x,n_g} and σ_{x,n_g} are subgroup parameters and have little dependency with specific questions. Subgroup parameters can be obtained by the least square fit method from effective resonance integral table, shown as **Eq. 2**. As for the subgroup flux, it can be calculated by the subgroup fixed source equation, which costs a large sum of calculation amount. Therefore, the subgroup flux is obtained approximately by intermediate resonance (IR) flux result, shown as **Eq. 3**. The background cross section $\sigma_{b,n}$ is obtained by equivalent cross-section interpolation table. Finally, the cross section can be rewritten and calculated in the form of **Eq. 4**. Besides, the Bondarenko-iteration method is adopted to deal with multi-nuclide resonance interface effect.

$$RI_x = \sum_n w_{x,n}\sigma_{x,n}\frac{\sigma_{b,n}}{\sigma_{a,n}+\sigma_{b,n}} \tag{2}$$

$$\phi_n \approx \frac{\sigma_{b,n}}{\sigma_{a,n}+\sigma_{b,n}} \tag{3}$$

$$\sigma_x \approx \frac{\sum_n w_{x,n}\sigma_{x,n}\frac{\sigma_{b,n}}{\sigma_{a,n}+\sigma_{b,n}}}{\sum_n w_{a,n}\frac{\sigma_{b,n}}{\sigma_{a,n}+\sigma_{b,n}}} \tag{4}$$

where RI_x is the effective resonance integral table for reaction x.

6 DIRECT TRANSPORT METHOD

6.1 2D/1D and quasi-3D methods

As for the direct transport method, two options are provided in SHARK, including the 2D/1D method and the quasi-3D method. The 2D/1D method has the efficiency and memory cost advantages on most cases such as the C5G7 benchmark and large-scale PWR cases. However, the 2D/1D method will suffer instability issues considering the negative sources introduced by traverse leakage terms (Stimpson et al., 2013; Zhao et al., 2018). Axial difference relationship is introduced in the quasi-3D method and negative sources can be avoided in the two-dimensional MOC calculation. Therefore, the quasi-3D method has better stability performance in theory with poor efficiency. Besides, no isotropic approximation is introduced in the equation derivation of the quasi-3D method. The quasi-3D method has better calculation accuracy in the strong anisotropic cases, such as the KUCA benchmark. The detailed analysis and comparison of these two methods can be found in previous work (Zhao et al., 2021b).

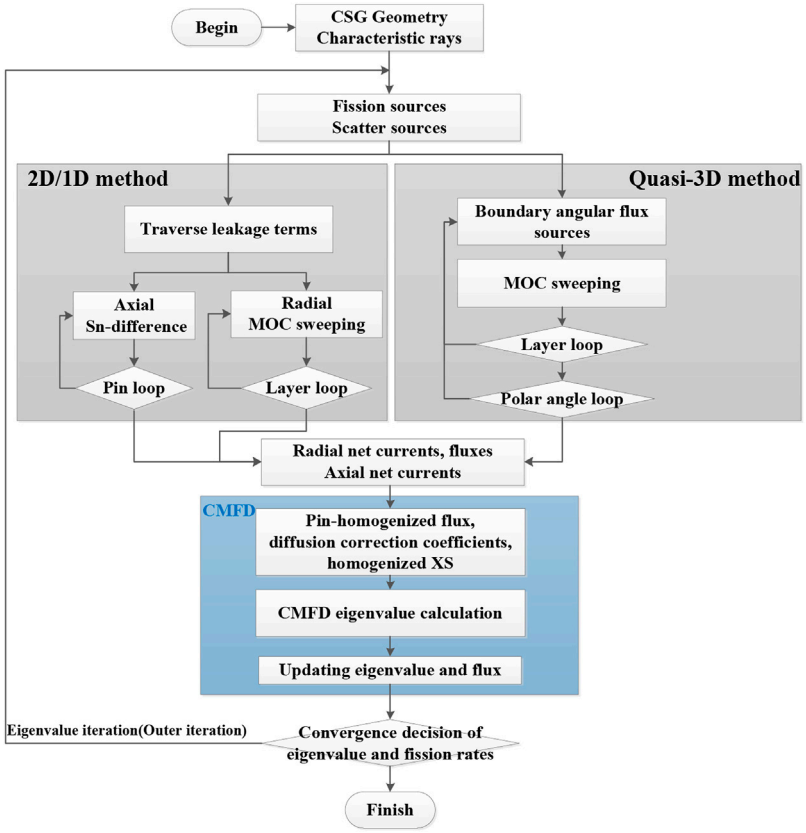

FIGURE 4 | The diagram of the coarse-mesh finite difference (CMFD) acceleration in SHARK.

6.2 odCMFD acceleration method

Coarse-mesh finite difference (CMFD) method (Zhu et al., 2016; Li et al., 2020) has already become an established method in the high-order calculation, especially in the direct transport method. Several advanced CMFD acceleration methods, such as odCMFD (Zhu et al., 2016) and lpCMFD (Li et al., 2020), have been proposed these years. These methods have little variations on the basic theory of the CMFD method. Current diffusion and correction coefficients are introduced with the high-order results of net currents and fluxes. The diagram of CMFD acceleration in SHARK is shown in **Figure 4**. The MOC-based transport calculation is conducted to provide radial, axial net currents, and fine-mesh fluxes. In the CMFD module, pin-homogenized fluxes, cross-sections, and coefficients need to be prepared before eigenvalue calculation. Eigenvalue and fine-mesh fluxes are updated by CMFD results. In this way, the convergence of eigenvalue iteration can be accelerated.

However, the traditional CMFD method suffers the poor stability issue. In SHARK, the odCMFD (Zhu et al., 2016) method is applied. In the theory of odCMFD, an additive component is added in the diffusion coefficient calculation, shown as **Eq. 5**.

$$D_{g,i} = \frac{1}{3\Sigma_{tr,g,i}} + \theta_{od}\Delta_i \tag{5}$$

where, $D_{g,i}$ is the diffusion coefficient on cell i and group g. $\Sigma_{tr,g,i}$ is the total cross section. Δ_i is the width of cell i. θ_{od} is the additive component, which needs to be 0–0.25. According to the research of the odCMFD method, θ_{od} is set to be 0.25 to have the best stability performance in SHARK.

6.3 Spatial parallel method

Advanced parallel algorithm is applied in the spatial domain-decomposition method in SHARK. Memory cost can be divided and decomposed before calculation. Ray sweeping happens on the certain domain for each CPU, and the communication only happens on the inner boundary for each domain. In this way, memory cost can be decreased for each node, and the large-scale calculation can be realized. Furthermore, non-blocking strategy is applied for communication, which improves parallel efficiency. The diagram of domain decomposition in SHARK is shown in **Figure 5**.

7 NUMERICAL RESULTS

7.1 The macro benchmark

7.1.1 Hexagonal assembly case

To validate the hexagonal calculation ability, a hexagonal assembly seven-group case is designed, as is shown in the

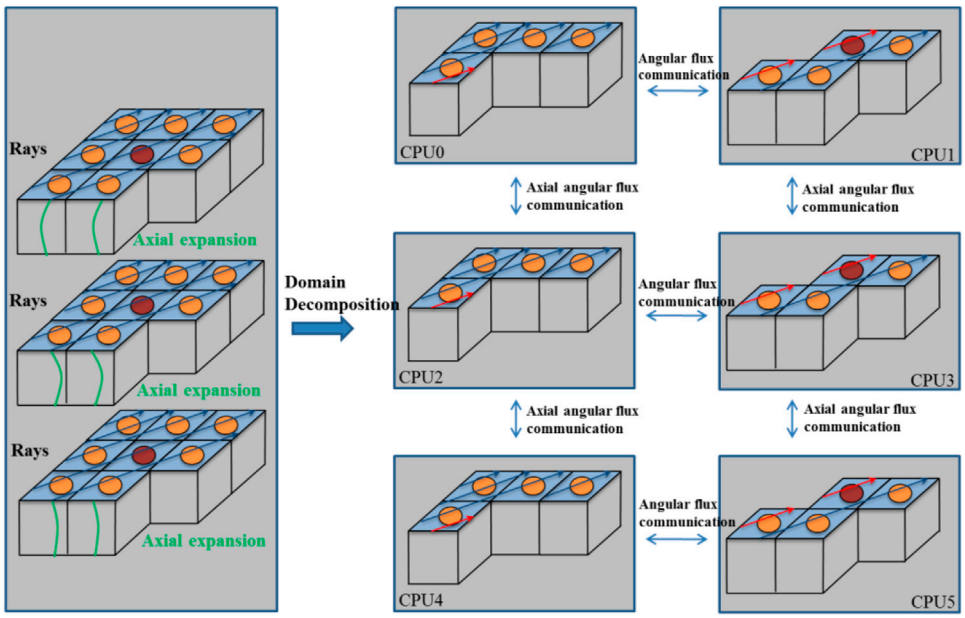

FIGURE 5 | The diagram of domain decomposition in SHARK.

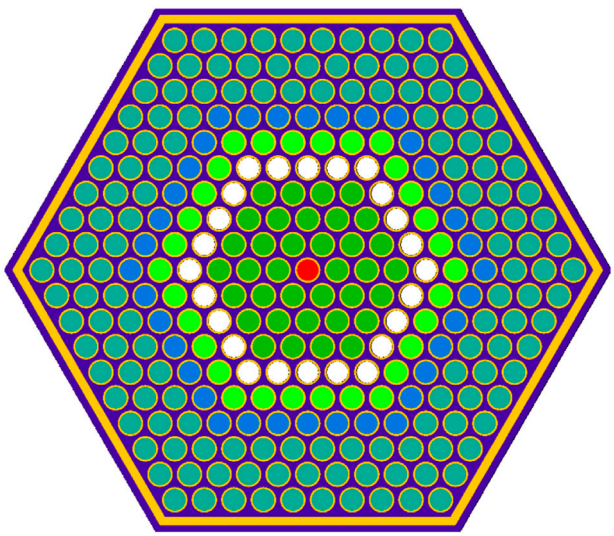

FIGURE 6 | Hexagonal assembly geometry modeling of SHARK.

Figure 6. Ten rings are arranged, including three MOX-8.7% rings, MOX-7% ring, MOX-4.3% ring, control rod ring, 3 UO_2 fuel rings, and fission chamber from outside to inside. The assembly box can be explicitly modeled. The pitch of the hexagonal pin cell is 0.91 cm. Radiuses of the inner and outer fuel pellets are 0.33 and 0.39 cm. Thicknesses of the assembly box and assembly gap are 0.26 and 0.22 cm separately. The multi-group cross-sections are from the C5G7 benchmark (OECD, 2005).

TABLE 1 | The eigenvalue and fission rate results of the hexagonal assembly case.

	Eigenvalue result	Pin-cell fission rate results/%		
		MAX	AVG	RMS
OpenMC	1.00213 ± 0.00001	—	—	—
SHARK	1.00159	0.200	0.040	0.005

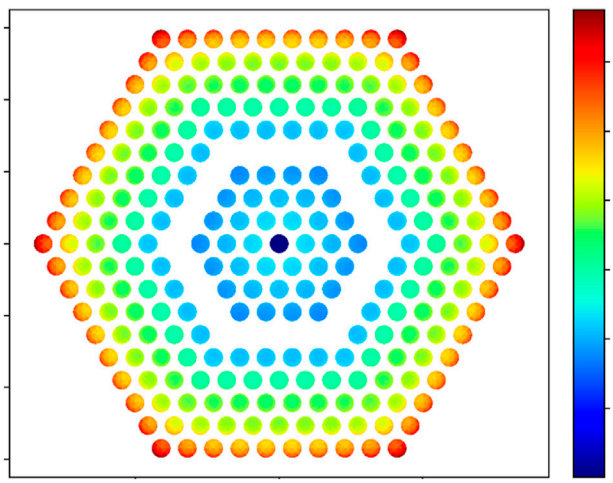

FIGURE 7 | The pin-cell fission rate results of the hexagonal assembly case.

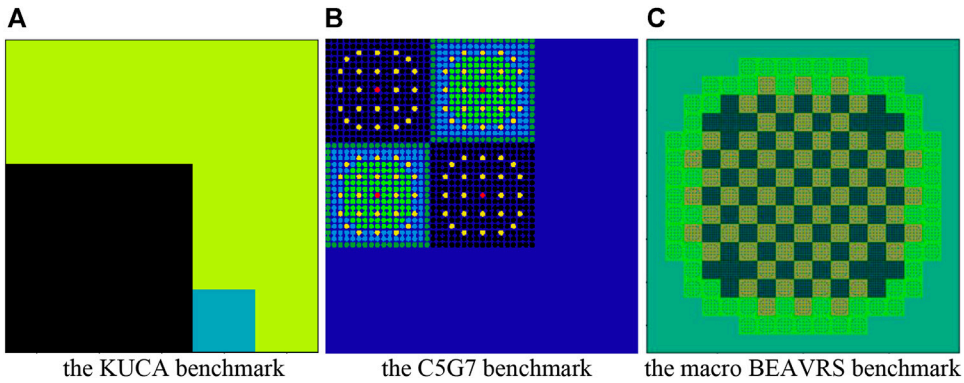

FIGURE 8 | Modeling of the pin-cell geometry cases with SHARK.

Reference result is from the Monte Carlo code OpenMC (Romano and Forget, 2013). Three billion active particles are used (3,000 generations consisting of 1,000,000 neutrons per generation, of which 100 generations are skipped). The standard deviation of the Monte Carlo result is 1 pcm. As for SHARK, 32 flat source regions are divided in the fuel rod pin cell. Sixty azimuthal angles, six polar angles, Yamamoto quadrature set, and 0.03-cm ray spacing are adopted. Eigenvalue and fission rate distribution results are shown in the **Table 1**. The pin-cell fission rate distribution results are shown in the **Figure 7**. As is shown in the table, the eigenvalue difference is 54 pcm, and the maximum pin-cell fission rate difference is 0.2%. These results show the good accuracy of the hexagonal calculation ability in SHARK.

7.1.2 Pin-cell geometry cases

The pin-cell geometry case is the basic calculation target for SHARK. The KUCA benchmark, C5G7 benchmark, and macro BEAVRS benchmark have already been applied in the validation of the transport module (Zhao et al., 2021b). Geometry modeling of these three cases is shown in **Figure 8**.

In the validation of these three cases, the 2D/1D transport method and the quasi-3D method have been compared with numerical results. In the KUCA benchmark and the C5G7 benchmark, the quasi-3D method shows better accuracy because of the strong anisotropic effect in these two cases. In the macro BEAVRS benchmark, the 2D/1D method has efficiency advantage.

Besides, the odCMFD acceleration and spatial parallel method also show good effect on the direct transport calculation. The traditional CMFD method without additive component in the diffusion coefficient has divergence problem in the KUCA and C5G7 benchmark calculation. The odCMFD method solves the issue and improves the stability of the traditional CMFD method. As for the spatial parallel method, 578 cores are adopted for the large-scale parallel calculation in the macro BEAVRS benchmark. The parallel algorithm improves the calculation efficiency, as well as realizing the memory cost decomposition and decreasing the memory cost for each node. The detailed numerical results of the macro benchmarks can be found in previous research (Zhao et al., 2021b).

7.2 The micro benchmark

7.2.1 The VERA-2 lattice benchmark

The VERA benchmark (Godfrey, 2014) is a series of benchmark published in the CASL project. The benchmark is modeled by Watts Bar nuclear plant and includes several cases from two-dimensional pin cell to three-dimensional whole core.

VERA-2 consists of 16 two-dimensional lattice cases in the VERA benchmark. Fuel enrichment, burnup poison, control rod, and gadolinium rod are considered in the VERA-2 benchmark.

Reference results are from the Monte Carlo code KENO using ENDF/B-VI.8. The calculation condition for SHARK is eight azimuthal angles and three polar angles in each octant with Yamamoto optimal quadrature set. The ray spacing is 0.01 cm. The library used in the subgroup method is also generated from ENDF/B-VI.8. Results of the VERA-2 benchmark are shown in **Table 2**. The average eigenvalue difference is 152 pcm, and the average maximum pin power difference is 1.34%. These results show the good accuracy of the subgroup resonance method in SHARK. As for the 2G and 2H cases, both the eigenvalue and pin power differences are relatively large. It is caused by the complex resonance phenomenon for AIC and B_4C control rod absorbers. It needs to be researched in the future.

7.2.2 The VERA-3 assembly benchmark

The VERA-3 assembly benchmark is a 3D single-assembly problem: Case 3A is a 3.1 w/o fuel assembly without burnable absorber at 600 K, and Case 3B is a 2.619 w/o fuel assembly with 16 Pyrex rods at 565 K. In addition to the radial arrangement, the benchmark problem tries to restore the structural details of the fuel assembly in the axial direction, such as end plugs, plenums, springs, nozzles, core plates, and spacer grids. Therefore, the problem provides a full picture of the ability of the software to simulate the heterogeneous effects of PWR assembly in the axial direction.

Two 3D assembly cases are modeled faithfully and accurately with SHARK. The axial active segment is divided into 49 layers, which is exactly consistent with the reference solution. Inflow

TABLE 2 | Numerical results of the VERA-2 benchmark.

Case	KENO-VI	SHARK	Eigenvalue difference	Pin power difference/%	
				Max	RMS
2A	1.17852	1.18099	247	0.76	0.32
2B	1.17977	1.18192	215	0.63	0.28
2C	1.17031	1.17202	171	0.68	0.28
2D	1.16215	1.16366	151	0.65	0.27
2E	1.06660	1.06707	47	1.34	0.59
2F	0.97338	0.97320	−18	1.64	0.68
2G	0.84563	0.84755	192	2.48	1.15
2H	0.78567	0.78701	134	2.75	1.28
2I	1.17637	1.17879	242	0.79	0.31
2J	0.97262	0.97248	−14	1.36	0.65
2K	1.01735	1.01718	−17	1.81	0.72
2L	1.01606	1.01947	341	0.83	0.28
2M	0.93642	0.94010	368	0.46	0.18
2N	0.86773	0.86765	−7	1.90	0.83
2O	1.04575	1.04495	−80	1.74	0.62
2P	0.92664	0.92474	−190	1.54	0.69
Average	—	—	152	1.34	0.57

TABLE 3 | Numerical results of the VERA-3 benchmark.

Case	Description	Reference k_{eff}	SHARK Δk_{eff}(pcm)	Radial power error (%)		Axial power error		
				MAX	RMS	MAX	AVG	RMS
3A	No poison	1.17572	−195	0.15	0.05	2.61	0.80	1.07
3B	16 Pyrex	1.00015	−20	−0.16	0.07	1.70	0.71	0.90

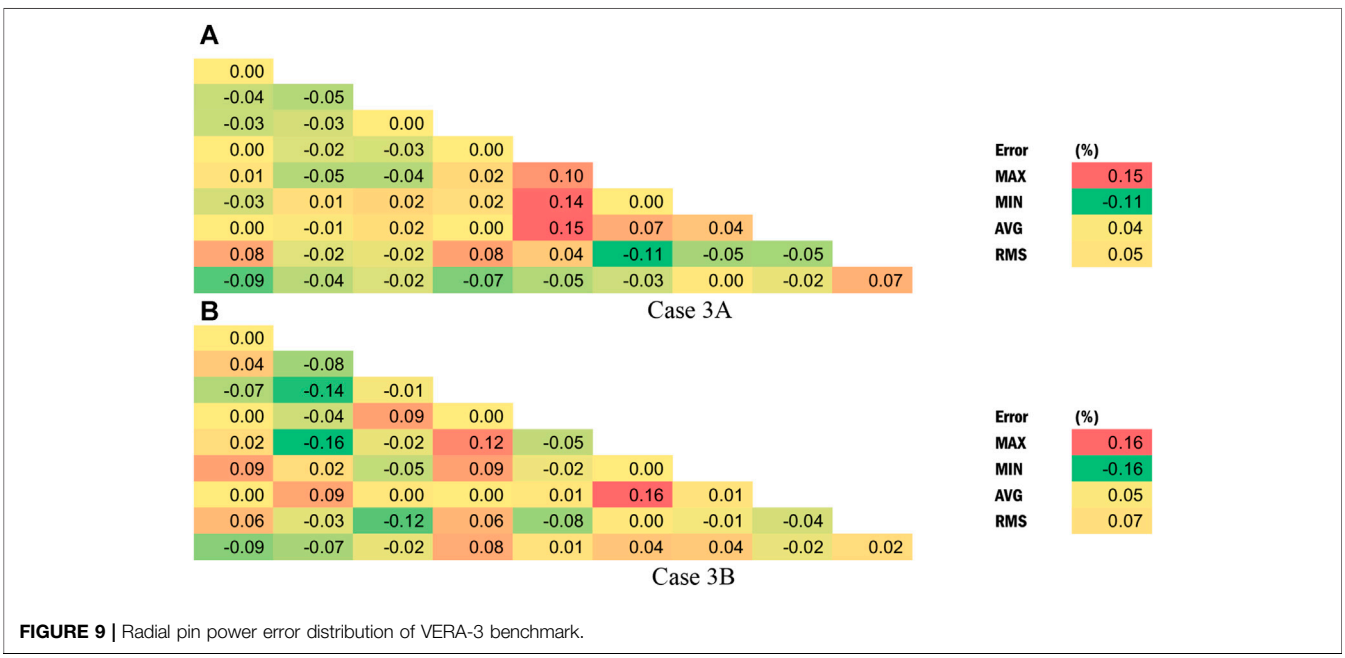

FIGURE 9 | Radial pin power error distribution of VERA-3 benchmark.

transport correction has been applied in calculation of the VERA-3 benchmark. The 2D/1D solver is adopted as the default choice in micro cases considering the better efficiency performance. Compared with the reference results from KENO-VI, the results of the VERA-3 benchmark in SHARK are given in **Table 3** and the radial and axial pin power results are shown in **Figure 9** and **10**. Deviations of eigenvalue results are less than 200 pcm, and the maximum radial pin power differences are 0.15% and 0.16% for

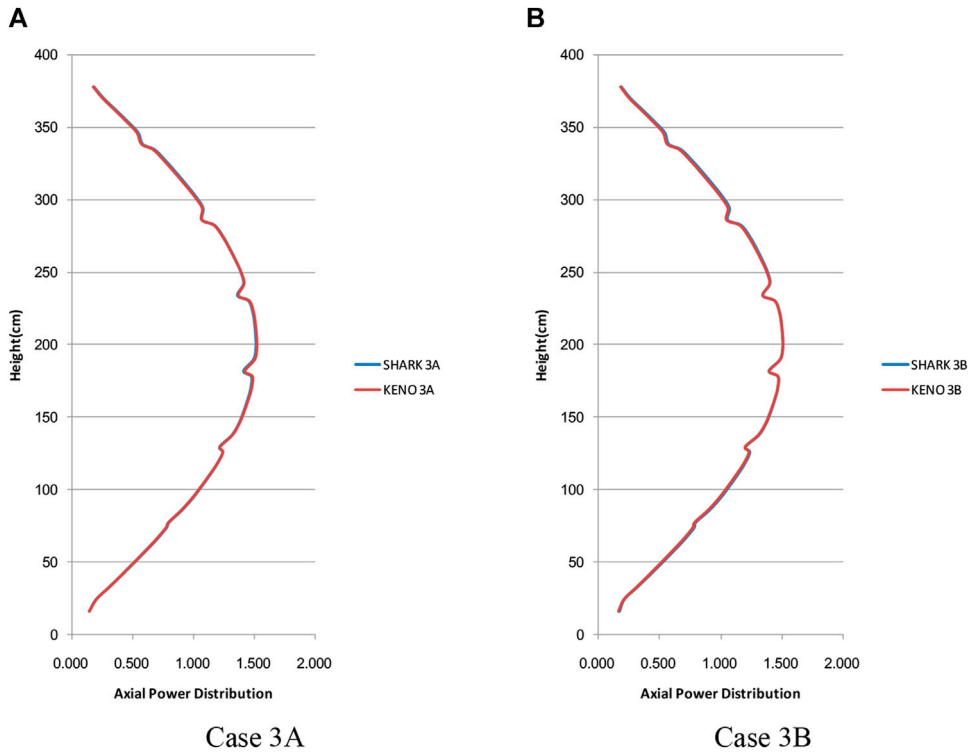

FIGURE 10 | Axial power distribution of VERA Problem #3.

the VERA-3A and VERA-3B cases. As for the axial power distribution, the maximum deviation of SHARK is only 2.61% and occurs in the low-power region near the top reflector layer. Meanwhile, the axial average (AVG) error and RMS error also reflect the accuracy of the program in modeling the axial heterogeneousity. As seen in **Figure 10A**, **B**, the axial power shape fits the KENO-VI reference well, and the spacer grid effects are accurately represented.

8 CONCLUSION

In this paper, a numerical nuclear reactor neutronics code SHARK is newly developed in the Nuclear Power Institute of China (NPIC). The framework and several significant sections of SHARK are introduced, including geometry modeling, characteristic ray tracing, library, subgroup resonance method, 2D/1D and quasi-3D direct transport method, odCMFD acceleration, and spatial parallel method. In numerical results, verification of SHARK is conducted by several macro and micro benchmark cases, including the macro hexagonal assembly case, the micro VERA-2 lattice benchmark, and the VERA-3 assembly benchmark. Eigenvalue difference is 54 pcm, and maximum pin power difference is 0.2% for the macro hexagonal assembly case. As for the micro benchmark, axial power differences are 2.61% and 1.70% for VERA-3A and VERA-3B benchmarks separately. These results show the good accuracy of SHARK.

DATA AVAILABILITY STATEMENT

The original contributions presented in the study are included in the article/Supplementary Material. Further inquiries can be directed to the corresponding author.

AUTHOR CONTRIBUTIONS

All authors listed have made a substantial, direct, and intellectual contribution to the work and approved it for publication.

FUNDING

This work is supported by the National Natural Science Foundation of China (Grant No. 12005214, 11905214) and the China Association for Science and Technology (Young Elite Scientists Sponsorship Program 2019QNRC001).

REFERENCES

Cao, L., Liu, Z. Y., Cao, L. Z., He, Q., and Zhou, X. (2019). "Implementation and Application of the CSG Method in the NECP-X Code[C]," in 27th International Conference on Nuclear Engineering (ICONE-27), Ibaraki, Japan, May 19–24, 2019.

Casl, D. B. (2010). *The Consortium for Advanced Simulation of Light Water Reactors[R]*. Bulletin of the American Physical Society.

CASL Project Summary Slides (2011). *CASL: The Consortium for Advanced Simulation of Light Water Reactors*. CASL-U-2011-0137-000.

Chen, J., Liu, Z., Zhao, C., He, Q., Zu, T., Cao, L., et al. (2018). A New High-Fidelity Neutronics Code NECP-X. *Ann. Nucl. Energ.* 116, 417–428. doi:10.1016/j.anucene.2018.02.049

Cho, J. Y., Kim, K. S., Shim, H. J., Song, J. S., Lee, C. C., and Joo, H. G. (2008). Whole Core Transport Calculation Employing Hexagonal Modular Ray Tracing and CMFD Formulation[J]. *J. Nucl. Sci. Techn.* 45 (8). doi:10.1080/18811248.2008.9711475

Choi, S., Choe, J., Hoang, K., Lee, W., Kim, W., Kim, H., et al. (2019). *Recent Development Status of Neutron Transport Code STREAM[C]*. Korea: Transactions of the Korean Nuclear Society Spring Meeting Jeju.

Cullen, D. E. (1977). *Calculation of Probability Table Parameters to Include Intermediate Resonance Self-Shielding*. LLNL.

Godfrey, A. T. (2014). *VERA Core Physics Benchmark Progression Problem Specifications, Revision 3[R]*. CASL-U-2012-0131-004, CASL.

HELIOS Methods (2001). *HELIOS Methods: III—Resonance Treatment*. Studsvik Scandpower.

Hong, S. G., and Cho, N. Z. (1998). CRX: A Code for Rectangular and Hexagonal Lattices Based on the Method of Characteristics. *Ann. Nucl. Energ.* 25 (8), 547–565. doi:10.1016/s0306-4549(97)00113-8

Hursin, M. (2010). *Full Core, Heterogeneous, Time Dependent Neutron Transport Calculation with the 3D Code DeCART[D]*. Berkeley, CA: University of California, Berkeley.

Iwasaki, J., Tsuruta, H., and Ichikawa, H. (1985). *Neutronics Calculation of Upgraded JRR-3[R]*. JAERI-M, 85–062.

Jung, Y. S. (2013). *Development of Practical Numerical Nuclear Reactor for High Fidelity Core analysis[D]*. Korea: Seoul National University.

Kelley, B. W., and Larsen, E. W. (2013). "2D/1D Approximations to the 3D Neutron Transport Equation," in I: Theory," Proc. M&C 2013, Sun Valley, ID, May 5–9, 2013.

Li, J., Xu, Y., Wang, D., and Shen, C. (2020). "Demonstration of a Linear Prolongation CMFD Method on MOC[C]," in PHYSOR2020, Cambridge, United Kingdom, March 29–April 2, 2020.

Liu, S., Wang, G., Wu, G., and Wang, K. (2015). Neutronics Comparative Analysis of Plate-type Research Reactor Using Deterministic and Stochastic Methods. *Ann. Nucl. Energ.* 79, 133–142. doi:10.1016/j.anucene.2015.01.027

Muir, D. W., Boicourt, R. M., Kahler, A. C., and Jeremy Lloyd, C. (2016). *The NJOY Nuclear Data Processing System, Version 2016*. Los Alamos: Los Alamos National Laboratory. Available at: https://www.osti.gov/biblio/1338791.

OECD (2005). Benchmark on Deterministic Transport Calculations Without Spatial Homogenization (MOX Fuel Assembly 3-D Extension Case)[J]. OECD/NEA Report, *Nucl. Sci. NEA/NSC/DOC* 2005, 16.

Romano, P. K., and Forget, B. (2013). The OpenMC Monte Carlo Particle Transport Code. *Ann. Nucl. Energ.* 51, 274–281. doi:10.1016/j.anucene.2012.06.040

Stimpson, S., Young, M., Collins, B., Kelly, B., and Downar, T. (2013). "Assessment and Improvement of the 2D/1D Method Stability in DeCART[C]," in M&C 2013, Sun Valley, ID, May 5–9, 2013.

Suslov, I. (2001). Improvements in the Long Characteristics Method and Their Efficiency for Deep Penetration Calculations. *Prog. Nucl. Energ.* 39 (2), 223–242. doi:10.1016/s0149-1970(01)00014-2

Wemple, C. A., Gheorghiu, H. N., Stamm'ler, R. J. J., and Eduardo, V. (2008). *The HELIOS-2 Lattice Physics code[JJ]*. Interlaken, Switzerland: Physor2008.

Zhang, T., Wang, Y., Lewis, E., Smith, M. A., Yang, W. S., and Wu, H. (2017). A Three-Dimensional Variational Nodal Method for Pin-Resolved Neutron Transport Analysis of Pressurized Water Reactors [J]. *Nucl. Sci. Eng.* 188 (2), 160–174. doi:10.1080/00295639.2017.1350002

Zhang, T., Lewis, E. E., Smith, M. A., Yang, W. S., and Wu, H. (2017). A Variational Nodal Approach to 2D/1D Pin Resolved Neutron Transport for Pressurized Water Reactors. *Nucl. Sci. Eng.* 186, 120–133. doi:10.1080/00295639.2016.1273023

Zhao, C., Peng, X. J., Zhang, H. B., Zhao, W., Li, Q., and Chen, Z. (2021). Analysis and Comparison of the 2D/1D and Quasi-3D Methods with the Direct Transport Code SHARK[J]. *Nucl. Eng. Techn.* doi:10.1016/j.net.2021.07.038

Zhao, C., Liu, Z., Liang, L., Chen, J., Cao, L., and Wu, H. (2018). Improved Leakage Splitting Method for the 2D/1D Transport Calculation. *Prog. Nucl. Energ.* 105, 202–210. doi:10.1016/j.pnucene.2018.01.007

Zhao, C., Peng, X., Zhang, H., Zhao, W., Chen, Z., and Li, Q. (2021). A Linear Source Scheme for the 2D/1D Transport Method in SHARK. *Ann. Nucl. Energ.* 161, 108479. doi:10.1016/j.anucene.2021.108479

Zhu, A., Jarrett, M., Xu, Y., Kochunas, B., Larsen, E., and Downar, T. (2016). An Optimally Diffusive Coarse Mesh Finite Difference Method to Accelerate Neutron Transport Calculations. *Ann. Nucl. Energ.* 95, 116–124. doi:10.1016/j.anucene.2016.05.004

Conflict of Interest: Authors CZ, XP, HZ, WZ, JR, KL, ZC, ZG, WZ, and QL were employed by the company Nuclear Power Institute of China.

frontiers in Energy Research

ORIGINAL RESEARCH
published: 15 December 2021
doi: 10.3389/fenrg.2021.765865

Refinements of Pin-Based Pointwise Energy Slowing-Down Method for Resonance Self-Shielding Calculation-II: Verifications

Wonkyeong Kim[1], *Sooyoung Choi*[2] *and Deokjung Lee*[1]*

[1]Department of Nuclear Engineering, Ulsan National Institute of Science and Technology, Eonyang, South Korea, [2]Department of Nuclear Engineering and Radiological Sciences, University of Michigan, Ann Arbor, MI, United States

The pin-based pointwise energy slowing-down method (PSM) has been refined through eliminating the approximation for using the pre-tabulated collision probability during the slowing-down calculation. A collision probability table is generated by assuming that material composition and temperature are constant in the fuel pellet using the collision probability method (CPM). Refined PSM (PSM-CPM), which calculates the collision probability in the isolated fuel pellet during the slowing-down calculation using CPM, can consider nonuniform material and temperature distribution. For the methods, the extensive comparative analysis is performed with problems representing various possible conditions in a light water reactor (LWR) design. Conditions are categorized with the geometry, material distribution, temperature profile in the fuel pellet, and burnup. With test problems, PSMs (PSM and PSM-CPM) have been compared with conventional methods based on the equivalence theory. With overall calculation results, PSMs show the accuracy in the eigenvalue with differences in the order of 100 pcm compared to the reference results. There was no noticeable difference in the multigroup cross sections, reaction rates, and pin power distributions. However, PSM-CPM maintains the accuracy in the calculation of the fuel temperature coefficient under the condition with 200% power and nonuniform temperature distribution in the fuel pellet. PSM shows the difference in the eigenvalue in the order of 2,000 pcm for the fictitious pin-cell problem with highly steep temperature profiles and material compositions, but PSM-CPM shows the difference in the eigenvalue within 100 pcm.

Keywords: reactor physics, resonance treatment, resonance self-shielding calculation, slowing-down, equivalence theory, light water reactor (LWR)

OPEN ACCESS

Edited by:
Ding She,
Tsinghua University, China

Reviewed by:
Qian Zhang,
Harbin Engineering University, China
Jinfeng Li,
Imperial College London,
United Kingdom

****Correspondence:***
Deokjung Lee
deokjung@unist.ac.kr

Specialty section:
This article was submitted to Nuclear Energy, a section of the journal Frontiers in Energy Research

Received: *27 August 2021*
Accepted: *02 November 2021*
Published: *15 December 2021*

Citation:
Kim W, Choi S and Lee D (2021) Refinements of Pin-Based Pointwise Energy Slowing-Down Method for Resonance Self-Shielding Calculation-II: Verifications. Front. Energy Res. 9:765865. doi: 10.3389/fenrg.2021.765865

INTRODUCTION

The resonance treatment (or resonance self-shielding calculation) is an essential and challenging process to solve the multigroup neutron transport equation that requires the effective multigroup cross sections (XSs). The equivalence theory is one of the resonance treatment methods which have an ultimate purpose to accurately predict the effective multigroup XSs (Knott et al., 2010; Stamm'ler and Abbate, 1983). The equivalence theory, in the literal sense, is to create a homogeneous system (infinite dilution system) that is equivalent to a heterogeneous system by utilizing background XSs. The equivalence theory has been widely used by providing a reasonable solution with a short

computation time, as standard resonance treatment method, and has been adopted by conventional codes such as CASMO (Rhodes et al., 2006a), WIMS (Powney and Newton, 2004), and APOLLO (Knott et al., 2010). However, there have been several fundamental approximations which impede its accuracy. The clumsy problem results from not considering a spatial effect of the resonance self-shielding by subdivided regions in the fuel pellet. In other words, a fuel pellet is assumed as a medium. Other important approximations are the resonance interference effect and the scattering source approximation. In order to reduce the error caused from the approximations, many studies have been conducted in the equivalence theory field. To consider the self-shielding effect for subdivided regions in the fuel pellet, the spatially dependent Dancoff method (SDDM) (Matsumoto et al., 2005) calculates the coefficients of the rational approximation incorporating the Dancoff factor for the fuel pellet as a medium and applies a weighting function for the spatial self-shielding for each subdivided region in the fuel pellet using the Stoke–Weiss method (Stoker and Weiss, 1996). SDDM adopts the Dancoff correction with the black limit approximation based on Stamm'ler correction (Stamm'ler and Abbate, 1983). In black limit approximation, the resonance material is the perfect neutron absorber. In contrast, the spatially dependent gray resonance self-shielding method (SDGM) (Koike et al., 2012) improves the coefficients in the rational approximation by considering gray resonance. In a similar manner, the spatially dependent resonance self-shielding method (SDSS) is implemented in CASMO5 (Ferrer and Hykes, 2019). SDGM and SDSS use the Stoke–Weiss method to compute the fuel escape probability for subdivided regions in the isolated fuel, and both methods consider gray resonance with optimum rational approximation (Rhodes et al., 2006b; Choi et al., 2015).

Another error source of the equivalence-based methods is the approximation of the scattering source with narrow or intermediate resonance approximation. The scattering source approximation is caused by the overestimation of the ^{238}U effective XS (Choi et al., 2021; Choi et al., 2017). Some studies have addressed the issue (Powney and Newton, 2004; Yamamoto et al., 2011; Zhang et al., 2015) but still require drastic improvements.

A new resonance treatment method was also developed to overcome limitations of the equivalence theory (Choi et al., 2017). The new method utilizes the pointwise energy XSs to solve the slowing-down equation based on a subdivided fuel pellet and a fictitious moderator region, which is called the pin-based pointwise energy slowing-down method (PSM) (Choi et al., 2021; Choi et al., 2017; Choi, 2022). Solving the pointwise energy slowing-down addresses two main issues in the equivalence theory, namely, the resonance scattering and the resonance interference effect. Another advantage of the PSM is what does not use the resonance integral (RI) table. PSM allows to calculate the effective XS for the nonuniform material compositions and temperature profiles in the fuel pellet. The accuracy of the effective XSs calculated shows good agreements with the effective XSs calculated by Monte Carlo calculation.

In the accompanying paper (Choi, 2022), PSM was reviewed and PSM-CPM, the refined method of PSM with collision probability method (CPM), was introduced. PSMs (PSM and PSM-CPM) are verified with a few of light-water (LWR) reactor problems with the uniform material composition and temperature profile. PSM generates the table of the collision probability as a function of the total XS for the isolated fuel pellet before slowing-down calculation, where it is assumed that the total XS of all the subdivided regions in the fuel pellet is constant. In this case, the average total XS in the entire fuel pellet is used in the lookup of the collision probability. Because PSM-CPM calculates the collision probability in the isolated fuel pellet solving the pointwise slowing-down equation, different total XSs in each subdivided region with the nonuniform material compositions or temperature profiles are explicitly considered. When the fuel is burned and the thermal hydraulic feedback is involved with the neutron transport calculation, the nonuniformity of the material compositions and temperature profiles in the fuel pellet appears. In this case, PSM-CPM is an alternative option to calculate the collision probability of subdivided regions in the isolated fuel pellet under the nonuniform material composition and temperature profile. With the development of PSM, there have been the resonance self-shielding methods which adopt the ultra-fine-group (UFG) method to solve the slowing-down equation (Liu et al., 2015; Zhang et al., 2018). Along with this study, the nonuniformity problem has also been the central issue by many studies which have addressed the difficulties of rigorously predicting the effective XSs by the nonuniformity of the material compositions or temperature profiles (Liu et al., 2015; Zhang et al., 2018; Li, 2020; Zhang et al., 2020). There have also been cutting-edge approaches on treating the nonuniformity in the resonance self-shielding calculation using the machine learning technique (Qin et al., 2020a; Qin et al., 2020b).

In this paper, PSM and PSM-CPM (PSMs) are reviewed, and comparative analyses are presented extensively with various test cases with the condition of nonuniform material compositions and temperature profiles. The purpose of comparative analysis is to present the limitation of PSM as well as the accuracy of PSMs representing the effect depending on how to calculate the collision probability in the isolated fuel pellet. Test cases for the accuracy assessments consist of various conditions of the geometry, material distribution, temperature profile, and burnup. A total of five sections are presented with the problem descriptions and the results. In each section, the detailed XS and reaction rate comparison is presented to show the accuracy of PSMs, in which it is also compared with the results of the conventional equivalence theory methods.

METHODS

Conventional Equivalence Theory Methods

The equivalence theory is derived with the transport equation with collision probabilities for the two-region problem and with

the scattering source approximation with the intermediate resonance (IR) approximation as follows:

$$\sum_{t,F}(E)\phi_F(E)V_F = P_{FF}(E)V_F Q_{s,F}(E) + P_{MF}(E)V_M Q_{s,M}(E) \quad (1)$$

where

$$\begin{cases} Q_{s,F}(E) = \sum_{r\in F} N^r\left(\lambda^r\sigma_p^r\frac{1}{E} + (1-\lambda^r)\sigma_s^r(E)\phi_F(E)\right) \\ Q_{s,M}(E) = \sum_{r\in M} N^r\left(\lambda^r\sigma_p^r\frac{1}{E}\right) \end{cases} \quad (2)$$

F is the index of the fuel pellet; M is the index of moderator; $\sum_{t,F}(E)$ is the total XS of fuel; $\phi_F(E)$ is the flux in fuel; V_F is the volume of the fuel pellet, $P_{FF}(E)$ is the fuel-to-fuel collision probability; $P_{MF}(E)$ is the collision probability from M to F; N^r is the number density of the nuclide r; $\sigma_s^r(E)$ is the scattering XS of the nuclide r; λ^r is the IR parameter; and Σ_p^r is the potential XS of the nuclide r.

Equation 1 is rewritten by using the approximated scattering source and the reciprocity theorem in **Eq. 4** as follows:

$$\sum_{t,F}(E)\phi_F(E) = P_{FF}(E)\left[\lambda_F\Sigma_{p,F}\frac{1}{E} + (1-\lambda_F)\Sigma_{s,F}(E)\phi_F(E)\right] + P_{FM}(E)\sum_{t,F}(E)V_F\frac{1}{E} \quad (3)$$

where $\lambda_X\Sigma_{p,X} = \sum_{r\in X}\lambda^r N^r\sigma_p^r$, $(X = F\text{or}M)$, and the reciprocity theorem is

$$P_{FM}(E)\sum_{t,F}(E)V_F = P_{MF}(E)\Sigma_{t,M}V_M \approx P_{MF}(E)\lambda_M\Sigma_{p,M}V_M \quad (4)$$

Then, the fuel-to-fuel collision probability is approximated by the rational equation as follows:

$$P_{FF}(E) = 1 - P_{FM}(E) = \sum_{n=1}^{N}\frac{\beta_n\Sigma_{t,F}(E)}{\Sigma_{t,F}(E)+\alpha_n\Sigma_e} \quad (5)$$

where N is the number of rational expressions; α_n and β_n are the coefficients of the nth rational term for the fuel rod; and Σ_e is the escape XS of the fuel rod (Knott et al., 2010).

It should be noted that the subscript F is not indicated in a_n, β_n, and Σ_e for simplification, even though the parameters are for the fuel rod. When the multi-term rational approximation is used, the total flux is approximated as a linear combination of the nth fluxes. By substituting **Eq. 5** into **Eq. 3** with the approximation, the flux is

$$\phi_F(E) = \sum_{n=1}^{N}\beta_n\phi_{F,n}(E) = \sum_{n=1}^{N}\beta_n\frac{\lambda_F\Sigma_{p,F}+\alpha_n\Sigma_e}{\Sigma_{a,F}(E)+\lambda_F\Sigma_{rs,F}(E)+\lambda_F\Sigma_{p,F}+\alpha_n\Sigma_e}\frac{1}{E} \quad (6)$$

where $\Sigma_{rs,F}(E)$ is the resonance scattering XS of the fuel.

In the equivalence theory, it is assumed that the fuel contains only one resonant nuclide and only the nuclide has the absorption XS. Therefore, $\Sigma_{a,F}(E)$ and $\Sigma_{rs,F}(E)$ are assumed to be both macroscopic XSs of the fuel and the resonant nuclide r (i.e., $\Sigma_{a,F}(E) = N^r\sigma_a^r(E)$). The flux in the fuel is rewritten as **Eq. 7** by dividing the numerator and denominator by the number density of the target nuclide r, and **Eq. 7** is presented as the lethargy form.

$$\phi_F(u) = \sum_{n=1}^{N}\beta_n\frac{\sigma_{b,n}^r}{\sigma_a^r(u)+\sigma_{b,n}^r} \quad (7)$$

where $\sigma_a^r(E)$ is the absorption XS of the nuclide r; $\lambda^r\sigma_{rs}^r(E)$ is the resonance scattering XS multiplied by the IR parameter of the nuclide r; and $\sigma_{b,n}^r$ is the nth term background XS of the nuclide r and is defined as follows:

$$\sigma_{b,n}^r = \frac{1}{N^r}\left(\lambda_F\Sigma_{p,F}+\alpha_n\Sigma_e\right) \quad (8)$$

The resonance scattering XS in **Eq. 7** is usually dropped for simplicity. The effective multigroup XS is calculated as a ratio of the reaction rate to the flux integrated over the energy range. Therefore, the multigroup XS for the reaction x is calculated as follows:

$$\sigma_{x,g}^r = \frac{\int_{\Delta u_g}\sigma_x^r(u)\phi_F(u)du}{\int_{\Delta u_g}\phi_F(u)du} = \frac{\int_{\Delta u_g}\sigma_x^r(u)\sum_{n=1}^{N}\beta_n\frac{\sigma_{b,n}}{\sigma_a^r(u)+\sigma_{b,n}}du}{\int_{\Delta u_g}\sum_{n=1}^{N}\beta_n\frac{\sigma_{b,n}}{\sigma_a(u)+\sigma_{b,n}}du} = \frac{\sum_{n=1}^{N}\beta_{n,g}\sigma_{x,n,g}^r\phi_{n,g}}{\sum_{n=1}^{N}\beta_{n,g}\phi_{n,g}} \quad (9)$$

where

$$\sigma_{x,n,g}^r = \sigma_{x,g}^r\left(\sigma_{b,n,g}^r\right)x = a,s,f \quad (10)$$

$$\phi_{n,g} = \phi_g\left(\sigma_{b,n,g}^r\right) = \frac{\sigma_{b,n,g}^r}{\sigma_{a,n,g}^r+\sigma_{b,n,g}^r} \quad (11)$$

$$\sigma_{b,n,g}^r = \frac{1}{N^r}\left(\sum_r\lambda_g^r N^r\sigma_p^r + \alpha_{n,g}\Sigma_e\right) \quad (12)$$

Actually, the IR parameter has energy dependency because every resonance has a different width. Therefore, the energy-integrated IR parameter λ_g^r has energy group dependency. The multigroup parameters such as $\alpha_{n,g}$, $\beta_{n,g}$, and $\sigma_{b,n,g}^r$ also have energy group dependency.

There are various calculation methods for the coefficients of the first flight collision probability shown in **Eq. 5**. The enhanced neutron current method (Yamamoto, 2008) and gray resonance treatment method (Koike et al., 2012) solve the fixed-source transport equation without the resonance scattering XS, as follows:

$$\Omega\cdot\nabla\psi_g(v,\Omega) + \left[\Sigma_{a,g}^*(v)+\lambda_g\Sigma_p(v)\right]\psi_g(v,\Omega) = \frac{1}{4\pi}\lambda_g\Sigma_p(v) \quad (13)$$

where $\psi_g(v,\Omega)$ is the angular flux for the position v and angle Ω, and $\Sigma_{x,g}^*(v)$ is the approximated XS of the reaction x.

In the enhanced neutron current method, the total XS or the absorption XS are assumed to be infinite, and the Dancoff factor is calculated from the total reaction rate of the fuel region. The

Dancoff factor can be used in the calculation of the rational approximation with Wigner's one-term or Carlvik's two-term method (Knott et al., 2010). In the gray resonance treatment method, the fuel flux is calculated with several discrete values of the fuel XSs, and then the rational approximation is calculated through the least square fitting process to the fuel flux. In their methods, the resonance scattering XS was omitted, but **Eq. 13** can be easily rewritten with the resonance scattering XS as follows:

$$\Omega \cdot \nabla \psi_g(\nu,\Omega) + \left[\Sigma^*_{a,g}(\nu) + \lambda_g \Sigma^*_{rs,g}(\nu) + \lambda_g \Sigma_p(\nu)\right]\psi_g(\nu,\Omega) = \frac{1}{4\pi}\lambda_g \Sigma_p(\nu) \tag{14}$$

There are several existing methods for spatial self-shielding calculation inside a fuel pellet with the equivalence theory. In this study, recent methods such as SDGM and SDSS as mentioned in *Introduction* section are not considered as the comparable methods. In the Distributed Resonance Integral (DRI) method (Xu et al., 2009), the legacy method implemented in CASMO-5, the average effective XS of the fuel pellet is calculated with a single region, and then an empirical radial distribution function is applied. The function is generated from Monte Carlo calculations, for the ^{238}U resonance integral (Xu et al., 2009). Matsumoto developed the SDDM (Matsumoto et al., 2005) based on the idea of Stoker–Weiss (Stoker and Weiss, 1996). SDDM calculates the coefficients of the rational approximation using the Dancoff factor for the fuel pellet with a single region and applies a weighting function for the spatial self-shielding inside the fuel pellet. Both the DRI method and the SDDM can consider the radial self-shielding effect inside the fuel pellet and calculate the spatially dependent multigroup XSs. However, both methods have the following two drawbacks. First, the methods use the multi-term rational approximation (Carlvik's two-term) and the effective XSs come from the XS lookup table using the multiple background XSs. Second, the methods use the resonance parameters or the effective XSs calculated for the fuel pellet with a single region. In the DRI method, the corrected effective XS is normalized as follows:

$$\sum_{i\in F} N_i^{U238} V_i \sigma_{a,i,g}^{U238} = \sum_{i\in F} N_i^{U238} V_i \bar{\sigma}_{a,g}^{U238} \tag{15}$$

where N_i^{U238} is the number density of ^{238}U in a subdivided region i; $\bar{\sigma}_{a,g}^{U238}$ is the average absorption XS of ^{238}U; and $\sigma_{a,i,g}^{U238}$ is the corrected absorption XS of ^{238}U in a subdivided i with the empirical correction factor w_i. as

$$\sigma_{a,i,g}^{\mathrm{U238}} = w_i \bar{\sigma}_{a,g}^{\mathrm{U238}} \tag{16}$$

If the averaged ^{238}U absorption XS is not calculated properly, the distributed absorption XS still has bias in the averaged XS. SDDM calculates the effective XS of a subdivided region i using the coefficients of rational approximation for averaged fuel as follows:

$$\frac{\sigma^r_{x,i,g} = \sum_{m=1}^4 F_{i,m} \sum_{n=1}^N \beta_{n,g} RI^r_{x,g}\left(\sigma^r_{b,i,n,m,g}\right)}{1 - \sum_{m=1}^4 F_{i,m} \sum_{n=1}^N \beta_{n,g} \frac{RI^r_{a,g}\left(\sigma^r_{b,i,n,m,g}\right)}{\sigma^r_{b,i,n,m,g}}} \tag{17}$$

where $F_{i,m}$ is the weighting function, and $\sigma^r_{b,i,n,m,g}$ is the background XS defined as

$$\sigma^r_{b,i,n,m,g} = \frac{1}{N^r}\left(\sum_r \lambda^r_g N^r \sigma^r_p + \alpha_{n,g}\Sigma_{e,i,m}\right) \tag{18}$$

where $\Sigma_{e,i,m}$ is the escape XS of a subdivided region i and the shape m.

The fuel-to-fuel collision probability generated for the fuel pellet with a single region has a significant error because of the scattering source distribution inside the fuel. Therefore, SDDM also has the same problem as long as $\alpha_{n,g}$ and $\beta_{n,g}$ are calculated for the fuel lump.

Pin-Based Pointwise Energy Slowing-Down Method

For a subdivided region in the fuel pellet and a nonfuel region, the pointwise energy slowing-down equations can be reformulated by ignoring the fission source and inelastic scattering source and using the reciprocity relation as follows:

$$\phi_i(u) = \sum_{j\in F} \frac{P_{ij}(u)}{\Sigma_{t,j}(u)} Q_{s,j}(u) + \frac{P_{iM}(u)}{\Sigma_{p,M}} Q_{s,M}(u), i \in F \tag{19}$$

$$\phi_M(u) = \sum_{i\in F} \frac{P_{Mi}(u)}{\Sigma_{t,i}(u)} Q_{s,i}(u) + \frac{P_{MM}(u)}{\Sigma_{p,M}} Q_{s,M}(u) \tag{20}$$

where i and j are the indexes of the subdivided regions of the fuel pellet; F and M are the fuel pellet and the nonfuel region, respectively.

PSMs (PSM and PSM-CPM) calculate $P_{ij}(u)$, $P_{iM}(u)$, $P_{Mi}(u)$, and $P_{MM}(u)$ to obtain the fluxes and scattering sources shown in **Eq. 19** and **20** by solving the neutron slowing-down equations with a fixed source at high energy.

A two-step approach is used to calculate the collision probabilities. In the first step, the collision probabilities of the subdivided regions in the isolated fuel pellet are calculated. The collision probability of the isolated fuel pellet is denoted as P_{ij}^{iso}. In the PSM (not PSM-CPM), $\hat{P}_{ij}^{iso}$ is tabulated as a function of the total XS of the fuel pellet before solving slowing-down equations, and then P_{ij}^{iso} is interpolated from the $\hat{P}_{ij}^{iso}$ table. In this tabulation, the total XS of fuel is assumed to be constant for the entire fuel pellet. The assumption of the constant material composition and temperature in the fuel pellet is not exact for the burned fuel and nonuniform temperature profile. In this case, the total XS of the entire fuel pellet for interpolating P_{ij}^{iso} at certain energy is replaced by the average total XS of the entire fuel pellet. This is the fundamental inconsistency for calculating the collision probability of the isolated fuel in PSM. The validity of the assumption and the effect of the effective XS by the theoretical inconsistency have been addressed in studies (Liu et al., 2015; Zhang et al., 2018; Zhang et al., 2020).

On the other hand, PSM-CPM calculates P_{ij}^{iso} by using the CPM solvers for all energy points during solving of slowing-down equations without the assumption in that of PSM. Depending on how to calculate P_{ij}^{iso}, the distinction is made between PSM and

TABLE 1 | Summary of test cases (Choi et al., 2021).

Section	Test name	Geometry	Material distribution	Temperature profile	Method	Note
Pin-Cell With Nonuniform Material Composition and Uniform Temperature Profile	Highly burned UO_2 pin-cell	Pin-cell	Nonuniform	Uniform	EQ, DRI, SDDM, MCXS, PSM, PSM-CPM	60 MWd/kgU burned fuel
17 × 17 Fuel Assembly Depletion Benchmark	VERA depletion	FA	Nonuniform	Uniform	EQ, DRI, SDDM, PSM, PSM-CPM	Depletion calculation for two FAs
Pin-Cell With Nonuniform Material Composition and Temperature Profile	Highly burned UO_2 pin-cell with TH feedback	Pin-cell	Nonuniform	Nonuniform	EQ, DRI, SDDM, MCXS, PSM, PSM-CPM	60 MWd/kgU burned fuel
SNU Nonuniform Temperature Pin-Cell Benchmark	SNU benchmark	Pin cell	Uniform	Nonuniform	EQ, DRI, SDDM, MCXS, PSM, PSM-CPM	Wide range of power
Pin-Cell of Annular Type With Centered Burnable Absorber	UO_2 pin-cell with centered burnable absorber	Pin cell	Nonuniform	Uniform	PSM, PSM-CPM	Annular type, fresh fuel

PSM-CPM. Introducing the $\hat{P}_{ij}^{iso}$ table can lead to an error in computing the collision probability even though it can reduce significant calculation time. In particular, the annular type of fuel pellet which has an extreme variation of total XSs in each subdivided region is caused by the significant error.

In PSMs (i.e., PSM and PSM-CPM), Carlvik's two-term rational approximation in the equivalence theory is incorporated to correct the shadowing effect from neighboring fuel rods and structural materials. Since P_{ij}^{iso} is calculated in an isolated fuel rod, a correction is required to consider the shadowing effect properly.

The shadowing effect correction factor, which adjusts the fuel escape probability of isolated fuel pin to consider the shadowing effect, is defined as a ratio of the fuel escape probabilities of two systems as follows:

$$\eta_i(u) \approx \eta_F(u) = \frac{P_{e,F}(u)}{P_{e,F}^{iso}(u)} \tag{21}$$

where $P_{e,F}^{iso}$ is the fuel escape probability of an isolated fuel pin and $P_{e,F}$ is that of the fuel pin in the lattice.

The shadowing effect correction factor is multiplied to the fuel escape probability in each subdivided region of the fuel pellets as follows:

$$P_{iM}(u) = P_{e,i}(u) = \eta_i(u) P_{e,i}^{iso}(u) \tag{22}$$

where

$$P_{iM}^{iso}(u) = P_{e,i}^{iso}(u) = 1 - \sum_{j \in F} P_{ij}^{iso}(u) \tag{23}$$

It is assumed that the subdivided regions of the fuel pellet have the same shadowing effect. The collision probability is then normalized to consider the changes in the fuel escape probability as follows:

$$P_{ij}(u) = P_{ij}^{iso}(u) \frac{1 - P_{e,i}(u)}{1 - P_{e,i}^{iso}(u)} \tag{24}$$

The collision probabilities from the non-fuel region are written as follows:

$$P_{Mi}(u) = \frac{P_{iM}(u) \Sigma_{t,i}(u) V_i}{\Sigma_{p,M} V_M} \tag{25}$$

$$P_{MM}(u) = 1 - \sum_{i \in F} P_{Mi}(u) = 1 - \sum_{i \in F} \frac{P_{iM}(u) \Sigma_{t,i}(u) V_i}{\Sigma_{p,M} V_M} \tag{26}$$

Finally, all the collision probabilities and escape probabilities are derived to solve the slowing-down equations in **Eqs. 19, 20**.

ACCURACY ASSESSMENT

Various LWR problems are solved to verify the accuracy of the PSMs. **Table 1** presents a summary of test cases and methods used in the verifications. The test cases include various conditions of the geometry (i.e., pin-cell and FA), material distribution (i.e., uniform and nonuniform), temperature profile (i.e., pin-cell and FA), and burnup (i.e., fresh fuel and burned fuel). The methods used in the comparisons are as follows:

1) EQ: the conventional equivalence theory
2) DRI: the distributed resonance integral method used in CASMO-5 (Xu et al., 2009)
3) SDDM: the spatially dependent Dancoff method used in PARAGON (Matsumoto et al., 2005)
4) MCXS: simulation with tallied multigroup XSs using the MCNP6 code
5) PSM: the pin-based pointwise slowing-down method with the $\hat{P}_{ij}^{iso}$ table (Choi et al., 2017)
6) PSM-CPM: the pin-based pointwise slowing-down method with the CPM (Choi, 2022)

MCXS means the multigroup transport simulation with multigroup absorption and nu*fission XSs calculated from the continuous energy Monte Carlo code (i.e., MCNP6 (Goorley et al., 2012)). $(n, 2n)$ and $(n, 3n)$ XSs are also tallied to calculate absorption XSs for the simulation. The scattering matrix is not tallied from the MCNP6, because MCNP6 cannot calculate the multigroup scattering XS matrix. From

the perspective of the resonance self-shielding calculation, the first purpose is to calculate the exact multigroup XSs. However, the multigroup simulation cannot completely reproduce the continuous energy solution, even though the exact multigroup XS is used in the simulation. Using the exact multigroup XS does not guarantee that the reaction rate is exact. There are still many error sources in the multigroup calculations (e.g., anisotropy, angular dependency of the multigroup XSs). This problem has not been clearly solved. Some studies tried to apply an artificial correction factor (i.e., SPH method) to reproduce the continuous energy solution (SUGIMURA and Yamamoto, 2007; Joo et al., 2009). The SPH method is not applied in this work because of the following reasons. First, the SPH method still cannot completely reproduce the continuous energy solution because the SPH factor is generated with a local continuous energy solution (i.e., pin cell). Second, the source from the continuous energy solution is assumed to be same as the source in the multigroup calculation during the SPH iteration. Third, the SPH factor is only applied in the resonance energy range. How to preserve the continuous energy reaction rate is still an open problem. Fortunately, the error in the reaction rate is not significant if the exact multigroup XS is used (see *Pin-Cell With Nonuniform Material Composition and Uniform Temperature Profile*, *17 × 17 Fuel Assembly Depletion Benchmark* and *Pin-Cell With Nonuniform Material Composition and Temperature Profile* sections).

All the methods listed above are implemented in the STREAM code to compare the accuracy of the methods in the following sections. It should be noted that the results in this work do not mean that the CASMO-5 and PARAGON codes are the same as those of DRI and SDDM. There may be many unpublished methods used in the vendor codes. In other words, the resonance self-shielding methods of CASMO-5 and PARAGON are not completely the same as the STREAM code with DRI and SDDM, respectively. Although the overall theories are the same as that of the STREAM code, the detailed implementations may be different. For example, a vendor code uses an empirical correction factor to correct the fuel escape probabilities (SUGIMURA and Yamamoto, 2007), but the detailed values of the correction factor are not shown. In addition, some codes adjust the resonance integral table to obtain an accurate result (Koike et al., 2012). In treating the resonance interference effect, the Bondarenko iteration is usually used in the equivalence theory. However, some codes try to consider the resonance interference effect in the process, which generates the multigroup XS library by solving the slowing-down equations with typical mixed fuel materials (Koike et al., 2012). Some codes use many energy groups (*e.g.*, ~300 groups) to reduce the error from the resonance interference effect (Knott et al., 2010). As discussed above, the detailed methods implemented in lattice physics codes are slightly different from the basic equivalence theory. Most of the methods are empirical corrections applied to fit the results to the Monte Carlo solution or experimental data. It is difficult to compare the methods consistently, because the information of the empirical corrections is insufficient and there are excessively various modified methods to implement. Therefore, the theoretical methods are implemented in the STREAM code to compare with the PSMs. DRI is also one of the empirical corrections, but there are sufficient descriptions to implement. There is no empirical correction (except DRI) in the STREAM code and the STREAM libraries.

In solving LWR problems, various parameters are compared to examine the accuracy and the calculation efficiency of the PSMs. In some problems (*Pin-Cell With Nonuniform Material Composition and Uniform Temperature Profile*, *17 × 17 Fuel Assembly Depletion Benchmark*, and *Pin-Cell With Nonuniform Material Composition and Temperature Profile* sections), the multigroup reaction rates are compared to examine the accuracy of the resonance self-shielding methods in detail. The eigenvalue represents the global condition of the problem. The eigenvalue can agree well with the reference solution, owing to error cancellation of some local errors in the reaction rates. Therefore, it is important to compare the reaction rates and the XSs. The difference in k-inf can be reconstructed with the difference of the absorption and fission reaction rates as follows:

$$\begin{aligned} dk_{\text{inf}} &= k_{\text{STREAM}} - k_{\text{Ref.}} = d\left(\frac{P}{A}\right) = \frac{AdP - PdA}{A^2} \\ &= dP - PdA = \sum_{r,i,g} \Delta P_{r,i,g} - P_{\text{STREAM}} \sum_{r,i,g} A_{r,i,g} \end{aligned}, \tag{27}$$

where dk_{inf} is the difference in k-inf between k-inf from the STREAM code (k_{STREAM}) and MCNP6 ($k_{\text{Ref.}}$); P is the sum of the neutron production rate, which is identical to the nu*fission rates; A is the sum of absorption rates; r is the index of the region; i is the index of the nuclide; g is the index of the energy group; $\Delta P_{r,i,g}$ is the difference in the production rate in region r, nuclide i, and group g; and $\Delta A_{r,i,g}$ is the difference in the absorption rate in region r, nuclide i, and group g.

The sum of the absorption rates from both STREAM and MCNP6 are normalized to unity. Therefore, there is no A in the second line of **Eq. 27**. From the normalization, $P_{r,i,g}$ and $-P_{\text{STREAM}}A_{r,i,g}$ mean contribution of k-inf in elements r, i, and g from the production rate and absorption rate, respectively. $\Delta P_{r,i,g}$ means the contribution to the difference in k-inf from the difference in the production rates of elements r, i, and g. In the same context, $-P_{\text{STREAM}}\Delta A_{r,i,g}$ is the contribution to the difference in k-inf from the difference in the absorption rates. The sum of $\Delta P_{r,i,g}$ and $-P_{\text{STREAM}}\Delta A_{r,i,g}$ is the total contribution to the difference in k-inf from the two reactions. From the equations, it is convenient to calculate which elements make the significant differences from the perspective of the eigenvalue.

Pin-Cell With Nonuniform Material Composition and Uniform Temperature Profile

The burned pin-cell problem was designed to examine the accuracy of PSMs for the pin-cell with the nonuniform material composition in the fuel pellet. When the collision probability is calculated, PSM uses one more approximation, which is that the material composition is constant in the fuel pellet, as described in an accompanying paper (Choi, 2022). PSM-

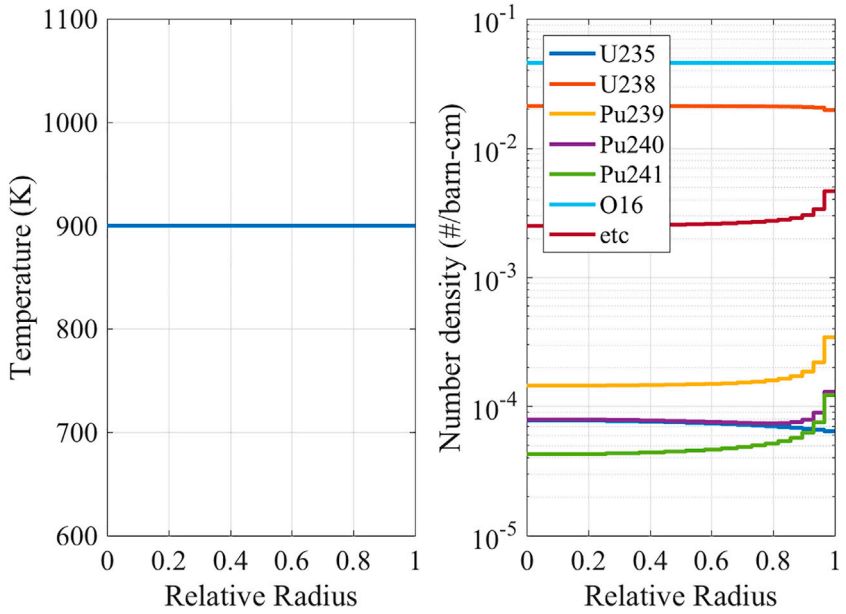

FIGURE 1 | Temperature profile and number densities (60 MWd/kg burned fuel pin-cell) (Choi et al., 2021).

TABLE 2 | k-inf and difference (60 MWd/kg burned fuel pin-cell) (Choi et al., 2021).

Method	k-inf	Difference (pcm)
MCNP6 (reference)	0.79383 ± 0.00014	—
EQ	0.79008	−375
DRI	0.78959	−424
SDDM	0.79016	−367
MCXS	0.79493	110
PSM	0.79498	115
PSM-CPM	0.79471	88

TABLE 3 | Nuclide-wise contribution to k-inf difference (60 MWd/kg burned fuel pin-cell) (Choi et al., 2021).

Nuclide	Contribution to k-inf difference (pcm)					
	EQ	DRI	SDDM	MCXS	PSM	PSM-CPM
^{239}Pu	−159	−179	−158	31	34	24
^{238}U	−170	−202	−101	−5	33	7
^{150}Sm	−93	−93	−95	−1	−1	−1
^{152}Sm	76	76	72	6	5	6
^{99}Tc	−60	−60	−64	5	6	7
^{147}Pm	−57	−57	−59	3	5	5
^{235}U	−49	−52	−50	12	13	11
^{238}Np	−26	−26	−26	0	−26	−26
^{236}U	−32	−33	−32	4	10	10
^{10}B	19	25	18	15	11	13
^{240}Pu	30	33	32	2	2	3
etc.	22	22	−4	20	14	19
Overall	−373	−422	−365	112	117	90

CPM was developed as a rigorous version of PSM. PSM-CPM uses a more rigorous method to calculate the collision probabilities in the subregions of the pellet. The 3.1-wt.% UO_2 pin cell was burned up to 60 MWd/kgHM with an initial power density of 40 W/gHM. The discharge burnup of the fuel assembly in the actual reactor design was approximately 45 MWd/kgHM. The problem has more difficult conditions in terms of the heterogeneous material distributions. The materials used in the problem are as follows: 3.1 wt% UO_2 fuel, air gap, Zircaloy-4 cladding, and H_2O moderator with 1,300 ppm boron. The geometries of the pin-cell are the fuel pellet of outer radius 0.4096 cm; the cladding of inner radius 0.4180 cm; the cladding of thickness 0.057 cm; the gap placed between the fuel pellet and the cladding; and the pin-pitch of 1.26 cm.

The depletion calculation was performed with the STREAM code using PSM. In the calculation, the fuel pellet was divided into 15 subregions of equal volume. The depletion calculation was performed for the individual subregions. Therefore, the material compositions of the submehes are different from each other after the depletion. The STREAM code uses a depletion chain with 1,304 nuclides. Among the nuclides, 393 nuclides have neutron XS data. In order to reduce the calculation time in generating the reference solution, the 160 most important nuclides were selected in terms of the eigenvalue, and the modified pin-cell model was constructed. The difference in the eigenvalue between the original model and the modified model was less than 10 pcm. **Figure 1** shows the temperature profile and the distribution of the material composition in the fuel pellet. The MCNP6 and STREAM codes solved the modified problem, and the results from the codes were compared.

The k-inf results are compared in **Table 2**. PSM-CPM is used in this comparison in addition to PSM. EQ, DRI, and SDDM have differences of the order of 400 pcm in k-inf. MCXS, PSM, and PSM-CPM show more accurate results, with differences in k-inf of the order of 100 pcm. There is a difference of 27 pcm in k-inf

between PSM and PSM-CPM. In order to compare the results in detail, the nuclide-wise reaction rates are compared in **Table 3**. In the nuclide-wise reaction rate comparison, various actinides and the fission products cause differences in the reaction rates. Among the actinides, ^{239}Pu and ^{238}U are the major error sources. With EQ, DRI, and SDDM, differences of 100–200 pcm occur from ^{239}Pu and ^{238}U. PSM-CPM calculates the reaction rates of ^{239}Pu and ^{238}U with differences of less than 30 pcm. Various fission products cause significant differences in the reaction rate for EQ, DRI, and SDDM. ^{150}Sm causes differences of the order of 90 pcm in the reaction rate for the three methods. However, PSM and PSM-CPM calculate quite accurate reaction rates of ^{150}Sm, with differences of 1 pcm.

Supplementary Figure S1 [contribution to the k-inf difference for ^{239}Pu in all regions (Burned UO_2 pin-cell) (Choi et al., 2021)] shows the group-wise reaction rate comparison results for ^{239}Pu. There are significant differences in the reaction rate of ^{239}Pu with EQ, DRI, and SDDM. In particular, differences of 30–40 pcm occur in Groups 25 and 29. The significant differences are successfully reduced by PSM and PSM-CPM. In Groups 25 and 29, the differences of the reaction rates are less than 5 pcm.

In **Supplementary Figure S2** [comparison of absorption and nu*fission reaction rates for ^{239}Pu in resonance energy groups (Burned UO_2 pin-cell) (Choi et al., 2021)] and **Supplementary Figure S3** (comparison of absorption XS and reaction rate for ^{239}Pu in Group 29 (Burned UO_2 pin-cell) (Choi et al., 2021)), the region-wise reaction rates are compared. The reaction rates in the resonance energy ranges are integrated and compared in **Supplementary Figure S2**. It is shown that the magnitude of the reaction rates from EQ, DRI, and SDDM tends to be underestimated for both the absorption and production rates. DRI and SDDM do not show noticeable improvement in the reaction rate compared to that of EQ. PSM and PSM-CPM calculate more accurate reaction rates in the fuel pellet. The absorption XSs and reaction rates in Group 29 are compared in **Supplementary Figure S3**. The absorption XSs from EQ, DRI, and SDDM are underestimated by 15%. The underestimated absorption XS causes underestimated absorption rates. A similar bias occurs in the production rates. PSM and PSM-CPM show greatly improved results. The differences in the reaction rates from PSM and PSM-CPM are negligible.

Supplementary Figure S4 [contribution to the k-inf difference for ^{238}U in all regions (Burned UO_2 pin-cell) (Choi et al., 2021)] shows the group-wise reaction rate comparison for ^{238}U. The reaction rates of ^{238}U with EQ, DRI, and SDDM are significantly different from the reference, causing differences of the order of 100 pcm in Groups 26 and 27. PSM and PSM-CPM have differences of less than 30 pcm in these groups. **Supplementary Figure S5** [comparison of absorption XS and reaction rate for ^{238}U in Group 27 (burned UO_2 pin-cell) (Choi et al., 2021)] shows the region-wise absorption XSs and reaction rates. The absorption XSs in the inner regions are significantly overestimated by EQ and DRI. SDDM has more accurate absorption XSs. However, the differences are still significant. The difference in the absorption XSs with PSM and PSM-CPM are quite accurate. There are no noticeable differences in the absorption XSs. There are differences of 10–30 pcm in the absorption reaction rates of the outermost region from MCXS, PSM, and PSM-CPM.

Supplementary Figure S6 [contribution to k-inf difference for ^{150}Sm in all regions (burned UO_2 pin-cell) (Choi et al., 2021)] shows the comparison of the group-wise reaction rate of ^{150}Sm. In order to calculate accurate multigroup XSs of the fission products, it is important to consider the resonance interference effect as well as the fuel escape probability. Resonant nuclides (i.e., ^{238}U) have relatively more contributions to the multigroup XSs of the fission products. In Group 27, differences of more than 90 pcm in the reaction rates occur with EQ, DRI, and SDDM. In the region-wise comparison for Group 27, there are significant differences in the XSs and the reaction rates from the three methods {see **Supplementary Figure S7** (comparison of absorption XS and reaction rate for ^{150}Sm in group 27 (burned UO_2 pin cell) (Choi et al., 2021)]}. The major source of the differences is the resonance interference effect. This should be considered with the detailed pointwise XSs and flux distributions because the positions of the resonance peaks have very significant impacts on the interference effect. However, the Bondarenko iteration method in the conventional equivalence theory considers the resonance interference effect in the multigroup parameters. PSM and PSM-CPM solve the pointwise energy equations with the fuel material with mixed nuclides, such that the resonance interference effect is considered spontaneously. There is no noticeable difference in the XSs and reaction rates.

From the verification with the burned pin-cell problem, it is concluded that PSM and PSM-CPM calculate considerably accurate multigroup XSs and reaction rates. PSM and PSM-CPM always exhibit superior results to those of EQ, DRI, and SDDM. EQ, DRI, and SDDM exhibit significant differences in the XSs and the reaction rates of actinides and the fission products. Because PSM and PSM-CPM solve the pointwise energy slowing-down equations on the fly, the resonance interference effect can be accurately considered. Therefore, high accuracy can be achieved with PSM and PSM-CPM for the highly burned pin-cell problem.

17 × 17 Fuel Assembly Depletion Benchmark

The depletion problems were solved to verify the accuracy of the XS for the depletion calculation. Because the reaction rates are used in the depletion calculation, it is important to calculate the accurate multigroup XS and reaction rates to achieve high accuracy in the final solution. Two types of FA problems were solved, as shown in **Table 4**. Problem A is the normal UO_2 FA without any burnable poison. Twenty-four gadolinia fuel rods are used in problem B. The two FAs were burned with a power density of 40 W/g. The final burnup is 60 MWd/kgHM. The verification problems came from the VERA depletion benchmark (Kim, 2015). Problems A and B are identical to problems 2C and 2P in the VERA depletion benchmark, respectively.

TABLE 4 | Description for fuel assembly depletion problems (Choi et al., 2021).

Problem	Description	UO_2 enrichment (%)	Moderator temperature (K)	Fuel temperature (K)	Moderator density (g/cc)	Boron concentration (ppm)
A	No poison	3.1	600	900	0.700	1,300
B	24 Gadolinia	1.8, 3.1				

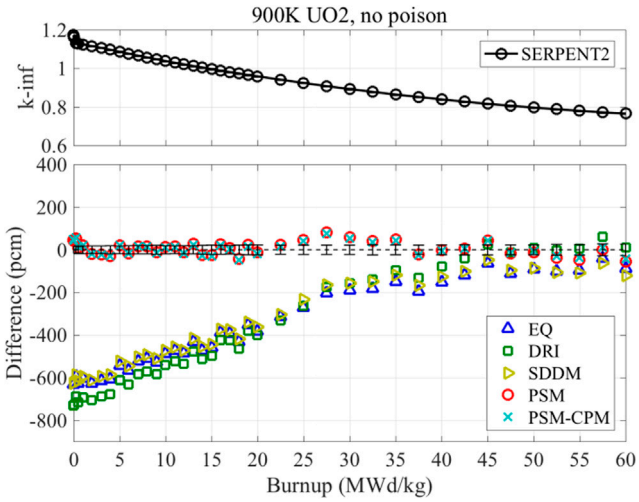

FIGURE 2 | Analysis result of 17 × 17 fuel assembly without poison (Choi et al., 2021).

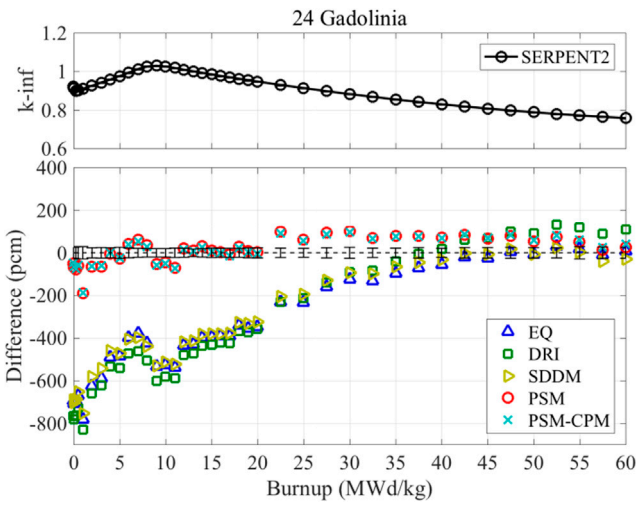

FIGURE 3 | Analysis result of 17 × 17 fuel assembly with 24 gadolinia fuel rods (Choi et al., 2021).

The reference data were generated by the SERPENT2 Monte Carlo code (Leppänen, 2015). The STREAM and SERPENT codes utilized a common recoverable energy per fission (which is usually called kappa) to be compared consistently. STREAM and SERPENT2 used their data for the depletion chain, decay, and yield. SERPENT2 uses more than 3,000 nuclides in the depletion chain. SERPENT2 uses an algorithm to determine the nuclides in the depletion chain depending on the problem. STREAM uses 1,304 nuclides in the depletion chain. The fuel pellet was divided into 15 subregions, such that each pellet had 15 different depletion zones. In order to obtain reliable results, sufficiently many depletion steps must be used in the depletion calculation. In the STREAM and SERPENT2 calculations, 40 steps are used for both the UO_2 FA without

poison and the FA with Pyrex. Forty steps are sufficient to calculate the converged k-inf for both codes. With the SERPENT code, more than 300 steps are needed to obtain fully converged solutions for the FA with the 24 gadolinia fuel rods. STREAM uses quadratic depletion methods to reduce the discretization error (Lee et al., 2013). With the quadratic depletion method (Lee et al., 2013), STREAM can yield a converged solution within 40–50 depletion steps. The FA depletion problems were solved with rigorous mesh divisions and the number of time steps. The obtained results are shown in **Figures 2**, **3**.

EQ, DRI, and SDDM have significant bias in k-inf as a function of the burnup. The initial k-inf is underestimated by 600 pcm. The difference in k-inf decreases as the burnup increases. In the comparisons of the reaction rates in the previous sections, ^{238}U absorption reaction rates are significantly overestimated by the three methods, leading to a negative contribution to the difference in k-inf. Therefore, the number density of ^{239}Pu is overestimated with the three methods. This is the major reason for the trends in k-inf. PSM and PSM-CPM show very accurate and consistent results of k-inf. The differences in k-inf are of the order of 100 pcm from 0 to 60 MWd/kgHM burnup. It is important to note that the difference between PSM and PSM-CPM is less than 10 pcm for all the depletion steps in the two FA problems. It is noted that PSM has bias when the nonuniform temperature profile is used. However, the nonuniform material compositions do not cause a noticeable bias in the results of PSM.

Although STREAM and SERPENT2 use common kappa data, they still use many different data and libraries for the depletion calculations. Therefore, the error from the use of different data is included in the comparisons. It is difficult to say how much difference in k-inf is caused by the difference in the depletion libraries. Because the depletion results with PSM and PSM-CPM show very good agreement with that of SERPENT2, it is expected that the error is not significant. A more detailed examination is necessary.

From the verification with the depletion problem, it is confirmed that PSM and PSM-CPM calculate accurate and consistent results for the depletion. To obtain high accuracy in the depletion calculation, it is important to calculate accurate reaction rates for every single nuclide. The resonance interference treatment is also important because many resonant nuclides are mixed together. Although the material compositions are not uniform in the fuel pellet, PSM calculates very close results to PSM-CPM. The difference between PSM and PSM-CPM is less than 10 pcm.

Pin-Cell With Nonuniform Material Composition and Temperature Profile

In *Pin-Cell With Nonuniform Material Composition and Uniform Temperature Profile* and *17 × 17 Fuel Assembly Depletion Benchmark* sections, the verification problem had nonuniform material compositions in the fuel pellets. In this section, both the material composition and temperature profiles are nonuniform. Currently, the whole-core transport calculation with multiphysics coupling is one of the main issues. If the TH feedback calculation is coupled, the fuel pellet has a nonuniform temperature profile. Obviously, the temperature has an impact on the XSs. PSM approximates the constant pointwise energy XS in the fuel pellet in computing the collision probability. Therefore, the approximation cannot work with the nonuniform temperature profile. Because of this issue, PSM-CPM is also developed to eliminate the approximation. Both methods are verified with the highly burned UO_2 pin-cell problem with the temperature profile. An identical pin-cell to that in *Pin-Cell With Nonuniform Material Composition and Uniform Temperature Profile* section is used in the verification. However, the depletion calculation is performed with the TH feedback. The parameters used in the TH feedback are described as follows: inlet temperature of 565 K, mass flux of 3,706 kg/m^2·s, initial power density of 40 W/gHM, and height of 380 cm.

Similarly to the pin-cell problem in *Pin-Cell With Nonuniform Material Composition and Uniform Temperature Profile* section, the 160 most important nuclides of the fuel were selected, and the new modified pin-cell problem was made to reduce the calculation time elapsed in generating the reference solution. **Figure 4** shows the temperature profile and the material distribution in the fuel pellet. The STREAM code with the different methods and the MCNP6 code were used in the modified pin-cell problem for the verification.

Here, some remarks on generating the reference solution are offered. The original MCNP6 data library is given for temperatures with 300-K intervals. Therefore, it is necessary to generate the ACE library for all the temperatures of interest. In order to obtain an accurate reference solution, the ACE library for MCNP6 was generated for all temperatures in the problem. The MAKXSF program in the MCNP6 code package was used to generate the S(α, β) data of hydrogen in light water. One may use the LEAPR module in the NJOY code to generate the S(α, β) data for the temperature (Kahler et al., 2012), which is not given in ENDF. However, it was concluded that MAKXSF can generate more reasonable S(α, β) data in terms of the trend of k-inf versus the temperature.

The STREAM code performs linear interpolation to calculate the XSs of any temperature of interest. The temperature interval of the pointwise energy XS library is approximately 100 K between 293.6 and 1800 K. The 100-K interval is sufficient to calculate an accurate multigroup XS from the pointwise energy slowing-down calculation. The interval for the multigroup XS library is also 100 K.

The results for k-inf and the nuclide-wise reaction rate comparison are shown in **Tables 5**, **6**, respectively. The results are very similar to the results in the *Pin-Cell With Nonuniform Material Composition and Uniform Temperature Profile* section. EQ, DRI, and SDDM show differences of the order of 300 pcm in k-inf, whereas PSM and PSM calculate k-inf with differences of the order of 100 pcm. In the nuclide-wise comparison, EQ, DRI, and SDDM have significant differences in the various actinide and fission products. PSM and PSM-CPM show good agreement in the nuclide-wise reaction rate. The maximum difference is less

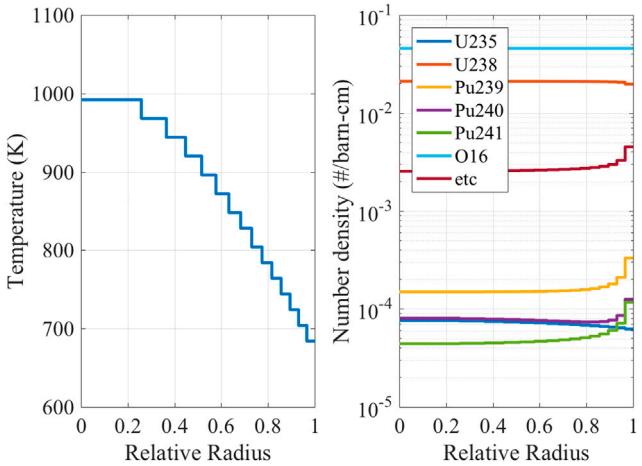

FIGURE 4 | Temperature profile and number densities (60 MWd/kg burned fuel pin-cell with TH feedback) (Choi et al., 2021).

TABLE 5 | k-inf and difference (60 MWd/kg burned fuel pin-cell with TH feedback) (Choi et al., 2021).

Method	k-inf	Difference (pcm)
MCNP6 (reference)	0.79285 ± 0.00014	—
EQ	0.78914	−371
DRI	0.78916	−369
SDDM	0.79030	−255
MCXS	0.79412	127
PSM	0.79398	113
PSM-CPM	0.79385	100

TABLE 6 | Nuclide-wise contribution to k-inf difference (60 MWd/kg burned fuel pin-cell with TH feedback) (Choi et al., 2021).

Nuclide	Contribution to k-inf difference (pcm)					
	EQ	DRI	SDDM	MCXS	PSM	PSM-CPM
^{239}Pu	−156	−157	−115	39	36	31
^{238}U	−184	−175	−27	−3	19	3
^{150}Sm	−91	−91	−93	−1	−1	−1
^{152}Sm	76	76	71	6	6	6
^{99}Tc	−59	−60	−65	4	6	6
^{147}Pm	−57	−57	−60	3	5	5
^{235}U	−51	−50	−45	10	9	9
^{238}Np	−26	−26	−26	0	−27	−27
^{236}U	−32	−33	−34	4	9	9
^{10}B	34	34	29	6	6	7
^{240}Pu	21	21	9	16	13	14
etc.	19	19	−7	19	13	17
Overall	−373	−371	−257	125	112	98

than 40 pcm. The difference between PSM and PSM-CPM is not noticeable.

Supplementary Figure S8 [contribution to k-inf difference for ^{239}Pu in all regions (burned UO_2 pin-cell with TH feedback) (Choi et al., 2021)] shows the comparison of the reaction rate of ^{239}Pu. EQ, DRI, and SDDM have significant differences in the reaction in Groups 25, 27, and 29. PSM and PSM-CPM have differences of less than 5 pcm in the reactions of the groups. In the region-wise comparison {see **Supplementary Figure S9** [comparison of absorption XS and reaction rate for ^{239}Pu in Group 29 (burned UO_2 pin-cell with TH feedback) (Choi et al., 2021)]}, the absorption is accurately calculated with PSM and PSM-CPM, whereas there are differences of the order of 15% in the XSs with EQ, DRI, and SDDM. There is a slight difference in the XSs from PSM and PSM-CPM. In comparison to PSM-CPM, PSM calculates slightly smaller XSs in the inner regions and larger XSs in the outer regions. The XSs from PSM are slightly tilted compared to those of PSM-CPM. The difference is less than 0.5%.

Supplementary Figure S10 (contribution to k-inf difference for ^{238}U in all regions [burned UO_2 pin-cell with TH feedback) (Choi et al., 2021)] shows the comparison of the group-wise reaction rates of ^{238}U. EQ, DRI, and SDDM have differences of the order of 100 pcm in Groups 26 and 27. PSM and PSM-CPM have differences of less than 30 pcm in the reaction rates in these groups. The difference between the PSM and PSM-CPM is not noticeable. In **Supplementary Figure S11** [comparison of absorption XS and reaction rate for ^{238}U in Group 27 (burned UO_2 pin-cell with TH feedback) (Choi et al., 2021)], the region-wise XSs and the reaction rates of ^{238}U are compared. PSM-CPM calculates quite an accurate multigroup XS. The differences in the XSs are less than 1% in all the subregions of the pellet. Similarly to the comparison with ^{239}Pu, the XSs from PSM are slightly tilted compared to those from PSM-CPM. In comparing with PSM-CPM, PSM calculates overestimated XSs in the inner regions and underestimated XSs in the outer regions.

From the verification with the burned pin cell with the nonuniform temperature profile, it is verified that PSM and PSM-CPM calculate the accurate multigroup XSs and the reaction rates. PSM-CPM show reasonable accuracy for the problem with the nonuniform temperature profile and material distributions. However, PSM has a slight in–out tilt in the XS compared to that of PSM-CPM. The

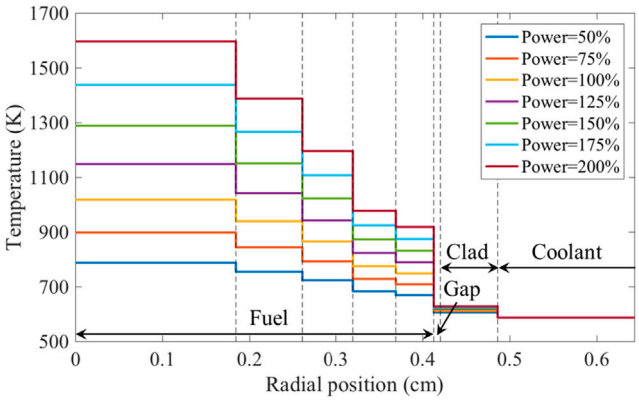

FIGURE 5 | Temperature profiles of nonuniform temperature cases (SNU benchmark) (Choi et al., 2021).

nonuniform temperature profile causes a bias in PSM. The reason for the bias will be discussed in the next section with a more significantly nonuniform temperature profile.

SNU Nonuniform Temperature Pin-Cell Benchmark

A research team in Seoul National University (SNU) developed a nonuniform fuel temperature benchmark (Jung et al., 2016) to examine the accuracy of the subgroup method of the pin-cell problem with a nonuniform temperature profile. The benchmark includes 14 pin-cell problems with the seven different power levels and two sets of temperature profiles (*i.e.*, uniform and nonuniform temperature profiles). The materials used in the problem are as follows: 3 wt% UO_2 fuel, air gap, natural zirconium cladding, and H_2O moderator. The fuel pellet is divided into five subregions of equal volume.

There are a set of temperature profiles, as shown in **Figure 5**. The profiles are given for the difference power levels from 50 to 200%. The 100% power level corresponds to full-power operation. In case of uniform temperature profiles, an average temperature for the fuel region is given for difference power levels. More detailed specifications are available elsewhere (Jung et al., 2016). The reference solution was generated using MCNP6. The default scattering kernel (*i.e.*, SVT) was used in the calculation. For a consistent comparison, the STREAM code also used the SVT upscattering correction to treat the resonance upscattering effect. Although five subregions were used in the fuel pellet in the benchmark, each subregion was divided into three regions to examine the information in more detail. Therefore, 15 subregions were used in the calculation using the MCNP6 and STREAM codes.

The pin-cell problems in the benchmark were solved with the different methods, and the obtained reactivities are compared in **Figure 6**. The reactivities and the differences are plotted as functions of the average temperature of the fuel pellet. EQ, DRI, and SDDM show the significantly underestimated reactivities. Differences of approximately 500 pcm are observed in the results. The reactivities are biased as a function of the average fuel temperature. PSM and PSM-CPM calculate the reactivities with differences of less than 100 pcm for all the cases. There is no noticeable bias in the results with PSM-CPM. The results with MCXS are similar to those with PSM-CPM. In the nonuniform cases, PSM shows a slightly biased reactivity. As the power increases, the reactivity with PSM is underestimated. In order to examine the temperature bias, the fuel temperature coefficient (FTC) was calculated. The FTC was calculated with least-square fitting to the reactivities versus the average fuel temperatures, and the results are shown in **Table 7**.

There are significant differences in the FTCs with the EQ, DRI, and SDDM. For the cases with the uniform temperature profile, the three methods have differences of the order of 10% in the FTCs. If the nonuniform temperature profile is used, the three methods still have quite significant differences in the FTCs. The FTCs with DRI and SDDM are not consistent for the two profiles. The differences in the FTCs with DRI change from −10.02% to 10.18% when the temperature profile is changed. The differences in the FTCs with SDDM change from −10.65% to −3.45%. The FTC with PSM is quite accurate, with a difference of 1.67% if the uniform temperature profile is used. However, PSM has a difference of 7.77% in the FTC for the problem with the nonuniform temperature profile. PSM shows a significant bias in the FTC. However, PSM-CPM shows consistent and accurate results for both temperature profiles. The differences in the FTCs are 1.65% and 0.56% for each profile.

In order to examine the bias in the FTC, the detailed reaction rates are compared for the problem with 200% power and the nonuniform temperature profile. **Supplementary Figure S12** [contribution to k-inf difference for ^{238}U in all regions (200% power nonuniform temperature case) (Choi et al., 2021)] shows the group-wise comparison of the reaction rates. PSM and PSM-CPM show relatively accurate results in the reaction rates of the resonance energy groups. There are differences of 5–30 pcm in

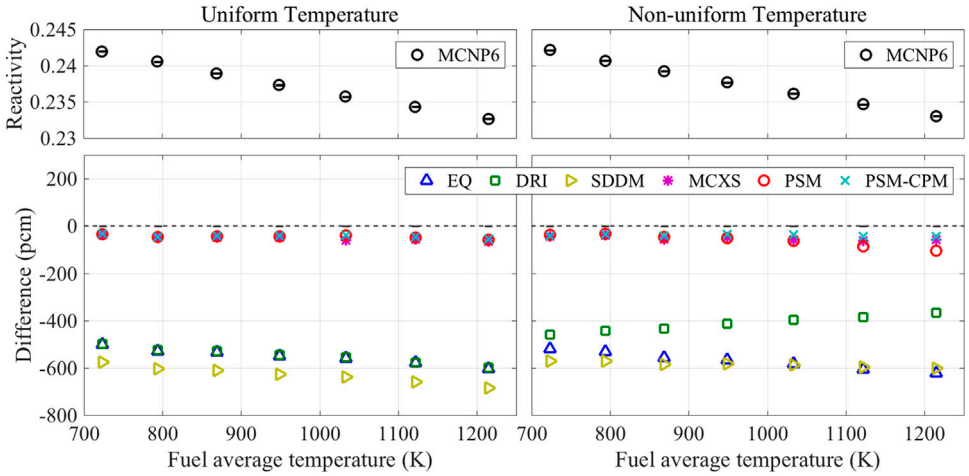

FIGURE 6 | Comparison of reactivity (SNU benchmark) (Choi et al., 2021).

TABLE 7 | Fuel temperature coefficients (SNU benchmark) (Choi et al., 2021).

Method	Uniform temperature profile		Nonuniform temperature profile	
	FTC (pcm/K)	Difference (%)	FTC (pcm/K)	Difference (%)
MCNP6	−1.896	-	−1.849	-
EQ	−2.083	−9.86	−2.056	−11.22
DRI	−2.087	−10.02	−1.661	10.18
SDDM	−2.098	−10.65	−1.913	−3.45
MCXS	−1.944	−2.51	−1.891	−2.25
PSM	−1.928	−1.67	−1.993	−7.77
PSM-CPM	−1.928	−1.65	−1.859	−0.56

k-inf between PSM and PSM-CPM. In **Supplementary Figure S13** [comparison of absorption XS for ^{238}U in Group 29 (200% power nonuniform temperature case) (Choi et al., 2021)], the region-wise absorption XSs and the reaction rates in Group 29 are compared, respectively. The absorption XSs with PSM are tilted along the radial direction. The XSs in the inner regions are overestimated, whereas the XSs in the outer regions are underestimated. The maximum difference in the XS with PSM is 9%. However, PSM-CPM shows negligible differences in the XSs.

The differences in the XSs between PSM and PSM-CPM are caused by their methods of calculating the collision probabilities. PSM calculates the average total XS and then interpolates the collision probability from the $\hat{P}_{ij}^{iso}$ table using the average pointwise energy total XS.

Figure 7 shows the macroscopic pointwise energy total XSs and the ratio of the XSs in each region to the average XS in the pellet between 4 and 27.7 eV. When the temperature increases, the overall resonance XSs increase. In calculating the collision probability with PSM, the resonance XSs in the inner regions are underestimated. With the underestimated XSs, PSM overestimates the fuel escape probabilities in the inner regions and then overestimates the scattering sources from the moderator. Finally, the reaction rates of the resonance are overestimated, and therefore the multigroup XSs are overestimated in the inner regions. The reaction rates in the outer regions are underestimated because of the overestimated fuel escape probabilities. Therefore, the multigroup XS is underestimated in the outer regions.

From the verification with the SNU benchmark, it is concluded that accurate k-inf values can be calculated with PSM and PSM-CPM. For the pin cell with 200% power, PSM has a bias in calculating the FTC for the problems with the nonuniform temperature profile. PSM calculates tilted multigroup XSs in the fuel pellet because of the approximation in calculating the collision probability. It is verified that PSM-CPM can consider the nonuniform temperature profile accurately because the approximation is not used in the PSM-CPM. The FTCs, multigroup XSs, and reaction rates from PSM-CPM are very accurate compared to the reference solutions.

Pin-Cell of Annular Type With Centered Burnable Absorber

The pin-cell problem was virtually designed to examine the accuracy of PSM-CPM for the pin cell with the extremely nonuniform material composition in the fuel pellet. The

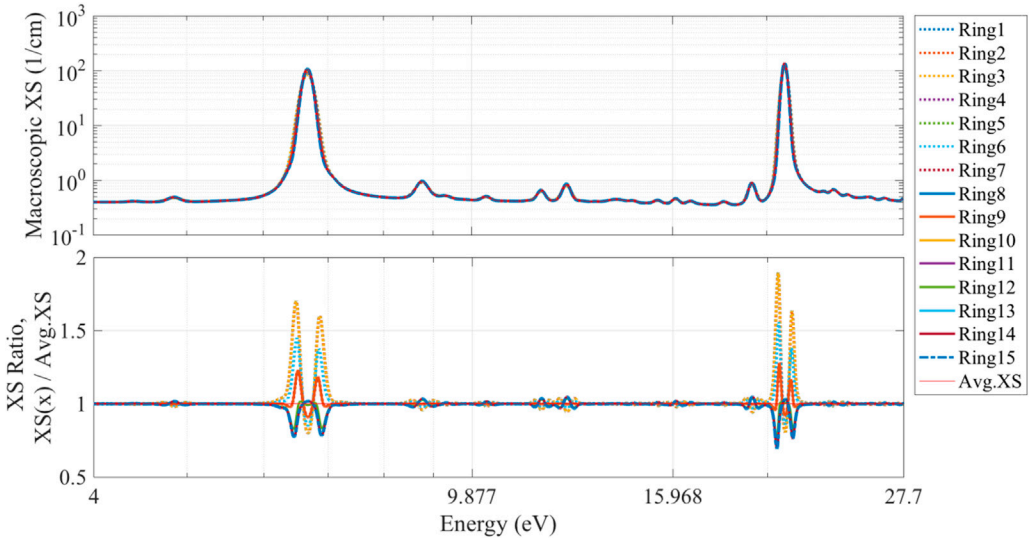

FIGURE 7 | Macroscopic total XSs in fuel pellet (200% power nonuniform temperature case) (Choi et al., 2021).

TABLE 8 | k-inf and difference (annular fuel pin cell).

Method	k-inf	Difference (pcm)
MCS (reference)	0.98933 ± 0.00007	—
PSM	0.96324	−2,609
PSM-CPM	0.98875	−58

problem has most difficult conditions in terms of the heterogeneous material distributions. The materials used in the problem are as follows: Gd_2O_3 burnable absorber, coated molybdenum (Mo) alloys cladding, UO_2 fuel, air gap, Zirlo cladding, and H_2O moderator. The geometries of the pin cell are: the absorber of outer radius 0.065 cm; the Mo cladding of outer radius 0.070 cm; the UO_2 fuel of inner radius 0.075 cm; the UO_2 fuel of outer radius 0.4096 cm; the Zirlo cladding of inner radius 0.4178 cm; the Zirlo of outer radius 0.4750 cm; the gaps filled with the air placed between fuel and both claddings; and the pin pitch of 1.26 cm.

The UO_2 region in the fuel pellet was divided into 11 subregions of equal outer radius. The reference was calculated by MCS Monte Carlo code (Lee et al., 2020). The results from the codes were compared.

The k-inf results are compared in **Table 8**. PSM has a significant difference of −2,609 pcm in k-inf. PSM-CPM shows an accurate result, with a difference in k-inf of -58 pcm.

Figure 8 shows the group-wise reaction rate comparison for ^{238}U in the resonance region. The reaction rates of ^{238}U with PSM are significantly different from the reference, causing a difference in the order of 300 pcm in Group 29. PSM-CPMs show very accurate results in the reaction rates of the resonance energy groups. **Figure 9** shows the region-wise absorption XSs and reaction rates. The absorption XSs in the inner UO_2 regions are significantly overestimated by PSM. The difference in the

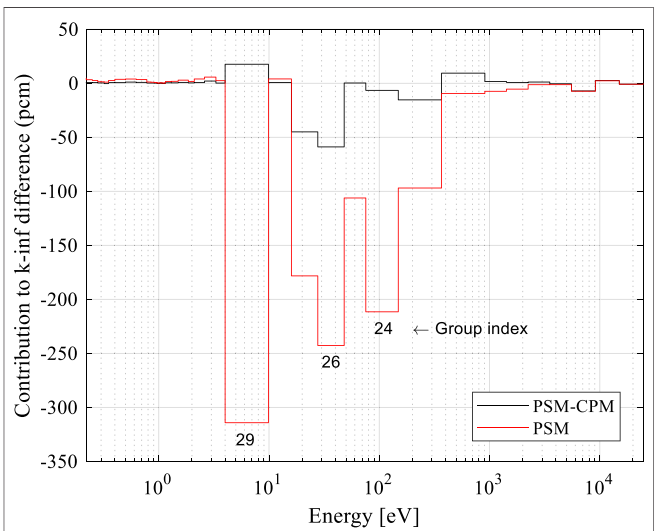

FIGURE 8 | Contribution to k-inf difference for ^{238}U in the resonance region.

absorption XSs with PSM-CPM are quite accurately less than 2% of relative error compared to the reference. There are differences of 100–150 pcm in the absorption reaction rates of the outermost and inner region from PSM. However, there is a difference of less than 50 pcm in that of the outermost region from PSM-CPM.

The major source of the differences is how they calculate the collision probability for the isolated fuel pellet. This problem has extreme stiffness of total XS distribution due to the centered burnable absorber in the fuel pellet. In the case of PSM which assumes that total XS is constant in the fuel pellet, it should cause an error. For general LWR problems in the previous sections, the assumption in PSM has not introduced significant errors and has

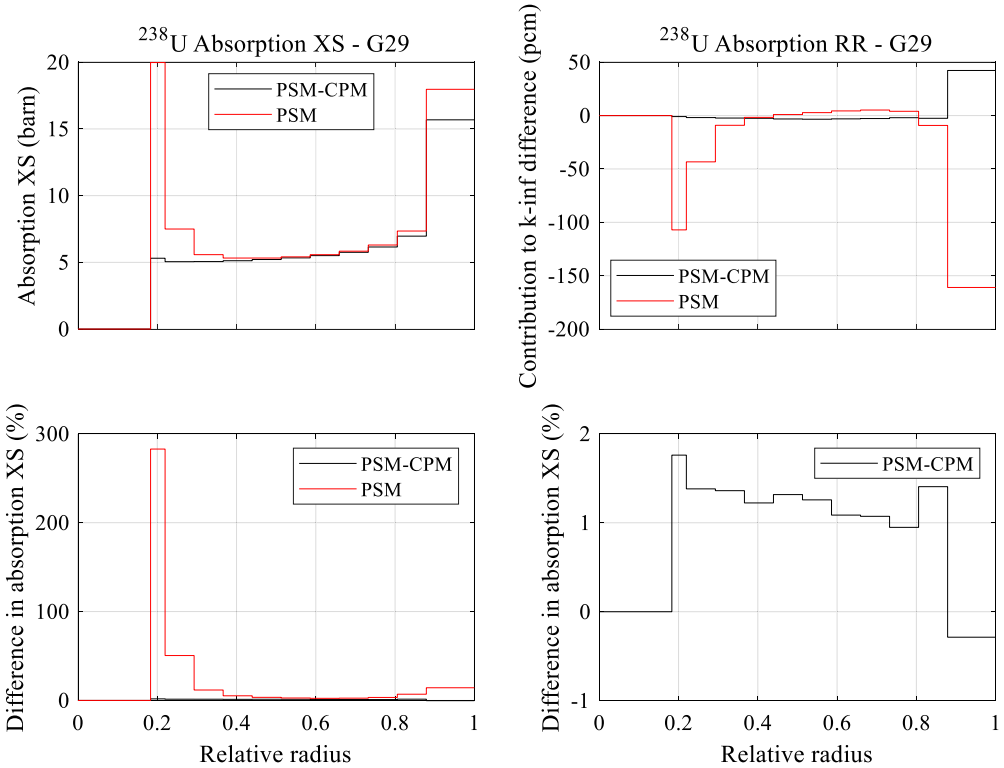

FIGURE 9 | Comparison of absorption XS and reaction rate for ^{238}U in Group 29 (Annular pin-cell).

shown the same level of accuracy as compared to PSM-CPM. However, PSM should not be an option in such a problem that the total XS has varied with a large difference in the fuel pellet. It is noted that both PSM and PSM-CPM use Carlvik's two-term rational approximation to calculate the collision probability in the fuel pellet in the lattice. It is assumed that the shadowing effect is not significantly different for the individual subregions of the fuel pellet. The effect by the assumption is one of the issues that need to be further investigated.

From the verification with the annular pin-cell problem which has a burnable absorber in the center region of the fuel pellet, it is concluded that PSM-CPM calculates considerably accurate multigroup XSs and reaction rates. PSM exhibits significant differences in the XSs and the reaction rates of ^{238}U. Because PSM-CPMs solve the pointwise energy slowing-down equations calculating the collision probability corresponding to the variation of the material compositions and the temperature profiles, high accuracy can be achieved even for the highly stiff pin-cell problem.

CONCLUSION

PSM has been briefly reviewed, and a PSM-CPM that is refined with respect to the way to calculate the collision probability in the isolated fuel pellet is introduced. PSM-CPM calculates the collision probability during solving of the pointwise slowing-down equation, but PSM uses pre-tabulated collision probability as a function of the total XS for a fuel pellet lump and indices of subdivided regions. Then, the collision probability is interpolated during the slowing-down calculation. The discrepancy in the effective XSs caused by the assumption in PSM is investigated through the comparative analysis. The comparative analysis is performed compared to legacy equivalence theory methods such as SDDM and DRI with various LWR problems, which have uniform and nonuniform material compositions and temperature profiles in the fuel pellets. By combination with various conditions (geometry, material composition distribution, temperature profile in the fuel pellet, and burnup), various test cases have represented problems under possible conditions in the LWR design.

First, the accuracy of PSMs (PSM and PSM-CPM) has been examined with the burned pin-cell problem that has the nonuniform material composition in the fuel pellet. This test has demonstrated that PSMs calculate the accurate multigroup XSs and reaction rates and show superior accuracy than that of conventional methods.

Second, the accuracy of PSMs and conventional methods is tested with the depletion problems. The accuracy of the depletion calculation is directly related to the accuracy of the reaction rates for every single nuclide with the burnup. When the material composition is not uniform in the fuel pellets, PSM showed a result with a difference of less than 10 pcm from PSM-CPM. It showed that the accuracy of PSM-CPM under nonuniformity of material composition by the depletion does not demonstrate a noticeable difference in PSM.

Third, PSMs have been verified with test cases which have nonuniform material composition and temperature profiles in the fuel pellet. The condition represents the effect of the TH feedback and the depletion in the fuel pellet. For the highly burned UO_2 pin-cell problem with a nonuniform temperature profile, the accuracy of PSMs has been verified with the comparisons of multigroup XSs and the reaction rates with the reference solutions. However, the XS from PSM has shown a slight in–out tilt compared to that of PSM-CPM.

Fourth, a bias in PSM, as mentioned above, has been investigated by solving the SNU benchmark which includes the pin-cell problems with the nonuniform temperature profile. It was demonstrated that PSMs show great accuracy in the calculation of the eigenvalue. PSM has a bias in calculating the FTC for the pin cell with a two times higher-power level than that in full-power operation. PSM calculates tilted multigroup XSs in the fuel pellet due to the approximation in calculating the collision probability. However, it is verified that PSM-CPM eliminates the approximation of PSM, giving the result of accurate FTCs, multigroup XSs, and reaction rates.

Finally, the annular pin-cell problem which has a burnable absorber in the center region of the fuel pellet has been tested with PSMs. PSM showed significant differences in the eigenvalue and XSs. However, it was clearly demonstrated that PSM-CPM achieves high accuracy in the calculation of XSs and reaction rates for the problem that has a highly stiff distribution in terms of the XS in the fuel pellet.

More improvement in the computational efficiency of PSM-CPM and the verifications with the up-to-date resonance self-shielding methods based on the equivalence theory, the subgroup method, and the UFG method will be performed in the future work.

DATA AVAILABILITY STATEMENT

The original contributions presented in the study are included in the article/**Supplementary Material**; further inquiries can be directed to the corresponding author.

AUTHOR CONTRIBUTIONS

WK and SC contributed to verifications. WK wrote the first draft of the manuscript. SC and WK wrote sections of the manuscript. SC reviewed and edited the manuscript. DL supervised all the activity for the manuscript. All authors contributed to the manuscript revision and read and approved the submitted version.

FUNDING

This work was supported by the National Research Foundation of Korea (NRF) grant funded by the government of Korea (MSIT). (No.NRF-2019M2D2A1A03058371). This work was partially supported by Korea Institute of Energy Technology Evaluation and Planning(KETEP) grant funded by the Korea government (MOTIE) (20206510100040).

SUPPLEMENTARY MATERIAL

The Supplementary Material for this article can be found online at: https://www.frontiersin.org/articles/10.3389/fenrg.2021.765865/full#supplementary-material.

REFERENCES

Choi, S., Lee, C., and Lee, D. (2017). Resonance Treatment Using Pin-Based Pointwise Energy Slowing-Down Method, Ulsan: Republic of Korea. *J. Comput. Phys.* 330, 134–155. doi:10.1016/j.jcp.2016.11.007

Choi, S., Lee, H., Hong, S. G., and Lee, D. (2015). Resonance Self-Shielding Methodology of New Neutron Transport Code STREAM. *J. Nucl. Sci. Tech.* 52, 1133–1150. doi:10.1080/00223131.2014.993738

Choi, S., Kim, W., and Lee, D. (2021). Refinements of Pin-based Pointwise Energy Slowing-down Method for Resonance Self-shielding Calculation-I: Theory. *Front. Energ. Res.*

Choi, S. (2022). Refinements of Pin-Based Pointwise Energy Slowing-Down Method for Resonance Self-Shielding Calculation-I: Theory. *Front. Energ. Res.*

Ferrer, R., and Hykes, J. (2019). *Development of A Spatially-dependent Resonance Self-Shielding Method in Casmo5, M&C 2019*. Portland: OR.

Goorley, T., James, M., Booth, T., Brown, F., Bull, J., Cox, L. J., et al. (2012). Initial MCNP6 Release Overview. *Nucl. Tech.* 180, 298–315. doi:10.13182/NT11-135

Joo, H. G., Kim, G. Y., and Pogosbekyan, L. (2009). Subgroup Weight Generation Based on Shielded Pin-Cell Cross Section Conservation. *Ann. Nucl. Energ.* 36, 859–868. doi:10.1016/j.anucene.2009.03.017

Jung, Y. S., Lim, C. H., and Joo, H. G. (2016). Temperature Dependent Subgroup Formulation with Number Density Adjustment for Direct Whole Core Power Reactor Calculation. *Ann. Nucl. Energ.* 96, 249–263. doi:10.1016/j.anucene.2016.06.001

Kahler, A. C., MacFarlane, R. E., Muir, D. W., and Boicourt, R. M. (2012). *The NJOY Nuclear Data Processing System*. Version 2012. Los Alamos: New Mexico National Laboratory. LA-UR-12-27079.

Kim, K. S. (2015). *Specification for the VERA Depletion Benchmark Suite*. Oak Ridge: United States National Laboratory. CASL-X-2015-1014-000.

Knott, D., and Yamamoto, A. (2010). "Lattice Physics Computations," in *Handbook of Nuclear Engineering*. Editor D. G. Cacuci (Boston, MA: Springer US), 913–1239. doi:10.1007/978-0-387-98149-9_9

Koike, H., Yamaji, K., Kirimura, K., Sato, D., Matsumoto, H., and Yamamoto, A. (2012). Advanced Resonance Self-Shielding Method for gray Resonance Treatment in Lattice Physics Code GALAXY. *J. Nucl. Sci. Tech.* 49, 725–747. doi:10.1080/00223131.2012.693885

Lee, D., Rhodes, J., and Smith, K. (2013). Quadratic Depletion Method for Gadolinium Isotopes in CASMO-5. *Nucl. Sci. Eng.* 174, 79–86. doi:10.13182/NSE12-20

Lee, H., Kim, W., Zhang, P., Lemaire, M., Khassenov, A., Yu, J., et al. (2020). MCS - A Monte Carlo Particle Transport Code for Large-Scale Power Reactor Analysis. *Ann. Nucl. Energ.* 139, 107276. doi:10.1016/j.anucene.2019.107276

Leppänen, J. (2015). *Serpent – a Continuous-Energy Monte Carlo Reactor Physics Burnup Calculation Code*. Espoo: VTT Technical Research Centre of Finland.

Li, J. (2020).Multi-ring Subgroup Method in Characterising Highly Self-Shielded Gadolinia Burnable Poison Pins for the UK EPR Nuclear Fuel Assembly. In International Conference on Computing. New York, NY: Electronics & Communications Engineering, 196–200. doi:10.1109/iCCECE49321.2020.9231157

Liu, Y., Martin, W., Williams, M., and Kim, K.-S. (2015). A Full-Core Resonance Self-Shielding Method Using a Continuous-Energy Quasi-One-Dimensional Slowing-Down Solution that Accounts for Temperature-dependent Fuel Subregions and Resonance Interference. *Nucl. Sci. Eng.* 180 (3), 247–272. doi:10.13182/nse14-65

Matsumoto, H., Ouisloumen, M., and Takeda, T. (2005). Development of Spatially Dependent Resonance Shielding Method. *J. Nucl. Sci. Tech.* 42, 688–694. doi:10.1080/18811248.2004.9726438

Powney, D. J., and Newton, T. D. (2004). Overview of the WIMS 9 Resonance Treatment. *Serco Assur. Dorchester, ANSWERS/WIMS/TR.* 26.

Qin, S., Zhang, Q., Liang, L., Zhao, Q., Zhang, Z., Wu, H., et al. (2020). Fitting-based Resonance Database Method for Resonance Self-Shielding Calculations of Large-Scale Task Considering Depletion and Intra-pin Distribution. *Ann. Nucl. Energ.* 139, 107247. doi:10.1016/j.anucene.2019.107247

Qin, S., Zhang, Q., Zhang, J., Liang, L., Zhao, Q., Wu, H., et al. (2020). Application of Deep Neural Network for Generating Resonance Self-Shielded Cross-Section. *Ann. Nucl. Energ.* 149, 107785. doi:10.1016/j.anucene.2020.107785

Rhodes, J., Smith, K., and Lee, D. (2006). Vancouver, BC: Canada, 10–14.CASMO-5 Development and ApplicationsProc. Int. Conf. on Advances in Nuclear Analysis and Simulation (PHYSOR 2006)*September*

Rhodes, J., Smith, K., and Lee, D. (2006). *CASMO-5 Development and Applications, PHYSOR-2006*. Vancouver, BC: Canada.

Stamm'ler, R. J. J., and Abbate, M. J. (1983). *Methods of Steady-State Reactor Physics in Nuclear Design*. London: Academic Press.

Stoker, C. C., and Weiss, Z. J. (1996). Spatially Dependent Resonance Cross Sections in a Fuel Rod. *Ann. Nucl. Energ.* 23, 765–778. doi:10.1016/0306-4549(95)00074-7

Sugimura, N., and Yamamoto, A. (2007). Resonance Treatment Based on Ultra-fine-group Spectrum Calculation in the AEGIS Code. *J. Nucl. Sci. Tech.* 44, 958–966. doi:10.1080/18811248.2007.9711335

Xu, Z., Rhodes, J., and Smith, K. (2009). *Casmo-5 versus Mcnp-5 Benchmark of Radial Power Profile in A Fuel Pin*. Lagrange Park, IL: M&C 2009.

Yamamoto, A., Endo, T., and Koike, H. (2011). Improved Derivation of Multigroup Effective Cross Section for Heterogeneous System by Equivalence Theory. *Nucl. Sci. Eng.* 168, 75–92. doi:10.13182/NSE10-50

Yamamoto, A. (2008). Evaluation of Background Cross Section for Heterogeneous and Complicated Geometry by the Enhanced Neutron Current Method. *J. Nucl. Sci. Tech.* 45, 1287–1292. doi:10.1080/18811248.2008.9711916

Zhang, Q., Jiang, R., Zhao, Q., Cao, L., and Wu, H. (2018). Accurate Resonance Absorption Calculation for Fuel Pins with Non-uniform Intra-pellet Temperature Profile Based on ultra-fine-group Slowing-Down Calculations. *Ann. Nucl. Energ.* 120, 392–401. doi:10.1016/j.anucene.2018.06.005

Zhang, Q., Shuai, Q., Zhao, Q., Liang, L., Wu, H., and Cao, L. (2020). Improvements on the Method of ultra-fine-group Slowing-Down Solution Coupled with Method of Characteristics on Irregular Geometries. *Ann. Nucl. Energ.* 136, 1070171–1107017.15. doi:10.1016/j.anucene.2019.107017

Zhang, Q., Wu, H., Cao, L., and Zheng, Y. (2015). An Improved Resonance Self-Shielding Calculation Method Based on Equivalence Theory. *Nucl. Sci. Eng.* 179, 233–252. doi:10.13182/NSE13-108

Conflict of Interest: The authors declare that the research was conducted in the absence of any commercial or financial relationships that could be construed as a potential conflict of interest.

Publisher's Note: All claims expressed in this article are solely those of the authors and do not necessarily represent those of their affiliated organizations, or those of the publisher, the editors, and the reviewers. Any product that may be evaluated in this article, or claim that may be made by its manufacturer, is not guaranteed or endorsed by the publisher.

frontiers in Energy Research

METHODS
published: 17 December 2021
doi: 10.3389/fenrg.2021.766449

The Application of the Combined Fission Matrix Theory in Fast Reactors

Donghao He, Tengfei Zhang and Xiaojing Liu*

Shanghai Jiaotong University, Shanghai, China

The combined fission matrix theory is a recently-developed hybrid neutron transport method. It features high efficiency, fidelity, and resolution whole-core transport calculation. The theory is based on the assumption that the fission matrix element $a_{i,j}$ is dominated by the property of the destination cell *i*. This assumption can be well explained in thermal reactors, and the combined fission matrix method has been validated in a series of thermal neutron system benchmarks. This work examines the feasibility of the combined fission matrix theory in fast reactors. The European Sodium Fast Reactor is used as the numerical benchmark. Compared to the Monte Carlo method, the combined fission matrix theory reports a 64 pcm k_{eff} difference and 8.3% 2D RMS error. The error is much larger than that in thermal reactors, and the correction ratio cannot significantly reduce the material discontinuity error in fast reactors. Overall, the combined fission matrix theory is more suited for thermal reactor transport calculations. Its application in fast reactors needs further developments.

OPEN ACCESS

Edited by:
Mingjun Wang,
Xi'an Jiaotong University, China

Reviewed by:
Guang Hu,
Xi'an Jiaotong University, China
Jiankai Yu,
Massachusetts Institute of Technology, United States

****Correspondence:***
Donghao He
donghaohe@sjtu.edu.cn

Specialty section:
This article was submitted to Nuclear Energy, a section of the journal Frontiers in Energy Research

Received: *29 August 2021*
Accepted: *18 October 2021*
Published: *17 December 2021*

Citation:
He D, Zhang T and Liu X (2021) The Application of the Combined Fission Matrix Theory in Fast Reactors. Front. Energy Res. 9:766449. doi: 10.3389/fenrg.2021.766449

Keywords: fission matrix, Monte Carlo, fast reactor, neutron transport, reactor physics

1 INTRODUCTION

The high-fidelity neutron transport method is a key technique in reactor design and safety analysis. There have been many such methods developed, including the deterministic MOC (Liu et al., 2011) method; the VNM method (Zhang et al., 2013, 2018); and the stochastic Monte Carlo method. Other than these traditional methods, the hybrid neutron transport method is gaining popularity in recent years. It pre-calculates a series of response functions and solves for the neutron transport deterministically relying on response functions. Such methods feature the combination of high accuracy from the Monte Carlo method and the high efficiency from the deterministic method.

The fission matrix method is originally proposed as an acceleration to the Monte Carlo neutron transport solver. A fission matrix describes the response of fission neutrons to a source neutron between spatial cells. The fission matrix element $a_{i,j}$ is defined as the number of fission neutrons produced in cell *i* per source neutron in cell *j*, and its detailed theory can be found in (Carney et al., 2014). The fission matrix from the neutron transport eigenmode equation can be written as:

$$F_i = \frac{1}{k} \sum_{j=1}^{N} a_{i,j} F_j \tag{1}$$

Where k is the multiplication factor, F_j and F_i are the source and fission neutron distributions, and $a_{i,j}$ is the fission matrix element. The eigenvalue and the eigenvector represent the multiplication factor and fission source distribution of the system. However, the calculation of the fission matrix could be memory-challenging and time-consuming in an extensive system, such as a whole-core calculation. There are typically two methods to tally the fission matrix through Monte Carlo calculations, which are the

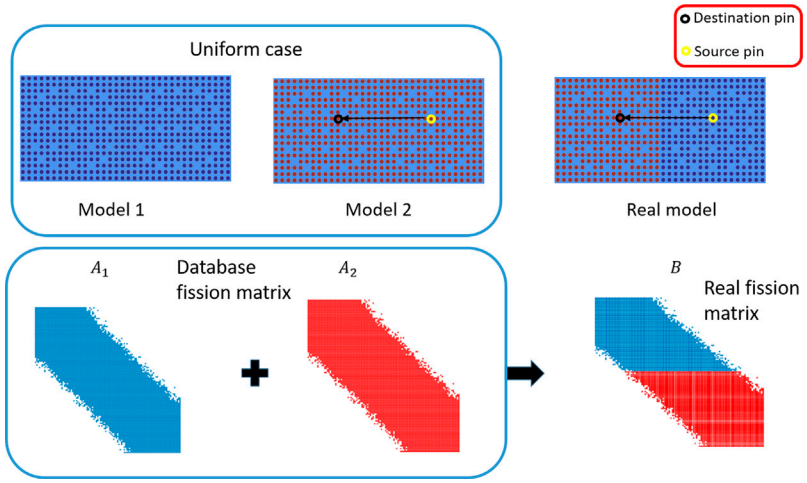

FIGURE 1 | A diagram of the combined fission matrix theory in a two-assembly model.

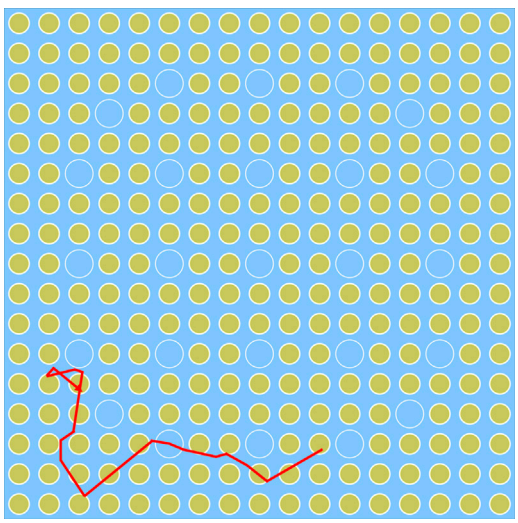

FIGURE 2 | The track of a neutron transport in a PWR assembly.

criticality calculation and the fixed-source calculation. Taking a whole-core calculation as an example, the criticality calculation runs the iterative Monte Carlo simulation and tallies the fission matrix in each iterative cycle. Therefore, the fission matrix is tallied from a converged whole-core fission source and considered the most accurate result. On the other hand, a fission matrix can also be composed of a set of fixed-source calculations, each of which will yield a fission matrix column. However, the fixed-source calculation assumes a uniform source in each mesh cell, so the mesh used to perform the fixed-source calculation has to be fine enough to guarantee the fission matrix is not biased by the source distribution. Overall, the fission matrix derivation is time-consuming and memory-prohibitive for a whole core problem.

In order to obtain the system fission matrix efficiently, a fission matrix combination theory has been developed (Walters et al., 2018; Terlizzi and Kotlyar, 2019; Laureau et al., 2015). It assumes that the system fission matrix element $a_{i,j}$ is dependent only on the property of the destination cell i. Therefore, the system fission matrix can be estimated by combining a set of pre-calculated database fission matrices. The assumption relies on the fact that

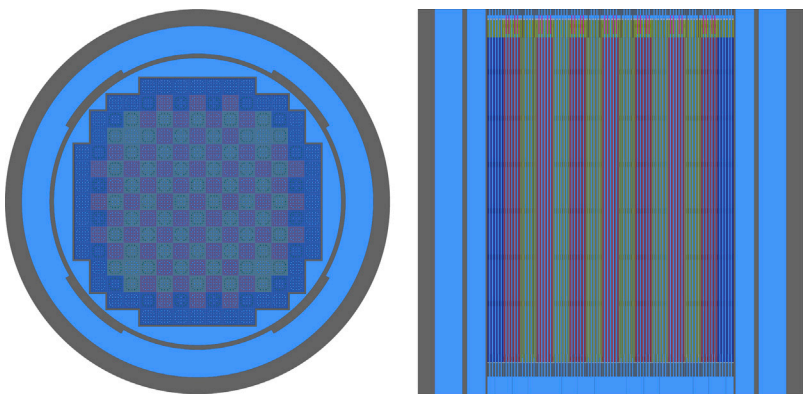

FIGURE 3 | The BEAVRS benchmark model.

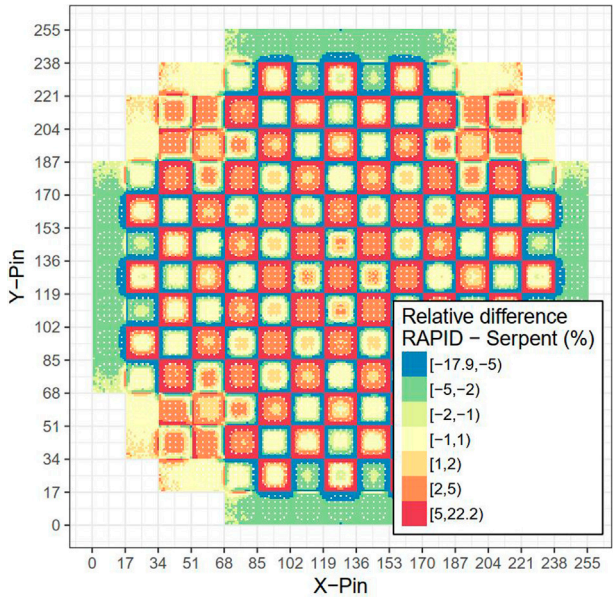

FIGURE 4 | The pin-wise relative error between the combined fission matrix method and the Monte Carlo calculation.

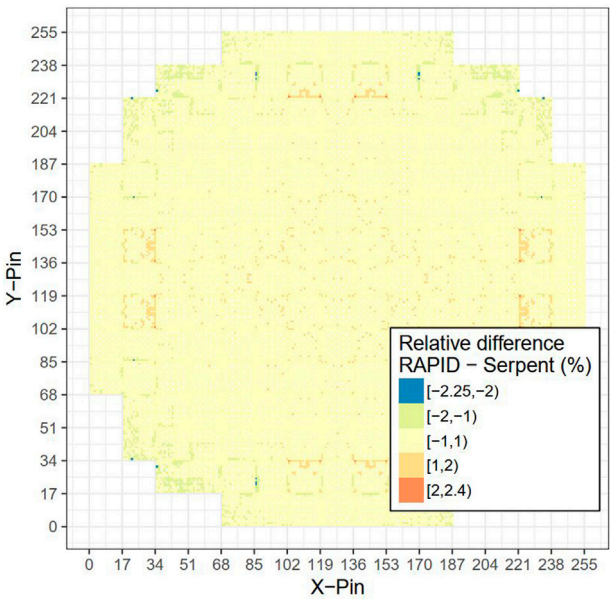

FIGURE 6 | The pin-wise relative error between the combined fission matrix method and the Monte Carlo calculation.

neutrons are thermalized before fissioning, and the thermal fission cross-section is much larger than the scattering cross-section. As a result, the destination cell property is more dominating in the number of fission neutrons than the intermediate or born cells. Based on the theory, a hybrid neutron transport code called RAPID has been developed. The combined fission matrix theory can perform high-fidelity and efficient whole-core pin-wise transport calculations. It is validated on the BEAVRS PWR benchmark (He and Walters, 2019, 2020), PSBR TRIGA reactor core (Topham et al., 2020; Rau and Walters, 2020), and UNF spent fuel cask benchmark (Mascolino et al., 2017). However, the promising methodology is mainly used and validated in thermal neutron systems. This paper will examine the validity of the combined fission matrix theory in the fast reactor whole-core transport calculations.

The paper will be organized as the following: In **Section 2**, a detailed overview of the combined fission matrix theory will be given for completeness of the paper. In **Section 3**, a Sodium Fast Reactor (SFR) numerical benchmark will be presented for the theory validation. Numerical results are shown in **Section 4**. Conclusions and future improvements are summarized in **Section 5**.

2 OVERVIEW OF THE COMBINED FISSION MATRIX THEORY

The combined fission matrix theory, as the core of the RAPID code scheme, estimates the core fission matrix instantly from pre-calculated database fission matrices. The theory states that the

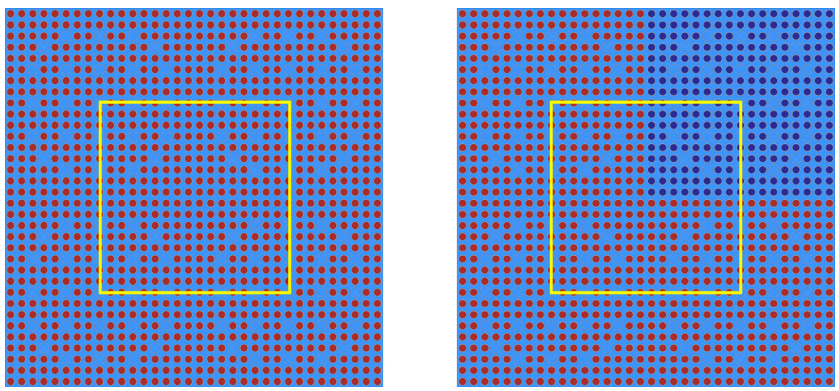

FIGURE 5 | The mini four assembly model to calculate the correction ratio with **(A)** no perturbation **(B)** perturbation on the upper right.

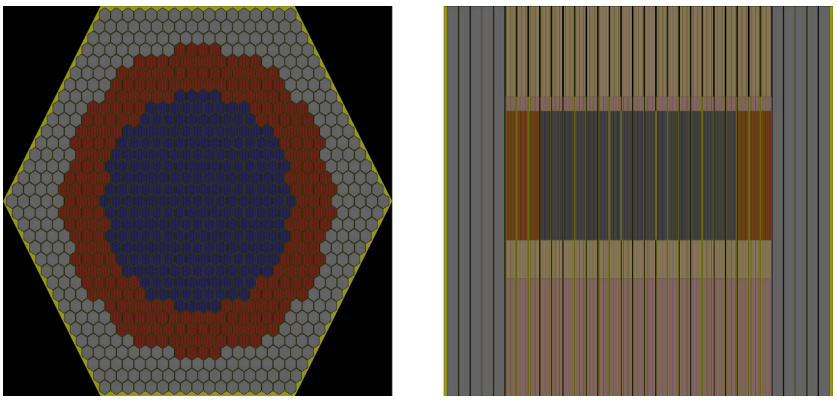

FIGURE 7 | The radial and axial cross sections of the sodium fast reactor benchmark.

TABLE 1 | Geometry Parameters of the ESFR model.

Parameter	Value (cm)
Fuel rod pitch	1.174
Fuel rod outer diameter	1.076
Fuel rod inner diameter	0.94
Fuel active zone height	100
Number of pins in an assembly	271
Assembly pitch	21.08
Inner fuel assemblies	241
Outer fuel assemblies	246
Reflector assemblies	330

system fission matrix element $a_{i,j}$ equals to the database fission matrix element $a_{i,j}^{'}$ if the destination cell i has the same transport property, such as the fuel enrichment, depletion, and the fuel and moderator temperature. Take a two-assembly model as an example, the diagram to combine fission matrices is shown in **Figure 1**. The two-assembly fission matrix is estimated by combining each half of the database fission matrices obtained in uniform-assembly cases. In order to explain the theory from the fission perspective of view, a neutron will be thermalized by scattering with water or other moderators. It finally gets absorbed in the low energy range and fission, where there is a much larger absorption and fission cross-section than those in the high energy range. **Figure 2** shows the track of a neutron in a PWR assembly with the Monte Carlo method. It can be observed that the neutron transports further and has fewer collisions at the beginning because of higher energy. Then it gets more easily scattered, and the transport length between collisions is smaller. Therefore, the cell properties in the intermediate regions or the beginning location are less likely to influence the neutron transport. The number of fission neutrons born in the process is mainly dominated by the destination and surrounding cells' properties. Then it is reasonable to assume that the fission matrix element $a_{i,j}$ is only dependent on the property of the destination cell i.

In a whole-core transport calculation, the core fission matrix is estimated by combining database fission matrices following the above assumption. The database fission matrices are calculated in uniform-assembly loading cases, where the same assemblies fill the infinite geometry. However, as explained before, the fission matrix combination theory assumes that only the destination cell dominates the fission matrix element $a_{i,j}$. The neutrons are also in a low energy range in the destination nearby cells. So a surrounding cell of different properties from the destination cell may introduce a perturbation to the fission matrix element $a_{i,j}$. Taking the BEAVRS benchmark as an example, the core is composed of different enrichment assemblies shown in **Figure 3**. For each type of assembly, the database fission matrices are pre-calculated and combined to build to a whole-core fission matrix. The details can be found in (He and Walters, 2019). The eigenpair of the fission matrix represents the multiplication factor and the fission source distribution, respectively. The pin-wise fission rate distribution obtained with the combined fission matrix method has been compared against the Monte Carlo reference calculation, and the relative error is shown in **Figure 4**. The k_{eff} difference is 156 pcm and the 2D root mean square (RMS) error is 6.26%.

Due to the perturbation a different surrounding cell brings to the fission matrix element $a_{i,j}$, the cells at the assembly boundary have relatively large errors. In order to reduce the error the material discontinuity brings to the combined fission matrix theory, a correction ratio method has been developed. The detail of the theory can be found in (He and Walters, 2019). The correction ratio estimates the perturbation a different surrounding assembly brings to the destination assembly. The pin-wise correction ratios are defined as the fission rates with perturbation assembly divided by those in uniform cases. In thermal reactors, due to the limited transport length of neutrons, only perturbation assemblies adjacent to the destination assembly are assumed to contribute to the correction ratios. Therefore, correction ratios are calculated corresponding to different perturbation assembly locations in a mini-four assembly model, as shown in **Figure 5**. With the correction ratio applied to the combined fission matrix theory in the whole-core problem, the relative error is significantly reduced, as shown in **Figure 6**. The k_{eff} difference is 26 pcm

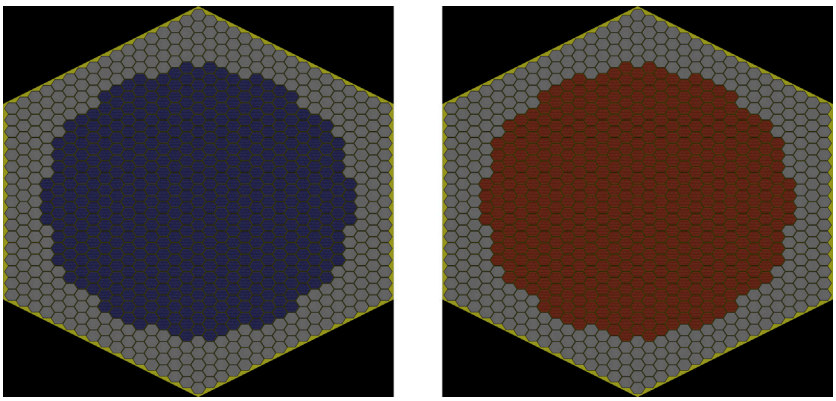

FIGURE 8 | The uniform models to tally the database fission matrices.

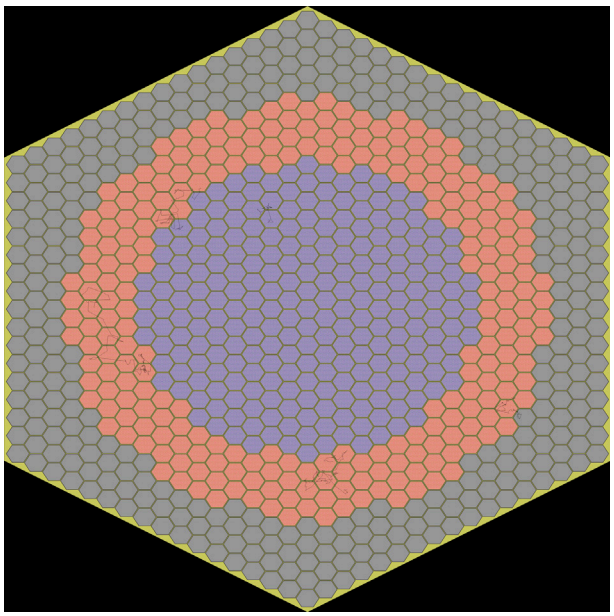

FIGURE 9 | The neutron transport tracks in a fast reactor.

with a 3 pcm uncertainty and the 2D RMS error is 0.54% with a 0.21% uncertainty. The Monte Carlo reference calculation takes about 80 h and the RAPID calculation can be finished within minutes. Note, the RAPID run time does not take the database preparation into account since the database does not need to be prepared again when performing additional RAPID calculations. Overall, the combined fission matrix theory with correction ratio has achieved high accuracy in thermal reactors.

3 SODIUM FAST REACTOR BENCHMARK

This work takes the European Sodium Fast Reactor as the benchmark problem (Fiorini and Vasile, 2011). The radial and axial cross-sections of the core are shown in **Figure 7**. The core is composed of three layers: the inner fuel regions, the outer fuel regions, and the outermost reflector regions. The inner and outer fuel regions have different Pu enrichment at 14.05 and 16.35%, respectively. The core is slightly modified in this work that the control and shutdown assemblies are switched with inner fuel assemblies for the convenience of fission matrix tally. Since the purpose of the work is to validate the combined fission matrix theory in a fast reactor, such a modification will not bias the conclusion. The main parameters of the reactor core and assembly are summarized in **Table 1**. The core is modeled at hot-zero-power condition, with the fuel and moderator temperature equal to 300*K*.

4 RESULTS

The combined fission matrix method is compared against the Monte Carlo calculation on the ESFR model. The database fission matrix is composed of two fission matrices. The two fission matrices represent the cases where inner and outer fuel assemblies fill the entire core as shown in **Figure 8**. The database fission matrix in this study is obtained through the Monte Carlo code OpenMC (Romano and Forget, 2013) criticality calculation due to its high fidelity. The mesh to tally the fission matrix is based on assemblies, i.e., there are 487 fuel assemblies in the core, which corresponds to a 487 × 487 fission matrix. The whole-core reference calculation is also using criticality calculation. The criticality calculations use 500 inactive cycles and 2000 active cycles, with 10, 000, 000 neutron histories simulated per cycle.

Before applying the combined fission matrix theory to the whole-core problem, we will first compare the neutron transport track between the thermal and fast reactors. As shown in **Figure 9**, the neutron transport from born to death may cover several assemblies in a fast reactor, which is much longer than that in thermal reactors.

The whole-core fission matrix is estimated by combining two database fission matrices, and its eigenvalue and

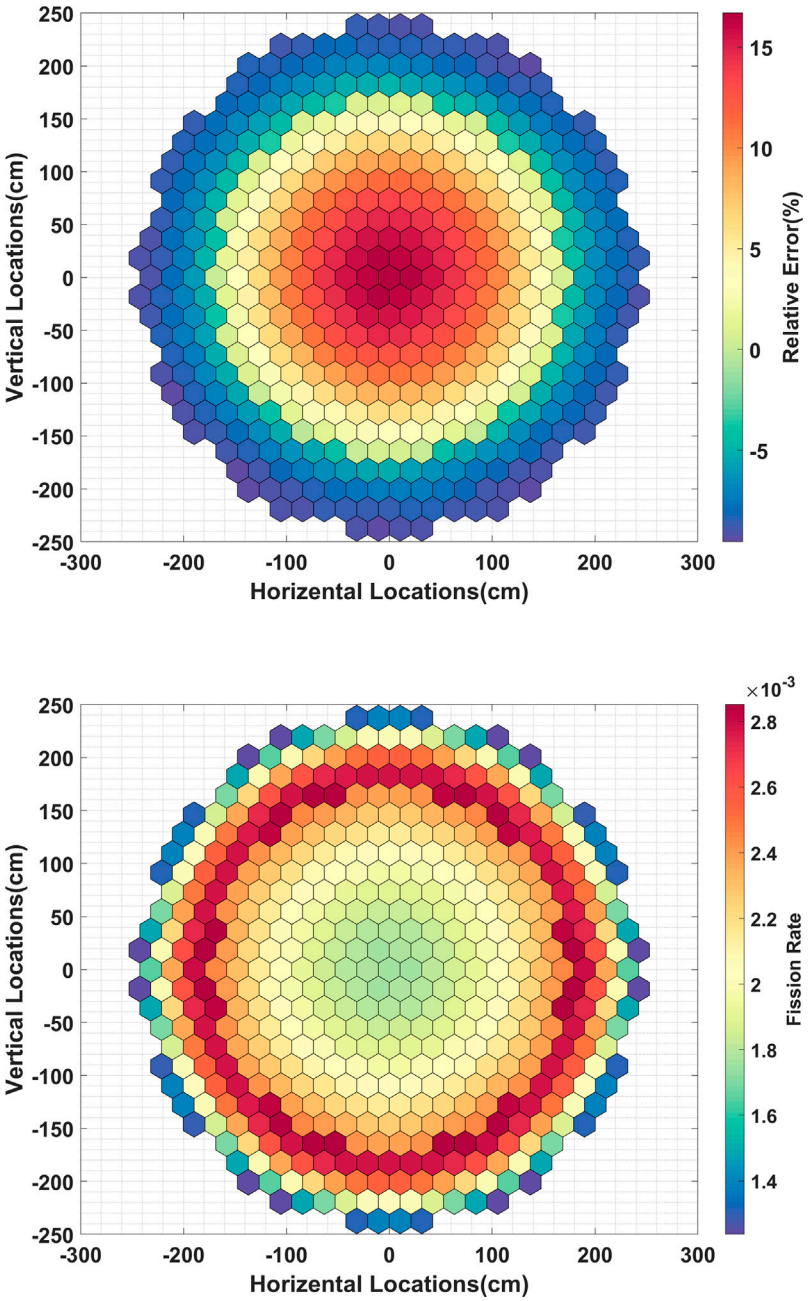

FIGURE 10 | The fission rate from Monte Carlo calculation and its relative error with that from the combined fission matrix theory.

eigenvector represent the multiplication factor and assembly-wise fission rate. The fission rate calculated from the Monte Carlo reference calculation and its difference with that from the combined fission matrix method are shown in **Figure 10**. The 2D RMS error is 8.3% and the k_{eff} difference is 64 pcm with a roughly 4 pcm uncertainty. The relatively large error in a fast reactor can be explained from the neutron transport point of view: the neutron remains high energy from birth to death in a fast reactor. The absorption and scattering in the intermediate cells have a competing impact with the absorption and fission in the destination cell. It implies that the destination cell property is not dominating in the fission matrix element $a_{i,j}$. On the other hand, because the neutron transports a long way in such a reactor, the destination is subject to perturbations from a large number of assemblies, i,e. the destination assembly is easier to be perturbed.

In this work, a whole-core correction ratio has also been tested. That is, the whole-core fission source from criticality calculation in the fast reactor is used to calculate the fission source in the uniform models, and then derive the correction

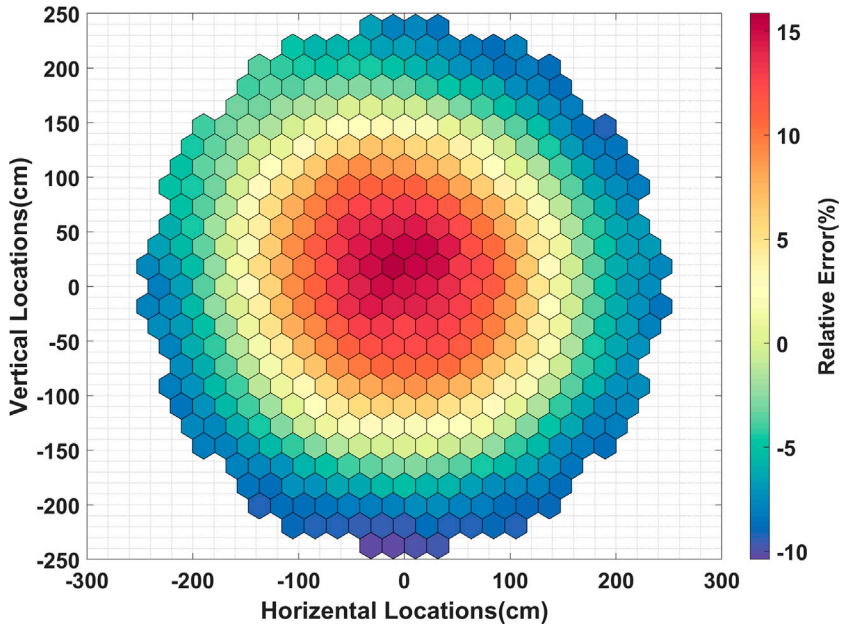

FIGURE 11 | The fission rate relative error between the Monte Carlo calculation and the combined fission matrix theory with correction ratio.

ratios separately for the inner fuel and outer fuel assemblies as in

$$R_i^{inner} = \frac{F_i^{real}}{F_i^{inner_uniform}}$$
$$R_i^{outer} = \frac{F_i^{real}}{F_i^{outer_uniform}} \quad (2)$$

Where, R_i and F_i are correction ratios and fission rates in assembly i. With the correction ratio applied, the 2D relative error is shown in **Figure 11**. The k_{eff} difference is 48 pcm, and the 2D RMS error is 7.3%. It can be seen that the combined fission matrix method in the fast reactor has lower accuracy than in the thermal reactor. The long length of the neutron transport in a fast reactor also makes the correction ratio generation a challenging problem. Overall, the combined fission matrix theory can provide a rough estimation of k_{eff} and fission source distribution in fast reactors, but it cannot restore the high-fidelity as in thermal reactors.

5 CONCLUSION

The combined fission matrix theory features an efficient and high-fidelity calculation. The method has been validated in a series of thermal reactors. This paper examines its application in fast reactors. Theoretically, the mechanism of combining database fission matrices by the destination cell property is more suited for a thermal neutron system. In fast reactors, the destination cell property is no more dominating in the fission matrix element, and the fission matrix element is more affected by intermediate cells. Finally, the combined fission matrix theory is validated in an SFR benchmark problem. Compared to the Monte Carlo reference calculation, the combined fission matrix theory has a larger error in the SFR than thermal reactors. It can be concluded that the combined fission matrix theory still needs further development in fast reactor applications.

DATA AVAILABILITY STATEMENT

The original contributions presented in the study are included in the article/supplementary material, further inquiries can be directed to the corresponding author.

AUTHOR CONTRIBUTIONS

DH proposes the idea and finishes the calculations in this work. TZ and XL helps organizes and edit the paper.

ACKNOWLEDGMENTS

The authors would like to acknowledge that this research is sponsored by Shanghai Sailing Program (21YF1421200) and Natural Science Foundation of Shanghai (21ZR1429700).

REFERENCES

Carney, S., Brown, F., Kiedrowski, B., and Martin, W. (2014). Theory and Applications of the Fission Matrix Method for Continuous-Energy Monte Carlo. *Ann. Nucl. Energ.* 73, 423–431. doi:10.1016/j.anucene.2014.07.020

Fiorini, G. L., and Vasile, A. (2011). European Commission - 7th Framework Programme. *Nucl. Eng. Des.* 241, 3461–3469. doi:10.1016/j.nucengdes.2011.01.052

He, D., and Walters, W. J. (2020). A Correction Method for RAPID Fission Matrix Calculations with Control Rod Movement. *Prog. Nucl. Energ.* 121, 103226. doi:10.1016/j.pnucene.2019.103226

He, D., and Walters, W. J. (2019). A Local Fission Matrix Correction Method for Heterogeneous Whole Core Transport with RAPID. *Ann. Nucl. Energ.* 134, 263–272. doi:10.1016/j.anucene.2019.06.008

Laureau, A., Aufiero, M., Rubiolo, P. R., Merle-Lucotte, E., and Heuer, D. (2015). Transient Fission Matrix: Kinetic Calculation and Kinetic Parameters βeff and Λeff Calculation. *Ann. Nucl. Energ.* 85, 1035–1044. doi:10.1016/j.anucene.2015.07.023

Liu, Z., Wu, H., Cao, L., Chen, Q., and Li, Y. (2011). A New Three-Dimensional Method of Characteristics for the Neutron Transport Calculation. *Ann. Nucl. Energ.* 38, 447–454. doi:10.1016/j.anucene.2010.09.021

Mascolino, V., Haghighat, A., and Roskoff, N. J. (2017). Evaluation of RAPID for a UNF Cask Benchmark Problem. *EPJ Web Conf.* 153, 05025. doi:10.1051/epjconf/201715305025

Rau, A., and Walters, W. J. (2020). Validation of Coupled Fission Matrix - TRACE Methods for thermal-hydraulic and Control Feedback on the Penn State Breazeale Reactor. *Prog. Nucl. Energ.* 123, 103273. doi:10.1016/j.pnucene.2020.103273

Romano, P. K., and Forget, B. (2013). The OpenMC Monte Carlo Particle Transport Code. *Ann. Nucl. Energ.* 51, 274–281. doi:10.1016/j.anucene.2012.06.040

Terlizzi, S., and Kotlyar, D. (2019). Fission Matrix Decomposition Method for Criticality Calculations: Theory and Proof of Concept. *Nucl. Sci. Eng.* 193, 948–965. doi:10.1080/00295639.2019.1583948

Topham, T. J., Rau, A., and Walters, W. J. (2020). An Iterative Fission Matrix Scheme for Calculating Steady-State Power and Critical Control Rod Position in a TRIGA Reactor. *Ann. Nucl. Energ.* 135, 106984. doi:10.1016/j.anucene.2019.106984

Walters, W. J., Roskoff, N. J., and Haghighat, A. (2018). The RAPID Fission Matrix Approach to Reactor Core Criticality Calculations. *Nucl. Sci. Eng.* 192, 21–39. doi:10.1080/00295639.2018.1497395

Zhang, M., Cao, Z., Xie, J., Zhu, W., Zhou, P., Gu, H., et al. (2013). Mutagenesis Analysis of Porcine Reproductive and Respiratory Syndrome Virus Nonstructural Protein 7. *Virus Genes* 47, 467–477. doi:10.1007/s11262-013-0957-4

Zhang, T., Wu, H., Cao, L., and Li, Y. (2018). Acceleration of 3d Pin-By-Pin Calculations Based on the Heterogeneous Variational Nodal Method. *Ann. Nucl. Energ.* 114, 165–174. doi:10.1016/j.anucene.2017.12.012

Conflict of Interest: The authors declare that the research was conducted in the absence of any commercial or financial relationships that could be construed as a potential conflict of interest.

frontiers in Energy Research

ORIGINAL RESEARCH
published: 20 December 2021
doi: 10.3389/fenrg.2021.765863

Refinements of the Pin-Based Pointwise Energy Slowing-Down Method for Resonance Self-Shielding Calculation—I: Theory

Sooyoung Choi[1], *Wonkyeong Kim*[2] *and Deokjung Lee*[2]*

[1]Department of Nuclear Engineering and Radiological Sciences, University of Michigan, Ann Arbor, MI, United States,
[2]Department of Nuclear Engineering, Ulsan National Institute of Science and Technology, Ulsan, South Korea

The pin-based pointwise energy slowing-down method (PSM), which is a resonance self-shielding method, has been refined to treat the nonuniformity of material compositions and temperature profile in the fuel pellet by calculating the exact collision probability in the radially subdivided fuel pellet under the isolated system. The PSM has generated the collision probability table before solving the pointwise energy slowing-down equation. It is not exact if the fuel pellet has nonuniform material compositions or temperature profile in all the subdivided regions. In the refined PSM-CPM, the pre-generated table is not required for directly calculating the collision probability in all the subdivided regions of the fuel pellet while solving the slowing-down equation. There are an advantage and a disadvantage to the method. The advantage is to exactly consider the nonuniformity of the material compositions and temperature profile in the fuel pellet. The disadvantage is the longer computing time than that of the PSM when the fuel pellet has more than five subdivided regions. However, in the practical use for UO_2 pin-cells, it is still comparable for the computation time with the PSM and the conventional equivalence theory methods. In this article, using simple light water reactor 17 × 17 F A problems with a uniform material composition and temperature profile, it is demonstrated that PSMs (PSM and PSM-CPM) exhibit consistent accuracy in calculating the multiplication factor and the pin power distribution with no compromise in the computation time. More detailed accuracy assessments with various test cases, including problems representing the nonuniformity, are presented in the accompanying article.

Keywords: resonance self-shielding calculation, equivalence theory, pointwise energy slowing-down method, resonance treatment, light water reactor, reactor physics

OPEN ACCESS

Edited by:
Ding She,
Tsinghua University, China

Reviewed by:
Qian Zhang,
Harbin Engineering University, China
Guang Hu,
Xi'an Jiaotong University, China

***Correspondence:**
Deokjung Lee
deokjung@unist.ac.kr

Specialty section:
This article was submitted to Nuclear Energy, a section of the journal Frontiers in Energy Research

Received: *27 August 2021*
Accepted: *08 November 2021*
Published: *20 December 2021*

Citation:
Choi S, Kim W and Lee D (2021) Refinements of the Pin-Based Pointwise Energy Slowing-Down Method for Resonance Self-Shielding Calculation—I: Theory. Front. Energy Res. 9:765863. doi: 10.3389/fenrg.2021.765863

1 INTRODUCTION

In reactor physics, all calculations are conducted with cross sections (XSs). The actual XSs for nuclides describe the very detailed energy resolution. XS data are composed of hundreds of thousands of energy points for major resonant nuclides (*e.g.*, ^{238}U). Even with modern computing resources, it is still time consuming and impractical to directly utilize raw XS data in lattice physics calculations. Because of this, XSs, especially in the resonance energy range that requires high-energy resolution, must be condensed during neutron transport computations. A resonance self-shielding calculation (or resonance treatment) is performed to condense a detailed XS into the multigroup level (*e.g.*, ~100 groups).

Therefore, if the resonance self-shielding calculation is not accurate, all the subsequent calculations would not be meaningful. The resonance treatment is one of the most difficult and challenging parts of reactor physics.

The equivalence theory has been widely used for resonance treatment (Knott et al., 2010; Stamm'ler and Abbate, 1983). The equivalence theory gives a reasonable solution within a short computation time. Owing to this advantage, many lattice physics codes adopt the equivalence theory to generate effective multigroup XSs (Powney and Hutton, 2002; Rhodes et al., 2006). There has been much research into the equivalence theory to improve the accuracy of effective multigroup XSs and the applicability to general geometry (Koike et al., 2012; Godfrey, 2014; Choi et al., 2015a). However, there are still many points missing from the resonance calculation. The author's previous works have determined that resonance scattering causes the overestimation of the ^{238}U effective XS (Choi, 2017; Choi et al., 2017).

In one of the authors' previous work (Choi et al., 2017), a new resonance self-shielding method, the pin-based pointwise slowing-down method (PSM), was developed to resolve limitations, that is, the overestimation of ^{238}U XS due to resonance scattering sources, in the conventional equivalence theory. However, the PSM has an assumption for treating with the total XSs in the subdivided regions of the fuel pellet. As one of the techniques for achieving high performance, the PSM generates the collision probability of the isolated fuel pellet before solving the pointwise slowing-down equation. The collision probability is generated with the grid of the total XSs that is assumed to be constant in the subdivided regions of the fuel pellet. With the nonuniform material and temperature distribution, the total XSs in the subdivided regions are different from each other so that the accuracy of the effective XSs is impeded by the constant total XS assumption (Zhang et al., 2018; Zhang et al., 2020). Therefore, generating the collision probability during solving the slowing-down equation on the fly, a more rigorous method, PSM-CPM, has been developed to treat nonuniform material and temperature distributions in the fuel pellet.

This work reviews the PSM in brief and introduces PSM-CPM with the refinement. The work demonstrates the accuracy of the PSM and PSM-CPM with several light water reactor problems with only uniform material and temperature distributions. The computing time for the two methods is also estimated and compared. Detailed verifications of the PSM-CPM are performed with various light water reactor (LWR) problems with a nonuniform material composition and temperature profile, and the detailed XS comparison is presented to show the superior accuracy of the method in the accompanying article (Kim et al., 2021).

2 PIN-BASED POINTWISE ENERGY SLOWING-DOWN METHODS (PSMS)

The achievements of the PSM are summarized as follows: RI or XS look-up tables are not required for resonance treatment; the distribution of the scattering sources in the fuel pellet is accurately modeled; and PSMs have a comparable computational cost with the equivalence theory.

The neutron transport equation can be expressed with the radially subdivided regions (Stoker and Weiss, 1996) and collision probabilities for the two-region problem (*i.e.*, fuel and moderator) in the resonance energy range as follows:

$$\Sigma_{t,i}(E)\phi_i(E)V_i = \sum_{j\in F} P_{ji}(E)V_j Q_{s,j}(E) + P_{Mi}(E)V_M Q_{s,M}(E), \tag{1}$$

where i and j are the indexes of the radially subdivided regions of the fuel pellet, $\Sigma_{t,i}(E)$ is the total XS of the radially subdivided region i of the fuel pellet, $\phi_i(E)$ is the flux in the subdivided region i, V_i is the volume of the subdivided region i, F is the index of the fuel pellet, M is the index of the moderator, $P_{ji}(E)$ is the collision probability from the subdivided region j to the subdivided region i, and the slowing-down scattering source of the subdivided region j is defined as follows:

$$Q_{s,j}(E) = \sum_{r\in j} N^r \int_E^{E/\alpha^r} \sigma_s^r\left(E'\right)\phi_j\left(E'\right)\frac{1}{1-\alpha^r}\frac{dE'}{E'}. \tag{2}$$

Using the lethargy form and the reciprocity relation, **Eq. 1** is written as follows:

$$\sum_{t,i}(u)\phi_i(u) = \sum_{j\in F} P_{ij}(u)\frac{\Sigma_{t,i}(u)}{\Sigma_{t,j}(u)}Q_{s,j}(u) + P_{iM}(u)\frac{\Sigma_{t,i}(u)}{\Sigma_{p,M}}Q_{s,M}(u), \quad i\in F. \tag{3}$$

The flux of the subdivided region i by rearranging **Eq. 3** is expressed as follows:

$$\phi_i(u) = \sum_{j\in F}\frac{P_{ij}(u)}{\Sigma_{t,j}(u)}Q_{s,j}(u) + \frac{P_{iM}(u)}{\Sigma_{p,M}}Q_{s,M}(u), \quad i\in F. \tag{4}$$

In **Eq. 3**, the index M also indicates the nonfuel region. It is assumed that materials in the nonfuel region only have a potential XS. In case of the multiregion problem, the nonfuel regions (*i.e.*, gap/clad/moderator) in a unit pin-cell are merged into a single region with the volume weighting by assuming constant spatial fluxes in the nonfuel regions.

The transport equation for the nonfuel region is written as follows:

$$\Sigma_{p,M}\phi_M(u)V_M = \sum_{i\in F} P_{iM}(u)V_i Q_{s,i}(u) + P_{MM}(u)V_M Q_{s,M}(u), \tag{5}$$

where $P_{MM}(u)$ is the nonfuel-to-nonfuel collision probability.

The flux of the nonfuel region M by rearranging **Eq. 5** is as follows:

$$\phi_M(u) = \sum_{i\in F}\frac{P_{Mi}(u)}{\Sigma_{t,i}(u)}Q_{s,i}(u) + \frac{P_{MM}(u)}{\Sigma_{p,M}}Q_{s,M}(u). \tag{6}$$

If $P_{ij}(u)$, $P_{iM}(u)$, $P_{Mi}(u)$, and $P_{MM}(u)$ are known, the fluxes and scattering sources in **Eqs 4–6** can be calculated by solving a fixed source transport equation.

The PSM and PSM-CPM calculate the collision probability with a two-step approach. In the first step, the collision probabilities of the subdivided regions in the isolated fuel pellet are calculated.

The difference between PSM and PSM-CPM is the way to calculate P_{ij}^{iso}, whereby a neutron uniformly born in the subdivided region i has its first collision in the subdivided region j. The PSM-CPM calculates P_{ij}^{iso} by using the CPM (Carlvik, 1996) for all energy points while solving the slowing-down equations with pointwise XSs.

In the PSM, however, P_{ij}^{iso} is tabulated as a function of the total XS of the fuel pellet before solving the slowing-down equations, and then P_{ij}^{iso} is interpolated using the total XS of any energy of interest. While solving the slowing-down equations, P_{ij}^{iso} is interpolated from the $\hat{P}_{ij}^{iso}$ table using the total XS of the fuel pellet at any energy of interest as follows:

$$P_{ij}^{iso}(u) = \hat{P}_{ij}^{iso}\left(\Sigma_{t,F}(u)\right). \tag{7}$$

Equation 7 is only exact if the fuel pellet has a constant material composition and temperature profile in all the subdivided regions. However, if the fuel is burned, the material compositions in the subdivided regions change differently from each other. For the burned fuel pellet, the burnup of the outermost subregion is higher than that in the inner subregion because of the spatial self-shielding effect. In addition, the thermal–hydraulic (TH) calculation is coupled with neutronics to analyze the power reactor. The fuel pellet must be divided into several rings to model the temperature profile from TH feedback. With the TH feedback, the temperature in the inner region is higher than that in the outer region. Obviously, the pointwise energy XSs depend on the material composition and the temperature. With nonuniform material compositions and temperatures, the total XSs of the subdivided regions are different from each other. In this case, an average total XS (*i.e.*, $\bar{\Sigma}_{t,F}$) is defined with **Eq. 8**, and the total XS of the entire fuel pellet (*i.e.*, $\Sigma_{t,F}$) in **Eq. 7** is replaced by the average total XS.

$$\Sigma_{t,F}(u) \approx \bar{\Sigma}_{t,F}(u) = \frac{\sum_{i\in F}\Sigma_{t,i}(u)\phi_i(u^h)V_i}{\sum_{i\in F}\phi_i(u^h)V_i}, \tag{8}$$

where energy u^h is one point higher than energy u.

Introducing the $\hat{P}_{ij}^{iso}$ table can lead error in computing the collision probability, even though it can significantly reduce the calculation time. The accuracy and efficiency on the use of the pre-generated table are estimated and compared in Section 3 and the accompanying article (Kim et al., 2021) in detail.

P_{ij}^{iso} considers the collision probability of an isolated fuel rod. Therefore, a proper correction is required to consider the shadowing effect from neighboring fuel rods and structural materials. In this second step of the collision probability calculation, it is assumed that the shadowing effect is not significantly different for the individually subdivided regions of the fuel pellet. In other words, the subdivided regions of the fuel pellet have the same shadowing effect. Under this assumption, a multiterm rational equation in the equivalence theory is used.

In PSMs, the shadowing correction factor is calculated with two escape probabilities. One is the fuel escape probability of an isolated fuel pin, and the other is that of the fuel pin in the lattice (or core). Carlvik's two-term rational approximation (Knott et al., 2010) is applied for a cylindrical geometry to calculate $P_{e,F}^{iso}(u)$ and $P_{e,F}(u)$ in **Eqs 22, 23**. $P_{e,F}^{iso}$ is the fuel escape probability of the isolated fuel pellet, and $P_{e,F}$ is the fuel escape probability of the fuel pellet in the lattice.

$$P_{e,F}^{iso}(u) = 1 - P_{FF}^{iso}(u) = 2\frac{2\Sigma_{e,F}}{\Sigma_{t,F}(u) + 2\Sigma_{e,F}} - \frac{3\Sigma_{e,F}}{\Sigma_{t,F}(u) + 3\Sigma_{e,F}}; \tag{9}$$

$$P_{e,F}(u) = 1 - P_{FF}(u) = \beta_1\frac{\alpha_1\Sigma_{e,F}}{\Sigma_{t,F}(u) + \alpha_1\Sigma_{e,F}} + \beta_2\frac{\alpha_2\Sigma_{e,F}}{\Sigma_{t,F}(u) + \alpha_2\Sigma_{e,F}}, \tag{10}$$

where $P_{e,F}^{iso}$ is the fuel escape probability of the isolated fuel pellet, $P_{e,F}$ is the fuel escape probability of the fuel pellet in lattice, and the coefficients in Eq. **10** are defined with the Dancoff factor as follows:

$$\begin{cases} A = \Gamma/(1-\Gamma) \\ \alpha_{1,2} = \left(5A + 6 \mp \sqrt{A^2 + 36A + 36}\right)\Big/(2A+2) \\ \beta_1 = \left(\dfrac{4A+6}{A+1} - \alpha_1\right)\Big/(\alpha_2 - \alpha_1) \\ \beta_2 = 1 - \beta_1 \end{cases}, \tag{11}$$

where Γ is the Dancoff factor of the fuel pellet.

It should be noted that $P_{e,F}^{iso}$ and $P_{e,F}$ are probabilities for the fuel pellet, not individual subregions of the pellet. The total XS of the fuel pellet, $\Sigma_{t,F}$, to calculate both escape probabilities is calculated by taking the average of the total XSs of the subdivided regions of the fuel pellet. Although Eq. 8 is only used for the PSM, the average XS of the fuel pellet is needed for both PSM and PSM-CPM to consider the shadowing effect.

The shadowing effect correction factor, which adjusts the fuel escape probability of an isolated fuel pin to consider the shadowing effect, is defined as a ratio of the fuel escape probabilities of two systems in the isolated fuel pellet and the lattice as follows:

$$\eta_F(u) = \frac{P_{e,F}(u)}{P_{e,F}^{iso}(u)}. \tag{12}$$

The shadowing effect correction factor is multiplied by the fuel escape probability in each subregion of the fuel pellets as follows:

$$P_{iM}(u) = P_{e,i}(u) = \eta_i(u)P_{e,i}^{iso}(u), \tag{13}$$

where

$$P_{iM}^{iso}(u) = P_{e,i}^{iso}(u) = 1 - \sum_{j\in F}P_{ij}^{iso}(u); \tag{14}$$

$$\eta_i(u) \approx \eta_F(u). \tag{15}$$

It is assumed that the shadowing effect correction factor of the subdivided region i is equal to that of the fuel pellet, as shown in Eq. **15**. The source distribution in the fuel pellet is very important because it has a significant effect on the fuel escape probability. When $P_{e,F}$ and $P_{e,F}^{iso}$ are calculated, a constant source distribution

in the fuel pellet is assumed. Therefore, the probabilities are not exact. The error from the constant source assumption exists in both $P_{e,F}$ and $P_{e,F}^{iso}$. However, the error existing in both escape probabilities is not expected to appear in the final products because the ratio of $P_{e,F}$ and $P_{e,F}^{iso}$ is used. The error existing in both the numerator and denominator of the shadowing effect correction factor in Eq. **12** can be canceled out.

The collision probabilities from the nonfuel region are expressed as follows:

$$P_{Mi}(u) = \frac{P_{iM}(u)\Sigma_{t,i}(u)V_i}{\Sigma_{p,M}V_M}; \tag{16}$$

$$P_{MM}(u) = 1 - \sum_{i\in F} P_{Mi}(u) = 1 - \sum_{i\in F} \frac{P_{iM}(u)\Sigma_{t,i}(u)V_i}{\Sigma_{p,M}V_M}. \tag{17}$$

Finally, all the collision probabilities and escape probabilities, which are needed to solve the slowing-down equations in **Eqs 4–6**, are derived.

2.1 Calculation Flow

There are two different options depending on how the collision probabilities of the subdivided regions of the isolated fuel pellet (*i.e.*, P_{ij}^{iso}) are calculated. The flowchart of PSMs is shown in **Figure 1**. The boxes with the dashed line are processes for only the PSM but not the PSM-CPM. The calculation process is as follows:

1. Read input information in a given problem.
2. Read the 72-group multigroup XS library and the 5·104 equal-lethargy pointwise energy XS library.
3. Generate the $\hat{P}_{ij}^{iso}$ vs total XS table for all the pin-geometry types in the given problem by using the CPM solver.
4. Perform the fixed-source MOC transport calculation for the whole-problem domain, and then calculate the individual Dancoff factors of the fuel pins with the enhanced neutron current method (Yamamoto, 2012).
5. Calculate $P_{e,F}^{iso}$ and $P_{e,F}$ with Carlvik's two-term method (Knott et al., 2010) and then calculate the shadowing effect correction factor η_F using Eq. **12**.
6. Interpolate $\hat{P}_{ij}^{iso}$ from the $\hat{P}_{ij}^{iso}$ table using the pointwise total XS of the fuel pellet for energy u (PSM) or calculate P_{ij}^{iso} using the CPM solver with the spatially dependent pointwise total XSs in the fuel pellet for energy u (PSM-CPM).
7. Correct the shadowing effect using the shadowing effect correction factor as in **Eq. 13**, and then calculate P_{ij}, P_{iM}, P_{Mi}, and P_{MM} with **Eqs 13–17**.
8. Solve the pointwise energy slowing-down equations in **Eqs 4–6**. Repeat steps 6–8 for all the pointwise energy points from high to low energy.
9. Condense the pointwise XS to the position-dependent multigroup XS. Consider the resonance upscattering effect for ^{238}U (Choi, 2017; Choi et al., 2017). Return to step 5) until all the fuel pins in the problem are treated.

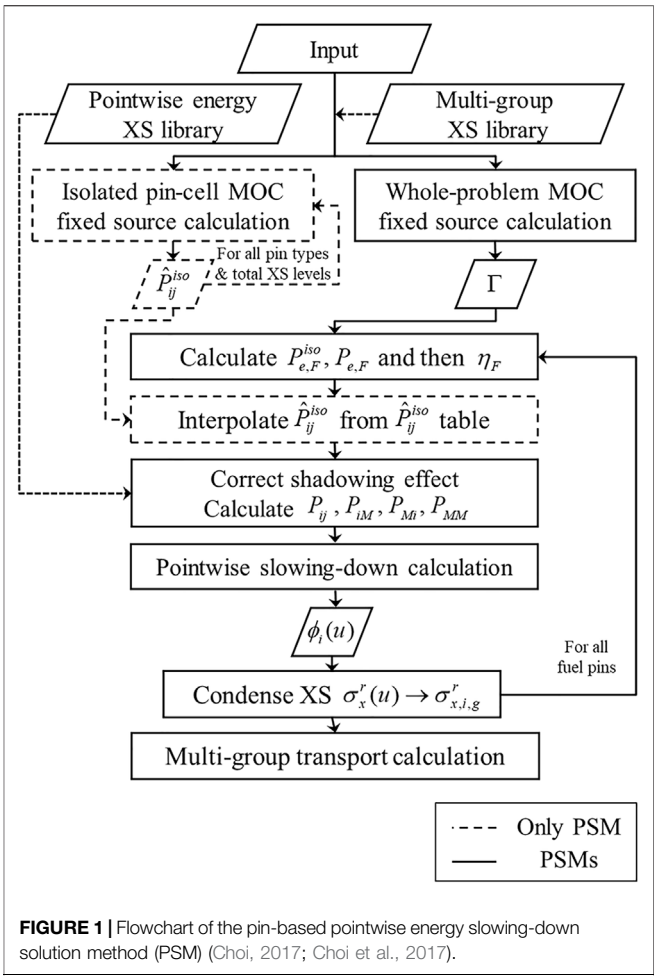

FIGURE 1 | Flowchart of the pin-based pointwise energy slowing-down solution method (PSM) (Choi, 2017; Choi et al., 2017).

3 NUMERICAL RESULTS

Several LWR problems are solved to verify the accuracy of the PSMs. **Table 1** presents a summary of test cases and methods used in the verifications. The test cases include the pin-cell and FA geometry with uniform material distribution, uniform temperature profile, and fresh fuel. The methods used in the comparisons are as follows:

1. EQ: The conventional equivalence theory.
2. PSM: The pin-based pointwise slowing-down method with the $\hat{P}_{ij}^{iso}$ table.
3. PSM-CPM: The pin-based pointwise slowing-down method with the CPM.

The following option was used in all the calculations in *Sensitivity Test for Energy Points in the Pointwise Cross-Section Library* and *VERA 17 × 17 Fuel Assembly Problem*: MOC condition: 0.01 cm ray spacing, 128 azimuthal angles, and T–Y optimized three polar angles (Yamamoto et al., 2007). It should be also noted that those calculation results in *Sensitivity Test for Energy Points in the Pointwise Cross-Section Library* and *VERA 17 × 17 Fuel Assembly Problem* were calculated with the P_2 high-order scattering model to reduce errors from the anisotropic source. The reference was the MCS Monte Carlo code (Lee et al., 2020). The numerical test was performed with the lattice physics code STREAM (Choi et al., 2015b). STREAM uses the method of

TABLE 1 | Summary of test cases (Choi, 2017).

Section	Test name	Geometry	Material distribution	Temperature profile	Method	Note
3.1	Sensitivity test for energy points in the PW XS library	Pin-cell	Uniform, nonuniform	Uniform	PSM, PSM-CPM	Computing time and eigenvalue
3.2	VERA FA	FA	Uniform	Uniform	PSM	Various FA types
3.3	17 × 17 FA	FA	Uniform	Uniform	EQ, PSM, PSM-CPM	Computing time test

characteristics (MOC) for the transport calculation and the equivalence theory for resonance treatment.

3.1 Sensitivity Test for Energy Points in the Pointwise Cross-Section Library

Sensitivity test was performed to determine a reliable option to give accurate results by PSMs. The parameter to test is the number of energy points in the PW XS libraries.

The number of energy points is important in terms of accuracy and computational efficiency. When many energy points are used, the solution from the slowing-down calculation is accurate. However, the calculation time is proportional to the number of energy points. Four pointwise energy libraries, which have different numbers of energy points, were used in the sensitivity test. A normal UO_2 pin-cell depletion problem was solved with PSMs. The reason that the depletion problem was selected is that light nuclides usually do not need many energy points, whereas heavy nuclides need many energy points because of their many resonances in XSs. Pointwise energy XS libraries with 5,000, 10,000, 50,000, and 100,000 points were used in the test. The energy between 0.3 eV and 30 keV was divided with equal lethargy depending on the libraries. The result with 100,000 points was set as a reference. From the internal test, it was verified that more than 100,000 points do not have noticeable effect on the results.

Figure 2 shows the results with the four libraries. The result with 50,000 energy points is quite close to the reference. The differences in the eigenvalue are less than 5 pcm over all the depletion steps. The result with 10,000 energy points is also reliable in terms of the eigenvalue. The maximum difference is 17 pcm. However, the result with 5,000 energy points is significantly different from the reference, with a maximum difference of 133 pcm. From this sensitivity test for the number of energy points, it is verified that 50,000 energy points are sufficient to get an accurate result. In the STREAM code, the pointwise energy XS library with 10,000 points is used as a default. The library is accurate enough to get reasonable solutions for practical use. The library with 50,000 points is used as an option when a user wants to get the most accurate result. All the results in this work were generated with 50,000 energy points to get the highest accuracy. The number of energy points can be further reduced by using a small lethargy width for high energy and a large lethargy width for low energy because resonances at high energy are narrower and more densely distributed.

The calculation times elapsed in PSMs were tested. A UO_2 fuel burnup level of 60 MW d/kg was used in this test. The number of

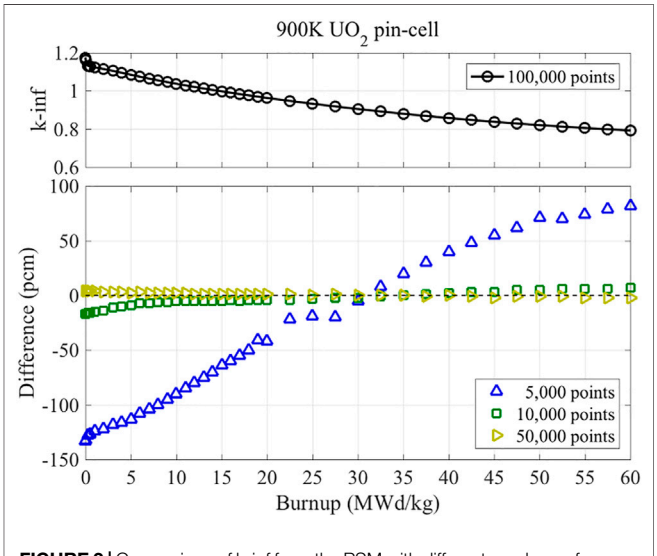

FIGURE 2 | Comparison of k-inf from the PSM with different numbers of energy points in the XS libraries (Choi, 2017).

TABLE 2 | Elapsed time in resonance treatment with PSMs (Choi, 2017).

Method →		PSM-CPM	PSM
k-inf →		0.79267	0.79282
Elapsed time (sec)	PSM solution[a]	0.148	0.011
	XS condensation[b]	0.102	0.115
	Nuclide grouping[c]	0.104	0.104
	$\hat{P}_{ij}^{iso}$ table[d]	—	0.003
	PSM total[e]	0.354	0.233

[a]*Elapsed time in solving the slowing-down equation and calculating collision probabilities.*
[b]*Elapsed time in condensing the pointwise XS, to multigroup XS.*
[c]*Elapsed time in calculating the macroscopic XSs, and the average mass for the each nuclide group.*
[d]*Elapsed time in generating the collision probability table.*
[e]*Total elapsed time in all calculations related to the PSM.*

the subdivided regions of the pellet is 5. Because of the spatial self-shielding effect in the fuel pellet, the material compositions are nonuniform in the pellet. The number of nuclides in the fuel is 198. The library with 50,000 points was used in this test. The eigenvalue results and elapsed time are shown in **Table 2**.

When the $\hat{P}_{ij}^{iso}$ table is used to calculate the collision probabilities of the isolated fuel pellet (*i.e.*, P_{ij}^{iso}), the elapsed time used in "PSM solution" is reduced by a factor of 13.5. There

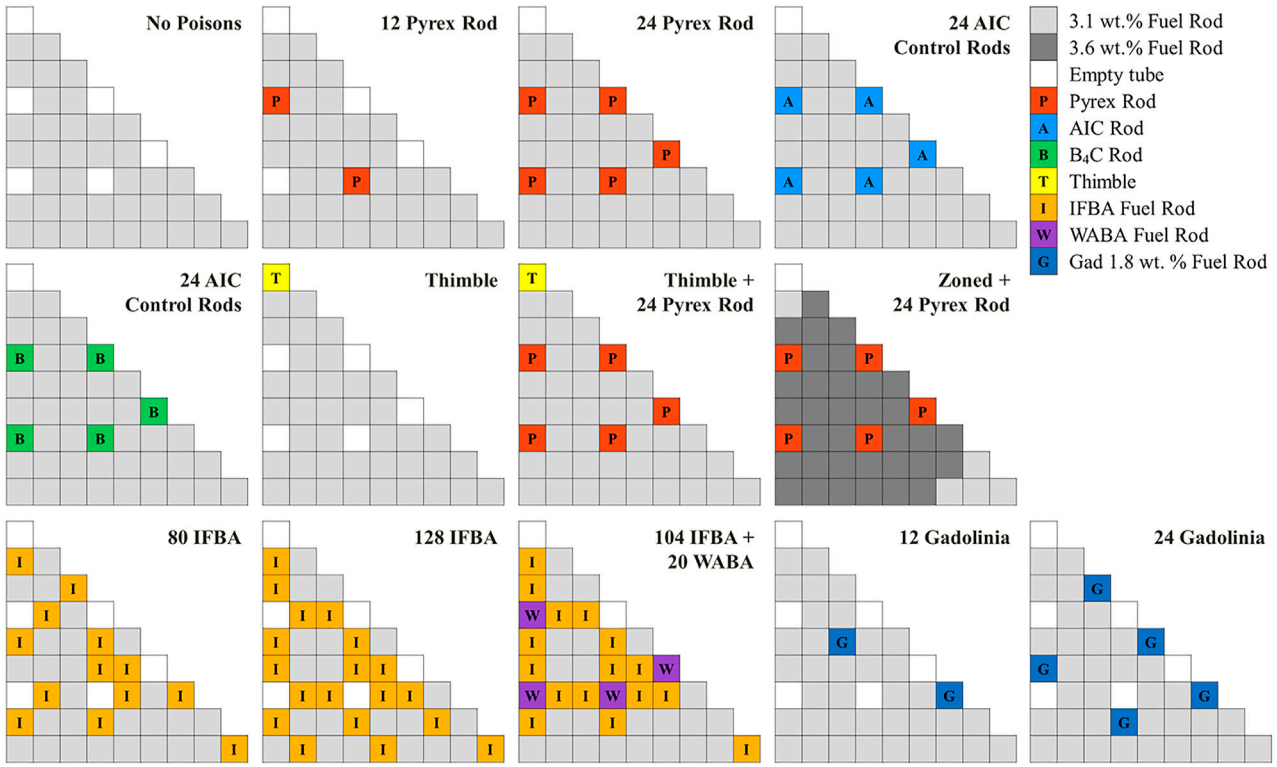

FIGURE 3 | Configuration of rods in the 17 × 17 fuel assembly problem (Choi, 2017).

are two error sources for the $\hat{P}_{ij}^{iso}$ table. One is error from interpolating $\hat{P}_{ij}^{iso}$. The $\hat{P}_{ij}^{iso}$ table is generated as a function of the total XS of the fuel pellet. From the internal test, it was concluded that the error from the interpolation is less than 4 pcm. The second error source is in approximation in the $\hat{P}_{ij}^{iso}$ table. The $\hat{P}_{ij}^{iso}$ table is made with a constant pointwise XS approximation in the fuel pellet. Overall, an error of 15 pcm occurs from the $\hat{P}_{ij}^{iso}$ table. The second error source is the major difference between PSM and PSM-CPM. More detailed comparisons are performed in the accompanying article (Kim et al., 2021). The $\hat{P}_{ij}^{iso}$ table effectively reduces the calculation time without a significant loss of accuracy. The additional calculation time required in generating the $\hat{P}_{ij}^{iso}$ table is 0.003 s, which is negligible. The PSM takes 0.233 s to calculate the effective multigroup XS of the burned fuel pellet with five submeshes. Although the XS condensation and the grouping are quite a simple calculation, they are the major time-consuming tasks in PSMs. The code must be further optimized to reduce the calculation time in the XS condensation and the grouping. With the 10,000-point library, the calculation time can be further reduced by a factor of 5.

3.2 VERA 17 × 17 Fuel Assembly Problem

17 × 17 fuel assembly (FA) problems were solved to verify PSMs. The 17 × 17 FAs in the VERA benchmark problem (Godfrey, 2014) were selected and solved as described in this section. **Figure 3** shows the configuration of the rods for various types of FAs. Various burnable poisons and control rods were used in the FA design. **Table 3** summarizes the material information and short descriptions of the FAs. The detailed specifications of the geometry and the material compositions are well described in the reference (Godfrey, 2014). The solutions for the 17 × 17 FAs were generated by the PSM. The fuel pellets used in this problem have a uniform material composition and a uniform temperature profile.

The results for k-inf and the pin power distribution were obtained with PSMs as shown in **Table 4** and **Table 5**, respectively. PSMs show quite accurate and consistent results. The differences in k-inf are of the order of 100 pcm. For the FA with AIC control rods, the PSM-CPM has a difference of 216 pcm in k-inf. The RMS difference and the maximum difference in the power distribution are approximately 0.17 and 0.41%, respectively.

From the verification with the various types of 17 × 17 FAs, it is verified that PSMs calculate accurate and consistent results in k-inf and the pin power distribution.

The PSM and PSM-CPM calculate identical solutions for the condition (*i.e.*, a uniform material composition and temperature profile in the fuel pellet). There is a slight difference (*i.e.*, less than 3 pcm in the eigenvalue) between PSM and PSM-CPM caused by the $\hat{P}_{ij}^{iso}$ table interpolation.

3.3 Test for Computing Time

The PSM and PSM-CPM showed high accuracy in the reactor parameters for the various verification problems. In order to use

TABLE 3 | Description for the fuel assembly problem (Choi, 2017).

Problem	Description	UO_2 enrichment (%)	Moderator temperature (K)	Fuel temperature (K)	Moderator density (g/cc)	Boron concentration (ppm)
A	No poison	3.1	565	565	0.743	1,300
B	No poison		600	600	0.661	
C	No poison			900		
D	No poison			1,200		
E	12 Pyrex			600	0.743	
F	24 Pyrex					
G	24 AIC					
H	24 B4C					
I	Thimble					
J	Thimble, 24 Pyrex					
K	Zoned, 24 Pyrex	3.1, 3.6				
L	80 IFBA	3.1				
M	128 IFBA					
N	104 IFBA, 20 WABA					
O	12 Gadolinia	1.8, 3.1				
P	24 Gadolinia					

TABLE 4 | k-inf results—PSM and PSM-CPM.

Problem	Description	k-inf				
		MCS	PSM	Difference (pcm)	PSM-CPM	Difference (pcm)
A	No poison	1.18165 ± 0.00007	1.18179	14	1.18181	16
B	No poison	1.18298 ± 0.00007	1.18303	14	1.18306	17
C	No poison	1.17371 ± 0.00008	1.17357	−14	1.17360	−11
D	No poison	1.16597 ± 0.00007	1.16567	−30	1.16570	−27
E	12 Pyrex	1.06915 ± 0.00007	1.06922	7	1.06924	9
F	24 Pyrex	0.97554 ± 0.00007	0.97569	15	0.97571	17
G	24 AIC	0.84743 ± 0.00007	0.84957	214	0.84959	216
H	24 B4C	0.78759 ± 0.00008	0.78865	106	0.78867	108
I	Thimble	1.17931 ± 0.00007	1.17960	29	1.17962	31
J	Thimble, 24 Pyrex	0.97475 ± 0.00007	0.97494	19	0.97497	22
K	Zoned, 24 Pyrex	1.01944 ± 0.00007	1.01987	43	1.01989	45
L	80 IFBA	1.01837 ± 0.00007	1.01896	59	1.01898	61
M	128 IFBA	0.93838 ± 0.00007	0.93914	76	0.93916	78
N	104 IFBA, 20 WABA	0.86919 ± 0.00007	0.86977	58	0.86978	59
O	12 Gadolinia	1.04722 ± 0.00007	1.04694	−28	1.04697	−25
P	24 Gadolinia	0.92683 ± 0.00007	0.92646	−37	0.92648	−35

the PSM and PSM-CPM in a practical design, it should be confirmed that they calculate the effective multigroup XS within a reasonable computation time.

The 17 × 17 FA problem was selected for the computation time comparison. The EQ was compared to the PSM. The FA was modeled with octant symmetry. For this section, the following option was used in the calculation: MOC condition: 0.05 cm ray spacing, 48 azimuthal angles, and three polar angles. In the test, each pin-cell had eight azimuthal sectors, three radial subregions in the coolant, and five radial subregions in the fuel pellet. The number of flat source regions is 2,842. The number of macroscopic XS sets is 242. The inflow transport corrected P0 (TCP0) model is used for both options (Choi et al., 2015c). Generally, these MOC conditions and the TCP0 model are used for practical calculations.

The time comparison results are shown in **Table 6**. The results were generated on an OSX system with a 3.1-GHz Intel Core i7 processor. PSMs perform the energy-independent fixed-source calculations to consider the shadowing effect. However, the EQ needs 15 fixed-source solutions for the fuel. The STREAM code performs the fixed-source MOC calculation for the resonance energy groups above 4 eV (Choi et al., 2015a). In case of the 17 × 17 FA problem, the Dancoff factors are calculated for the fuel and the cladding. PSMs are not applied on the resonance treatment for the cladding. Both PSMs and EQ use a common resonance treatment method (Choi et al., 2015a) for the cladding. The cladding resonance treatment method is based on the equivalence theory, and therefore PSMs and EQ perform energy-group–dependent MOC fixed-source calculations. Finally, PSM requires 16 MOC fixed-source solutions (1 for the fuel; 15 for the cladding), whereas EQ requires 30 fixed-source solutions (15 for the fuel; 15 for the cladding). This is why PSMs need approximately half the computation time in the fixed-source calculation (MOC FSP in **Table 6**) compared to EQ. Obviously, the elapsed time in the fixed-source MOC calculation depends on the MOC ray conditions. PSMs solve the slowing-down equations for the individual fuel pins. In the case of the 17 × 17 FA problem with

TABLE 5 | Pin power distribution results—PSM and PSM-CPM.

Problem	Description	Pin power difference (%)			
		PSM vs MCS		PSM-CPM vs MCS	
		RMS	Max	RMS	Max
A	No poison	0.116 ± 0.001	0.217 ± 0.001	0.116 ± 0.001	0.217 ± 0.001
B	No poison	0.103 ± 0.001	0.205 ± 0.001	0.103 ± 0.001	0.205 ± 0.001
C	No poison	0.151 ± 0.001	0.345 ± 0.001	0.151 ± 0.001	0.345 ± 0.001
D	No poison	0.127 ± 0.001	0.254 ± 0.001	0.127 ± 0.001	0.254 ± 0.001
E	12 Pyrex	0.109 ± 0.001	0.303 ± 0.001	0.109 ± 0.001	0.303 ± 0.001
F	24 Pyrex	0.126 ± 0.001	0.264 ± 0.001	0.126 ± 0.001	0.264 ± 0.001
G	24 AIC	0.172 ± 0.001	0.357 ± 0.002	0.172 ± 0.001	0.357 ± 0.001
H	24 B4C	0.153 ± 0.001	0.408 ± 0.002	0.153 ± 0.001	0.408 ± 0.001
I	Thimble	0.143 ± 0.001	0.340 ± 0.001	0.143 ± 0.001	0.340 ± 0.001
J	Thimble, 24 Pyrex	0.153 ± 0.001	0.351 ± 0.001	0.153 ± 0.001	0.351 ± 0.001
K	Zoned, 24 Pyrex	0.129 ± 0.001	0.297 ± 0.002	0.129 ± 0.001	0.297 ± 0.002
L	80 IFBA	0.108 ± 0.001	0.317 ± 0.001	0.108 ± 0.001	0.317 ± 0.001
M	128 IFBA	0.140 ± 0.001	0.285 ± 0.002	0.140 ± 0.001	0.285 ± 0.002
N	104 IFBA, 20 WABA	0.154 ± 0.001	0.414 ± 0.002	0.154 ± 0.001	0.414 ± 0.002
O	12 Gadolinia	0.148 ± 0.001	0.370 ± 0.001	0.148 ± 0.001	0.370 ± 0.001
P	24 Gadolinia	0.159 ± 0.001	0.339 ± 0.001	0.159 ± 0.001	0.339 ± 0.001

TABLE 6 | Comparison for elapsed time (unit: s) (Choi, 2017).

Category	EQ	PSM	PSM-CPM
Reading library[a]	0.36	0.37	0.37
MOC FSP solver for fuel[b]	0.36	0.03	0.03
MOC FSP solver for cladding[c]	0.36	0.35	0.36
Interpolation in multigroup XS and RI libraries[d]	0.97	0.15	0.14
Nuclide grouping[e]	—	0.23	0.22
XS condensation[f]			
Slowing-down solver[g]	—	0.42	5.21
Total XS generation[h]	2.25	1.67	6.44
Total simulation	7.78	7.16	11.95

[a]*Elapsed time in reading the XS and RI libraries.*
[b]*Elapsed time in solving the MOC fixed-source problem for the fuel.*
[c]*Elapsed time in solving the MOC fixed-source problem for the cladding.*
[d]*Elapsed time in interpolating the multigroup XS and RI, from the multigroup XS library and the RI library.*
[e]*Elapsed time in calculating the macroscopic pointwise energy XSs of the nuclide groups.*
[f]*Elapsed time in collapsing the pointwise energy XS to the multigroup XSs.*
[g]*Elapsed time in solving the slowing-down equation and calculating the collision probabilities.*
[h]*Total elapsed time in calculating the multigroup XSs.*

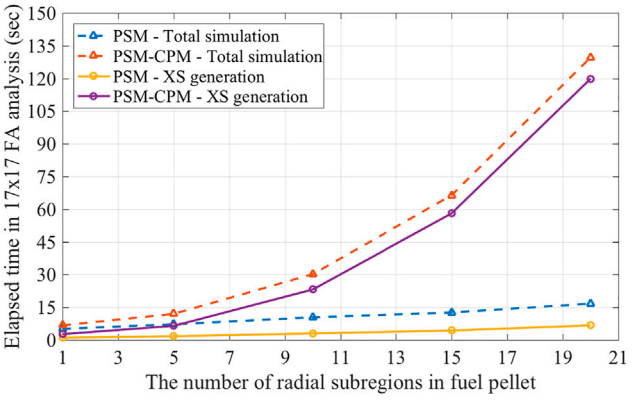

FIGURE 4 | Elapsed time as a function of the number of radial meshes (Choi, 2017).

octant symmetry, the slowing-down equations are solved for 39 fuel pins. Approximately 0.41 s is spent on the pointwise energy slowing-down calculations for all the fuel pins in the problem. PSMs spend additional time on grouping the nuclides and the energy condensations. A non-negligible time is consumed for these calculations, although the calculations are quite simple. Because the pointwise energy XS data are used in PSMs, these calculations are inevitable. The PSM-CPM takes a longer time in the slowing-down solver because it calculates the collision probability with the CPM solver for all energy points. PSMs spend less time in interpolating the RI from the multigroup RI library because they do not use the RI look-up table to calculate the effective XSs of fuel materials.

The same problem was solved with different numbers of the radially subdivided regions in the fuel pellet. **Figure 4** shows the calculation time as a function of the number of the subdivided regions in the fuel pellet. Both PSM and PSM-CPM were tested with different numbers of regions. When the number of radially subdivided regions is small, the differences in the calculation time between PSMs are not noticeable. As the number of the subdivided regions increases, the elapsed time used in the XS generation significantly increases with the PSM-CPM. With the PSM-CPM, the XS generation accounts for a very large portion of the total simulation. However, the elapsed time in the XS generation with the PSM is not very long compared to the total simulation time. The PSM is very effective in reducing the calculation time in the XS generation.

In conclusion, PSMs can calculate the multigroup XS within a reasonable computation time. PSMs save the calculation time by reducing the number of MOC fixed-source calculations. Even though PSMs solve the pointwise energy slowing-down equations, the calculation time is not problematic because various techniques are applied to enhance the performance of PSMs (Choi, 2017). The PSM-CPM takes a longer time in

calculating the multigroup XSs with many subdivided regions in the fuel pellet. Nevertheless, the PSM-CPM is still useful because more than five subdivided regions are hardly used in the practical calculations for UO_2 pin-cells. For a uniform material distribution and temperature profile, PSMs show consistent results. The comparative analysis between PSM and PSM-CPM for a nonuniform material distribution and temperature profile is presented in the accompanying article (Kim et al., 2021).

4 CONCLUSION

The PSM has been refined to exactly consider the collision probability in the subdivided regions of the isolated fuel pellet. The collision probabilities of an isolated pellet with the radial subdivisions are calculated by using the CPM. The PSM calculates the collision probability corresponding to the grid of the total XSs which is assumed to be constant in all the subdivided regions of the fuel pellet before solving the slowing-down equation. Then, the PSM uses a pre-generated look-up table for the collision probability to reduce the calculation time, but it is only valid if the fuel pellet has a uniform material composition and temperature profile in the subdivided regions of the fuel pellet. On the other hand, the PSM-CPM directly calculates the collision probability in the fuel pellet while solving the slowing-down equation so that exact collision probabilities in all the subdivided regions for the isolated fuel pellet are calculated.

The PSM-CPM has been verified with a few types of LWR FA. PSMs generate consistent results for specified problems in this article. The verification calculations showed good agreement in the eigenvalues, with differences of the order of 100 pcm compared to those of the reference solutions. The pin power distributions were also sufficiently accurate. It has also been demonstrated that the computation times using the PSM-CPM are comparable to those with the conventional equivalence theory methods in the practical use. The accompanying article demonstrates more comparative analysis to verify the PSM-CPM for nonuniform material and temperature distributions in the fuel pellet.

DATA AVAILABILITY STATEMENT

The original contributions presented in the study are included in the article/Supplementary Material; further inquiries can be directed to the corresponding author.

AUTHOR CONTRIBUTIONS

SC contributed to the conception and design of the methodology. SC wrote the first draft of the manuscript. SC and WK wrote sections of the manuscript. WK reviewed and edited the manuscript. DL supervised all the activity for the manuscript. All authors contributed to manuscript revision and read and approved the submitted version.

FUNDING

This work was supported by the National Research Foundation of Korea (NRF) grant funded by the government of Korea (MSIT) (No. NRF-2019M2D2A1A03058371). This work was partially supported by Korea Institute of Energy Technology Evaluation and Planning (KETEP) grant funded by the Korea government (MOTIE) (20206510100040).

REFERENCES

Carlvik, I. (1964). *A Method for Calculating Collision Probabilities in General Cylindrical Geometry and Applications to Flux Distributions and Dancoff Factors*. Stockholm (Sweden): Aktiebolaget Atomenergi. A/CONF. 28/P/681.

Choi, S., Khassenov, A., and Lee, D. (2015). Resonance Self-Shielding Method Using Resonance Interference Factor Library for Practical Lattice Physics Computations of LWRs. *J. Nucl. Sci. Technol.* 53, 1142–1154. doi:10.1080/00223131.2015.1095686

Choi, S., Lee, H., Hong, S. G., and Lee, D. (2015). Resonance Self-Shielding Methodology of New Neutron Transport Code Stream. *J. Nucl. Sci. Technol.* 52, 1133–1150. doi:10.1080/00223131.2014.993738

Choi, S., Smith, K., Lee, H. C., and Lee, D. (2015). Impact of Inflow Transport Approximation on Light Water Reactor Analysis. *J. Comput. Phys.* 299, 352–373. doi:10.1016/j.jcp.2015.07.005

Choi, S., Lee, C., and Lee, D. (2017). Resonance Treatment Using Pin-Based Pointwise Energy Slowing-Down Method. *J. Comput. Phys.* 330, 134–155. doi:10.1016/j.jcp.2016.11.007

Choi, S. (2017). *Pin-Based Pointwise Energy Slowing-Down Method for Resonance Self-Shielding Calculation*. Doctoral Thesis. Ulsan National Institute of Science and Technology.

Godfrey, A. T. (2014). *VERA Core Physics Benchmark Progression Problem Specifications*. Oak Ridge National Laboratory, Oak Ridge National Laboratory. CASL-U-2012-0131-004.

Kim, W., Choi, S., and Lee, D. (2021). Refinements of Pin-Based Pointwise Energy Slowing-Down Method for Resonance Self-Shielding Calculation-II: Verifications. *Front. Energy Res.* 9, 765865. doi:10.3389/fenrg.2021.765865

Knott, D., and Yamamoto, A. (2010). "Lattice Physics Computations," in *Handbook of Nuclear Engineering*. Editor D.G. Cacuci (Boston, MA: Springer US), 913–1239. doi:10.1007/978-0-387-98149-9_9

Koike, H., Yamaji, K., Kirimura, K., Sato, D., Matsumoto, H., and Yamamoto, A. (2012). Advanced Resonance Self-Shielding Method for gray Resonance Treatment in Lattice Physics Code GALAXY. *J. Nucl. Sci. Technol.* 49, 725–747. doi:10.1080/00223131.2012.693885

Lee, H., Kim, W., Zhang, P., Lemaire, M., Khassenov, A., Yu, J., et al. (2020). MCS - A Monte Carlo Particle Transport Code for Large-Scale Power Reactor Analysis. *Ann. Nucl. Energ.* 139, 107276. doi:10.1016/j.anucene.2019.107276

Powney, D. J., and Hutton, J. L. (2002). *The Next Generation WIMS Lattice Code : WIMS9*. Seoul, Korea: PHYSOR-2002.

Rhodes, J., Smith, K., and Lee, D. (2006). *CASMO-5 Development and Applications*. Vancouver, BC, Canada: PHYSOR-2006.

Stamm'ler, R. J. J., and Abbate, M. J. (1983). *Methods of Steady-State Reactor Physics in Nuclear Design*. London: Academic Press.

Stoker, C. C., and Weiss, Z. J. (1996). Spatially Dependent Resonance Cross Sections in a Fuel Rod. *Ann. Nucl. Energ.* 23, 765–778. doi:10.1016/0306-4549(95)00074-7

Yamamoto, A., Tabuchi, M., Sugimura, N., Ushio, T., and Mori, M. (2007). Derivation of Optimum Polar Angle Quadrature Set for the Method of

Characteristics Based on Approximation Error for the Bickley Function. *J. Nucl. Sci. Technol.* 44, 129–136. doi:10.1080/18811248.2007.9711266

Yamamoto, A. (2012). Evaluation of Background Cross Section for Heterogeneous and Complicated Geometry by the Enhanced Neutron Current Method. *J. Nucl. Sci. Technol.* 45, 1287–1292. doi:10.1080/18811248.2008.9711916

Zhang, Q., Jiang, R., Zhao, Q., Cao, L., and Wu, H. (2018). Accurate Resonance Absorption Calculation for Fuel Pins with Non-uniform Intra-pellet Temperature Profile Based on ultra-fine-group Slowing-Down Calculations. *Ann. Nucl. Energ.* 120, 392–401. doi:10.1016/j.anucene.2018.06.005

Zhang, Q., Shuai, Q., Zhao, Q., Liang, L., Wu, H., and Cao, L. (2020). Improvements on the Method of Ultra-Fine-Group Slowing-Down Solution Coupled with Method of Characteristics on Irregular Geometries. *Ann. Nucl. Energ.* 136, 1070171. doi:10.1016/j.anucene.2019.107017

Conflict of Interest: The authors declare that the research was conducted in the absence of any commercial or financial relationships that could be construed as a potential conflict of interest.

frontiers in Energy Research

ORIGINAL RESEARCH
published: 22 December 2021
doi: 10.3389/fenrg.2021.777286

Neutronics Perturbation Calculation Method Study of Solid Breeder Tritium Breeding Blanket for TBR Enhancement

Shen Qu[1]*, *Qixiang Cao*[1], *Fengchao Zhao*[1], *Xueren Wang*[1,2], *Xuru Duan*[1] and *Xiaoyu Wang*[1]

[1]Southwestern Institute of Physics, Chengdu, China, [2]Fusion Power System, San Diego, CA, United States

Tritium breeding blanket (TBB) is an essential component in a fusion reactor, which has functions of tritium breeding, energy generation, and neutron shielding. Tritium breeding ratio (TBR) is a key parameter to evaluate whether the TBB could produce enough tritium to achieve the tritium self-sufficiency (TBR >1) for fusion reactor. Current codes or software are hard to meet the requirements of high efficiency, high resolution, and high automation for neutronic optimization of TBB. In this article, the application of the density perturbation calculation on a solid breeder TBB was first performed. Then, the method of the geometry perturbation calculation based on the virtual density theory was studied. Results and comparison analysis indicate that the 1st + 2nd-order neutronic perturbation calculations (including the density perturbation and the geometry perturbation) results are consistent with the transport results under a perturbation of −15% to +15%. It is proven to be valid to use the perturbation calculation for rapid TBR enhancement study of the solid breeder TBB.

Keywords: neutronics, HCCB TBB, TBR, perturbation calculation, virtual density theory

OPEN ACCESS

Edited by:
Tengfei Zhang,
Shanghai Jiao Tong University, China

Reviewed by:
Liangzhi Cao,
Xi'an Jiaotong University, China
Chen Zhao,
Nuclear Power Institute of China (NPIC), China
Shichang Liu,
North China Electric Power University, China

***Correspondence:**
Shen Qu
qushen@swip.ac.cn

Specialty section:
This article was submitted to Nuclear Energy, a section of the journal Frontiers in Energy Research

Received: *15 September 2021*
Accepted: *25 November 2021*
Published: *22 December 2021*

Citation:
Qu S, Cao Q, Zhao F, Wang X, Duan X and Wang X (2021) Neutronics Perturbation Calculation Method Study of Solid Breeder Tritium Breeding Blanket for TBR Enhancement. Front. Energy Res. 9:777286. doi: 10.3389/fenrg.2021.777286

INTRODUCTION

The tritium breeding blanket (TBB) is an essential component to achieve the tritium production, energy generation, and extraction in the fusion reactor. The solid breeder TBB is an important alternative for a demonstration fusion reactor (DEMO) or a fusion power plant. The tritium self-sufficiency is a significant goal, and the tritium breeding ratio (TBR) is a key parameter to evaluate whether the TBB can produce enough tritium to achieve the tritium self-sufficiency for fusion reactor, which could be calculated as follows: (Wan et al., 2017; Zhuang et al., 2019).

$$\mathrm{TBR} = \frac{\iint \left[N_{^6\mathrm{Li}} \sigma_{^6\mathrm{Li}(n,\alpha)} \left(\vec{r}, E\right) + N_{^7\mathrm{Li}} \sigma_{^7\mathrm{Li}(n,\alpha)} \left(\vec{r}, E\right) \right] \cdot \phi\left(\vec{r}, E, t\right) dE d\vec{r}}{S_{plasma}}. \quad (1)$$

N^6_{Li} and N^7_{Li} are the atom densities of 6Li and 7Li separately, σ^6_{Li} and σ^7_{Li} are the cross sections of (n, T) reaction of 6Li and 7Li separately, $\Phi(r, E, t)$ is the neutron flux distribution, S_{plasma} is the generation rate of fusion neutron in plasma. In brief, TBR represents the average atom number of tritium produced in TBB for every fusion neutron consumed.

However, the TBR of the fusion reactor will be impacted by a number of factors, including the geometries (the opening ports to install the corresponding heating and diagnostic equipment [Cao et al., 2021], and a heterogeneous model of the blanket [Qu et al., 2020]), materials (type, density,

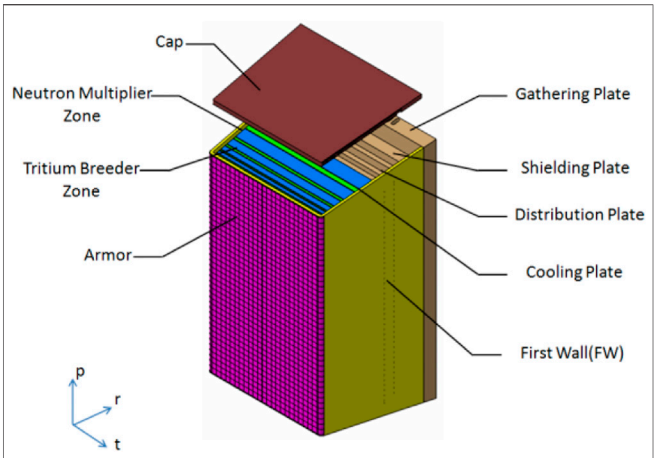

FIGURE 1 | CAD model of the CFETR HCCB blanket typical module.

TABLE 1 | The initial radial dimensions of the blanket module.

Structure	Radial length/cm	Structure	Radial length/cm
FW	2.5	CP-5	1.0
Li_4SiO_4-1	1.7	Be-3	11.0
CP-1	1.0	CP-6	1.0
Be-1	5.0	Li_4SiO_4-4	5.5
CP-2	1.0	CP-7	1.0
Li_4SiO_4-2	2.2	Be-4	6.0
CP-3	1.0	CP-8	1.0
Be-2	8.0	Li_4SiO_4-5	6.0
CP-4	1.0	Manifold	14.0
Li_4SiO_4-3	3.1	Back plate	7.0

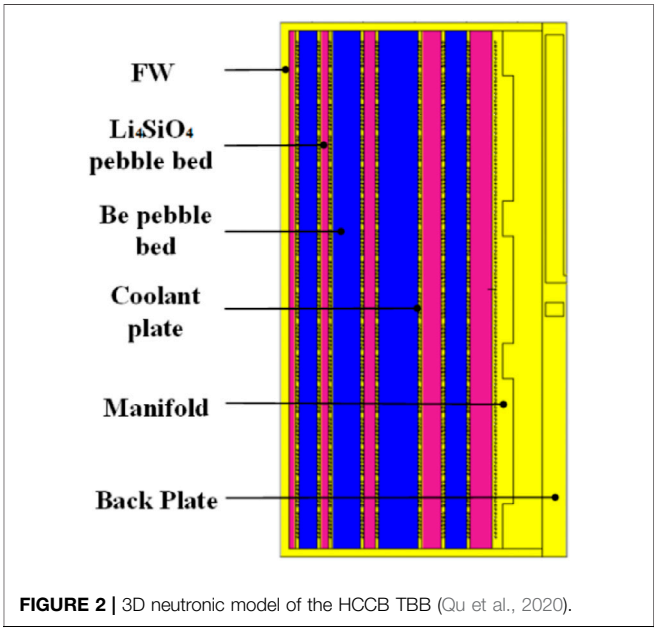

FIGURE 2 | 3D neutronic model of the HCCB TBB (Qu et al., 2020).

enrichment), nuclear libraries (uncertainty), and neutron transport codes (uncertainty). Meanwhile, the tritium losses occur during the fuel cycle because of the tritium decay, leakage, extraction, and retention, which is a considerable challenge to the tritium self-sufficiency. Therefore, a higher TBR is needed. Taking the above facts into account, the TBR design goal of a fusion reactor is set as 1.15 (Fischer et al., 2005).

Consequently, neutronic optimization study toward the solid breeder TBB is imperative in blanket design, which is a process to enhance the TBR (by means of density and geometric adjustments) as much as possible on the basis of engineering feasibilities (Qu et al., 2021). The current neutronic optimization methods are based on multiple neutronic transport calculation. Monte-Carlo codes MCNP-4C based on FENDL-3.2 are selected for the neutronic transport calculation and optimization for the solid breeder TBB (Forster and Godfrey, 1985). However, the following concerns will be arisen:

(1) As for the neutronic optimization for a typical solid breeder TBB module, multiple neutronic transport calculation will lead to a considerable amount of computation and a low efficiency. However, this method could not be adopted for the neutronic optimization for the whole solid breeder TBBs of a fusion reactor. (2) Small density or geometric adjustments will be performed in the neutronic optimization, and there will be an extremely little change for the TBR. This has the same order magnitude with the standard deviation of Monte-Carlo codes. As a response, accurate change results of TBR may not be obtained through multiple neutronic transport calculation.

The above two concerns can be effectively avoided by using the neutronic perturbation calculation instead. The variation of the neutron flux can be obtained by solving the neutronic perturbation equation based on the neutron flux before adjustments in the condition that no significant distortion of the neutron flux distribution occurs. Currently, the perturbation calculation is widely used in the neutronic analysis and design of fission reactors.

In this article, the verification of the density perturbation calculation on the solid breeder TBB was first performed. Then, the method of the geometry perturbation calculation was studied and verified. The work can provide a solid foundation for the rapid neutronic optimization of the solid breeder TBB.

NEUTRONICS MODEL

A helium-cooled ceramic breeder (HCCB) TBB typical module based on the latest design of China Fusion Engineering Test Reactor (CFETR) HCCB blanket (Wang et al., 2019; Qu et al., 2020) (shown as **Figure 1**) was selected for the neutronic analysis and the verification of the density perturbation calculation. The toroidal width and poloidal length of the blanket module are both 120 cm, and the radial thickness is 80 cm (2.5 cm for first wall (FW), 56.5 cm for breeding zone, 14 cm for manifold, and 7 cm for back plate). The tungsten armor with 3 mm in radial before the FW is omitted in this article. The poloidal length of caps is the same as that of the FW thickness.

CLF-1 steel was selected as the structure material, Li_4SiO_4 (the enrichment of 6Li is 90%) as the tritium breeder, and beryllium as the neutron multiplier in the pebble bed regions. The packing

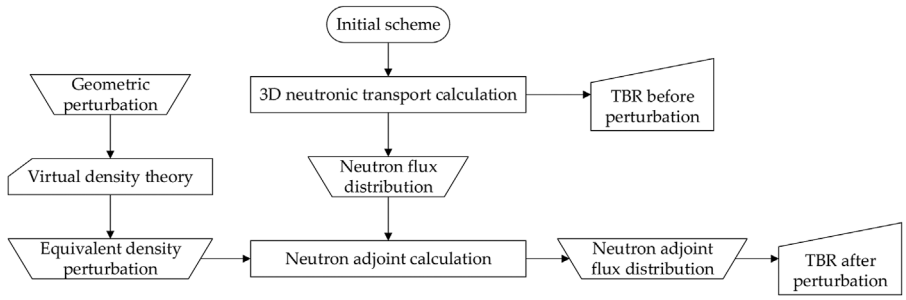

FIGURE 3 | Flowchart of TBR calculation with a geometric perturbation of the solid breeder TBB.

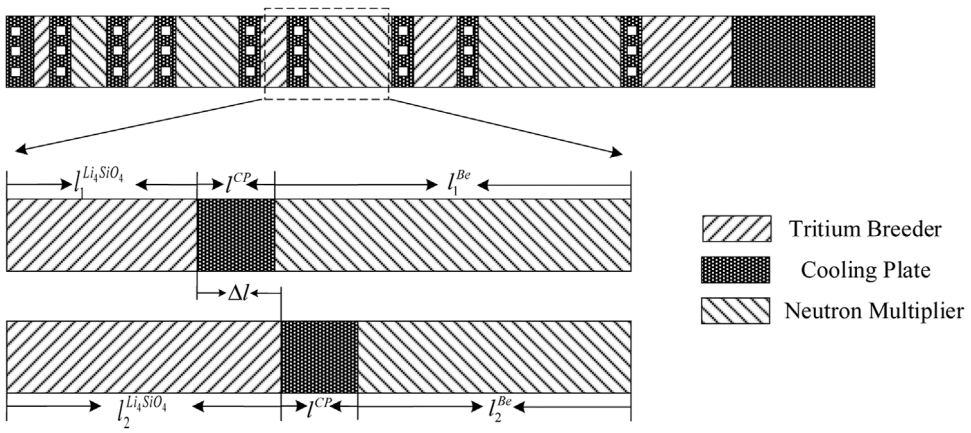

FIGURE 4 | Local layout of the HCCB TBB before **(middle)** and after **(bottom)** the geometry adjustment.

fractions for the Li_4SiO_4 and Be pebble beds were assumed to be 62% and 80%, respectively. The whole breeding zone was divided into nine regions in radial: five regions for the tritium breeding, four regions for the neutron multiplication, and there are eight cooling plates (CPs), which provide cooling function and structural support for the blanket box. The initial radial dimensions of the blanket module are summarized in **Table 1**.

Based on the HCCB CAD model, the homogeneous neutronic model was produced for 3D transport calculation, shown as **Figure 2**. In the homogeneous model, different materials of the breeding blanket were mixed according to their volume fractions in each functional region. Reflecting boundaries were applied, including both the toroidal and poloidal directions. In radial direction, reflecting boundary was also adopted in the surface near plasma, and free boundary was adopted in the outer surface of the back plate. A general neutron source of a Gaussian fusion energy spectrum was added in the front of the FW.

METHODS

Perturbation Theory

The perturbation theory could be adopted for the cases that there is no obvious change of neutron flux distribution for a specific neutronic system before and after a perturbation. Based on the neutron flux distribution before the perturbation, the neutron flux distribution after the perturbation could be obtained by solving the neutron adjoined equation (shown as **Eq. 2**).

$$-\frac{1}{v}\frac{\partial \phi^*}{\partial t} - \Omega \cdot \nabla \phi^* + \Sigma \phi^* - \int_0^\infty dE' \int_{\Omega'} \Sigma_s(r; E, \Omega \rightarrow E', \Omega')\phi^*(r, E', \Omega', t)d\Omega', = \frac{\nu \Sigma_f(r, E)}{4\pi} \int_0^\infty dE' \int_{\Omega'} \chi(E')\phi^*(r', E', \Omega', t)d\Omega'. \quad (2)$$

Φ fnlowast(r, E, t) is the adjoined neutron flux which is the distribution of neutron value.

The perturbation calculation has been widely used in reactor physics calculation for fission reactors, including the core Doppler coefficient calculation, the differential value calculation of control rods, coolant cavitation value calculation, and so on. The type of perturbation includes density perturbation, cross-section perturbation, temperature perturbation, and so on.

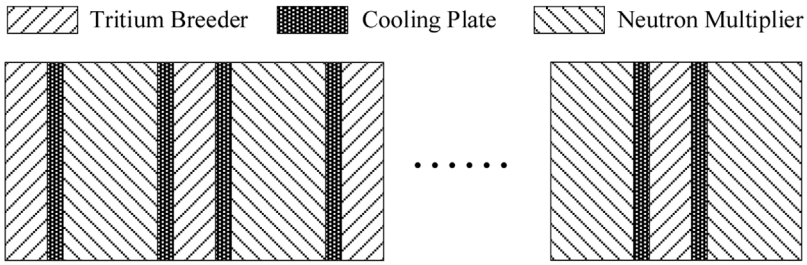

FIGURE 5 | Layout of the HCCB TBB typical module.

TABLE 2 | Details of the three cases for the neutronic perturbation calculation.

Case	Region of perturbation	Material	Type of perturbation
1	Tritium breeding region	Li_4SiO_4	Density
2	Neutron multiplier region	Be	Density
3	Cooling plates region	CLF-1	Density

The perturbation theory could also be put to use for the rapid calculation of neutron flux distribution of the solid breeder TBB of fusion reactors. As for a density perturbation, the TBR could be rapidly calculated through **Eq. 1** based on the perturbation calculation. As for a geometric perturbation, the TBR could be rapidly calculated through the following flowchart (shown as **Figure 3**).

Virtual Density Theory

The density perturbation calculation for the change of the TBR on the TBB was verified. Comprehensively, the study for the geometry perturbation calculation for the change of the TBR on the TBB based on the virtual density theory could be performed (Hess et al., 1998).

According to the expression for isotropic deformation calculation based on the virtual density theory, the equivalent coefficient can be calculated as follows:

$$\varepsilon = \frac{N_2 - N_1}{N_1} = \frac{\kappa_d \kappa_l N_1 - N_1}{N_1} = \kappa_d \kappa_l - 1. \tag{3}$$

ε is the equivalent coefficient of a specific kind of material that indicates the rate of change of atom density (shown as the following formula); N_1 is the atom density before the deformation, and N_2 is the equivalent atom density; κ_d is the density change coefficient; κ_l is the linear scale change coefficient; δ_N and δ_ρ are the variation of the atom density and mass density of the specific material, separately.

$$\varepsilon = \frac{\delta N}{N} = \frac{\delta \rho}{\rho}. \tag{4}$$

According to the isotropic expansion case of a sphere, the density change coefficient and the linear scale change coefficient are expressed as follows:

$$\kappa_d = \frac{1}{f^3}. \tag{5}$$

$$\kappa_l = f, \tag{6}$$

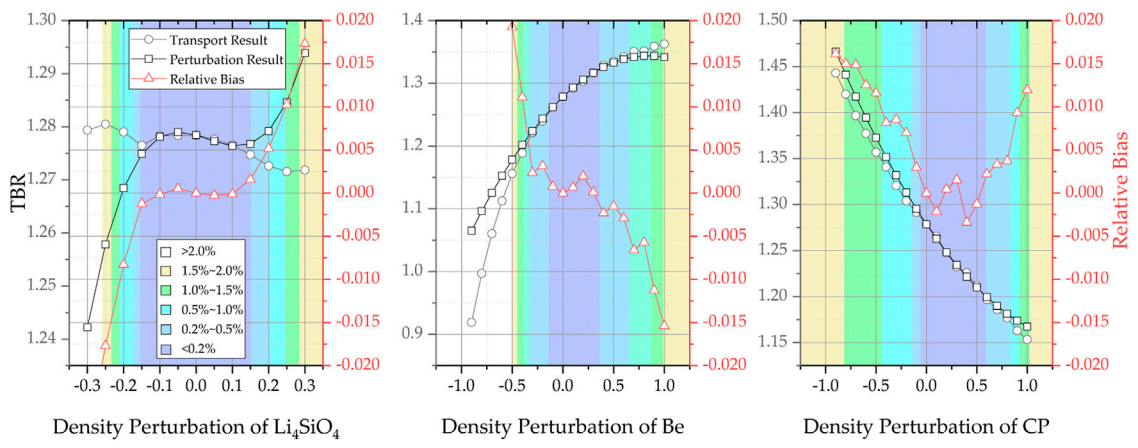

FIGURE 6 | Curves of the TBR versus the density perturbation of the HCCB TBB under each case.

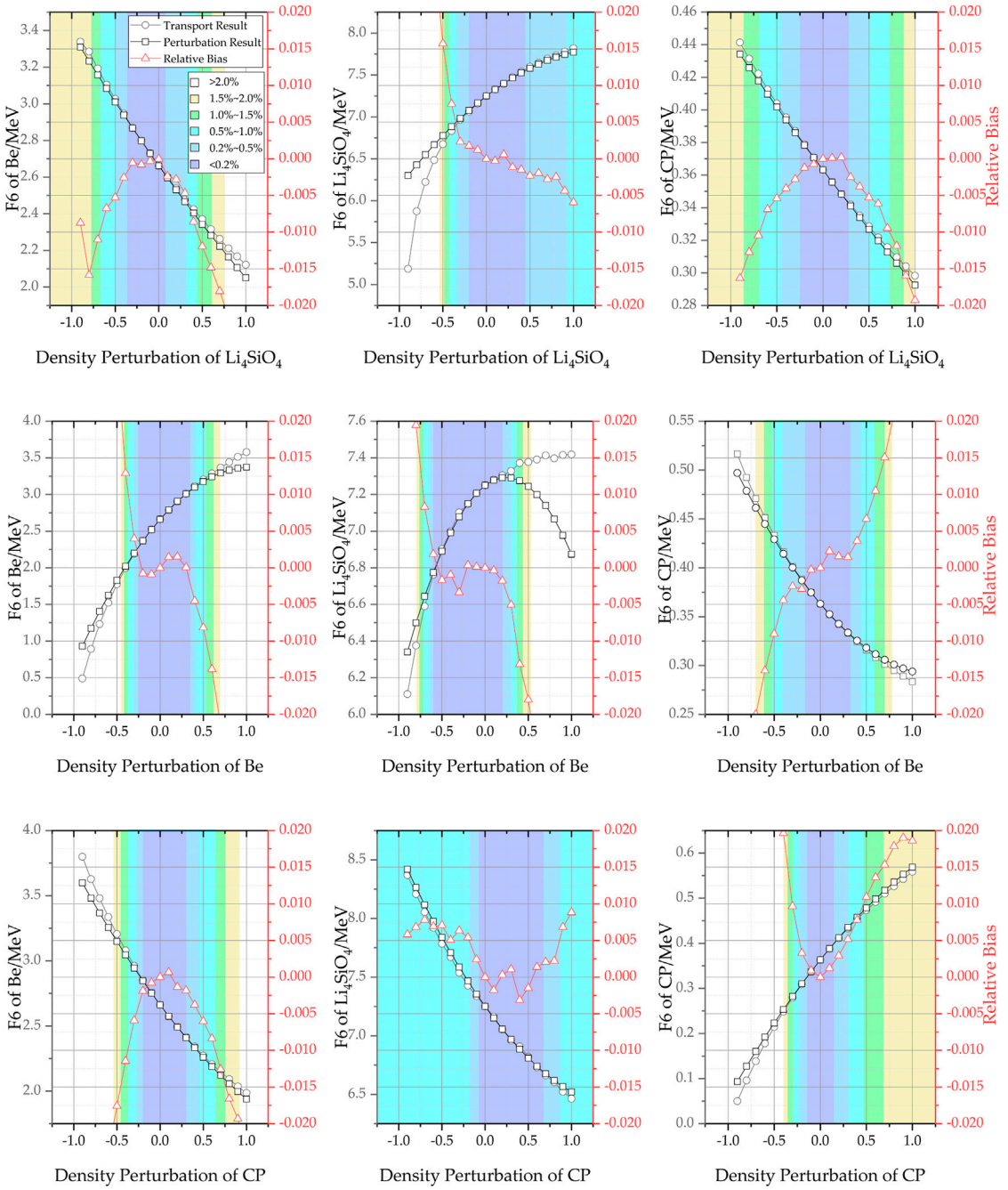

FIGURE 7 | Curves of the F6 versus the density perturbation of the HCCB TBB under each case.

f is the change coefficient of radium. If $f = 1.01$, the radium will be increased by 1%. Thus, the equivalent coefficient of an isotropic expansion case can be calculated as follows:

$$\varepsilon = \kappa_d \kappa_l - 1 = \frac{1}{f^2} - 1. \tag{7}$$

As for the geometry adjustment (radial expansion or compression of each tritium breeder region or the neutron multiplier region for the HCCB TBB) of the TBB for the neutronic optimization, it is not an isotropic deformation case but an anisotropic deformation one.

In this article, the CFETR HCCB TBB typical module with a sandwich-like breeder zone was also selected for the geometry perturbation method study. According to **Figure 1**, both the tritium breeder regions and neutron multiplier regions are rectangular solids, which can be described with the radial thickness, toroidal width, and poloidal length. The toroidal

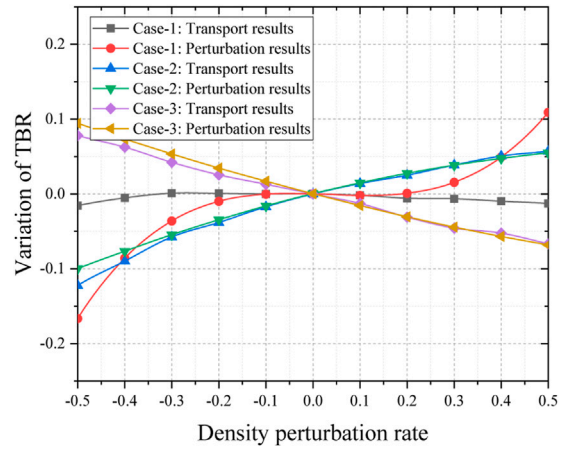

FIGURE 8 | Curves of variation of TBR versus the density perturbation rate under each case.

width and poloidal length keep as constant during the neutronic optimization and the geometry adjustment for the neutronic optimization can be regarded as the radial expansion or compression case. In this case, there will be a change for the radial thickness ($\kappa_d = f$) and the density change ($\kappa_l = 1/f$) in a specific region, so the radial equivalent coefficient can be calculated as follows:

$$\varepsilon_r = \frac{f}{f} - 1 = 0. \tag{8}$$

Meanwhile, there is no change in the toroidal width and the poloidal length ($d_o = 1$) and a reduction in the density ($\kappa_l = 1/f$); consequently, the toroidal and poloidal equivalent coefficient can be calculated as follows:

$$\varepsilon_t = \varepsilon_p = \frac{1}{f} - 1. \tag{9}$$

Figure 4 shows the local layout of the HCCB TBB before and after the geometric adjustment. The local layout model consists of the tritium breeder regions, CPs, and neutron multiplier regions. The total radial thickness of the local layout model is assumed to be constant during the geometry adjustment. According to the local layout, l^{CP} is the radial thickness of the CP, which is also be assumed to be a constant during the neutronic optimization. $l_1^{Li4SiO4}$ and $l_2^{Li4SiO4}$ are the radial thickness of the tritium breeder region before and after the geometry adjustment, separately, and Δl is the increment of the tritium breeding region. Correspondingly, l_1^{Be} and l_2^{Be} are the radial thickness of the neutron multiplier region before and after the geometry adjustment, separately, and Δl is the decrement of the Be region. $\rho_1^{Li4SiO4}$ and ρ_1^{Be} are the densities of the tritium breeder region and the neutron multiplier region before the geometry adjustment separately, and $\rho_2^{Li4SiO4}$ and ρ_2^{Be} are the densities of the tritium breeder region and the neutron multiplier region after the geometry adjustment. The equivalent coefficients of the tritium breeder region and the neutron multiplier region can be calculated as follows:

$$\varepsilon^{Li_4SiO_4} = \frac{1}{f} - 1 = \frac{-\Delta l}{l_1^{Li_4SiO_4} + \Delta l}, \tag{10}$$

$$\varepsilon^{Be} = \frac{1}{f} - 1 = \frac{\Delta l}{l_1^{Be} - \Delta l}. \tag{11}$$

The equivalent density change of these two regions can be calculated as follows:

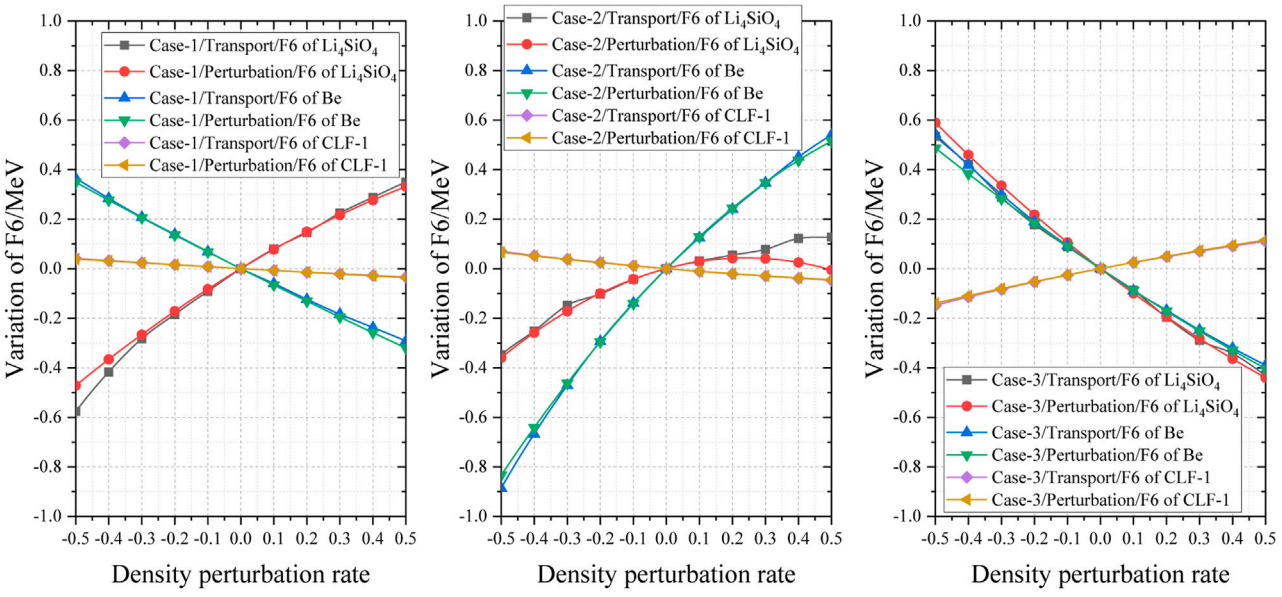

FIGURE 9 | Curves of the variation of F6 versus the density perturbation rate under each case.

TABLE 3 | Radial geometry adjustment of each region of the HCCB TBB typical module for each case.

Case	Radial adjustment of each tritium breeder/cm					Radial adjustment of each neutron multiplier/cm			
	Li-1	Li-2	Li-3	Li-4	Li-5	Be-1	Be-2	Be-3	Be-4
0	0.0	0.0	0.0	0.0	0.0	0.0	0.0	0.0	0.0
1	+0.05	+0.05	+0.05	+0.05	+0.05	−0.05	−0.05	−0.05	−0.10
2	+0.10	+0.10	+0.10	+0.10	+0.10	−0.10	−0.10	−0.10	−0.20
3	+0.15	+0.15	+0.15	+0.15	+0.15	−0.15	−0.15	−0.15	−0.30
4	+0.20	+0.20	+0.20	+0.20	+0.20	−0.20	−0.20	−0.20	−0.40
5	+0.25	+0.25	+0.25	+0.25	+0.25	−0.25	−0.25	−0.25	−0.50

TABLE 4 | Equivalent mass densities of each region under each case.

Case	Equivalent mass densities of each tritium breeder region and neutron multiplier region/g·cm^{-3}								
	Li-1	Li-2	Li-3	Li-4	Li-5	Be-1	Be-2	Be-3	Be-4
0	1.361	1.361	1.361	1.361	1.361	1.472	1.472	1.472	1.472
1	1.322	1.331	1.339	1.349	1.350	1.487	1.481	1.479	1.497
2	1.285	1.302	1.318	1.337	1.339	1.502	1.491	1.486	1.523
3	1.251	1.274	1.298	1.325	1.328	1.518	1.500	1.492	1.549
4	1.218	1.247	1.278	1.313	1.317	1.533	1.510	1.499	1.577
5	1.186	1.222	1.259	1.302	1.306	1.549	1.519	1.506	1.606

TABLE 5 | Variation of the neutron flux of each tritium breeding region calculated by each method of each case.

Case	Method A (ref)					Method B									
	Neutron flux/10^{12} n · cm^{-2} · s^{-1}					Neutron flux/10^{12} n · cm^{-2} · s^{-1}					Relative deviation/%				
	Li-1	Li-2	Li-3	Li-4	Li-5	Li-1	Li-2	Li-3	Li-4	Li-5	Li-1	Li-2	Li-3	Li-4	Li-5
1	597	355	139	31.2	9.82	601	358	141	31.3	9.81	0.67	0.84	1.42	0.32	−0.10
2	593	351	138	31	9.83	598	356	140	31.1	9.79	0.84	1.40	1.43	0.32	−0.41
3	587	350	138	30.7	9.97	593	354	140	30.8	9.91	1.01	1.13	1.43	0.32	−0.61
4	583	348	137	30.6	10	590	352	138	30.8	10.05	1.19	1.14	0.72	0.65	0.50
5	579	346	136	30.6	10	589	351	138	30.7	9.97	1.70	1.42	1.45	0.33	−0.30

$$\delta\rho^{\mathrm{Li_4SiO_4}} = \frac{-\Delta l \cdot \rho_1^{\mathrm{Li_4SiO_4}}}{l_1^{\mathrm{Li_4SiO_4}} + \Delta l} = \frac{-\Delta l \cdot \rho_1^{\mathrm{Li_4SiO_4}}}{l_2^{\mathrm{Li_4SiO_4}}}, \tag{12}$$

$$\delta\rho^{Be} = \frac{\Delta l \cdot \rho_1^{Be}}{l_1^{Be} - \Delta l} = \frac{\Delta l \cdot \rho_1^{Be}}{l_2^{Be}}. \tag{13}$$

$\varepsilon^{\mathrm{Li4SiO4}}$ and $\varepsilon^{\mathrm{Be}}$ are the equivalent coefficients of the tritium breeder region and the neutron multiplier region, respectively. $\delta\rho^{\mathrm{Li4SiO4}}$ and $\delta\rho^{\mathrm{Be}}$ are the equivalent density change of the tritium breeder region and the neutron multiplier, individually.

Then, the conclusions are made from the local layout model to the HCCB TBB typical model, which can be shown as **Figure 5**.

In the HCCB TBB typical module with the sandwich-like breeder zone, there are m tritium breeder regions, n neutron multiplier regions, and k CPs ($k = m + n - 1$). Before the geometry adjustment, the radial thickness and the density of each tritium breeder region are expressed by l_i^{Li4SiO4} and $\rho_i^{\mathrm{Li4SiO4}}$ ($i = 1,2 \ldots m$), respectively. The radial thickness and the density of each neutron multiplier region are defined as l_j^{Be} and ρ_j^{Be} ($j = 1,2 \ldots n$), separately. After the geometry adjustment, the change of the radial thickness and the change of the density of each tritium breeder region are $\Delta l_i^{\mathrm{Li4SiO4}}$ and $\Delta\rho_i^{\mathrm{Li4SiO4}}$ ($i = 1,2 \ldots m$), individually. The change of the radial thickness and the change of the density of each neutron multiplier region are Δl_j^{Be} and $\Delta\rho_j^{\mathrm{Be}}$ ($j = 1,2 \ldots n$). The total radial thickness of the breeder zone of the TBB remains unchanged (shown as the following equation).

$$\sum_{i=1}^{m} \Delta l_i^{Li_4SiO_4} + \sum_{j=1}^{n} \Delta l_j^{Be} = 0. \tag{14}$$

Based on the conclusions above, the equivalent coefficients and equivalent change of the density of each tritium breeder region and neutron multiplier region can be calculated as follows:

$$\varepsilon_i^{Li_4SiO_4} = \frac{-\Delta l_i^{Li_4SiO_4}}{l_i^{Li_4SiO_4} + \Delta l_i^{Li_4SiO_4}} \ (i = 1, 2 \cdots m), \tag{15}$$

TABLE 6 | Variation of the neutron flux of each neutron multiplier region calculated by each method of each case.

Case	Method A (ref)				Method B							
	Neutron flux/10^{12} n · cm^{-2} · s^{-1}				Neutron flux/10^{12} n · cm^{-2} · s^{-1}				Relative deviation/%			
	Be-1	Be-2	Be-3	Be-4	Be-1	Be-2	Be-3	Be-4	Be-1	Be-2	Be-3	Be-4
1	540	312	117	23.8	544	313	118	23.6	0.74	0.32	0.85	−0.84
2	535	311	116	23.6	540	314	117	23.6	0.93	0.96	0.86	0.00
3	530	310	116	23.5	535	312	118	23.5	0.94	0.65	1.72	0.00
4	526	306	114	23.4	531	309	115	23.5	0.95	0.98	0.88	0.43
5	523	306	114	23.4	530	309	115	23.4	1.34	0.98	0.88	0.00

TABLE 7 | Variation of the TBR calculated by each method of each case.

Case	Method A	Method B		Method C	
	TBR (references)	TBR	Relative deviation/%	TBR	Relative deviation/%
1	1.3166	1.3181	0.11	1.3182	0.12
2	1.3152	1.3177	0.19	1.3178	0.20
3	1.3144	1.3182	0.29	1.3185	0.31
4	1.3104	1.3158	0.41	1.3157	0.40
5	1.3102	1.3169	0.51	1.317	0.52

$$\varepsilon_j^{Be} = \frac{-\Delta l_j^{Be}}{l_j^{Be} + \Delta l_j^{Be}} \ (j = 1, 2 \cdots n). \tag{16}$$

$$\delta\rho_i^{Li_4SiO_4} = \frac{-\Delta l_i^{Li_4SiO_4} \cdot \rho_i^{Li_4SiO_4}}{l_i^{Li_4SiO_4} + \Delta l_i^{Li_4SiO_4}} \ (i = 1, 2 \cdots m), \tag{17}$$

$$\delta\rho_j^{Be} = \frac{-\Delta l_j^{Be} \cdot \rho_j^{Be}}{l_j^{Be} + \Delta l_j^{Be}} \ (j = 1, 2 \cdots n). \tag{18}$$

VERIFICATION

Density Perturbation

The neutronic perturbation calculation for the change of the TBR and nuclear heat of each part on the TBB of three cases was performed, and the details of the three cases are listed in **Table 2** (Mckinney and Iverson, 1996; Schnabel et al., 2021). Ten percent is selected for the interval of density perturbation (5% is selected for the TBR comparison under case 1).

Two kinds of the results were calculated for comparison: the transport results, and the 1st + 2nd order of the neutronic perturbation results. The TBR comparison of the HCCB TBB of cases 1, 2, and 3 are shown as **Figure 6**. The nuclear heat comparison (F6 tally results are compared) is shown as **Figure 7**. The curve of relative bias is also shown in each figure (in red). Regions of each relative bias band are marked with different colors. The variation of TBR and F6 calculated by transport code and perturbation method under each case is shown as **Figure 8** and **Figure 9** individually. The MC transport results were regarded as the reference. In this article, 1E7 particles are simulated, and some variance reduction techniques (such as weight windows, forced collision, energy splitting, and roulette) are used in the MCNP-4C calculation. In this way, the Monte-Carlo relative deviation could reduce to ~0.01%. Therefore, the change of TBB neutronics performances were large enough (an order of magnitude larger) compared with the standard deviation of MCNP-4C code, and the perturbation problem could be verified using the MC method.

Analysis toward the above results indicates that the 1st + 2nd order of the neutronic perturbation calculation results (including TBR and nuclear heat) is consistent with the transport results under a density perturbation of -15% to +15% under each case (with a relative bias <0.2%). Meanwhile, the neutronic perturbation calculation is much faster than the transport calculation (the efficiency could be improved by more than 100 times in conservative estimating). Therefore, the perturbation calculation can be a substitute for the transport calculation, which will be a better choice for the rapid neutronic optimization for the TBB.

Geometric Perturbation

The CFETR HCCB TBB typical module was chosen for the verification of the geometry perturbation calculation. Geometry adjustments toward the CFETR HCCB TBB of five cases were performed, and the radial adjustment of each region of the HCCB TBB typical module of each case are listed in **Table 3**. Case 0 is the initial scheme of the CFETR HCCB TBB, which the radial lengths of each region can be found in **Table 1**. The maximum geometry adjustment of all regions is less than 15% (case 5 in Li-1 region). According to the virtual density theory, the equivalent mass densities of each tritium breeder region and neutron multiplier region can be summarized in **Table 4**.

Three methods (methods A, B, and C) were used for the neutronic calculation for the HCCB TBB. The model with the geometry adjustment (shown in **Table 3**) of each case was

adopted, and 3D neutronic transport calculation was performed in method A; 3D neutronic transport calculation based on the model with the equivalent density adjustment (shown in **Table 4**) of each case was made in method B; 3D neutronic transport calculation of the initial scheme was performed, and perturbation calculation (the 1st + 2nd order) based on the virtual density theory of each case was made in model C. The neutron flux of each region calculated by methods A and B is listed and compared in **Table 5** (the tritium breeding region) and **Table 6** (the neutron multiplier region), separately. According to the design parameters of CFETR phase II, a fusion power of 1.5 GW was assumed, based on which a neutron wall load of 1.69 MW/m^2 was adopted in the calculations for a single TBB module (Cao et al., 2021). The TBRs calculated by using the three methods are listed in **Table 7**. The MCNP-4C code was adopted for the 3D neutronic and perturbation calculation based on FENDL-3.2. All the results calculated by method A are regarded as the references. The analysis and conclusions can be portrayed as follows:

(1) Relative deviations that the neutron flux of each region and the TBR are listed in **Tables 5**, **6**, **7**, separately for using methods A and B generally showing an increasing trend as the radial geometry variation of each region goes up.
(2) The closer the specific region is to plasma, the larger the relative deviation of the neutron flux is.
(3) The maximum relative deviation of the neutron flux is less than 1.5% in the vast majority of cases.
(4) The maximum relative deviation of the TBR between methods A and B is less than or equal to 0.51%. However, the deviation is no more than 0.2% in the case that the perturbation rate is less than 15%, which showed a good coincidence with the transport results and fully met the requirements for TBB neutronics optimization. The TBR calculated by method C is almost identical to that obtained by method B, but it is much faster in terms of efficiency.

Therefore, the geometry perturbation calculation can be adopted for the solid breeder TBB of the fusion reactor for the rapid neutronic optimization based on the virtual density theory.

CONCLUSION

In this article, the verification of the density perturbation calculation on the solid TBB was first performed. Then, method of the geometry perturbation calculation based on the virtual density theory was studied. Results indicate that the neutronic perturbation calculation, including the density perturbation and the geometry perturbation, has been proven to be valid for the rapid TBR enhancement of the solid TBB.

The Monte Carlo transport calculation results in this article could meet the requirements of neutronics optimization of TBB, and a detailed test of the effects of perturbation calculations by deterministic calculations will be mentioned in a future study (Zheng et al., 2017; Wang, 2019).

DATA AVAILABILITY STATEMENT

The original contributions presented in the study are included in the article/supplementary material, further inquiries can be directed to the corresponding author.

AUTHOR CONTRIBUTIONS

SQ: Methodology, Software, Writing—original draft. QC: Visualization, Validation. FZ: Validation. XD: Supervision. XRW: Supervision. XYW: Writing—Reviewing and Editing.

FUNDING

The work at Southwestern Institute of Physics (SWIP) is supported by the National Natural Science Foundation of China Number 11905046, China ITER HCCB TBS project Number CGB-TBM-HCCB, National Key R&D Program of China Number 2017YFE0300601 and Talent Project of SWIP Number 202001XWCXRC013.

ACKNOWLEDGMENTS

Acknowledge to the KIT (Karlsruhe Institute of Technology) for the development of McCAD code.

REFERENCES

Cao, Q., Wang, X., Wu, X., Yin, M., Qu, S., Zhao, F., et al. (2021). Neutronics And Shielding Design Of Cfetr Hccb Blanket. *Fusion Eng. Des.* 172 (3), 112918. doi:10.1016/j.fusengdes.2021.112918

Fischer, U., Pereslavtsev, P., and Hermsmeyer, S. (2005). Neutronic Design Optimisation of Modular HCPB Blankets for Fusion Power Reactors. *Fusion Eng. Des.* 75-79 (0), 751–757. doi:10.1016/j.fusengdes.2005.06.222

Forster, R. A., and Godfrey, T. N. K., 1985 "MCNP- A General Monte-Carlo Code for Neutrons and Photon Transport." In Proceedings of the Joint Los Alamos National Laboratory. 240 33–55. April 1985.France.

Hess, A. K., Mckinney, G. W., Hendricks, J. S., and Carter, L. L.. (1998). *Verification of the MCNP (TM) Perturbation Correction Feature for Cross-Section Dependent Tallies[J]*. Office of Scientific & Technical Information Technical Reports. United states. doi:10.2172/1197

Mckinney, G. W., and Iverson, J. L. (1996). *Verification of the MCNP{trademark Perturbation Technique*[J]. office of scientific & technical information technical reportsUnited states. doi:10.2172/221051

Qu, S., Cao, Q., Duan, X., Wang, X., Li, Z., and Wang, X. (2020). Neutronics Effects of Homogeneous Model on Solid Breeder Blanket of CFETR. *Fusion Eng. Des.* 160, 111825. doi:10.1016/j.fusengdes.2020.111825

Qu, S., Cao, Q., Duan, X., Wang, X., and Wang, X. (2021). Study on Multiphysics Coupling and Automatic Neutronic Optimization for Solid Tritium Breeding

Blanket of Fusion Reactor. *Energies* 14 (17), 5442, 2021 . Sep. 2021. doi:10.3390/en14175442

Schnabel, G., Capote, R., and Trkov, A. (2021). Fusion Evaluated Nuclear Data Library-FENDL-3.2. Available at: https://www-nds.iaea.org/fendl/.

Wan, Y. X., Li, J. G., Liu, Y., Wang, X., Chan, V., and Chen, C. (2017). Overview of the Present Progress and Activities on the CFETR. *Nucl. Fusion* 57, 10. doi:10.1088/1741-4326/aa686a

Wang, X. Y. (2019). *Development Status of Helium Cooled Ceramic Breeder Tritium Breeding Blanket (HCCB TBB) in China [R]*. Budapest Hungary.

Wang, X. Y., Feng, K. M., Chen, Y. J., Zhang, L., Feng, Y., and Wu, X. H. (2019). Current Design And R&D Progress Of Cn Hccb Tbs. " *Nucl. Fusion*. 59(7). 10. 1088/1741-4326/ab0c32.

Zheng, Y., Xiao, Y., and Wu, H., (2017). Application of the Virtual Density Theory in Fast Reactor Analysis Based on the Neutron Transport Calculation. *Nucl. Eng. Des.* 320, 200–206. doi:10.1016/j.nucengdes.2017.05.020

Zhuang, G., Li, G. Q., Li, J. G., Wan, Y. X., Liu, Y., and Wang, X. (2019). Progress of the CFETR Design. " *Nucl. Fusion*. 59(11) 112010. 10.1088/1741-4326/ab0e27.

Conflict of Interest: The authors declare that the research was conducted in the absence of any commercial or financial relationships that could be construed as a potential conflict of interest.

Publisher's Note: All claims expressed in this article are solely those of the authors and do not necessarily represent those of their affiliated organizations, or those of the publisher, the editors and the reviewers. Any product that may be evaluated in this article, or claim that may be made by its manufacturer, is not guaranteed or endorsed by the publisher.

frontiers in Energy Research

ORIGINAL RESEARCH
published: 23 December 2021
doi: 10.3389/fenrg.2021.773255

ACCRUE—An Integral Index for Measuring Experimental Relevance in Support of Neutronic Model Validation

Jeongwon Seo[1]*, *Hany S. Abdel-Khalik*[1] and *Aaron S. Epiney*[2]

[1]School of Nuclear Engineering, Purdue University, West Lafayette, IN, United States, [2]Idaho National Laboratory, Idaho Falls, ID, United States

A key challenge for the introduction of any design changes, e.g., advanced fuel concepts, first-of-a-kind nuclear reactor designs, etc., is the cost of the associated experiments, which are required by law to validate the use of computer models for the various stages, starting from conceptual design, to deployment, licensing, operation, and safety. To achieve that, a criterion is needed to decide on whether a given experiment, past or planned, is relevant to the application of interest. This allows the analyst to select the best experiments for the given application leading to the highest measures of confidence for the computer model predictions. The state-of-the-art methods rely on the concept of similarity or representativity, which is a linear Gaussian-based inner-product metric measuring the angle—as weighted by a prior model parameters covariance matrix—between two gradients, one representing the application and the other a single validation experiment. This manuscript emphasizes the concept of experimental relevance which extends the basic similarity index to account for the value accrued from past experiments and the associated experimental uncertainties, both currently missing from the extant similarity methods. Accounting for multiple experiments is key to the overall experimental cost reduction by prescreening for redundant information from multiple equally-relevant experiments as measured by the basic similarity index. Accounting for experimental uncertainties is also important as it allows one to select between two different experimental setups, thus providing for a quantitative basis for sensor selection and optimization. The proposed metric is denoted by ACCRUE, short for Accumulative Correlation Coefficient for Relevance of Uncertainties in Experimental validation. Using a number of criticality experiments for highly enriched fast metal systems and low enriched thermal compound systems with accident tolerant fuel concept, the manuscript will compare the performance of the ACCRUE and basic similarity indices for prioritizing the relevance of a group of experiments to the given application.

Keywords: similarity index, generalized linear least squares, model validation, criticality safety, correlation coefficient

OPEN ACCESS

Edited by:
Tengfei Zhang,
Shanghai Jiao Tong University, China

Reviewed by:
Qian Zhang,
Harbin Engineering University, China
Tomasz Kozlowski,
University of Illinois at Urbana-Champaign, United States
Chenghui Wan,
Xi'an Jiaotong University, China

***Correspondence:**
Jeongwon Seo
seo71@purdue.edu

Specialty section:
This article was submitted to Nuclear Energy, a section of the journal Frontiers in Energy Research

Received: *09 September 2021*
Accepted: *25 November 2021*
Published: *23 December 2021*

Citation:
Seo J, Abdel-Khalik HS and Epiney AS (2021) ACCRUE—An Integral Index for Measuring Experimental Relevance in Support of Neutronic Model Validation. Front. Energy Res. 9:773255. doi: 10.3389/fenrg.2021.773255

1 INTRODUCTION

Model validation is one of the key regulatory requirements to develop a scientifically-defendable process in support of establishing confidence in the results of computerized physics models for the various developmental stages starting from conceptual design to deployment, licensing, operation, and safety. To ensure that model predictions can be trusted for a given application, e.g., the domain envisaged for code usage, the regulatory process requires the consolidation of two independent sources of knowledge, one from measurements collected from experimental conditions that are similar to the application, and the other from code predictions that model the same experimental conditions. For criticality safety applications, representing the focus of this manuscript, model validation plays a critical role in supporting design changes, e.g., the introduction of high burnup fuel, high assay low enrichment fuel, etc., or new fuel designs, e.g., accident tolerant fuel, both typically challenged by the scarcity of experimental data.

It is thus paramount to devise a methodology that can consolidate knowledge from both the experimental and computational domains in some optimal manner. The optimality of this consolidation process needs to recognize the possible scarcity of relevant experimental data expected with new designs, the cost for constructing new validation experiments, and the infeasibility of duplicating of all application conditions in the experimental domain. Ideally, the consolidation methodology should be able to optimally leverage existing experimental data in order to minimize the need for new experiments.

In our context, model validation entails a mapping process in which the experimental biases (differences between measurements and model predictions) are to be mapped to the application's responses of interest in the form of calculational (i.e., best-estimate) biases along with their uncertainties. The goal is to improve the analyst's confidence in the calculated application response. Mathematically, the confidence is measured in terms of the response uncertainty. The initial uncertainty propagated throughout the model is referred to as the prior uncertainty which accounts for parameter uncertainties, modeling assumptions, numerical approximations, initial, and boundary conditions, etc. The consolidation of experimental biases with the prior uncertainties results in a calculational bias that is intended to correct for the prior uncertainties. A successful consolidation process would result in a reduced bias uncertainty, i.e., as compared to the prior uncertainty, implying increased confidence in the calculated response.

The prior uncertainties are often grouped into two categories, aleatory, and epistemic. This manuscript will focus on epistemic uncertainties resulting from the lack of knowledge of the true values of the nuclear cross-section data. The implied assumption here is that cross-sections constitute the major source of uncertainty in neutronic calculations (Glaeser, 2008; Avramova and Ivanov, 2010; Abdel-Khalik et al., 2013; Wieselquist, 2016). Specifically, we focus on a single consolidation methodology for reducing the impact of epistemic uncertainties, the so-called generalized linear least-squares (GLLS) methodology which may be derived using Bayesian estimation theory (Williams et al., 2016). It is designed to calculate an optimal bias for any calculated response based on an optimal adjustment of the nuclear cross-sections.

In the neutronic community, the GLLS methodology has been independently developed by various researchers (Gandini, 1967; Salvatores, 1973; Broadhead et al., 2004; Cacuci and Ionescu-Bujor, 2010) with varying levels of generalization and mathematical formulation, e.g., Gaussianity assumption of the uncertainty source, degree of nonlinearity of the response variations with cross-sections, mathematical formulation in the cross-section space or the response space, etc. Under the same set of assumptions however, one can show the equivalence of these various formulations. For example, for Gaussian prior cross-section uncertainties and assumed linear approximations, the noted GLLS optimality criterion reduces to an L_2 minimization of the sum of two terms, see **Eq. 4**. The first term minimizes the L_2 norm of the adjustments of the cross-sections to ensure their consistency with their prior values, and the second term minimizes the discrepancy between the measurements and predictions for the selected experimental responses. The GLLS methodology is briefly discussed in **Section 2**.

A prerequisite for the GLLS methodology is to select the experiments that are most relevant to the application conditions[1]. The premise is that with higher relevance biases with higher confidence, i.e., reduced uncertainties, can be calculated. In the neutronic community, sensitivity methods have been adopted to determine experimental relevance using a scalar quantity, denoted by the similarity index c_k (Broadhead et al., 2004)—also called representativity factor by other researchers (Palmiotti and Salvatores, 2012)—which can be used to prioritize/rank the experiments and possibly judge the value of a new experiment before it is constructed.

To measure the similarity index c_k, sensitivity methods are first employed to calculate the first-order variations in select quantities of interest that can be experimentally measured, e.g., critical eigenvalue, reaction rate ratios, etc., with respect to the cross-section variations by isotope, reaction type, and incident neutron energy. This is done with both the experimental models as well as the application model of interest, e.g., calculating the criticality conditions for a new fuel design, resulting in one sensitivity vector per model. The sensitivity vector comprises the first-order derivatives, i.e., sensitivity coefficients, of a given response with respect to all cross-sections. Next, the sensitivity vector of the experiment is folded with that of the application and the prior cross-section covariance matrix to calculate the similarity index.

The result of this folding process, see **Eq. 5**, is an integral quantity (c_k) taken to measure the degree of similarity between the first order derivatives of a single quantity of interest with respect to all cross-sections as calculated from both the

[1]In theory the GLLS can incorporate any experimental data regardless of their relevance to the application conditions. In practice however, one limits the analysis to the most relevant experiments for various practical considerations. For example, inclusion of many weakly-relevant experiments may adversely impact the χ^2 value making it difficult to interpret the GLLS results.

experiment and the application models[2]. The prior uncertainties are used as weighting parameters, assigning more weight to cross-sections with higher uncertainties. The resulting similarity index c_k is thus expected to be heavily influenced by cross-sections exhibiting both high prior uncertainties as well as strong sensitivities. This helps the GLLS methodology find the optimal adjustments for cross-sections with strong sensitivities as well as high uncertainties. This is justified as follows: cross-sections with weak sensitivities would require large adjustments to change the response, potentially rendering them statistically inconsistent with their prior values. Similarly, adjusting low-uncertainty cross-sections would violate their prior values, also considered a form of fudging that cannot be mathematically justified as it violates the basic assumption of the GLLS methodology, that is the observed discrepancies are mainly originating from the prior cross-section uncertainties.

The resulting similarity index c_k is a scalar quantity which lies between −1.0 and 1.0 and may be interpreted as follows: a zero value implies no correlations, i.e., cross-sections with strong sensitivities and high uncertainties, exist between the application, and the experimental conditions. This implies that experimental bias cannot be used to infer the application bias, i.e., it cannot be used to improve the prior estimate of the application response and hence the experiment is judged to have no value to the given application. Conversely, a high similarity value, i.e., close to 1.0, implies that the associated experimental bias can be reliably used to infer the application bias. More important, the bias uncertainty can be reduced with highly relevant experiments. Theoretically, the inclusion of a zero-similarity experiment would keep the prior uncertainty for the application unchanged—not increasing the confidence—while a perfectly similar experiment, e.g., c_k = 1.0, would result in the minimum bias uncertainty, i.e., the maximum attainable confidence[3].

One key limitation of the similarity index is that it does not account for the impact of measurement uncertainties. Essentially, the c_k value is obtained by normalizing the covariance matrix for the calculated responses. This further implies that the measurements uncertainties have no impact on the c_k value calculation. To explain this, consider two experiments with analogous similarity as measured by the c_k value but with different measurement uncertainties. The experiment with the lower uncertainty would result in the calculation of lower bias uncertainty, i.e., more confidence. This implies that an experiment with a lower c_k value and a low measurement uncertainty could result in a lower bias uncertainty than that obtained from an experiment with higher c_k value and higher measurement uncertainty. Thus, it is important to include the measurement uncertainty in the definition of relevance. This brings value to the design of future experiments, often involving an optimization of sensors' types and placements. Inclusion of measurement uncertainty would allow the analyst to compare the value of different experiments (and sensors selection) prior to the conduction of the experiment.

Another limitation of the similarity index is that it does not consider the impact of past experiments. As the c_k value is calculated by normalizing the weighted inner product of two sensitivity vectors, with more experiments involved in the relevance evaluation process, the c_k value cannot be employed to capture a weighted relevance between two subspaces. To explain this, consider that the analyst has calculated the application bias using ideal conditions, i.e., with a highly relevant experiment and near zero measurement uncertainty. In this scenario, the inclusion of additional experiments, even if highly relevant, is unlikely to lead to further noticeable reduction in the bias uncertainty. Thus, two experiments with the same c_k value should be assigned different relevance depending on which experiment is employed first. This provides a lot of value when designing new experiments by quantifying the maximum possible increase in confidence while accounting for past experiments. Addressing these two limitations will help analysts determine the minimum number of experiments required to meet a preset level of increased confidence as well as compare the value of planned experiments, providing a quantitative approach for their optimization.

In response to these limitations, this manuscript employs the concept of experimental relevance as opposed to similarity in order to distinguish between the possible added value of a new experiment, if any, and the value available from past experiments. This is possible by extending the definition of the c_k similarity index[4] *via* a new analytical expression for experimental relevance, denoted by the ACCRUE index, designed to account for the experiment's measurement uncertainty and the prior confidence associated with past experiments. The symbol j_k is used to distinguish the ACCRUE index from the similarity index c_k, where the j denotes the ability to jointly assess the relevance of an experiment with past experiments. The ACCRUE index is short for Accumulated Correlation Coefficient for Relevance of Uncertainties in Experimental validation.

The TSURFER code, representing the GLLS rendition under the ORNL's SCALE code suite, is employed to exemplify the application of the ACCRUE index j_k. Specifically, we develop three sorting methods for the available experiments based respectively on the similarity index c_k, the ACCRUE index j_k, and pure random sampling. Two different sets of experiments are employed to compare the performance of the various sorting methods. The first set involves low-enriched uranium thermal compound systems with the accident-tolerant fuel (ATF) concept BWR assembly, and the second comprises highly enriched uranium fast metal systems. Finally, numerical experiments will be employed to verify the analytically-calculated values for j_k.

[2]Other empirical forms for the similarity index have been proposed, but are not covered here. (Broadhead et al., 2004). Examples include the use of the absolute difference in the sensitivity coefficients, D, and the inner products of two sensitivity profiles, E, etc.

[3]In this hypothetical scenario, the minimum uncertainty would be controlled by the measurement uncertainty and other administrative uncertainties that are typically added for unaccounted sources of uncertainties.

[4]The development here will be limited to the GLLS methodology; it is thus implicitly assumed that the GLLS assumptions are satisfied, i.e., Gaussianity of the cross-section prior uncertainty and linearity of the response variation with cross-section perturbations.

This manuscript is organized as follows. **Section 2** provides a background on sensitivity theory and the details of mathematical description of the GLLS nuclear data adjustment methodology. **Section 3** introduces ACCRUE algorithm and an extension of the non-intrusive stochastic verification with mathematical details. **Section 4** verifies the performance of the proposed algorithm by numerical experiments to compare the results made by one of the conventional integral similarity indices, c_k, and the ACCRUE index, j_k. Concluding remarks and further research are summarized in **Section 5**.

2 BACKGROUND AND RELEVANCE

This section presents a brief background on three key topics: 1) sensitivity methods employed for the calculation of first-order derivatives; 2) the GLLS adjustment theory, employed to calculate the application bias; and 3) the extant similarity index c_k definition. The material in this section may be found in the literature, however compiled here to help set the stage for the proposed ACCRUE index.

2.1 Sensitivity Theory

Sensitivity coefficients are the key ingredients for the GLLS methodology, as they are used to relate the response variations to the model parameter variations, with the latter assumed to represent the dominant sources of uncertainties. A sensitivity coefficient measures the first-order variation of a response that is caused by a change in one input model parameter. For the numerical experiments employed in this paper, we focus on the multiplication factor, k_{eff}, i.e., critical eigenvalue, as the response of interest and the reaction-wise cross-sections by isotope and energy group as the model parameters.

While sensitivity coefficients can be readily evaluated using finite differencing, the adjoint-based perturbation theory methodology (Usachev, 1964; Gandini, 1967; Stacey, 1974; Oblow, 1976; Cacuci and Ionescu-Bujor, 2010) has been adopted as the most efficient way to calculate derivatives. This follows because adjoint-based sensitivity theory requires one adjoint solution per response, implying that one can calculate the first-order derivatives of the given response with respect to all cross-sections using a single adjoint model evaluation, whereas finite differencing requires an additional forward model evaluation for each cross-section. The general idea behind adjoint-based sensitivity analysis is summarized below for the evaluation of the first order derivatives of the critical eigenvalue.

The Boltzmann transport equation for an assembly containing fissionable material, referred to as the forward model, can be symbolically expressed as (Williams, Broadhead and Parks, 2001):

$$\left(\boldsymbol{M}(\alpha) - \frac{1}{k}\boldsymbol{F}(\alpha)\right)\psi = 0 \tag{1}$$

where

$\boldsymbol{M}(\alpha)$ = Multigroup form of the Boltzmann loss operator.

$\boldsymbol{F}(\alpha)$ = Multigroup form of the Boltzmann production operator.

$\psi = \psi(r, \Omega, g)$ = Multigroup angular flux. where ψ is a function of

r = position.

Ω = neutron moving direction.

g = energy group.

The two operators $\boldsymbol{M}(\alpha)$ and $\boldsymbol{F}(\alpha)$ are functions of the reference multi-group cross-section data which may be described by an n-dimensional vector, $\alpha = [\,\alpha_1 \quad \alpha_2 \quad \cdots \quad \alpha_n\,]^T$ whose n components are the reaction-wise cross-sections by energy-group and isotope[5]. Thus, the solution of this equation yielding the eigenvalue may be compactly written as follows:

$$k_j = f_j(\alpha)$$

where k_j is the code-predicted eigenvalue[6], i.e., k_{eff}, of jth critical experiment model and f_j is a compact representation of the solution of **Eq. 1** implying its dependence on α. Analytically, the first-order derivatives of k_{eff} with respect to each cross-section can be expressed in a relative sense—referred to as the sensitivity coefficients—using a first-order Taylor series expansion:

$$S_{k_j,\alpha_i} = \frac{\alpha_i}{k_j}\frac{f_j(\alpha_1, \ldots, \alpha_i + \Delta\alpha_i, \ldots, \alpha_n) - f_j(\alpha_1, \ldots, \alpha_i, \ldots, \alpha_n)}{\Delta\alpha_i} \tag{2}$$

and aggregated in a vector (referred to as the sensitivity vector or profile) with the superscript "T" representing vector/matrix transpose:

$$s_j = \left[\, S_{k_j,\alpha_1} \quad S_{k_j,\alpha_2} \quad \cdots \quad S_{k_j,\alpha_n} \,\right]^T$$

Eq. 2 implies that a finite-difference-based sensitivity analysis would require $n+1$ forward model executions, one with the reference cross-section values, and one additional execution per cross-section. For most practical neutronic problems, this is computationally infeasible because cross-sections often number in the 10^4 to 10^5 range.

The adjoint formulation of sensitivity coefficients may be described by the following equation:

$$S_{k_j\alpha_i} = \frac{\alpha_i}{k_j}\frac{\left\langle \psi^* \dfrac{\partial}{\partial\alpha_i}\left(\dfrac{1}{k}\boldsymbol{F} - \boldsymbol{M}\right)\psi \right\rangle}{\langle \psi^* \boldsymbol{F}\psi \rangle} \tag{3}$$

The brackets represent an inner product operation corresponding to an integration over entire phase-space (e.g., energy groups, direction of neutron travel, and space) using the forward solution obtained from **Eq. 1** and a new quantity, called the adjoint solution, obtained from:

[5]Other dependencies for the two operators, such as geometry, composition, etc., are suppressed in the current discussion, since GLLS focuses only on the epistemic uncertainties associated with nuclear cross-sections.

[6]The subscript j (denoting the jth experiment) will be suppressed for other quantities in **Eqs. 2**, **3** to reduce notational clutter, and because they do not contribute to the discussion.

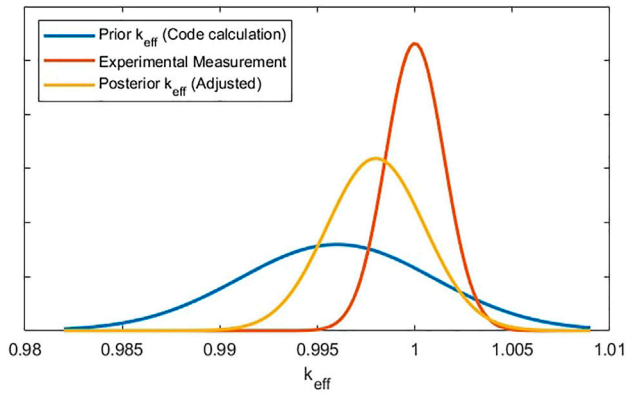

FIGURE 1 | k_{eff} consolidated confidence from experiment and prior calculations.

$$\left(\boldsymbol{M}^{*}-\frac{1}{k}\boldsymbol{F}^{*}\right)\psi^{*}=0$$

where $\boldsymbol{M}^{*}$ and $\boldsymbol{F}^{*}$ are the adjoint operators of the forward operators $\boldsymbol{M}$ and $\boldsymbol{F}$, evaluated at the reference cross-section values. The $\frac{\partial}{\partial\alpha_i}$ term differentiates the operators $\boldsymbol{M}$ and $\boldsymbol{F}$ with respect to the ith cross-section, with the derivative taken around the reference cross-section values. Since the mathematical expressions for $\boldsymbol{M}$ and $\boldsymbol{F}$ are known, these changes can be analytically calculated. More importantly, they do not require re-execution of the forward or the adjoint model. The implication is that one can evaluate the derivatives with respect to all cross-sections using a single forward and a single adjoint model evaluation.

Several computer codes have embodied the adjoint methodology to calculate sensitivity coefficients (Lucius et al., 1981; Becker et al., 1982; Gerald; Rimpault et al., 2002). Of interest to us is the SCALE TSUNAMI methodology (Rearden and Jessee, 2016) which is used as a basis for the evaluation of the sensitivity coefficients for the GLLS-based TSURFER code, discussed in the next section.

2.2 GLLS Adjustment Methodology

As discussed earlier, the main goal of GLLS is to consolidate knowledge from computations and experiments. This is illustrated in **Figure 1** using two representative PDFs describing the best available knowledge about the k_{eff} from the experiments (shown in red) and model predictions (blue). The spread of each PDF is taken as a measure of confidence. The confidence in the model predictions is determined by the propagated prior uncertainties, and the experiment's confidence is tied to its measurement uncertainties. The GLLS methodology represents a disciplined mathematical approach to consolidate these two PDFs into one (yellow) that provides higher confidence for the calculated response as compared to the prior confidence from model predictions.

To achieve that, GLLS assumes that the uncertainties originate from the cross-sections. Therefore, it attempts to identify the optimal cross-section adjustments which minimize the discrepancies between measured and predicted responses. Based on the optimal adjustments, one can calculate the corresponding change in the application's response, with the application representing the conditions for which no experimental values exist. The change in the code-calculated application response, i.e., from its prior value, is denoted by the application bias.

Considering that the analyst is interested in calculating the bias for the k_{eff} value for a given application, and there exist M available experiments, the corresponding prior values may be aggregated in a vector $k \in \mathbb{R}^{M+1}$ such that:

$$k = [k_1 \;\; k_2 \;\; \cdots \;\; k_{M+1}]^T$$

where the last component is the prior value for the application k_{eff}. The corresponding measurements for the first M values are designated by another vector $m \in \mathbb{R}^{M+1}$. In this formulation, the last element of m is set to the prior value of k_{eff}, assumed to have no corresponding experimental value.

The prior cross-section uncertainties are described by a multi-variable Gaussian PDF with a vector of means representing the reference multi-group cross-sections and a covariance matrix given by:

$$\boldsymbol{C}_{\alpha\alpha}=\begin{bmatrix} cov(\alpha_1,\alpha_1) & cov(\alpha_1,\alpha_2) & \cdots & cov(\alpha_1,\alpha_n) \\ cov(\alpha_2,\alpha_1) & cov(\alpha_2,\alpha_2) & \cdots & cov(\alpha_2,\alpha_n) \\ \vdots & \vdots & \ddots & \vdots \\ cov(\alpha_n,\alpha_1) & cov(\alpha_n,\alpha_2) & \cdots & cov(\alpha_n,\alpha_n) \end{bmatrix} \in \mathbb{R}^{n\times n}$$

The adjusted cross-sections are calculated as the minimizer of the following minimization problem subject to the constraint $k'(\alpha') = m'$:

$$\alpha^{*}=\underset{\alpha'}{\operatorname{argmin}}\left[\alpha'-\alpha\right]^{T}\boldsymbol{C}_{\alpha\alpha}^{-1}\left[\alpha'-\alpha\right]+\left[m'-m\right]^{T}\boldsymbol{C}_{mm}^{-1}\left[m'-m\right] \tag{4}$$

where $\boldsymbol{C}_{mm} \in \mathbb{R}^{(M+1)\times(M+1)}$ is the covariance matrix for the measured k_{eff}. The constraint implies that the adjusted cross-sections α' will update the best-estimated values (the components of m') for all M experiments as well as the application. The last element of the vector m' is taken to represent the best-estimate for the application k_{eff} value, and the last component of $m' - m$ is referred to as the application bias. Note that $k_j - m_j$ represents the initial discrepancy between the prior code-calculated and measured k_{eff} values for the jth experiment, and $m' - m$ represents the discrepancy after the cross-sections are adjusted.

The objective function in **Eq. 4** may be re-written in terms of the calculated and adjusted k_{eff} values as:

$$\chi_M^2=\left[k'-k\right]^{T}\boldsymbol{C}_{kk}^{-1}\left[k'-k\right]+\left[m'-m\right]^{T}\boldsymbol{C}_{mm}^{-1}\left[m'-m\right]$$

where χ_M^2 is the M -degrees of freedom chi-square value describing the discrepancies between the prior and adjusted k_{eff} values. The $\boldsymbol{C}_{kk} \in \mathbb{R}^{(M+1)\times(M+1)}$ matrix denotes the prior covariance matrix for the calculated k_{eff} values given by:

$$\boldsymbol{C}_{kk}=\boldsymbol{S}_{k\alpha}\boldsymbol{C}_{\alpha\alpha}\boldsymbol{S}_{k\alpha}^{T} \tag{5}$$

and $\boldsymbol{S}_{k\alpha} \in \mathbb{R}^{(M+1)\times n}$ matrix aggregates the sensitivity profiles for all M experiments and the application:

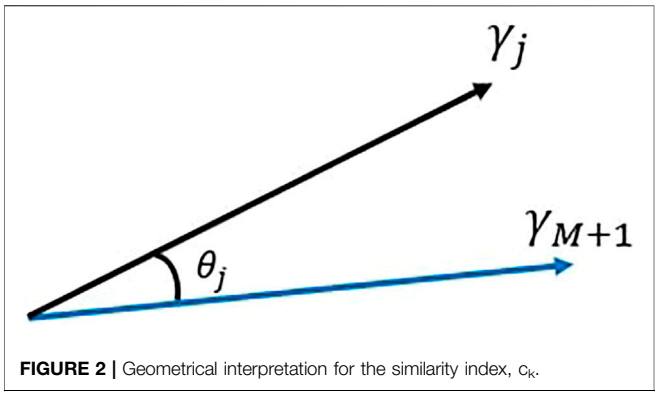

FIGURE 2 | Geometrical interpretation for the similarity index, c_k.

$$\boldsymbol{S_{k\alpha}} = \begin{bmatrix} S_{1,1} & S_{1,2} & \cdots & S_{1,i} & \cdots & S_{1,n} \\ S_{2,1} & S_{2,2} & \cdots & S_{2,i} & \cdots & S_{2,n} \\ \vdots & \vdots & \ddots & \vdots & \vdots & \vdots \\ S_{j,1} & S_{j,2} & \cdots & S_{j,i} & \cdots & S_{j,n} \\ \vdots & \vdots & \cdots & \vdots & \ddots & \vdots \\ S_{M,1} & S_{M,2} & \cdots & S_{M,i} & \cdots & S_{M,n} \\ S_{M+1,1} & S_{M+1,2} & \cdots & S_{M+1,i} & \cdots & S_{M+1,n} \end{bmatrix}$$

where (j, i) element represents the relative sensitivity coefficient of the jth experiment [or application, $(M + 1)$th row] with respect to the ith multi-group cross-section.

Assuming that the linearization of the constraint $k'(\alpha') = m'$ is sufficiently accurate within the limitations of first-order sensitivity theory, the minimizer of the objective function in **Eq. 4** may be given by:

$$\Delta k = -\boldsymbol{C_{kk}}\left(\boldsymbol{C_{kk}} + \boldsymbol{C_{mm}}\right)^{-1} d$$

where $\Delta k = k' - k$ and $d \in \mathbb{R}^{M+1}$ is the discrepancy vector, $d = k - m$

The posterior (i.e., post the consolidation of experimental and prior values) covariance matrix for the k_{eff} values is given by:

$$\boldsymbol{C_{k'k'}} = \boldsymbol{C_{kk}} - \boldsymbol{C_{kk}}\left(\boldsymbol{C_{kk}} + \boldsymbol{C_{mm}}\right)^{-1}\boldsymbol{C_{kk}} \tag{6}$$

The diagonal elements of this matrix describe the confidence one has in the posterior k_{eff} values. The $(M + 1)$th diagonal element of the $\boldsymbol{C_{kk}}$ matrix ($\boldsymbol{C_{kk}}[M + 1, M + 1]$) measures the prior confidence one has in the calculated application k_{eff} value. If the experiments are relevant to the application, the posterior confidence, ($\boldsymbol{C_{k'k'}}[M + 1, M + 1]$) should provide higher confidence, i.e., $\boldsymbol{C_{k'k'}}[M + 1, M + 1] < \boldsymbol{C_{kk}}[M + 1, M + 1]$.

2.3 Similarity Index, c_k

The definition of the similarity index c_k naturally appears in the GLLS formulation of the prior covariance matrix. Specifically, one can expand **Eq. 5** as follows:

$$\boldsymbol{C_{kk}} = \begin{bmatrix} s_1^T\boldsymbol{C_{\alpha\alpha}}s_1 & s_1^T\boldsymbol{C_{\alpha\alpha}}s_2 & \cdots & s_1^T\boldsymbol{C_{\alpha\alpha}}s_{M+1} \\ s_2^T\boldsymbol{C_{\alpha\alpha}}s_2 & s_2^T\boldsymbol{C_{\alpha\alpha}}s_2 & \cdots & s_2^T\boldsymbol{C_{\alpha\alpha}}s_{M+1} \\ \vdots & \vdots & \ddots & \vdots \\ s_{M+1}^T\boldsymbol{C_{\alpha\alpha}}s_1 & s_{M+1}^T\boldsymbol{C_{\alpha\alpha}}s_2 & \cdots & s_{M+1}^T\boldsymbol{C_{\alpha\alpha}}s_{M+1} \end{bmatrix} \tag{7}$$

The diagonal entries of this matrix represent the uncertainty (in the units of variance) of the prior k_{eff} values and the off-diagonal entries are the correlations between these uncertainties. Ideally, one would want to maximize the correlations between the application and all experiments, described by the last row or last column of the matrix. A standardized form of this matrix may be obtained by multiplying it from both sides by the inverse of the square root of its diagonal elements to produce the matrix $\boldsymbol{R} \in \mathbb{R}^{(M+1)\times(M+1)}$:

$$\boldsymbol{R} = \begin{bmatrix} 1 & \frac{s_1^T\boldsymbol{C_{\alpha\alpha}}s_2}{\sqrt{s_1^T\boldsymbol{C_{\alpha\alpha}}s_1}\sqrt{s_2^T\boldsymbol{C_{\alpha\alpha}}s_2}} & \cdots & \frac{s_1^T\boldsymbol{C_{\alpha\alpha}}s_{M+1}}{\sqrt{s_1^T\boldsymbol{C_{\alpha\alpha}}s_1}\sqrt{s_{M+1}^T\boldsymbol{C_{\alpha\alpha}}s_{M+1}}} \\ \frac{s_2^T\boldsymbol{C_{\alpha\alpha}}s_1}{\sqrt{s_2^T\boldsymbol{C_{\alpha\alpha}}s_2}\sqrt{s_1^T\boldsymbol{C_{\alpha\alpha}}s_1}} & 1 & \cdots & \frac{s_2^T\boldsymbol{C_{\alpha\alpha}}s_{M+1}}{\sqrt{s_2^T\boldsymbol{C_{\alpha\alpha}}s_2}\sqrt{s_{M+1}^T\boldsymbol{C_{\alpha\alpha}}s_{M+1}}} \\ \vdots & \vdots & \ddots & \vdots \\ \frac{s_{M+1}^T\boldsymbol{C_{\alpha\alpha}}s_1}{\sqrt{s_{M+1}^T\boldsymbol{C_{\alpha\alpha}}s_{M+1}}\sqrt{s_1^T\boldsymbol{C_{\alpha\alpha}}s_1}} & \frac{s_{M+1}^T\boldsymbol{C_{\alpha\alpha}}s_2}{\sqrt{s_{M+1}^T\boldsymbol{C_{\alpha\alpha}}s_{M+1}}\sqrt{s_2^T\boldsymbol{C_{\alpha\alpha}}s_2}} & \cdots & 1 \end{bmatrix}$$

In this representation, the value of any off-diagonal terms is standardized between −1.0 and 1.0 which is equivalent to the definition of the standard correlation coefficient between two random variables. Appearing naturally in the GLLS formulation, these off-diagonal terms have been adopted as to measure experimental relevance. Specifically, the similarity index c_k between the application and the jth experiment is given by:

$$c_k\left(k_j, k_{M+1}\right) = \frac{s_j^T\boldsymbol{C_{\alpha\alpha}}s_{M+1}}{\sqrt{s_j^T\boldsymbol{C_{\alpha\alpha}}s_j}\sqrt{s_{M+1}^T\boldsymbol{C_{\alpha\alpha}}s_{M+1}}} \tag{8}$$

This equation may be used to pre-calculate the similarities of all available experiments with respect to the given application. To achieve that one needs to calculate the corresponding sensitivity profiles for the experiments and the application which are readily calculated using the adjoint sensitivity theory presented in **Section 2.1**. In our work, the SCALE TSUNAMI code is employed to calculate the sensitivity profiles as well as the similarity indices.

Next, it is instructive to give a geometric interpretation of the similarity index. To do that, rewrite the expressions in **Eq. 8** using the Cholesky decomposition of $\boldsymbol{C_{kk}}$ as:

$$\boldsymbol{C_{kk}} = \boldsymbol{\Gamma}^T\boldsymbol{\Gamma}$$

where $\boldsymbol{\Gamma} = [\,\gamma_1 \quad \gamma_2 \quad \cdots \quad \gamma_{M+1}\,]$, where the inner-product of any of two columns of $\boldsymbol{\Gamma}$ gives:

$$\gamma_i^T\gamma_j = \boldsymbol{C_{kk}}[i, j],\ i, j = 1, 2, \ldots,\ M + 1$$

Performing this transformation for both the numerator and denominator in **Eq. 8**, the c_k index reduces to:

$$\begin{aligned} c_k\left(k_j, k_{M+1}\right) &= \frac{\gamma_j^T\gamma_{M+1}}{\sqrt{\gamma_j^T\gamma_j}\sqrt{\gamma_{M+1}^T\gamma_{M+1}}} \\ &= \frac{\boldsymbol{C_{kk}}[j, M+1]}{\sqrt{\boldsymbol{C_{kk}}[j, j]}\sqrt{\boldsymbol{C_{kk}}[M+1, M+1]}} = \cos\theta\left(\gamma_j, \gamma_{M+1}\right) \end{aligned} \tag{9}$$

As illustrated in **Figure 2**, this expression is interpreted as cosine angle between two vectors, one related to the application and the other to an experiment.

Further, it has been shown in earlier research (Huang et al., 2020) that one can calculate c_k using randomized forward model evaluations taking advantage of the equivalence between the c_k definition and the standard correlation coefficient. This requires sampling of the cross-sections within their prior uncertainties a few hundred times to obtain sufficiently approximate estimates of the similarity index, as shown below. As demonstrated in earlier work using the Sampler code under the SCALE environment (Wieselquist, 2016), this forward-based approach provides two advantages; first, it allows one to calculate similarity indices when the adjoint solver is not available; and second, it provides a way to verify the results of adjoint-based calculations.

It has been shown in earlier work that these two vectors may be interpreted as the directional sensitivity profiles with respect to the dominant eigen directions of the prior covariance matrix. To illustrate the mechanics of the forward-based approach for calculating the similarity index, first consider re-writing the cross-section covariance matrix decomposed by Cholesky methodology as follows:

$$\boldsymbol{C}_{\alpha\alpha} = \boldsymbol{U}\boldsymbol{\Lambda}^2\boldsymbol{U}^T \tag{10}$$

where $\boldsymbol{U} \in \mathbb{R}^{n\times n}$ a unitary matrix; $\boldsymbol{U}^T\boldsymbol{U} = \boldsymbol{U}\boldsymbol{U}^T = \boldsymbol{I}$ and $\boldsymbol{\Lambda} \in \mathbb{R}^{n\times n}$ is a diagonal matrix whose elements are square root of the singular values of $\boldsymbol{C}_{\alpha\alpha}$.

If $\xi^{(p)} \in \mathbb{R}^n$ is a Gaussian variable, one can generate N random samples for the cross-sections which respect their covariance structure, such that:

$$\Delta\alpha^{(p)} = \boldsymbol{U}\boldsymbol{\Lambda}\xi^{(p)},\ p = 1, 2, \ldots, N$$

By the law of large numbers, one can show that as N increases (Stark and Woods, 2012)

$$\lim_{N\to\infty}\left(\frac{1}{N}\sum_{p=1}^{N}\xi^{(p)}\xi^{(p)^T}\right) = \boldsymbol{I}$$

This limit is readily reached with a few hundred samples. Verification with numerical experiments is provided in the following section.

Then, **Eq. 10** can be re-written by the cross-section samples, such as:

$$\begin{aligned}\boldsymbol{C}_{\alpha\alpha} &= \lim_{N\to\infty}\boldsymbol{U}\boldsymbol{\Lambda}\left(\frac{1}{N}\sum_{p=1}^{N}\xi^{(p)}\xi^{(p)^T}\right)\boldsymbol{\Lambda}^T\boldsymbol{U}^T\\ &= \lim_{N\to\infty}\left(\frac{1}{N}\sum_{p=1}^{N}\Delta\alpha^{(p)}\Delta\alpha^{(p)^T}\right)\end{aligned}$$

With the linearity assumption valid, e.g., $\boldsymbol{S}_{k\alpha}\Delta\alpha^{(p)} = \Delta k^{(p)}$, samples for the code-calculated responses also can be calculated by the sandwich rule in **Eq. 5**, and thus the covariance matrix for calculated responses can be re-written as:

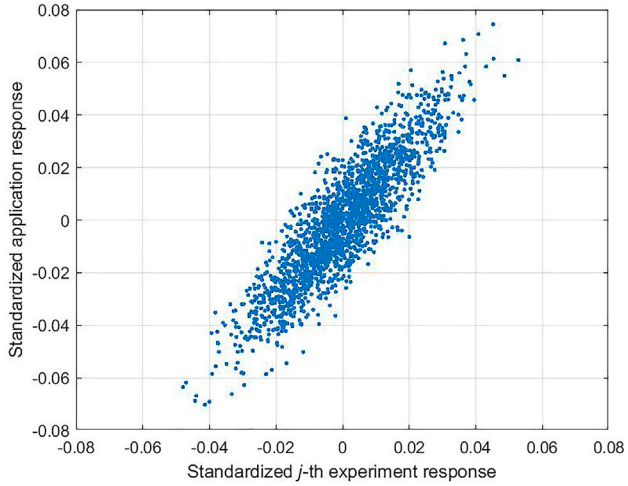

FIGURE 3 | Representative scatter plot of two perturbation vectors.

$$\begin{aligned}\boldsymbol{C}_{kk} = \boldsymbol{S}_{k\alpha}\boldsymbol{U}\boldsymbol{\Lambda}^2\boldsymbol{U}^T\boldsymbol{S}_{k\alpha}^T &= \lim_{N\to\infty}\left(\frac{1}{N}\sum_{p=1}^{N}\boldsymbol{S}_{k\alpha}\Delta\alpha^{(p)}\Delta\alpha^{(p)T}\boldsymbol{S}_{k\alpha}^T\right)\\ &= \lim_{N\to\infty}\left(\frac{1}{N}\sum_{p=1}^{N}\Delta k^{(p)}\Delta k^{(p)T}\right)\end{aligned}$$

where Δk transforms the sensitivity matrix $\boldsymbol{S}_{k\alpha}$ using the Chelosky factor of $\boldsymbol{C}_{\alpha\alpha}$.

Thus, the construction of the $\boldsymbol{C}_{kk}$ matrix effectively reduces to the following three steps; first, it transforms the original variables into a set that are uncorrelated; second, it calculates the sensitivities along the directions of the transformed variables (referred to as directional sensitivity in the calculus literature); and third, it weighs each directional sensitivity by its corresponding prior uncertainty.

The deviation vector of jth experiment (or application denoted by subscript $M + 1$) code-calculated samples from its reference value can be written as:

$$\Delta k_j = \begin{bmatrix}\dfrac{k_j^{(1)} - k_j^{(ref)}}{k_j^{(ref)}}\\ \dfrac{k_j^{(2)} - k_j^{(ref)}}{k_j^{(ref)}}\\ \vdots\\ \dfrac{k_j^{(N)} - k_j^{(ref)}}{k_j^{(ref)}}\end{bmatrix},\ j = 1, 2, \ldots, M+1$$

Each term in Δk_j may be considered as a sample resulting from executing the forward model with a random cross-section perturbation. Thus, Δk_j is a vector of N sampled perturbations of the jth response. Graphically, these perturbation vectors can be displayed via a scatter plot. For example, **Figure 3** shows a

representative scatter plot of the perturbation vectors for the *j*th experiment and the application.

Their similarity index thus reduces to the standard correlation coefficient between the two vectors Δk_j and Δk_{M+1} similarly to **Eq. 9** such that:

$$\cos\theta\left(\Delta k_j, \Delta k_{M+1}\right) = \frac{\Delta k_j^{\mathrm{T}} \Delta k_{M+1}}{\sqrt{\Delta k_j^T \Delta k_j}\sqrt{\Delta k_{M+1}^T \Delta k_{M+1}}}$$

With a large number of samples, the inner-products of any two sample vectors reduce to the elements of the $\boldsymbol{C_{kk}}$ matrix, such that:

$$\lim_{N\to\infty} \Delta k_i^T \Delta k_j = \boldsymbol{C_{kk}}[i, j]$$

Thus,

$$c_k\left(k_j, k_{M+1}\right) = \lim_{N\to\infty} \frac{\Delta k_j^{\mathrm{T}} \Delta k_{M+1}}{\sqrt{\Delta k_j^T \Delta k_j}\sqrt{\Delta k_{M+1}^T \Delta k_{M+1}}}$$

In this manuscript, the ACCRUE index will be calculated using both the analytical definition, presented in **Section 3**, as well as the noted forward-based approach for verification.

3 ACCRUE INDEX AND VERIFICATION ALGORITHM

This section details the theoretical derivation of the ACCRUE index j_k, discusses its relationship to the c_k index, and shows how it can be calculated both analytically using the adjoint approach and statistically using the forward approach. The j_k index is designed to address two limitations of the c_k index, first the impact of measurement uncertainty on the relevance of a given experiment, and second, the diminished value of an experiment resulting from its similarity with previously consolidated experiments. With regard to the first limitation, the c_k index bases the similarity on the code-calculated values only. In practice however, an experiment with a high c_k index could prove less valuable to estimating the application bias if its measurements have high uncertainties. The second limitation calls for an approach to identify experimental redundancy. The high level premise of any inference procedure is that additional measurements will result in more confidence in the calculated application bias. In practice however, the confidence gleaned from multiple highly relevant experiments could be equally obtained from a smaller number of experiments if high level of redundancy exists between the experiments, a common phenomenon observed in many fields, often referred to as the law of diminished return. The c_k index does not capture this effect because it is based on a single experiment.

3.1 Impact of Measurement Uncertainty

Different from the c_k index which relies on the $\boldsymbol{C_{kk}}$ matrix, the j_k index leverages the $\boldsymbol{C_{kk}} + \boldsymbol{C_{mm}}$ matrix which appears in the GLLS procedure to weigh the prior values and the experimental measurements. This matrix can be shown to be the covariance matrix for the discrepancies between the calculated and measured values, whereas the $\boldsymbol{C_{kk}}$ matrix is the covariance matrix for the calculated values only.

The discrepancies can be aggregated in a vector such that:

$$d = \begin{bmatrix} k_1 - m_1 & k_2 - m_2 & \cdots & k_M - m_M & k_{M+1} \end{bmatrix}^T$$

where the last element, k_{M+1}, of the discrepancy vector remains the same as k, since measurement uncertainty for the application is not applicable.

Then the covariance matrix for the discrepancy vector, d, is:

$$\boldsymbol{C_{dd}} = \begin{bmatrix} D_{1,1} & D_{1,2} & \cdots & D_{1,M} & D_{1,M+1} \\ D_{2,1} & D_{2,2} & \cdots & D_{2,M} & D_{2,M+1} \\ \vdots & \vdots & \ddots & \vdots & \vdots \\ D_{M,1} & D_{M,2} & \cdots & D_{M,M} & D_{M,M+1} \\ D_{M+1,1} & D_{M+1,2} & \cdots & D_{M+1,M} & D_{M+1,M+1} \end{bmatrix} \in \mathbb{R}^{(M+1)\times(M+1)} \tag{11}$$

where $D_{i,j} = \boldsymbol{C_{kk}}[i, j] + \boldsymbol{C_{mm}}[i, j]$ and $\boldsymbol{C_{mm}}[i, j]$ describes the possible correlations between the experimental measurements. The elements of the last column or the last row of the $\boldsymbol{C_{dd}}$ are the same as those of the $\boldsymbol{C_{kk}}$ matrix since no measurement is applicable for the application. If the experiments are independent, then the $\boldsymbol{C_{mm}}$ matrix reduces to a diagonal matrix.

Similarly to before, consider the expressions in **Eq. 11** using the Cholesky decomposition of $\boldsymbol{C_{dd}}$ as:

$$\boldsymbol{C_{dd}} = \boldsymbol{D}^T \boldsymbol{D}$$

where $\boldsymbol{D} = [\,\delta_1 \quad \delta_2 \quad \cdots \quad \delta_{M+1}\,]$, where the inner-product of any of two columns of $\boldsymbol{D}$ gives:

$$7\delta_i^T \delta_j = \boldsymbol{C_{dd}}[i, j],\ i, j = 1, 2, \ldots, M+1$$

Geometrically, the ACCRUE index j_k with a single experiment thus is defined as the cosine angle defined by two vectors of $\boldsymbol{D}$, specifically one related to the application and the other to an experiment as:

$$\begin{aligned} j_k\left(d_j; d_{M+1}\right) &= \frac{\delta_j^T \delta_{M+1}}{\sqrt{\delta_j^T \delta_j}\sqrt{\delta_{M+1}^T \delta_{M+1}}} \\ &= \frac{\boldsymbol{C_{dd}}[j, M+1]}{\sqrt{\boldsymbol{C_{dd}}[j, j]}\sqrt{\boldsymbol{C_{dd}}[M+1, M+1]}} \\ &= \cos\theta\left(\delta_j, \delta_{M+1}\right) \end{aligned} \tag{12}$$

Figure 4 graphically shows how the measurement uncertainty impacts on the j_k value with a single experiment (the *j*th experiment denoted by subscript "*j*") as compared to the c_k value. Due to the measurement uncertainty, the cosine angles estimated by c_k and j_k respectively change from $\cos\theta_j$ to $\cos\varphi_j$. If the associate measurement uncertainty of the given experiment is zero, the j_k value reduces to the c_k value. In any other cases where the measurement uncertainty of the given experiment is not zero, the cosine angle given by j_k is always smaller than that by c_k as illustrated, e.g., $\cos\varphi_j < \cos\theta_j$ or $\varphi_j > \theta_j$. This can be readily proved by comparing the

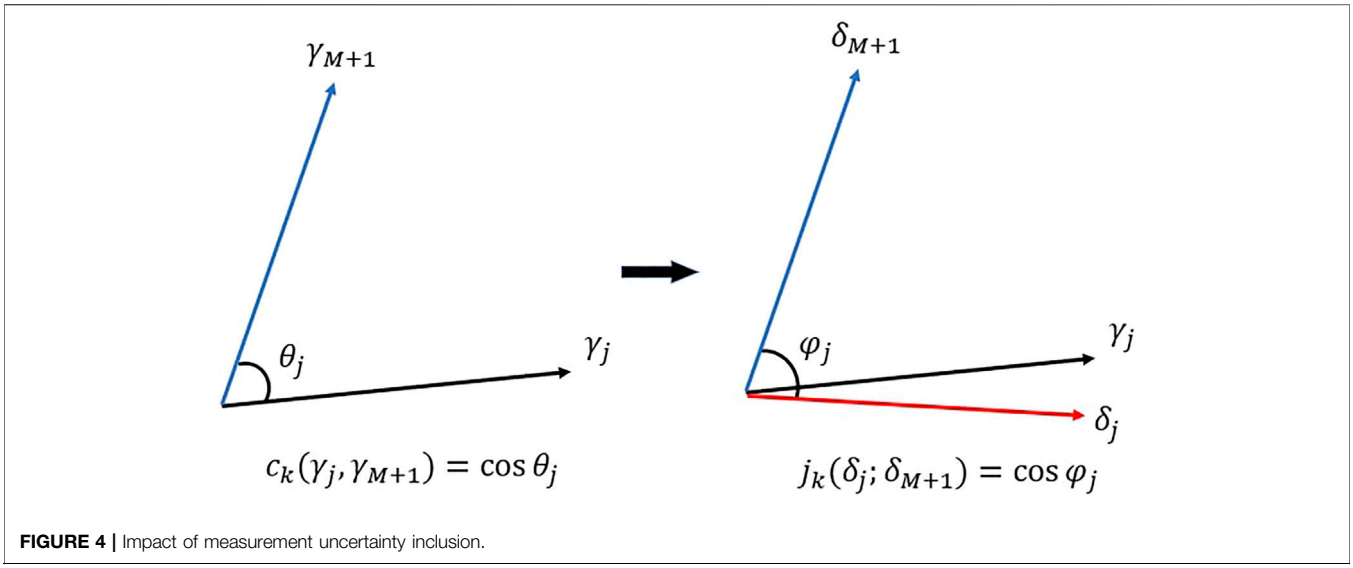

FIGURE 4 | Impact of measurement uncertainty inclusion.

analytical expressions for each c_k and j_k value shown in **Eqs. 9**, **12**, respectively.

With regard to the matrix notations of both equations, $\boldsymbol{C_{kk}}[j, M+1]$ and $\boldsymbol{C_{dd}}[j, M+1]$, $\boldsymbol{C_{kk}}[M+1, M+1]$ and $\boldsymbol{C_{dd}}[M+1, M+1]$ are the same respectively since measurement is not applicable for the application, while $\boldsymbol{C_{dd}}[j, j]$ is always greater than $\boldsymbol{C_{kk}}[j, j]$ since $\boldsymbol{C_{dd}}[j, j] = \boldsymbol{C_{kk}}[j, j] + \boldsymbol{C_{mm}}[j, j]$. As a result, the cosine angle is reduced proportional to $\sqrt{\boldsymbol{C_{kk}}[j, j]/\boldsymbol{C_{dd}}[j, j]}$ with experimental measurement uncertainty present.

As discussed in **Section 2.3**, the covariance matrix, $\boldsymbol{C_{mm}}$, can be written as:

$$\boldsymbol{C_{mm}} = \boldsymbol{L}\boldsymbol{L}^{\boldsymbol{T}} = \lim_{N\to\infty}\left(\boldsymbol{L}\frac{1}{N}\sum_{i=1}^{N}\zeta^{(p)}\zeta^{(p)T}\boldsymbol{L}^{\boldsymbol{T}}\right)$$
$$= \lim_{N\to\infty}\left(\frac{1}{N}\sum_{p=1}^{N}\Delta m^{(p)}\Delta m^{(p)T}\right)$$

where $\boldsymbol{L} \in \mathbb{R}^{M\times M}$ a low triangular matrix.

Then the measurement sample vector for jth experiment, $\Delta m_j \in \mathbb{R}^N$, is defined as:

$$\Delta m_j = \begin{bmatrix} \dfrac{m_j^{(1)} - m_j^{(ref)}}{m_j^{(ref)}} \\ \dfrac{m_j^{(2)} - m_j^{(ref)}}{m_j^{(ref)}} \\ \vdots \\ \dfrac{m_j^{(N)} - m_j^{(ref)}}{m_j^{(ref)}} \end{bmatrix}, j = 1, 2, \ldots, M$$

Thus, the discrepancy sample vector for jth experiment, $\Delta d_j \in \mathbb{R}^N$, is:

$$\Delta d_j = \Delta k_j - F_j \Delta m_j$$

where F_j is a scalar quantity representing a ratio of experimental to calculated response values of jth experiment

$$\lim_{N\to\infty}\Delta d_i^T \Delta d_j = \boldsymbol{C_{dd}}[i, j]$$

Thus,

$$j_k\left(d_j; d_{M+1}\right) = \lim_{N\to\infty}\frac{\Delta d_j^{\mathrm{T}}\Delta d_{M+1}}{\sqrt{\Delta d_j^T \Delta d_j}\sqrt{\Delta d_{M+1}^T \Delta d_{M+1}}}$$

3.2 Impact of Multiple Experiments

The ACCRUE index may be viewed as the similarity between a group of experiments and the application of interest when the experimental uncertainties are excluded from the analysis. Its true value however is in assessing the relevance of a new experiment by taking into account both the experiment's measurement uncertainty and the value gleaned from past experiments. In this section, the detailed analytical derivation for j_k value with multiple experiments is provided with the δ vectors. However, if analysts are not interested in including the impact of measurement uncertainties, they can work directly with the γ vectors instead of δ vectors.

Analytically, the j_k index for the first L experiments is given using the elements of the $\boldsymbol{C_{dd}}$ matrix in **Eq. 11** by:

$$j_k = \sqrt{\sum_{i=1}^{L}\frac{\left(E_{i,M+1}\right)^2}{E_{i,i}\, D_{M+1,M+1}}} \tag{13}$$

where the E terms are defined by the following recurring relation:

$$E_{1,j} = D_{1,j}$$
$$E_{i,j} = D_{i,j} - \sum_{k=1}^{i-1}\frac{E_{k,i}}{E_{k,k}}E_{k,j}$$

These terms can be evaluated analytically given access to the sensitivity coefficients, the prior cross-section covariance matrix,

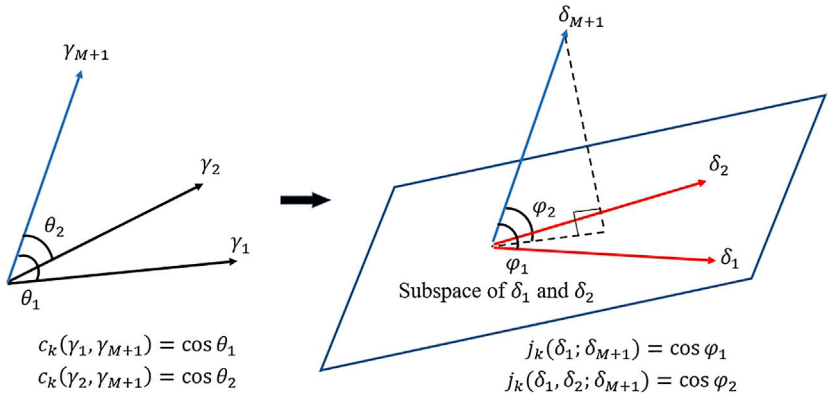

FIGURE 5 | Geometrical interpretation of j_k value with two experiments.

and the measurement uncertainties. By way of an example, consider the simple case with $L = 1$, i.e., a single experiment, where the j_k reduces to:

$$j_k(d_1; d_{M+1}) = \sqrt{\frac{(D_{1,M+1})^2}{D_{1,1}\, D_{M+1,M+1}}} = \frac{s_1 \boldsymbol{C}_{\alpha\alpha} s_{M+1}^T}{\sqrt{s_1^T \boldsymbol{C}_{\alpha\alpha} s_1 + \sigma_{m_1}^2}\sqrt{s_{M+1}^T \boldsymbol{C}_{\alpha\alpha} s_{M+1}}} \tag{14}$$

This expression equivalent to the c_k index assuming zero measurement uncertainty, i.e., $\sigma_{m_1}^2 = 0.0$. The implication is the j_k will always have a lower value than the corresponding c_k value for any realistic non-zero experimental uncertainties. With $L = 2$, and assuming the measurement uncertainties are uncorrelated, i.e., $\boldsymbol{C_{mm}}[1,2] = \boldsymbol{C_{mm}}[2,1] = 0$, the j_k value becomes:

$$\begin{aligned} j_k(d_1, d_2; d_{M+1}) &= \sqrt{\frac{(E_{1,M+1})^2}{E_{1,1}\, D_{M+1,M+1}} + \frac{(E_{2,M+1})^2}{E_{2,2}\, D_{M+1,M+1}}} \\ &= \sqrt{\frac{(D_{1,M+1})^2}{D_{1,1}\, D_{M+1,M+1}} + \frac{\left(D_{2,M+1} - \frac{D_{1,2}}{D_{1,1}} D_{1,M+1}\right)^2}{\left(D_{2,2} - \frac{D_{1,2}}{D_{1,1}} D_{1,2}\right) D_{M+1,M+1}}} \\ &= \sqrt{\frac{\left(s_1^T \boldsymbol{C}_{\alpha\alpha} s_a\right)^2}{\left(s_1^T \boldsymbol{C}_{\alpha\alpha} s_1 + \sigma_{m_1}^2\right)\left(s_a^T \boldsymbol{C}_{\alpha\alpha} s_a\right)} + \frac{\left(s_2^T \boldsymbol{C}_{\alpha\alpha} s_a - \frac{s_1^T \boldsymbol{C}_{\alpha\alpha} s_2}{s_1^T \boldsymbol{C}_{\alpha\alpha} s_1 + \sigma_{m_1}^2} s_2^T \boldsymbol{C}_{\alpha\alpha} s_a\right)^2}{\left(s_2^T \boldsymbol{C}_{\alpha\alpha} s_2 + \sigma_{m_2}^2 - \frac{s_1^T \boldsymbol{C}_{\alpha\alpha} s_2}{s_1^T \boldsymbol{C}_{\alpha\alpha} s_1 + \sigma_{m_1}^2} s_1^T \boldsymbol{C}_{\alpha\alpha} s_2\right) s_a^T \boldsymbol{C}_{\alpha\alpha} s_a}} \end{aligned} \tag{15}$$

Eq. 15 shows that the relevance of two experiments may be expressed as the sum of two terms, one very similar to the c_k index representing the relevance of the first experiment, and the other subtracting away the impact of the first experiment. To help interpret the j_k index for L experiments, we resort to the geometrical and statistical interpretations provided earlier in **Section 3.1**.

Consider the case with two experiments (denoted by the subscripts "1" and "2", respectively) as illustrated in **Figure 5**, where j_k calculates the angle between the δ_{M+1} vector (representing the application) and the subspace formed by δ_1 and δ_2 (representing the two experiments). As long as the second experiment provides additional information which is not duplicated by the first experiment, the j_k value is expected to increase as compared to the value obtained with a single experiment, i.e., $j_k(\delta_1, \delta_2; \delta_{M+1}) > j_k(\delta_1; \delta_{M+1})$ or $\varphi_2 < \varphi_1$ as shown in **Figure 5**. In the case that the second experiment carries no additional information, e.g., the j_k value remains the same. The implication is that the second experiments provides no value to the GLLS inference procedure, and hence can be excluded.

The cosine angle between any two subspaces can be calculated by orthogonal projection techniques, e.g., QR decomposition or Singular Value Decomposition (SVD). For example, consider the j_k value of the first L experiments and the application, the corresponding δ vectors can be aggregated as:

$$\boldsymbol{D}_L = [\ \delta_1 \quad \delta_2 \quad \cdots \quad \delta_L\ ]$$

Then, the associated j_k expression can be written as:

$$\begin{aligned} j_k(\boldsymbol{D}_L; \delta_{M+1}) &= \cos\theta(\boldsymbol{D}_L, \delta_{M+1}) = \cos\theta(\boldsymbol{Q}_L, v) = \left\|\boldsymbol{Q}_L^T v\right\| \\ &= \sqrt{(q_1^T v)^2 + (q_2^T v)^2 + \cdots (q_L^T v)^2} \end{aligned}$$

where q_j $(j = 1, 2, \ldots, L)$ is jth q vector of the $\mathbf{Q}_L$ matrix from QR decomposition and v is a normalized δ_{M+1} vector for the application such as $v = \delta_{M+1}/||\delta_{M+1}||$.

For example, consider the case where D_1 contains only δ_1 vector corresponding to the first experiment, i.e., $D_1 = \delta_1$, then the j_k value is calculated as:

$$j_k(D_1, \delta_{M+1}) = \sqrt{(q_1^T v)^2}$$

where q_1 is a normalized directional vector of δ_1:

$$q_1 = \frac{\delta_1}{||\delta_1||}$$

Thus, the j_k value is

$$j_k = \sqrt{\frac{\left(\delta_1^T \delta_{M+1}\right)^2}{\delta_1^T \delta_1 \delta_{M+1}^T \delta_{M+1}}} = \frac{\delta_1^T \delta_{M+1}}{\sqrt{\delta_1^T \delta_1}\sqrt{\delta_{M+1}^T \delta_{M+1}}}$$
$$= \frac{s_1^T \boldsymbol{C}_{\alpha\alpha} s_a}{\sqrt{s_1^T \boldsymbol{C}_{\alpha\alpha} s_1 + \sigma_{m_1}^2}\sqrt{s_a^T \boldsymbol{C}_{\alpha\alpha} s_a}}$$

which is equivalent to **Eq. 14**

If $\boldsymbol{D}_2$ contains two δ vectors (δ_1 and δ_2) corresponding to the first two experiments, then the j_k value is calculated as:

$$j_k(\boldsymbol{D}_2, \delta_{M+1}) = \sqrt{\left(q_1^T v\right)^2 + \left(q_2^T v\right)^2}$$

where q_2 is defined by Gram-Schmidt process such as:

$$q_2 = \frac{\left(\delta_2 - \frac{\delta_1^T \delta_2}{\delta_1^T \delta_1}\delta_1\right)}{\sqrt{\delta_2^T \delta_2\left(1 - \frac{\delta_1^T \delta_2 \delta_1^T \delta_2}{\delta_1^T \delta_1 \delta_2^T \delta_2}\right)}}$$

Thus, the j_k value is:

$$j_k = \sqrt{\frac{\left(\delta_1^T \delta_{M+1}\right)^2}{\delta_1^T \delta_1 \delta_{M+1}^T \delta_{M+1}} + \frac{\left(\delta_2 \gamma_a - \frac{\delta_1^T \delta_2}{\delta_1^T \delta_1}\delta_1 \delta_{M+1}\right)^2}{\left(\delta_2^T \delta_2 - \delta_2^T \delta_1 \frac{\delta_1^T \delta_2}{\delta_1^T \delta_1}\right)\delta_{M+1}^T \delta_{M+1}}}$$
$$= \sqrt{\frac{\left(s_1^T \boldsymbol{C}_{\alpha\alpha} s_a\right)^2}{\left(s_1^T \boldsymbol{C}_{\alpha\alpha} s_1 + \sigma_{m_1}^2\right)\left(s_a^T \boldsymbol{C}_{\alpha\alpha} s_a\right)} + \frac{\left(s_2^T \boldsymbol{C}_{\alpha\alpha} s_a - s_2^T \boldsymbol{C}_{\alpha\alpha} s_a \frac{s_1^T \boldsymbol{C}_{\alpha\alpha} s_2}{s_1^T \boldsymbol{C}_{\alpha\alpha} s_1 + \sigma_{m_1}^2}\right)^2}{\left(s_2^T \boldsymbol{C}_{\alpha\alpha} s_2 + \sigma_{m_2}^2 - s_1^T \boldsymbol{C}_{\alpha\alpha} s_2 \frac{s_1^T \boldsymbol{C}_{\alpha\alpha} s_2}{s_1^T \boldsymbol{C}_{\alpha\alpha} s_1 + \sigma_{m_1}^2}\right) s_a^T \boldsymbol{C}_{\alpha\alpha} s_a}}$$

which is equivalent to **Eq. 15**

Consequently, the general expression for j_k value can be written as:

$$j_k = \sqrt{\sum_{i=1}^{L} \frac{\left(u_i^T \delta_{M+1}\right)^2}{u_i^T u_i \, \delta_{M+1}^T \delta_{M+1}}}$$

where

$$u_1 = \delta_1$$
$$u_i = \delta_i - \sum_{k=1}^{i-1} \frac{u_k^T \delta_i}{u_k^T u_k} u_k, \quad i = 2, 3, \ldots, L$$

which evaluates the same scalar quantity as that calculated by the matrix element notations in earlier this section.

3.3 Overall Process

Figure 6 shows the overall process for evaluating the similarity or relevance of an experiment to a given application. The similarity accounts for the correlation between two responses, e.g., one from the application and the other from the experiment, as calculated by a computer code. The ACCRUE index extends the concept of similarity to quantify the relevance, as measured by the added value of the experiment, taking into account both the experiment's measurement uncertainties as well as past experiments. As shown in this figure, the first step is to check if an adjoint solver is available which allows one to employ sensitivity coefficients. If no experimental measurement uncertainty is available and only a single experiment is available, the ACCRUE index j_k reduces to the similarity index c_k. If the experimental uncertainty is available, **Eq. 12** is employed to evaluate the j_k index. If additional experiments are available, then the most general expression for j_k is employed per **Eq. 13**.

4 NUMERICAL EXPERIMENTS

Numerical experiments have been conducted with two different case studies. The first case study assumes that the applications have low c_k values for all available experiments which are in the order of 0.7, referred to as the low relevance applications, and the second case study considers applications with high c_k values that are greater than 0.9. An application with low relevant experiments represents a realistic scenario expected with first-of-a-kind designs, i.e., advanced reactor designs and new fuel concepts, with no prior or rare strongly relevant experiments. It also highlights the expected high cost of new experiments, and the need to employ modeling and simulation to design a minimal number of targeted validation experiments. When the c_k values are low for the given application, it is important to figure out a way to prioritize the selection of past available experiments, as well as judge the value of new/planned experiments. We compare the performance of the j_k and c_k indices for both the high relevance and low relevance applications for a range of assumed values for the experimental uncertainties. This is also important when designing new experiments, as it provides quantitative value for different types of instrumentations with varying levels of measurement uncertainties.

The low relevance case study employs 17 critical benchmark experiments from the low enriched uranium thermal compound systems (LCT-008-001—LCT-008-017) in the ICSBEP handbook (NEA, 2011) as experiments and the accident-tolerant fuel (ATF) concept BWR assembly as an application. The selected LCT benchmark experiment set (LCT-008) cases are critical lattices with UO_2 fuel rods of 2.9% enrichment and perturbing rods in borated water in common, but have different boron concentrations and various rods arrangements. Their similarity indices, c_k, to the BWR ATF model are all around 0.7 as reported by TSUNAMI-IP. The BWR ATF model is a 10×10 GE14 dominant lattice with UO_2 fuel and FeCrAl cladding. This model comprises 92 UO_2 fuel pins, 78 out of which are fuel with various enrichments from 2 to 4% and the remaining are 14 rods with gadolinium, surrounded by water coolant in a channel box structure (Jessee, 2020). The layouts of a representative LCT benchmark experiment (LCT-008-001) and the application model are shown in **Figure 7**. The high relevance case study employs 42 critical experiments from highly enriched uranium fast metal systems (HMF set, short for HEU-MET-FAST) in ICSBEP handbook. In this study, application models are selected among these benchmark experiments and similarity indices are in the 0.9 range (NEA, 2011). All the critical benchmarks employ highly enriched uranium fuel with a variety of design configurations and different enrichments. **Figure 8** shows two representative benchmark experiments one of which is used as an experiment (HMF-020-001, Polyethylene-reflected spherical

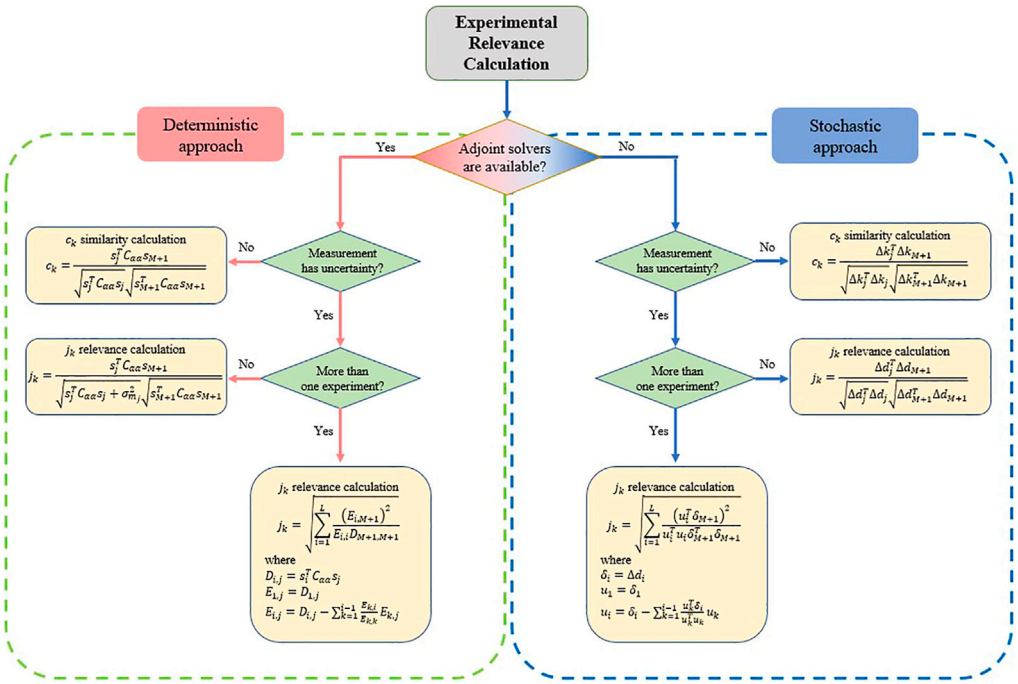

FIGURE 6 | Approach for evaluating experimental relevance.

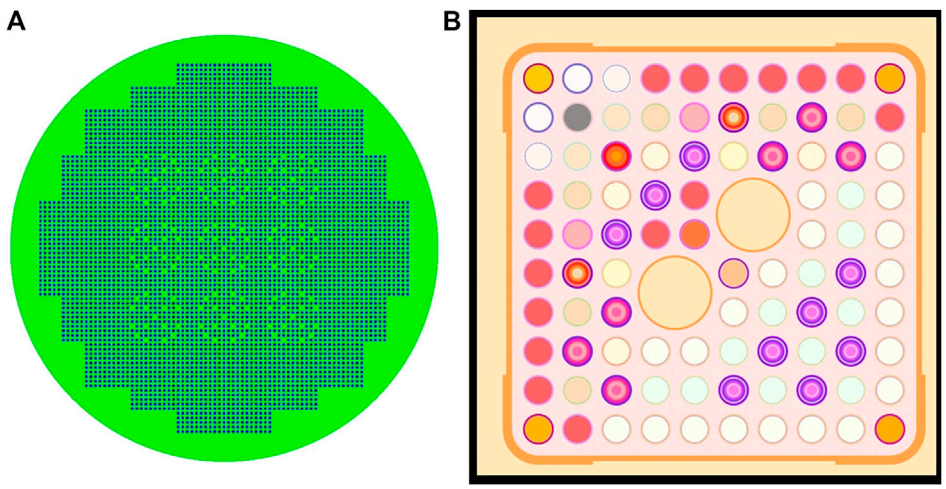

FIGURE 7 | Low-relevant case layouts of the representative models. **(A)** Experiment model: LCT-008-001 **(B)** Application model: ATF assembly.

assembly of ^{235}U) and the other as an application (HMF-019-001, Graphite-reflected spherical assembly of ^{235}U).

To identify the possible impact of initial discrepancies, i.e., differences between calculated and measured responses, on the GLLS-estimated biases, three critical experiments having different biases (high, intermediate, and low) are selected as applications and the remaining experiments are used as validation experiments. The high bias application is selected to have an initial k_{eff} discrepancy in the order of 1,000 pcm, while the intermediate in the order of 300–500 pcm, and the low 200 pcm.

4.1 Comparison of j_k *vs.* c_k-Sorting

Figure 9 shows representative results for the high relevance case study for three different applications with high, intermediate, and low biases. The *x*-axis explores the change in the GLLS-estimated biases when adding one experiment at a time, wherein the experiments are ordered according to their c_k values (top

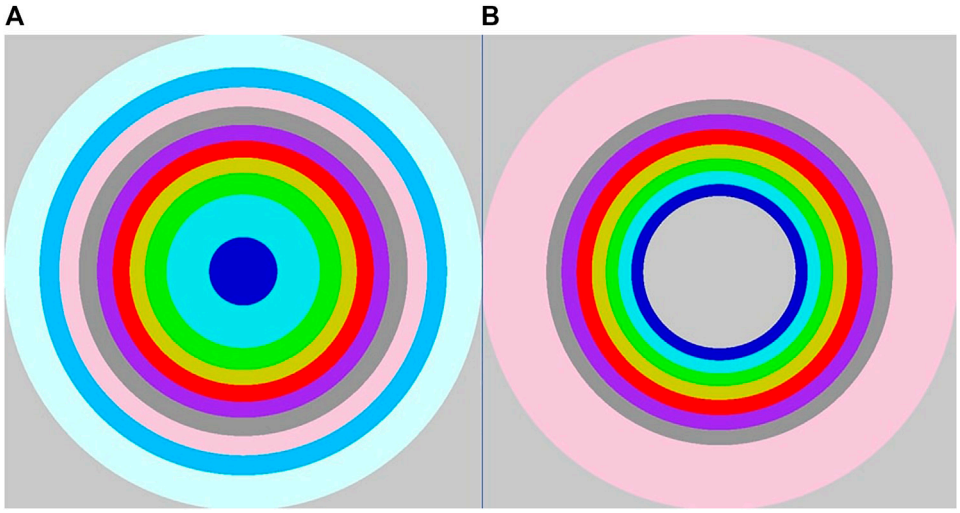

FIGURE 8 | High-relevant case layouts of the representative models. **(A)** Experiment model: HMF-020-001 **(B)** Application model: HMF-019-001.

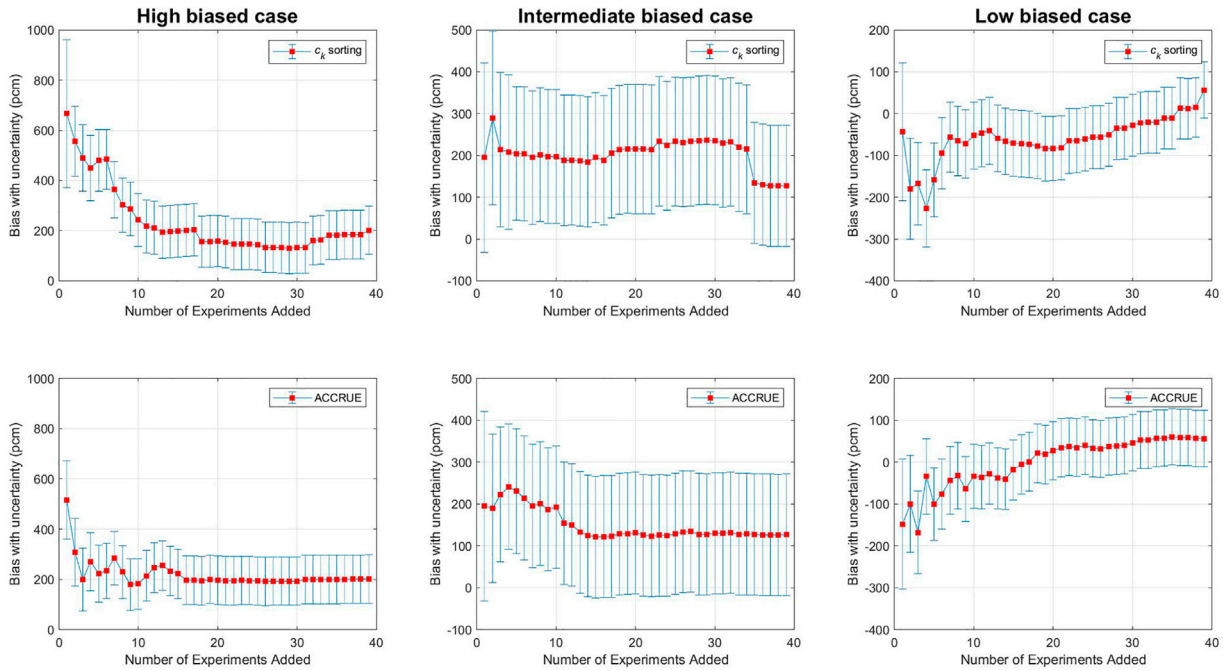

FIGURE 9 | Bias and uncertainty estimation for high relevance case.

graphs), and j_k values (bottom graphs). The c_k-sorting is straightforward as each experiment is employed once in conjunction with the given application. Markedly different, the j_k value depends on the number and order of experiments included, hence each sorting is expected to give rise to different profiles for j_k and the associated bias and bias uncertainty. The goal is thus to identify the order that allows the analyst to reach a certain level of confidence in the calculated bias with minimal number of experiments. In the current study, the search for this optimal order is initiated with the experiment having the highest c_k value, with the second experiment selected to maximize the j_k value among all remaining experiments, and so on. In practice, one may start with any experiment, and adds experiments as they become available, or may employ the j_k value to quantify the value of new/planned experiments. For each added experiment, the GLLS bias and bias uncertainty are calculated to help compare the c_k and j_k-sorting. The goal is to achieve a stable prediction of the bias with minimal uncertainty.

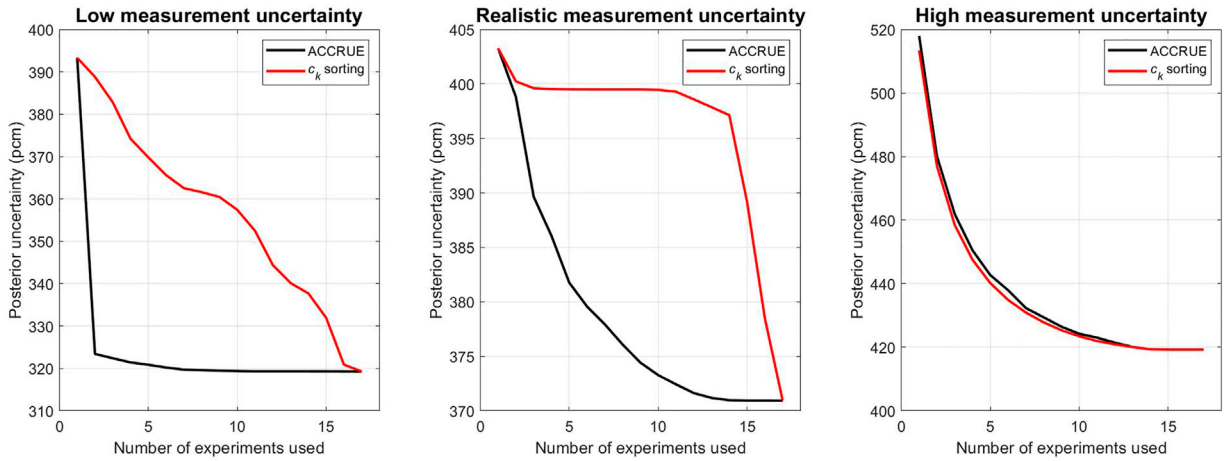

FIGURE 10 | Bias uncertainty reduction for a low relevance application.

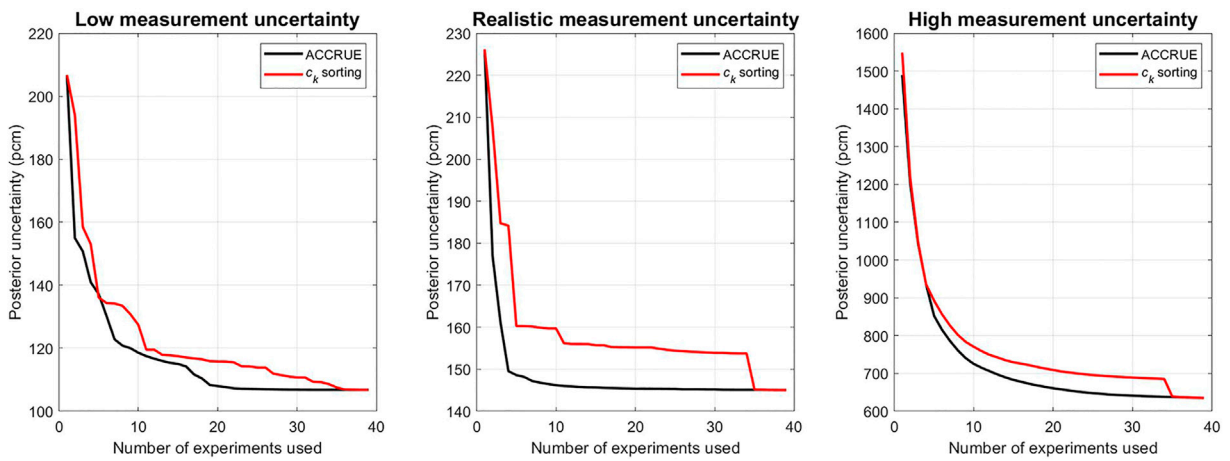

FIGURE 11 | Bias uncertainty reduction for a high relevance application.

These results show that the bias stabilizes quicker with the j_k sorting. More important, the c_k-sorting could show sudden changes after a period of stable behavior. For all considered applications using the c_k-sorting, the biases continue to experience sudden or gradual changes following a period of stable behavior. For example, for the low bias application, the estimated bias exhibits an upward trend after the 20th experiment. The implication is that the additional experiments continue to provide value to the GLLS procedure despite their lower relevance. With the j_k-sorting, a more explainable trend is achieved whereby the bias trend shows stable behavior after the 20th experiment.

Regarding the bias uncertainties, shown in **Figure 9** as error bars, they are plotted in **Figures 10**, **11** as a function of the number of experiments using both the c_k and j_k-sorting for, respectively, one application with high relevance experiments and one application with low relevance experiments. The results highlight a key limitation of the c_k-sorting, that is the addition of low relevance experiments could change the trend of both the bias and the bias uncertainty. The j_k-sorting however does not suffer from this limitation, implying that one can select the minimal number of experiments required to reach a certain pre-determined level of confidence for the calculated bias. Comparison of the uncertainty values in both figures indicate that the impact is much less pronounced when highly relevant experiments are available. This highlights the value of the j_k-sorting when limited number of experiments are available, as is the case with first-of-a-kind designs.

These results are compared in **Figure 12** with randomized orders (shown as multi-color solid lines) for one of the low relevance applications at different levels of measurement uncertainty, specifically 10 pcm (representing a highly accurate measurement), 100 pcm (a realistic measurement), and 500 pcm (a low confidence measurement) for the measured k_{eff} values. The

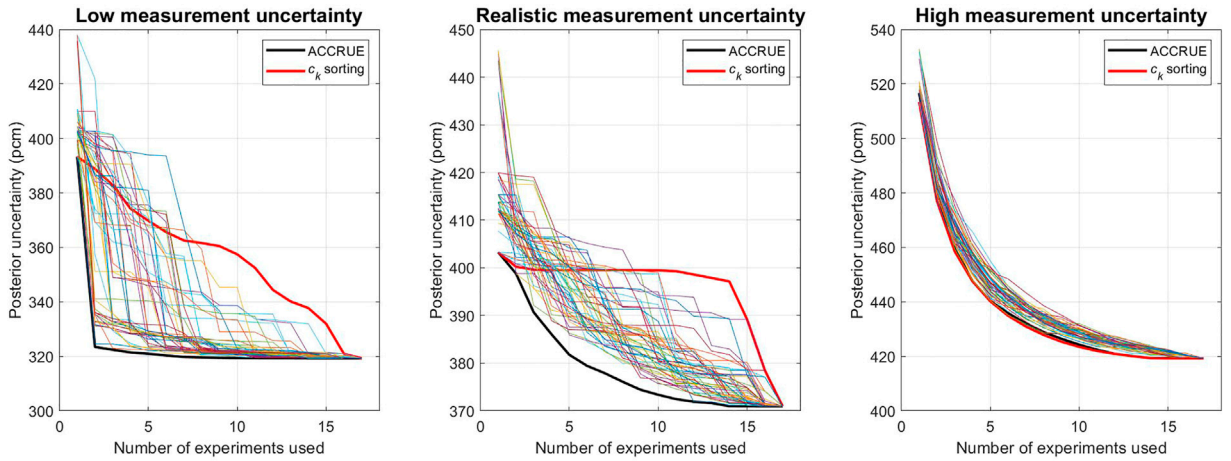

FIGURE 12 | Bias uncertainty reduction with random orders.

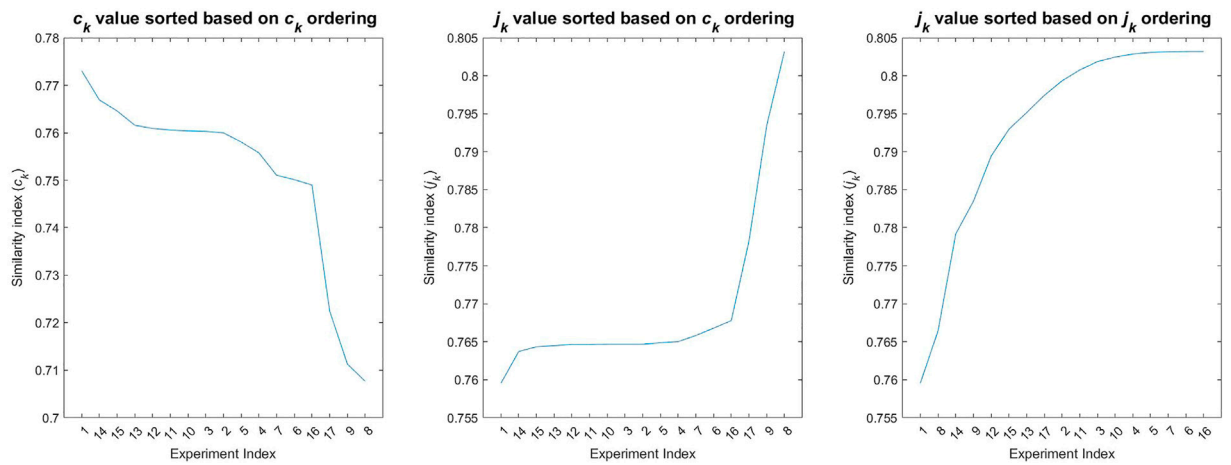

FIGURE 13 | Comparison of the c_k and j_k profiles.

results show that pure random sampling could be superior to c_k-sorting, with the j_k sorting still exhibiting the best behavior in terms of reducing the bias uncertainty with minimal number of experiments. When the measurement uncertainty is too high, the ordering of the experiments is no longer important. This is a key observation highlighting the value of ordering experiments as experimentalists continue to improve their measurements in support of model validation.

To help understand the changes in the bias and bias uncertainty associated with the c_k-sorting, the left plot in **Figure 13** orders the experiments according to their c_k values, and the middle plot calculates the corresponding j_k values using the c_k-sorting. Notice that although the first few experiments, i.e., #15, #13, #12, . . ., to #4 have higher relevance than later experiments, they do not change the j_k value, and hence the bias and bias uncertainty as shown in the earlier figures. The j_k values start to show larger increase when additional lower relevance experiments are added, explaining the sudden or gradual change in the bias and its uncertainty. However, when the experiments are ordered according to their j_k values, as shown in the right plot, a smoother j_k profile is obtained which is consistent with the bias and bias uncertainty profiles obtained using the GLLS procedure. The implication is that one can employ the j_k profile to develop insight into the amount of experimental effort necessary to reach a target confidence in the calculated bias, even before the actual measurements are recorded. This follows because j_k only requires access to the prior uncertainties and the expected measurement uncertainty, not the actual measured bias.

4.2 Stochastic Non-Intrusive Verification

As mentioned earlier, the analytical expressions for the similarity or relevance metrics such as c_k and j_k require access to derivatives which may not be readily available. To address this challenge, earlier work has developed an alternative to the estimation of c_k

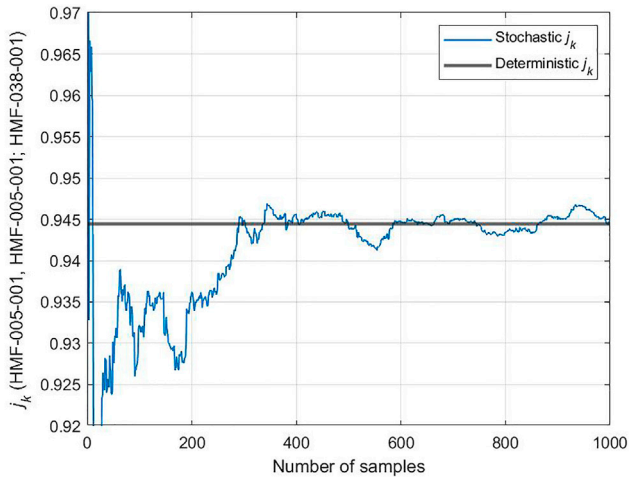

FIGURE 14 | Non-intrusive stochastic estimation of j_k.

value using a non-intrusive forward-based stochastic method (Huang et al., 2020). In this section, we present numerical results comparing the results of the analytically-calculated j_k value to that estimated by the noted stochastic method. This will serve two purposes: the first is to provide a simple approach for the calculation of the j_k value when derivatives are unavailable, and the second to help verify the calculated j_k value using the stochastic method by comparing it to the analytically-calculated value. To achieve that, two benchmark experiments (HMF-005-001 and 005-002) are selected to calculate the j_k value. Their calculated response uncertainties are 1,492 pcm and 1721 pcm respectively, and measurement uncertainties are 360 pcm. A total of 1,000 samples are generated to examine the convergence of forward-based j_k value, whose corresponding analytical value is 0.9445 as given by **Eq. 15**, shown in **Figure 14** as a horizontal line. The results indicate that the forward-based approach produces acceptable approximation of the analytical value using few hundred simulations, which is consistent with the results reported previously for the c_k value (Huang et al., 2020).

5 CONCLUSION AND FURTHER RESEARCH

This manuscript has introduced an extension of the basic similarity metric, denoted by the ACCRUE metric and mathematically symbolized by the j_k index to distinguish it from the c_k similarity metric. The ACCRUE metric takes into account the impact of multiple experiments and the associated experimental uncertainties, both currently missing from the extant similarity definition. The results show that the ACCRUE metric is capable of finding the optimal sorting of the experiments, the one that leads to the most stable variation in the GLLS calculated bias and bias uncertainty. When the experiments available are highly relevant and numerous, the performance of the c_k metric approaches that of the j_k metric. However, when highly-relevant experiments are scarce and when experimental uncertainties are low, the j_k metric is capable of identifying the minimal number of experiments required to reach a certain confidence for the calculated bias, whereas the c_k metric may be outperformed by random sorting of the experiments. The results of this work are expected to be valuable to the validation of computer models for first-of-a-kind designs where little or rare experimental data exist. Another important value for the j_k metric is that it can be calculated using forward samples of the model responses, thereby precluding the need for derivatives, which allows one to extend the concept to non-k_{eff} responses. This will allow one to extend its definition to models exhibiting nonlinear behavior often resulting from multi-physics coupling, e.g., different geometry, compositions, and types of reactor. This will pave the way to the development of relevance metrics that goes beyond the first-order variations currently captured by the extant similarity analysis.

DATA AVAILABILITY STATEMENT

The raw data supporting the conclusion of this article will be made available by the authors, without undue reservation.

AUTHOR CONTRIBUTIONS

JS: Writing the original draft, methodology, investigation, visualization. HA-K: Conceptualization, methodology, writing/editing, supervision. AE: Supervision, review/editing.

FUNDING

This work was supported in part by an Idaho National Laboratory project (Grant no. 74000576).

ACKNOWLEDGMENTS

The authors would like to acknowledge Dr. Ugur Mertyurek of Oak Ridge National Laboratory for providing the models used in this study.

REFERENCES

Abdel-Khalik, H. S., Bang, Y., and Wang, C. (2013). Overview of Hybrid Subspace Methods for Uncertainty Quantification, Sensitivity Analysis. *Ann. Nucl. Energ.* 52, 28–46. doi:10.1016/j.anucene.2012.07.020

Avramova, M. N., and Ivanov, K. N. (2010). Verification, Validation and Uncertainty Quantification in Multi-Physics Modeling for Nuclear Reactor Design and Safety Analysis. *Prog. Nucl. Energ.* 52, 601–614. doi:10.1016/j.pnucene.2010.03.009

Becker, M., Henley, E. J., and Oshima, K. (1982). *Advances in Nuclear Science and Technology*.

Broadhead, B. L., Rearden, B. T., Hopper, C. M., Wagschal, J. J., and Parks, C. V. (2004). Sensitivity- and Uncertainty-Based Criticality Safety Validation Techniques. *Nucl. Sci. Eng.* 146, 340–366. doi:10.13182/NSE03-2

Cacuci, D. G., and Ionescu-Bujor, M. (2010). Best-Estimate Model Calibration and Prediction through Experimental Data Assimilation-I: Mathematical Framework. *Nucl. Sci. Eng.* 165, 18–44. doi:10.13182/NSE09-37B

Gandini, A. (1967). A Generalized Perturbation Method for Bi-linear Functionals of the Real and Adjoint Neutron Fluxes. *J. Nucl. Energ.* 21, 755–765. doi:10.1016/0022-3107(67)90086-X

Glaeser, H. (20082008). GRS Method for Uncertainty and Sensitivity Evaluation of Code Results and Applications. *Sci. Tech. Nucl. Installations* 2008, 1–7. doi:10.1155/2008/798901

Huang, D., Mertyurek, U., and Abdel-Khalik, H. (2020). Verification of the Sensitivity and Uncertainty-Based Criticality Safety Validation Techniques: ORNL's SCALE Case Study. *Nucl. Eng. Des.* 361, 110571. doi:10.1016/j.nucengdes.2020.110571

Jessee, M. (2020). *SCALE Lattice Physics Code Assessments of Accident-Tolerant Fuel*.

Lucius, J. L., Weisbin, C. R., Marable, J. H., Drischler, J. D., Wright, R. Q., and White, J. E. (1981). *Users Manual for the FORSS Sensitivity and Uncertainty Analysis Code System*. Oak Ridge, TN. doi:10.2172/6735933

NEA (2011). *International Handbook of Evaluated Criticality Safety Benchmark Experiments 2015*.

Oblow, E. M. (1976). Sensitivity Theory from a Differential Viewpoint. *Nucl. Sci. Eng.* 59, 187–189. doi:10.13182/nse76-a15688

Palmiotti, G., and Salvatores, M. (20122012). Developments in Sensitivity Methodologies and the Validation of Reactor Physics Calculations. *Sci. Tech. Nucl. Installations* 2012, 1–14. doi:10.1155/2012/529623

Rearden, B. T., and Jessee, M. A. (2016). *TSUNAMI Utility Modules*. Ornl/Tm-2005/39.

Rimpault, G., Plisson, D., Tommasi, J., Jacqmin, R., Rieunier, J-M., Verrier, D., et al. (2002). *The ERANOS Code and Data System for Fast Reactor Neutronic Analysis*.

Salvatores, M. (1973). Adjustment of Multigroup Neutron Cross Sections by a Correlation Method. *Nucl. Sci. Eng.* 50, 345–353. doi:10.13182/nse73-a26569

Stacey, W. B. (1974). *Variational Methods in Nuclear Reactor Physics*. Academic Press. doi:10.1016/b978-0-12-662060-3.x5001-2

Stark, H., and Woods, J. W. (2012). *Probability, Statistics, and Random Processes for Engineers*. Fourth Edition4th editio. Upper Saddle River: Pearson.

Usachev, L. N. (1964). Perturbation Theory for the Breeding Ratio and for Other Number Ratios Pertaining to Various Reactor Processes. *J. Nucl. Energ. Parts A/B. Reactor Sci. Tech.* 18, 571–583. doi:10.1016/0368-3230(64)90142-9

Wieselquist, W. A., 2016. SAMPLER: A Module for Statistical Uncertainty Analysis with SCALE Sequences, 6.2.3. ed. Ornl/Tm-2005/39.

Williams, M. L., Broadhead, B. L., Jessee, M. A., Wagschal, J. J., and Lefebvre, R. A., 2016. TSURFER: An Adjustment Code to Determine Biases and Uncertainties in Nuclear System Responses by Consolidating Differential Data and Benchmark Integral Experiments, 6.2.3. ed.

Conflict of Interest: The authors declare that the research was conducted in the absence of any commercial or financial relationships that could be construed as a potential conflict of interest.

Publisher's Note: All claims expressed in this article are solely those of the authors and do not necessarily represent those of their affiliated organizations, or those of the publisher, the editors and the reviewers. Any product that may be evaluated in this article, or claim that may be made by its manufacturer, is not guaranteed or endorsed by the publisher.

frontiers in Energy Research

METHODS
published: 05 January 2022
doi: 10.3389/fenrg.2021.804018

Generalized Empirical Interpolation Method With H^1 Regularization: Application to Nuclear Reactor Physics

Helin Gong, Zhang Chen and Qing Li**

Science and Technology on Reactor System Design Technology Laboratory, Nuclear Power Institute of China, Chengdu, China

The generalized empirical interpolation method (GEIM) can be used to estimate the physical field by combining observation data acquired from the physical system itself and a reduced model of the underlying physical system. In presence of observation noise, the estimation error of the GEIM is blurred even diverged. We propose to address this issue by imposing a smooth constraint, namely, to constrain the H^1 semi-norm of the reconstructed field of the reduced model. The efficiency of the approach, which we will call the H^1 regularization GEIM (R-GEIM), is illustrated by numerical experiments of a typical IAEA benchmark problem in nuclear reactor physics. A theoretical analysis of the proposed R-GEIM will be presented in future works.

Keywords: generalized empirical interpolation method, model order reduction, observations, regularization, nuclear reactor physics

OPEN ACCESS

Edited by:
Qian Zhang,
Harbin Engineering University, China

Reviewed by:
Bertrand Bouriquet,
Electricité de France, France
Zhang Chunyu,
Sun Yat-Sen University, China
Jean-Philippe Argaud,
Electricité de France, France

****Correspondence:***
Helin Gong
gonghelin06@qq.com
Qing Li
liqing_npic@163.com

Specialty section:
This article was submitted to Nuclear Energy, a section of the journal Frontiers in Energy Research

Received: *28 October 2021*
Accepted: *01 December 2021*
Published: *05 January 2022*

Citation:
Gong H, Chen Z and Li Q (2022) Generalized Empirical Interpolation Method With H[1] Regularization: Application to Nuclear Reactor Physics. Front. Energy Res. 9:804018. doi: 10.3389/fenrg.2021.804018

1 INTRODUCTION AND PRELIMINARIES

In nuclear reactor simulations, data assimilation (DA) with reduced basis (RB) enables the reconstruction of the physical field, e.g., for constructing a fast/thermal flux and power field within a nuclear core in an optimal way based on neutronic transport/diffusion model and observations (Gong et al., 2016; Argaud et al., 2017a; Gong et al., 2017; Argaud et al., 2018; Gong, 2018). In practice, the existing methods are based on a reduced basis, however, this approach is not robust with respect to observation noise and there are some additional constraints or regularization on the low-dimensional subspaces, i.e., the related coefficients, have been proposed as possible remedies in several recent works (Argaud et al., 2017b; Gong et al., 2020; Gong et al., 2021). The idea of introducing box constraints was originally introduced in Argaud et al. (2017a) to stabilize the generalized empirical interpolation method in the presence of noise (Maday and Mula, 2013). The same idea has been applied to the POD basis and the background space (Gong et al., 2019) of the so-called parametrized-background data-weak (PBDW) data assimilation (Maday et al., 2015a). Recently, the regularization of the GEIM/POD coefficients has been studied in Gong et al. (2021). The corresponding theoretical analysis can be found in Gong (2018), Herzet et al. (2018), and Gong et al. (2019). This article introduces H^1 regularization schemes for the approximation, and numerical experiments in nuclear reactor physics indicate its potential to address this obstruction.

Our goal is to approximate the physical state u from a given compact set $\mathcal{M} \subset \mathcal{X}$ (manifold), which represents the possible state of a physical system taking place in Ω. Where $\mathcal{X}$ is a Banach space over a domain $\Omega \subset \mathbb{R}^d$ $(d \geq 1)$ being equipped with the norm $\|.\|_{\mathcal{X}}$. In the framework of data assimilation with reduced basis, any $u \in \mathcal{M}$ can be estimated by combining two parts. The first term

is a certain amount (m) of observation of u acquired directly from sensors of the underline physical system, which can be represented by a combination of linear functionals of $\mathcal{X}'$ (the dual space of $\mathcal{X}$) evaluated on u. The second term is the use of a family of (reduced) subspaces $\mathcal{Z}_n$ of finite dimension n which is assumed to approximate well with the manifold $\mathcal{M}$ in a given accuracy.

The algorithms used to build the reduced subspace $\{\mathcal{Z}_n\}_n$ and find appropriate linear functionals have already been reported in the community of reduced modeling [see Maday and Mula, 2013; Maday et al., 2015b; Maday et al., 2015c; Maday et al., 2016]. Note that even if this is not necessary in the previous statements, the construction of the reduced spaces $\mathcal{Z}_n$ could be recursive, i.e., we have $\mathcal{Z}_{n-1} \subset \mathcal{Z}_n$. The field $u \in \mathcal{M}$ can be approximated by interpolation (Argaud et al., 2018) or data assimilation (Gong, 2018; Gong et al., 2019).

For reading convenience, let us first introduce some notations used throughout this article. We first introduces the standard $L^2(\Omega)$ or $\mathcal{H}$ Hilbert space over the special domain $\Omega \subset \mathbb{R}^d$ equipped with an inner product $(w, v)_{L^2(\Omega)} \equiv \int_\Omega wvdx$ and the induced norm $\|w\|_{L^2(\Omega)} = \sqrt{(w, w)_{L^2(\Omega)}}$. The semi-norm H^1 is defined by $|w|_{H^1(\Omega)} = \sqrt{(\nabla w, \nabla w)_{H^1(\Omega)}}$, where the inner product is $(w, v)_{H^1(\Omega)} \equiv \int_\Omega \nabla w \nabla v dx$. For a given Hilbert space $\mathcal{U}$ and the related dual space $\mathcal{U}'$, the Riesz operator $R_{\mathcal{U}}$: $\mathcal{U}' \to \mathcal{U}$ satisfies: for any given $\ell \in \mathcal{U}'$, we have $(R_{\mathcal{U}}\ell, v) = \ell(v), \forall v \in \mathcal{U}$.

Let us denote by $u(\boldsymbol{r}; \mu)$ the solution of a parameter-dependent partial differential equation (PDE) set on Ω and on a closed parametric domain $\mathcal{D} \subset \mathbb{R}^p$. For any given $\mu \in \mathcal{D}$, the physical field $u(\boldsymbol{r}; \mu)$ belongs to $\mathcal{U} \subset L^2(\Omega)$ or $H^1(\Omega)$, a functional space derived from the PDE. We call the set $\mathcal{M} \equiv \{u(\boldsymbol{r}; \mu); \mu \in \mathcal{D}\}$ of all parameter-dependent solution manifold. Let $\mathcal{L}_M$: $\mathcal{U} \to \mathbb{R}^M$ be the vector-valued observation functional $\mathcal{L}_M(u) = (\ell_1(u), \ldots, \ell_M(u))^T$ of $u \in \mathcal{U}$.

2 FIELD RECONSTRUCTION WITH REGULARIZATION

Our goal in this work is to infer any state $u \in \mathcal{U}$ over a spacial domain $\Omega \in \mathbb{R}^d$ given only some corresponding noisy observations $\boldsymbol{y} = (y_1^{obs}, \ldots, y_M^{obs})^T$. This empirical learning problem from a limited data set is always underdetermined. In general, with observation noise, a regularization term $R(u)$ is added to the loss function, and then a general convex model fitting problem can be written in the form:

$$\underset{u \in \mathcal{U}}{\text{minimize}} \; J(u) \coloneqq V(\mathcal{L}(u), \boldsymbol{y}) + \lambda R(u), \tag{2.1}$$

where V: $\mathbb{R}^M \to \mathbb{R}$ is a convex loss function that describes the cost of predicting u when the observation is $\boldsymbol{y}$. λ is a parameter which presents the importance of the regularization term. $R(u)$ is usually a convex regularization function to impose a penalty on the complexity of u through some prior knowledge.

2.1 H^1 Regularization

The goal of regularization is to prevent overfitting or to denoise in mathematics and particularly in the fields of inverse problems (Ivanov, 1976; Andreui et al., 1977; Balas, 1995; Arnold, 1998; Vladimir, 2012; Benning and Burger, 2018), by introducing additional information in order to solve ill-posed problems. From a *Bayesian* (James Press, 1989) point of view, regularization techniques correspond to introduce some prior distributions on model parameters. The general choice of $R(u)$ is a norm-like form $\|u\|_\chi^2$, where χ represents different kinds of norm depending on the underlying application. The simplest choice of $R(u)$ is L^2 norm, say, $\|u\|_{L^2(\Omega)}^2$, which has been well studied in the literature, either from a theoretical or algorithmic point of view. The regularization is also called *Tikhonov regularization* (Andreui et al., 1977), which is essentially a trade-off between fitting the data and reducing the norm of the solution. For some real-world problems, there has been much interest in alternative regularization terms. For example, total variation (TV) regularization, $R(u) = \|\nabla u\|_{L^1(\Omega)}$, is popular in image reconstruction or other domains (Rudin et al., 1992; Rudin et al., 1992; Chan et al., 1997; Chan and Tai, 2003; Wachsmuth and Wachsmuth, 2011; De los Reyes and Schönlieb, 2012). By using a L^1 norm, sharp edges would be allowed as the penalty is finite, and it also allows discontinuous controls which can be important in certain applications.

If one would like to impose a smooth control, the H^1 semi-norm can be used:

$$R(u) = \|\nabla u\|_{L^2(\Omega)}. \tag{2.2}$$

Examples can be found in the context of parameter estimation problems (Keung and Zou, 1998; Cai et al., 2008; Wilson et al., 2009; Barker et al., 2016), image-deblurring (Chan et al., 1997; Li et al., 2010; Cimrák and Melicher, 2012), image reconstruction (Ng et al., 2000), and flow control (Heinkenschloss, 1998; Collis et al., 2001). The work in Van Den Doel et al. (2012) shows that the proposed H^1 semi-norm regularization performs better than L^1 regularization cousin, total variation, for problems with very noisy data due to the smooth nature of controlled variables. The authors in Srikant did a comparison of H^1 and TV regularization methods and also studied the shortcomings and limitations of some of the implementations schemes, such as a Gaussian filter. H^1 regularization would perform well over uniform regions in the domain but would perform poorly over edges. Furthermore, to solve the PDE-constrained optimization problem as reported in Haber and Hanson (2007), the authors suggested a synthetic regularization functional of the form:

$$R(u) = \|u\|_{L^2(\Omega)}^2 + \gamma \|\nabla u\|_{L^2(\Omega)}, \tag{2.3}$$

where the parameter γ can be adapted. Note that this synthetic regularization is now commonly used to solve the ill-posed inverse problems.

2.2 Generalized Empirical Interpolation Method

Recall that our goal is to estimate the state $u^{true}[\mu] \in \mathcal{U}$ of a physical system for a given parameter $\mu \in \mathcal{D}$, by using a

parameterized best-knowledge model and M (potentially noisy) observations.

The first step is to choose a sequence of n-dimensional subspaces $\{\mathcal{Z}_n\}_n$ such that the best approximation of any given $u^{true}[\mu]$ in the space $\mathcal{Z}_n$ converges to zero when n goes to infinity, i.e.,

$$\lim_{n\to\infty} \inf_{w\in\mathcal{Z}_n} \|u^{true}[\mu] - w\| \le \epsilon_{\mathcal{Z}} \quad \forall \mu \in \mathcal{D} \tag{2.4}$$

for an acceptable tolerance $\epsilon_{\mathcal{Z}}$. We further assume that the selected subspaces satisfy

$$\mathcal{Z}_1 \subset \cdots \subset \mathcal{Z}_{N_{max}} \subset \cdots \subset \mathcal{U}. \tag{2.5}$$

In other words, we choose the subspaces such that the most dominant physical system is well represented for a relatively small n. In particular, these subspaces may be constructed through the application of model reduction methods to a parameterized PDE.

The second step is to model the data acquisition procedure. Given a system in of a parameter $\mu \in \mathcal{D}$, we assume the observations are of the form

$$\forall m = 1, \ldots, M, \quad y_m^{obs}[\mu] = \ell_m(u^{true}[\mu]) + e_m, \tag{2.6}$$

where $y_m^{obs}[\mu]$ is the value of the mth observation, ℓ_m is the linear functional associated with the mth sensor, and e_m is the observation noise associated with the mth sensor. The detailed form of the functional ℓ_m depends on the specific sensor used to acquire data. For example, if the sensor measures a local value of the state, then we may model the observation value as Gaussian convolution

$$\ell_m(v) \equiv \int_\Omega \left((2\pi r_m^2)^{-d/2} \exp\left(-\frac{\|x - x_m^c\|^2_{\ell^2(\mathbb{R}^d)}}{2r_m^2} \right) \right) v(x)dx, \tag{2.7}$$

where $(2\pi r_m^2)^{-d/2}\exp(-\frac{\|x-x_m^c\|^2_{\ell^2(\mathbb{R}^d)}}{2r_m^2})$ is a Gaussian distributed function to present the response of the sensor for a given physical field v, and $x_m^c \in \mathbb{R}^d$ is the center of the sensor in the special domain Ω, and $r_m \in \mathbb{R}_{>0}$ is the physical width of the sensor. In particular, the localized sensor is of interest in this work.

We assume that e_m is independent and identically distributed (IID), and with a density of p_m on $\mathbb{R}$. In practice, the mean and covariance of the observation data acquired are more readily quantifiable than the distribution p_m. Thus, we assume the mean and the covariance of the distribution exist and make the following assumptions on the noise term: (i) zero mean: $E[e_m] = 0$, $m = 1, \ldots, M$; (ii) variance: $E[e_m^2] = \sigma_m^2$, $m = 1, \ldots, M$; (iii) and uncorrelated: $E[e_m e_n] = 0$, $m \neq n$.

By running the greedy algorithm of the so-called generalized empirical interpolation method [GEIM (Maday and Mula, 2013)], a set of basis $\{q_n\}_n$ is generated and spanned the reduced space $\mathcal{Z}_n = \text{span}\{q_1, \ldots, q_n\}$. Then, the generalized interpolation process is well defined as follows:

$$\mathcal{I}_N[u] = \sum_{j=1}^N \alpha_j q_j \quad \text{subject to: } \forall i = 1, \ldots, M,\ \ell_i(\mathcal{I}_N[u]) = \ell_i(u). \tag{2.8}$$

With noisy observations, GEIM is, however, not robust with respect to observation noise (Argaud et al., 2017b), and in that work, a so-called constrained stabilized GEIM (CS-GEIM) by using a constrained least squares approximation was proposed to address this obstruction, where numerical experiments indicate its potential.

3 H^1 REGULARIZATION FORMULATION OF GEIM

Now, we state the H^1 regularization scheme for GEIM (R-GEIM). Given a reduced space $\mathcal{Z}_N = \text{span}\{q_1, \ldots, q_N\} \subset \mathcal{U}$ of dimension N spanned by N basis $\{q_i\}_{i=1}^N$ and M measurement functionals $\mathcal{L}_M \coloneqq (\ell_1, \ldots, \ell_M)^T$ and the corresponding noisy measurements $\boldsymbol{y} = (y_1^{obs}, \ldots, y_M^{obs})^T$, $M \ge N$, then the reconstruction problem from measurements is: find $u \in \mathcal{Z}_N$ such that:

$$u = \underset{u\in\mathcal{Z}_N}{\text{argmin}}\ V(\mathcal{L}(u), \boldsymbol{y}) + \xi\|\nabla u\|^2_{L^2(\Omega)}, \tag{3.1}$$

where $V: \mathbb{R}^M \to \mathbb{R}$ is loss function that evaluates the cost of estimating u giving the observation $\boldsymbol{y}$ which depends on the underlying application. The symbol "*argmin*" is argument of the minimum, thus $argmin\, f(u)$ is the value of u for which $f(u)$ attains its minimum. The parameter ξ is a trade-off factor between the regularization term and the loss function term. Furthermore, if we have no information about the noise distribution, three proposed typical forms of V could be $\|\mathcal{L}(u) - \boldsymbol{y}\|_l^2$,, where $l = \infty$, 1, 2. For the above R-GEIM, we have the following remarks:

- The basis and measurements of the chosen scheme could be based on GEIM, POD, or any other approach.
- Later, we will show that $l = 2$ corresponds to the least squares method, and $l = 1$ corresponds to the least absolute deviations (LAD) (Bloomfield and Steiger, 1980). Compared to the traditional least squares method, the LAD is much robust and finds its applications in many areas.
- By using the H^1 regularization for the reduced basis field reconstruction, the first assumption is that the field u is in H^1 space; for the most regular physical problem, this condition is satisfied automatically, and the H^1 regularization term is a kind of smooth control for the underlying field reconstruction problem.

If we have no prior information about noise, a commonly used way to formulize **Eq. 3.1** is taking 2 norm for the loss function term, we have the following results:

R-GEIM: Given a reduced space $\mathcal{Z}_N = \text{span}\{q_1, \ldots, q_N\} \subset \mathcal{U}$ of dimension N spanned by N basis $\{q_i\}_{i=1}^N$ and $M(\ge N)$ measurement functionals $\mathcal{L}_M \coloneqq (\ell_1, \ldots, \ell_M)^T$ and the

corresponding noisy measurements $\boldsymbol{y} = (y_1^{obs}, \ldots, y_M^{obs})^T$, then the reconstruction problem from measurements is: find $u \in \mathcal{Z}_N$ such that:

$$u = \underset{u \in \mathcal{Z}_N}{\operatorname{argmin}} \ \frac{1}{M}\|\mathcal{L}(u) - \boldsymbol{y}\|_2^2 + \xi\|\nabla u\|_{L^2(\Omega)}^2. \tag{3.2}$$

Let $\mathbb{M}$ be an $M \times N$ full-column rank matrix with elements $\mathbb{M}_{i,j} = \ell_i(q_j)$, $i = 1, \ldots, M$, $j = 1, \ldots, N$ and $\mathbb{N}$ be an $N \times N$ matrix with elements $\mathbb{N}_{i,j} = (\nabla q_i, \nabla q_j)$, $i, j = 1, \ldots, N$, then the algebraic form of **Eq. 3.2** is: find $\boldsymbol{\alpha} = (\alpha_1, \ldots, \alpha_N)^T \in \mathbb{R}^N$ or $v = \sum_{j=1}^N \alpha_j q_j \in \mathcal{Z}_N$ such that:

$$\boldsymbol{\alpha}^* = \arg\min_{\boldsymbol{\alpha} \in \mathbb{R}^N} \ (\mathbb{M}\boldsymbol{\alpha} - \boldsymbol{y})^T(\mathbb{M}\boldsymbol{\alpha} - \boldsymbol{y}) + M\xi\boldsymbol{\alpha}^T\mathbb{N}\boldsymbol{\alpha}, \tag{3.3}$$

the solution is

$$\boldsymbol{\alpha}^* = (\mathbb{M}^T\mathbb{M} + M\xi\mathbb{N})^{-1}\mathbb{M}^T\boldsymbol{y}. \tag{3.4}$$

Proof. Let $J(\boldsymbol{\alpha}, \boldsymbol{y}) = (\mathbb{M}\boldsymbol{\alpha} - \boldsymbol{y})^T(\mathbb{M}\boldsymbol{\alpha} - \boldsymbol{y}) + M\xi\boldsymbol{\alpha}^T\mathbb{N}\boldsymbol{\alpha}$, then we have:

$$\nabla J(\boldsymbol{\alpha}, \boldsymbol{y}) = 2\mathbb{M}^T\mathbb{M}\boldsymbol{\alpha} + 2M\xi\mathbb{N}\boldsymbol{\alpha} - 2\mathbb{M}^T\boldsymbol{y},$$

the solution to minimize $J(\boldsymbol{\alpha},\boldsymbol{y})$ is the $\boldsymbol{\alpha}*$ that satisfies $\nabla J(\boldsymbol{\alpha}*,\boldsymbol{y}) = 0$. Because, $\mathbb{M}$ is an $M \times N$ full-column rank matrix, so that $\mathbb{M}^T\mathbb{M}$ is a symmetric positive definite (SPD) matrix.From the definition of $\mathbb{N}$, it is a symmetric positive semi-definite matrix, so $\mathbb{M}^T\mathbb{M} + M\xi\mathbb{N}$ is an $N \times N$ invertible matrix, which completes the proof.

Let $\mathbb{D}$ be the $M \times M$ covariance matrix of the measurement with elements $\mathbb{D}_{i,j} = E[e_i e_j]$, $i, j = 1, \ldots, M$. If e_m is uncorrelated, $\mathbb{D}_{i,j} = 0$ for $i \neq j$, then $\mathbb{D}$ is a diagonal matrix with $\mathbb{D}_{i,i} = \sigma_i^2$ and the variance of the ith measurement, **Eq. 3.3** can be improved by

$$\boldsymbol{\alpha}^* = \underset{\boldsymbol{\alpha} \in \mathbb{R}^N}{\operatorname{argmin}} \ (\mathbb{M}\boldsymbol{\alpha} - \boldsymbol{y})^T\mathbb{D}^{-1}(\mathbb{M}\boldsymbol{\alpha} - \boldsymbol{y}) + M\xi\boldsymbol{\alpha}^T\mathbb{N}\boldsymbol{\alpha}, \tag{3.5}$$

and the solution is

$$\boldsymbol{\alpha}^* = (\mathbb{M}^T\mathbb{D}^{-1}\mathbb{M} + M\xi\mathbb{N})^{-1}\mathbb{M}^T\mathbb{D}^{-1}\boldsymbol{y}. \tag{3.6}$$

Later, we will show this is also the algebraic formulation for Gaussian noise with covariance $\mathbb{D}$. If we can make use of the prior information of noise, we have the following remark:

Remark. Let $r(u)$ be the bias of the reduced model from the truth $\mathcal{L}(u) - \boldsymbol{y} = \boldsymbol{e} + r(u)$. By using maximum likelihood (ML) estimation for the following common noise densities, we have:

- Uniform noise, when the noise term e_m is uniformly independent and identically distributed on $(-e_0, e_0)$, then the reconstruction problem is: find $u \in \mathcal{Z}_N$ such that:

$$u = \underset{u \in \mathcal{Z}_N}{\operatorname{argmin}} \ \|\nabla u\|_{L^2(\Omega)}^2, \quad \text{subject to } \|\mathcal{L}(u) - \boldsymbol{y}\|_\infty \leq e_0 + \|r(u)\|_\infty. \tag{3.7}$$

If the noise bounds are different for different measurements, the constraint in **Eq. 3.7** becomes $|\ell_m(u) - y_m^{obs}| \leq e_m + |r_m(u)|, m = 1, \ldots, M$.

- Gaussian noise, when the noise e_m is Gaussian with the zero mean and covariance matrix $\mathbb{D}$, then the reconstruction problem is: find $u \in \mathcal{Z}_N$ such that

$$u = \underset{u \in \mathcal{Z}_N}{\operatorname{argmin}} \ (\mathcal{L}(u) - \boldsymbol{y})^T\mathbb{D}^{-1}(\mathcal{L}(u) - \boldsymbol{y}) + M\xi\|\nabla u\|_{L^2(\Omega)}^2. \tag{3.8}$$

- Laplacian noise, when the noise e_m is Laplacian independent, identically distributed with density $p(e) = \frac{1}{2e_0}e^{-|e|/e_0}$, then the reconstruction problem is: find $u \in \mathcal{Z}_N$ such that

$$u = \underset{u \in \mathcal{Z}_N}{\operatorname{argmin}} \ \|\mathcal{L}(u) - \boldsymbol{y}\|_1^2 + \xi\|\nabla u\|_{L^2(\Omega)}^2. \tag{3.9}$$

We refer readers to Boyd and Vandenberghe (2004) for further theoretical analysis on this remark. Through this remark, the physical means of the term $\|\mathcal{L}(u) - \boldsymbol{y}\|_l^2$ in **Eq. 3.1** for different l is easier to understand. The ∞, 1, and 2 norms interpret the maximum likelihood estimation with a noise density, that is, uniform, Laplacian, and Gaussian, respectively. Considering for the most engineering problems, the noise density is Gaussian and also bounded, and thus we only present numerical results of uniform noise and Gaussian noise in this work.

Another remark is that, in this work, numerical results are illustrated based on GEIM, more precisely. The reduced basis in **Eq. 3.2** is derived with GEIM, but this regularization is fit for the POD basis or the basis selected from the greedy reduced basis method (Grepl et al., 2007) without any modification.

4 NUMERICAL RESULTS AND ANALYSIS

In this section, we illustrate the performance of R-GEIM on a typical benchmark problem in nuclear reactor physics. The test example is adapted based on the classical 2D IAEA benchmark problem (Benchmark Problem Book, 1977; Gong et al., 2017); the geometry of the 2D core is shown in **Figure 1**. This problem represents the mid-plane $z = 190\ cm$ of the 3D IAEA benchmark problem, that is used by references (Theler et al., 2011). The reactor spacial domain is Ω = region (1, 2, 3, 4). The core and control regions are Ω_{core} = region (1, 2, 3) and $\Omega_{control}$ = region (3), respectively. We consider the value of $\Sigma_{a,2}|_{\Omega_1}$, $\Sigma_{a,2}|_{\Omega_2}$, and $\Sigma_{a,2}|_{\Omega_3}$ in the core region $\Omega_{1,2,3}$ as a parameter (so $p = 3$ and $\mu = [\Sigma_{a,2}|_{\Omega_1}, \Sigma_{a,2}|_{\Omega_2}, \Sigma_{a,2}|_{\Omega_3}]$). We assume that $\Sigma_{a,2}|_{\Omega_i} \in [0.080, 0.150]$ for $i = 1, 2, 3$. The rest of the coefficients of the diffusion model are fixed to the values indicated in **Table 1** of Gong et al. (2017).

The neutronic field (fast and thermal flux, power distribution) is derived by solving two group diffusion equations. The numerical algorithm is implemented by employing the free finite elements solver FreeFem++ (Hecht, 2012). The norm $\|\cdot\|_{L^2(\Omega)}$ is induced by the inner product $(w, v)_{L^2(\Omega)} = \int_\Omega wv dx$, and the semi-norm $\|\cdot\|_{H^1(\Omega)}$ is induced by the inner product $(w, v)_{H^1(\Omega)} = \int_\Omega \nabla w \nabla v dx$. The measurement we employed here is same as **Eq. 2.7** with $r_m = 1$ cm and set $\{w_i\}_{i=1}^N$ being the corresponding Riesz representation with H^1 inner product. Finally, we set the finite element size

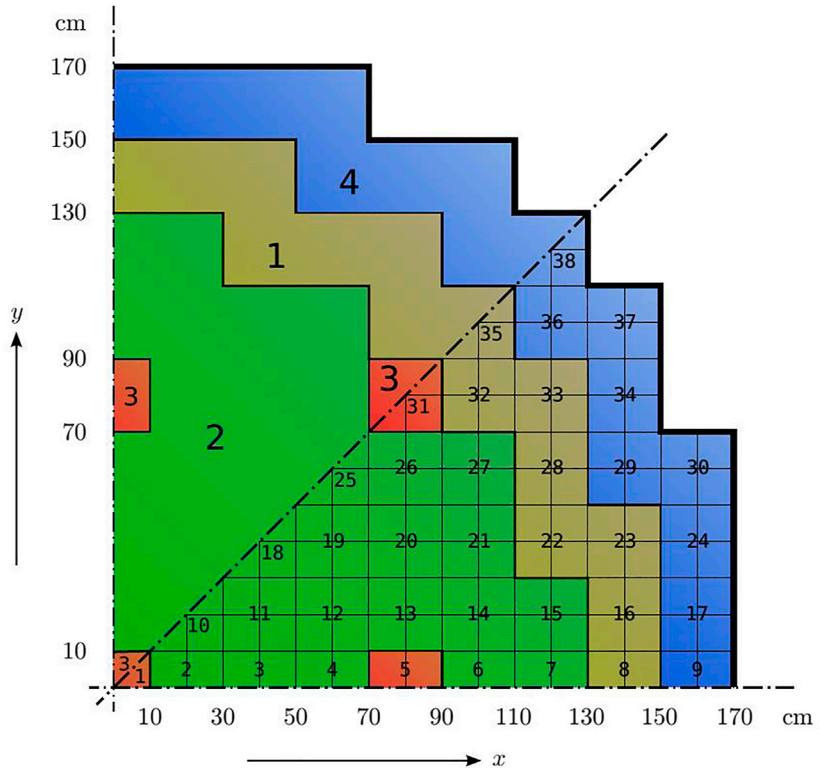

FIGURE 1 | Geometry of a 2D IAEA benchmark. Upper octant: region assignments; lower octant: fuel assembly identification [from reference (Benchmark Problem Book, 1977; Theler et al., 2011)].

TABLE 1 | Coefficient value: diffusion coefficients D_i (in cm) and macroscopic cross sections (in cm^{-1}).

Region	D_1	D_2	$\Sigma_{1\to2}$	Σ_{a1}	Σ_{a2}	$\nu\Sigma_{f2}$	Material[a]
1	1.5	0.4	0.02	0.01	0.080	0.135	Fuel 1
2	1.5	0.4	0.02	0.01	0.085	0.135	Fuel 2
3	1.5	0.4	0.02	0.01	0.130	0.135	Fuel 2 + rod
4	[1.0,3.0] or 2.0[b]	0.3	0.04	0	0.010	0	Reflector

[a] *Axial bucking $B^2_{zg} = 0.8 \cdot 10^{-4}$ for all regions and energy groups*
[b] *Here 2.0 is the exact value from Reference (Theler et al., 2011).*

to $d = 0.1$ cm, which is enough for our analysis. We refer to Argaud et al. (2017b) for detailed implementation of this problem with FreeFem++.

The regularization factor ξ is essential for R-GEIM. It can significantly affect the reconstruction error of R-GEIM, and if they are incorrectly specified then the field reconstructed with R-GEIM is suboptimal. We show the variation of the errors in L^∞, H^1, and L^2 norms for R-GEIM with respect to different regularization factors ξ in **Figure 2**. The dimension of reduced basis is fixed to $n = 80$, the number of measurements is set to $m =$

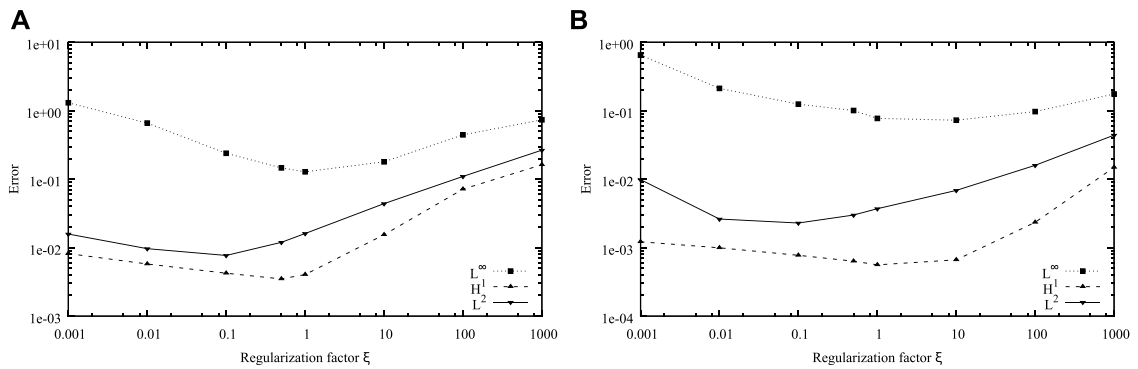

FIGURE 2 | Variation of the errors in L^∞, H^1, and L^2 norms for R-GEIM with respect to the different regularization factor ξ. The reduced dimension is $n = 80$, number of measurement is $m = 2n$, and the observation noise is uniformly distributed with noise levels 10^{-2} **(A)** and 10^{-3} **(B)**.

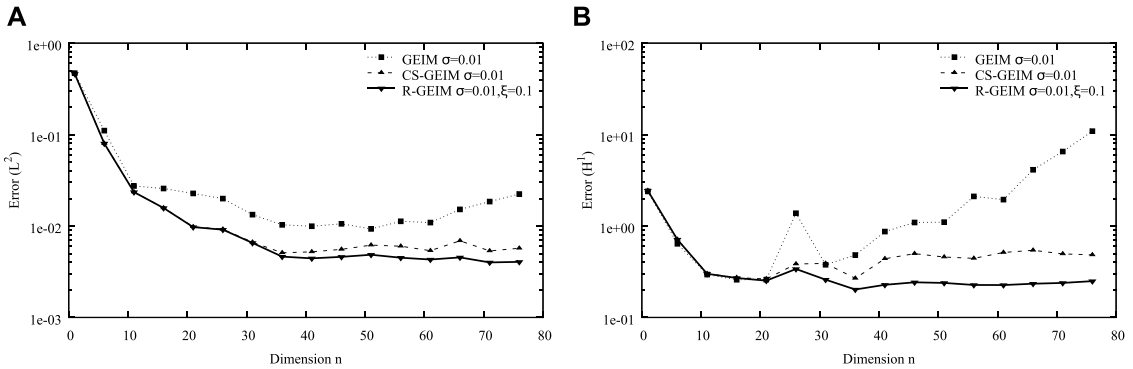

FIGURE 3 | The variation of the errors in L^2 norm **(A)** H^1 norm **(B)** for GEIM, CS-GEIM, and R-GEIM with respect to different reduced dimension n. The number of measurement is $m = 2n$, and the observation noise is uniformly distributed with a noise level $\sigma = 10^{-2}$.

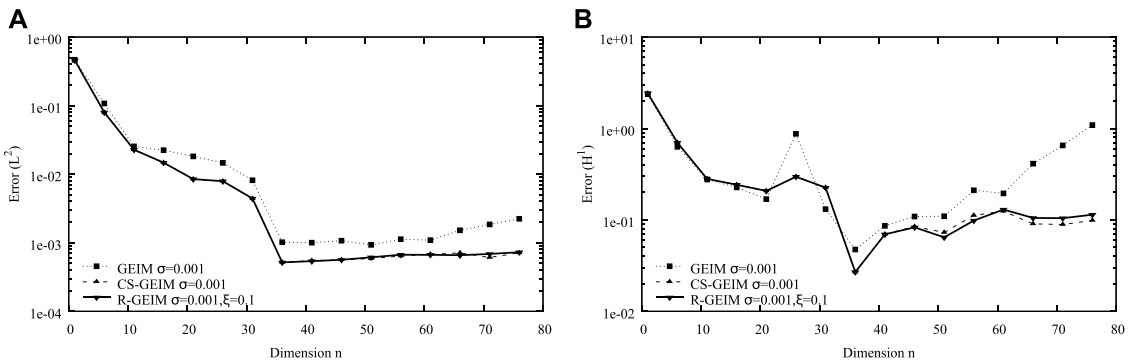

FIGURE 4 | Variation of the errors in L^2 norm **(A)** and H^1 norm **(B)** for GEIM, CS-GEIM, and R-GEIM with respect to different reduced dimension n. The number of measurement is $m = 2n$, and the observation noise is uniformly distributed with a noise level $\sigma = 10^{-3}$.

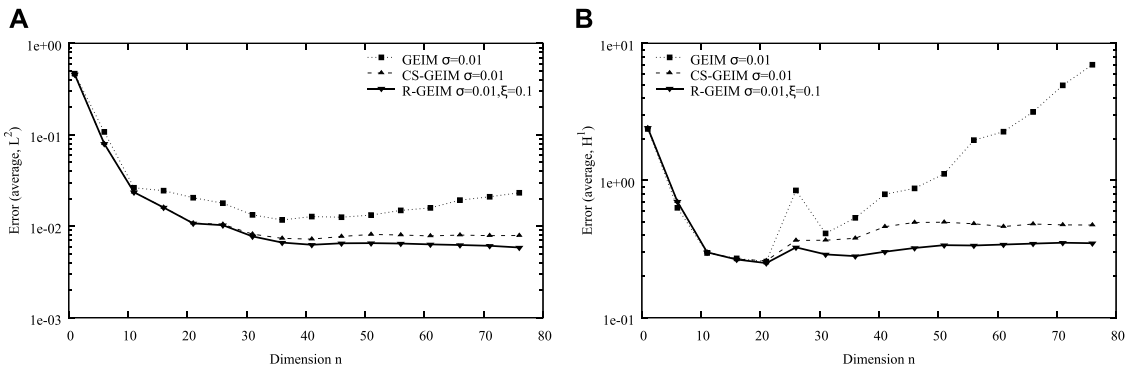

FIGURE 5 | Variation of the errors in L^2 norm **(A)** and H^1 norm **(B)** for GEIM, CS-GEIM, and R-GEIM with respect to different reduced dimension n. The number of measurement is $m = 2n$, and the observation noise is Gaussian distributed with a noise level $\sigma = 10^{-2}$.

$2n$, and the observation noise is uniformly distributed, with a noise level $\sigma = 10^{-2}$, 10^{-3}. It can be observed that the optimal ξ is different for different error metrics. For the errors evaluated in L^2 norm, the optimal $\xi_{op} \sim 0.1$, and for L^∞ norm or H^1 norm, the optimal $\xi_{op} \sim 1$. In the left of this work, we fix ξ to be the optimal value and evaluate the errors in L^2 norm and H^1 norm, which reflect the average error of the reconstructed field itself and its gradient.

This section illustrates the behavior of GEIM, CS-GEIM, and R-GEIM, in case of noisy observations. We first show the variation of the errors in L^2 norm and H^1 norm for GEIM,

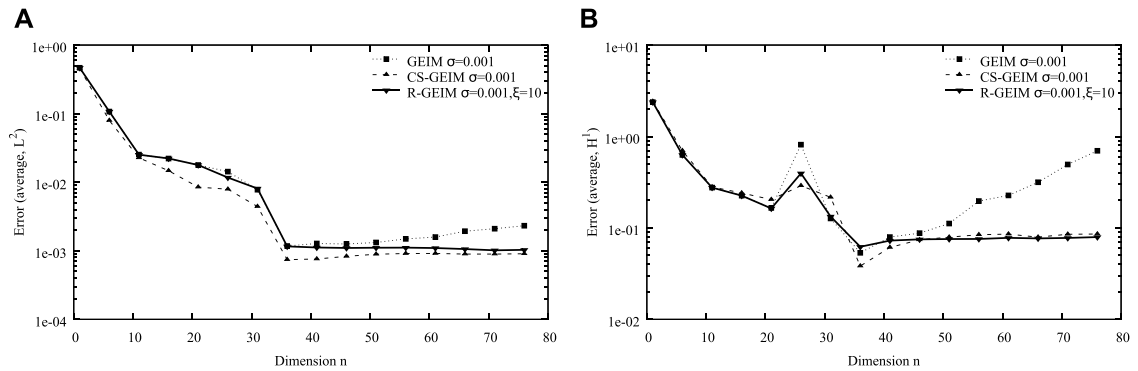

FIGURE 6 | Variation of the errors in L^2 norm **(A)** and H^1 norm **(B)** for GEIM, CS-GEIM, and R-GEIM with respect to different reduced dimension n. The number of measurement is $m = 2n$, and the observation noise is Gaussian distributed with a noise level $\sigma = 10^{-3}$.

CS-GEIM, and R-GEIM with respect to different reduced dimensions n in **Figure 3**. The observation noise is assumed to be uniformly distributed, with a noise level $\sigma = 10^{-2}$. The number of measurements is $m = 2n$. **Figure 4** illustrates the case for the noise level $\sigma = 10^{-3}$. The cases with Gaussian-distributed observation noise are shown in **Figure 5** for the noise level $\sigma = 10^{-2}$ and in **Figure 6** for the noise level 10^{-3}.

From these figures, we can conclude that R-GEIM shows a better stability performance in the case of noisy measurement. The accuracy can be as good as CS-GEIM, but the R-GEIM algorithm is much simpler, with relatively low computational cost; the main cost for the online stage is to solve the matrix system **Eq. 3.4**. But for CS-GEIM, the relative complex constrained quadratic programming problem has to be solved.

5 CONCLUSION AND FUTURE WORKS

The traditional generalized empirical interpolation method is well studied for data assimilation in many domains. However, this reduced modeling-based data assimilation method is not robust with respect to observation noise. We propose addressing this issue by imposing a smooth constraint, namely, an H^1 semi-norm of the reconstructed field to involve some prior knowledge of the noise. The efficiency of the approach, which we call R-GEIM, is illustrated by an IAEA benchmark numerical experiment, dealing with the reconstruction of the neutronic field derived from neutron diffusion equations in nuclear reactor physics. With H^1 regularization, the behavior of the reconstruction is improved in the case of noisy observation. Further works are ongoing: i) mathematical analysis of the stable and accurate behavior of this regularization approach and ii) the regularization trade-off factor will be studied to give an outline on how to choose these factors for generic problems.

DATA AVAILABILITY STATEMENT

The raw data supporting the conclusion of this article will be made available by the authors, without undue reservation.

AUTHOR CONTRIBUTIONS

HG contributed to conceptualization, methodology, software, data curation, and writing—original draft and editing. ZC contributed to conceptualization. QL contributed to conceptualization, supervision, and review.

FUNDING

This work is supported by the National Natural Science Foundation of China (Grant No. 11905216 and Grant No. 12175220).

ACKNOWLEDGMENTS

The authors are grateful to three reviewers for the useful remarks on the manuscript.

REFERENCES

Andreui, N. T., Vasiliui, I. A., and Fritz, J. (1977). *Solutions of Ill-Posed Problems, Volume 14*. Washington, DC: Winston.

Argaud, J.-P., Bouriquet, B., Gong, H., Maday, Y., and Mula, O. (2017). "Stabilization of (G) EIM in Presence of Measurement Noise: Application to Nuclear Reactor Physics," in Spectral and High Order Methods for Partial Differential Equations ICOSAHOM 2016 (Berlin, Germany: Springer), 133–145.

Argaud, J.-P., Bouriquet, B., de Caso, F., Gong, H., Maday, Y., and Mula, O. (2018). Sensor Placement in Nuclear Reactors Based on the Generalized Empirical Interpolation Method. *J. Comput. Phys.* 363, 354–370. doi:10.1016/j.jcp.2018.02.050

Argaud, J. P., Bouriquet, B., Gong, H., Maday, Y., and Mula, O. (2017). *Stabilization of (G)EIM in Presence of Measurement Noise: Application to Nuclear Reactor*

Physics. Cham: Springer International Publishing, 133–145. doi:10.1007/978-3-319-65870-4_8

Arnold, N. (1998). Solving Ill-Conditioned and Singular Linear Systems: A Tutorial on Regularization. *SIAM Rev.* 40 (3), 636–666.

Balas, K. N. (1995). Sparse Approximate Solutions to Linear Systems. *SIAM J. Comput.* 24 (2), 227–234.

Barker, A. T., Rees, T., and Stoll, M. (2016). A Fast Solver for anH1Regularized PDE-Constrained Optimization Problem. *Commun. Comput. Phys.* 19 (1), 143–167. doi:10.4208/cicp.190914.080415a

Benchmark Problem Book (1977). *Computational Benchmark Problem Comitee for the Mathematics and Computation Division of the American Nuclear Society*. Argonne Code Center: Benchmark Problem Book.

Benning, M., and Burger, M. (2018). Modern Regularization Methods for Inverse Problems. *Acta Numerica* 27, 1–111. doi:10.1017/s0962492918000016

Bloomfield, P., and Steiger, W. (1980). Least Absolute Deviations Curve-Fitting. *SIAM J. Sci. Stat. Comput.* 1 (2), 290–301. doi:10.1137/0901019

Boyd, S., and Vandenberghe, L. (2004). *Convex Optimization*. Cambridge: Cambridge University Press.

Cai, X-C., Liu, S., and Zou, J. (2008). An Overlapping Domain Decomposition Method for Parameter Identification Problems. *Domain Decomposition Methods Sci. Eng. XVII* 2008, 451–458.

Chan, R. H., Chan, T. F., and Wan, W. L. (1997). Multigrid for Differential-Convolution Problems Arising from Image Processing. *Proc. Workshop Scientific Comput.* 1997, 58–72.

Chan, T. F., and Tai, X.-C. (2003). Identification of Discontinuous Coefficients in Elliptic Problems Using Total Variation Regularization. *SIAM J. Sci. Comput.* 25 (3), 881–904. doi:10.1137/s1064827599326020

Cimrák, I., and Melicher, V. (2012). Mixed Tikhonov Regularization in Banach Spaces Based on Domain Decomposition. *Appl. Maths. Comput.* 218 (23), 11583–11596.

Collis, S. S., Ghayour, K., Heinkenschloss, M., Ulbrich, M., and Ulbrich, S. (2001). Numerical Solution of Optimal Control Problems Governed by the Compressible Navier-Stokes Equations. *Int. Ser. Numer. Math.* 139, 43–55. doi:10.1007/978-3-0348-8148-7_4

De los Reyes, J-C., and Schönlieb, C-B. (2012). Image Denoising: Learning Noise Distribution via Pde-Constrained Optimization. *arXiv preprint arXiv:1207.3425*.

Gong, H., Argaud, J.-P., Bouriquet, B., and Maday., Y. (2016). "The Empirical Interpolation Method Applied to the Neutron Diffusion Equations with Parameter Dependence," in Proceedings of PHYSOR.

Gong, H., Argaud, J. P., Bouriquet, B., Maday, Y., and Mula, O. (2017). "Monitoring Flux and Power in Nuclear Reactors with Data Assimilation and Reduced Models," in International Conference on Mathematics and Computational Methods Applied to Nuclear Science and Engineering (M&C 2017), Jeju, Korea.

Gong, H. (2018). "Data Assimilation with Reduced Basis and Noisy Measurement: Applications to Nuclear Reactor Cores," (Paris, France: Sorbonne University). PhD thesis.

Gong, H., Maday, Y., Mula, O., and Tommaso, T. (2019). Pbdw Method for State Estimation: Error Analysis for Noisy Data and Nonlinear Formulation. *arXiv preprint arXiv:1906.00810*.

Gong, H., Chen, Z., Maday, Y., and Li, Q. (2021). Optimal and Fast Field Reconstruction with Reduced Basis and Limited Observations: Application to Reactor Core Online Monitoring. *Nucl. Eng. Des.* 377, 111113. doi:10.1016/j.nucengdes.2021.111113

Gong, H., Yu, Y., and Li, Q. (2020). Reactor Power Distribution Detection and Estimation via a Stabilized Gappy Proper Orthogonal Decomposition Method. *Nucl. Eng. Des.* 370, 110833. doi:10.1016/j.nucengdes.2020.110833

Grepl, M. A., Maday, Y., Nguyen, N. C., and Patera, A. T. (2007). Efficient Reduced-Basis Treatment of Nonaffine and Nonlinear Partial Differential Equations. *Esaim: M2an* 41 (3), 575–605. doi:10.1051/m2an:2007031

Haber, E., and Hanson, L. (2007). *Model Problems in PDE-Constrained Optimization. Report*. Atlanta, GA, USA: Emory University.

Hecht, F. (2012). New Development in FreeFem++. *J. Numer. Math.* 20 (3-4), 251–265. doi:10.1515/jnum-2012-0013

Heinkenschloss, M. (1998). "Formulation and Analysis of a Sequential Quadratic Programming Method for the Optimal Dirichlet Boundary Control of Navier-Stokes Flow," in *Optimal Control, Theory, Algorithms, and Applications* (Alphen aan den Rijn, Netherlands: Kluwer Academic Publishers BV). doi:10.1007/978-1-4757-6095-8_9

Herzet, C., Diallo, M., and Héas, P. (2018). An Instance Optimality Property for Approximation Problems with Multiple Approximation Subspaces. *hal-01913339*.

Ivanov, A. A. (1976). *The Theory of Approximate Methods and Their Applications to the Numerical Solution of Singular Integral Equations, Volume 2*. Berlin, Germany: Springer Science & Business Media.

James Press, S. (1989). *Bayesian Statistics: Principles, Models, and Applications, Volume 210*. Hoboken, NJ, USA: John Wiley & Sons.

Keung, Y. L., and Zou, J. (1998). Numerical Identifications of Parameters in Parabolic Systems. *Inverse Probl.* 14 (1), 83–100. doi:10.1088/0266-5611/14/1/009

Li, F., Shen, C., and Li, C. (2010). Multiphase Soft Segmentation with Total Variation and H 1 Regularization. *J. Math. Imaging Vis.* 37 (2), 98–111. doi:10.1007/s10851-010-0195-5

Maday, Y., and Mula, O. (2013). "A Generalized Empirical Interpolation Method: Application of Reduced Basis Techniques to Data Assimilation," in *Analysis and Numerics of Partial Differential Equations* (Berlin, Germany: Springer), 221–235. doi:10.1007/978-88-470-2592-9_13

Maday, Y., Mula, O., and Turinici, G. (2016). Convergence Analysis of the Generalized Empirical Interpolation Method. *SIAM J. Numer. Anal.* 54 (3), 1713–1731. doi:10.1137/140978843

Maday, Y., Patera, A. T., Penn, J. D., and Yano, M. (2015). A Parameterized-Background Data-Weak Approach to Variational Data Assimilation: Formulation, Analysis, and Application to Acoustics. *Int. J. Numer. Meth. Engng* 102 (5), 933–965. doi:10.1002/nme.4747

Maday, Y., T, A., Penn, J. D., and Yano, M. (2015). PBDW State Estimation: Noisy Observations; Configuration-Adaptive Background Spaces; Physical Interpretations. *Esaim: Proc.* 50, 144–168. doi:10.1051/proc/201550008

Maday, Y., T, A., Penn, J. D., and Yano, M. (2015). Pbdw State Estimation: Noisy Observations; Configuration-Adaptive Background Spaces; Physical Interpretations. *Esaim: Proc.* 50, 144–168. doi:10.1051/proc/201550008

Ng, M. K., Chan, R. H., Chan, T. F., and Yip, A. M. (2000). Cosine Transform Preconditioners for High Resolution Image Reconstruction. *Linear Algebra its Appl.* 316 (1-3), 89–104. doi:10.1016/s0024-3795(99)00274-8

Rudin, L. I., Stanley, O., and Fatemi, E. (1992). Nonlinear Total Variation Based Noise Removal Algorithms. *Physica D: Nonlinear Phenomena* 60 (1-4), 259–268. doi:10.1016/0167-2789(92)90242-f

Srikant, K. I. (0000). *Comparison of H1 and Tv De-noising Schemes and Their Implementation*.

Theler, G., Bonetto, F. J., and Clausse, A. (2011). Solution of the 2D IAEA PWR Benchmark with the Neutronic Code Milonga. *Actas de la Reunión Anual de la Asociación Argentina de Tecnología Nucl.* XXXVIII.

Van Den Doel, K., Ascher, U., and Haber, E. (2012). The Lost Honour of L2-Based Regularization. *Large Scale Inverse Problems, Radon Ser. Comput. Appl. Math.* 13, 181–203.

Vladimir, A. M. (2012). *Methods for Solving Incorrectly Posed Problems*. Berlin, Germany: Springer Science & Business Media.

Wachsmuth, D., and Wachsmuth, G. (2011). "Necessary Conditions for Convergence Rates of Regularizations of Optimal Control Problems," in *System Modelling and Optimization* (Berlin, Germany: Springer), 145–154.

Wilson, J., Neal, P., and Guevara Vasquez, F. (2009). "Regularization Methods for Radio Tomographic Imaging," in *2009 Virginia Tech Symposium on Wireless Personal Communications*.

Conflict of Interest: The authors declare that the research was conducted in the absence of any commercial or financial relationships that could be construed as a potential conflict of interest.

frontiers in Energy Research

ORIGINAL RESEARCH
published: 24 January 2022
doi: 10.3389/fenrg.2021.779243

Validation of PWR Neutronics Code Package TORCH V2.0 With Nuclear Power Plant Measurements

Bin Zhang, Xingjie Peng, Chen Zhao, Wenbo Zhao and Qing Li*

China Nuclear Power Research and Design Institute, Key Laboratory of Nuclear Reactor System Design Technology, Chengdu, China

This article presents the verification and validation (V and V) of PWR neutronics code package TORCH V2.0 with nuclear power plant (NPP) measurements. The advanced nuclear power engineering design software, TORCH V2.0, was developed by the Nuclear Power Institute of China (NPIC), China National Nuclear Corporation (CNNC). Based on the two-step calculation scheme, TORCH V2.0 mainly contains lattice physics code for assembly homogenization, link calculation code for few-group constant parameterization, and core simulation code for few-group core calculation. The calculation modules of each code were already verified against various benchmark problems, whereas this article focuses on the V and V of linked code system. The measured values of the reactor startup physics test and NPP operation from six PWR NPPs (Daya Bay NPP, Ling Ao NPP, Fangjiashan NPP, Qinshan NPP, Hainan Changjiang NPP, and Fuqing NPP) were utilized to perform the comparison and analysis of V and V. Compared parameters of the reactor startup physics test include critical boron concentration, control rod integral value, boron differential value, and isothermal temperature coefficient. Compared parameters of the NPP operation contain critical boron concentration, assembly-wise power distribution, hot spot factor, and nuclear enthalpy rise factor. The results show that the software TORCH V2.0 has reliable calculation ability and can be applied in the PWR nuclear power engineering design which is based on square fuel assembly.

Keywords: validation and verification, TORCH V2.0, nuclear power plant operation data, measurements, startup physics test

OPEN ACCESS

Edited by:
Jun Wang,
University of Wisconsin-Madison, United States

Reviewed by:
A. Abdelghafar Galahom,
Higher Technological Institute, Egypt
Zhuo Li,
Sun Yat-sen University, China

****Correspondence:***
Xingjie Peng
pengxingjiets@126.com

Specialty section:
This article was submitted to Nuclear Energy, a section of the journal Frontiers in Energy Research

Received: *18 September 2021*
Accepted: *27 December 2021*
Published: *24 January 2022*

Citation:
Zhang B, Peng X, Zhao C, Zhao W and Li Q (2022) Validation of PWR Neutronics Code Package TORCH V2.0 With Nuclear Power Plant Measurements. Front. Energy Res. 9:779243. doi: 10.3389/fenrg.2021.779243

INTRODUCTION

A conventional two-step approach of a transport calculation and a nodal diffusion calculation, such as CASMO/SIMULATE, PARAGON (or PHOENIX)/ANC, and APOLLO/SMART (Liu and Meliksetian, 1986; Studsvik of American, 1994; Studsvik of American, 1995; Westinghouse Electric Company, 2005; Adrien, 2014; Vidal et al., 2014; Zhang et al., 2018), has been used in the light water reactor core design for decades. These conventional code systems have been in use for commercial PWR core designs for a long time, and they have been upgraded continuously based on numerous core calculations. However, the conventional code systems usually adopt methodologies developed in the past. A PWR core design software package named TORCH V2.0 has been developed by the Nuclear Power Institute of China (NPIC), CNNC. Many advanced methodologies (Zhang et al., 2019) have

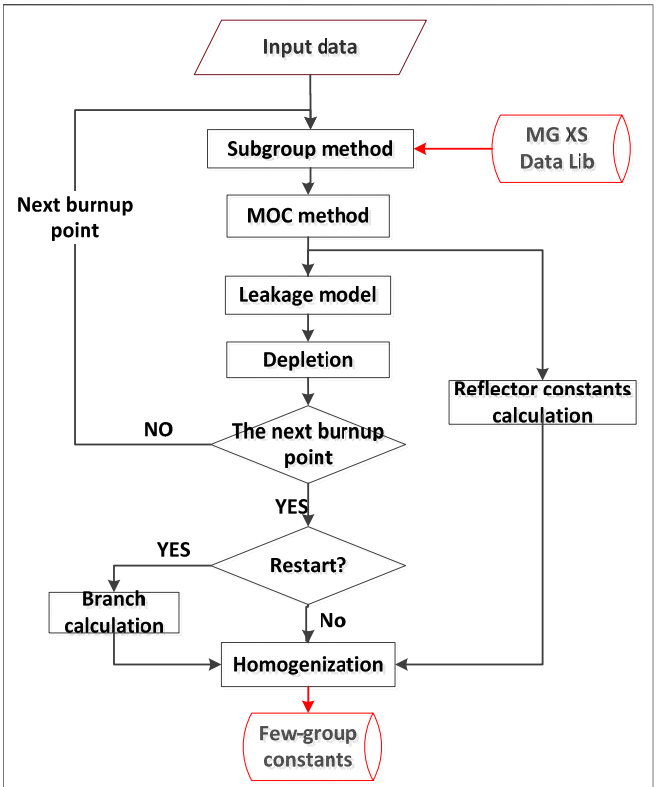

FIGURE 1 | Main calculation flow chart of the KYLIN V2.0 program.

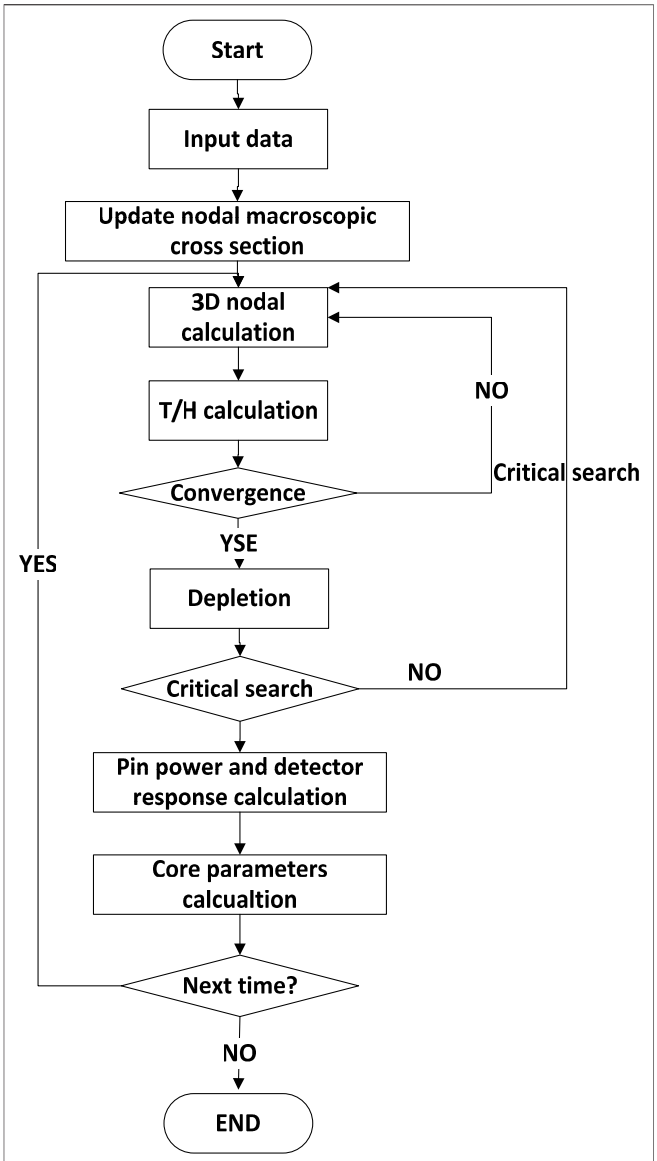

FIGURE 2 | Main calculation flow chart of the CORCA-3D code.

been implemented in TORCH V2.0 to enhance the accuracy and performance. TORCH V2.0 has been developed to be a multi-scale, multi-physics analysis code system; thus, it can be a platform in terms of a neutronics code for coupling with thermal/hydraulic code and fuel performance code. TORCH V2.0 is a property code which is mainly used for the PWR nuclear power engineering design with square fuel assembly, and it is developed along with China's third-generation nuclear power HPR1000.

The results show that the software TORCH V2.0 has reliable calculation ability and can be applied in the PWR nuclear power engineering design which is based on square fuel assembly.

TORCH V2.0 is a PWR core design software package, which mainly includes a lattice physics code named KYLIN V2.0 (Tu et al., 2016; Chai et al., 2017), linking a calculation code named PACFAC and a few-group core simulation code named CORCA-3D (An et al., 2019). KYLIN V2.0 has powerful geometric processing ability, which can perform one-step two-dimensional neutron transport calculation and analysis on various fuel assemblies with complex structures in advanced nuclear reactors, and is mainly used to provide the few-group assembly-homogenized parameters for the three-dimensional core computing software CORCA-3D. PACFAC is a linking code which uses the interpolation/fitting method to parameterize the few-group assembly-homogenized parameters generated by KYLIN V2.0 and provides the polynomial parameters to CORCA-3D to calculate the few-group constants which can be determined by the core state. CORCA-3D software adopts an advanced nodal method to solve the few-group diffusion equation and can perform core depletion calculation, power reconstruction, and physical and thermal coupling calculations.

The reactor cores of six PWR nuclear power plants (Daya Bay NPP, Ling Ao NPP, Fangjiashan NPP, Qinshan NPP, Hainan Changjiang NPP, and Fuqing NPP) have been 85 cycles for 14 NPP units reactor startup physics tests and a total of were simulated by TORCH V2.0. Compared parameters of the reactor startup physics test include critical boron concentration, control rod integral value, boron differential value, and isothermal temperature coefficient. Compared parameters of the nuclear power plant (NPP) operation include critical boron concentration, assembly-wise power distribution, hot spot factor, and nuclear enthalpy rise factor.

TABLE 1 | The details information of simulated six PWR NPPs.

NPP	Unit	Simulated cycles of startup physics test	Simulated cycles of reactor operation
Daya Bay NPP	Unit 1	9–20	9, 12, 15, 17
	Unit 2	9–20	9, 12, 15, 17
Ling Ao NPP	Unit 1	5–16	—
	Unit 2	5–15	
Fangjiashan NPP	Unit 1	1–4	1–4
	Unit 2	1–4	1–4
Qinshan NPP	Unit 1	1–15	1–15
	Unit 3	1–8	1–8
Hainan Changjiang NPP	Unit 1	1–4	1–4
	Unit 2	1–3	1–3
Fuqing NPP	Unit 1	1–4	1–2
	Unit 2	1–3	1–2
	Unit 3	1–3	1
	Unit 4	1–2	—

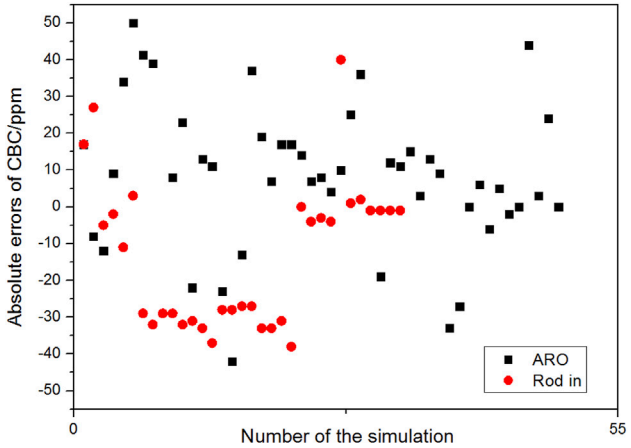

FIGURE 3 | Results of critical boron concentration.

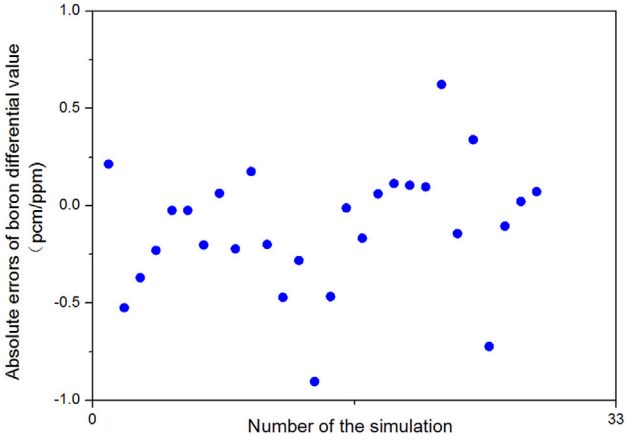

FIGURE 5 | Results of the boron differential value.

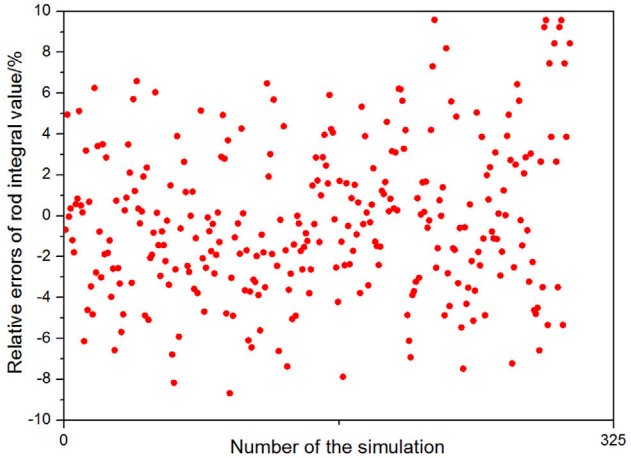

FIGURE 4 | Results of the control rod integral value.

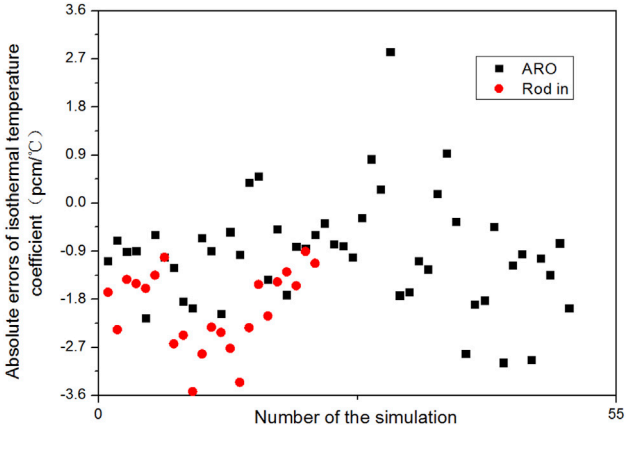

FIGURE 6 | Results of the isothermal temperature coefficient.

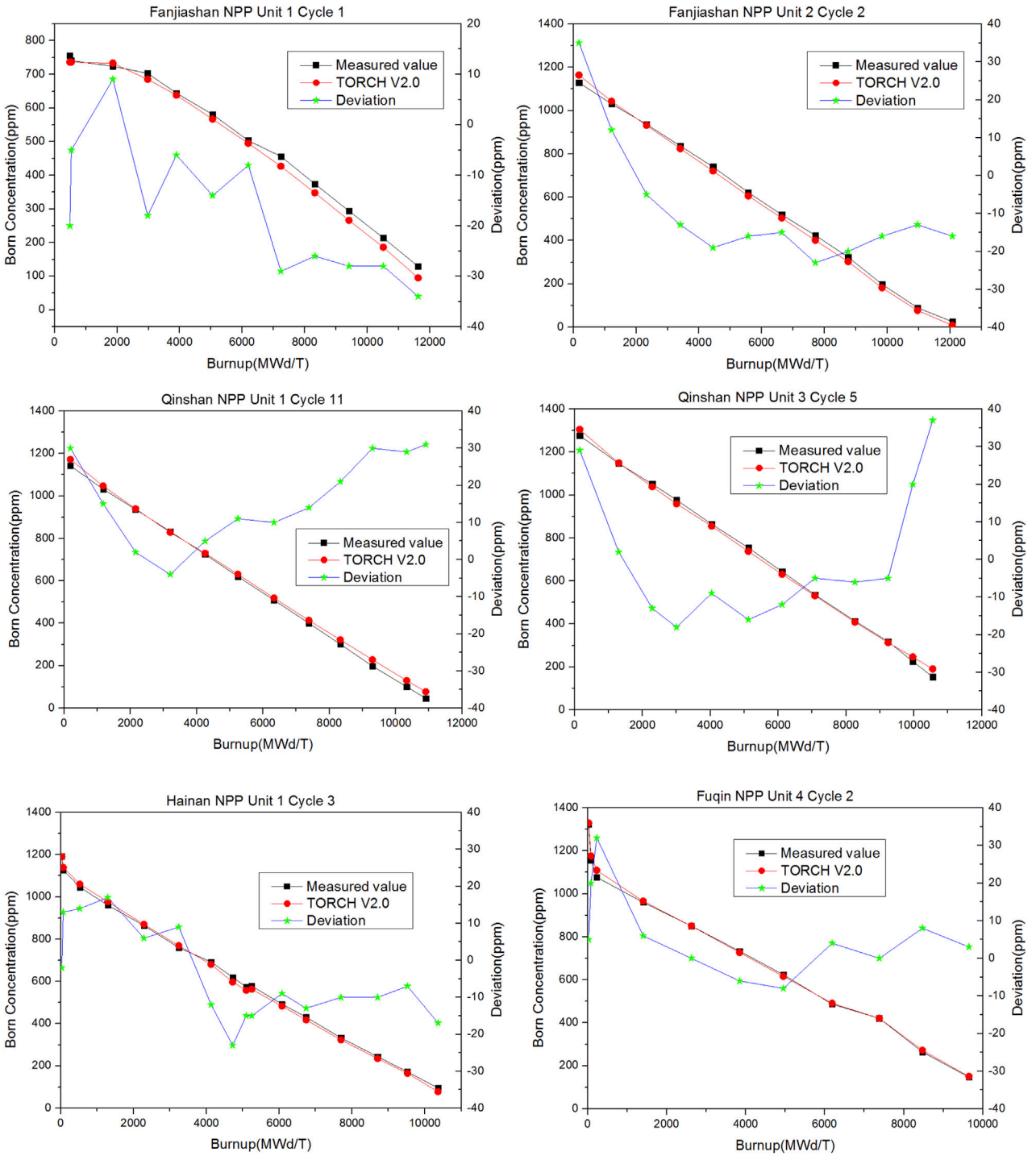

FIGURE 7 | Partial results of critical boron concentration.

CHARACTERISTICS OF TORCH V2.0

TORCH V2.0 adopts a two-step approach to simulate PWR cores. The one-step direct heterogenous calculation code KYLIN V2.0 based on a fine-group structure is used. KYLIN V2.0 is used to generate homogenized parameters, including homogenized cross-section, diffusion coefficients, and discontinuity factors. Considering the fact that a certain state required by the reactor core calculation may be different from the ones provided by KYLIN V2.0, a process is required to provide a table between those neutronics few-group constants and state parameters based on the discrete points provided by lattice

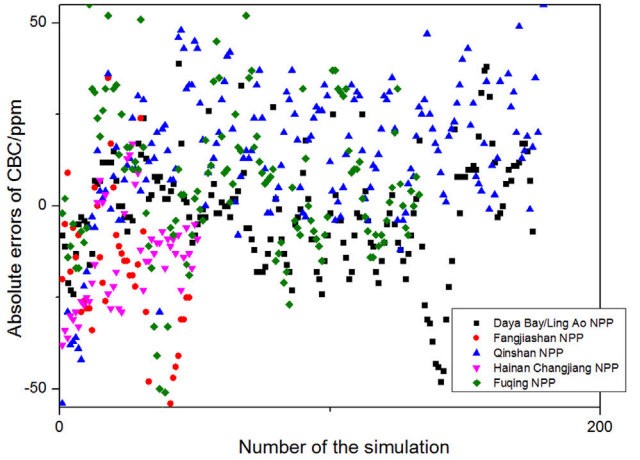

FIGURE 8 | Results of critical boron concentration.

calculations. The code named PACFAC is used to provide the table for the core simulator CORCA-3D. The neutron diffusion equation would be calculated for core fuel management in CORCA-3D.

KYLIN V2.0 Code

The flow chart of the lattice physics code KYLIN V2.0 is shown in **Figure 1**; the program is mainly used for neutron simulation calculation and analysis of two-dimensional problems and provides assembly-homogenized parameters for three-dimensional core simulation software. The KYLIN V2.0 program can select the 45-/190-group structure of multi-group cross-section libraries for calculation. It adopts an advanced subgroup method (Nikilaev et al., 1970; Hebert, 2004) to solve the effective resonance cross-section of resonance nuclides, adopts an MOC method (Hong and Cho, 1998; Kosaka and Takeda, 2004) to calculate the neutron transport of complex structure geometry, and adopts a generalized coarse mesh finite difference (GCMFD) acceleration method to accelerate

TABLE 2 | Results of Daya Bay NPP (Unit 1 Cycle 11) assembly-wise power.

Burnup (MWd/tU)	Relative assembly power ≥0.9		Relative assembly power<0.9	
	Max relative error (%)	Acceptance standard (%)	Max relative error (%)	Acceptance standard (%)
250	2.71	±5	−2.20	±8
1,492	2.56	±5	1.85	±8
2,610	3.27	±5	2.91	±8
3,810	3.48	±5	3.10	±8
5,000	3.63	±5	3.29	±8
6,250	4.19	±5	3.90	±8
7,494	3.68	±5	3.34	±8
8,650	4.08	±5	4.14	±8
11,090	3.62	±5	3.74	±8
12,289	3.02	±5	3.17	±8
13,529	2.79	±5	2.49	±8
14,456	3.19	±5	−2.42	±8
15,929	3.09	±5	−2.45	±8
17,128	3.11	±5	−2.48	±8
18,746	3.15	±5	−2.56	±8

TABLE 3 | Results of Ling Ao NPP (Unit 2 Cycle 7) assembly-wise power.

Burnup (MWd/tU)	Relative assembly power ≥0.9		Relative assembly power<0.9	
	Max relative error (%)	Acceptance standard (%)	Max relative error (%)	Acceptance standard (%)
220	2.77	±5	4.07	±8
1,260	2.75	±5	3.93	±8
2,420	2.75	±5	3.69	±8
3,700	2.85	±5	3.38	±8
4,970	3.02	±5	3.43	±8
6,220	3.04	±5	3.28	±8
7,340	−2.96	±5	3.11	±8
8,620	−2.80	±5	3.04	±8
9,860	−2.66	±5	3.02	±8
11,000	2.84	±5	3.39	±8
12,240	2.73	±5	3.25	±8
12,920	−2.79	±5	3.23	±8

TABLE 4 | Results of Fangjiashan NPP (Unit 2 Cycle 4) assembly-wise power.

Burnup (MWd/tU)	Relative assembly power ≥0.9		Relative assembly power<0.9	
	Max relative error (%)	Acceptance standard (%)	Max relative error (%)	Acceptance standard (%)
179	1.84	±5	2.32	±8
1,216	1.46	±5	2.09	±8
2,332	2.19	±5	2.91	±8
3,408	2.67	±5	3.58	±8
4,451	3.05	±5	4.05	±8
5,576	3.21	±5	3.96	±8
6,642	3.69	±5	4.87	±8
7,711	3.61	±5	4.84	±8
8,755	3.63	±5	4.99	±8
9,837	3.66	±5	4.68	±8
10,966	3.77	±5	5.05	±8

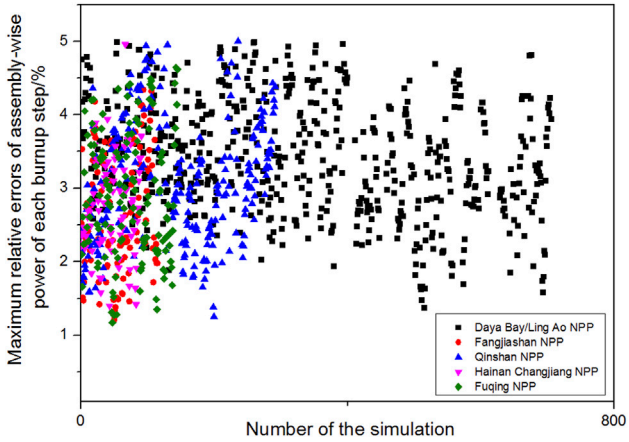

FIGURE 9 | Results of assembly-wise power (greater than 0.9).

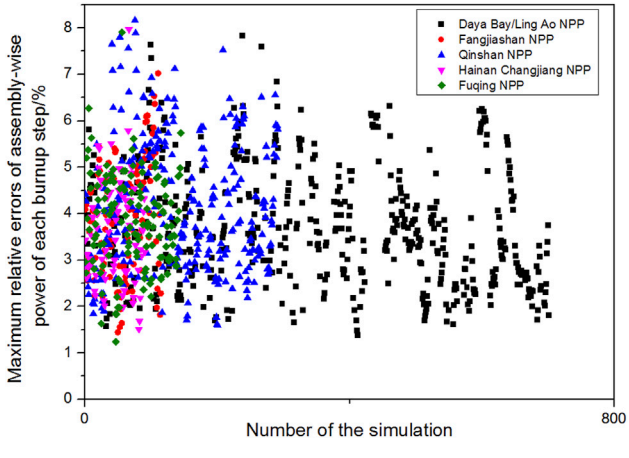

FIGURE 10 | Results of assembly-wise power (less than 0.9).

neutron transport calculation. The depletion calculation is carried out based on the improved predictive-corrected critical-fuel consumption iterative method (Yamamoto et al., 2009), and the burnup equation is solved by the Chebyshev method. At the same time, for the convenience of users, the program also has a graphical modeling tool for components with complex structure geometry and a post-processing display tool.

Specifically, KYLIN V2.0 software mainly has the following characteristics:

1) It can accurately describe geometric shape, mesh division, material distribution of various grids, or components with different geometric structures (including the bar bundle type and plate type) and provide users with clear and convenient input methods.
2) It can accurately read the input parameters necessary for grid (component) calculation, including multi-group constant library, temperature of each region, and resonance effective temperature of important nuclides.
3) It can accurately deal with complex geometric resonance problems and can also consider the influence of fuel core temperature, multi-resonance nuclide interference, and other influence factors.
4) The fine energy spectrum and homogenized cross-section parameters of various types of grids (assemblies) can be solved by using a fine energy group structure.
5) It can deal with heavy nuclear burnup chains, such as uranium series, plutonium series, and fine fission product chains, and can carry out burnup calculation of important combustible poisons (such as boron and gadolinium).
6) One-step two-dimensional heterogenous multi-assembly calculations can be performed, and restart calculations such as continuous calculation and variable working conditions can be performed.
7) It can output main calculation results, such as infinite multiplication coefficient, relative power distribution, and nuclear density of important nuclides.

PACFAC Code

The PACFAC code adopts the interpolation/fitting method to parameterize the few-group assembly-homogenized parameters generated by KYLIN V2.0 and provides the polynomial parameters to CORCA-3D to calculate the few-group constants which can be determined by the core state (Li et al., 2016). The main functions of PACFAC contain the few-group constant parameterization model of few-group constants and the inverse

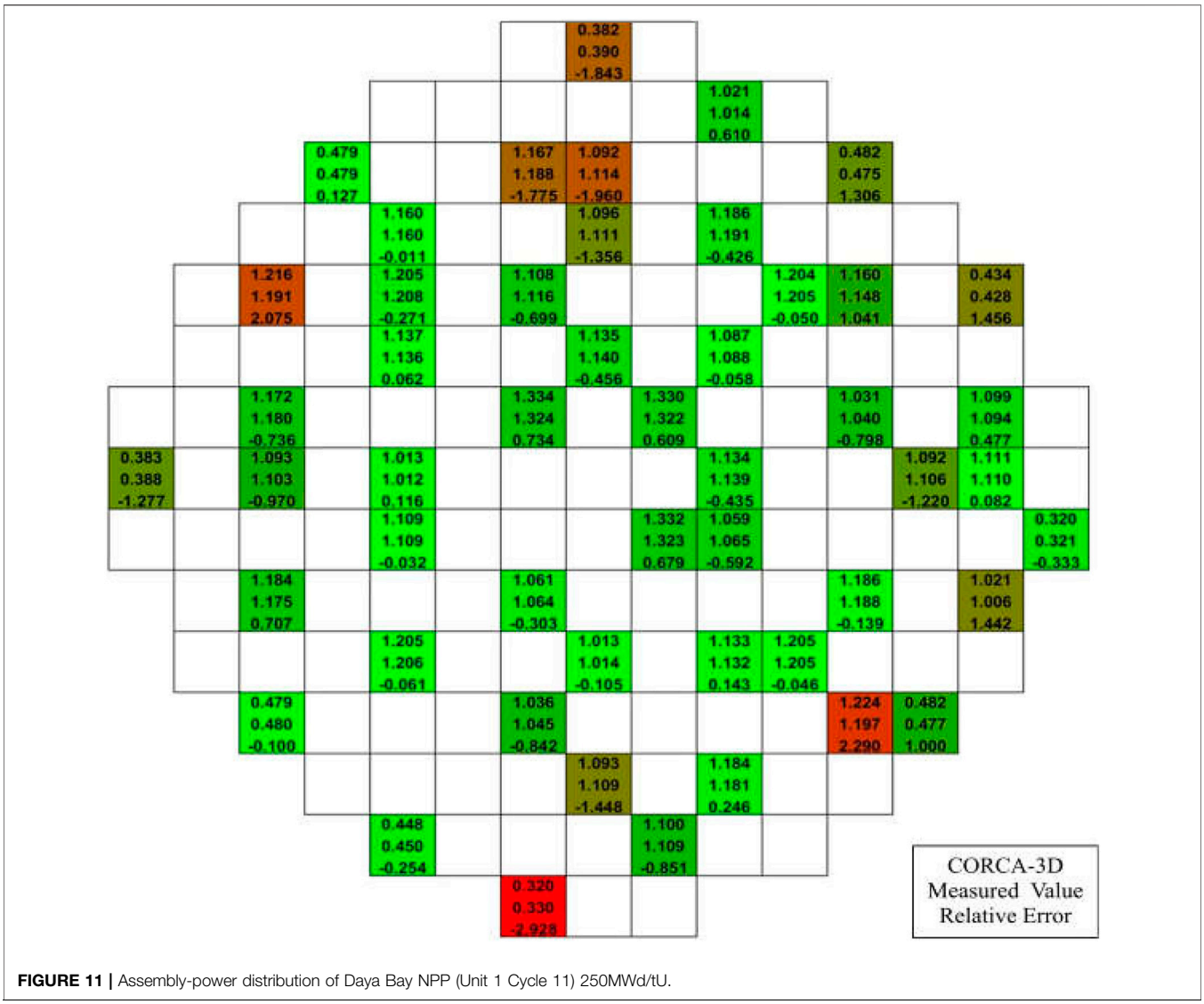

FIGURE 11 | Assembly-power distribution of Daya Bay NPP (Unit 1 Cycle 11) 250MWd/tU.

calculation model of cross-section parameters. The former provides the polynomial parameters of the interpolation/fitting relationship between the few-group constants (few-group cross-section, shape factor, and so on) and core state parameters. The inverse calculation model is mainly used to determine the few-group constants in the core simulator, which is closely related to polynomial parameters in the interpolation/fitting relation. The parameterization formulation of PACFA is shown in the following equation:

$$\sum^{actual} = \sum_{i=1}^{n} N_i^{actual} \sigma_i (DM, Bu, FT, \ldots) + \sum^{pis} (DM, \ldots) + \Delta\Sigma_{rod} (DM, \ldots).$$

Here, $\sum^{pis}$ means the contribution of pseudo-nuclides to the macroscopic cross section, which is caused by the difference between the species of nuclides in the burnup chain of CORCA-3D and burnup chain of KYLIN V2.0. $\Delta\Sigma_{rod}$ means the influence component of the control rod on the cross section.

CORCA-3D Code

The main calculation flow chart of CORCA-3D is shown in **Figure 2**, which is mainly used for the simulation of three-dimensional steady-state core, and is one of the most important calculation software for core fuel management. CORCA-3D can carry out the diffusion calculation based on the few-group constants calculated *via* the homogenized cross-section parameter library, the burnup calculation of important actinides, fission products, and combustible poisons. CORCA-3D can perform thermal-hydraulic feedback calculation, pin-power reconstruction calculation, and is able to calculate the equilibrium concentration of iodine and xenon. CORCA-3D can read multiple-cycle databases for refueling core modeling calculation. At the same time, it has the basic functions of core design, such as coefficient calculation, variable parameter calculation, boron concentration/control rod position critical search calculation, and control rod differential/integral value calculation.

The CORCA-3D code mainly has the following characteristics:

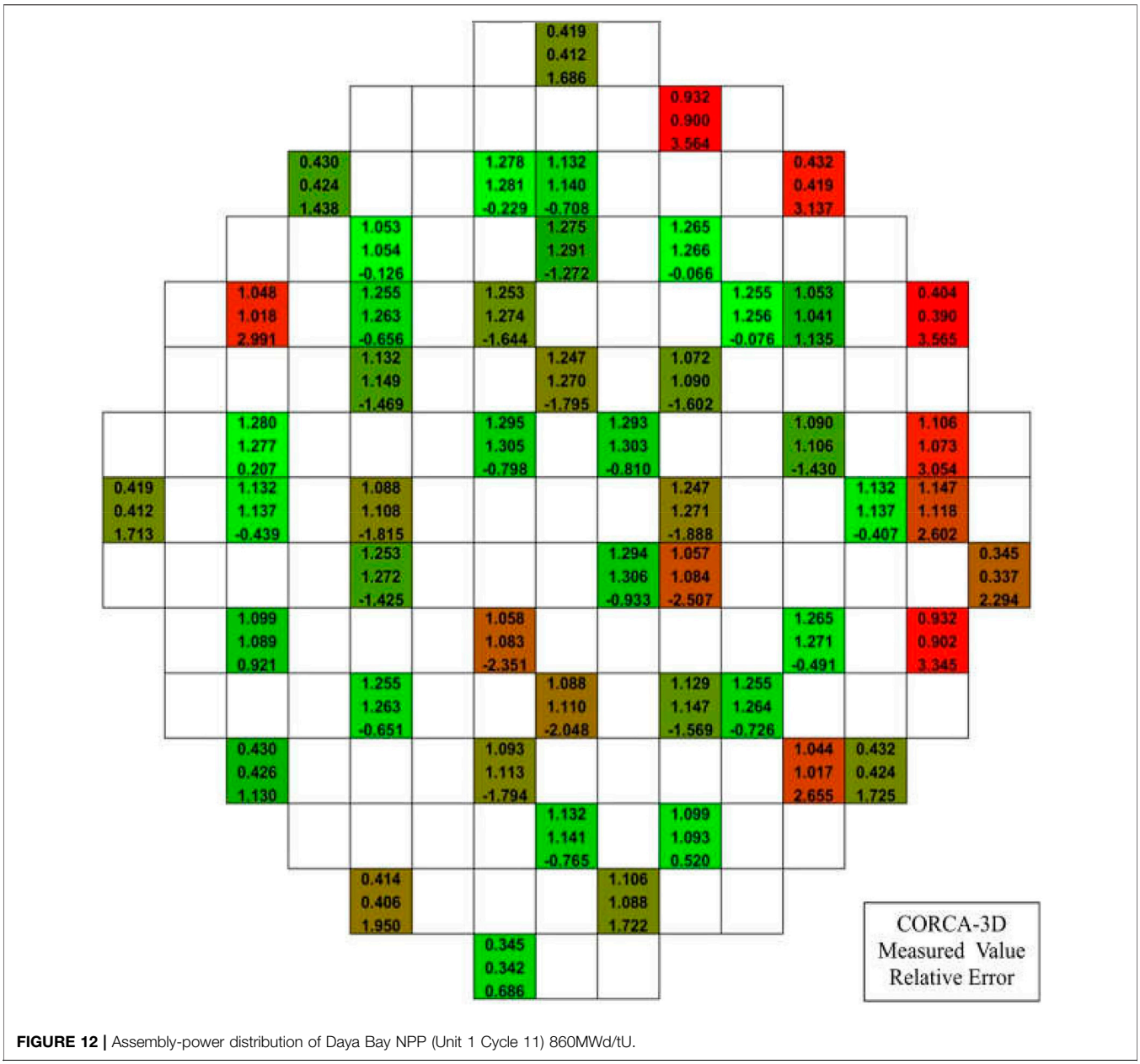

FIGURE 12 | Assembly-power distribution of Daya Bay NPP (Unit 1 Cycle 11) 860MWd/tU.

1) According to the current core information and historical information of the component (including burnup depth, boron concentration, effective fuel temperature, moderator density, xenon concentration, and control rod status), the few-group cross-section parameters of each segment in the core can be calculated from the multi-parameter cross-section library provided by the linking code PACFAC.
2) It can quickly and accurately solve the diffusion equation of few groups (two groups and four groups) in the core.
3) The power reconstruction calculation of rectangular geometry can be carried out, and the pin-power distribution and the detector response can be obtained.
4) It can solve the single-channel thermal hydraulic equation of the reactor core and calculate the enthalpy field distribution of the coolant in the reactor;
5) It can accurately solve the burnup equation of important nuclides in the reactor core and calculate the accumulation and consumption process of important nuclides (such as actinides and combustible poisons) in the reactor.
6) It can calculate the equilibrium concentration of xenon.
7) It is can search boron concentration or rod position of the control rod group to make the core eigenvalue reach the target value;
8) Parameters such as boron concentration, relative power, and control rod position can be changed at any burning time for calculation.

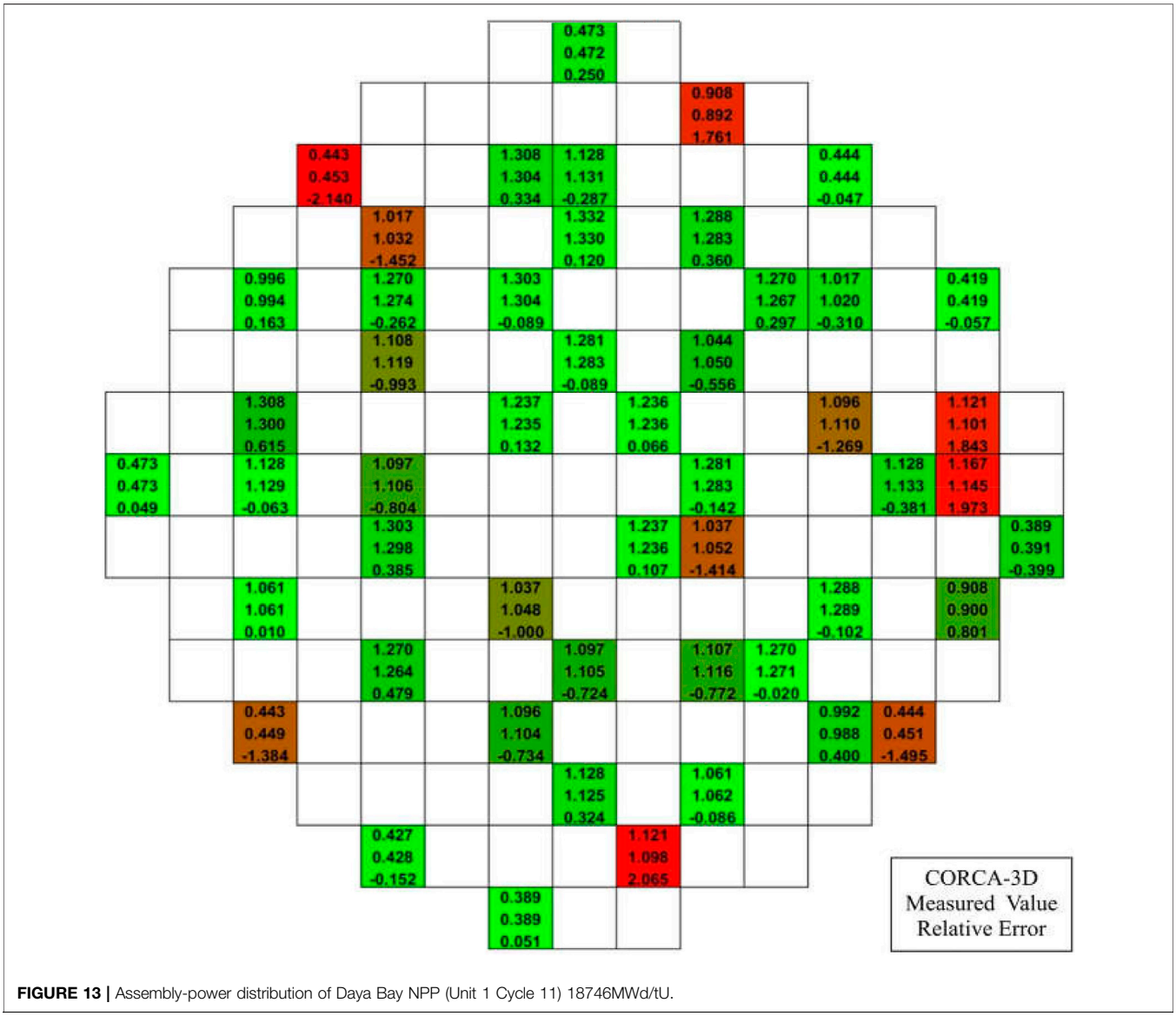

FIGURE 13 | Assembly-power distribution of Daya Bay NPP (Unit 1 Cycle 11) 18746MWd/tU.

VERIFICATION AND VALIDATION RESULTS

The reactor cores of six PWR NPPs are simulated. The analyzed NPPs shown in **Table 1** are Daya Bay NPP (DYBU1C9-WRS-410100-BG1 Rev. 0, 2010), Ling Ao NPP (LAU1C5-WRS-410100-BG1 Rev. 0, 2009), Fangjiashan NPP (FJSU1C1-WRS-410100-BG1 Rev. 0, 2016), Qinshan NPP (QSU1C1-WRS-410100-BG1 Rev. 0, 2005), Hainan Changjiang NPP (CJU1C1-WRS-410100-BG1 Rev. 0, 2016), and Fuqing NPP (FQU1C1-WRS-410100-BG1 Rev. 0, 2016). Part of reactor startup physics tests and a total of 85 cycles of 14 NPP units were simulated by TORCH V2.0. However, the content of the reactor startup physics tests varies in different cycles.

Reactor Startup Physics Test

Compared parameters of the reactor startup physics test include critical boron concentration (CBC), control rod integral value, boron differential value, and isothermal temperature coefficient.

The results of critical boron concentration are shown in **Figure 3**. The absolute errors of the critical boron concentration in the all-rod-out (ARO) state are within ±50 ppm and those of the rod-inserted state agreed with the rod-inserted criterion. The formula of the rod-inserted criterion is as follows:

$$(\mathrm{CBC})_{\mathrm{R}}^{\mathrm{M}} = (\mathrm{CBC})_{\mathrm{R}}^{\mathrm{P}} + \left[(\mathrm{CBC})_{\mathrm{ARO}}^{\mathrm{M}} - (\mathrm{CBC})_{\mathrm{R_0}}^{\mathrm{M}}\right] \pm f\left((\mathrm{CBC})_{\mathrm{R_0}}^{\mathrm{M}}, (\mathrm{CBC})_{\mathrm{R}}^{\mathrm{M}}, (\mathrm{CBC})_{\mathrm{R_0}}^{\mathrm{P}}, (\mathrm{CBC})_{\mathrm{R}}^{\mathrm{P}}\right),$$

where M means the measured value, P means the predicted value, R_0/R means the initial/final rod position at the time of measurement, and f is the value of the uncertainty of the measurement, including chemical analysis uncertainty.

The results indicate that the accuracy of ARO calculation is better than that of rod-inserted calculation with the exception of a

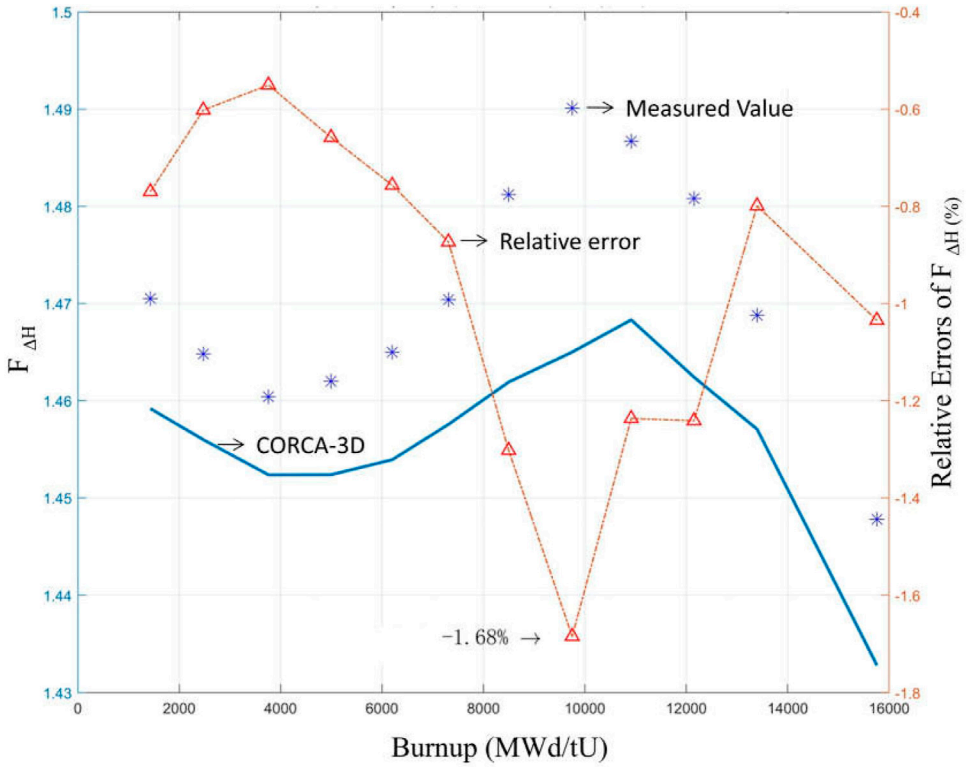

FIGURE 14 | Hot spot factors of Daya Bay NPP (Unit 1 Cycle 11).

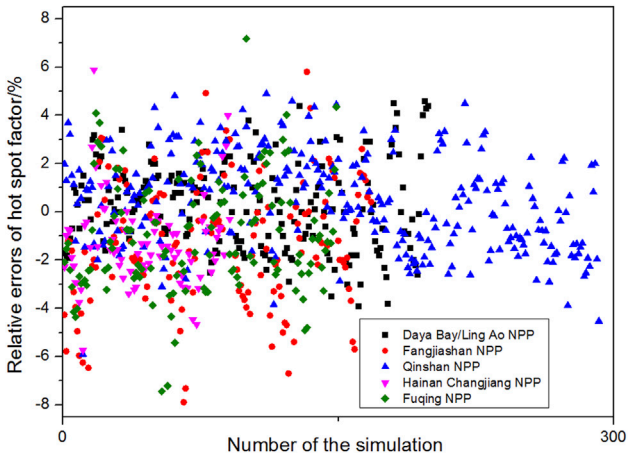

FIGURE 15 | Results of the hot spot factor.

very few calculations. It is because when the control rods are inside the core, the effect and shadow effect would increase the difficulty for the core simulation.

The results of control rod integral value, boron differential value, and isothermal temperature coefficient are shown in **Figure 4**, **Figure 5**, and **Figure 6**, respectively. The relative errors of control rod integral value are within 10%, the absolute errors of boron differential value are within 1.0 pcm/ppm, and the absolute errors of isothermal temperature coefficient are within 3.6 pcm/°C. The large errors appearing in the results belong to the subsequent cycles. It is caused by the core historical effect. In CORCA-3D, the micro burnup method is applied to handle this problem. The models which are based on the two-step calculation scheme adopted in the software cannot fully account for the historical processes. Anyway, all of them agreed with the acceptance criteria. It is indicated that TORCH V2.0 software has enough accuracy in predicting the reactor startup physics test parameters.

Nuclear Power Plant Operation

Compared parameters of the NPP operation include critical boron concentration, assembly-wise power distribution, hot spot factor, and nuclear enthalpy rise factor. The partial results of critical boron concentration are shown in **Figure 7**. The absolute errors of critical boron concentration of all the measured points shown in **Figure 8** are within ±50 ppm except for very few points. At the beginning and end of the core cycle life, the absolute errors are almost worse than those of other times. The changes in xenon concentration and distribution at the beginning of the core cycle life and the core historical effect enhanced with depletion lead to increased errors.

The partial results of maximum assembly-wise power relative error are shown in **Tables 2**–**4**, summary of the maximum assembly-wise power relative errors of all burnup steps is shown in **Figure 9** and **Figure 10**, and the maximum relative errors are within 5% when the relative assembly power is greater than 0.9 and within 8% when it

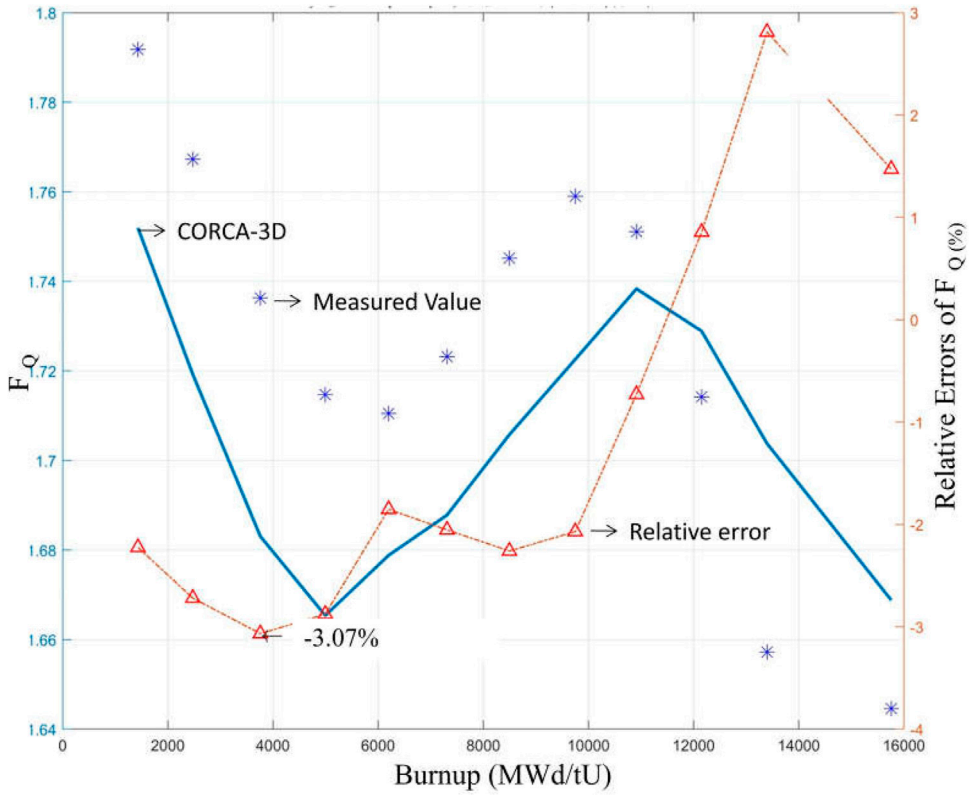

FIGURE 16 | Nuclear enthalpy rise factors of Daya Bay NPP (Unit 1 Cycle 11).

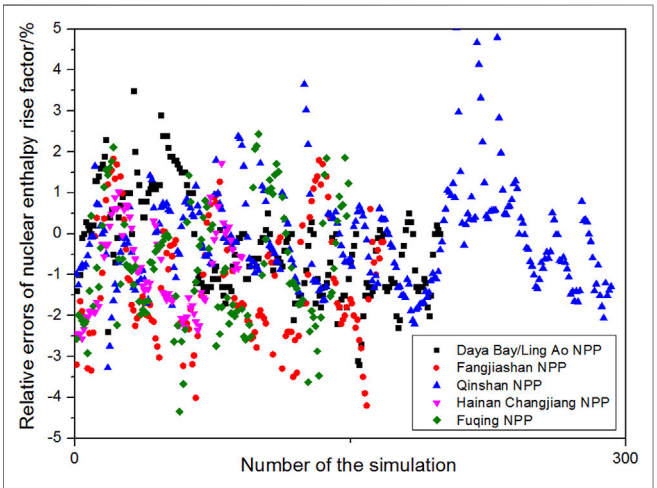

FIGURE 17 | Results of the nuclear enthalpy rise factor.

is less than 0.9, except for very few points. The assembly-wise power distributions of Daya Bay NPP (Unit 1 Cycle 11) at the beginning, middle, and end of the core life are shown in **Figures 11–13** respectively. It can be found that the calculation accuracy does not get worse with the increase in depletion.

The hot spot factors of Daya Bay NPP (Unit 1 Cycle 11) are shown in **Figure 14**. The relative errors of hot spot factors of all cycles are shown in **Figure 15**; the relative errors of hot spot factor are within 8%. The nuclear enthalpy rise factors of Daya Bay NPP (Unit 1 Cycle 11) are shown in **Figure 16**. All the relative error results of nuclear enthalpy rise factor are shown in **Figure 17**; the relative errors are within 5%.

All the calculated parameters are in good accordance with the measured values, which are in agreement with the acceptance criteria. For each core cycle of the NPP used to perform the validation, the average computer processing time of calculations is several minutes. Before the core simulation, the assembly-homogenized few-group constants and the databank of core front-order loops should be ready. The results show that TORCH V2.0 software has high calculation accuracy and efficiency for each cycle operation data of each power plant.

CONCLUSION

In this article, the main components of the PWR core design software package TORCH V2.0 and the main theoretical models and program features adopted in different codes are briefly introduced, and TORCH V2.0 software is verified by using the data of the reactor startup physics test and NPP operation of each power plant. With the exception of very few results of critical boron concentration for some deep operation

cycles, all the results of the compared parameters are in good accordance with the measured values, which are in agreement with the industrial acceptance criteria. The results show that the software TORCH V2.0 has reliable calculation ability and can be applied in the PWR nuclear power engineering design which is based on square fuel assembly. In the future, the uncertainty analysis of TORCH V2.0 would be carried out for the comprehensive verification and validation.

DATA AVAILABILITY STATEMENT

The raw data supporting the conclusions of this article will be made available by the authors, without undue reservation.

AUTHOR CONTRIBUTIONS

XP contributed significantly to analysis and manuscript preparation; CZ performed the data analysis; WZ contributed to analysis and manuscript preparation; QL performed the data analyses and wrote the manuscript. All authors contributed to the article and approved the submitted version.

FUNDING

This study is supported by the National Natural Science Foundation of China (Grant No. 11905214, 12005215) and China Association for Science and Technology (Young Elite Scientists Sponsorship Program 2019QNRC001).

REFERENCES

Adrien, M. (2014). *Applicability of SCIENCE V2 Physical Validation to FA3 EPRTM Reactor* Rouen, Normandie: Framatome.

An, P., Ma, Y. Q., and Guo, F. C. (2019). Development and Validation of Critical Boron Concentration and Burnup Calculation of Software CORCA-3D[J]. *Nucl. Power Eng.* 40 (4), 161–165. doi:10.13832/j.jnpe.2019.04.0161

Chai, X. M., Tu, X. L., and Guo, F. C. (2017). Development and Preliminary Verification of Advanced Neutronics Grid Program KYIN-2[J]. *High Power Laser Part. Beams* 29 (1), 1–7. doi:10.11884/HPLPB201729.160306

CJU1C1-WRS-410100-BG1 Rev. 0 (2016). *The Nuclear Design Report for Hainan Changjiang Nuclear Power Plant Unite 1 Cycle 1*. Chengdu: China Nuclear Power Research and Design Institute.

DYBU1C9-WRS-410100-BG1 Rev. 0 (2010). *The Nuclear Design Report for Daya Bay Nuclear Power Plant Unite 1 Cycle 9*. Chengdu: China Nuclear Power Research and Design Institute.

FJSU1C1-WRS-410100-BG1 Rev. 0 (2016). *The Nuclear Design Report for Fangjiashan Nuclear Power Plant Unite 1 Cycle 1*. Chengdu: China Nuclear Power Research and Design Institute.

FQU1C1-WRS-410100-BG1 Rev. 0 (2016). *The Nuclear Design Report for Hainan Fuqing Nuclear Power Plant Unite 1 Cycle 1*. Chengdu: China Nuclear Power Research and Design Institute.

Hebert, A. (2004). *A Mutual Resonance Shielding Model Consistent with Ribon Subgroup equations[C]*. Chicago: PHYSOR 2004.

Hong, S. G., and Cho, N. Z. (1998). CRX: A Code for Rectangular and Hexagonal Lattices Based on the Method of Characteristics. *Ann. Nucl. Energ.* 25 (8), 547–565. doi:10.1016/s0306-4549(97)00113-8

Kosaka, S., and Takeda, T. (2004). Verification of 3D Heterogeneous Core Transport Calculation Utilizing Non-linear Iteration Technique. *J. Nucl. Sci. Tech.* 41 (6), 645–654. doi:10.1080/18811248.2004.9715529

LAU1C5-WRS-410100-BG1 Rev. 0 (2009). *The Nuclear Design Report for Ling Ao Nuclear Power Plant Unite 1 Cycle 5*. Chengdu: China Nuclear Power Research and Design Institute.

Li, Y., Gao, S., Wu, H., Cao, L., and Shen, W. (2016). PWR Few-Group Constants Parameterization Analysis. *Prog. Nucl. Energ.* 88, 104–117. doi:10.1016/j.pnucene.2015.12.011

Liu, Y. S., and Meliksetian, A. (1986). *ANC – A Multi-Dimensional Neutronic Advanced Nodal Code[R]*. USA: Westinghouse Electric Company.

Nikilaev, M., Ignatcv, A., and Isaev, N. (1970). The Method of Subgroups for Considering the Resonance Structure of Cross Sections in Neutron Calculations [J]. *Atomnaya Energiya* 29, 11–16. doi:10.1007/BF01408755

QSU1C1-WRS-410100-BG1 Rev. 0 (2005). *The Nuclear Design Report for Qinshan Nuclear Power Plant Unite 1 Cycle 1*. Chengdu: China Nuclear Power Research and Design Institute.

Studsvik of American (1994). *CASMO-3 User's Manual[R]*. Chicago, Illinois: Studsvik of American.

Studsvik of American (1995). *SIMULATE-3 Methodology[R]*. Chicago, Illinois: Studsvik of American.

Tu, X. L., Chai, X. M., and Lu, K. (2016). "Development and Preliminary Verification of Characteristic Line Method Module in Advanced Neutronics Grid Program KYLIN-2[C]," in China Annual Conference on Reactor Physics, Beijing, China Beijing, China: China Nuclear Society (CNS).

Vidal, J. F., Bay, C., and Archier, P. (2014). *Transport Core Solver Validation for the Astride Conceptual Design Study with APOLLO3[C]. PHYSOR2014*. Japan: Kyoto.

Westinghouse Electric Company (2005). *PARAGON User Manual[R]*. USA: Westinghouse Electric Company.

Yamamoto, A., Tatsumi, M., and Sugimura, N. (2009). Projected Predictor-Corrector Method for Lattice Physics Burnup Calculations. *Nucl. Sci. Eng.* 163 (2), 144–151. doi:10.13182/nse08-80

Zhang, T. F., Wu, H. C., Cao, L. Z., and Li, Y. Z. (2018). An Improved Variational Nodal Method for the Solution of the Three Dimensional Steady-State Multi-Group Neutron Transport Equation. *Nucl. Eng. Des.* 337, 419–427. doi:10.1016/j.nucengdes.2018.07.009

Zhang, T. F., Xiong, J. B., Li, Z. P., and Zhuang, K. (2019). Development and Implementation of an Integral Variational Nodal Method to the Hexagonal Geometry Nuclear Reactors. *Annal. Nucl. Energy 131*, 210–220. doi:10.1016/j.anucene.2019.03.031

Conflict of Interest: The authors declare that the research was conducted in the absence of any commercial or financial relationships that could be construed as a potential conflict of interest.

Publisher's Note: All claims expressed in this article are solely those of the authors and do not necessarily represent those of their affiliated organizations, or those of the publisher, the editors, and the reviewers. Any product that may be evaluated in this article, or claim that may be made by its manufacturer, is not guaranteed or endorsed by the publisher.

frontiers in Energy Research

ORIGINAL RESEARCH
published: 26 January 2022
doi: 10.3389/fenrg.2021.822780

High-Fidelity MC-DEM Modeling and Uncertainty Analysis of HTR-PM First Criticality

Ruihan Li[1], Zhaoyuan Liu[2], Zhiyuan Feng[3], Jingang Liang[1] and Liguo Zhang[1]*

[1]Institute of Nuclear and New Energy Technology, Tsinghua University, Beijing, China, [2]Shandong Computer Science Center (National Supercomputer Center in Jinan), Qilu University of Technology (Shandong Academy of Sciences), Jinan, China, [3]Department of Engineering Physics, Tsinghua University, Beijing, China

A high-fidelity model for the first criticality of pebble-bed reactor HTR-PM is built using Monte Carlo (MC) code RMC and discrete element method (DEM) code LAMMPS. Randomly packed TRi-structural ISOtropic (TRISO) particles and fuel pebbles are modeled explicitly. A cone structure on the top of the pebble bed is also taken into account. Criticality calculation result agrees well with the experiment. Uncertainty analysis is carried out considering three inherent aspects: the randomness of MC code, the randomness of TRISO particle and pebble position, and the randomness of mixed pebbles. Results show that these factors have a significant impact on the uncertainty of effective multiplication factor (k_{eff}). And the most influential factor is expected to be the randomness of mixed pebbles. The influence of several configuration factors is studied as well. It is observed that the effects of cross-section library, the heterogeneity of TRISO particles, and the angle of pebble bed cone are nonnegligible contributors. However, the results between randomly and regularly placed TRISO particles are not noticeably different.

Keywords: HTR-PM, Monte Carlo, discrete element method, high-fidelity, uncertainty, double heterogeneity

OPEN ACCESS

Edited by:
Tengfei Zhang,
Shanghai Jiao Tong University, China

Reviewed by:
Jiankai Yu,
Massachusetts Institute of Technology, United States
Qian Zhang,
Harbin Engineering University, China

****Correspondence:***
Jingang Liang
jingang@tsinghua.edu.cn

Specialty section:
This article was submitted to Nuclear Energy, a section of the journal Frontiers in Energy Research

Received: *26 November 2021*
Accepted: *20 December 2021*
Published: *26 January 2022*

Citation:
Li R, Liu Z, Feng Z, Liang J and Zhang L (2022) High-Fidelity MC-DEM Modeling and Uncertainty Analysis of HTR-PM First Criticality. Front. Energy Res. 9:822780. doi: 10.3389/fenrg.2021.822780

1 INTRODUCTION

As the fourth-generation nuclear power plant, high-temperature gas-cooled reactors (HTGRs) have been gaining attention because of their safety features. Recently, the world's first 200 MWe pebble-bed modular high-temperature gas-cooled reactor demonstration plant (HTR-PM) (Zhang et al., 2006) built in Shandong, China, reached its first criticality. With the experiment data provided, it is a good opportunity to carry out high-fidelity modeling research. As a pebble-bed reactor like HTR-10, HTR-PM has the feature of double heterogeneity and randomness as well, but the reactor core is larger and has more pebbles. It would be more challenging to perform a high-precision modeling for HTR-PM.

There has been research on the simulation of pebble-bed reactors. For example, the high-fidelity model of HTR-10 was built using MCNP (Version 5) (X-5 Monte Carlo Team, 2003) with double heterogeneity taken into account (Abedi and Vosoughi, 2012). HTR-10 was also modeled using a regularly packed pebble bed (Abedi et al., 2011). The influence of the heterogeneity of the pebble bed was studied based on HTR-PROTEUS (Auwerda et al., 2010). HTR-10 was studied focusing on the effect of the randomness of TRi-structural ISOtropic (TRISO) particles (Çolak and Seker, 2005). The first solid-fueled thorium molten salt reactor (TMSR-SF1) was modeled explicitly, and the influence of randomness of TRISO particles was studied (Sun et al., 2018). The influence of a cross-section library was studied based on the explicit model of the pebble bed reactor of ASTRA facility (Rintala

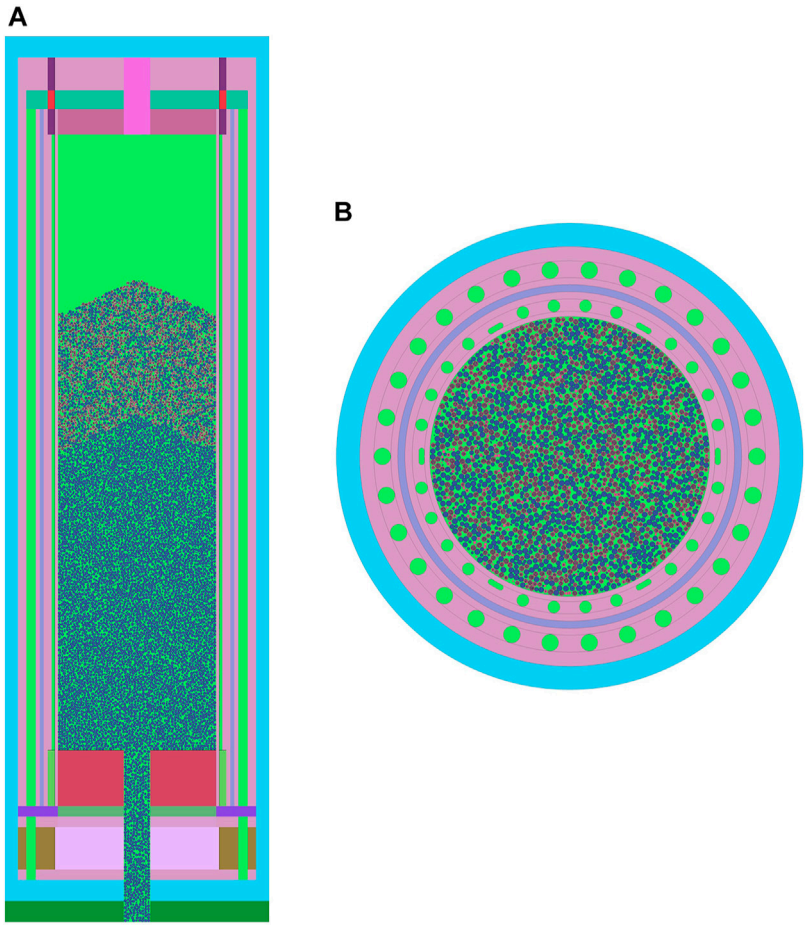

FIGURE 1 | (A) The axial cross section at the center of the model and **(B)** radial cross section at the height of 1,026.17 cm from the bottom.

et al., 2015). Even so, comparing to these facilities, the scale of HTR-PM is significantly larger, resulting in higher complexity of the model.

There are also several research projects on HTR-PM. She et al. (2021) studied the high-fidelity model based on deterministic code PANGU; sensitivity analysis was carried out focusing on filling fraction and uranium loading (Hao et al., 2015); uncertainty analysis on thermal features was launched using CUSA and ATHENA codes (Hao et al., 2020). However, research on HTR-PM Monte Carlo (MC) high-fidelity model and uncertainty is relatively insufficient.

This study builds a high-fidelity model of the first criticality of HTR-PM, realizing the meticulous modeling of large-scale pebble-bed reactor. MC code RMC (Wang et al., 2015) and discrete element method (DEM) code LAMMPS (Plimpton, 1995) are used. The randomly packed pebbles and TRISO particles are modeled explicitly. Uncertainty analysis is carried out, and the uncertainty of mixed pebbles is proposed. The influence of cross-section library, heterogeneity of TRISO particles, and angle of pebble bed cone is also studied.

The paper is organized as follows. **Section 2** shows the details of the model. **Section 3** describes the uncertainty analysis of inherent factors. **Section 4** presents the effects of several configuration aspects. And **Section 5** summarizes this paper.

2 HIGH-FIDELITY MC-DEM MODEL AND CRITICALITY CALCULATION

The reactor core vessel of HTR-PM is a large cylinder with a cone structure and discharge tube at the bottom. The core is filled with pebbles, including fuel pebble and graphite pebble. Within each fuel pebble, UO_2 fuel is contained in separate TRISO particles instead of evenly distributed. These features make the double heterogeneity of the pebble-bed reactor. In the first criticality condition, the core is first filled with graphite pebbles, on the top of which a mixture of fuel pebbles and graphite pebbles is loaded with a ratio of 7:8.

In this study, a high-fidelity model of HTR-PM is built according to the information of "base condition" provided by She et al. (2021). In the base condition, the core is filled with air instead of helium. The temperature of the whole model is set at 293.6 K. The layout of the model is shown in **Figure 1**. The cone structure at the bottom is converted equivalently to cylinder as

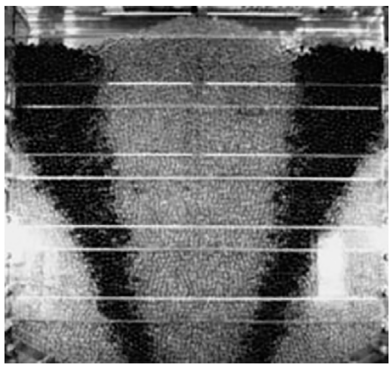

FIGURE 2 | Photo of the pebble packing experiment (Yang et al., 2009).

She et al. (2021) did. To model double heterogeneity explicitly, the positions of pebbles are firstly determined using DEM method with LAMMPS code. These positions are then used to construct the MC model with RMC code. And positions of TRISO particles are directly determined by RMC code, using RSA method (Liu et al., 2015). Though TRISO particles are randomly placed, fuel pebbles have identical inner TRISO particle distributions in order to save calculation time.

LAMMPS code can model the movement of pebbles according to Newton's laws. To generate the pebble bed, a process of packing pebbles is modeled. Pebbles are first randomly placed at the top of the reactor core vessel. They then drop freely under the influence of gravity and are accumulated at the bottom of the vessel. The simulation ends when enough pebbles are packed. Parameters used in this model, such as elastic constant and friction coefficient, are referenced from Rycroft et al. (2013). It should be noted that the time step is set to be 10 times larger than the reference, which is $2.5 \times 10^{-4}\tau$ with the time scale $\tau = 0.0782$ **s**, in order to save calculation time. This change will not significantly affect the packed pebble bed. A total of 2.3 million time steps are calculated, and the time consumption is 93 min using 64-core parallel computing. The packing fraction of the generated pebble bed is 61%, which agrees well with the value used by She et al. (2021).

Pebbles modeled by the LAMMPS code are described as elastic spheres. Thus, the packed pebbles can be slightly overlapped. However, when modeling the pebble bed geometry using the MC code RMC, any overlap is unacceptable. Therefore, the size of pebbles is set to be a little larger in the LAMMPS model to eliminate overlap. When packing pebbles with a diameter of 6 cm, a maximum overlap of 0.002 cm is observed, so the diameter of pebbles in the LAMMPS model is set to 6.002 cm. Using the position information derived by LAMMPS, the diameter of pebbles in RMC model is still set to 6 cm. Thus, no overlapping is observed in RMC model, and the influence on pebble packing fraction can be neglected.

In the first criticality experiment of HTR-PM, pebbles are loaded into the reactor vessel from a single tube. Obviously, a cone structure will form at the top of the pebble bed. As the mixed pebbles are loaded after graphite pebbles, there will be a cone structure at the top of the graphite pebble pile as well. Because of the similar mass and friction coefficient of fuel and graphite pebble, the cone angles of the graphite pebble pile and the mixed pebble pile are the same, as shown in **Figure 1A**. The k_{eff} of the reactor can be significantly affected by the cone angle (will be further discussed in **Section 4**), making it necessary to model the cone correctly. However, no experiment result of HTR-PM cone angle is currently available. Thus, this study refers to a previous experiment done by Yang et al. (2009). According to the photo taken from the pebble packing experiment (**Figure 2**), the cone angle is approximately 25°, which is chosen to be the cone angle value in this model. To generate the cone structure, using LAMMPS directly is highly time-consuming because more time steps must be calculated if the pebbles are inserted one by one. So this study uses the following method instead. First, a cylinder-shaped pebble bed with larger height but no cone is generated using LAMMPS. Then, pebbles are examined by a Python script according to the expected cone geometry. Pebbles in different regions are defined as graphite pebble or mixed pebble or deleted respectively. Thus, the cone structure shown in **Figure 1A** is achieved. This method is also applied to model different cone angles in **Section 4.3**.

The equivalent height of the graphite pebble pile is 6.05 m, with a packing fraction of 61% (She et al., 2021). Note that there are also graphite pebbles in the discharge tube at the bottom of the core. The total number of graphite pebbles is estimated to be 234,957. According to the first criticality experiment in Shandong, China, the number of mixed pebbles is approximately 102,300 when reaching criticality.

Using the parameters mentioned above, k_{eff} obtained by RMC is 0.99968, which is very close to the experimental value of 1. The uncertainty of k_{eff} will be further discussed in **Section 3**.

3 QUANTIFICATION OF THE INHERENT STOCHASTICITY

3.1 Factors Causing Uncertainty

The actual pebble-bed reactor can be uncertain in may parameters, such as the diameter of pebbles or mass of uranium in each pebble. Uncertainty of these parameters will result in the uncertainty of reactor physics or thermal property (Guo et al., 2021). However, for a computer simulation model, most of these parameters are completely certain, which means the uncertainty of the model results from only a few factors. As for the model used in this study, inherent uncertainty is only caused by the following three factors.

The first factor is the uncertainty of MC method. Because MC method is essentially statistical, results obtained by MC calculation always come with statistical uncertainties. It should be noted that the uncertainty of MC method is related to the number of neutrons simulated. In this study, all RMC calculations are carried out with 50 million neutron histories in total where 100 inactive generations, 900 active generations, and 50,000 particles per generation were used. This will result in a k_{eff} standard deviation of 10 pcm.

The second factor is the randomness of TRISO particles and pebble positions. Obviously, the calculation result will be

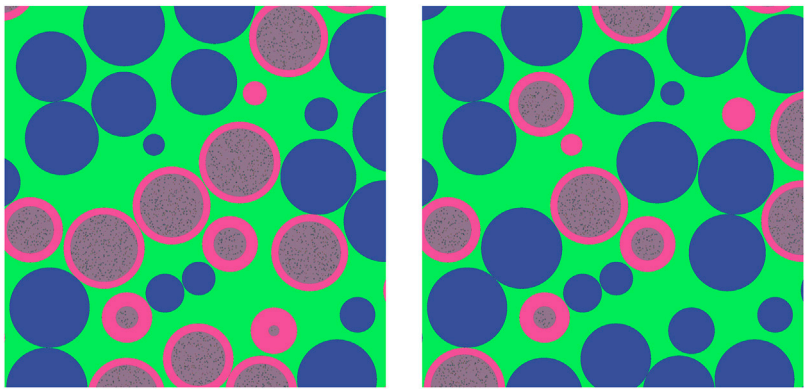

FIGURE 3 | Different mixed pebbles with the same pebble position.

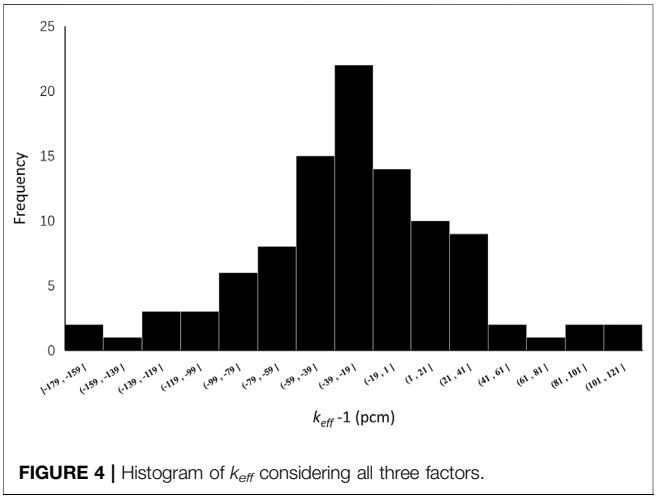

FIGURE 4 | Histogram of k_{eff} considering all three factors.

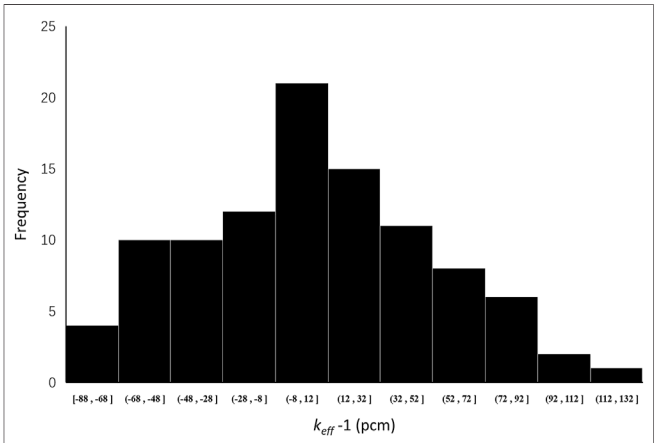

FIGURE 5 | Histogram of k_{eff} considering the randomness of MC method and mixed pebbles.

uncertain because TRISO particles and pebbles are randomly packed.

The third factor is the randomness of the mixed pebbles. In order to discuss this factor, the method used in this study to model the mixed pebbles needs to be first explained.

HTR-PM first criticality core contains a mixture of fuel pebbles and graphite pebbles with a ratio of 7:8. To model this mixture, a randomly packed pebble pile with 102,300 pebbles is first generated using LAMMPS. In this step, there is no difference among pebbles. Then 47,740 of these pebbles are randomly chosen to be fuel pebble, and the remaining 54,560 pebbles will be graphite pebbles. The choosing process is done using *random.sample* function in *Python 3.9.5*.

Rigorously speaking, the mixture of fuel and graphite pebbles is not completely random. If the bed is packed with pebbles with different densities, the proportion of light pebbles would be larger near the wall, and heavy pebbles would be more concentrated near the center (Wu et al., 2019). However, considering that the difference between fuel and graphite pebble density is relatively small (about 3%), this phenomenon is neglected in this study.

It is observed that even the positions of 102,300 pebbles are fixed; the k_{eff} calculation result can be different if the 47,740 fuel pebbles are chosen differently. As shown in **Figure 3**, the positions of each pebble in these two pebble piles are completely the same. The only difference is which pebble is fuel and which pebble is graphite. In this study, this feature is called the randomness of mixed pebbles.

3.2 Standard Deviation of k_{eff} Caused by the Factors

Quantitative study of uncertainty is carried out using statistical sampling method (Helton et al., 2006). When investigating the influence of some factors, 100 examples are calculated considering these factors. And the standard deviation of k_{eff} is derived from the result.

First, the uncertainty under the influence of all the three factors is studied. One hundred examples with random TRISO particle and pebble positions, and randomly chosen fuel pebbles, are calculated. A histogram of results is shown in **Figure 4**. The

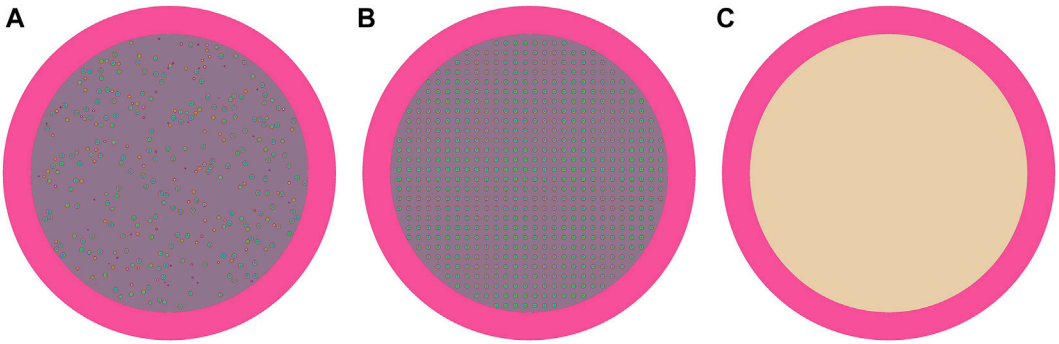

FIGURE 6 | (A) randomly placed TRISO particles; **(B)** regularly placed TRISO particles; and **(C)** homogeneous material.

TABLE 1 | Calculation results of different fuel patterns.

	Single fuel pebble		Reactor core	
	k_{inf}	Difference	k_{eff}	Difference
Randomly placed TRISO particles	1.43796	Reference	0.99968	Reference
Regularly placed TRISO particles	1.43572	−224 pcm	0.99935	−33 pcm
Homogeneous material	1.33422	−10374 pcm	0.96860	−3,108 pcm

TABLE 2 | Calculation results of different fuel enrichments.

Enrichment (%)	k_{eff} of regularly placed TRISO particles	k_{eff} of randomly placed TRISO particles	Difference (pcm)
1	0.45766	0.45792	26
2	0.70956	0.70983	27
3	0.86964	0.87024	60
4	0.98084	0.98138	54
4.2	0.99935	0.99968	33
5	1.06235	1.06295	60
6	1.12539	1.12589	50
7	1.17494	1.17571	77
8	1.21544	1.21599	55
8.5	1.23262	1.23351	89

mean value of k_{eff} is 0.99972, and the standard deviation is 53 pcm. This indicates that when modeling HTR-PM, the inherent uncertainty is not only caused by MC calculation. Thus, it is unnecessary to excessively reduce the uncertainty of MC calculation by increasing the neutron history.

Next, the influence of each factor is studied respectively. However, it should be stressed that some factors cannot be separated, including: 1) MC method is applied in every example, making it difficult to separate its effect, and 2) when positions of pebbles change, it is meaningless to make the mixed pebble stay the same. Thus, the effect of random pebble position cannot be separated from the effect of mixed pebbles.

Considering the facts mentioned above, the following studies are carried out: 1) uncertainty under the influence of MC method and mixed pebbles and 2) uncertainty under the influence of MC method and TRISO particle positions.

In order to study the influence of MC method and mixed pebbles, 100 examples are calculated with fixed TRISO particle and pebble positions and randomly chosen fuel pebbles. A histogram of results is shown in **Figure 5**. The mean value of k_{eff} is 1.00006, and the standard deviation is 46 pcm. The mean value of k_{eff} here (1.00006) is different from that in **Figure 4** (0.99972). The reason is that although the fixed TRISO particle and pebble positions chosen in this calculation are from 1 of the 100 examples in **Figure 4**, it is not the one whose result is closest to the mean value of **Figure 4**.

To study the influence of MC method and TRISO particle positions, 100 examples are calculated with fixed pebble positions and mixed pebbles and random TRISO particle positions. Results show that the standard deviation of k_{eff} is 10 pcm. Note that the standard deviation under only the influence of MC method is 10 pcm. It can be inferred from this result that the influence of

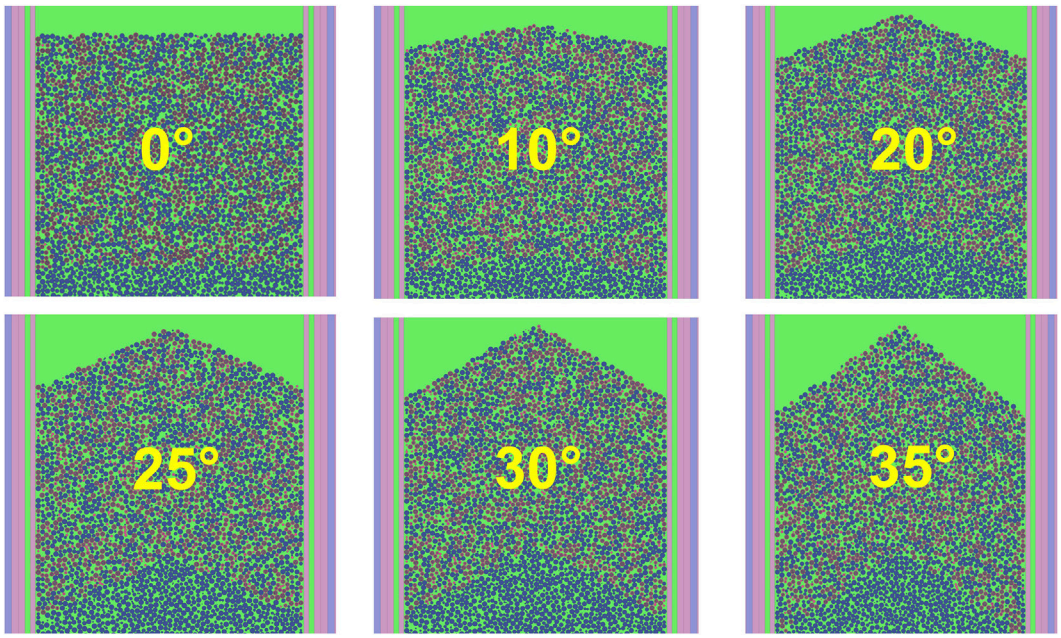

FIGURE 7 | Axial cross sections of different cone angles.

TABLE 3 | k_{eff} results with different cone angle.

Angle (degree)	0	10	20	25	30	35
k_{eff}	1.00442	1.00416	1.00206	0.99968	0.99758	0.99319

randomness of TRISO particle positions can be neglected. The same conclusion was obtained by Çolak and Seker when studying HTR-10 (Çolak and Seker, 2005).

Results shown in this section suggest that the randomness of mixed pebbles is the main factor causing the uncertainty of the HTR-PM high-fidelity model.

Section 4 shows the influence of several configuration factors on the k_{eff} value. To compare these results, it is necessary to determine their standard deviations. These results may be influenced by different factors mentioned in **Section 3.1**, which means different standard deviations should be applied. This will be further discussed in **Section 4**.

4 UNCERTAINTY ANALYSIS OF CONFIGURATION FACTORS

This section shows the influence of several configuration factors on the high-fidelity model, including the cross-section library, the heterogeneity of TRISO particles, and the angle of the cone formed by pebble packing.

4.1 Influence of Cross-Section Library

The high-fidelity model described in **Section 2** is calculated based on ENDF/B-VIII.0 library. Its k_{eff} result is 0.99968. When using ENDF/B-VII.1 library, the k_{eff} is 0.99797, with a difference of approximately 200 pcm, which is significantly larger than the standard deviation of 10 pcm from the MC calculation. The positions of TRISO particles and pebbles, as well as the mixed pebbles, are set to be the same between these two examples, which indicates that this error is caused by the difference of nuclear data libraries.

The source of this difference is speculated to be the difference of graphite cross sections between the two libraries, especially the difference of thermal neutron scattering cross sections of "Reactor Graphite" (Brown et al., 2018). Since carbon-based graphite is the moderator in HTR-PM, the change of graphite cross sections is supposed to have an appreciable impact on the simulation.

4.2 Influence of Heterogeneity of TRISO Particles

Within the fuel pebble, UO_2 fuel is contained in separately distributed TRISO particles, forming the heterogeneity of TRISO particles. To study its effect, three examples are considered using randomly placed TRISO particles, regularly placed TRISO particles, and homogeneous material, respectively, as shown in **Figure 6**. Material compositions in the fuel pebbles are kept the same between the three examples.

The k_{eff} of the reactor and k_{inf} of a single fuel pebble are calculated. The results are shown in **Table 1**.

The difference of k_{eff} of the reactor using different fuel enrichment is also calculated. The results are shown in **Table 2**. Note that the enrichment of the high-fidelity model is 4.2%.

It is worth mentioning that the regularly placed TRISO particle model is not directly generated using the lattice geometry (Liu et al., 2015) of RMC code. Instead, the positions of TRISO particles are determined using a Python script. The script first generates a large lattice of particles, with the lattice pitch determined based on the packing fraction. Then particles located beyond the fuel pebble region are deleted. Using this method, regularly placed TRISO particles without overlapping with the fuel pebble boundary are generated, as shown in **Figure 6B**. The packing fraction of regularly and randomly placed TRISO particles used in this study are very close, with 11,665 and 11,666 particles in each pebble, respectively.

Pebble positions and mixed pebbles are set to be the same between these three examples; thus, the uncertainty is only influenced by MC method and TRISO particle positions. According to **Section 3.2**, the standard deviation of multiplication factor from MC calculation is 10 pcm. The results suggest that the difference between randomly and regularly placed TRISO particles are insignificant, but the result using homogeneous material is unacceptable.

4.3 Influence of Pebble Bed Cone Angle

To study the effect of the pebble bed cone angle, six models with different cone angles (as shown in **Figure 7**) are constructed and calculated. The consistent 234,957 graphite pebbles and 102,300 mixed pebbles are used in each model. The results are shown in **Table 3**.

Obviously, pebble positions and mixed pebbles cannot stay the same when the cone angle changes. Thus, the uncertainty of this result is influenced by all the three factors mentioned in **Section 3.1**, making the standard deviation 53 pcm.

The results show that the cone angle can significantly influence k_{eff}. With a larger cone angle, the k_{eff} is smaller. This is because a larger cone angle results in more neutron leakage. It should also be noticed that at the angle of 25°, a change of 5° in the cone angle can lead to a difference of 200 pcm in k_{eff}, indicating that it is necessary to use the correct angle when modeling HTR-PM.

5 CONCLUSION

A high-fidelity model for the first criticality of pebble-bed reactor HTR-PM is built using MC code RMC and DEM code LAMMPS. The uncertainty of the model is studied based on three inherent factors: randomness of MC method, randomness of TRISO particle and pebble positions, and randomness of mixed pebbles. Results suggest that the main factor causing uncertainty of the model is the randomness of mixed pebbles, and the influence of TRISO particle positions can be neglected.

The effects of cross-section library, heterogeneity of TRISO particles, and angle of cone formed by pebble packing are also studied. Results show that these factors can significantly influence the k_{eff} result. k_{eff} using ENDF/B-VIII.0 is about 200 pcm larger than that of ENDF/B-VII.1. The results of randomly or regularly placed TRISO particles are not remarkably different, but it is not favorable to simply homogenize the material in MC simulation. The influence of pebble bed cone angle is relatively large. With larger cone angle, the k_{eff} is smaller. A difference of 200 pcm can result from a change of 5° in the cone angle at 25°.

Due to the limitation of calculation time, the cone structure of the pebble bed is not generated directly by LAMMPS code, which can be improved in further studies. It is also suggested in future work to carry out MC depletion calculation of HTR-PM considering pebble flow.

DATA AVAILABILITY STATEMENT

The original contributions presented in the study are included in the article/Supplementary Material, further inquiries can be directed to the corresponding author.

AUTHOR CONTRIBUTIONS

RL: methodology, numerical simulation, and writing—original draft preparation. ZL: computing resources, simulation result evaluation, and writing—reviewing and editing. ZF: code development and simulation result evaluation. JL: conceptualization, supervision, writing—reviewing and editing, and funding acquisition. LZ: supervision and resources.

FUNDING

The research was supported by the faculty startup funds of Tsinghua University.

ACKNOWLEDGMENTS

We gratefully acknowledge the reactor physics team of the Institute of Nuclear and New Energy Technology, Tsinghua University, for providing recommendations in constructing the model. We acknowledge RMC development team from the Department of Engineering Physics, Tsinghua University, for providing the RMC code used in this work.

REFERENCES

Abedi, A., Vosoughi, N., and Ghofrani, M. B. (2011). "An Exact MCNP Modeling of Pebble Bed Reactors," in 2011 International Nuclear Atlantic Conference, Belo Horizonte, MG, Brazil, October 24–28, 2011.

Abedi, A., and Vosoughi, N. (2012). Neutronic Simulation of a Pebble Bed Reactor Considering its Double Heterogeneous Nature. *Nucl. Eng. Des.* 253, 277–284. doi:10.1016/j.nucengdes.2012.08.030

Auwerda, G. J., Kloosterman, J. L., Lathouwers, D., and van der Hagen, T. H. J. J. (2010). Effects of Random Pebble Distribution on the Multiplication Factor in HTR Pebble Bed Reactors. *Ann. Nucl. Energ.* 37, 1056–1066. doi:10.1016/j.anucene.2010.04.008

Brown, D. A., Chadwick, M. B., Capote, R., Kahler, A. C., Trkov, A., Herman, M. W., et al. (2018). ENDF/B-VIII.0: The 8 Th Major Release of the Nuclear Reaction Data Library with CIELO-Project Cross Sections, New Standards and Thermal Scattering Data. *Nucl. Data Sheets* 148, 1–142. doi:10.1016/j.nds.2018.02.001

Chen, H., Fu, L., Jiong, G., and Lidong, W. (2015). Uncertainty and Sensitivity Analysis of Filling Fraction of Pebble Bed in Pebble Bed HTR. *Nucl. Eng. Des.* 292, 123–132. doi:10.1016/j.nucengdes.2015.05.032

Çolak, Ü., and Seker, V. (2005). Monte Carlo Criticality Calculations for a Pebble Bed Reactor with MCNP. *Nucl. Sci. Eng.* 149 (2), 131–137. doi:10.13182/NSE04-17

Guo, J., Wang, Y., Zhang, H., Cui, M., and Li, F. (2021). Challenges and Progress of Uncertainty Analysis for the Pebble-Bed High-Temperature Gas-Cooled Reactor. *Prog. Nucl. Energ.* 138, 103827. doi:10.1016/j.pnucene.2021.103827

Hao, C., Li, P., She, D., Zhou, X., and Yang, R. (2020). Sensitivity and Uncertainty Analysis of the Maximum Fuel Temperature under Accident Condition of HTR-PM. *Sci. Technol. Nucl. Installations* 2020, 1–21. doi:10.1155/2020/9235783

Helton, J. C., Johnson, J. D., Sallaberry, C. J., and Storlie, C. B. (2006). Survey of Sampling-Based Methods for Uncertainty and Sensitivity Analysis. *Reliability Eng. Syst. Saf.* 91, 1175–1209. doi:10.1016/j.ress.2005.11.017

Liu, S., She, D., Liang, J.-G., and Wang, K. (2015). Development of Random Geometry Capability in RMC Code for Stochastic Media Analysis. *Ann. Nucl. Energ.* 85, 903–908. doi:10.1016/j.anucene.2015.07.008

Plimpton, S. (1995). Fast Parallel Algorithms for Short-Range Molecular Dynamics. *J. Comput. Phys.* 117, 1–19. doi:10.1006/jcph.1995.1039

Rintala, V., Suikkanen, H., Leppänen, J., and Kyrki-Rajamäki, R. (2015). Modeling of Realistic Pebble Bed Reactor Geometries Using the Serpent Monte Carlo Code. *Ann. Nucl. Energ.* 77, 223–230. doi:10.1016/j.anucene.2014.11.018

Rycroft, C. H., Dehbi, A., Lind, T., and Güntay, S. (2013). Granular Flow in Pebble-Bed Nuclear Reactors: Scaling, Dust Generation, and Stress. *Nucl. Eng. Des.* 265, 69–84. doi:10.1016/j.nucengdes.2013.07.010

She, D., Xia, B., Guo, J., Wei, C.-L., Zhang, J., Li, F., et al. (2021). Prediction Calculations for the First Criticality of the HTR-PM Using the PANGU Code. *Nucl. Sci. Tech.* 32, 90. doi:10.1007/s41365-021-00936-5

Sun, K., Wilson, J., Hauptman, S., Ji, R., Dave, A. J., Zou, Y., et al. (2018). Neutronics Modeling and Analysis of the TMSR-SF1 Fuel Lattice and Full Core with Explicit Fuel Particle Distribution and Random Pebble Loadings. *Prog. Nucl. Energ.* 109, 171–179. doi:10.1016/j.pnucene.2018.08.005

Wang, K., Li, Z., She, D., Liang, J. G., Xu, Q., Qiu, Y., et al. (2015). RMC - A Monte Carlo Code for Reactor Core Analysis. *Ann. Nucl. Energ.* 82, 121–129. doi:10.1016/j.anucene.2014.08.048

Wu, M., Gui, N., Wu, H., Yang, X., Tu, J., and Jiang, S. (2019). Numerical Study of Mixing Pebble Flow with Different Density in Circulating Packed Bed. *Ann. Nucl. Energ.* 130, 483–492. doi:10.1016/j.anucene.2019.03.020

X-5 Monte Carlo Team (2003). MCNP-A General Monte Carlo N-Particle Transport Code, Version 5, Vol. I & II: User's Guide. Los Alamos National Laboratory. LA-13709-M.

Yang, X., Hu, W., and Jiang, S. (2009). Experimental Investigation on Feasibility of Two-Region-Designed Pebble-Bed High-Temperature Gas-Cooled Reactor. *J. Nucl. Sci. Technol.* 46, 374–381. doi:10.3327/jnst.46.37410.1080/18811248.2007.9711543

Zhang, Z., Wu, Z., Sun, Y., and Li, F. (2006). Design Aspects of the Chinese Modular High-Temperature Gas-Cooled Reactor HTR-PM. *Nucl. Eng. Des.* 236, 485–490. doi:10.1016/j.nucengdes.2005.11.024

Conflict of Interest: The authors declare that the research was conducted in the absence of any commercial or financial relationships that could be construed as a potential conflict of interest.

frontiers in Energy Research

BRIEF RESEARCH REPORT
published: 04 February 2022
doi: 10.3389/fenrg.2022.788753

A Lightweight Verification Method Based on Metamorphic Relation for Nuclear Power Software

Meng Li[1,2,3], *Xiaohua Yang*[1,2,3]*, *Shiyu Yan*[1,2,3], *Jie Liu*[1,2,3], *Yusheng Liu*[4] *and Jun Sun*[5]

[1]School of Computing, University of South China, Hengyang, China, [2]Engineering and Technology Research Center of Software Evaluation and Testing for Intellectual Equipment of Hunan Province, Hengyang, China, [3]CNNC Key Laboratory on High Trusted Computing, Hengyang, China, [4]Nuclear and Radiation Safety Center, Ministry of Ecological Environment of China, Beijing, China, [5]Institute of Nuclear and New Energy Technology, Tsinghua University, Beijing, China

The verification of nuclear design software commonly uses direct comparison methods. Benchmark questions, classical programs, experimental data, manual solutions, etc., would be used as expected results to compare with program outputs to evaluate the reliability of software coding and the accuracy of the numerical solution. Because nuclear power software numerically simulates complex physical processes, it involves many partial differential equations. It is usually challenging to construct analytical or accurate solutions and is expensive to develop benchmark questions and experimental data. Hence, the quantity of verification examples is small. By using the direct comparison method, verification is complicated, high cost, and inadequate. Entering the validation process without adequate proof will adversely impact the effectiveness and efficiency of validation. Metamorphic testing is an indirect verification technology that cleverly combines the nature of the model with software verification. It evaluates the correctness of the code by examining whether the program satisfies the metamorphic relation. Without manual solutions or benchmark examples, it has broad application prospects in the field of nuclear power. A lightweight verification method based on metamorphic relation has been produced here. Metamorphic relations are identified from physical equations, numerical algorithms, and program specifications. Next, they are explicitly used to system, integration, and unit tests to improve test adequacy. Because no need to develop verification examples, this method can detect code errors as soon as possible at a low cost, improve test efficiency, avoid mistakes remaining in subsequent stages and reduce the overall cost of verification.

Keywords: nuclear power software, metamorphic relation, lightweight verification method, software verification, metamorphic testing

OPEN ACCESS

Edited by:
Qian Zhang,
Harbin Engineering University, China

Reviewed by:
Xiaoyuan Xie,
Wuhan University, China
Yu Ma,
Sun Yat-sen University, China
Tao Zhang,
Macau University of Science and Technology, Macao SAR, China

***Correspondence:**
Xiaohua Yang
xiaohua1963@foxmail.com

Specialty section:
This article was submitted to Nuclear Energy, a section of the journal Frontiers in Energy Research

Received: *03 October 2021*
Accepted: *13 January 2022*
Published: *04 February 2022*

Citation:
Li M, Yang X, Yan S, Liu J, Liu Y and Sun J (2022) A Lightweight Verification Method Based on Metamorphic Relation for Nuclear Power Software. Front. Energy Res. 10:788753. doi: 10.3389/fenrg.2022.788753

INTRODUCTION

The development of nuclear power software usually includes the stages of physical equation modeling, numerical method selection, and code programming. Verification evaluates whether the algorithm is suitable for equations and whether the code accurately implements the algorithm. Verification is the prerequisite for validation. Without adequate verification, it will substantially adversely impact the effectiveness and efficiency of validation.

Software verification usually uses direct comparison methods. Benchmark questions, classical programs, experimental data, manual solutions, etc., would be used as expected results to compare with program outputs to evaluate the reliability of software coding and the accuracy of the numerical solution. These verification examples are part of system-level information and can only be used for system and acceptance testing. While failures have been detected in those testing levels, revealing and locating defects in functions and solvers is a great challenge. As a result, the cost is exceptionally high, even leading to the collapse of the entire project. Because nuclear power software numerically simulates complex physical processes, it involves many partial differential equations. It is usually impossible to construct analytical or accurate solutions and is expensive to develop benchmark questions and experimental data. Hence, the small number of verification examples further aggravates nuclear software verification's difficulty.

In the process of software verification, tester often implicitly check whether the code satisfies the specific characteristics of the physical equation, numerical solution method, and program specification. If the above rules are violated, it indicates that the code has defects and verification is false. Metamorphic testing (MT) is a rapid indirect verification method for qualitative evaluation. MT cleverly combines the evaluation of the model nature with software verification. Without manual solutions or benchmark questions, it assesses the code reliability by examining whether the code satisfies the metamorphic relation (MR). It has broad application prospects in the nuclear field.

The main innovation points in this article include: 1) A lightweight verification method based on metamorphic relation has been developed. It employs MRs to rapidly evaluate the code reliability at a low cost before the traditional methods estimate the solution accuracy expensively. The former is a supplement to the latter. 2) It makes the verification of nuclear power software more reasonable, reveals defects in the early stage of verification, and reduces the total cost of development. 3) The study of MR is helpful to deep insight into the characters of equations and algorithms, improve the quality of code and continuously increase the developer's confidence in the program. In other words, MRs are the domain knowledge, and the research on them is profit to understand the system better and reuse that knowledge.

Specifically, a group of metamorphic relations is identified from the characteristics of physical equations and numerical algorithms. Then, metamorphic relations are explicitly used to evaluate whether the code keeps the specific rules of equations and algorithms. Two types of code errors can be revealed out quickly and efficiently. The first one is that the code does not accurately implement the numerical algorithm, and the second one is that the numerical method does not correctly solve the physical model.

For the application of this method, the point-depletion computing code, namely NUIT, was used as the experimental object. Without verification examples, the code failures were found by the metamorphic relation. This method significantly alleviates the requirement for verification examples and improves verification efficiency and adequacy.

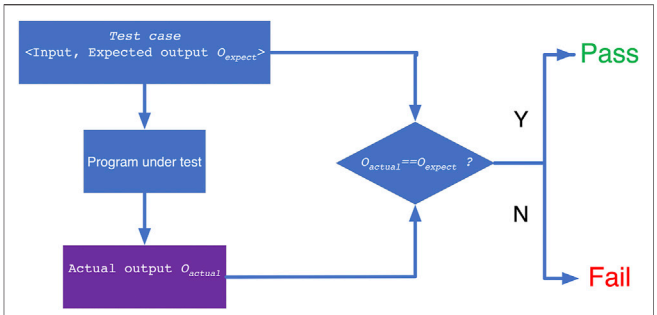

FIGURE 1 | The working principle of the direct comparison method.

Direct Comparison Method

At present, nuclear power software verification usually adopts a direct comparison method, which verifies the correctness of the code by comparing the actual output with the expected result. The working principle is shown in **Figure 1**.

The expected result mainly employs typical benchmark questions, power plant operating data, and experimental bench data. For example, software package NESTOR is verified by international benchmark questions, Qinshan Nuclear Power Plant Unit 1 and Unit 2 operating data, and Hualong No. 1 Unit bench data (Lu et al., 2018). Furthermore, verification of PCM adopts benchmark questions, CPR1000/M310 power plant data, critical reactor test data, and similar software (Wang et al., 2018). The classical program is also a kind of expected result, such as the ORIGEN program for fuel consumption analysis (Hermann and Westfall 1998), APOLLO (Sanchez et al., 1988) and CASMO (Rhodes, Smith, and Lee 2006) for assembly calculation, MCNP(Brown et al., 2002) for radiation shielding, RELAP (Andrs et al., 2012) for system program and so on.

Oracle Problem

Oracle is a mechanism used to determine whether the execution result of the program under test is correct. It is challenging to construct when the expected result does not exist or the construction cost is exceptionally high; it is called an Oracle problem (Barr et al., 2015). Nuclear power software involves the numerical solution of many partial differential equations. It is usually tricky to construct analytical or accurate solutions. Furthermore, for fourth-generation reactors, such as high-temperature gas-cooled reactors, sodium-cooled fast reactors, molten salt reactors, lead reactors et al., and modern designs, e.g., high-fidelity, one-step method, multi-physics coupling, etc., new-generation software has almost no comparable programs and benchmark questions. In addition, benchmark questions, power plant operating data, and experimental bench data are only applicable to specific reactor types due to differences in the neutron energy spectrum, geometric configuration, and core materials. For verification examples, the development cost is high, the cycle is long, and the quantity is small. Therefore, the Oracle problem of nuclear power software is particularly prominent.

Compared with traditional testing methods, i.e., the direct comparison method, this type of software is called a non-testable

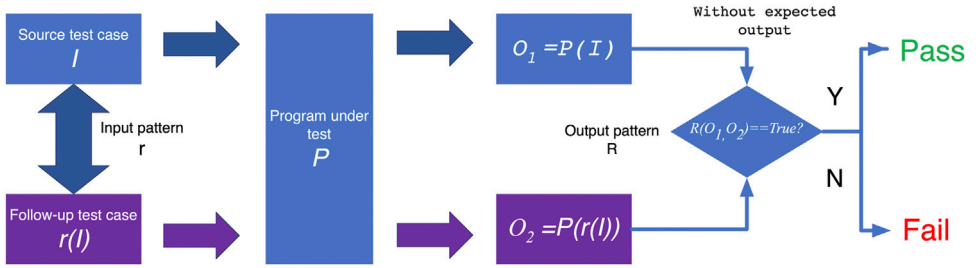

FIGURE 2 | The working principle of the metamorphic testing.

system (Patel and Hierons 2018). Oracle problem makes nuclear power software testing insufficient. Hence, defects are challenging to find, which affects the safety and economy of engineering design. The sharp-jump problem is found in the classic burnup program ORIGEN when it calculates the decay chain of ^{239}Pu and ^{233}U (Isotalo and Aarnio 2011). If the half-life of some daughter-nucleus meets a specific relationship with the burnup step length, the calculation error will suddenly increase. Without adequate verification, such situations would remain.

Generally, software verification includes four test levels: unit testing, integration testing, system testing, and acceptance testing. Each level requires differently corresponding expected results. However, benchmark questions are only applicable to acceptance testing, and the expected results are seriously insufficient in other test levels. Code bugs are challenging to find early, making it challenging to locate defects and high costs for debugging and repairing. The characteristics of nuclear power software essentially cause the Oracle problem. Even if developing more benchmark questions, this problem can only be alleviated but cannot be solved. Therefore, there is an urgent need to introduce new software verification technologies.

Metamorphic Testing

Most scientific computing software is untestable software (Kanewala and Bieman 2014). Software verification often implicitly checks whether the code satisfies the specific characteristics of the physical equations, numerical methods, and program specifications. If those characteristics are violated, the code should have errors and could not pass the test. Metamorphic testing is an indirect verification technology that skillfully combines the program's specific characteristics checking with software verification without constructing verification examples. The correctness of the code is evaluated by examining whether the code meets the metamorphic relation (MR). Its working principle is shown in **Figure 2**.

MRs are necessary properties of the target function or algorithm in relation to multiple inputs and their expected outputs (Chen et al., 2018; Chen and Tse 2021). For example, a program P implements sine function. It is hard to construct an oracle to determine whether P(x) is correct. However, applying her periodicity, i.e., sin(x) = sin (x+2π), an MR can be obtained as following: if $x_2 = x_1 + 2\pi$, then P (x_2) = P (x_1). As a result, using a group of inputs that satisfied such input pattern, if twice execution results violate the output pattern, it will indicate that P does not agree with MR. In other words, P conflicts with the basic property of sine. Thus, P has a failure. MRs are essential properties that are meaningful for software verification, and codes should abide by them.

Metamorphic testing is one of the effective means to solve Oracle problems (Chen et al., 1998; Liu et al., 2014; Segura et al., 2018; Kanewala and Yueh Chen 2019). Studies have shown that MT has the advantages of reasonable cost and a more vital ability to expose errors (Hu et al., 2006). It is used for software verification, software validation, and software quality assurance (Segura and Zhou 2018). Furthermore, it appears to be the only technique applicable to all three areas of verification, namely testing, proving, and debugging (Chen and Tse 2021). MT has broad application prospects in the nuclear field.

LIGHTWEIGHT VERIFICATION METHOD BASED ON METAMORPHIC RELATION

For relieving the Oracle problem, this paper developed a lightweight verification method based on metamorphic relation. The MR hierarchical classification model (Xiaohua et al., 2020) identifies MRs from the specific property of physical equations, numerical algorithms, and program specifications. Then applying them to system testing, integration testing, and unit testing, respectively, to improve the adequacy of testing. Because there is no need to develop verification examples, this method can reveal code failures at the earliest opportunity. As a result, it will improve verification efficiency at a lower cost. In addition, it is also a necessary supplement to the traditional verification technology.

NUIT is a burnup calculation code independently developed by the Institute of Nuclear and New Energy Technology of Tsinghua University (Jian et al., 2020). NUIT implements a variety of burnup algorithms, including the transmutation trajectory analysis method (TTA), the Chebyshev Rational Approximation Method (CRAM), Quadrature group Rational Approximation Method (QRAM), Laguerre Polynomial Approximation method (LPAM), and Mini-Max Polynomial Approximation method (MMPA). For ease of understanding, the rest of this article uses NUIT for discussion.

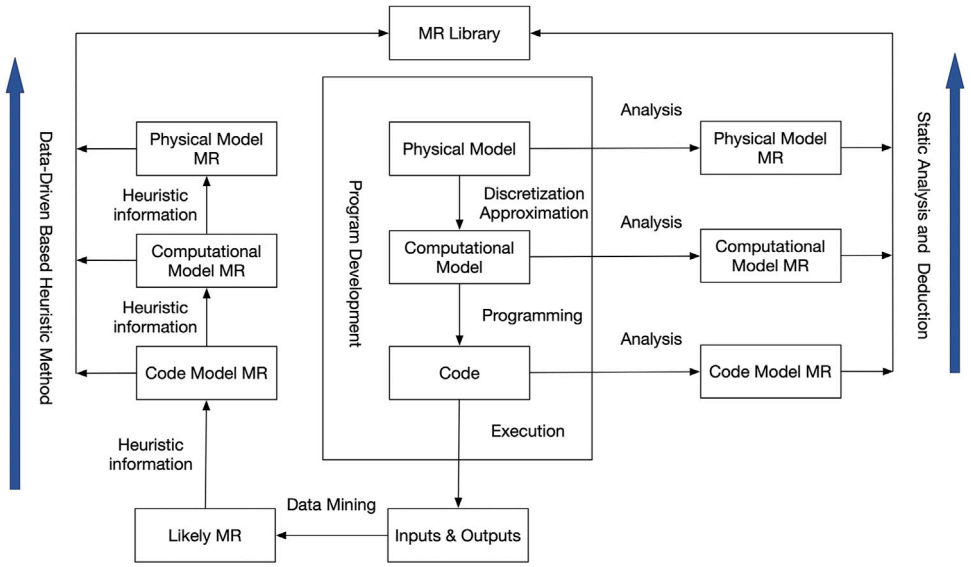

FIGURE 3 | Metamorphic relation identification model.

MR Identification Model

MR is the key in MT. According to current research literature (Sun et al., 2019; Segura et al., 2016), there are several MR identification techniques, such as machine-learning-based, search-based, pattern-based, data mutation-based, and existing MRs' composition etc. We divide them into two categories, namely static analysis, and dynamic discovery, from the perspective of whether to execute the program under test. The former does not execute the program and derives MR by analyzing physical equations' properties, numerical algorithms, and program specifications. The latter reveals MR from inputs and outputs. Because these relations are fitted from data, their validity has not been proved theoretically, thus called likely relations. However, they can provide heuristic information for MR identification. As a result, one abstract MR identification model has been constructed, illustrated in **Figure 3**. This model has four types of MR, i.e., physics model, computational model, code model, and likely MR. Besides them, a single MR should be formally described with the template approach (Segura et al., 2017).

The Verification Processes

It is assumed that a group of MR has been obtained. The lightweight verification method includes two core stages: MR identification and program evaluation. Specifically, we describe the main activities as follows: 1) Analyzing the nature of the physical equation. 2) Investigating the properties of the numerical algorithm. 3) Studying the characteristic of the program specification. 4) Revealing the metamorphic relation by techniques in the identification model, i.e., transforming the above rules into a hierarchical MR model. 5) In accordance with MR, a group of MR test input pairs is generated, and the program under test is evaluated with MR. If the MR is satisfied, the test passes. Otherwise, it indicates that at least a failure in the code.

For demonstrating the details, there are several examples as follows.

Example 1: We are analyzing the nature of the physical equation. In the case of the fission reaction, the density of ^{135}Xe gradually increases and does not change until production and consumption reach a dynamic balance after about 2–3 days. According to this rule, we can identify a physical model MR. Specifically, suppose t is the burnup time, D(t) is the nuclide density of ^{135}Xe, T is the threshold at which the reaction reaches balance. Before balance, $(t1, t2) < T$, $if\ t1 < t2$, $then\ D(t1) < D(t2)$; after balance, $(t1, t2) > \mathrm{T}, if\ t1 < t2, then\ D(t1)£\mathrm{D}(t2)$. We construct two sets of test inputs. One set of the total time is less than the balance time, and the other set is greater than the balance time. The failure can be detected if the density of ^{135}Xe violates MR.

Example 2: One property of the numerical algorithm is that the nuclide density should smoothly change with the burnup step. The corresponding computational model MR is described as follows. Similarly, t1 and t2 is the burnup time, D(t) is the nuclide density, T is the error threshold. If t2 is next to t1, then$|\mathrm{D}(t1)-\mathrm{D}(t2)| < \mathrm{T}$. A set of test inputs with continuous changes in burnup step length is constructed, and the failure can be found if the absolute deviation is greater than the threshold.

Example 3: After studying the characteristics of the program specification of the matrix exponent method, we find one rule that the result should not be affected by the nuclide ranking rule in the matrix. Hence, a code model MR is obtained. It assumes that o is the sorting rule, D(o) is the nuclide density when the burnup matrix is sorted by rule o, T is the error threshold. If o1

and o2 are different, then $|D(o1) - D(o2)| < T$. Next, it orders the burnup matrix with three rules: ascending, descending, and random. It indicates that a failure exists while the change of actual outputs has occurred.

Automation Execution Algorithm

It supposes that a set of MR has been obtained. The automation execution algorithm is as follows: 1) Reading a metamorphic relation. 2) Generating a set of test inputs according to the input pattern r and driving the program under test to execute to obtain the calculation outputs. 3) Evaluate whether those results comply with the output pattern R. If R is violated, the verification fails, and the process ends. Else 4) checking whether there is still a metamorphic relation that has not been adopted. If not, terminate the process, else do activity 1)–3) repeatedly.

CASE STUDY

The burnup program describes the law of nuclide density changes over time. It is an essential part of the reactor's physical design. It plays a crucial role in calculating the breeding and consumption of fuel in the reactor and changes in reactivity. The density of a particular nuclide can be expressed by **Eq. 1**.

$$\frac{dn_i}{dt} = \sum_{j=1} l_{ij}\lambda_j n_j + \varnothing \sum_{k=1} f_{ik}\sigma_k n_k - (\lambda_i + \varnothing\sigma_i)n_i \tag{1}$$

n_i is the density of nuclide i, l_{ij} is the production rate of nuclide j decaying into nuclide i, λ_j is the decay constant of nuclide j, $\varnothing$ is the space and energy average neutron flux, f_{ik} is the production rate that nuclide k fission into nuclide i, σ_i is the average neutron absorption cross-section of nuclide i.

The burnup equation can also be rewritten in matrix form, as shown in **Eq. 2**, where A is the coefficient matrix of the N-order nuclide depletion equation, and N is the number of nuclides.

$$\frac{d\vec{N}(t)}{dt} = A(t)\vec{N}(t) \tag{2}$$

Experiment

Twenty-eight MRs have been identified from NUIT using the static analysis technique, of which eighteen are physical model MR, and the rest are computational model MR (Meng et al., 2020; Li et al., 2020a; Li et al., 2020b; Li et al., 2021). Specifically, they are listed as follows.

The input parameters of NUIT mainly include initial fuel enrichment, mass, burnup step length, step unit, and the number of steps. The burnup calculation types include pure decay, constant flux, and constant power. The parameters constrained by the calculation type have neutron fluence rate and power. The solver mainly includes TTA and CRAM. The solver parameters include approximate order and truncation threshold. The output parameters mainly include nuclide density, radioactivity, neutron reaction rate, neutron absorption rate, decay heat, and other physical quantities.

By analyzing the physical model MRs, the adjustable input parameters include fuel enrichment, mass, total burnup time, neutron flux, and power. Since the neutron flux and power can be converted to each other, and the obtained properties are equivalent. Thus only power is taken here. The source test case of MT uses the verification example of the user manual. The burnup database adopts the high-temperature gas-cooled reactor HTGR nuclide database. The solver employs CRAM. The initial values of other parameters involve that the fuel enrichment is 8.5 percent, mass is one ton, power is 20 MW. The total burnup time is 340 days, of which the step length of the first stage is 1 day, the second stage is 4 days, and the third stage is 12 days, with twenty steps in each stage. The nuclide density is selected as the output parameter.

Figure 4 illustrates the trend relation between the density of some nuclides and the burnup level. A linear function y = ax + b can express some relations, such as ^{135}Cs and ^{235}U, the coefficient a is greater than zero in the former, while a is less than zero in the latter. A power function $y = ax^2+bx + c$ can also denote ones; for example, ^{237}Np and ^{135}Xe, the parameter a is greater than zero in the former, while a is less than zero in the latter. These observations can guide MR identification.

Assuming that the input pattern of MR is inequality, the single factor approach is used to design test cases, i.e., only one parameter changes at a time. To accurately describe the physical laws, the number of samples is more than 20. Therefore, the design results are as follows: 1) the fuel enrichment is from 1 to 20 percent, increasing by 1 percent each time; 2) The fuel mass is from 500 to 10000 kg, increasing by 500 kg each time; 3) The power is from 20 to 210 MW, increasing or decreasing by 10 MW each time. To sum up, a total of 160 test cases are designed.

Result

A total of forty-six defects were found, of which thirteen bugs were contributed by the lightweight method. After analyzing carefully, we can divide the defects of NUIT into three categories. The first one is that the code does not accurately implement the numerical algorithm. The second one is that the numerical algorithm does not correctly solve the physical equation; It results in the applicable scope of the code being narrower than that agreed in the requirements document. The last one is that the parameters of the algorithm are set inappropriately for specific calculation conditions. Hence, the first type error number is thirteen, and the second type error is three. Half of them are contributed by the lightweight method.

For example, 1) when solving the short half-life nuclides, such as ^{134}Cs, ^{242}Cm, and ^{244}Cm, etc., by the TTA method, it is necessary to shorten the burnup step length; otherwise, the deviation will increase significantly. 2) Since time-consuming and significant deviation, the TTA method is not suitable for solving non-homogeneous burnup equations. 3) Matrix exponent numerical algorithms, like CRAM, QRAM, LPAM, and others, are more stable and reliable in the constant power than constant neutron flux. 4) Similarly, their results of the instantaneous are better than integral.

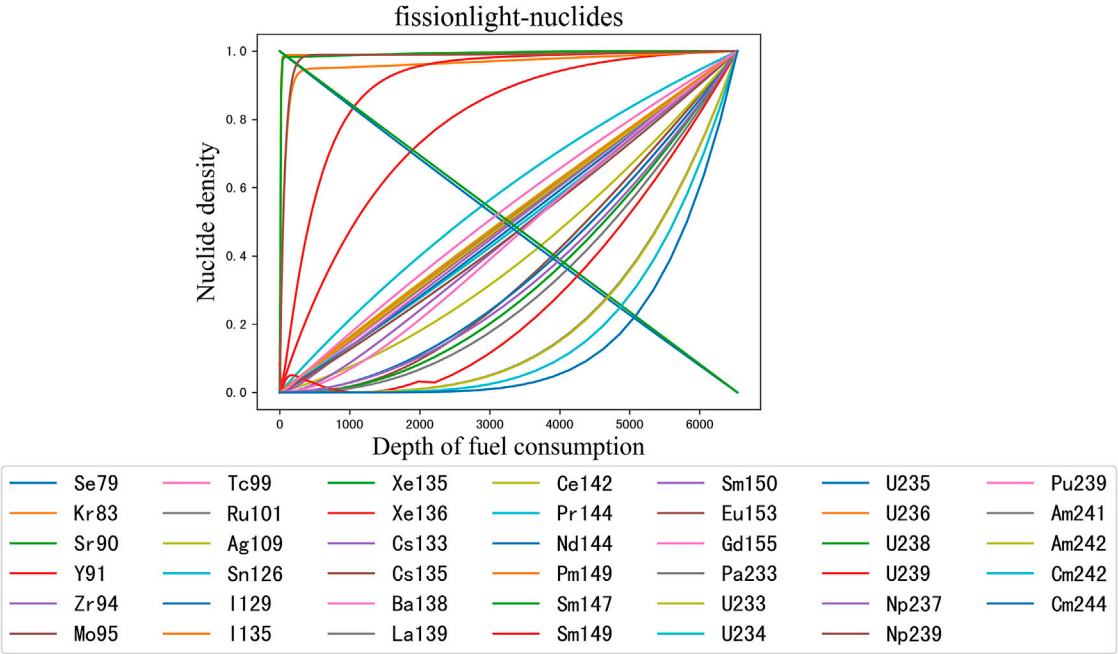

FIGURE 4 | The relation between nuclide density and burnup level.

DISCUSSION

The program model MR is applied for unit testing to evaluate whether the code correctly performs the program design specifications. Next, the computational model MR is employed for integration testing to estimate whether the code accurately implements the numerical solution algorithm. Moreover, the physical model MR is performed for system testing to ensure that the code correctly explains the physical equations.

Compared with the traditional verification model, this paper clearly defines the nature of verification activity. It makes the implicit evaluation of the program's properties explicating. Furthermore, we can perform qualitative verification on nuclear power software without benchmarks at a low cost by taking advantage of MT. It should be compliance testing before any quantitative examinations at every test level.

The lightweight verification method has the following advantages:

1) It assumes that the program accurately implements the numerical algorithm. Then, the code should maintain the specific properties of the algorithm, such as symmetry, homogeneity, conjugation, error convergence, etc. Similarly, if the numerical algorithm correctly solves the physical equation, it should keep the expected natures of the equation even though there are no verification examples. If the actual outputs violate the above assumptions, there must be bugs in the program under test. Therefore, the lightweight verification method can significantly reduce verification costs and improve verification efficiency.
2) The properties of numerical algorithms and physical equations belong to high-order rules independent of the specific implementation of code. The program should keep these high-order regulations, whether the programming language is Python or C/C + +, whether the mathematical library is Intel MKL, OPENBLAS, or EIGEN. Therefore, lightweight verification has broader applicability and stronger reusability, which is helpful to improve the evaluation level of nuclear power software. It has important practical significance for shortening software certification time.

With advantage 1, the actual test time of NUIT only took 3 months, and there was no development cost of verification example for improvement of the test coverage. Based on advantage 2, the physical MRs are applied at the different solvers of NUIT, such as TTA, CRAM, and others. It reduces the test time significantly. Moreover, MRs identified from NUIT can verify other burnup calculation programs, such as KYLIN-2 developed by NPIC.

To sum up, the lightweight verification method based on MR alleviates the Oracle problem better compared with the traditional direct comparison method. It uses a lower cost to increase the test adequacy, reveal code bugs in early stage of verification, and avoid leaving defects to the subsequent testing level. Since reducing the cost of defect location and repair, improving the efficiency of research and development, it has broad application prospects in nuclear power software verification.

The main limitations of this method come from MR and source test cases. At present, MR identification technology mainly depends on manual analysis and inference, so data-driven MR mining technology is a promising research direction.

DATA AVAILABILITY STATEMENT

The original contributions presented in the study are included in the article/Supplementary Material, further inquiries can be directed to the corresponding author.

AUTHOR CONTRIBUTIONS

XY: Supervision, Conceptualization, Methodology. ML: Conceptualization, Methodology, Writing an original draft and editing. SY: Methodology, Analysis. JL: Methodology, Analysis. YL: Methodology, Experiment. JS: Conceptualization, Experiment.

FUNDING

Financial support of National Science and Technology Major Project of China (2019ZX06005001), Natural Science Foundation of Hunan Province of China (2020JJ4519), Scientific Research Project of Department of Education of Hunan Province of China (19C1608), Teaching Reform Research Project of Hunan Province of China (Xiang Jiaotong 2018; No. 436-327).

REFERENCES

Andrs, D., Berry, R., Gaston, D., Martineau, R., Peterson, J., Zhang, H., et al. (2012). *Relap-7 Level 2 Milestone Report: Demonstration of a Steady State Single Phase Pwr Simulation with Relap-7*. Idaho Falls: Idaho National Laboratory.

Barr, E. T., Harman, M., McMinn, P., Shahbaz, M., and Yoo, S. (2015). The Oracle Problem in Software Testing: A Survey. *IIEEE Trans. Softw. Eng.* 41 (5), 507–525. doi:10.1109/TSE.2014.2372785

Brown, F. B., Barrett, R. F., Booth, T. E., Bull, J. S., Cox, L. J., Forster, R. A., et al. (2002). MCNP Version 5. *Trans. Am. Nucl. Soc.* 87 (273), 2–3935.

Chen, T. Y., Cheung, S. C., and Yiu, S. M. (1998). *Metamorphic Testing: A New Approach for Generating Next Test Cases. Technical Report HKUSTCS98-01*. HongKong: Department of Computer Science, Hong Kong University of Science and Technology. Available from: https://www.cse.ust.hk/~scc/publ/CS98-01-metamorphictesting.pdf.

Chen, T. Y., Kuo, F.-C., Liu, H., Poon, P.-L., Towey, D., Tse, T. H., et al. (2019). Metamorphic Testing. *ACM Comput. Surv.* 51 (1), 1–27. doi:10.1145/3143561

Chen, T. Y., and Tse, T. H. (2021). "New Visions on Metamorphic Testing after a Quarter of a Century of Inception," in ESEC/FSE 2021 - Proceedings of the 29th ACM Joint Meeting European Software Engineering Conference and Symposium on the Foundations of Software Engineering, August 2021 (New York, NY: Association for Computing Machinery), 1487–1490. doi:10.1145/3468264.3473136

Hermann, O. W., and Westfall, R. M. (1998). *ORIGEN-S: SCALE System Module to Calculate Fuel Depletion, Actinide Transmutation, Fission Product Buildup and Decay, and Associated Radiation Source Terms*. Washington, DC: Citeseer.

Hu, P., Zhang, Z., Chan, W. K., and Tse, T. H. (2006). "An Empirical Comparison between Direct and Indirect Test Result Checking Approaches," in Proceedings of the Third International Workshop on Software Quality Assurance, SOQUA 2006, New York, USA, November 2006 (New York, NY: Association for Computing Machinery), 6–13. doi:10.1145/1188895.1188901

Isotalo, A. E., and Aarnio, P. A. (2011). Comparison of Depletion Algorithms for Large Systems of Nuclides. *Ann. Nucl. Energ.* 38 (2–3), 261–268. doi:10.1016/j.anucene.2010.10.019

Kanewala, U., and Bieman, J. M. (2014). Testing Scientific Software: A Systematic Literature Review. *Inf. Softw. Tech.* 56 (10), 1219–1232. doi:10.1016/j.infsof.2014.05.006

Kanewala, U., and Yueh Chen, T. (2019). Metamorphic Testing: A Simple yet Effective Approach for Testing Scientific Software. *Comput. Sci. Eng.* 21 (1), 66–72. doi:10.1109/MCSE.2018.2875368

Li, J., She, D., Shi, L., and Liang, J. g. (2020). The NUIT Code for Nuclide Inventory Calculations. *Ann. Nucl. Energ.* 148, 107690. doi:10.1016/j.anucene.2020.107690

Li, M., Wang, L., Yan, S., Yang, X., Liu, J., and Wan, Y. (2020a). "Metamorphic Relations Identification on Chebyshev Rational Approximation Method in the Nuclide Depletion Calculation Program," in Proceedings of 2020 IEEE 20th International Conference on Software Quality, Reliability and Security Companin(QRS-C), Macau, China, Dec. 2020 (IEEE), 1–6. doi:10.1109/QRS-C51114.2020.00013December 11-14

Li, M., Yan, S., Yang, X., and Liu, J. (2020b). "Metamorphic Testing on Nuclide Inventory Tool." In Proceedings of the 2020 28th International Conference on Nuclear Engineering, V003T14A001. August 2020, American Society of Mechanical Engineers. doi:10.1115/ICONE2020-16403

Li, M., Wang, L., Yue, W., Liu, B., Liu, J., Liu, Z., et al. (2021). Metamorphic Testing of the NUIT Code Based on Burnup Time. *Ann. Nucl. Energ.* 153 (April), 108027. doi:10.1016/j.anucene.2020.108027

Liu, H., Kuo, F.-C., Towey, D., and Chen, T. Y. (2014). How Effectively Does Metamorphic Testing Alleviate the Oracle Problem. *IIEEE Trans. Softw. Eng.* 40 (1), 4–22. doi:10.1109/TSE.2013.46

Lu, Z., Li, Q., Dong, L., Chai, X., Fang, H., and Gong, Z. (2018). Engineering Applicability Strengthening Design and Practice of NESTOR Software Package. *Nucl. Power Eng.* 39 (1), 161–164. doi:10.13832/j.jnpe.2018.01.0161

Meng, L., Lijun, W., Shiyu, Y., and Xiaohua, Y. (2020). Metamorphic Relation Generation for Physics Burnup Program Testing. *Int. J. Performability Eng.* 16 (2), 297–306. doi:10.23940/ijpe.20.02.p12.297306

Patel, K., and Hierons, R. M. (2018). A Mapping Study on Testing Non-testable Systems. *Softw. Qual J* 26 (4), 1373–1413. doi:10.1007/s11219-017-9392-4

Rhodes, J., Smith, K., and Lee, D. (2006). "CASMO-5 Development and Applications," in Proceedings of the PHYSOR-2006 Conference, ANS Topical Meeting on Reactor Physics, Vancouver BC Canada, January 2006, 144.

Sanchez, R., Mondot, J., Stankovski, Ž., Cossic, A., and Zmijarevic, I. (1988). APOLLO II: A User-Oriented, Portable, Modular Code for Multigroup Transport Assembly Calculations. *Nucl. Sci. Eng.* 100 (3), 352–362. doi:10.13182/NSE88-3

Segura, S., Duran, A., Troya, J., and Cortes, A. R. (2017). "A Template-Based Approach to Describing Metamorphic Relations," in Proceedings of the 2nd International Workshop on Metamorphic Testing MET '17, Buenos Aires, Argentina, May 2017 (IEEE Press), 3–9. doi:10.1109/MET.2017.3

Segura, S., Fraser, G., Sanchez, A. B., and Ruiz-Cortes, A. (2016). A Survey on Metamorphic Testing. *IIEEE Trans. Softw. Eng.* 42 (9), 805–824. doi:10.1109/TSE.2016.2532875

Segura, S., Towey, D., Zhou, Z. Q., and Chen, T. Y. (2020). Metamorphic Testing: Testing the Untestable. *IEEE Softw.* 37, 46–53. doi:10.1109/MS.2018.2875968

Segura, S., and Zhou, Z. Q. (2018). "Metamorphic Testing 20 Years Later," in Proceedings of the 2018 ACM/IEEE 40th International Conference on Software Engineering, Gothenburg, Sweden, May 2018 (IEEE Computer Society), 538–539. doi:10.1145/3183440.3183468

Sun, C.-A., Fu, A., Poon, P.-L., Xie, X., Liu, H., and Chen, T. Y. (2019). METRIC+: A Metamorphic Relation Identification Technique Based on

Input Plus Output Domains. *IIEEE Trans. Softw. Eng.* 47, 1. doi:10.1109/tse.2019.2934848

Wang, C., Yang, S., Peng, S., Li, G., Ma, Y., Chen, J., et al. (2018). Automated Validation of CGN Nuclear Software Package PCM. *Nucl. Power Eng.* 39 (S2), 43–46. doi:10.13832/j.jnpe.2018.S2.0043

Xiaohua, Y., Shiyu, Y., Jie, L., and Meng, L. (2020). Hierarchical Classification Model for Metamorphic Relations of Scientific Computing Programs. *Computer Science* 47 (11A), 557–561. doi:10.11896/jsjkx.200200015

Conflict of Interest: The authors declare that the research was conducted in the absence of any commercial or financial relationships that could be construed as a potential conflict of interest.

Publisher's Note: All claims expressed in this article are solely those of the authors and do not necessarily represent those of their affiliated organizations, or those of the publisher, the editors and the reviewers. Any product that may be evaluated in this article, or claim that may be made by its manufacturer, is not guaranteed or endorsed by the publisher.

frontiers in Energy Research

ORIGINAL RESEARCH
published: 09 February 2022
doi: 10.3389/fenrg.2021.773067

Theoretically Modified Optical Length Research on the Physical Boundary of the Double-Heterogeneous System

Lou Lei, Chai Xiaoming, Yao Dong, Wang Lianjie, Li Mancang, Chen Liang, Liu Xiaoli, Zhang Hongbo, Li Sinan, Tang Xiao and Zhou Nan*

Science and Technology on Reactor System Design Technology Laboratory, Nuclear Power Institute of China, Chengdu, China

Because of the double-heterogeneity (DH), dispersed particle-type systems cannot be described by traditional neutronic programs, and the volumetric homogenization method (VHM) will bring reactivity calculation deviation because of ignoring the spatial self-shielding effect of the particles. In this article, the relationship between the reactivity calculation deviation and the optical length of dispersed particle-type fuel and different types of burnable poisons is analyzed. Also then, it was proposed that the influencing factors of reactivity calculation deviation can be integrated to a physical quantity named theoretically modified optical length containing the influencing factors mentioned earlier. In addition, the DH physical boundary has forward that, when the theoretically modified optical length is larger than 10^{-4}, reactivity calculation deviation of volumetric homogenization method will be larger than 100 pcm, and the DH of the dispersed particle-type systems should be considered.

Keywords: dispersed particle-type systems, double-heterogeneity, physical boundary, volumetric homogenization method, reactivity calculation deviation, optical length, corrected optical length

OPEN ACCESS

Edited by:
Tengfei Zhang,
Shanghai Jiao Tong University, China

Reviewed by:
Tiejun Zu,
Xi'an Jiaotong University, China
Zhitao Xu,
North China University of Water Resources and Electric Power, China

****Correspondence:***
Chai Xiaoming
chaixm@163.com

Specialty section:
This article was submitted to Nuclear Energy, a section of the journal Frontiers in Energy Research

Received: *09 September 2021*
Accepted: *28 December 2021*
Published: *09 February 2022*

Citation:
Lei L, Xiaoming C, Dong Y, Lianjie W, Mancang L, Liang C, Xiaoli L, Hongbo Z, Sinan L, Xiao T and Nan Z (2022) Theoretically Modified Optical Length Research on the Physical Boundary of the Double-Heterogeneous System. Front. Energy Res. 9:773067. doi: 10.3389/fenrg.2021.773067

INTRODUCTION

Particle-dispersed fuel can contain fission products under high temperature and deep burnup conditions and block the release of fission gas and fission fragments out of the fuel pellets. Because of its accident resistance and inherent safety, it has been widely used in fully ceramic microencapsulated (FCM) fuel (Cole and Maldonado, 2013; Xiang et al., 2014) of pressurized water reactors and the tristructural isotropic (TRISO) particle fuel of high-temperature gas-cooled reactors (Zhai et al., 2004; Zhang et al., 2021).

Particle-dispersed burnable poisons can increase the surface compatibility between the dispersed particles and the matrix by adding a coating layer on the surface of the particles and can improve the flexibility of the use of burnable poison. At the same time, because of the space self-shielding effect of the burnable poison particles, its burn speed is relatively slower than when a burnable poison is uniformed dispersed. So, the appropriate particle-dispersed burnable poison can be selected by selecting the type and particle size of the burnable poison to improve the flexibility of reactivity control (van Dam, 2000a; van Dam, 2000b; Kloosterman, 2003; Talamo, 2006).

Particle-dispersed fuels and burnable poisons have gradually attracted attention and applications due to the excellent characteristics mentioned earlier, but they have double-heterogeneity (DH), which cannot be described by traditional neutronic calculation programs (Sanchez and Pomraning, 1991; Hébert, 1993; Kim et al., 2005; Zhang et al.,

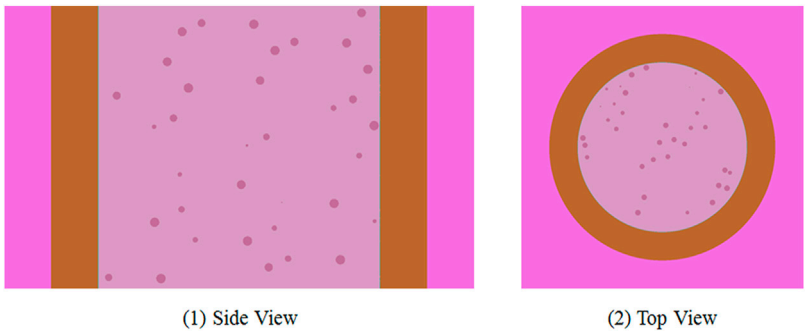

FIGURE 1 | Schematic diagram of random distribution of dispersed particles.

TABLE 1 | Main parameters of fuel cell.

Parameters	Values
Pitch, cm	1.26
Radius of fuel region, cm	0.4096
Thickness of air gas, cm	0.0084
Thickness of zirconium clad, cm	0.057
Density of zirconium clad, g/cm^3	6.5
Density of moderate H_2O, g/cm^3	1.0

2017a; Zhang et al., 2017b). The so-called DH refers to the heterogeneity of the core, cladding, and moderator on the macroscopic level and the heterogeneity of the dispersed particles and the matrix on the microscopic level. The traditional neutronic calculation program can only describe the macroscopic heterogeneity, and the simplest processing method for the DH is the Volumetric Homogenization Method (VHM), that is, the dispersed particles and the matrix are homogenized according to the volume weight, and then, the traditional neutronic calculation program can be used to model and calculate. In the world, a variety of types of DH processing methods have been proposed, e.g., the Sanchez–Pomraning method (Hébert, 1993; Sanchez and Pomraning, 1991) implemented in Dragon and Apollo, the reactivity equivalent-physical transformation method (Lei and Dong, 2020; Li et al., 2018) for treating the FCM (Kurt, 2012) fuel in advanced pressurized water reactor, and the equivalent homogenization method (She et al., 2017) implemented in VSOP (Teuchert et al., 1994) and PANGU (She et al., 2018; She et al., 2021) for treating the TRISO type fuel in high-temperature gas-cooled reactors.

Because the dispersed particles have a spatial self-shielding effect, the materials inside the particles cannot reflect the neutron absorption effect, and the direct use of the VHM will bring a certain degree of reactivity calculation deviation. It is necessary to study the size and influencing factors of the reactivity calculation deviation of the VHM and finally give the DH physical boundary of the dispersed particle system and point out when the VHM can be used for directly processing and when the DH of the system must be considered.

CALCULATION OBJECT

The Monte Carlo program RMC (Wang et al., 2013) developed by Tsinghua University is used to model the random distribution of dispersed particles. A schematic diagram of the random distribution of dispersed particles in the matrix is shown in **Figure 1**.

To analyze the spatial self-shielding effect of dispersed particles, a fuel cell is structured as the calculation model, and the main parameters of the fuel cell are shown in **Table 1**.

First, the fuel particles with different enrichments, volume fractions, and particle radii are dispersed in the zirconium matrix, and the calculation deviation of the VHM of the dispersed fuel is analyzed. Then, the burnable poison particles of different burnable poison types, particle sizes, and volume fractions are dispersed in the fuel matrix with different enrichments, and the calculation deviation of the VHM of the particle-dispersed burnable poisons is analyzed. The detailed calculation parameters are shown in **Table 2**.

It should be noted that the calculation deviation of VHM in this paper is the reactivity calculation deviation between the grain model and the VHM model of RMC, and the calculation deviation caused by different programs can be ignored. The grain model is performed by the dispersion particle calculation function in RMC, which can simulate the random distribution of dispersed particles. Also, the variance of the results obtained by RMC remains within 0.0003, which is equivalent to 30 pcm, to maintain the accuracy of the calculation results.

CALCULATION DEVIATION ANALYSIS OF VOLUMETRIC HOMOGENIZATION METHOD

Particle-Dispersed Fuel

To analyze the reactivity calculation deviation of VHM on particle-dispersed fuel, in this section, the calculation cases cover three influencing factors, which is the fuel volumetric fraction in the range of 3–30%, the fuel enrichment in the range of 10–90%, and the particle radius in the range of 100–400 μm. Although 3–10% of the fuel volumetric fraction is difficult to encounter in engineering, here is a regular study for

TABLE 2 | Parameters of particle-dispersed fuel and burnable poisons.

Parameters	Values
Types of burnable poisons	Ag/In/Cd/Hf/B_4C/Dy_2O_3/Er_2O_3/Eu_2O_3/Gd_2O_3
Radius of burnable poison particle, μm	10–250
Volumetric fraction of burnable poison particles, %	1–10
Type of fuel matrix	UO_2
Enrichment of fuel, %	10–90
Type of fuel particle	UO_2
Radius of fuel particle, μm	100–400
Volumetric fraction of fuel particles, %	3–30
Enrichment of fuel particle core, %	10–90
Matrix of dispersed particle system	Zr

considering extreme cases. The main calculation results are shown in **Figure 2**, in which E10–E90 indicates that the enrichment degree is 10–90%. Each figure shows the reactivity calculation deviation curve with particle size between the VHM and particle model of the Monte Carlo program under different fuel volumetric fractions and different fuel enrichment.

It can be seen from **Figure 2** that when the fuel volumetric fraction is 3 or 5%, if the dispersed particle radius is 100 μm, the calculation deviation of VHM will be greater than 100 pcm. Also, when the fuel volumetric fraction is 10%, even if the dispersed particle radius reaches 400 μm, the calculation deviation of the VHM is still less than 100 pcm. In addition, when the fuel volumetric fraction continues to increase to 20–30%, if the fuel enrichment is 90% and the radius of the dispersed particles is greater than 200 μm, the calculation deviation of VHM will be greater than 100 pcm.

If the radius of the dispersed particles is less than 100 μm and the fuel volumetric fraction is 10–30%, the calculation deviation of VHM will be less than 100 pcm, and there is no need to consider the DH. Also, if the radius of the dispersed particles is 250 μm, which is the typical size of the TRISO particle core, the fuel enrichment is higher than 20%, the calculation deviation of VHM will be greater than 100 pcm, and DH needs to be considered.

For dispersed UO_2 particles, the calculation deviation of VHM decreases with the increase of the volumetric fraction of the dispersed particles, and the calculation deviation is the smallest at approximately 10% of the volumetric fraction. Also, the calculation deviations of VHM will increase with the increase of the size of the dispersed particles and the fuel enrichment.

The volumetric fraction of the dispersed fuel particles affects the probability that the neutrons flying out of the fuel particles will encounter the fuel particles again in the matrix, which may affect the self-shielding effect. As the calculation deviation of the VHM does not change significantly in the range of 10–30%, the in-depth analysis of the influencing factors of the volumetric fraction will not be done here.

Particle-Dispersed Burnable Poison

To comprehensively analyze the size of the DH of the cells containing different particle-dispersed burnable poison materials, in this section, the calculation deviations of different types of burnable poison particle systems will be compared, and the factors of different matrix fuel enrichment and poison particle volumetric fraction will be considered. Also, then, the calculation deviation of VHM with the particle radius will be analyzed. The main results are shown in **Figure 3**, in which "E90%V1%" indicates that the matrix fuel enrichment is 90%, and the volumetric fraction of burnable poison is 1%.

From the calculation results in **Figure 3**, it can be seen that the self-shielding effect of the dispersed particles of different burnable poison materials is different due to the different absorption cross-sections. The horizontally comparing results of different burnable poison materials show that when the fuel enrichment is 90% and the dispersed burnable poison volumetric fraction is as small as 1%, the DH of the system is the smallest. To ensure that the calculation deviation of the VHM is still less than 100 pcm, the radius of the dispersed B_4C, Er_2O_3, Dy_2O_3, and Ag particles needs to be less than 20 μm. Therefore, in most cases of burnable poison particles, the calculation deviation of the VHM is relatively large, and its DH should be considered.

For different burnable poison materials, under the same particle size, particle volumetric fraction, and matrix fuel enrichment, the reactivity calculation deviation of the VHM is directly related to the absorption cross-section of the burnable poison. The larger the absorption cross-section, the stronger the self-shielding effect of the particles and the DH of the system, and the larger the deviation of the reactivity calculation of the VHM.

RELATION BETWEEN VOLUMETRIC HOMOGENIZATION METHOD DEVIATION AND OPTICAL LENGTH

Relation Between Self-Shielding of Single Particle and Optical Length

From the analysis of the self-shielding effect of the particle-dispersed fuel and burnable poisons, it can be seen that the calculation deviation of the reactivity of VHM is related to many factors. To obtain the judgment condition of whether the DH system can be processed by VHM, the material cross-section and particle size of the dispersed particles should be considered comprehensively to the optical length to judge whether the system needs to consider DH (Pogosbekyan and Han, 2007):

$$\left|\Sigma_{\text{matrix}} - \Sigma_{\text{particle}}\right| \cdot d_{\text{particle}} > \varepsilon \tag{1}$$

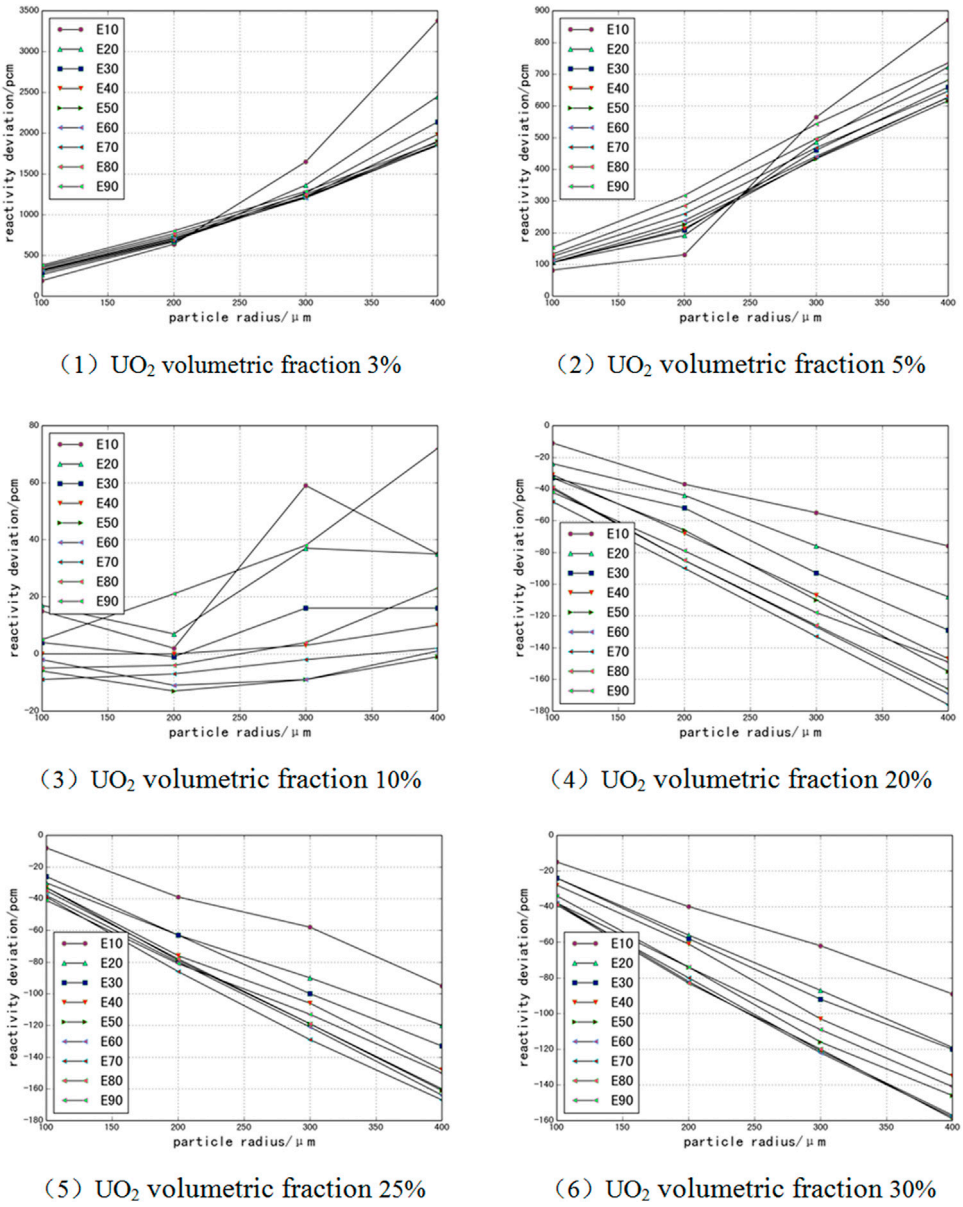

FIGURE 2 | Reactivity calculation deviation curve of different UO_2 volumetric fraction.

The formula Σ_{matrix} represents the macroscopic cross-section of the matrix material, and the unit is cm^{-1}. The formula Σ_{particle} represents the macroscopic cross-section of the particle material, and the unit is cm^{-1}. The formula d_{particle} represents the particle diameter, and the unit is cm. The formula ε represents the optical length limit, and it has no unit.

The physical meaning of **Eq. 1** is that when the material cross-section of the particle and the matrix differs to a certain degree, it will cause the flux difference between the materials. Also, when the particle size increases to a certain degree, the internal flux gradient inside the particle will also be caused by the space self-shielding effect. In addition, when the flux difference is greater than a certain level (10% is generally considered), the calculation deviation of VHM will not be negligible, and so, the general optical length limit of **Eq. 1** is 0.1. When the inequality relationship in **Eq. 1** holds, the DH effects of the system need to be considered.

Relation Between Self-Shielding of System and Optical Length

The calculation formula discussed earlier of the optical length only considers the effect between the matrix and a single particle and does not consider the influence of the mutual

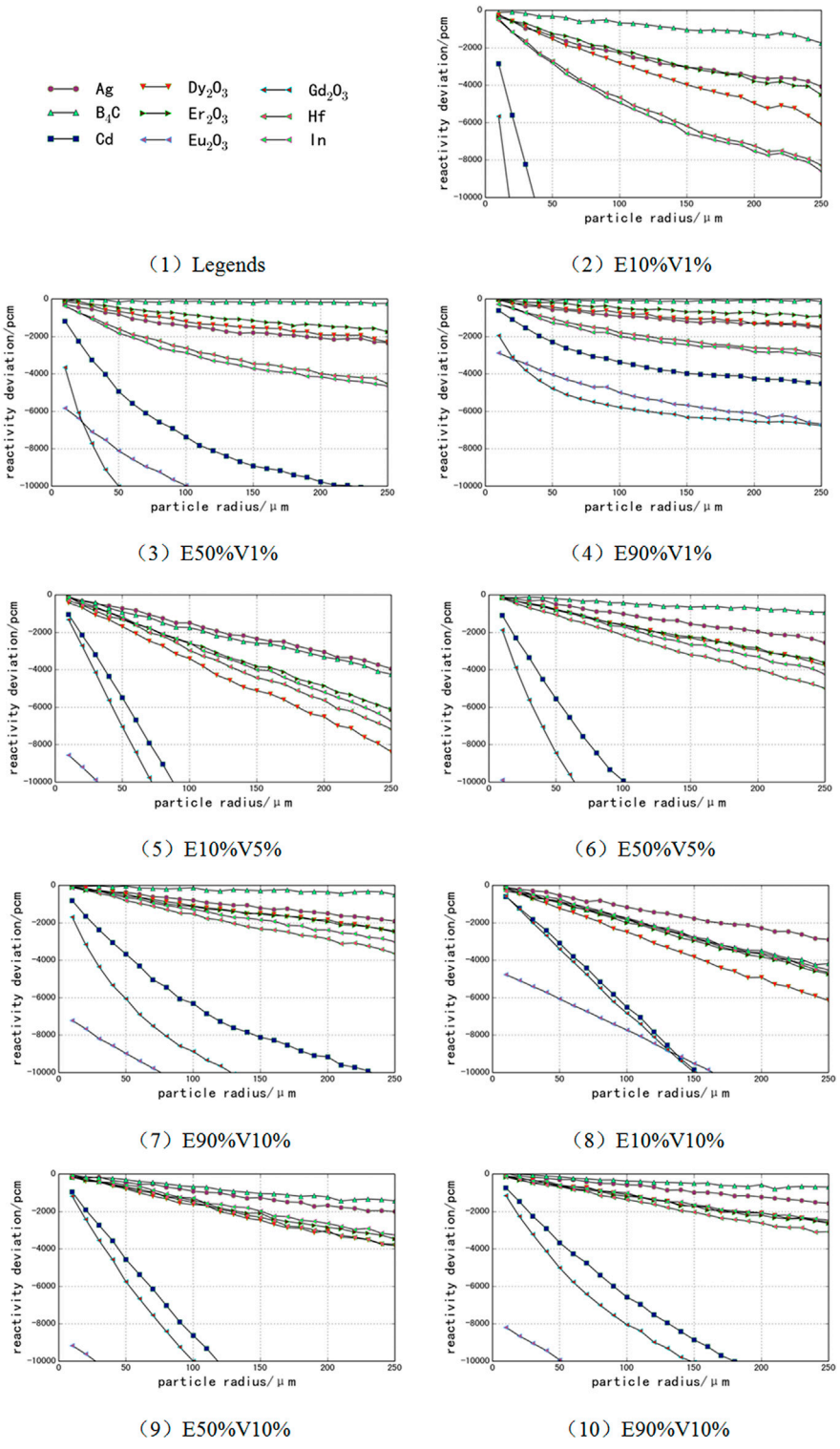

FIGURE 3 | Reactivity calculation deviation curve of different burnable poisons.

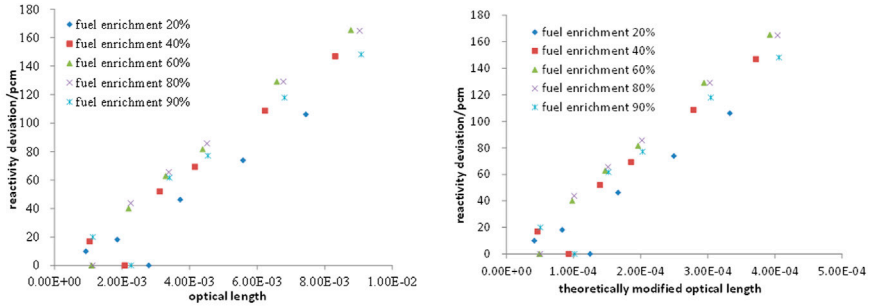

（1）Volumetric fraction of UO_2 particles 20%

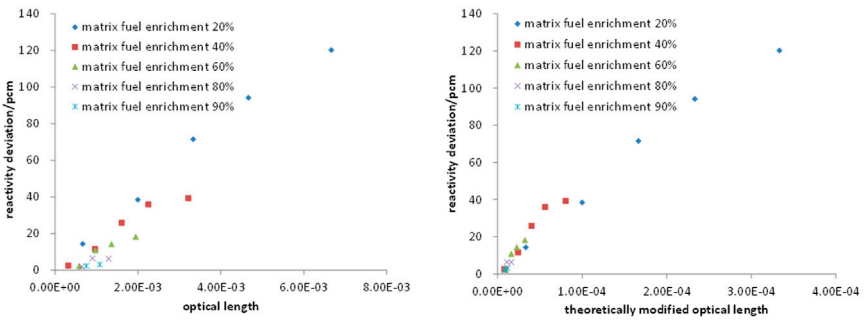

（2）Volumetric fraction of B_4C particles 1%

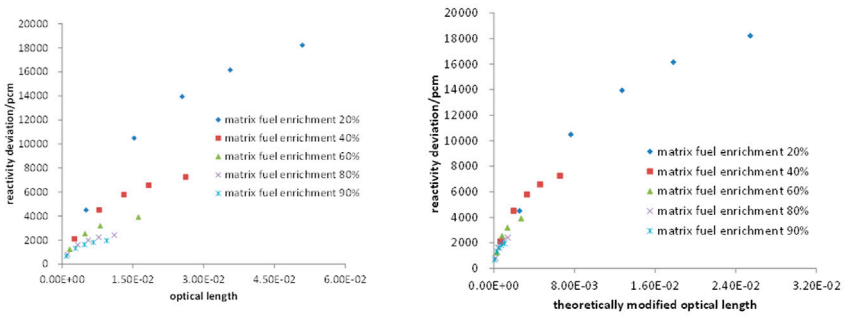

（3）Volumetric fraction of Gd_2O_3 particles 1%

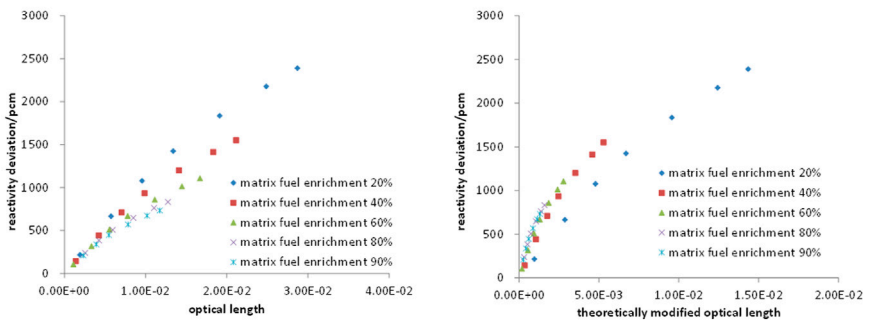

（4）Volumetric fraction of Hf particles 1%

FIGURE 4 | Relationship between reactivity deviation and optical length or theoretically modified optical length under different fuel enrichment of matrix.

shielding effect between the particles on the cross-section, especially the resonance interference effect between the particles. After analysis, **Eq. 1** can be revised as **Eq. 2**:

$$
\begin{aligned}
&|\Sigma_{\text{matrix}} - \Sigma_{\text{particle}}|\cdot d_{\text{particle}} \cdot \frac{\sqrt{V_{\text{particle}}}}{10} > \tilde{\varepsilon}, \text{UO}_2 \text{ fuel particle},\\
&|\Sigma_{\text{matrix}} - \Sigma_{\text{particle}}|\cdot d_{\text{particle}} \cdot \frac{\sqrt{V_{\text{particle}}}}{E_{\text{matrix}}} > \tilde{\varepsilon}, \text{ resonance particle such as } Gd_2O_3,\\
&|\Sigma_{\text{matrix}} - \Sigma_{\text{particle}}|\cdot d_{\text{particle}} \cdot \frac{\sqrt{V_{\text{particle}}}}{E_{\text{matrix}}} > \tilde{\varepsilon}, \text{ no resonance particle such as } B_4C.
\end{aligned}
\tag{2}
$$

The formula $\Sigma_{\text{matrix}}E_{\text{matrix}}$ represents the enrichment of the matrix fuel, without units and ranging from 0 to 1.0. The formula V_{particle} represents the volumetric fraction of dispersed particles, without units and ranging from 0 to 1.0. The formula $\tilde{\varepsilon}$ is the modified optical length limit, without units. Here, $\tilde{\varepsilon}$ and ε have similar physical significance, which are used to characterize the size of DH of the system, and some other items are added in the calculation formula $\tilde{\varepsilon}$, so the value of $\tilde{\varepsilon}$ should be determined by the new numerical calculation results. Also, based on numerical analysis, the result $\tilde{\varepsilon}$ should be 10^{-4}.

The theoretically modified optical length takes into account the volumetric fraction of dispersed particles and the enrichment of matrix fuel. For a specific cell, the larger the volumetric fraction of dispersed particles, the stronger the mutual shielding effect between particles, and so, the larger the theoretically modified optical length. For resonant nuclides, when the volumetric fraction of dispersed particles is large, the resonance interference effect between particles needs to be considered. Numerical fitting results show that the theoretically modified optical length is proportional to the square root of the volumetric fraction of dispersed particles for particles containing resonant nuclides, and the theoretically modified optical length is proportional to the volumetric fraction of dispersed particles for particles without resonant nuclides. Also, the theoretically modified optical length has an inverse relationship with the fuel enrichment of the matrix.

For a fuel cell, when the volumetric fraction of particles and the fuel enrichment of the matrix are determined, a very small particle size, such as the radius of 10 μm, can be used to calculate the material cross-section of the dispersed particles without self-shielding. Also, the cross-section of the matrix is less affected by the size of the dispersed particles and can be taken directly from the cross-section of the matrix when the particle size is 10 μm. At this time, the value on the left side of the **Eq. 2** is related to the size of the dispersed particles. When the size of the dispersed particles is greater than a certain value, the theoretically modified optical length calculated according to the **Eq. 2** is greater than the limit 10^{-4}, the calculation deviation of VHM will be greater than 100 pcm, and the DH of the system needs to be considered.

Numerical Results

For the DH system of dispersed particles and burnable poisons described in this article, the relationship between the reactivity calculation deviation of VHM and the optical length or the theoretically modified optical length at different fuel enrichment and the fixed volumetric fraction of dispersed particles is shown in **Figure 4**, Also, then, the relationship between the reactivity calculation deviation of VHM and the optical length or the theoretically modified optical length under a different volumetric fraction of dispersed particles and the fixed matrix fuel enrichment is shown in **Figure 5**. Finally, the relationship between the calculation deviation of VHM and the theoretically modified optical length changes with the matrix fuel enrichment and the volumetric fraction of the dispersed particle is shown in **Figure 6**.

It can be seen from **Figure 4** that after fixing the volumetric fraction of the dispersed particles, while changing the size of the dispersed particles, the reactivity calculation deviation of VHM and the theoretically modified optical length are almost linear at different enrichment of UO_2 fuel particles or fuel matrix. The larger the theoretically modified optical length, the larger the calculation deviation of VHM. The use of theoretically modified optical length can reflect the law of different matrix enrichment better than optical length.

It can be seen from **Figure 5** that after fixing the fuel enrichment, while changing the volumetric fraction of the dispersed fuel particles or burnable poisons, and changing the dispersed particle size at the same time, the reactivity calculation deviation of VHM and the theoretically modified optical length is also almost linear, except for the case where the fuel phase volume is less than 10%. The larger the theoretically modified optical length, the greater the reactivity calculation deviation of VHM. Because the fuel volumetric fraction of less than 10% rarely occurs, we will not analyze it in detail here. The use of theoretically modified optical length can reflect the law of different volumetric fractions of particles better than optical length.

It can be seen from **Figure 6** that the relationship between the reactivity calculation deviation of VHM and the theoretically modified optical length are almost linear when the influence factors of fuel enrichment, particle phase volume, and particle size change. The greater the theoretically modified optical length, the larger the calculation deviation of VHM. When the theoretically modified optical length is 10^{-4}, the cell reactivity calculation deviation of VHM is about 100 pcm.

CONCLUSION

In this paper, by analyzing the reactivity calculation deviation of VHM on particle-dispersed fuel and burnable poisons and its influencing factors, the type of dispersed particles, the type of matrix, the particle size, and other factors are integrated into the optical length, and further research is carried out to integrate the enrichment of fuel matrix and particles, the volumetric fraction of the dispersed particles, and the size of dispersed particles are into the physical quantity of the theoretically modified optical length, and the judgment methods of the particle-dispersed fuel and burnable poisons are integrated into a calculation formula, and the intuitive physical boundary of whether the DH system needs to be considered is given. For particle-dispersed fuel and burnable

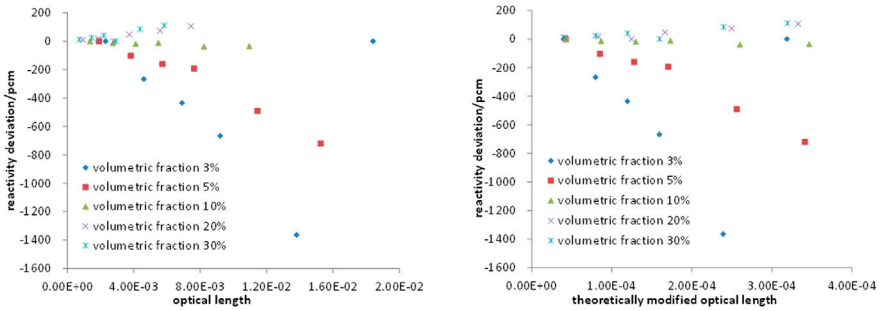

（1）Fuel enrichment of dispersed UO_2 particles 20%

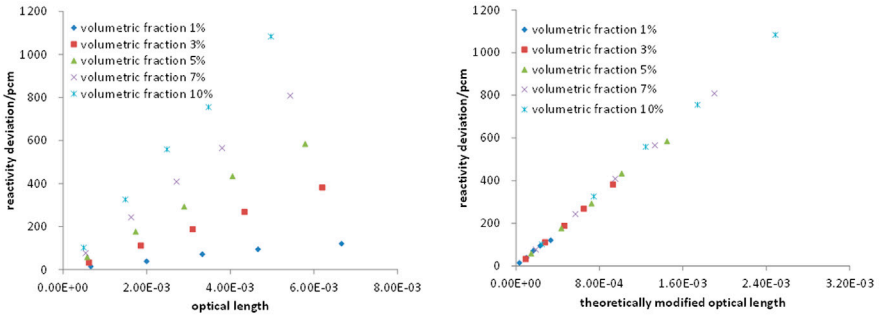

（2）B_4C particles dispersed in matrix fuel enrichment 20%

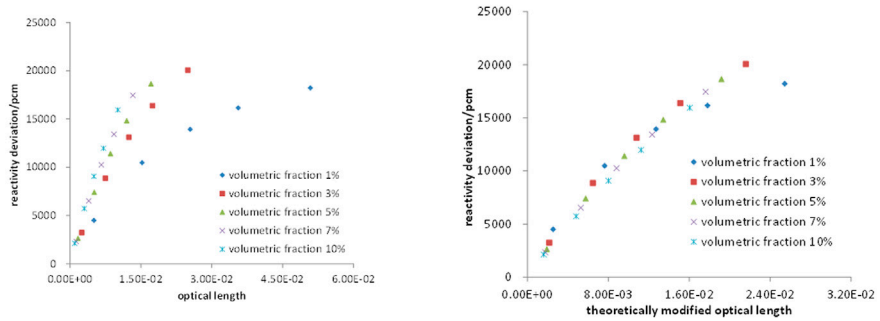

（3）Gd_2O_3 particles dispersed in matrix fuel enrichment 20%

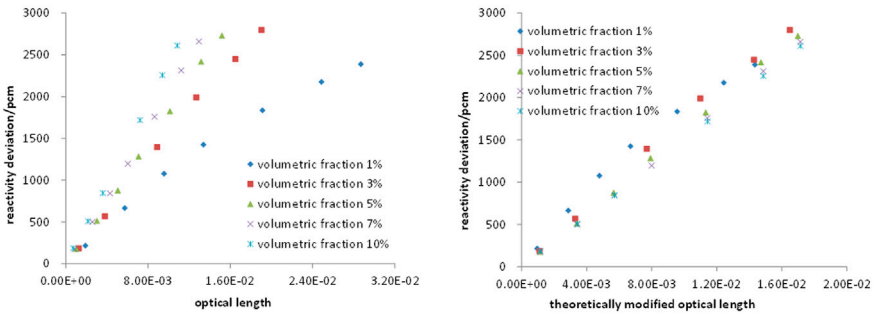

（4）Hf particles dispersed in matrix fuel enrichment 20%

FIGURE 5 | Relationship between reactivity deviation and optical length or theoretically modified optical length under different volumetric fraction of particles.

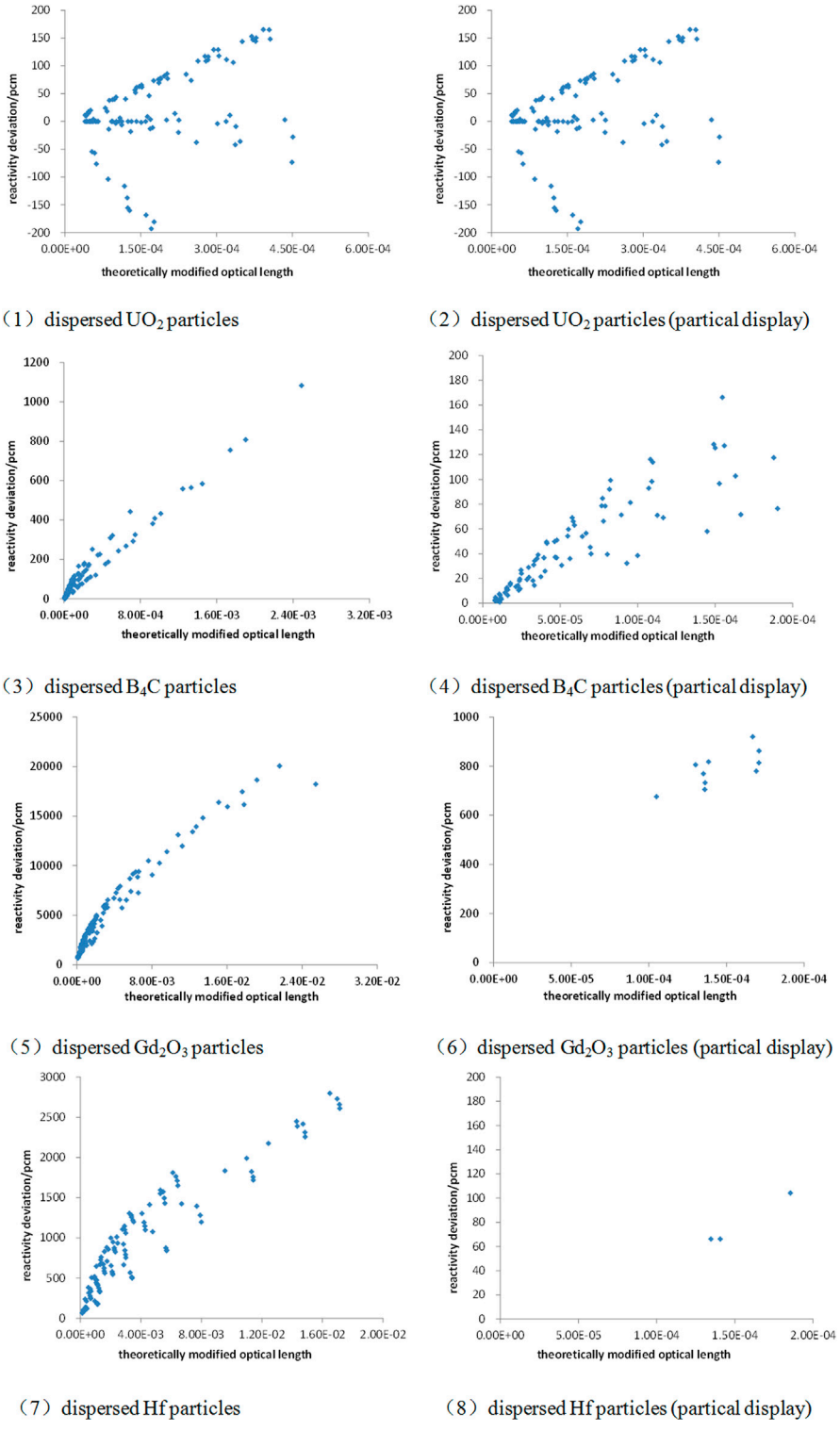

FIGURE 6 | Relationship between reactivity deviation and optical length or theoretically modified optical length.

poison systems in FCM fuel loaded in pressurized water reactor, if the theoretically modified optical length is greater than 10^{-4}, the reactivity calculation deviation of VHM will be greater than 100 pcm, and a DH calculation program needs to be used to consider the DH of the dispersed particles and the matrix in the system.

DATA AVAILABILITY STATEMENT

The raw data supporting the conclusion of this article will be made available by the authors without undue reservation.

AUTHOR CONTRIBUTIONS

LL: conceptualization, methodology, and software. CX: conceptualization. YD: conceptualization. WL: conceptualization. LM: visualization and investigation. CL: visualization and investigation. LX: visualization and investigation. ZH: visualization and investigation. LS: visualization and investigation. TX: funding acquisition and supervision. ZN: funding acquisition and supervision.

FUNDING

This work is supported by the National Natural Science Foundation of China (approved no: 1170051016).

REFERENCES

Cole, G., and Maldonado, I. (2013). A Neutronic Investigation of the Use of Fully Ceramic Microencapsulated Fuel for Pu/Np Burning in PWRs [J]. *Fuel Cycle Management*. doi:10.13182/NT13-75

Hébert, A. (1993). A Collision Probability Analysis of the Double-Heterogeneity Problem. *Nucl. Sci. Eng.* 115 (2), 177–184. doi:10.13182/nse115-177

Kim, Y., Kim, K., and Noh, J. (2005). *Reactivity-Equivalent Physical Transformation for Homogenization of Double-Heterogeneous Fuels [C]*. Busan, Korea: Transactions of Korean Nuclear Society Autumn Meeting.

Kloosterman, J. L. (2003). Application of Boron and Gadolinium Burnable Poison Particles in UO2 and PUO2 Fuels in HTRs. *Ann. Nucl. Energ.* 30, 1807–1819. doi:10.1016/s0306-4549(03)00134-8

Kurt, A. T. (2012). Microencapsulated Fuel Technology for Commercial Light Water and Advanced Reactor Application. *Journals Nucl. Mater.* 427, 209–224. doi:10.1016/j.jnucmat.2012.05.021

Lei, L., and Dong, Y. (2020). A Novel Reactivity-Equivalent Physical Transformation Method for Homogenization of Double-Heterogeneous Systems. *Ann. Nucl. Energ.* 142, 107396. doi:10.1080/00295639.2016.1272363

Li, J., She, D., and Shi, L. (2018). An Improved Reactivity-Equivalent Physical Transformation for Treating FCM Fuel with Burnable Poisons. *Ann. Nucl. Energ.* 121 (11), 577–581. doi:10.1016/j.anucene.2018.08.024

Pogosbekyan, L., and Han, G. (2007). *Implementation of the Sanchez-Pomraning Double Heterogeneity Treatment Method in DeCART, Reactor Physics Laboratory*.Seoul: Seoul National University.

Sanchez, R., and Pomraning, G. C. (1991). A Statistical Analysis of the Double Heterogeneity Problem. *Ann. Nucl. Energ.* 18 (7), 371–395. doi:10.1016/0306-4549(91)90073-7

She, D., Guo, J., and Liu, Z. (2018). PANGU Code for Pebble-Bed HTGR Reactor Physics and Fuel Cycle Simulations[J]. *Ann. Nucl. Energ.* 126, 48–58. doi:10.1016/j.anucene.2018.11.005

She, D., Xia, B., and Guo, J. (2021). Prediction Calculations for the First Criticality of the HTR-PM Using the PANGU Code[J]. *Nucl. Sci. Tech.* 32 (9), 1–7. doi:10.1007/s41365-021-00936-5

She, D., Liu, Z., and Shi, L. (2017). An Equivalent Homogenization Method for Treating the Stochastic media. *Nucl. Sci. Eng.* 185, 351–360. doi:10.1080/00295639.2016.1272363

Talamo, A. (2006). Effects of the Burnable Poison Heterogeneity on the Long Term Control of Excess of Reactivity. *Ann. Nucl. Energ.* 33, 794–803. doi:10.1016/j.anucene.2006.04.009

Teuchert, E., Haas, K. A., Rütten, H. J., Brockmann, H., Gerwin, H., Ohlig, U., et al. (1994). *V.S.O.P. (94) Computer Code System for Reactor Physics and Fuel Cycle Simulation*. Jülich, Germany: Forschungszentrum Jülich

van Dam, H. (2000a). Long-Term Control of Excess Reactivity by Burnable Particles. *Ann. Nucl. Energ.* 27, 733–743. doi:10.1016/s0306-4549(00)82014-9

van Dam, H. (2000b). Long-Term Control of Excess Reactivity by Burnable Poison in Reflector Regions. *Ann. Nucl. Energ.* 27, 63–69. doi:10.1016/s0306-4549(00)82005-8

Wang, K., Li, Z. G., and She, D. (2013). *RMC-A Monte Carlo Code for Reactor Physics analysisJoint International Conference on Supercomputing in Nuclear Applications and Monte Carlo*. Paris: France.

Xiang, Dai., Cao, X., Yu, S., and Zhu, C. (2014). Conceptual Core Design of an Innovative Small PWR Utilizing Fully Ceramic Microencapsulated Fuel. *J. Prog. Nucl. Energ.* 75, 63–71. doi:10.1016/j.pnucene.2014.04.010

Zhai, T., Kadak, A. C., and No, H. C. (2004). LOCA and Air Ingress Accident Analysis of a Pebble Bed Reactor, MIT Center for Advanced Nuclear Energy Systems [J]. *MIT-ANP-TR-102*.

Zhang, T., Yin, H., Li, X., She, D., Pan, Q., He, D., et al. (2021). Studies on calculation models of ASTRA critical facility benchmark using OpenMC. *Ann. Nucl. Energy* 158, 108291. doi:10.1016/j.anucene.2021.108291

Zhang, T., Wang, Y., Lewis, E. E., Smith, M. A., Yang, W. S., and Wu, H. (2017a). A Three-Dimensional Variational Nodal Method for Pin-resolved Neutron Transport Analysis of Pressurized Water Reactors. *Nucl. Sci. Eng.* 188 (2), 160–174. doi:10.1080/00295639.2017.1350002

Zhang, T., Lewis, E. E., Smith, M. A., Yang, W. S., and Wu, H. (2017b). A Variational Nodal Approach to 2D/1D Pin Resolved Neutron Transport for Pressurized Water Reactors. *Nucl. Sci. Eng.* 186, 120–133. doi:10.1080/00295639.2016.1273023

Conflict of Interest: The authors declare that the research was conducted in the absence of any commercial or financial relationships that could be construed as a potential conflict of interest.

Publisher's Note: All claims expressed in this article are solely those of the authors and do not necessarily represent those of their affiliated organizations or those of the publisher, the editors, and the reviewers. Any product that may be evaluated in this article, or claim that may be made by its manufacturer, is not guaranteed or endorsed by the publisher.

frontiers | Frontiers in Energy Research

BRIEF RESEARCH REPORT
published: 31 May 2022
doi: 10.3389/fenrg.2022.836363

A Stable Condition and Adaptive Diffusion Coefficients for the Coarse-Mesh Finite Difference Method

Zhitao Xu[1]*, *Hongchun Wu*[2], *Youqi Zheng*[2] and *Qian Zhang*[3]

[1]School of Electric Power, North China University of Water Resources and Electric Power, Zhengzhou, China, [2]School of Nuclear Science and Technology, Xi'an Jiaotong University, Xi'an, China, [3]School of Physics, Zhejiang University, Hangzhou, China

Coarse-mesh finite difference (CMFD) method is a widely used numerical acceleration method. However, the stability of CMFD method is not good for the problems with optically thick regions. In this paper, a stability rule named the "sign preservation rule" in the field of numerical heat transfer is extended to the scheme of CMFD. It is required that the disturbance of neutron current is positively correlated with that of the negative value of flux gradient. A necessary condition for stability of the CMFD method is derived, an adaptive diffusion coefficient equation is proposed to improve the stability of CMFD method, and the corresponding revised CMFD method is called the rCMFD method. With a few modifications of the code, the rCMFD method was implemented in the hexagonal-Z nodal S_N (discrete-ordinates) solver in the NECP-SARAX code system. The rCMFD method and other similar acceleration methods were tested by three fast reactor problems which were obtained by modifying the hexagonal pitches of a benchmark problem. The numerical results indicated that the rCMFD method showed better stability than the traditional CMFD method and the artificially diffusive CMFD (adCMFD) method and a better convergence rate than the adCMFD method and the optimally diffusive CMFD (odCMFD) method for these fast reactor problems.

Keywords: stable condition, adaptive diffusion coefficients, rCMFD, acceleration method, stability, IFDF, nodal SN method

OPEN ACCESS

Edited by:
Shoaib Usman,
Missouri University of Science and Technology, United States

Reviewed by:
Tengfei Zhang,
Shanghai Jiao Tong University, China
Jiankai Yu,
Massachusetts Institute of Technology, United States
Zhipeng Li,
Institute of Applied Physics and Computational Mathematics (IAPCM), China

***Correspondence:**
Zhitao Xu
xuzhitao@ncwu.edu.cn

Specialty section:
This article was submitted to Nuclear Energy, a section of the journal Frontiers in Energy Research

Received: *15 December 2021*
Accepted: *25 April 2022*
Published: *31 May 2022*

Citation:
Xu Z, Wu H, Zheng Y and Zhang Q (2022) A Stable Condition and Adaptive Diffusion Coefficients for the Coarse-Mesh Finite Difference Method. Front. Energy Res. 10:836363. doi: 10.3389/fenrg.2022.836363

1 INTRODUCTION

The convergence rate (Kuzmin, 2010) of the source iteration (SI) (Adams and Larsen, 2002; Li et al., 2015b) is often low when solving the reactor neutron transport problem. Many acceleration methods (Adams and Larsen, 2002; Willert et al., 2014) have been developed to accelerate the iteration process, such as the extrapolation methods, the Krylov subspace methods, and the high-order/low-order (HOLO) methods which are usually found to be the most efficient (Kuzmin, 2010; Willert et al., 2014). Here, the HOLO methods refer to a series of acceleration methods with the same internal logic that employs proper coupling between high-order discretization and low-order discretization to obtain high-order accuracy and high convergence rate, such as the multigrid method (Wesseling, 1995), the partitioned-matrix (PM) method (Li et al., 2015b), the diffusion synthetic acceleration (DSA) method (Alcouffe, 1977), the coarse-mesh finite difference (CMFD) method (Smith, 2002), and so on (Adams and Larsen, 2002; Zhang, et al., 2018). Among them, the CMFD method and other similar methods which employ the neutron diffusion approximation for the low-order discretization

are widely used in solving the reactor neutron transport problem (Smith, 2002; Lee et al., 2014; Zhang et al., 2019; Xu et al., 2020; Hao et al., 2021; Chan and Xiao, 2021; Zhao et al., 2022; Zhou et al., 2022) in recent years. However, the traditional CMFD method tends to fail due to iterative divergence for reactors with optically thick regions.

By reducing the coarse mesh size of the diffusion problem, increasing the number of transport sweeps, and adding over relaxation factors (Li et al., 2015a; Jarrett et al., 2016), the stability (Kuzmin, 2010) of CMFD can be improved to a certain extent. Compared with the traditional CMFD method, the pCMFD method and its variants (Yuk and Cho, 2017; Zhang et al., 2019) have improved stability by using partial neutron currents to calculate the coupling factors between high-order discretization and low-order discretization. The artificially diffusive CMFD (adCMFD) (Jarrett et al., 2016) and the optimally diffusive CMFD (odCMFD) (Zhu et al., 2016) can also improve the stability of the traditional CMFD method by improving the diffusion coefficients. The lpCMFD (Wang and Xiao, 2018; Wang and Zhu, 2021) method improves the stability of CMFD by flux prolongation. Some analyses of the variants of CMFD are available (Zhu, et al., 2017; Wang and Zhu, 2021). The IFDF (Xu, et al., 2020; Xu, et al., 2022) method adopts a coupling scheme different from the CMFD method and adaptively adjusts the diffusion coefficients during the iterative process, which was found to have better stability than the CMFD and adCMFD.

A stability principle, sign preservation rule (Tao, 2001) also known as the positive coefficients rule (Patankar, 1980), is required to obtain a stable discrete scheme in the field of numerical heat transfer. Its connotation is that the positive disturbance introduced at any grid should have a positive impact on other grids, which is physically reasonable. Considering the CMFD method, we found that the traditional CMFD equation could not physically reflect the response relationship between neutron currents and neutron fluxes, which was believed to be at least one main reason that causes the divergence of the iterative acceleration process.

In this paper, the condition for diffusion coefficients at the mesh surface is derived to keep the positive correlation between the neutron current and the negative values of the flux gradient by observing the sign preservation rule, the adaptive diffusion coefficient equation for the CMFD method is proposed, and the traditional CMFD method is revised as the rCMFD method. The theoretical derivation is presented in **Section 2**, the numerical results of different acceleration methods for three fast reactor problems obtained by modifying the hexagonal pitches of a small fast reactor benchmark problem are presented in **Section 3**, and the discussion and conclusion of this work are presented in **Section 4**.

2 THEORETICAL DERIVATION

2.1 Source Iteration

For high-order discretization, the discrete orders of spatial and angular dimensions of the neutron transport equation are high enough to give high accuracy. Taking the S_N method based on hexagonal-Z meshes as an example, the k-eigenvalue problem can be written as

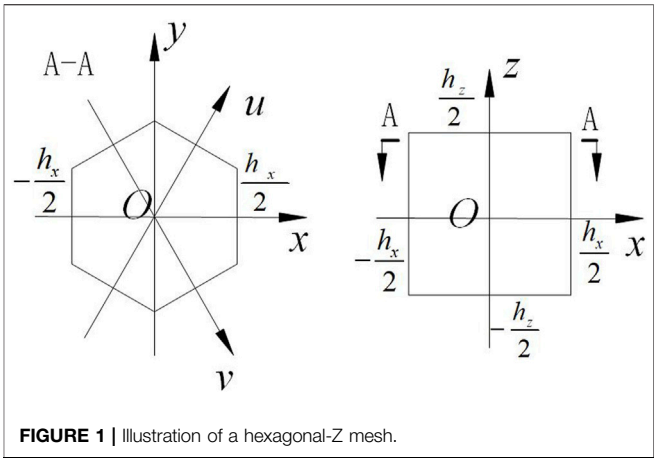

FIGURE 1 | Illustration of a hexagonal-Z mesh.

$$\boldsymbol{L\psi} = \boldsymbol{S\phi} + \frac{\mathbf{1}}{\boldsymbol{k}}\boldsymbol{F\phi}, \tag{1}$$

where L is the neutron leakage matrix, ψ is the angular flux vector of every energy group, every spatial moment, and every discrete angle, S is the neutron scattering matrix, ϕ is the scalar flux vector, k is the eigenvalue, and F is the neutron fission matrix. The scalar flux vector could be calculated by the angular flux vector with

$$\boldsymbol{\phi} = \boldsymbol{T\psi}, \tag{2}$$

where T is a matrix to calculate the scalar flux vector ϕ with the angular flux vector ψ. **Eqs 1**, **2** constitute the k-eigenvalue equations with high-order discretization, which could be solved by the classical power iteration also known as fission SI for the reactor problem:

$$\boldsymbol{\psi}^{(n)} = \frac{\mathbf{1}}{\boldsymbol{k}^{(n-1)}}(\boldsymbol{L} - \boldsymbol{ST})^{-1}\boldsymbol{F\phi}^{(n-1)}, \tag{3}$$

$$\boldsymbol{\phi}^{(n)} = \boldsymbol{T\psi}^{(n)}, \tag{4}$$

$$k^{(n)} = k^{(n-1)}\frac{\langle \boldsymbol{F\phi}^{(n)} \rangle}{\langle \boldsymbol{F\phi}^{(n-1)} \rangle}, \tag{5}$$

where the superscript (n) or (n-1) is the iteration index and the symbol $\langle\ \rangle$ means integration over the phase space with the energy, angular, and spatial dimensions. The dimension of the matrix $(L - ST)$ is usually very large, and its inverse is usually not conducted by direct matrix operation but achieved by transport sweeps of every mesh, angle, and energy group for the S_N method.

2.2 Traditional Coarse-Mesh Finite Difference Method

The stability of source iteration is good, but the convergence rate is usually low especially for large reactor problems. The CMFD acceleration method is commonly used in the solution of the S_N k-eigenvalue problem. In the process of source iteration, the k-eigenvalue problem of transport corrected finite difference diffusion equation (low-order discretization) is solved to correct the high-order iterative variables.

For a hexagonal-Z mesh as illustrated in **Figure 1**, the low-order neutron balance equation for every group to be solved can be written as

$$\sum_{d=v,x,u,z}\left(J_{K_d+1/2}-J_{K_d-1/2}\right)A_{K_d}+\Sigma_{r,K}\phi_K V_K=Q_K V_K, \quad (6)$$

where d is the dimension index with the possible values of v, x, u, z as illustrated in **Figure 1**, $J_{K_d\pm1/2}$ is the normal neutron current at the mesh surface indexed by $K_d \pm 1/2$, A_{K_d} is the surface area of mesh K along dimension d, $\Sigma_{r,K}$ is the removal cross section of mesh K, ϕ_K is the scalar neutron flux of mesh K, V_K is the volume of mesh K, and Q_K is the neutron source of mesh K including the fission source and scattering source from other groups.

For the CMFD method, the neutron currents and neutron fluxes in **Eq. 6** are related by the transport corrected Fick's law. For an inner mesh surface,

$$J_{K_d+1/2}=-\frac{D_{K_d+1/2}}{h_{K_d+1/2}}\left(\phi_{K_d+1}-\phi_K\right)-\frac{r_{K_d+1/2}}{h_{K_d+1/2}}\left(\phi_{K_d+1}+\phi_K\right), \quad (7)$$

where

$$D_{K_d+1/2}=\frac{2D_K D_{K_d+1}h_{K_d+1/2}}{h_{K_d}D_{K_d+1}+h_{K_d+1}D_K}, \quad (8)$$

$$r_{K_d+1/2}=-\frac{h_{K_d+1/2}J^{SN}_{K_d+1/2}+D_{K_d+1/2}\left(\phi^{SN}_{K_d+1}-\phi^{SN}_K\right)}{\phi^{SN}_{K_d+1}+\phi^{SN}_K}, \quad (9)$$

$$h_{K_d+1/2}=\frac{1}{2}\left(h_{K_d}+h_{K_d+1}\right), \quad (10)$$

where $D_{K_d+1/2}$ is the common diffusion coefficient at the mesh surface, $r_{K_d+1/2}$ is the transport correction factor, h is the mesh size, and the superscript SN means the value is from the high-order transport calculation. For the boundary cases, take the mesh surface in the positive coordinate direction of mesh K as an example:

$$J_{K_d+1/2}=\frac{D_{K_d+1/2}}{h_{K_d+1/2}}\phi_K-\frac{r_{K_d+1/2}}{h_{K_d+1/2}}\phi_K, \quad (11)$$

where

$$D_{K_d+1/2}=\frac{2D_K\alpha_{K_d+1/2}h_{K_d}}{\alpha_{K_d+1/2}h_{K_d}+2D_K}, \quad (12)$$

$$r_{K_d+1/2}=-\frac{h_{K_d+1/2}J^{SN}_{K_d+1/2}-D_{K_d+1/2}\phi^{SN}_K}{\phi^{SN}_K}, \quad (13)$$

in which $\alpha_{K_d+1/2}$ is the boundary parameter and equals 0 for the reflective boundary condition and 0.5 for the vacuum boundary condition.

Eqs 6–13 and the boundary equations for other cases constitute the coarse-mesh finite difference equations and can be solved with a linear solver for every group. Then, the low-order k-eigenvalue problem could be solved by source iteration or other more efficient algorithms. Details of the solution algorithm for the linear system with low-order discretization are not to be introduced here for simplicity. Finally, the iterative variables including k and scalar fluxes from high-order discretization are to be corrected:

$$k=k^{DIF}, \quad (14)$$

$$\phi_{i,K}=\phi^{SN}_{i,K}\frac{\phi^{DIF}_K}{\phi^{SN}_{0,K}}, i\geq 0, \quad (15)$$

where the superscript DIF means the value is the solution of the diffusion problem and the subscript i is the expansion order of the spatial moment for the nodal S_N method.

2.3 A Stable Condition and Adaptive Diffusion Coefficients

The convergence rate of the CMFD method is usually high. However, the stability of the CMFD method is a problem for the transport problem with optically thick regions. Let us check the CMFD equations from the stability rule in the field of numerical heat transfer. For an inner mesh surface, the traditional Fick's law without transport correction can be written as follows:

$$J_{K_d+1/2}h_{K_d+1/2}=-\phi_{K_d+1}D_{K_d+1/2}+\phi_K D_{K_d+1/2}. \quad (16)$$

It is seen that the mesh-surface diffusion coefficient $D_{K_d+1/2}$ is always positive from **Eq. 8**, which means that $J_{K_d+1/2}$ will always decrease when ϕ_{K_d+1} increases and always increase when ϕ_K increases. This phenomenon obeys the physical law of diffusion and should be established in the transport corrected cases. Let us check the case of CMFD by rewriting **Eq. 7** for inner mesh surfaces as follows:

$$J_{K_d+1/2}h_{K_d+1/2}=-\phi_{K_d+1}\left(D_{K_d+1/2}+r_{K_d+1/2}\right)+\phi_K\left(D_{K_d+1/2}-r_{K_d+1/2}\right). \quad (17)$$

From **Eqs 8**, **9** it is seen that the coefficient $(D_{K_d+1/2}+r_{K_d+1/2})$ of ϕ_{K_d+1} and the coefficient $(D_{K_d+1/2}-r_{K_d+1/2})$ of ϕ_K are not guaranteed to be always positive, which means that the physical law of diffusion could not be guaranteed. So, the following conditions are required:

$$D_{K_d+1/2}+r_{K_d+1/2}>0, \quad (18)$$

and

$$D_{K_d+1/2}-r_{K_d+1/2}>0. \quad (19)$$

After substituting **Eq. 9** into **Eqs 18**, **19**, the condition becomes

$$D_{K_d+1/2}>\frac{h_{K_d+1/2}}{2}\max\left(-\frac{J^{SN}_{K_d+1/2}}{\phi^{SN}_{K_d+1}},\frac{J^{SN}_{K_d+1/2}}{\phi^{SN}_K}\right). \quad (20)$$

Then, let us check **Eq. 11** for the boundary cases; the following condition is obtained with similar derivation to the case of inner mesh surfaces:

$$J^{SN}_{K_d+1/2}>0. \quad (21)$$

This condition is always met for the vacuum boundary condition. For the reflective boundary condition, nothing is required to meet the diffusion law since $J_{K_d+1/2}\equiv 0$. If the boundary surface is in the negative coordinate direction of mesh K, the response condition between the mesh-surface current and the mesh flux is also always met. All in all, only the condition of **Eq. 20** of the inner mesh surface is necessary.

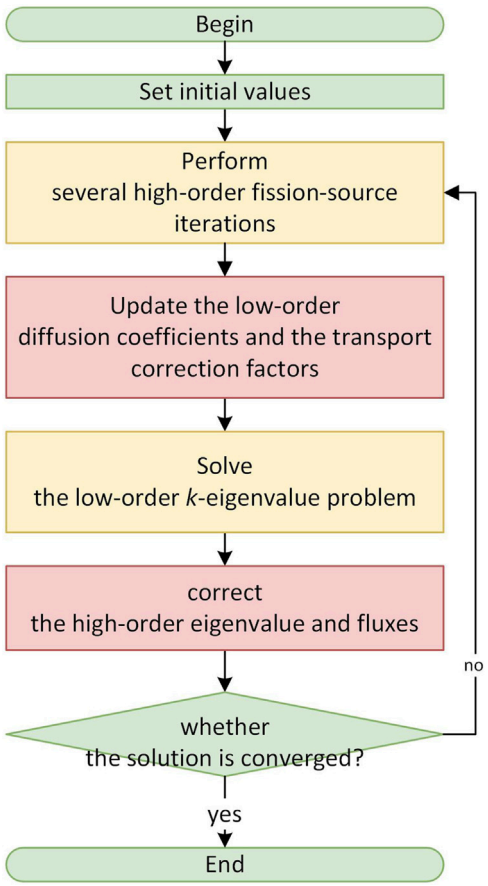

FIGURE 2 | Flowchart of the rCMFD acceleration method.

An interesting thing was found that **Eq. 20** was very similar to the stability equation of the IFDF method (Xu et al., 2020; Xu et al., 2022) which had been found to be more stable than the traditional CMFD method and the adCMFD method for a large fast reactor core. For one-dimensional (1D) meshes, the stability condition of the IFDF method is

$$D_K > \frac{h_K}{2}\max\left(-\frac{J^{SN}_{K_d-1/2}}{\phi^{SN}_K}, \frac{J^{SN}_{K_d+1/2}}{\phi^{SN}_K}\right). \tag{22}$$

The difference is in the subscripts, and the condition for the diffusion coefficient at the mesh surface becomes the condition for the diffusion coefficient in the mesh.

In order to guarantee the condition in **Eq. 20**, **Eq. (8)** is modified to the following equation of adaptive diffusion coefficient:

$$D_{K_d+1/2} = \max\left[\frac{2D_K D_{K_d+1}h_{K_d+1/2}}{h_{K_d}D_{K_d+1} + h_{K_d+1}D_K}, \frac{ch_{K_d+1/2}}{2}\right.$$
$$\left.\max\left(-\frac{J^{SN}_{K_d+1/2}}{\phi^{SN}_{K_d+1}}, \frac{J^{SN}_{K_d+1/2}}{\phi^{SN}_K}\right)\right], \tag{23}$$

where c is an additional damping parameter which should be larger than 1. With c larger than 1, **Eq. 23** gives a conservative condition to satisfy **Eq. 20**, and a larger value of c tends to increase the stability but decrease the convergence rate from our numerical tests. A value of 5 is recommended for c referring to the IFDF method and will be employed in the numerical tests of next section. When **Eq. 20** is met, the traditional mesh-surface diffusion coefficient in **Eq. 8** is employed to guarantee diagonal dominance of the low-order linear system, which will improve the solution speed of the low-order linear system; when **Eq. 20** is not met, **Eq. 23** will adaptively abandon **Eq. 8** and employ a more conservative mesh-surface diffusion coefficient equation in **Eq. 23** to meet the stable condition of **Eq. 20**.

Employing **Eq. 23**, the traditional CMFD method is improved to the revised CMFD (rCMFD) method. Few changes are needed to modify a CMFD acceleration process to an rCMFD acceleration process. What we should do is to replace **Eq. 8** with **Eq. 23** and update the mesh-surface diffusion coefficients before solving the low-order k-eigenvalue problem. The process of the rCMFD method is illustrated in **Figure 2**.

3 NUMERICAL RESULTS

3.1 Description of the Tests

Three fast reactor core problems were employed to test the methods. The first one (core 1) is a small fast reactor benchmark problem with hexagonal assemblies (Takeda and Ikeda, 1991). The hexagonal pitches are 12.9904 cm, and the total height of the model is 190 cm. Four-group cross sections are provided by the benchmark for different regions of the core. The case of half-inserted control rods is employed. The radial layout of the core is presented in **Figure 3**. The second one (core 2) and the third one (core 3) are obtained by changing the hexagonal pitches of core 1 to 50 and 100 cm, respectively, which may be not very rational for reactor design but helpful to test the convergence of numerical methods for problems with optically thick meshes.

The three problems have been calculated by the DNTH (Wang et al., 2020) solver in the NECP-SARAX (Zheng et al., 2018) code system with different methods including pure fission-source iteration (SI), fission-source iteration with CMFD acceleration (SI-CMFD), fission-source iteration with adCMFD (η = 1/4) acceleration (SI-adCMFD), fission-source iteration with odCMFD acceleration (SI-odCMFD), fission-source iteration with IFDF acceleration (SI-IFDF), and fission-source iteration with rCMFD acceleration (SI-rCMFD). The NECP-SARAX code system is a code system developed at Xi'an Jiaotong University for the neutronics analysis of advanced fast-spectrum reactors or facilities. The DNTH solver is an S_N nodal transport solver in NECP-SARAX for hexagonal-Z meshes with the capacity of large-scale parallel computing.

For all the cases, S_4 Legendre–Chebyshev angular quadrature was used; the number of hexagonal-Z meshes was 169 × 33; the nodal interior variables were expanded with second-order polynomials; the nodal surface variables were expanded with first-order polynomials; the fission-source iteration criterion of high-order discretization was 1×10^{-5}; the scattering-source iteration criterion of high-order

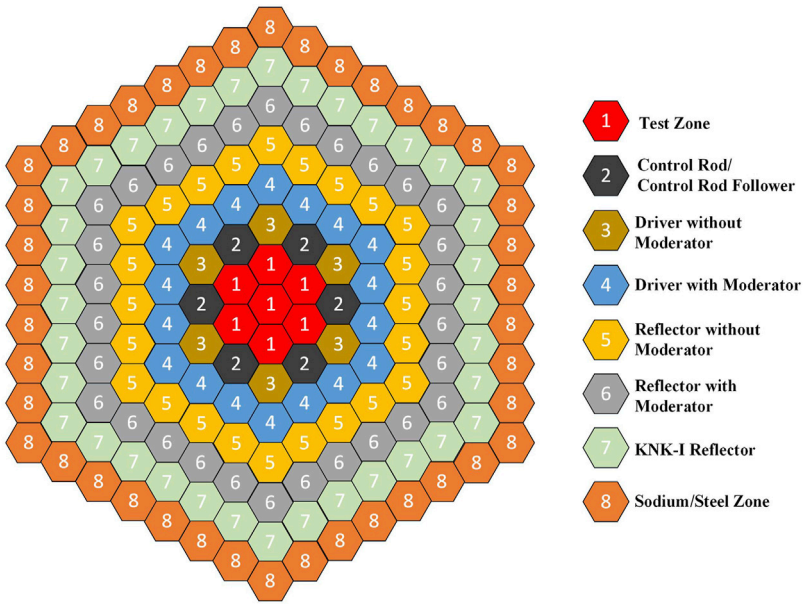

FIGURE 3 | Radial layout of the small fast reactor core.

TABLE 1 | Numerical results of the tests for different methods.

Item		SI	SI-CMFD	SI-adCMFD	SI-odCMFD	SI-IFDF	SI-rCMFD
Core (12.9904 cm pitches)	k_{eff}	0.98362	0.98368	0.98361	0.98363	0.98368	0.98368
	CPU time (s)	49	18	25	20	18	18
	Fission iteration count	81	29	43	37	29	29
	Transport sweep count	1480	518	687	586	523	518
	Speedup	1.0	2.7	2.0	2.5	2.7	2.7
Core 2 (50 cm pitches)	k_{eff}	1.48319	Divergent	Divergent	1.48310	1.48308	1.48311
	CPU time (s)	157			69	58	64
	Fission iteration count	253			101	90	98
	Transport sweep count	4922			1971	1736	1895
	Speedup	1.0			2.3	2.7	2.5
Core 3 (100 cm pitches)	k_{eff}	1.64874	Divergent	Divergent	Divergent	1.64843	Divergent
	CPU time (s)	240				121	
	Fission iteration count	383				177	
	Transport sweep count	7500				3453	
	Speedup	1.0				2.0	

discretization was 5×10^{-6}; an iteration limit of 5 was employed for the inner scattering-source iteration; the fission-source iteration criterion of low-order discretization was 2.5×10^{-6}; one low-order linear system was solved before four high-order fission-source iterations were performed. All the calculations were performed on 2.0 GHz AMD Ryzen PRO 2500U w CPU core.

3.2 Results for Different Cases

The results for the three reactor cores are presented in **Table 1**. In the table, one transport sweep means one update of all the mesh angular fluxes within one group, which is the main part of the time-consuming calculations, and the speedups are obtained by comparing the CPU time of every method with that of the SI scheme.

As shown in **Table 1**, for core 1, the radial hexagonal pitches were 12.9904 cm, and every method could give a convergent result; there were some deviations between the k_{eff} of different methods, which was caused by the different convergence degrees of the inner scattering-source iteration; the speedup of SI-rCMFD was 2.7, which was higher than those of adCMFD and odCMFD and close to those of SI-CMFD and SI-IFDF. For core 2, the radial hexagonal pitches were 50 cm, SI-CMFD and SI-adCMFD failed to converge, while SI, SI-odCMFD, SI-IFDF, and SI-rCMFD proposed in this work still could give convergent results; the speedup of SI-rCMFD for core 2 was 2.5, which was a bit lower than 2.7 of SI-IFDF but higher than 2.3 of odCMFD. For core 3, the radial hexagonal pitches were 100 cm, SI-rCMFD also failed to converge, and only SI and SI-IFDF could give convergent results.

4 DISCUSSION AND CONCLUSION

After numerical tests of three fast reactor problems with different radial hexagonal pitches from 12.9904 to 100 cm by different acceleration methods, the advantages and limitations of the proposed rCMFD method were clarified. It was seen that the adaptive diffusion coefficients of this work were helpful to improve the stability of the traditional CMFD method without obvious loss of the convergence rate, and the improvement was even higher than those of the adCMFD method and the odCMFD method which had been found to be more stable than the traditional CMFD method. However, the rCMFD method failed for the third core with radial hexagonal pitches of 100 cm, while the IFDF method still could give a convergent result with a speedup of 2.0, which indicated that the rCMFD was still not unconditionally stable and the stable region was narrower than that of the IFDF method although the adaptive diffusion coefficient equations were similar for the rCMFD and IFDF. The inferiority of the rCMFD method compared with the IFDF method may be due to the fact that Fick's law correction formula of the IFDF method is derived from the interface discontinuity relationship with clear physical significance, but Fick's law correction formula of rCMFD is based on a heuristic hypothesis as the traditional CMFD method.

It is concluded that the stable condition derived in this work is necessary for the CMFD stability but perhaps not sufficient for unconditional stability, and the adaptive diffusion coefficients can effectively improve the stability of the traditional CMFD method without obvious loss of the convergence rate. Further research on spectral radius analysis of the rCMFD method and comparison between different methods is expected, which may enlighten sufficient stable conditions or higher improvements of the CMFD method.

DATA AVAILABILITY STATEMENT

The original contributions presented in the study are included in the article/supplementary material, and further inquiries can be directed to the corresponding author.

AUTHOR CONTRIBUTIONS

ZX performed the methods and presented the results. HW supervised the work. YZ and QZ were advisers.

ACKNOWLEDGMENTS

This study was inspired by Professor Wenquan Tao's lecture on numerical heat transfer at Xi'an Jiaotong University. And we are very grateful to the reviewers for their helpful suggestions on this article.

REFERENCES

Adams, M. L., and Larsen, E. W. (2002). Fast Iterative Methods for Discrete-Ordinates Particle Transport Calculations. *Prog. Nucl. energy* 40 (1), 3–159. doi:10.1016/S0149-1970(01)00023-3

Alcouffe, R. E. (1977). Diffusion Synthetic Acceleration Methods for the Diamond-Differenced Discrete-Ordinates Equations. *Nucl. Sci. Eng.* 64 (2), 344–355. doi:10.13182/NSE77-1

Chan, Y., and Xiao, S. (2021). Numerical Stability Analysis of Lp-CMFD Acceleration for the Discrete Ordinates Neutron Transport Calculation Discretized with Discontinuous Galerkin Finite Element Method. *Ann. Nucl. Energy* 153, 108036. doi:10.1016/j.anucene.2020.108036

Hao, C., Liu, L., Kang, L., and Xu, Y. (2021). An Efficient Hybrid Multi-Level CMFD in Space and Energy for Accelerating the High-Fidelity Neutron Transport Calculation. *Ann. Nucl. Energy* 161, 108446. doi:10.1016/j.anucene.2021.108446

Jarrett, M., Kochunas, B., Zhu, A., and Downar, T. (2016). Analysis of Stabilization Techniques for CMFD Acceleration of Neutron Transport Problems. *Nucl. Sci. Eng.* 184 (2), 208–227. doi:10.13182/NSE16-51

Kuzmin, D. (2010). *A Guide to Numerical Methods for Transport Equations*. Erlangen, Germany: Friedrich–Alexander University Erlangen–Nürnberg.

Lee, M. J., Joo, H. G., Lee, D., and Smith, K. (2014). Coarse Mesh Finite Difference Formulation for Accelerated Monte Carlo Eigenvalue Calculation. *Ann. Nucl. Energy* 65, 101–113. doi:10.1016/j.anucene.2013.10.025

Li, L. L., Smith, K. S., and Forget, B. (2015a). *Techniques for Stabilizing Coarse-Mesh Finite Difference (CMFD) in Methods of Characteristics (MOC)*. Nashville, TN: ANS M&C2015.

Li, Y., Wang, Y., Liang, B., and Shen, W. (2015b). Partitioned-matrix Acceleration to the Fission-Source Iteration of the Variational Nodal Method. *Prog. Nucl. Energy* 85, 640–647. doi:10.1016/j.pnucene.2015.08.001

Patankar, S. V. (1980). *Numerical Heat Transfer and Fluid Flow*. Boca Raton, FL: CRC Press.

Smith, K. S. (2002). *Full-core, 2-D, LWR Core Calculations with CASMO-4E*. Seoul, Korea: PHYSOR 2002.

Takeda, T., and Ikeda, H. (1991). 3-D Neutron Transport Benchmarks. *J. Nucl. Sci. Technol.* 28 (7), 656–669. doi:10.1080/18811248.1991.9731408

Tao, W. (2001). *Numerical Heat Transfer*. Xi'an, China: Xi'an Jiaotong University Publishing Company.

Wang, D., and Xiao, S. (2018). A Linear Prolongation Approach to Stabilizing CMFD. *Nucl. Sci. Eng.* 190 (1), 45–55. doi:10.1080/00295639.2017.1417347

Wang, D., and Zhu, Z. (2021). A Revisit to CMFD Schemes: Fourier Analysis and Enhancement. *Energies* 14 (2), 424. doi:10.3390/en14020424

Wang, Y., Xu, Z., Zheng, Y., and Wu, H. (2020). A New Hexagonal-Z Nodal SN Method in SARAX Code System. *Ann. Nucl. Energy* 144, 107546. doi:10.1016/j.anucene.2020.107546

Wesseling, P. (1995). *Introduction to Multigrid Methods (No. NASA-CR-195045)*. Hampton, VA: NASA Langley Research Center.

Willert, J., Park, H., and Knoll, D. A. (2014). A Comparison of Acceleration Methods for Solving the Neutron Transport K -eigenvalue Problem. *J. Comput. Phys.* 274, 681–694. doi:10.1016/j.jcp.2014.06.044

Xu, Z., Zheng, Y., Wang, Y., and Wu, H. (2020). IFDF Acceleration Method with Adaptive Diffusion Coefficients for SN Nodal Calculation in SARAX Code System. *Ann. Nucl. Energy* 136, 107056. doi:10.1016/j.anucene.2019.107056

Xu, Z., Zheng, Y., and Wu, H. (2022). An IFDF Accelerated Parallel Nodal SN Method for XYZ Geometry in SARAX Code System. *Ann. Nucl. Energy* 166, 108710. doi:10.1016/j.anucene.2021.108710

Yuk, S., and Cho, N. Z. (2017). Two-level Convergence Speedup Schemes for P-CMFD Acceleration in Neutron Transport Calculation. *Nucl. Sci. Eng.* 188 (1), 1–14. doi:10.1080/00295639.2017.1332891

Zhang, G., Hsieh, A., Yang, W. S., and Jung, Y. S. (2019). Consistent pCMFD Acceleration Schemes of the Three-Dimensional Transport Code PROTEUS-MOC. *Nucl. Sci. Eng.* 193, 828–853. doi:10.1080/00295639.2018.1560854

Zhang, T., Wu, H., Cao, L., and Li, Y. (2018). Acceleration of 3D Pin-By-Pin Calculations Based on the Heterogeneous Variational Nodal

Method. *Ann. Nucl. Energy* 114, 165–174. doi:10.1016/j.anucene.2017.12.012

Zhao, W., Chai, X., Zhang, B., Liu, J., Peng, X., Li, T., et al. (2022). A Nodal Method Based on CMFD for Pin-By-Pin SP3 Calculation. *Ann. Nucl. Energy* 167, 108849. doi:10.1016/j.anucene.2021.108849

Zheng, Y., Du, X., Xu, Z., Zhou, S., Liu, Y., Wan, C., et al. (2018). SARAX: A New Code for Fast Reactor Analysis Part I: Methods. *Nucl. Eng. Des.* 340, 421–430. doi:10.1016/j.nucengdes.2018.10.008

Zhou, X., Liu, Z., Cao, L., and Wu, H. (2022). Convergence Analysis for the CMFD Accelerated 2D/1D Neutron Transport Calculation Method Based on Fourier Analysis. *Ann. Nucl. Energy* 170, 108982. doi:10.1016/j.anucene.2022.108982

Zhu, A., Jarrett, M., Xu, Y., Kochunas, B., Larsen, E., and Downar, T. (2016). An Optimally Diffusive Coarse Mesh Finite Difference Method to Accelerate Neutron Transport Calculations. *Ann. Nucl. Energy* 95, 116–124. doi:10.1016/j.anucene.2016.05.004

Zhu, A., Kochunas, B., Xu, Y., Jarrett, M., Larsen, E., and Downar, T. (2017). Theoretical Convergence Rate Lower Bounds for Variants of Coarse Mesh Finite Difference to Accelerate Neutron Transport Calculations. *Nucl. Sci. Eng.* 186 (3), 224–238. doi:10.1080/00295639.2017.1293408

Conflict of Interest: The authors declare that the research was conducted in the absence of any commercial or financial relationships that could be construed as a potential conflict of interest.

The reviewer TZ is currently organizing a research topic with the author QZ.

Advantages of publishing in Frontiers

OPEN ACCESS
Articles are free to read for greatest visibility and readership

FAST PUBLICATION
Around 90 days from submission to decision

HIGH QUALITY PEER-REVIEW
Rigorous, collaborative, and constructive peer-review

TRANSPARENT PEER-REVIEW
Editors and reviewers acknowledged by name on published articles

Frontiers
Avenue du Tribunal-Fédéral 34
1005 Lausanne | Switzerland

Visit us: www.frontiersin.org
Contact us: frontiersin.org/about/contact

REPRODUCIBILITY OF RESEARCH
Support open data and methods to enhance research reproducibility

DIGITAL PUBLISHING
Articles designed for optimal readership across devices

FOLLOW US
@frontiersin

IMPACT METRICS
Advanced article metrics track visibility across digital media

EXTENSIVE PROMOTION
Marketing and promotion of impactful research

LOOP RESEARCH NETWORK
Our network increases your article's readership